THE ROLE OF NON-STOICHIOMETRY IN THE FUNCTIONAL PROPERTIES OF OXIDE MATERIALS

EDITED BY: Maria Veronica Ganduglia-Pirovano, Javier Carrasco and Claudio Cazorla

PUBLISHED IN: Frontiers in Chemistry and Frontiers in Physics

frontiers Research Topics

ISSN 1664-8714
ISBN 978-2-88963-155-1
DOI 10.3389/978-2-88963-155-1

About Frontiers

Frontiers is more than just an open-access publisher of scholarly articles: it is a pioneering approach to the world of academia, radically improving the way scholarly research is managed. The grand vision of Frontiers is a world where all people have an equal opportunity to seek, share and generate knowledge. Frontiers provides immediate and permanent online open access to all its publications, but this alone is not enough to realize our grand goals.

Frontiers Journal Series

The Frontiers Journal Series is a multi-tier and interdisciplinary set of open-access, online journals, promising a paradigm shift from the current review, selection and dissemination processes in academic publishing. All Frontiers journals are driven by researchers for researchers; therefore, they constitute a service to the scholarly community. At the same time, the Frontiers Journal Series operates on a revolutionary invention, the tiered publishing system, initially addressing specific communities of scholars, and gradually climbing up to broader public understanding, thus serving the interests of the lay society, too.

Dedication to Quality

Each Frontiers article is a landmark of the highest quality, thanks to genuinely collaborative interactions between authors and review editors, who include some of the world's best academicians. Research must be certified by peers before entering a stream of knowledge that may eventually reach the public - and shape society; therefore, Frontiers only applies the most rigorous and unbiased reviews.
Frontiers revolutionizes research publishing by freely delivering the most outstanding research, evaluated with no bias from both the academic and social point of view. By applying the most advanced information technologies, Frontiers is catapulting scholarly publishing into a new generation.

What are Frontiers Research Topics?

Frontiers Research Topics are very popular trademarks of the Frontiers Journals Series: they are collections of at least ten articles, all centered on a particular subject. With their unique mix of varied contributions from Original Research to Review Articles, Frontiers Research Topics unify the most influential researchers, the latest key findings and historical advances in a hot research area! Find out more on how to host your own Frontiers Research Topic or contribute to one as an author by contacting the Frontiers Editorial Office: researchtopics@frontiersin.org

THE ROLE OF NON-STOICHIOMETRY IN THE FUNCTIONAL PROPERTIES OF OXIDE MATERIALS

Topic Editors:
Maria Veronica Ganduglia-Pirovano, Institute of Catalysis and Petrochemistry (ICP-CSIC), Spain
Javier Carrasco, CIC Energigune, Spain
Claudio Cazorla, UNSW Sydney, Australia

Citation: Ganduglia-Pirovano, M. V., Carrasco, J., Cazorla, C., eds. (2019). The Role of Non-Stoichiometry in the Functional Properties of Oxide Materials. Lausanne: Frontiers Media SA. doi: 10.3389/978-2-88963-155-1

Table of Contents

frontiers in Chemistry

EDITORIAL
published: 08 August 2019
doi: 10.3389/fchem.2019.00547

Editorial: The Role of Non-stoichiometry in the Functional Properties of Oxide Materials

Claudio Cazorla[1]*, *Maria Verónica Ganduglia-Pirovano*[2] *and Javier Carrasco*[3]

[1] School of Materials Science and Engineering, University of New South Wales, Sydney, NSW, Australia, [2] Institute of Catalysis and Petrochemistry-CSIC, Madrid, Spain, [3] CIC Energigune, Vitoria-Gasteiz, Spain

Keywords: oxide materials, density functional theory, experiments, oxygen vacancies, functionality

Editorial on the Research Topic

The Role of Non-stoichiometry in the Functional Properties of Oxide Materials

Oxides can show a plethora of emergent complex phenomena beyond their traditional role as dielectrics, which makes them attractive materials to a very broad range of scientific and technological processes. This includes areas such as catalysis, energy conversion and storage, and magnetism, to name just a few. Furthermore, nano-engineered oxides offer the possibility of realizing hitherto unobserved phenomena as due to their unique responsiveness to external stimuli, multiple order-parameter couplings, and increased volume-to-surface ratio. Yet, controlled synthesis and thorough microscopic understanding of functional oxide materials remain challenging. This is a complex task to accomplish due to the ubiquitous stoichiometry fluctuations found in oxides, which affect considerably their structural, chemical, and magnetic properties (Venkatesan et al., 2004; Herklotz et al., 2017).

Non-stoichiometry is indeed a pivotal facet of the functioning of oxide materials. For instance, the presence of oxygen vacancies in oxide-based heterogeneous catalysts is often necessary for any activity (Campbell and Peden, 2005; Jeen et al., 2013). Oxygen vacancies can also distort significantly the equilibrium arrangement of atoms and modify the super-exchange interactions between neighboring magnetic ions, thus inducing spin-order transformations (Wang et al., 2003; Eerenstein et al., 2005). Furthermore, extrinsic vacancies enable ionic conductivity in perovskite-based solid solutions to be used in electrochemical applications such as solid oxide fuel and electrolytic cells (Adler, 2004; Chroneos et al., 2011). Engineering of chemical defects in oxide compounds, therefore, emerges as a likely avenue for the design of new materials with tailored functionality. In this Research Topic, we present a collection of original articles that highlight how state-of-the-art theoretical and experimental approaches are leading to a better atomic-level understanding of non-stoichiometric oxide systems and improved design of novel functional materials.

From a theoretical viewpoint, the accurate description of the electronic structure of non-stoichiometric oxides of technological interest is not an easy task and requires efficient and robust theory (Ganduglia-Pirovano et al., 2007). Martínez-Casado et al. thoroughly analyze this issue for defective anatase surfaces and conclude that all-electron-based hybrid density functionals are required to yield accurate trends in the position of band gap states of defects and adsorbates in large model systems. Furthermore, Poli et al. efficiently combine non-local density functional theory (DFT) and linear-response time-dependent DFT to enable the interpretation of recent experimental

Edited and reviewed by:
Bretislav Friedrich,
Fritz-Haber-Institut, Germany

****Correspondence:***
Claudio Cazorla
c.cazorla@unsw.edu.au

Specialty section:
This article was submitted to Physical Chemistry and Chemical Physics,
a section of the journal Frontiers in Chemistry

Received: *17 June 2019*
Accepted: *18 July 2019*
Published: *08 August 2019*

Citation:
Cazorla C, Ganduglia-Pirovano MV and Carrasco J (2019) Editorial: The Role of Non-stoichiometry in the Functional Properties of Oxide Materials. Front. Chem. 7:547. doi: 10.3389/fchem.2019.00547

UV-vis spectra for cation-vacancy defects in aluminosilicate imogolite nanotubes, considering large supercells of around 1,000 atoms.

Research on non-stoichiometric oxide materials is typically focused on bulk and extended surfaces. Generally, the interaction of oxygen vacancies in such materials is poorly understood. Gao et al. address the mechanisms of aggregation of oxygen vacancies in SiO_2 and HfO_2 theoretically and suggest that electron trapping at oxygen vacancies may facilitate the creation of new neighboring vacancies and that this process becomes even more efficient with increasing vacancy cluster size. This finding is particularly relevant for improving the performance of such materials in applications where, for example, electrons can be injected via tunneling from an electrode in a device. At non-stoichiometric oxide surfaces, the structure and dynamics of the near-surface oxygen vacancies and excess charges are most relevant for technological applications such as catalysis. Wolf et al. address the heavily discussed appearance and properties of anionic defects at the (111)-oriented CeO_2 ceria surface in scanning tunneling microscopy (STM) images, and Han et al. investigate the effect of applied stress on the relative stability of isolated surface and subsurface oxygen vacancies at the same surface, the formation of vacancy pairs, and the localization of the excess charge. Noticeably, at moderate compressive strains the formation of first-neighbor surface oxygen vacancy pairs is energetically preferred over that of isolated vacancies, contrary to what it is predicted at null strain. Yet, little is known about nanosize effects on oxygen vacancy formation. This salient aspect of current materials design is theoretically explored by Cuko et al. considering as a case study titania, silica, and mixed $Ti_xSi_{1-x}O_2$ nanoclusters. Interestingly, the authors show that, in contrast to the results obtained for the bulk and for surfaces, silica nanoclusters are more reducible than titania, thus disclosing an unexpected chemical behavior at the nanoscale. Moreover, Rhatigan and Nolan model hydroxylated titania surfaces modified with dispersed Mn_4O_x nanoclusters and reveal important changes in light absorption and reactivity toward water splitting as a consequence of the formation of nanocluster-surface interactions that influence the system electronic structure. Furthermore, Kim et al. consider the effect that agglomeration of CeO_2 nanoparticles have on the stability and oxygen vacancy formation energy, applying a computational protocol based on a multiscale simulation approach. Surprisingly, for a possible {100}/{100} interface of two agglomerated $Ce_{40}O_{80}$ truncated octahedral, the energy cost to create an oxygen vacancy is negative, indicating that under reducing conditions, oxygen removal from the interface will have a stabilizing effect.

The structural changes of oxide surfaces during redox processes are essential to understanding their properties in many applications. Schöttner et al. track the evolution of the hematite a-Fe_2O_3(0001) surface under reducing conditions by polarization-resolved infrared reflection absorption spectroscopy (IRRAS) using CO as a probe molecule. Not only the formation of oxygen vacancies is observed, but a massive reconstruction yielding the formation of Fe_3O_4(111) domains. Such findings cannot be ignored when thinking about the surface chemistry of iron oxide surfaces. Furthermore, Luches et al. focus on the dynamics of the interaction between ceria epitaxial islands and films on Pt (111) during reduction and oxidation, and observe different reduced structural phases that include the formation of a Ce-Pt alloy. These results are most relevant for the understanding of Pt/CeO_2 catalysts, which can be used for low-temperature CO oxidation, as discussed by Kardash et al., who investigate Pt/CeO_x and Pt/$CeSnO_x$ systems by means of a synergistic approach that combines experiment and theory. It is found that the Sn-doping promotes oxygen removal and increases catalytic activity. The effect of catalyst doping is also considered by Alvarez-Galvan et al., who address the production of synthesis gas from methane over Rh-doped Ni-based catalysts, supported on Al_2O_3, CeO_2, La_2O_3, MgO, and ZrO_2. This is an important process for converting natural gas into added value high-quality liquid products. However, current catalysis methods for achieving partial oxidation of methane are energy-intensive and hence more energy-efficient alternatives to produce synthesis gas are highly desirable. It is found that Ni/CeO_2 catalyst shows the best behavior per surface area and that small amount of Rh improves the catalytic performance.

We believe that the Role of Non-stoichiometry in the Functional Properties of Oxide Materials Research Topic provides recent insights into our ongoing quest for rationalizing the intriguing phenomena observed in non-stoichiometric oxide systems and how this can affect their functionality, with special focus on energy harvesting applications.

AUTHOR CONTRIBUTIONS

All authors listed have made a substantial, direct and intellectual contribution to the work, and approved it for publication.

REFERENCES

Adler, S. B. (2004). Factors governing oxygen reduction in solid oxide fuel cell cathodes. *Chem. Rev.* 104, 4791–4844. doi: 10.1021/cr020724o

Campbell, C. T., and Peden, C. H. F. (2005). Oxygen vacancies and catalysis on ceria surfaces. *Science* 309, 713–714. doi: 10.1126/science.1113955

Chroneos, A., Yildiz, B., Tarancon, A., Parfitt, D., and Kilner, J. A. (2011). Oxygen diffusion in solid oxide fuel cell cathode and electrolyte materials: mechanistic insights from atomistic simulations. *Energy Environ. Sci.* 4, 2774–2789. doi: 10.1039/c0ee00717j

Eerenstein, W., Morrison, F. D., Dho, J., Blamire, M. G., Scott, J. F., and Mathur, N. D. (2005). Comment on "Epitaxial $BiFeO_3$ multiferroic thin film heterostructures". *Science* 307:1203. doi: 10.1126/science.1105422

Ganduglia-Pirovano, M. V., Hofmann, A., and Sauer, J. (2007). Oxygen vacancies in transition metal and rare earth oxides: current state of understanding and remaining challenges. *Surf. Sci. Rep.* 62, 219–270. doi: 10.1016/j.surfrep.2007.03.002

Herklotz, A., Lee, D., Guo, E.-J., Meyer, T. L., Petrie, J. R., and Lee, H. N. (2017). Strain coupling of oxygen non-stoichiometry in perovskite thin films. *J. Phys.* 29:493001. doi: 10.1088/1361-648x/aa949b

Jeen, H., Bi, Z., Choi, W. S., Chisholm, M. F., Bridges, C. A., Paranthaman, M. P., et al. (2013). Orienting oxygen vacancies for fast catalytic reaction. *Adv. Mater.* 25, 6459–6463. doi: 10.1002/adma.201302919

Venkatesan, M., Fitzgerald, C. B., and Coey, J. M. D. (2004). Unexpected magnetism in a dielectric oxide. *Nature* 430:630. doi: 10.1038/430630a

Wang, J., Neaton, J. B., Zheng, H., Nagarajan, V., Ogale, S. B., Liu, B., et al. (2003). Epitaxial $BiFeO_3$ multiferroic thin film heterostructures. *Science* 299, 1719–1722. doi: 10.1126/science.1080615

Conflict of Interest Statement: The authors declare that the research was conducted in the absence of any commercial or financial relationships that could be construed as a potential conflict of interest.

frontiers
in Chemistry

ORIGINAL RESEARCH
published: 25 June 2019
doi: 10.3389/fchem.2019.00451

Structural Evolution of α-Fe_2O_3(0001) Surfaces Under Reduction Conditions Monitored by Infrared Spectroscopy

Ludger Schöttner, Alexei Nefedov, Chengwu Yang, Stefan Heissler, Yuemin Wang* and Christof Wöll*

Institute of Functional Interfaces (IFG), Karlsruhe Institute of Technology, Karlsruhe, Germany

OPEN ACCESS

Edited by:
Maria Veronica Ganduglia-Pirovano,
Institute of Catalysis and Petrochemistry (ICP), Spain

Reviewed by:
Shamil Shaikhutdinov,
Fritz-Haber-Institut, Germany
Oscar Rodríguez De La Fuente,
Complutense University of Madrid, Spain
Geoff Thornton,
University College London, United Kingdom

****Correspondence:***
Yuemin Wang
yuemin.wang@kit.edu
Christof Wöll
christof.woell@kit.edu

Specialty section:
This article was submitted to Physical Chemistry and Chemical Physics,
a section of the journal Frontiers in Chemistry

Received: *01 March 2019*
Accepted: *05 June 2019*
Published: *25 June 2019*

Citation:
Schöttner L, Nefedov A, Yang C, Heissler S, Wang Y and Wöll C (2019) Structural Evolution of α-Fe_2O_3(0001) Surfaces Under Reduction Conditions Monitored by Infrared Spectroscopy. Front. Chem. 7:451. doi: 10.3389/fchem.2019.00451

The precise determination of the surface structure of iron oxides (hematite and magnetite) is a vital prerequisite to understand their unique chemical and physical properties under different conditions. Here, the atomic structure evolution of the hematite (0001) surface under reducing conditions was tracked by polarization-resolved infrared reflection absorption spectroscopy (IRRAS) using carbon monoxide (CO) as a probe molecule. The frequency and intensity of the CO stretch vibration is extremely sensitive to the valence state and electronic environments of surface iron cations. Our comprehensive IRRAS results provide direct evidence that the monocrystalline, stoichiometric α-Fe_2O_3(0001) surface is single Fe-terminated. The initial reduction induced by annealing at elevated temperatures produces surface oxygen vacancies, where the excess electrons are localized at adjacent subsurface iron ions (5-fold coordinated). A massive surface restructuring occurs upon further reduction by exposing to atomic hydrogen followed by Ar^+-sputtering and annealing under oxygen poor conditions. The restructured surface is identified as a Fe_3O_4(111)/$Fe_{1-x}O$(111)-biphase exposing both, Fe^{3+} and Fe^{2+} surface species. Here the well-defined surface domains of Fe_3O_4(111) exhibit a Fe_{oct2}-termination, while the reduced $Fe_{1-x}O$(111) is Fe^{2+}(oct)-terminated. These findings are supported by reference IRRAS data acquired for CO adsorption on magnetite (111) and (001) monocrystalline surfaces.

Keywords: iron oxide, CO adsorbed infrared spectroscopy, IR spectroscopy, reduced oxides, XPS

INTRODUCTION

Although iron oxides have been the topic of numerous studies, their surface is of complex nature and their structure depends strongly on the interaction with the ambience (Kuhlenbeck et al., 2013; Parkinson, 2016). Not only because of the comprehensive phase diagram and the ability to form polymorphs, but also because of the unique material properties including magnetism, the surface properties of iron oxide are among the most challenging research fields in inorganic chemistry and solid-state physics. In previous works, a number of structural conversions and surface reconstructions have been reported (Ketteler et al., 2001; Weiss and Ranke, 2002; Sakurai et al., 2009; Kuhlenbeck et al., 2013; Parkinson, 2016). It is therefore not surprising that the discussion on many common iron oxide facets toward surface stabilization and termination has remained controversial. For detailed insights, we refer the reader to two recent excellent review papers (Kuhlenbeck et al., 2013; Parkinson, 2016). In section Preview on Related Iron Oxide Crystal Structures, we have briefly summarized the important experimental and theoretical results reported in the literature for three relevant iron oxide surfaces [α-Fe_2O_3(0001), Fe_3O_4(111), Fe_3O_4(001)] in the form of both thin films and single crystals.

The chemical and physical properties of metal oxides strongly depend on the structural arrangement of atoms at their surfaces (Wang and Wöll, 2017). Furthermore, it has been shown that the chemical reactivity can be dramatically changed in the presence of defects like oxygen vacancies. Especially under reducing conditions there are numerous such defects, with their densities depending on temperature and the surrounding atmosphere (Parkinson, 2016). However, it is difficult to gain atomic-level information on metal oxide surface structures since some of the standard methods in surface science cannot be applied in a straightforward fashion, e.g., due to charging problems.

This problem can be avoided when using non-destructive surface analysis methods insensitive to charging effects. An important example is infrared (IR) spectroscopy. In combination with appropriate probe molecules like carbon monoxide (CO), this vibrational spectroscopy has been shown to provide insights into structural, electronic and reactive properties of model and nanostructured catalysts (Yang and Wöll, 2017). In addition, the interaction between CO and iron oxide (α-Fe_2O_3, hematite, Fe_3O_4, magnetite, $Fe_{1-x}O$, wüstite) is of great interest in itself because of detailed knowledge about the binding of CO to iron oxides is required for a fundamental understanding of industrial catalytic processes such as CO oxidation and water gas-shift reactions (de Smit and Weckhuysen, 2008; Freund et al., 2011; Zhu and Wachs, 2016; Wei et al., 2018). The adsorption of CO on various well-defined metal surfaces has been extensively studied by infrared reflection absorption spectroscopy (IRRAS). However, the application of this approach on metal oxide single-crystal surfaces is challenging due to the inherent experimental difficulties arising from the low reflectivity of dielectric substrates in the IR regime. Recent progress in instrumentation, however, has allowed us to obtain high-resolution data for a number of different oxide surfaces (e.g., CeO_2, TiO_2, ZnO, α-Fe_2O_3) (Buchholz et al., 2016; Yu et al., 2016; Yang et al., 2017a,b; Chen et al., 2019; Schöttner et al., 2019). These IRRAS results have demonstrated that CO is well suited as a probe molecule to monitor the atomic structure evolution of oxide surfaces under different conditions. In particular, defects like oxygen vacancies and surface restructuring could be clearly identified (Xu et al., 2012; Yang et al., 2014, 2017a,b).

To the best of our knowledge, no IRRAS data of CO adsorption on surfaces of macroscopic iron oxide single crystals have been reported so far. Several studies have been reported on related systems including CO adsorbed on α-Fe_2O_3 powders (Zecchina et al., 1988) and Fe_3O_4(111) thin films grown on Pt(111) (Lemire et al., 2004, 2005; Kuhlenbeck et al., 2013; Li et al., 2018). Here, we present a thorough polarization-resolved IRRAS study of CO adsorption on differently treated iron (III/II) oxide single-crystal surfaces, focusing on α-Fe_2O_3(0001) that has shown to be the most abundant facet exposed by hematite nanoparticles (Hartman, 1989). Our systematic IRRAS results allow to gain detailed insight into the structural evolution of the α-Fe_2O_3(0001) surface under reducing conditions. The assignment of the IR bands was assisted by additional reference measurements of CO adsorption on well-defined Fe_3O_4(111) and Fe_3O_4(001) monocrystalline substrates.

MODELS AND METHODS

Preview on Related Iron Oxide Crystal Structures

α-Fe_2O_3 crystallizes in a corundum structure characterized by a slightly distorted hexagonal close-packed oxide-ion lattice where 2/3 of the octahedral sites are occupied by Fe^{3+} ions with non-degenerated energy levels on metal d-electrons due to a ligand field splitting originating from Fe-O hybridization (**Figure S1**) (de Groot et al., 1989). Oxygen ions that are located parallel to (0001) plane levels, are separated by an iron double layer, yielding a stacking sequence of O_3-Fe-Fe repeat units. There are three different surface terminations possible for α-Fe_2O_3(0001): a single iron layer (Fe-O_3-Fe-R), a double iron layer (Fe-Fe-O_3-R) and an oxygen (O_3-Fe-Fe-R) layer (**Figure 1A**).

It is known that the structural and electronic properties of hematite (0001) depends strongly on the interaction with the ambience and the preparation parameters (Ketteler et al., 2001; Weiss and Ranke, 2002; Kuhlenbeck et al., 2013; Parkinson, 2016). In particular, the surface termination α-Fe_2O_3(0001) is highly sensitive to the oxygen partial pressure and preparation temperature. Freund and coworkers have systematically studied the surface structures of α-Fe_2O_3(0001) thin films supported on Pt(111) by scanning tunneling microscopy (STM) and IRRAS (Lemire et al., 2005). The results revealed a ferryl (Fe=O) termination coexisting with domains of the Fe-terminated surface in 10^{-3}-1 mbar O_2 at ∼1,050 K, while the preparation at higher pressures of O_2 (>1 mbar) yields O-terminated surfaces (Shaikhutdinov and Weiss, 1999). In contrast, an exclusive Fe-termination was reported on thin films (Thevuthasan et al., 1999) as well as on single crystal substrates under O-deficient conditions ($<10^{-5}$ mbar) (Yamamoto, 2010; Schöttner et al., 2019). For α-Fe_2O_3(0001) single crystals, it has been reported that Ar^+-sputtering followed by annealing in 10^{-6} mbar of O_2 at about 1,000 K leads to a massive surface restructuring, forming a Fe_3O_4(111) layer (Condon et al., 1994, 1998; Camillone et al., 2002). A biphase structure was observed upon heating in oxygen (10^{-6} mbar) to higher temperatures (∼1,100 K) (Condon et al., 1995, 1998; Camillone et al., 2002). The STM results revealed the formation of long-range order of α-Fe_2O_3(0001) and $Fe_{1-x}O$(111) domains, which are characterized by floret-like spots in the low-energy electron diffraction (LEED) pattern described as $(\sqrt{3} \times \sqrt{3})R30^\circ$ reconstruction (Kurtz and Henrich, 1983; Lad and Henrich, 1988; Condon et al., 1995). In addition, the surface chemistry and physics of α-Fe_2O_3(0001) has been studied by a number of theoretical groups [for details see the review by Parkinson, 2016] (Wang et al., 1998; Bergermayer et al., 2004; Trainor et al., 2004; Nguyen et al., 2014; Lewandowski et al., 2016; Ovcharenko et al., 2016).

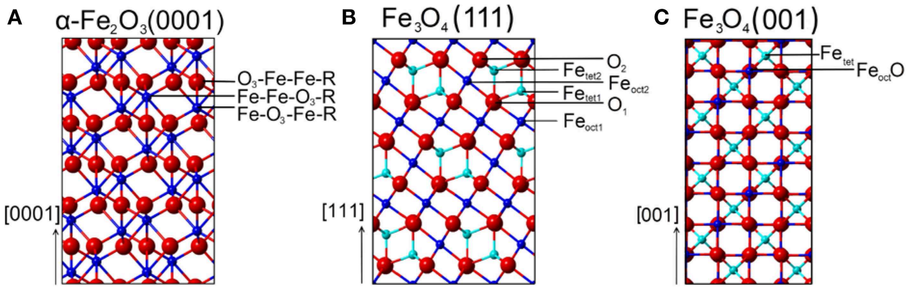

FIGURE 1 | Schematic representations (side view) of various surface terminations for **(A)** α-$Fe_2O_3(0001)$, **(B)** $Fe_3O_4(111)$, and **(C)** $Fe_3O_4(001)$ surfaces. Red spheres correspond to oxide lattice ions; dark blue spheres and cyan spheres represent iron ions on octahedral (oct) and tetrahedral (tet) lattice sites, respectively.

In the crystal structure of Fe_3O_4 oxygen anions are aligned in a cubic closed packing of equal spheres, where Fe^{3+} cations are located at tetrahedrally coordinated interstitial sites. Other cations are located at octahedrally coordinated lattice positions, among which 50% exhibit the valence state +3 while the other 50% are in the +2 oxidation state. This chemical composition is typical for inverse spinel bulk structures and can be written as $Fe^{3+}[Fe^{3+}Fe^{2+}]O_4$ to illustrate that the first type is tetrahedrally coordinated (A-type), whereas the parenthesized Fe^{2+} and Fe^{3+} ions occupy octahedrally coordinated sites (B-type). At low-pressure and low-temperature (CO measurement conditions), Fe_3O_4 consists of a crystal structure with monoclinic symmetry (Wright et al., 2002; Bengtson et al., 2013). Above 120 K, known as the Verwey temperature (Verwey, 1939), the octahedrally coordinated iron atoms in magnetite have an average oxidation state of Fe +2.5 due to electron hopping between equal numbers of Fe^{2+} and Fe^{3+} ions. Such electron movement is frozen in Fe_3O_4 below 120 K and therefore accompanied by a significant decrease in the electrical conductivity.

For $Fe_3O_4(111)$ surfaces, six terminations may occur when cleaving the (111) stacking sequence (**Figure 1B**). The different terminations exhibit Fe atoms on octahedral (Fe_{oct1} or Fe_{oct2}) and tetrahedral (Fe_{tet1} or Fe_{tet2}) lattice sites, as well as O layers (O_1 or O_2). The surface structure of $Fe_3O_4(111)$ has been the subject of numerous experimental and theoretical investigations. Quantum chemical calculations have predicted that the Fe_{oct2}-termination is energetically favored on $Fe_3O_4(111)$ under oxygen-deficient conditions, followed closely by the Fe_{tet1} termination (Ahdjoudj et al., 1999; Zhu et al., 2006; Grillo et al., 2008; Noh et al., 2015). Recent work combining IRRAS and DFT (Li et al., 2018) revealed that the regular $Fe_3O_4(111)$ thin film is Fe_{tet1}-terminated over close-packed oxygen layer, in line with the LEED *IV* results (Ritter and Weiss, 1999; Sala et al., 2012). STM studies provided further evidence for the Fe_{tet1} termination on the pristine $Fe_3O_4(111)$ surface, while the Fe_{oct2} termination was observed under oxygen-poor conditions (Lennie et al., 1996; Shimizu et al., 2010). In addition, a long-range ordered biphase structure was reported for reduced $Fe_3O_4(111)$ in the form of both thin films (Shaikhutdinov et al., 1999) and single-crystals (Condon et al., 1997; Paul et al., 2007). The STM and LEED data suggested the coexistence of $Fe_3O_4(111)$ and $Fe_{1-x}O(111)$ domains.

From the ideal $Fe_3O_4(001)$ model, only two surface terminations are possible, namely Fe_{tet} and $Fe_{oct}O$ layers (**Figure 1C**). Again, the surface structure of $Fe_3O_4(001)$ depends strongly on the preparation parameters (Tarrach et al., 1993; Parkinson et al., 2011; Bartelt et al., 2013). The polar $Fe_3O_4(001)$ surface is well-known to be stabilized by a $(\sqrt{2} \times \sqrt{2})R45^\circ$ reconstruction. The reconstructed surface was first studied using STM by Wiesendanger et al. (1992) and later by other groups [see e.g., Chambers and Joyce, 1999; Rustad et al., 1999; Stanka et al., 2000; Mariotto et al., 2002]. Recently, Parkinson et al. (Bliem et al., 2014) proposed a subsurface cation vacancy (SCV) model by using STM in conjunction with LEED *IV* analysis and theory. In this model, the reconstructed surface features a $Fe_{oct}O$ termination (B-layer) and is slightly distorted by a rearrangement of the cations in the subsurface layers.

Overall, due to the great complexity, an unambiguous experimental determination of the surface atomic structure for these iron oxides under different conditions is still a challenging task.

Experimental Details

The IR measurements were carried out in an UHV multi-chamber system (Prevac). The base pressure of the entire chambers is in 10^{-10} mbar range. The IR spectra were recorded in reflection absorption mode using a state-of-the-art Fourier-Transform (FT)-IR spectrometer (Bruker Vertex 80v) that is directly coupled to the UHV chamber via differentially pumped KBr-windows. The IR-spectrometer contains an internal polarizer module, which allows to carry out polarization-resolved IRRAS experiments. All CO adsorption measurements reported here were conducted for the respective iron oxide substrate mounted in a cryo-pumped IR-chamber at low temperatures. With liquid-He cooling, we could achieve sample temperatures of 65 K, which was sufficiently low to yield CO adsorption on all substrates studied here. Exposures to CO were carried out by using a leak-valve based directional doser. Gas dosages are quoted in Langmuir ($1\,L = 1.33 \cdot 10^{-6}$ mbar·s). The IR spectra were recorded after saturating the iron oxide surfaces with CO (1 L). The polarization-dependent IRRAS measurements were conducted with p- and/or s-polarized light at grazing incidence, with the angle of 80° with respect to the surface normal. The IRRA spectra are shown in absorbance mode. The resolution of the IR spectrometer was set to 4 cm^{-1} and 2,048 scans were accumulated for a single spectrum.

Iron oxide single crystals were mounted on a sample holder dedicated for e-beam heating. Temperatures were measured with a NiAl-NiCr thermocouple, that is spot-welded at a position between heating plate and backside of the sample. Surface quality and cleanliness were checked by XPS and LEED. Supplementary XPS measurements on the oxidation states of iron atoms for differently prepared iron oxide surfaces were conducted at the HESGM-beamline of the BESSY II storage ring, which is a part of the Helmholtz-Center Berlin.

The iron oxide single crystals used in this study were cut from minerals and polished (SurfaceNet GmbH). The α-Fe_2O_3(0001) substrate was cleaned by repeated cycles of annealing with stepwise heating from 850 K to 950 K in 10^{-5} mbar O_2 (Supporting information, **Figures S2A–C**) (Lübbe and Moritz, 2009; Schöttner et al., 2019). The slightly reduced Fe_2O_3(0001) was formed after over-annealing the sample by gradual heating from 950 K to 1,050 K in 10^{-5} mbar O_2. A highly reduced surface was prepared by exposing the clean and stoichiometric α-Fe_2O_3(0001) to atomic hydrogen followed by post-annealing at 1,000 K. Then the reduced α-Fe_2O_3(0001) surface was prepared by repeated cycles of sputtering with 1.0 keV Ar^+ for 15 min and subsequent annealing at 950 K in 10^{-6} mbar oxygen for 20 min until a LEED pattern gets visible.

The Fe_3O_4(111) single crystal surface was prepared by sputtering with 1.0 keV Ar^+ for 15 min and subsequent annealing at 920 K in 10^{-6} mbar oxygen for 20 min. The surface of Fe_3O_4(001) was cleaned by Ar^+-sputtering at 1.0 keV for 15 min and annealing at 870 K in a background of oxygen at 10^{-6} mbar for 20 min (**Figure S3**) (Nie et al., 2013).

RESULTS AND DISCUSSION

CO Adsorption on the Pristine α-Fe_2O_3(0001) Surface

In **Figure 2** we display polarization-resolved IRRAS data recorded after a saturating exposure of the pristine stoichiometric α-Fe_2O_3(0001) single crystal surface to CO at 65 K. For p-polarized light, we observe a single, symmetric band at 2,169 cm^{-1} which is characteristic for CO bound to the coordinatively unsaturated surface Fe^{3+} cations (Zecchina et al., 1988), indicating the presence of a well-defined surface with only one adsorption site. As mentioned above, the surface termination of iron oxides depends strongly on the preparation conditions (Kuhlenbeck et al., 2013; Parkinson, 2016). For example, the ferryl termination was observed for α-Fe_2O_3(0001) thin films after oxidation with O_2 partial pressures of up to 1 mbar, showing a typical IR band at 2,185 cm^{-1} (Lemire et al., 2005), which is not seen in the present IR spectra (**Figure 2**). Our IRRAS data provides direct spectroscopic evidence that the pristine α-Fe_2O_3(0001) surface is single Fe^{3+}-terminated.

The difference between p- and s-polarizations can be understood by considering the transition dipole moment (TDM) describing the vibrational excitation of CO. The intensity and sign of an IR peak is given by the interaction of the TDM with the vector of the E-field. Note that for metal surfaces including metal-supported oxide thin films, IRRAS data can only be obtained for IR light polarized perpendicular to the surface according to the so-called surface selection rule. In the case of dielectric bulk materials (e.g., metal oxide single crystals), however, both s- and p-polarized components can interact with adsorbate vibrations being highly dependent on the orientation of TDM, thus allowing for a determination of the adsorption geometry (Wang and Wöll, 2017). The absorbance bands excited by E_s are always negative, while the vibrations excited by p-polarized components (normal $E_{p,n}$ and tangential $E_{p,t}$, showing always opposite signs) can be negative or positive depending on the incidence angle Θ and the refractive index n of the substrate (Brunner et al., 1997).

For the adsorption of a full CO monolayer on α-Fe_2O_3(0001) at 65 K, a single IR band with negative sign was observed at 2,169 cm^{-1} for p-polarized light but not for s-polarized light (**Figure 2A**). Since the TDM is oriented parallel to the CO molecular axis, these polarization-dependent IRRAS results indicate that CO is bound to surface Fe^{3+} ions in an upright geometry. Furthermore, we observed a coverage-dependent frequency shift (**Figure S4**), in line with IR results reported for CO adsorbed on α-Fe_2O_3 powder samples (Zecchina et al., 1988). This coverage-induced frequency shift can be explained in terms of lateral adsorbate-adsorbate interactions including both dynamic and substrate-mediated static effects. For CO adsorption on oxide surfaces, the substrate mediated interactions (static shift) play a predominant role, whereas the contribution from dynamic interactions originating from the dipole-dipole coupling between CO adsorbates is rather small (Mahan and Lucas, 1978; Hollins and Pritchard, 1980).

The coverage-dependent frequency shift in CO stretch frequency was also observed after heating the sample to higher temperatures, i.e., with decreasing the CO coverage (temperature-induced CO desorption). The intensity of the CO vibrational band remains stable on α-Fe_2O_3(0001) up to 70 K (**Figure 2B**) but strongly decreases upon further heating. The IR band has disappeared at 100 K, indicating complete desorption of CO. The thermal desorption of CO is accompanied by a blue-shift in frequency from 2,169 to 2,178 cm^{-1}. A quantitative analysis of the temperature-dependent IRRAS results (CO coverage as a function of temperature, see **Figure 2C**) (Gottfried et al., 2003) yields an activation energy for CO desorption on α-Fe_2O_3(0001) of 24 kJ·mol^{-1} (using a frequency factor of 10^{13} s^{-1}), demonstrating that CO binds only weakly to the surface Fe^{3+} ions.

CO Adsorption on Reduced α-Fe_2O_3(0001)

In the next step the stoichiometric α-Fe_2O_3(0001) was subjected to annealing in 10^{-5} mbar oxygen at higher temperatures increased stepwise from 850 K to 1050 K. The corresponding structure evolution was tracked by measuring the vibrational frequency of adsorbed CO. Upon annealing to 950 K, the IRRA spectrum shows only a single CO band at 2,169 cm^{-1} (**Figure 3**), assigned to CO adsorbed at the 3-fold coordinated (Fe-O_3) Fe^{3+} sites of the stoichiometric α-Fe_2O_3(0001) surface, as discussed

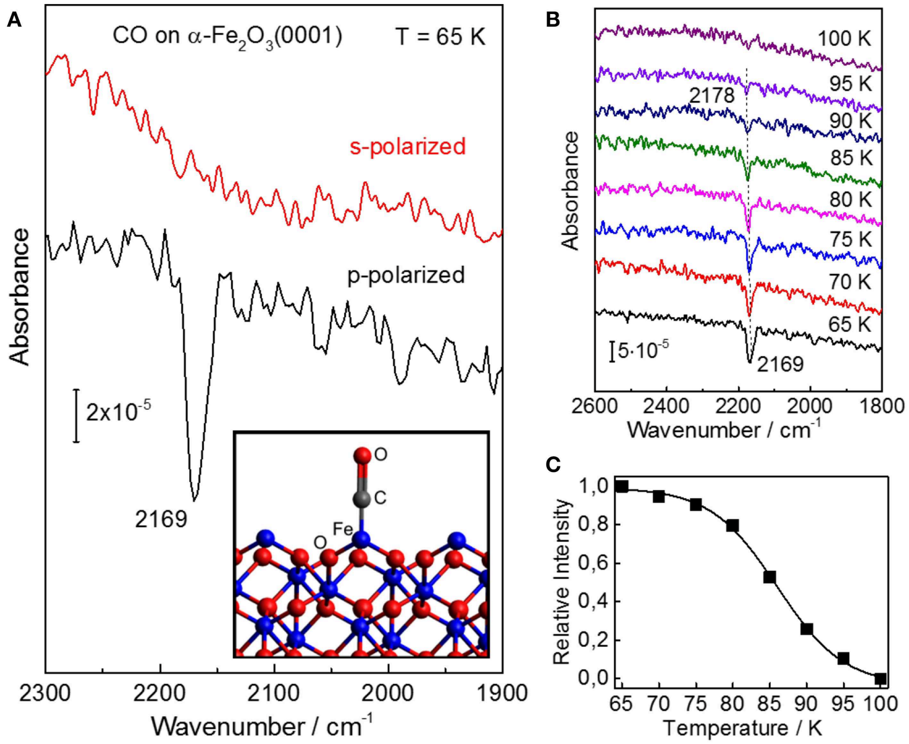

FIGURE 2 | IRRAS results for CO adsorption on the well-ordered stoichiometric α-Fe_2O_3(0001) surface. **(A)** Polarization-dependent IRRAS data recorded after exposing the clean surface of α-Fe_2O_3(0001) to 1 L CO at 65 K. The adsorption model is shown as inset. **(B)** Temperature-dependent IRRAS data starting from a saturated CO coverage at 65 K. Here, all spectra were recorded at an incidence angle of 80° with p-polarized light. **(C)** The relative CO band-intensity is shown as a function of the sample temperature.

above. A new CO band at 2,163 cm^{-1} appears and becomes the dominating one when increasing the sample temperature to 950–1000 K under O-poor conditions. After heating the sample to 1,000–1,050 K, only the 2,163 cm^{-1} band is detected, while the Fe^{3+}-related CO vibration at 2,169 cm^{-1} observed for the fully oxidized surface disappears completely (see **Figure 3**). Note that in the fitting process, the half width for all CO peaks was set to be equal.

Overall, the present IRRAS data indicate the presence of surface oxygen vacancies (V_O) created by annealing to elevated temperatures. Formation of V_O defects have been found to induce a red-shift of CO frequencies on other oxides [e.g., rutile TiO_2(110) surface; Xu et al., 2012]. Here, the slightly reduced α-Fe_2O_3(0001) surface (Fe-O_{3-x}-Fe-R) is characterized by a CO band position of 2,163 cm^{-1}, which we assign to CO bound to 2-fold coordinated (Fe-O_2) Fe^{3+} ions adjacent to O-vacancy sites. Importantly, the rather small red shift of 6 cm^{-1} stands for an only little electronic structure modification of surface iron cations, suggesting that the excess electrons are not trapped at the 2-fold coordinated surface Fe^{3+} ions. This finding is in excellent agreement with the DFT calculations made on the reduced α-Fe_2O_3(0001) surface (Ovcharenko et al., 2016). Along with the removal of a surface oxygen atom, two excess electrons were predicted to occupy the easily available Fe 3d states on two neighboring subsurface iron cations (5-fold coordinated).

We turn our attention to the experimental results for the highly reduced surface states of hematite, which were created by subjecting the stoichiometric Fe_2O_3(0001) to atomic hydrogen exposure followed by Ar^+-sputtering and annealing cycles. Again, the changes in surface structure were monitored by measuring the CO vibrational frequency. Our IRRAS data allow to gain detailed insight into the surface structure of highly reduced α-Fe_2O_3(0001).

After CO adsorption at 65 K, the p-polarized IRRAS data show a number of CO bands in the regions between 2,175–2,135 cm^{-1} and 2,125–2,025 cm^{-1} (**Figure 4A**), which are related respectively to CO species adsorbed on surface Fe^{3+} and Fe^{2+} sites, revealing substantial changes of the surface structure. To achieve a thorough analysis of the data, we subjected the IR spectra to a peak-fitting procedure starting with Lorentzian curves, which were centered at local maxima in the spectra. In the deconvoluted spectrum (**Figure 4A**), four distinct CO stretch bands are resolved at 2,166, 2,150, 2,104, and 2,085 cm^{-1} for highly reduced α-Fe_2O_3(0001), in full agreement with those obtained after CO adsorption on the reduced Fe_3O_4(111) surface [see section CO Adsorption on Fe_3O_4(111) and Fe_3O_4(001)].

Interestingly, **Figure 4A** shows that the intensity of the Fe^{2+}-related CO bands is much stronger than that of the Fe^{3+}-related CO vibrations at 2,166/2,150 cm^{-1}. A higher population of CO species adsorbed to Fe^{2+} sites could account for this

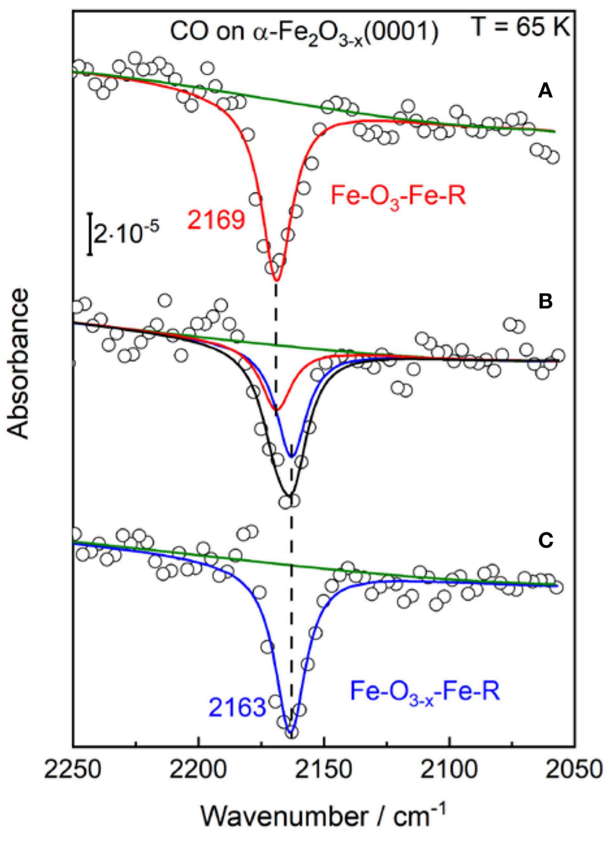

FIGURE 3 | The p-polarized IRRA spectra obtained after saturation adsorption of CO (1 L) on α-Fe_2O_3(0001) at 65 K. The α-Fe_2O_3(0001) samples were pretreated in 10^{-5} mbar O_2 at different temperatures: **(A)** 850–950 K; **(B)** 950–1,000 K; **(C)** 1,000–1,050 K.

observation. However, the substantial intensity difference should be also related to a larger transition dipole moment for CO-Fe^{2+}, resulting from the enhanced electron backdonation compared to CO/Fe^{3+}, as confirmed by the large red-shift in frequency of CO species bound to Fe^{2+} cations. A similar phenomenon has been reported for CO adsorption on differently charged (Cu^+ and Cu^{2+}) copper ions, where the CO stretch intensity was calculated to be more than a factor of five higher for the CO-Cu^+ than for the CO-Cu^{2+} complex (St. Petkov et al., 2012).

Our IRRAS data strongly suggests that the highly reduced α-Fe_2O_3(0001) surface reconstructs. This conclusion is further supported by the corresponding LEED pattern (**Figure 4B**), which reveal that the α-Fe_2O_3(0001) surface undergoes a complete structural conversion from α-Fe_2O_3(0001) to Fe_3O_4(111) termination, in agreement with literature (Condon et al., 1994, 1998; Camillone et al., 2002). Furthermore, the outer hexagon spots become much broader and more intense, which could be attributed to the presence of additional, ordered $Fe_{1-x}O$(111) domains [further detailed explanations are given in section CO Adsorption on Fe3O4(111) and Fe3O4(001)]. The surface structures of α-Fe_2O_3(0001), Fe_3O_4(111) and $Fe_{1-x}O$(111) are illustrated in **Figure 5**. The LEED results indicate the formation of a Fe_3O_4(111)/$Fe_{1-x}O$(111)-biphase structure on highly reduced α-Fe_2O_3(0001). The approach using non-destructive IR spectroscopy and CO as a probe molecule allows to provide more reliable information on the surface termination and chemical environments because CO only interacts with the outermost surface (Wang and Wöll, 2017; Chen et al., 2019). The CO vibrations at 2,166/2,104 cm^{-1} and 2,150 cm^{-1} could be attributed to octahedral Fe^{3+}/Fe^{2+} sites as well as to tetrahedral Fe^{3+} sites within Fe_3O_4(111) domains, while the CO band the 2,085 cm^{-1} implies the coexistence of reduced $Fe_{1-x}O$(111) islands terminated by octahedral Fe^{2+} cations. These assignments are corroborated by reference experiments where CO was adsorbed on Fe_3O_4(111) single-crystal surfaces, as discussed below in section CO adsorption on Fe_3O_4(111) and Fe_3O_4(001). Further evidence for this massive surface restructuring of the highly reduced α-Fe_2O_3(0001) is provided by photoelectron spectroscopy, where Fe^{2+} and Fe^{3+} species are clearly identified in both Fe 2p (**Figure S5A**) and valence band regions (**Figure S5B**) (Liu et al., 2012).

As mentioned in section Preview on Related Iron Oxide Crystal Structures, the highly reduced α-Fe_2O_3(0001) surface may also feature an ordered α-Fe_2O_3(0001)/$Fe_{1-x}O$(111)-biphase reconstruction which is characterized by floret-like satellite spots, positioned adjacent to the peaks for the pristine (1×1)-α-Fe_2O_3(0001) surface (Condon et al., 1995, 1998). However, this surface reconstruction is not supported by our combined results from IRRAS and LEED (**Figure 4**). Our observation is in line with the STM studies on α-Fe_2O_3(0001) single crystal surfaces (Condon et al., 1998), where a Fe_3O_4(111)-termination was created by annealing the sample at ∼1,000 K in 10^{-6} mbar O_2. The structural transformation to a α-Fe_2O_3(111)/$Fe_{1-x}O$(111)-biphase occurs only when increasing the temperature to about 1,100 K (Condon et al., 1998). In addition, more recent DFT calculations revealed that the α-Fe_2O_3(0001) surface can expose O-, Fe-, and ferryl-terminated regions, whose size varies depending on the oxygen chemical potential (Lewandowski et al., 2016). The long-range order was explained in terms of the dipole-dipole interaction between domains with different work functions.

CO Adsorption on Fe_3O_4(111) and Fe_3O_4(001)

In order to aid the assignment of the CO bands and to gain a thorough understanding of the structural evolution of the α-Fe_2O_3(0001) surface during reduction, we have carried out additional reference measurements on Fe_3O_4(111) and reconstructed Fe_3O_4(001)-$\sqrt{2} \times \sqrt{2}$R45° (**Figure S3**) single crystal surfaces. **Figure 6a** shows p-polarized IRRAS data recorded after saturating the slightly (two sputter/annealing cycles) and strongly (five sputter/annealing cycles) reduced Fe_3O_4(111) single-crystal surfaces with CO at 65 K, which is much lower than the Verwey transition temperature of ∼120 K (Verwey, 1939). The deconvoluted spectra display four CO stretch bands at 2,166, 2,150, 2,104, and 2,085 cm^{-1} (**Figure 6a**),

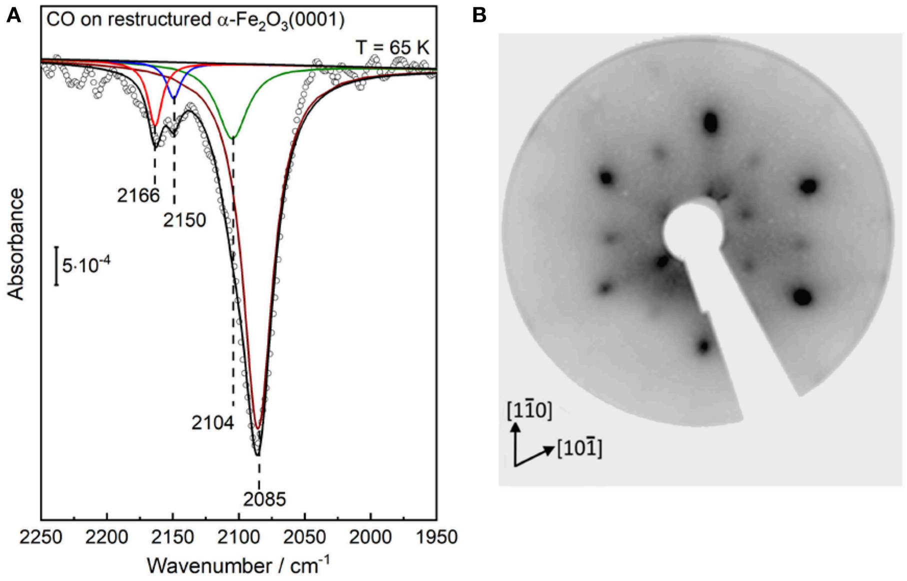

FIGURE 4 | (A) IRRA spectrum (p-polarized) obtained after saturation adsorption of CO (1 L) at 65 K on a highly reduced α-Fe_2O_3(0001) surface created via atomic hydrogen treatment at RT followed by Ar^+-sputtering and post-annealing at 950 K in 10^{-6} mbar oxygen. **(B)** LEED pattern of the corresponding highly reduced α-Fe_2O_3(0001) surfaces recorded at 90 eV.

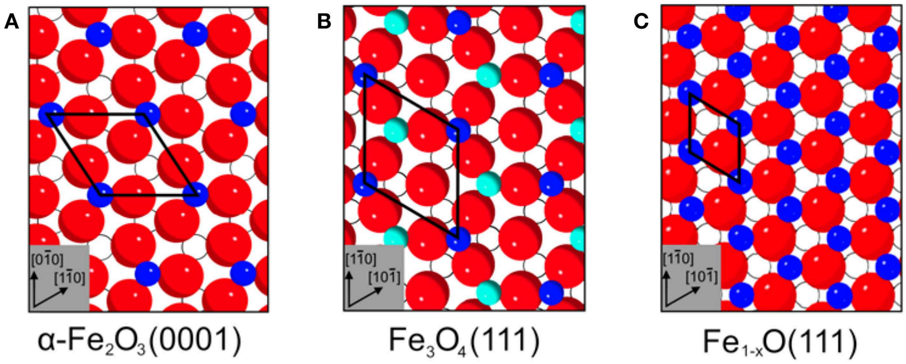

FIGURE 5 | Top view surface structures of **(A)** α-Fe_2O_3(0001), **(B)** Fe_3O_4(111), and **(C)** $Fe_{1-x}O$(111). The surface unit cells are **(A)** 5.04 Å, **(B)** 5.94 Å, and **(C)** 3.04 Å. Surface atoms are shown inked; subsurface atoms below the first oxide layer are depicted hollow. Red spheres correspond to oxide lattice ions; dark blue spheres and cyan spheres represent iron ions on octahedral and tetrahedral lattice sites, respectively.

in excellent agreement with the results found for the highly reduced surface of hematite α-Fe_2O_3(0001) (see **Figure 4A**).

As discussed in section Preview on Related Iron Oxide Crystal Structures, the surface structure of Fe_3O_4(111) is extremely sensitive to the preparation parameters (Kuhlenbeck et al., 2013; Parkinson, 2016). The experimental and theoretical studies revealed consistently that the regular Fe_3O_4(111) surface is Fe_{tet1}-terminated over a close-packed oxygen layer, whereas this surface is stabilized by the Fe_{oct2}-termination under oxygen-deficient conditions (Lennie et al., 1996; Ahdjoudj et al., 1999; Ritter and Weiss, 1999; Zhu et al., 2006; Grillo et al., 2008; Shimizu et al., 2010; Sala et al., 2012; Noh et al., 2015). The vibrational frequencies at 2,166/2,104 cm^{-1} and 2,150 cm^{-1} are assigned to CO species adsorbed to octahedral Fe^{3+}/Fe^{2+} sites (B type) as well as to tetrahedral Fe^{3+} sites (A type), respectively, indicating a Fe_{oct2}-terminated Fe_3O_4(111) structure (see **Figure 5B**).

The assignment of the CO bands is further assisted by additional IRRAS data obtained for CO adsorption on the highly reduced α-Fe_2O_3(0001) surface created by annealing at 950 K in a higher O_2 pressure of 10^{-4} mbar (see **Figure S6**). In this condition, the Fe_3O_4(111) layer within the Fe_3O_4(111)/$Fe_{1-x}O$ biphase should be dominated by the Fe_{tet1}-termination. Indeed, the corresponding IR data shows a single Fe^{3+}-related vibrational band at 2,153 cm^{-1}, which is attributed to CO molecules bound on surface Fe_{tet1} sites (see **Figure S6**).

Furthermore, we assign the low-lying IR band at 2,085 cm^{-1} to CO bound to Fe^{2+} surface sites from reduced $Fe_{1-x}O$ phases (see **Figure 5C**), as reported in the literature (Benziger and

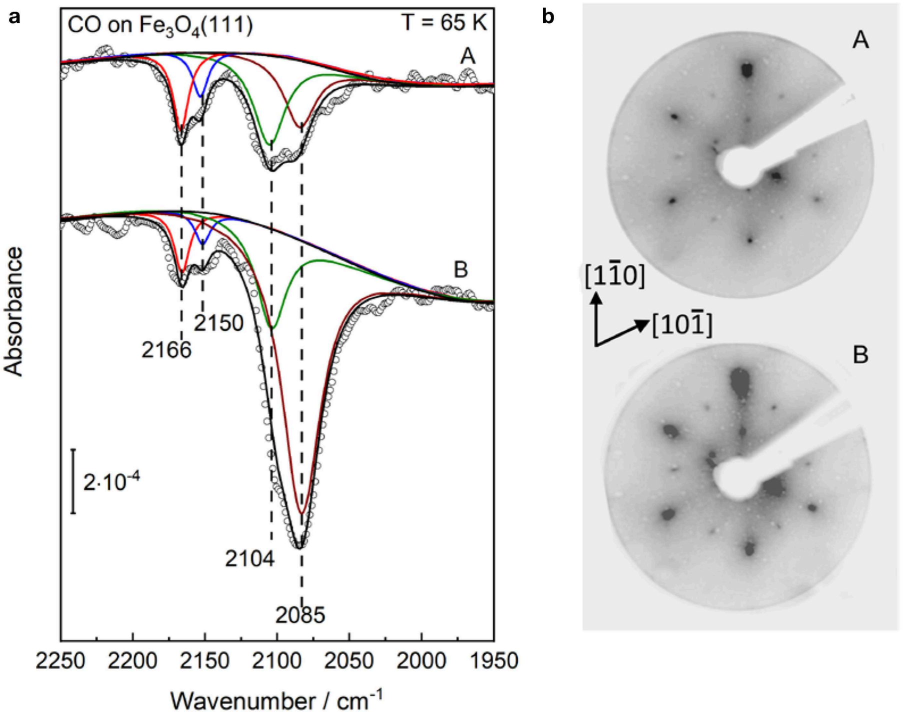

FIGURE 6 | Structural evolution of well-defined Fe_3O_4(111) single-crystal surfaces after (A) slight and (B) heavy Ar^+-sputtering treatment. Afterward such treatment the sample was annealed at 920 K in 10^{-6} mbar oxygen. **(a)** The p-polarized IRRAS data of CO adsorption on reduced Fe_3O_4(111) surfaces. The clean surfaces was saturated with a dose of 1 L CO at 65 K. **(b)** LEED patterns of the corresponding Fe_3O_4(111) surfaces recorded at 90 eV.

Larson, 1982). Again, the $Fe_{1-x}O$(111) surface can expose either Fe or O layers according to the preparation conditions. Whereas, the STM investigations suggested the presence of O-terminated $Fe_{1-x}O$(111) domains formed by oxidation of the Fe_3O_4(111) layer on α-Fe_2O_3(0001) (Tang et al., 2013), the DFT calculations predicted a Fe-termination in O-poor environments (Li et al., 2005). This assignment is supported by the observation that the 2,085 cm^{-1} band becomes more intense along with the Ar^+-sputtering/annealing treatment of the Fe_3O_4(111) single-crystal surface (**Figure 6a**), indicating the growth of ordered $Fe_{1-x}O$(111) domains, which coexist with the Fe_{oct2}-terminated Fe_3O_4(111) structures on the reduced Fe_3O_4(111) surface. The stretch frequencies of all CO species adsorbed on different iron(III/II) oxide single-crystal surfaces studied in the course of this work are summarized in **Table 1**.

Our IR data provide direct spectroscopic evidence for the formation of a Fe_3O_4(111)/$Fe_{1-x}O$(111) biphase structure on Fe_3O_4(111), in line with the results from STM and LEED (Condon et al., 1997; Shaikhutdinov et al., 1999; Paul et al., 2007). Here, the presence of a Fe_3O_4(111)/$Fe_{1-x}O$(111) biphase is also supported by the LEED patterns shown in **Figure 6B**. In addition to the pristine Fe_3O_4(111) structure (Tarrach et al., 1993), the spots at the outer hexagon become much broader and more intense under reducing conditions, which is also seen for the highly reduced α-Fe_2O_3(0001) surface (see **Figure 4B**). This should originate from the presence of ordered $Fe_{1-x}O$(111) domains. However, we did not see the floreted diffraction patterns as observed for a typical α-Fe_2O_3(0001)/$Fe_{1-x}O$(111) biphase. This can be attributed to the rather small lattice mismatch (2%) between Fe_3O_4(111) and $Fe_{1-x}O$(111), which makes an unambiguous observation of the floret-like satellite spots extremely difficult (Condon et al., 1997; Paul et al., 2007).

The temperature-dependent IRRAS data allows to gain deep insight into the interaction of CO molecule with various surface sites. As shown in **Figure 7A**, the Fe^{3+}-related CO bands at 2,166 and 2,150 cm^{-1} disappear after annealing the sample to ∼100 K, indicating a weak binding of CO to coordinatively unsaturated surface Fe^{3+} cations. The thermal stability and the frequency (blue-shifted compared to the gas phase value, see **Table 1**) are in good agreement with those observed on pristine

TABLE 1 | CO stretch frequencies collected on regular and restructured hematite (0001) as well as on magnetite (111) and (001) single-crystal surfaces.

Surface	Termination	CO stretch vibration (cm^{-1})		
		Fe^{3+}(oct)	Fe^{3+} (tet)	Fe^{2+}(oct)
α-Fe_2O_3(0001)	Fe_{oct}	2169	–	–
α-Fe_2O_{3-x}(0001)	Fe_{oct}	2163	–	–
Fe_3O_4(111)	Fe_{oct2}	2166	2150	2104
$Fe_{1-x}O$(111)	Fe_{oct}	–	–	2085
Fe_3O_4(001)	$Fe_{oct}O$	2169		–

The frequencies are shown for saturating CO exposures at 65 K.

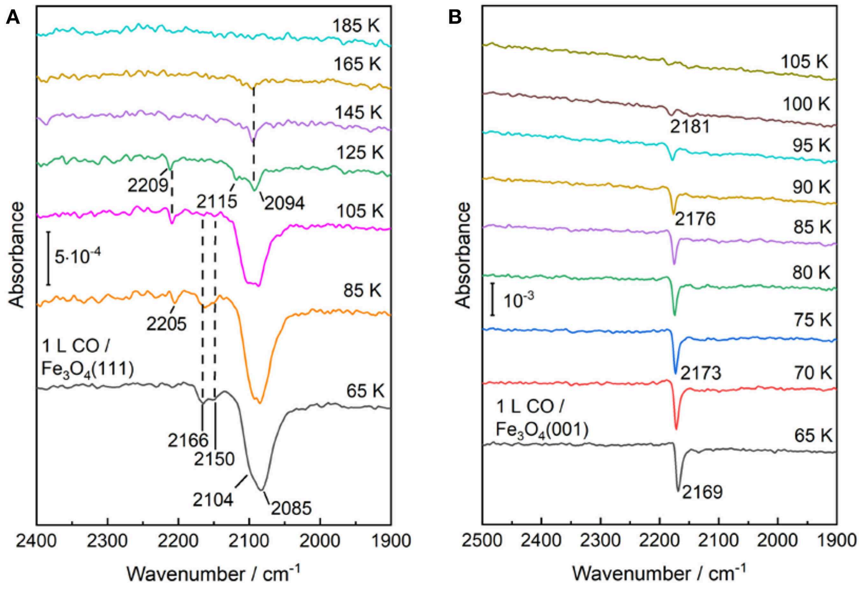

FIGURE 7 | Temperature-dependent IRRA spectra starting from CO saturated surfaces of **(A)** $Fe_3O_4(111)$ and **(B)** $Fe_3O_4(001)$ at 65 K and subsequently heating to indicated temperatures. All the spectra were recorded at an incidence angle of 80° with p-polarized light at 65 K.

α-$Fe_2O_3(0001)$ (**Figure 2B**) and $Fe_3O_4(001)$ surfaces (**Figure 7B**, see below), in which both are terminated by single Fe^{3+} species. In comparison, the Fe^{2+}-related CO species at 2,104 and 2,085 cm^{-1} are thermodynamic more stable and desorb completely only upon annealing to temperatures above 165 K (**Figure 7A**). Again, the stronger binding of CO to Fe^{2+} is attributed to the enhanced electron back-donation to the CO $2\pi^*$ antibonding orbital, thus strengthening the CO-substrate interaction and weakening the internal C–O bond (redshift in frequency).

In addition, a new weak IR band at 2,205–2,209 cm^{-1} is detected after annealing to temperatures above 85 K. The origin of this band is not clear, but a similar CO species has been reported for ZnO and Au/ZnO systems and is assigned to CO coadsorbed with carbonate species that increase the Lewis acidity of adjacent Zn^{2+} cations (Wang et al., 2007; Noei et al., 2012). Carbonate could be produced via the oxidation of adsorbed CO with surface O atoms on $Fe_3O_4(111)$ (Tinkle and Dumesic, 1987; Huang et al., 2006). In a recent study on $Fe_3O_4(111)$ thin films grown on Pt(111) (Li et al., 2018), a CO vibration at 2,204 cm^{-1} was also observed. According to the DFT calculations, this band was ascribed to CO adsorbed at Fe^{2+}_{oct2} ions located at step edges (defect sites). However, the $Fe_3O_4(111)$ thin film, prepared under oxidation conditions, features a Fe^{3+}_{tet}-termination over close-packed oxygen layer, which is quite different from the present work focusing on the structural evolution of iron oxides under reducing conditions.

We now turn to the experimental results obtained on the reconstructed $Fe_3O_4(001)$-($\sqrt{2} \times \sqrt{2}$)R45° surface. After adsorption of CO on the $Fe_3O_4(001)$ surface at 65 K only one single sharp CO band at 2,169 cm^{-1} is observed (**Figure 7B**), which is typical for CO bound to Fe^{3+} sites. As discussed in section Preview on Related Iron Oxide Crystal Structures, the ($\sqrt{2} \times \sqrt{2}$)R45°-reconstructed $Fe_3O_4(001)$ surface has been studied extensively by numerous groups (Wiesendanger et al., 1992; Tarrach et al., 1993; Chambers and Joyce, 1999; Rustad et al., 1999; Stanka et al., 2000; Mariotto et al., 2002; Parkinson et al., 2011; Bartelt et al., 2013; Bliem et al., 2014). Recently, Parkinson et al. (Bliem et al., 2014) presented a thorough study combining STM, LEED *IV* analysis and theory, in which a subsurface cation vacancy (SCV) model was developed. According to this model, the reconstructed surface is Fe_{oct}-O terminated, which is accompanied by a rearrangement of the cations in the subsurface layers (Bliem et al., 2014).

Our IRRAS results are fully consistent with the SCV structure in that the single IR band at 2,169 cm^{-1} is characteristic for CO bound to surface Fe^{3+}_{oct} sites. The assignment to Fe^{3+} is further supported by a temperature-programmed desorption measurement, where the IRRAS data reveal a complete desorption of CO species after heating to 105 K, in excellent agreement with the TPD results (Hulva et al., 2018). This finding demonstrates again a weak interaction between CO and surface Fe^{3+} cations as observed for CO adsorption on the Fe^{3+} sites of α-$Fe_2O_3(0001)$ and $Fe_3O_4(001)$ surfaces. In addition, the thermal desorption of CO leads to a blue shift in frequency from 2,169 to 2,181 cm^{-1} (**Figure 7B**), which is attributed to the lateral adsorbate-adsorbate interactions [for a detailed discussion see section CO Adsorption on the Pristine α-$Fe_2O_3(0001)$ Surface].

Overall, the IRRAS results, acquired for CO adsorption on the macroscopic $Fe_3O_4(111)$ and $Fe_3O_4(001)$ surfaces, provide a solid basis for a reliable assignment of the CO bands observed for the restructured α-$Fe_2O_3(0001)$ surface under different reduction conditions (**Table 1**). Importantly, the comprehensive IR data, together with XPS and LEED analysis, allow for identifying the

Fe_3O_4(111)/$Fe_{1-x}O$(111) biphase structure on highly reduced α-Fe_2O_3(0001) surfaces.

CONCLUSIONS

In summary, the structural evolution of differently treated iron(III/II) oxide single-crystal surfaces was monitored by polarization-resolved IRRAS using CO as a probe molecule. We presented a comprehensive investigation on stoichiometric and reduced α-Fe_2O_3(0001) surfaces as well as on Fe_3O_4(001) and Fe_3O_4(111) surfaces. The polarization-dependent IRRAS results demonstrate that the CO adsorption is well suited to monitor the atomic structure evolution of iron oxide surfaces under different conditions.

The pristine stoichiometric α-Fe_2O_3(0001) surface is terminated in a single-Fe^{3+} configuration as characterized by the single sharp IR band at 2,169 cm^{-1} (CO on 3-fold coordinated Fe^{3+}). Annealing the hematite (0001) surface to elevated temperatures leads to the formation of surface oxygen vacancies. The reduced α-Fe_2O_3(0001) surface shows a typical vibrational band at 2,163 cm^{-1} (CO on Fe^{3+} at O vacancy). A further reduction of α-Fe_2O_3(0001) induced by atomic hydrogen treatment followed by Ar^+-sputtering and annealing cycles under oxygen poor conditions causes a massive surface restructuring yielding a Fe_3O_4(111) overlayer, which coexists with $Fe_{1-x}O$(111) domains. The reconstructed Fe_3O_4(111) surface is Fe_{oct2}-terminated and shows typical CO bands at 2,166/2,150 and 2,104 cm^{-1}. They are assigned to Fe^{3+}(oct)/Fe^{3+}(tet) and Fe^{2+}(oct) sites, respectively. The $Fe_{1-x}O$(111) domains within the Fe_3O_4(111)/$Fe_{1-x}O$(111) biphase are characterized by the intense band at 2,085 cm^{-1} originating from CO adsorbed on Fe^{2+}(oct) sites. The assignment is further demonstrated by reference IRRAS data acquired for CO adsorption on Fe_3O_4(111) single-crystal surfaces. The surface of Fe_3O_4(001) is terminated with Fe^{3+}_{oct}-O in a SCV reconstruction as determined by the single intense IR band of CO at 2,169 cm^{-1}.

DATA AVAILABILITY

All datasets generated for this study are included in the manuscript and/or the **Supplementary Files**.

AUTHOR CONTRIBUTIONS

YW and CW conceived the idea of the experiment. LS and CY carried out the experiments, with additional help by AN and SH. Data analysis was carried out by LS, CY, and YW. The manuscript was written by LS, YW, and CW.

ACKNOWLEDGMENTS

The Helmholtz-Research-School Energy-related-catalysis is gratefully acknowledged for providing financial support and the donation of a Ph.D.-Scholarship to LS. We acknowledge funding from the Science and Technology of Nanosystems Program (432202). The authors thank Helmholtz-Zentrum Berlin for the allocation of synchrotron radiation beamtime at BESSY II.

SUPPLEMENTARY MATERIAL

The Supplementary Material for this article can be found online at: https://www.frontiersin.org/articles/10.3389/fchem.2019.00451/full#supplementary-material

Additional XPS, LEED, and polarization-resolved IRRAS analysis.

REFERENCES

Ahdjoudj, J., Martinsky, C., Minot, C., Van Hove, M. A., and Somorjai, G. A. (1999). Theoretical study of the termination of the Fe_3O_4 (111) surface. *Surf. Sci.* 443, 133–153. doi: 10.1016/S0039-6028(99)01008-0

Bartelt, N. C., Nie, S., Starodub, E., Bernal-Villamil, I., Gallego, S., Vergara, L., et al. (2013). Order-disorder phase transition on the (100) surface of magnetite. *Phys. Rev. B* 88:235436. doi: 10.1103/PhysRevB.88.235436

Bengtson, A., Morgan, D., and Becker, U. (2013). Spin state of iron in fe_3O_4 magnetite and h-Fe_3O_4. *Phys. Rev. B* 87:155141. doi: 10.1103/PhysRevB.87.155141

Benziger, J. B., and Larson, L. R. (1982). An infrared spectroscopy study of the adsorption of Co on Fe/Mgo. *J. Catal.* 77, 550–553. doi: 10.1016/0021-9517(82)90195-6

Bergermayer, W., Schweiger, H., and Wimmer, E. (2004). *Ab initio* thermodynamics of oxide surfaces: O_2 on Fe_2O_3(0001). *Phys. Rev. B* 69:195409. doi: 10.1103/PhysRevB.69.195409

Bliem, R., Mc Dermott, E., Ferstl, P., Setvin, M., Gamba, O., Pavelec, J., et al. (2014). Subsurface cation vacancy stabilization of the magnetite (001) surface. *Science* 346, 1215–1218. doi: 10.1126/science.1260556

Brunner, H., Mayer, U., and Hoffmann, H. (1997). External reflection infrared spectroscopy of anisotropic adsorbate layers on dielectric substrates. *Appl. Spectrosc.* 51, 209–217. doi: 10.1366/0003702971940143

Buchholz, M., Yu, X., Yang, C., Heißler, S., Nefedov, A., Wang, Y., et al. (2016). Ir-spectroscopy of CO adsorption on mixed-terminated ZnO surfaces. *Surf. Sci.* 652, 247–252. doi: 10.1016/j.susc.2015.12.029

Camillone, N. III., Adib, K., Fitts, J. P., Rim, K. T., Flynn, G. W., Joyce, S. A., et al. (2002). Surface termination dependence of the reactivity of single crystal hematite with CCl_4. *Surf. Sci.* 511, 267–282. doi: 10.1016/S0039-6028(02)01503-0

Chambers, S. A., and Joyce, S. A. (1999). Surface termination, composition and reconstruction of Fe_3O_4(001) and Γ-Fe_2O_3(001). *Surf. Sci.* 420, 111–122. doi: 10.1016/S0039-6028(98)00657-8

Chen, A. L., Yu, X., Zhou, Y., Miao, S., Li, Y., Kuld, S., et al., (2019). Structure of the catalytically active copper–ceria interfacial perimeter. *Nat. Catal.* 2, 334–341. doi: 10.1038/s41929-019-0226-6

Condon, N. G., Leibsle, F. M., Lennie, A. R., Murray, P. W., Parker, T. M., Vaughan, D. J., et al. (1998). Scanning tunnelling microscopy studies of α-Fe_2O_3(0001). *Surf. Sci.* 397, 278–287. doi: 10.1016/S0039-6028(97)00744-9

Condon, N. G., Leibsle, F. M., Lennie, A. R., Murray, P. W., Vaughan, D. J., Thornton, G., et al. (1995). Biphase ordering of iron oxide surfaces. *Phys. Rev. Lett.* 75, 1961–1964. doi: 10.1103/PhysRevLett.75.1961

Condon, N. G., Leibsle, F. M., Parker, T., Lennie, A. R., Vaughan, D. J., and Thornton, G. (1997). Biphase ordering on Fe_3O_4(111). *Phys. Rev. B* 55, 15885–15894. doi: 10.1103/PhysRevB.55.15885

Condon, N. G., Murray, P. W., Leibsle, F. M., Thornton, G., Lennie, A. R., and Vaughan, D. J. (1994). Fe_3O_4(111) termination of α- Fe_3O_3 (0001). *Surf. Sci.* 310, L609–L613. doi: 10.1016/0039-6028(94)91360-9 de Groot, F. M. F., Grioni, M., Fuggle, J. C., Ghijsen, J., Sawatzky, G. A., and Petersen, H. (1989). Oxygen 1s x-ray-absorption edges of transition-metal oxides. *Phys. Rev. B* 40, 5715–5723. doi: 10.1103/PhysRevB.40.5715

de Smit, E., and Weckhuysen, B. M. (2008). The renaissance of iron-based fischer–tropsch synthesis: on the multifaceted catalyst deactivation behaviour. *Chem. Soc. Rev.* 37, 2758–2781. doi: 10.1039/b805427d

Freund, H. J., Meijer, G., Scheffler, M., Schlögl, R., and Wolf, M. (2011). Co oxidation as a prototypical reaction for heterogeneous, processes. *Angew. Chem. Int. Ed.* 50, 10064–10094. doi: 10.1002/anie.201101378

Gottfried, J. M., Schmidt, K. J., Schroeder, S. L. M., and Christmann, K., (2003). Adsorption of Carbon Monoxide on Au(110)-(1×2). *Surface Science* 536, 206-224. doi: 10.1016/S0039-6028(03)00595-8

Grillo, M. E., Finnis, M. W., and Ranke, W. (2008). Surface structure and water adsorption on Fe_3O_4 (111): spin-density functional theory and on-site coulomb interactions. *Phys. Rev. B* 77:075407. doi: 10.1103/PhysRevB.77.075407

Hartman, P. (1989). The effect of surface relaxation on crystal habit: cases of corundum (α-Al_2O_3) and hematite (α-Fe_2O_3). *J. Cryst. Growth* 96, 667–672. doi: 10.1016/0022-0248(89)90065-1

Hollins, P., and Pritchard, J. (1980). Dipole coupling effects in the coverage-dependent infrared spectra of co chemisorbed on Cu(111). *Chem. Phys. Lett.* 75, 378–382.

Huang, D. M., Cao, D. B., Li, Y. W., and Jiao, H. (2006). Density function theory study of CO adsorption on Fe_3O_4(111) Surface. *J. Phys. Chem. B* 110, 13920–13925. doi: 10.1021/jp0568273

Hulva, J., Jakub, Z., Novotny, Z., Johansson, N., Knudsen, J., Schnadt, J., et al. (2018). Adsorption of CO on the Fe_3O_4 (001) Surface. *J. Phys. Chem. B* 122, 721–729. doi: 10.1021/acs.jpcb.7b06349

Ketteler, G., Weiss, W., Ranke, W., and Schlögl, R. (2001). Bulk and surface phases of iron oxides in an oxygen and water atmosphere at low pressure. *Phys. Chem. Chem. Phys.* 3, 1114–1122. doi: 10.1039/b009288f

Kuhlenbeck, H., Shaikhutdinov, S., and Freund, H. J. (2013). Well-ordered transition metal oxide layers in model catalysis – a series of case studies. *Chem. Rev.* 113, 3986–4034. doi: 10.1021/cr300312n

Kurtz, R. L., and Henrich, V. E. (1983). Geometric structure of the α-Fe_2O_3(0001) surface: a leed and Xps study. *Surf. Sci.* 129, 345–354. doi: 10.1016/0039-6028(83)90185-1

Lad, R. J., and Henrich, V. E. (1988). Structure of α-Fe_2O_3 single crystal surfaces following Ar+ ion bombardment and annealing in O_2. *Surf. Sci.* 193, 81–93. doi: 10.1016/0039-6028(88)90324-X

Lemire, C., Bertarione, S., Zecchina, A., Scarano, D., Chaka, A., Shaikhutdinov, S., et al. (2005). Ferryl (Fe=O) termination of the hematite α-Fe_2O_3 (0001) Surface. *Phys. Rev. Lett.* 94:166101. doi: 10.1103/PhysRevLett.94.166101

Lemire, C., Meyer, R., Henrich, V. E., Shaikhutdinov, S., and Freund, H. J. (2004). The surface structure of Fe_3O_4(111) films as studied by CO adsorption. *Surf. Sci.* 572, 103–114. doi: 10.1016/j.susc.2004.08.033

Lennie, A. R., Condon, N. G., Leibsle, F. M., Murray, P. W., Thornton, G., and Vaughan, D. J. (1996). Structures of Fe=O_4 (111) surfaces observed by scanning tunneling microscopy. *Phys. Rev. B* 53, 10244–10253. doi: 10.1103/PhysRevB.53.10244

Lewandowski, M., Groot, I. M. N., Qin, Z. H., Ossowski, T., Pabisiak, T., Kiejna, A., et al. (2016). Nanoscale patterns on polar oxide surfaces. *Chem. Mater.* 28, 7433–7443. doi: 10.1021/acs.chemmater.6b03040

Li, X., Paier, J., Sauer, J., Mirabella, F., Zaki, E., Ivars-Barceló, F., et al. (2018). Surface termination of Fe_3O_4(111) films studied by CO adsorption revisited. *J. Phys. Chem. B* 122, 527–533. doi: 10.1021/acs.jpcb.7b04228

Li, Y. L., Yao, K. L., Liu, Z. L., and Gao, G. Y. (2005). First-principles study of the composition, structure, and stability of the Feo (111) surface. *Phys. Rev. B* 72:155446. doi: 10.1103/PhysRevB.72.155446

Liu, S., Wang, S., Guo, J., and Guo, Q. (2012). Polarity and surface structural evolution of iron oxide films. *RSC Adv.* 2, 9938–9943. doi: 10.1039/c2ra21892e

Lübbe, M., and Moritz, W. A. (2009). Leed analysis of the clean surfaces of α-Fe_2O_3(0001) and α-Cr_2O_3(0001) bulk single crystals. *J. Phys. Condens. Matter* 21:134010. doi: 10.1088/0953-8984/21/13/134010

Mahan, G. D., and Lucas, A. A. (1978). Collective vibrational modes of adsorbed CO. *J. Chem. Phys.* 68, 1344–1348. doi: 10.1063/1.435952

Mariotto, G., Murphy, S., and Shvets, I. V. (2002). Charge ordering on the surface of Fe_3O_4(001). *Phys. Rev. B* 66:245426. doi: 10.1103/PhysRevB.66.245426

Nguyen, M. T., Seriani, N., and Gebauer, R. (2014). Defective α-Fe_2O_3 (0001): an ab initio study. *ChemPhysChem*. 15, 2930–2935. doi: 10.1002/cphc.201402153

Nie, S., Starodub, E., Monti, M., Siegel, D. A., Vergara, L., El Gabaly, F., et al. (2013). Insight into magnetite's redox catalysis from observing surface morphology during oxidation. *J. Am. Chem. Soc.* 135, 10091–10098. doi: 10.1021/ja402599t

Noei, H., Birkner, A., Merz, K., Muhler, M., and Wang, Y. (2012). Probing the mechanism of low-temperature CO oxidation on Au/Zno catalysts by vibrational spectroscopy. *J. Chem.* C 116, 11181–11188. doi: 10.1021/jp302723r

Noh, J., Osman, O. I., Aziz, S. G., Winget, P., and Brédas, J. L. (2015). Magnetite Fe_3O_4 (111) surfaces: impact of defects on structure, stability, and electronic properties. *Chem. Mater.* 27, 5856–5867. doi: 10.1021/acs.chemmater.5b02885

Ovcharenko, R., Voloshina, E., and Sauer, J. (2016). Water adsorption and O-defect formation on Fe_2O_3(0001) surfaces. *Phys. Chem. Chem. Phys.* 18, 25560–25568. doi: 10.1039/C6CP05313K

Parkinson, G. S. (2016). Iron oxide surfaces. *Surf. Sci. Rep.* 71, 272–365. doi: 10.1016/j.surfrep.2016.02.001

Parkinson, G. S., Novotný, Z., Jacobson, P., Schmid, M., and Diebold, U. (2011). A metastable Fe(A) termination at the Fe_3O_4(001) surface. *Surf. Sci.* 605, L42–L45. doi: 10.1016/j.susc.2011.05.018

Paul, M., Sing, M., Claessen, R., Schrupp, D., and Brabers, V. A. M. (2007). Thermodynamic stability and atomic and electronic structure of reduced Fe_3O_4 (111) single-crystal surfaces. *Phys. Rev. B* 76:075412. doi: 10.1103/PhysRevB.76.075412

Ritter, M., and Weiss, W. (1999). Fe_3O_4 (111) surface structure determined by leed crystallography. *Surf. Sci.* 432, 81–94. doi: 10.1016/S0039-6028(99)00518-X

Rustad, J. R., Wasserman, E., and Felmy, A. R. (1999). A molecular dynamics investigation of surface reconstruction on magnetite (001). *Surf. Sci.* 432, L583–L588. doi: 10.1016/S0039-6028(99)00581-6

Sakurai, S., Namai, A., Hashimoto, K., and Ohkoshi, S. I. (2009). First observation of phase transformation of all four fe_2O_3 phases ($\Gamma \rightarrow$ E $\rightarrow$ B $\rightarrow$ A-Phase). *J. Am. Chem. Soc.* 131, 18299–18303. doi: 10.1021/ja9046069

Sala, A., Marchetto, H., Qin, Z. H., Shaikhutdinov, S., Schmidt, T., and Freund, H. J. (2012). Defects and inhomogeneities in Fe_3O_4(111) Thin film growth on Pt(111). *Phys. Rev. B* 86:155430. doi: 10.1103/PhysRevB.86.155430

Schöttner, L., Ovcharenko, R., Nefedov, A., Voloshina, E., Wang, Y., Sauer, J., et al. (2019). Interaction of Water Molecules with the α-Fe_2O_3(0001) surface: a combined experimental and computational study. *J. Phys. Chem. C* 123, 8324–8335. doi: 10.1021/acs.jpcc.8b08819

Shaikhutdinov, S. K., Ritter, M., Wang, X. G., Over, H., and Weiss, W. (1999). Defect structures on epitaxial Fe_3O_4(111) films. *Phys. Rev. B* 60, 11062–11069. doi: 10.1103/PhysRevB.60.11062

Shaikhutdinov, S. K., and Weiss, W. (1999). Oxygen pressure dependence of the α-Fe_2O_3(0001) surface structure. *Surf. Sci.* 432, L627–L634. doi: 10.1016/S0039-6028(99)00643-3

Shimizu, T. K., Jung, J., Kato, H. S., Kim, Y., and Kawai, M. (2010). Termination and Verwey transition of the (111) surface of magnetite studied by scanning tunneling microscopy and first-principles calculations. *Phys. Rev. B* 81:235429. doi: 10.1103/PhysRevB.81.235429

Stanka, B., Hebenstreit, W., Diebold, U., and Chambers, S. A. (2000). Surface reconstructions of Fe_3O_4(001). *Surf. Sci.* 448, 49–63. doi: 10.1016/S0039-6028(99)01182-6

St. Petkov, P., Vayssilov, G. N., Liu, J., Shekhah, O., Wang, Y., Wöll, C., et al. (2012). Defects in MOFs: a thorough characterization. *ChemPhysChem*. 13, 2025–2029. doi: 10.1002/cphc.201200222

Tang, Y., Qin, H., Wu, K., Guo, Q., and Guo, J. (2013). The reduction and oxidation of Fe_2O_3(0001) surface investigated by scanning tunneling microscopy. *Surf. Sci.* 609, 67–72. doi: 10.1016/j.susc.2012.11.005

Tarrach, G., Bürgler, D., Schaub, T., Wiesendanger, R., and Güntherodt, H. J. (1993). Atomic surface structure of Fe_3O_4(001) in different preparation stages studied by scanning tunneling microscopy. *Surf. Sci.* 285, 1–14. doi: 10.1016/0039-6028(93)90908-3

Thevuthasan, S., Kim, Y. J., Yi, S. I., Chambers, S. A., Morais, J., Denecke, R., et al. (1999). Surface structure of MBE-grown a-Fe_2O_3(0001) by intermediate-energy X-ray photoelectron diffraction. *Surf. Sci.* 425, 276–286. doi: 10.1016/S0039-6028(99)00200-9

Tinkle, M., and Dumesic, J. A. (1987). Isotopic exchange measurements of the rates of adsorption desorption and interconversion of CO and CO_2 over chromia-promoted magnetite - implications for water-gas shift. *J. Catal.* 103, 65–78. doi: 10.1016/0021-9517(87)90093-5

Trainor, T. P., Chaka, A. M., Eng, P. J., Newville, M., Waychunas, G. A., Catalano, J. G., et al. (2004). Structure and reactivity of the hydrated hematite (0001) surface. *Surf. Sci.* 573, 204–224. doi: 10.1016/j.susc.2004.09.040

Verwey, E. J. W. (1939). Electronic conduction of magnetite (Fe_3O_4) and its transition point at low temperatures. *Nature* 14, 327–328. doi: 10.1038/144327b0

Wang, X. G., Weiss, W., Shaikhutdinov, S. K., Ritter, M., Petersen, M., Wagner, F., et al. (1998). The hematite (α-Fe_2O_3) (0001) surface: evidence for domains of distinct chemistry. *Phys. Rev. Lett.* 81, 1038–1041. doi: 10.1103/PhysRevLett.81.1038

Wang, Y., and Wöll, C. (2017). IR spectroscopic investigations of chemical and photochemical reactions on metal oxides: bridging the materials gap. *Chem. Soc. Rev.* 46, 1875–1932. doi: 10.1039/C6CS00914J

Wang, Y., Xia, X., Urban, A., Qiu, H., Strunk, J., Meyer, B., et.al. (2007). Tuning the reactivity of oxide surfaces by charge - accepting adsorbates. *Angew. Chem. Int. Ed.* 46, 7315–7318. doi: 10.1002/anie.200702815

Wei, X., Shao, B., Zhou, Y., Li, Y., Jin, C., Liu, J., et al. (2018). Geometrical structure of the gold–iron(iii) oxide interfacial perimeter for co oxidation. *Angew. Chem.* 130, 11459–11463. doi: 10.1002/ange.201805975

Weiss, W., and Ranke, W. (2002). Surface chemistry and catalysis on well-defined epitaxial iron-oxide layers. *Prog. Surf. Sci.* 70, 1–151. doi: 10.1016/S0079-6816(01)00056-9

Wiesendanger, R., Shvets, I. V., Bürgler, D., Tarrach, G., Güntherodt, H. J., Coey, J. M. D., et al. (1992). Topographic and magnetic-sensitive scanning tunneling microscope study of magnetite. *Science* 255, 583–586. doi: 10.1126/science.255.5044.583

Wright, J. P., Attfield, J. P., and Radaelli, P. G. (2002). Charge ordered structure of magnetite Fe_3O_4 below the verwey transition. *Phys. Rev. B* 66:214422. doi: 10.1103/PhysRevB.66.214422

Xu, M., Noei, H., Fink, K., Muhler, M., Wang, Y., and Wöll, C. (2012). The surface science approach for understanding reactions on oxide powders: the importance of ir spectroscopy. *Angew. Chem. Int. Ed.* 51, 4731–4734. doi: 10.1002/anie.201200585

Yamamoto, S. (2010). Water adsorption on α-Fe_2O_3(0001) at near ambient conditions. *J. Phys. Chem. C* 114, 2256–2266. doi: 10.1021/jp909876t

Yang, C., and Wöll, C. (2017). Ir spectroscopy applied to metal oxide surfaces: adsorbate vibrations and beyond. *Adv. Phys.* 2, 373–408. doi: 10.1080/23746149.2017.1296372

Yang, C., Yin, L.-L., Bebensee, F., Buchholz, M., Sezen, H., Heissler, S., et al. (2014). Chemical activity of oxygen vacancies on ceria: a combined experimental and theoretical study on Ceo_2(111). *Phys. Chem. Chem. Phys.* 16, 24165–24168. doi: 10.1039/C4CP02372B

Yang, C., Yu, X., Heißler, S., Nefedov, A., Colussi, S., Llorca, J., et al. (2017b). Surface faceting and reconstruction of ceria nanoparticles. *Angew. Chem. Int. Ed.* 56, 375–379. doi: 10.1002/anie.201609179

Yang, C., Yu, X., Heißler, S., Weidler, P. G., Nefedov, A., Wang, Y., et al. (2017a). O_2 activation on ceria catalysts - the importance of substrate crystallographic orientation. *Angew. Chem. Int. Ed.* 56, 16399–16404. doi: 10.1002/anie.201709199

Yu, X. J., Zhang, Z., Yang, C., and Wöll, C. (2016). Interaction of formaldehyde with the rutile Tio_2(110) surface: a combined experimental and theoretical study. *J. Phys. Chem. C* 120, 12626–12636. doi: 10.1021/acs.jpcc.6b03689

Zecchina, A., Scarano, D., and Reller, A. (1988). Infrared spectra of CO adsorbed on prismatic faces of α-Fe_2O_3. *J. Chem. Soc. Faraday Transac. 1: Phys. Chem. Condens. Phases* 84, 2327–2333. doi: 10.1039/f19888402327

Zhu, L., Yao, K. L., and Liu, Z. L. (2006). First-principles study of the polar (111) surface of Fe_3O_4. *Phys. Rev. B* 74:035409. doi: 10.1103/PhysRevB.74.035409

Zhu, M., and Wachs, I. E. (2016). Resolving the reaction mechanism for H_2 formation from high-temperature water–gas shift by chromium–iron oxide catalysts. *ACS Catal.* 6, 2827–2830. doi: 10.1021/acscatal.6b00659

Conflict of Interest Statement: The authors declare that the research was conducted in the absence of any commercial or financial relationships that could be construed as a potential conflict of interest.

frontiers in Chemistry

ORIGINAL RESEARCH
published: 18 June 2019
doi: 10.3389/fchem.2019.00436

The Structure of Oxygen Vacancies in the Near-Surface of Reduced CeO_2 (111) Under Strain

Zhong-Kang Han[1†‡], *Lei Zhang*[2†], *Meilin Liu*[2], *Maria Verónica Ganduglia-Pirovano*[3*] and *Yi Gao*[1,4*]

[1] Shanghai Institute of Applied Physics, Chinese Academy of Sciences, Shanghai, China, [2] Center for Innovative Fuel Cell and Battery Technologies, School of Materials Science and Engineering, Georgia Institute of Technology, Atlanta, GA, United States, [3] Institute of Catalysis and Petrochemistry, Spanish National Research Council (CSIC), Madrid, Spain, [4] Zhangjiang Laboratory, Shanghai Advanced Research Institute, Chinese Academy of Sciences, Shanghai, China

Strain has been widely recognized as important for tuning the behavior of defects in metal oxides since properties such as defect configuration, electronic structure, excess charge localization, and local atomic distortions may be affected by surface strain. In CeO_2, the most widely used promoter in three-way catalysts and solid state electrolyte in fuel cells, the behaviors of oxygen vacancies, and associated Ce^{3+} polarons are crucial in applications. Recent STM and AFM investigations as well as DFT-based calculations have indicated that in the near-surface of CeO_2 (111), at low temperatures and vacancy concentrations, subsurface oxygen vacancies are more stable than surface ones, and the Ce^{3+} ions are next-nearest neighbors to both types of vacancies, which can be explained by the better ability of the system to relax the lattice strain induced by vacancy formation as well as by the excess charge localization. The results also revealed that the interaction between first-neighbor vacancies is repulsive. In this work, the relative stability of surface and subsurface oxygen vacancies at the CeO_2 (111) surface under in-plane strain is investigated by means of DFT+*U* calculations. The tensile strain favors isolated surface vacancies with next nearest neighbor polarons, whereas isolated subsurface vacancies with nearest neighbor polarons are energetically favored under compressive strain. In addition, the formation of both surface and subsurface dimers is favored over having corresponding isolated species under compressive strain, which implies the possibility of controlling the formation of vacancy clusters using strain. In many applications, ceria is employed as a supported thin film or within a heterostructure in which ceria can be strained, and this study shows that strain can be a useful handle to tune properties of such materials.

Keywords: CeO_2, density functional theory, oxygen vacancy, strain, surface structures

Edited by:
Zhuhua Zhang,
Nanjing University of Aeronautics and Astronautics, China

Reviewed by:
Liangzhi Kou,
Queensland University of Technology, Australia
Luqing Wang,
Rice University, United States

***Correspondence:**
Maria Verónica Ganduglia-Pirovano
vgp@icp.csic.es
Yi Gao
gaoyi@sinap.ac.cn

†These authors have contributed equally to this work

‡Present address:
Zhong-Kang Han,
Fritz Haber Institute of the Max Planck Society, Berlin, Germany

Specialty section:
This article was submitted to Physical Chemistry and Chemical Physics, a section of the journal Frontiers in Chemistry

Received: *03 March 2019*
Accepted: *28 May 2019*
Published: *18 June 2019*

Citation:
Han Z-K, Zhang L, Liu M, Ganduglia-Pirovano MV and Gao Y (2019) The Structure of Oxygen Vacancies in the Near-Surface of Reduced CeO_2 (111) Under Strain. Front. Chem. 7:436. doi: 10.3389/fchem.2019.00436

INTRODUCTION

Ceria is widely used as solid oxide fuel cell electrolyte (Inaba and Tagawa, 1996) and in catalytic applications (Trovarelli, 1996; Fu et al., 2003; Vayssilov et al., 2011; Montini et al., 2016) largely due to its facile oxygen vacancy formation and diffusion, either within the bulk or at its surfaces. It has been previously reported (Skorodumova et al., 2002), and later supported by subsequent research (Ganduglia-Pirovano et al., 2007, 2009; Li et al., 2009; Shoko et al., 2010; Jerratsch et al., 2011; Paier et al., 2013), that the formation of an intrinsic neutral oxygen vacancy in ceria is accompanied by the formation of two nearby polarons (Ce^{3+} or Ce'_{Ce} in Kröger-Vink notation), which result from the transfer of two electrons originally residing in 2*p* states of the missing oxygen ion to Ce 4*f* states of two cations. For oxygen vacancies in the near-surface of CeO_2 (111), it has been predicted from Density Functional Theory (DFT) calculations that the two Ce^{3+} polarons are not necessarily NN (Nearest-Neighbor) to the oxygen vacancies, but rather prefer to locate at NNN (Next-Nearest-Neighbor) cationic sites (Ganduglia-Pirovano et al., 2007, 2009; Li et al., 2009; Paier et al., 2013), which has been later validated in Scanning Tunneling Microscope (STM) experiments (Jerratsch et al., 2011). The preference for the NNN positions upon localization of the excess charge has been explained by the better ability of the system to relax the lattice strain induced by the presence of the vacancies as well as by the excess charge localization; a Ce^{3+} ion is more spacious than its Ce^{4+} counterpart and at NN sites Ce^{3+} – O bonds would be compressed (Ganduglia-Pirovano et al., 2009). Moreover, the preferred sites for oxygen vacancies in the near-surface of CeO_2 (111) (Esch et al., 2005; Castleton et al., 2007; Torbrügge et al., 2007; Ganduglia-Pirovano et al., 2009; Li et al., 2009; Jerratsch et al., 2011; Murgida and Ganduglia-Pirovano, 2013; Sutton et al., 2015) as well as the type of interactions between them (Namai et al., 2003; Esch et al., 2005; Torbrügge et al., 2007; Conesa, 2009; Murgida and Ganduglia-Pirovano, 2013; Kullgren et al., 2014, 2017; Han et al., 2018), have also been assessed. Under zero applied stress, isolated subsurface vacancies are more stable than surface ones, and the interaction between nearest neighbor vacancies at the surface or in the subsurface is repulsive.

As for isolated oxygen vacancies in bulk ceria, most theoretical studies reported that the NNN Ce^{3+} locations are also preferred under zero applied stress (Kullgren et al., 2012; Allen and Watson, 2014; Murgida et al., 2014; Wang et al., 2014; Grieshammer et al., 2016; Han et al., 2017), i.e., at the calculated equilibrium volume of CeO_2. Moreover, it has been demonstrated that the ground-state configuration varies whether tensile or compressive stress is applied (Arapan et al., 2015), namely, at large volumes, both Ce^{3+} ions are in the second coordination sphere of the vacancy, and at small volumes, they are in the first. Additionally, it has been experimentally found that the lattice parameter of reduced ceria in the fluorite-type cubic structure is expanded (Rossignol et al., 2003), which has been consistently reproduced in DFT calculations (Arapan et al., 2015) that predict that the averaged lattice parameter over different configurations for the pair of Ce^{3+}'s is slightly larger than the equilibrium lattice parameter of perfect ceria.

Furthermore, for doped ceria with three-valent dopants (Andersson et al., 2006; Wang and Cormack, 2012; Grieshammer et al., 2016), the dependence of the location of the dopants on the dopant's ionic radius has been reported, in which larger ions such as La prefer NNN sites to vacancies, and smaller ions such as Gd prefer NN sites. It has been argued that it is the balance between repulsive elastic and attractive electronic contributions to the interaction between dopants and vacancies what determines the NN or NNN site preference (Andersson et al., 2006), and, as in the case of undoped ceria mentioned above, applied tensile or compressive stress can change the site preferences (Wang and Cormack, 2012). In addition, changes in the lattice parameter upon ceria doping have been reported, as, for example, the one of Gd-doped ceria (Artini et al., 2014; Žguns et al., 2019) that shows a maximum as a function of Gd content.

Strain in ceria has received considerable attention because oxygen vacancy migration can be modified through strain, which is most relevant for tuning ion conduction in ceria-based applications (De Souza et al., 2012; Hinterberg et al., 2013; Sun et al., 2015). It is fair to say that it is practically inevitable to avoid that ceria surfaces will experience strain effects, either induced by the lattice mismatch when created as a thin film on a substrate (Duchon et al., 2013; Luches et al., 2014), or when reduced (Grieshammer et al., 2016), particularly due to the higher stability of oxygen vacancies in the near-surface as compared to deeper layers (Duchon et al., 2013; Murgida and Ganduglia-Pirovano, 2013; Sutton et al., 2015; Olbrich et al., 2017) that are accompanied by the formation of Ce^{3+} ions which induces a near-surface lattice expansion. For reduced ceria nanoparticles, mainly expansions of the lattice have been observed, which were associated to the presence of Ce^{3+} cations (Rossignol et al., 2003; Wang and Cormack, 2012; Allen and Watson, 2014; Arapan et al., 2015), but also lattice contractions have been reported (Wang and Cormack, 2012), which were attributed to the additional pressure caused by the surface tension between the crystallite and the ambient atmosphere as the nanoparticle size decreases. Despite these efforts, the effect of applying a tensile or compressive stress to the reduced CeO_2 (111) surface has not yet been comprehensively studied.

In this article, using DFT-based methods, we systematically investigate the effect of applied stress on the reduced CeO_2 (111) surface and address how strain affects the relative stability of isolated surface and subsurface oxygen vacancies, the formation of vacancy pairs, and the localization of the excess charge. It turns out that, depending on strain, surface vacancies can be more stable than subsurface ones, the interaction between first nearest neighbor vacancies in the near-surface can be attractive, and different localized charge distributions can be attained.

METHODOLOGY

First-principles spin-polarized DFT-based calculations were carried out employing the VASP (Vienna *Ab-initio* Simulation Package) code. The DFT+*U* methodology (Dudarev et al., 1998) was used with the generalized gradient approximation (GGA) of Perdew-Burke-Ernzerhof (PBE) (Perdew et al., 1996), and an effective *U*-value of 5.0 eV. The value of the *U* parameter—necessary to describe localized electrons associated to Ce^{3+} ions—lies within the range of suitable values to describe reduced ceria-based systems (Castleton et al., 2007). We used projector augmented wave (PAW) potentials (Kresse and Joubert, 1999) with Ce (4*f*, 5*s*, 5*p*, 5*d*, 6*s*) and O (2*s*, 2*p*) electrons as valence states, and a plane-wave cutoff of 400 eV. The CeO_2 (111)

surface was modeled using three O-Ce-O trilayers separated by 15 Å vacuum space (i.e., a nine atomic layer slab) with both 5×5 and 2×2 periodicities. A $1 \times 1 \times 1$ ($3 \times 3 \times 1$) Gamma-centered Monkhorst-Pack grid was used for the *k*-point sampling of the Brillouin zone of the 5×5 (2×2) slab. Stress ranging from -5% (compressive) to $+5\%$ (tensile) has been applied to the CeO_2 (111) surface, i.e., to the two vectors which define the surface unit cell. It should be mentioned that for compressive stress, experiments show that CeO_2 transforms from a cubic fluorite-type structure to an orthorhombic cotunnite-type ($PbCl_2$) structure at a pressure of 31 GPa (Duclos et al., 1988). However, in this study, the underlying fluorite lattice is prevented from undergoing a phase transition. In all geometry optimizations, all atoms in the bottom trilayer were kept fixed after stress had been applied, whereas the rest of the atoms were allowed to fully relax. For all strained surfaces, the interlayer spacings within the bottom trilayer correspond to those of a bulk-truncated CeO_2 (111) under zero stress, and the in-plane atom positions correspond to those in the corresponding strained CeO_2 bulk.

To systematically investigate how strain affects the relative stability of isolated surface and subsurface oxygen vacancies in the near-surface of CeO_2 (111), as well as the formation of vacancy pairs, and the localization of the excess charge, reduced strained slabs were created. Isolated surface and subsurface vacancies with different configurations for the Ce^{3+}'s were considered with both 5×5 and 2×2 periodicities. Vacancies were placed near the surface, i.e., within the outermost trilayer, and the Ce^{3+}'s within the (two) outermost cationic plane(s) for the 5×5 (2×2) periodicity. Moreover, using the larger 5×5 surface unit cell, nearest and next-nearest neighbor surface and subsurface vacancy pairs with various configurations for the Ce^{3+}'s were considered. In order to obtain distinct configurations of the reduced Ce^{3+} sites, a two-step relaxation procedure was applied. In the first step, we replaced the selected Ce^{4+} with Ce^{3+} ions, i.e., for the latter we used PAW potentials for which the $4f^{\,1}$ state was moved to the core, and performed non-spin polarized calculations. The so-obtained relaxed structure was further optimized using the regular Ce^{4+} PAW potentials and spin-DFT. We limit the discussion to high-spin states because the difference between these states and any other spin state is <0.01 eV (Keating et al., 2009). The oxidation state of a given Ce atom has been estimated by considering its local magnetic moment (the difference between up and down spin on the atoms), which can be estimated by integrating the site- and angular momentum-projected spin-resolved density of states over spheres with radii chosen as the Wigner–Seitz radii of the PAW potentials. For reduced Ce ions, the occupation of Ce *f* states is close to one, and the magnetic moment is $\sim 1\ \mu_B$. Hence, those ions are referred to as Ce^{3+} ($4f^{\,1}$).

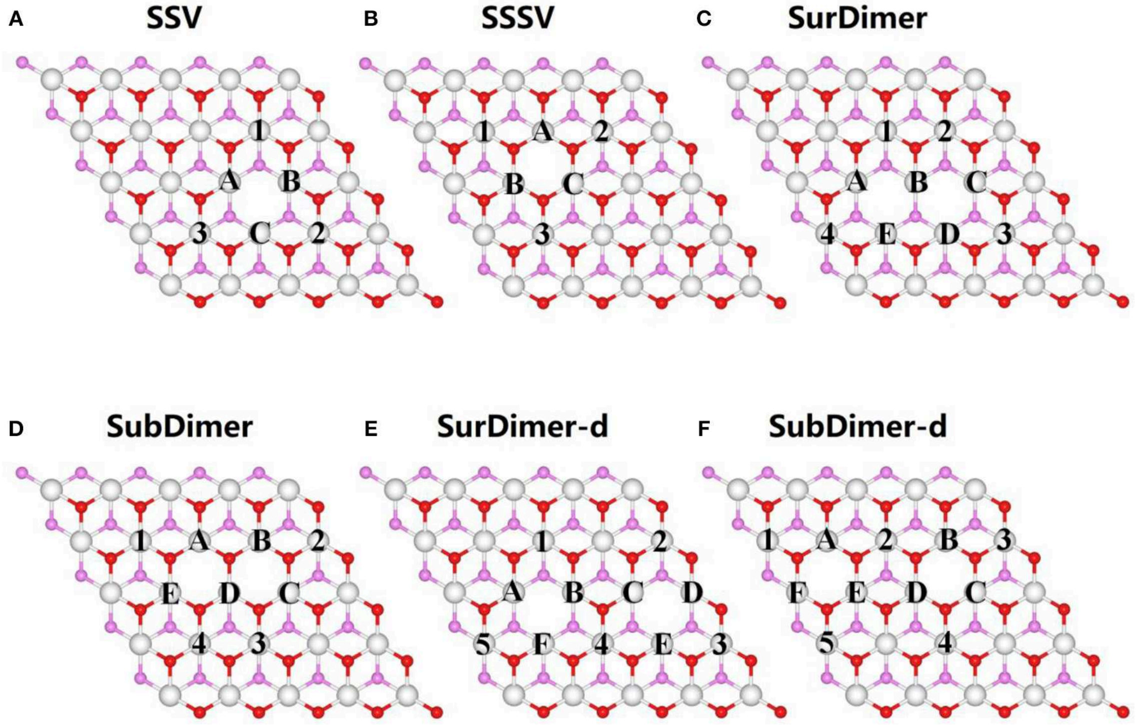

FIGURE 1 | Structural model of the CeO_2 (111) unit cell with 5×5 periodicity. **(A)** single surface vacancy, SSV, **(B)** single subsurface vacancy, SSSV, **(C)** nearest neighbor surface oxygen vacancy dimer, SurDimer, **(D)** nearest neighbor subsurface oxygen vacancy dimer, SubDimer, and **(E)** third-nearest neighbor surface oxygen vacancy pair, SurDimer-d. **(F)** third-nearest neighbor surface oxygen vacancy pair, SubDimer-d. Ce cations in the outermost trilayer are shown as white balls. Surface and subsurface oxygen atoms are shown as red and pink balls, respectively. The labeled cerium atoms denote possible Ce^{3+} locations on nearest-neighbor (A, B, C, D....) or next-nearest-neighbor (1, 2, 3, 4....) sites to the vacancies. Only the three outermost atomic layers are shown for simplicity.

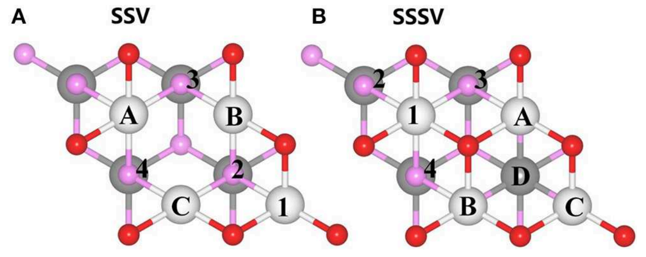

FIGURE 2 | Structural model of the CeO_2 (111) unit cell with 2×2 periodicity. **(A)** single surface vacancy, SSV, and **(B)** single subsurface vacancy, SSSV. The color scheme for atoms and vacancies corresponds to that used in **Figure 1**. The labeling scheme for the captions also corresponds to that in **Figure 1**. Only the five outermost atomic layers are shown for simplicity.

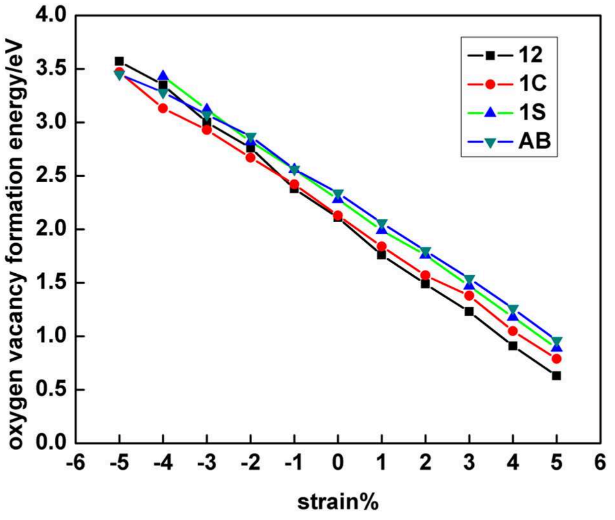

FIGURE 3 | Single surface oxygen vacancy (SSV) formation energy at the 5 × 5 CeO_2 (111) surface as a function of strain and for distinct polaronic structures, which are labeled according to the location of the two Ce^{3+} as shown in **Figure 1**.

RESULTS AND DISCUSSION

We have modeled the reduced CeO_2 (111) surface by removing one single surface (SSV) or subsurface (SSSV) vacancy from a supercell with 5 × 5 and 2 × 2 periodicities, as shown in **Figures 1**, **2**, respectively. Nearest (NN) and next-nearest neighbor (NNN) Ce ions to vacancies are labeled with uppercase letters (A, B, C, D, ...) and numerals (1, 2, 3, 4, ...), respectively. Employing the larger supercell, first-neighbor vacancy dimers at the surface or in the subsurface (SurDimer and SubDimer), as well as corresponding pairs with a vacancy separation corresponding to that of third-nearest neighbors in the oxygen plane (SurDimer-d and SubDimer-d), have also been considered (cf. **Figure 2**). Stress ranging from −5% (compressive) to +5% (tensile) has been applied to both supercells as mentioned in section Methodology. It is known that under zero applied stress, NNN sites in the outermost cerium layer are the energetically preferred locations of the Ce^{3+} ions, but they would rather be in NNN sites of a deeper layer than next to a vacancy in the outermost one (Murgida and Ganduglia-Pirovano, 2013). Since under applied stress preferences may change, for the strained surfaces with 5 × 5 (**Tables S1–S7**) or 2 × 2 (**Table S8**) periodicity, vacancy structures corresponding to the most relevant combinations of the possible locations of the Ce^{3+} ions have been considered.

The averaged vacancy formation energy (E_f) was calculated as:

$$E_f = \frac{1}{n}[E_{defect} + \frac{n}{2}E_{O_2} - E_{perfect}] \quad (1)$$

where E_{defect} and $E_{perfect}$ are the total energies of the (relaxed) defective (reduced) and perfect (clean) slabs, respectively, n is the number of oxygen vacancies, and E_{O_2} is the total energy of the isolated O_2 molecule in its triplet ground state.

Low Vacancy Concentration

Stability, Structural Relaxation, and Excess Charge Localization

Figures 3, **4** summarize the calculated vacancy formation energy for all 5 × 5 structures with a SSV and a SSSV vacancy, respectively. For the surface vacancy, configurations with both Ce^{3+} ions in the outermost cationic plane and either in the first coordination shell (AB), in the second (12), or one in each shell (1C) were considered (**Figure 1**). In addition, a configuration with both Ce^{3+} ions in the second coordination shell, but one in the outermost cationic plane and the other one in the plane beneath, was considered (1S) (**Figure S1**). Under 0% tension, the 12 configuration is by 0.23 eV more stable than the AB one (**Figure 3**), in line with previous works (Ganduglia-Pirovano et al., 2009; Li et al., 2009; Murgida and Ganduglia-Pirovano, 2013; Han et al., 2018). As the tensile strain is increased from 0 to +5%, the 12 >1C >1S >AB stability trend does not change although the difference between the most stable configuration (12) and the least stable one (AB) becomes larger (0.33 eV under +5% strain, **Table S1**). In contrast, if we look at the surface under large compressive strain (≥ −5%), the trend is reversed, i.e., AB >1C>12; (the 1S configuration is not stable); under −5% strain, the configuration with both Ce^{3+} ions in the first coordination shell (AB) is by 0.12 eV more stable than that with the Ce^{3+} ions in the second coordination shell (12).

For the subsurface vacancy, configurations with both Ce^{3+} ions in the outermost cationic plane and either in the first coordination shell (AB) or in the second (12), or one in each shell (1C), as well as with both Ce^{3+} ions in the second coordination shell, but one in the outermost cationic plane and the other one in the plane beneath (1S), were also considered (cf. **Figure 1** and **Figure S1**). The behavior of the SSSV is comparable to that of the SSV, although the slopes of the energy-strain curves for the SSSV are somewhat smaller than those of the SSV (cf. **Figures 3**, **4**). Under 0% tension, the SSSV-12 configuration is by 0.32 eV more stable than the AB one, in line with previous works (**Figure 4**) (Ganduglia-Pirovano et al., 2009; Li et al., 2009; Murgida and Ganduglia-Pirovano, 2013; Han et al., 2018). The

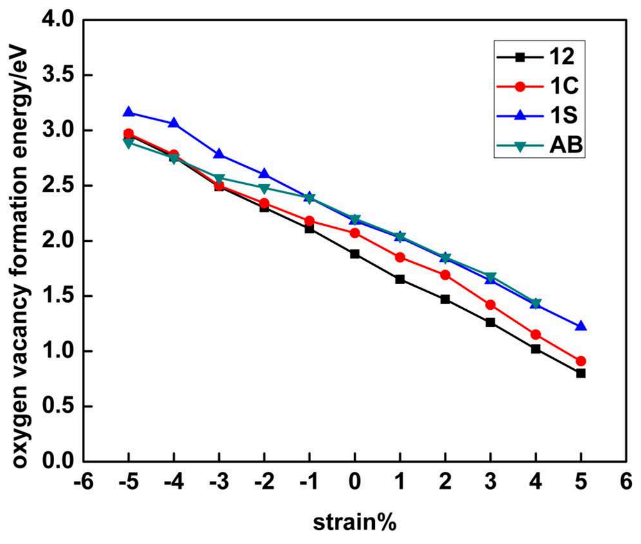

FIGURE 4 | Single subsurface oxygen vacancy (SSSV) formation energy at the 5 × 5 CeO_2 (111) surface as a function of strain and for distinct polaronic structures, which are labeled according to the location of the two Ce^{3+} as shown in **Figure 1**.

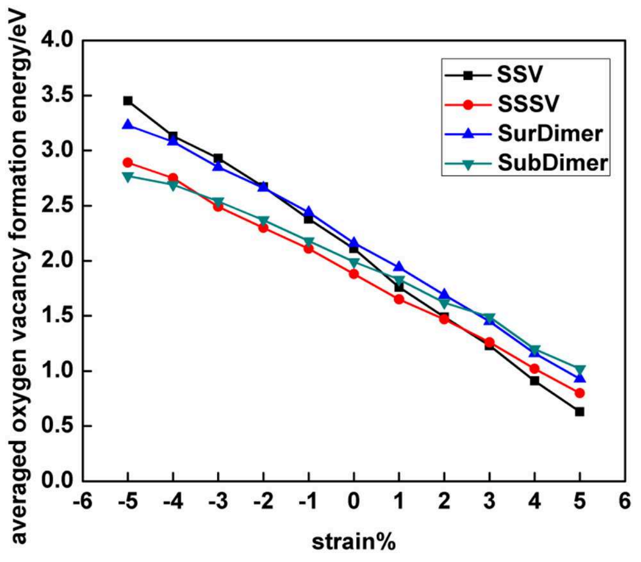

FIGURE 5 | The averaged oxygen vacancy formation energy of the most stable SSV, SSSV, SurDimer, and SubDimer structures with 5 × 5 periodicity as a function of strain.

12 >1C >1S >AB stability trend obtained under 0% tension, does not change upon increasing the tensile strain from 0 to +4% (the AB configuration is not stable under +5% strain), but the difference between the 12 and AB configurations becomes larger, for example, it is 0.42 eV under +4% strain (**Table S2**). If the surface is compressed, for example by −5%, the most stable configuration has both Ce^{3+} ions in the first coordination shell (AB), and that with the Ce^{3+} ions in the second coordination shell (12), is by 0.07 eV less stable.

Before analyzing the origin of the observed transitions between NNN-NNN (12) and NN-NN (AB) Ce^{3+} configurations for both vacancy types under large compressive strain (cf. section Electronic Density of States), we first discuss how their relative stability is influenced by strain. **Figure 5** collects the results of the most stable SSV and SSSV configurations for each value of the applied stress (cf. **Figures 3**, **4**, and **Tables S1, S2**, **S7**). In agreement with the literature (Ganduglia-Pirovano et al., 2009; Li et al., 2009; Murgida and Ganduglia-Pirovano, 2013), we find that under 0% tension, the subsurface vacancy position is by 0.23 eV more stable than the surface one. Under compressive strain, from 0 to −5%, the SSSV remains more stable than the SSV, but the difference becomes larger as the compression increases, for example under −5% compression, the SSSV is by 0.56 eV more stable than the SSV. However, as the tensile tension increases from +3%, the relative stability reverses and the SSV becomes more stable.

As vacancy-induced lattice relaxations are known to play an important role in the stabilization of both a particular Ce^{3+} configuration and the subsurface vacancy position in the near-surface of CeO_2 (111) under 0% strain, (Ganduglia-Pirovano et al., 2009; Li et al., 2009) we analyze their effects on the strained surfaces. To this end, we define two contributions to the vacancy formation energy, $E_f = E_b + E_r$ (cf. Equation 1), namely, the bond breaking energy, E_b, as the energy cost to create a vacancy without allowing for lattice relaxations, i.e., $E_b = E_{defect}^{unrelax} + \frac{1}{2}E_{O_2} - E_{perfect}$, and the energy gained from the structural relaxation in the presence of the vacancy, E_r, i.e., $E_r = E_{defect}^{relax} - E_{defect}^{unrelax}$. In **Figure 6** and **Table S9**, we show how these different contributions depend on strain.

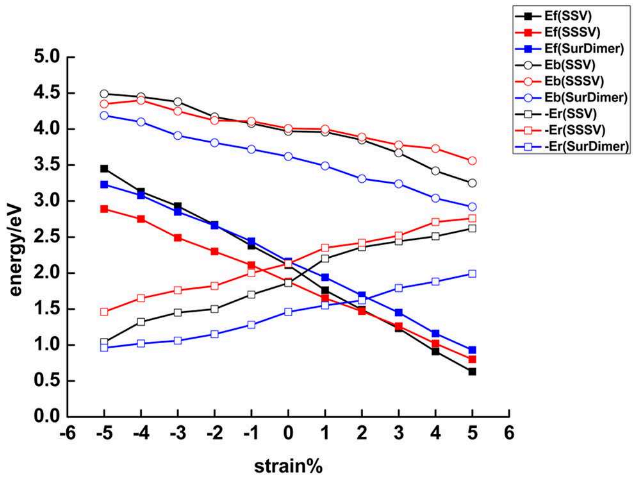

FIGURE 6 | The (average) near-surface oxygen vacancy formation energy, $E_f = E_b + E_r$, as a function of strain (5 × 5 periodicity). E_b is the energy cost to create a near-surface oxygen vacancy structure without allowing for lattice relaxations, i.e., the bond breaking energy, and E_r, the energy gained from lattice relaxations in the presence of the vacancies.

TABLE 1 | O–Ce bond lengths (in Å) between a surface oxygen atom at the fully oxidized strained CeO_2 (111) surface (5 × 5 periodicity), O_s, and its three nearest neighbor cerium atoms in the outermost cerium layer, Ce_1, as well as between a subsurface oxygen atom, O_{ss}, and its three (one) nearest neighbor cerium atoms in the first (second) cerium layer, Ce_1 (Ce_2).

Strain %	−5	−4	−3	−2	−1	0	+1	+2	+3	+4	+5
$O_s - Ce_1$	2.30	2.31	2.32	2.33	2.35	2.36	2.37	2.39	2.40	2.41	2.43
$O_{ss} - Ce_1$	2.29	2.30	2.32	2.33	2.35	2.36	2.38	2.40	2.41	2.43	2.45
$O_{ss} - Ce_2$	2.52	2.48	2.45	2.42	2.40	2.37	2.35	2.33	2.31	2.29	2.26

For both SSV and SSSV, E_b is largest for the highest compression and smallest for the largest tensile stress, i.e., the correlation between E_b and strain is negative. To create unrelaxed surface and subsurface oxygen vacancies, three Ce–O_s and four Ce–O_{ss} bonds, respectively, have to be cut. For the SSV, the Ce_1-O_s bond lengths (Ce_1 and O_s are in the outermost cationic and anionic layers, respectively) vary from 2.30 to 2.43 Å as the stress changes from −5 to +5% (**Table 1**), thus, the observed E_b vs. strain trend is in line with the weakening of the bonds upon increasing tensile strain. For the SSSV, the corresponding variations in the three Ce_1-O_{ss} bond lengths are practically identical to those of the SSV, but the Ce_2-O_{ss} bond (Ce_2 and O_{ss} are in the second cationic and anionic layers, respectively) is contracted from 2.52 (−5%) to 2.26 (+5%). In any case, the observed E_b vs. strain trend for the SSSV vacancy is in line with the weakening of the average Ce–O_{ss} bond length upon increasing tensile strain, which varies from 2.35 (−5%) to 2.40 (+5%).

Moreover, we observe that the E_b vs. strain curves for both the SSV and the SSSV resemble straight lines but with a different slope, i.e., the curves cross (**Figure 6**). Under the largest tensile strain (+5%), three Ce_1-O_s bonds of 2.43 Å for the SSV have to be cut (**Table 1**), whereas for the SSSV they are three Ce_1-O_{ss} bonds of 2.45 Å and one particularly strong Ce_2-O_{ss} bond of 2.26 Å; hence, creating an unrelaxed SSV is preferred. As already mentioned, upon compression the Ce_2-O_{ss} bond expands in such a way that for the largest compressive strain (−5%), three Ce–O_s bonds with an average distance of 2.30 Å and four Ce–O_{ss} ones of 2.35 Å have to be cut to create an unrelaxed SSV and SSSV, respectively (**Table 1**). The latter is energetically preferred.

In **Figure 6** we further compare the energy gained from structural relaxation in the presence of oxygen vacancies, E_r ($<$ 0), as a function of surface strain. The E_r vs. strain curves also resemble straight lines with a different slope for the SSV and SSSV, but the curves do not cross within the interval of −5 to +5% strain values. The lattice relaxations are the result of both the presence of the oxygen vacancy, which for example induces the neighboring O (Ce) ions to move toward (away from) the vacancy, and the localization of the excess charge driving the $Ce^{4+} \rightarrow Ce^{3+}$ reduction of two cations. For isolated oxygen vacancies in bulk ceria under strain (De Souza et al., 2012), it has been shown that the energy gained due to the displacements of the atoms upon relaxation increases almost linearly with the increasing of the tensile stress, independent of the sites on which the excess charge is localized, but the gain is more pronounced when the localization occurs at NNN cationic sites to the vacancy. Similarly, for both SSV and SSSV vacancies in the near-surface of CeO_2 (111), the energy gained from structural relaxation is smallest for the biggest compressive strain and largest for the highest tensile stress, i.e., the correlation between the absolute value of $E_r$and strain is positive. We note that the energy gain is always largest for the SSSV within the −5 to +5% strain interval, which is related to the fact that the numbers of neighboring O and Ce ions that will be displaced upon the creation of a SSSV are larger than the corresponding ones for a SSV. Moreover, the relaxation energy gained from the localization of the excess charge also favors the SSSV; for the unrelaxed SSSV and SSV structures, the two excess electrons are equally shared by four and three NN Ce ions, respectively, and thus, the energy gained due to the $4\times Ce^{0.5+} \rightarrow 2\times Ce^{3+}$ charge localization in the case of the SSSV, is larger than the corresponding one for the SSV, namely, $3\times Ce^{0.\hat{6}+} \rightarrow 2\times Ce^{3+}$. Furthermore, with respect to the above-mentioned smallest gain in the relaxation energy for the largest compressive strain for both SSV and SSSV, we recall here –and address below– that the Ce^{3+} ions in the first coordination sphere are preferred when the surface is substantially compressed and then, it is expected that the contribution associated with the relocation of electrons will be lower when it occurs between first neighbors.

Summarizing, there is an almost linear correlation between both contributions to the oxygen vacancy formation and the surface strain. The correlation between the bond breaking energy, E_b, and strain, is negative and that between the absolute energy gained due to relaxation, –E_r, and strain is positive. The slopes of the almost linear E_b vs. strain and E_r vs. strain relationships are not the same for the SSV than for the SSSV. The preference for the SSSV under compressive strain and for the SSV under tensile strain ($>$3%) is the result of the different behaviors of the contributions to create the corresponding vacancies with strain. For example, for the −5% compressed surface, both E_b and E_r favor the SSSV by 0.14 and 0.42 eV, respectively, and thus, the SSSV is by 0.56 eV more stable than the SSV. However, for the +5% strained surface, E_b favors the SSV by 0.31 eV and E_r the SSSV by 0.14 eV, and, as a result, the SSV is by 0.17 eV more stable than the SSSV.

Electronic Density of States

The effects of strain on the distribution of the excess charge are also reflected in the calculated densities of states (DOS). In pure CeO_2, all valence Ce states, including the 4*f* states, are empty and the system is a wide gap insulator with a measured fundamental band gap of 6 eV between the valence and the conduction bands (Pfau and Schierbaum, 1994), which are formed predominantly by the O 2*p* and Ce 5*d* states, respectively. The vacant 4*f* states lie in the O_{2p}-Ce_{5d} gap. PBE+*U* underestimates the O_{2p}-Ce_{5d} gap of bulk CeO_2 by ∼12% (5.3 eV) (Da Silva et al., 2007). The formation of a pair of Ce^{3+} ions following the creation of an oxygen vacancy results in the appearance of split-off (defect) states of the initially empty Ce 4*f* band, lying inside the O_{2p}-Ce_{5d} gap below the Fermi level (Jerratsch et al., 2011). If the two Ce^{3+} ions occupy different cationic shells around the vacancy,

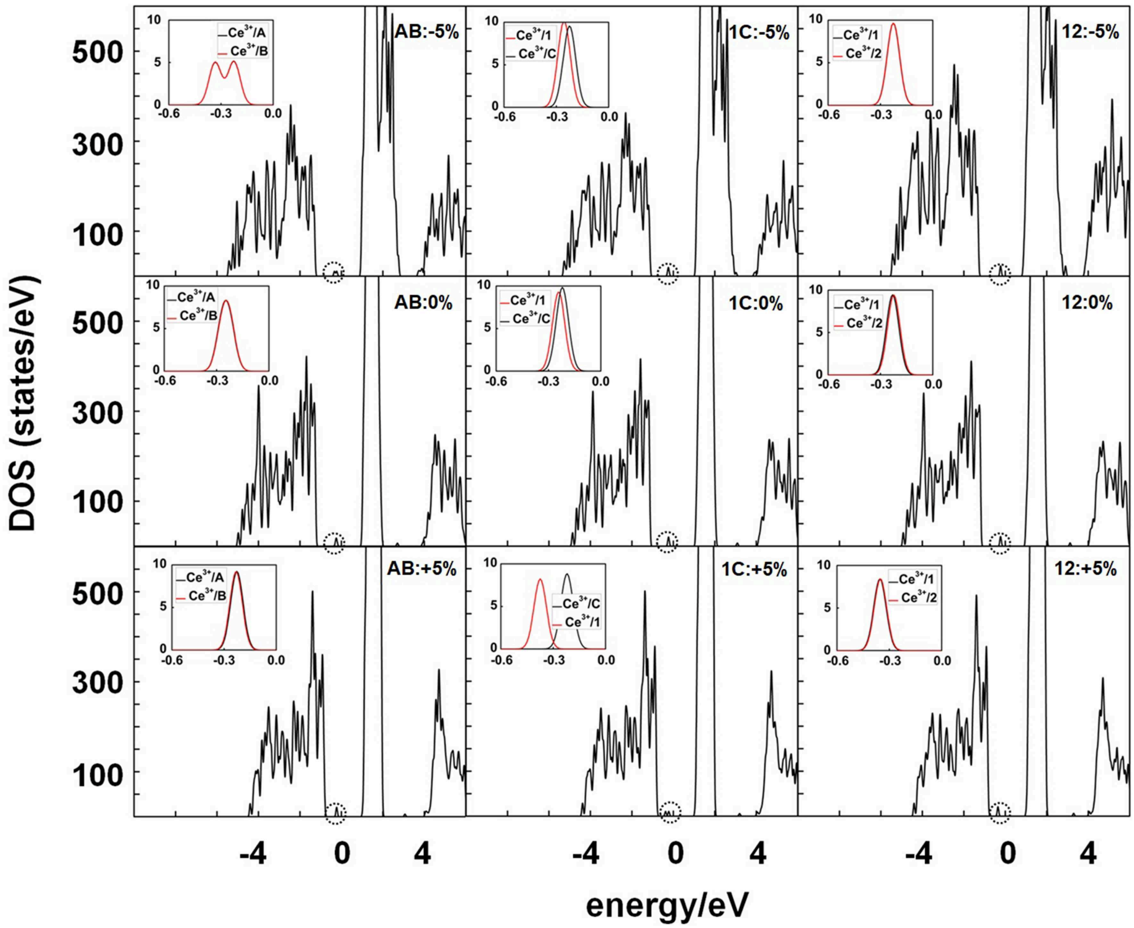

FIGURE 7 | Densities of states (DOS) summed over spin projections and all atoms for a SSV under −5, 0, and +5% strain with different Ce^{3+} configurations, namely, AB, 1C, and 12 and 5 × 5 periodicity. The Fermi level is set as the zero energy value, below which the states are occupied. The occupied Ce 4*f* states are marked with black dashed circles, which are shown magnified in the insets.

the resulting variation in the chemical environment leads to a splitting of the two filled Ce^{3+} *f* levels, which could be detected with STM spectroscopy (Jerratsch et al., 2011). The densities of states for the example of an SSV at the CeO_2 (111) surface with the Ce^{3+}s in either the 12, 1C, or AB configuration under −5, 0, or +5% strain (**Figure 7**) are discussed in the following.

In the 12 configuration, the two next-nearest neighbor Ce^{3+} ions have equal coordination number (CN = 7) and filled *f* orbitals with the same energy as they experience the same chemical environment, and hence no splitting of the *f* orbitals is expected; this is certainly observed for the 12 configurations within the −5 to +5% strain range (**Figure 7**; **Table S10**). Similarly, for the AB configuration with the two Ce^{3+} ions in nearest neighbor sites, and experiencing the same chemical environment (CN = 6), no splitting of the *f* orbitals is expected. However, two peaks are observed in the DOS for −5% compression with a splitting of the order of 0.16 eV. The reason for the splitting is not that the Ce^{3+}s are located in different environments but a hybridization of the polaronic states, which causes a spread of charges across both adjacent sites. That is, the polarons are no longer fully localized in one specific Ce site, rather, the polaronic charge is shared between the two sites in a sort of bonding/anti-bonding configuration (cf. isosurfaces in **Figure S2**). Finally, for the 1C configuration with one nearest and one next-nearest Ce^{3+} (CN = 6 and 7, respectively), we find a splitting of the *f* orbitals of the order of 0.1 eV for −5 and 0% strain, but increases to about 0.2 eV for +5% tensile strain (**Table S10**). Before discussing the changes in the positions of the occupied *f* states in the O_{2p}-Ce_{5d} gap as a consequence of in-plane strain here below, we note that both compressive and tensile strain decrease the O_{2p}-Ce_{5d} gap (**Figure 7**; **Table S10**), and that the width of the valence band widens (shrinks) as the lattice is compressed (expanded).

The position of the occupied *f* states in the O_{2p}-Ce_{5d} gap is hereby given as O_{2p}-Ce_{4f}, i.e., the difference between the eigenvalue of the lowest occupied *f* state and the top of the valence band. We note that, as the in-plane strain changes from −5 to +5%, the occupied *f* states are shifted toward the valence band (**Table S10**), but the amount by which they are shifted depends on the actual positions of the Ce^{3+} with respect to the

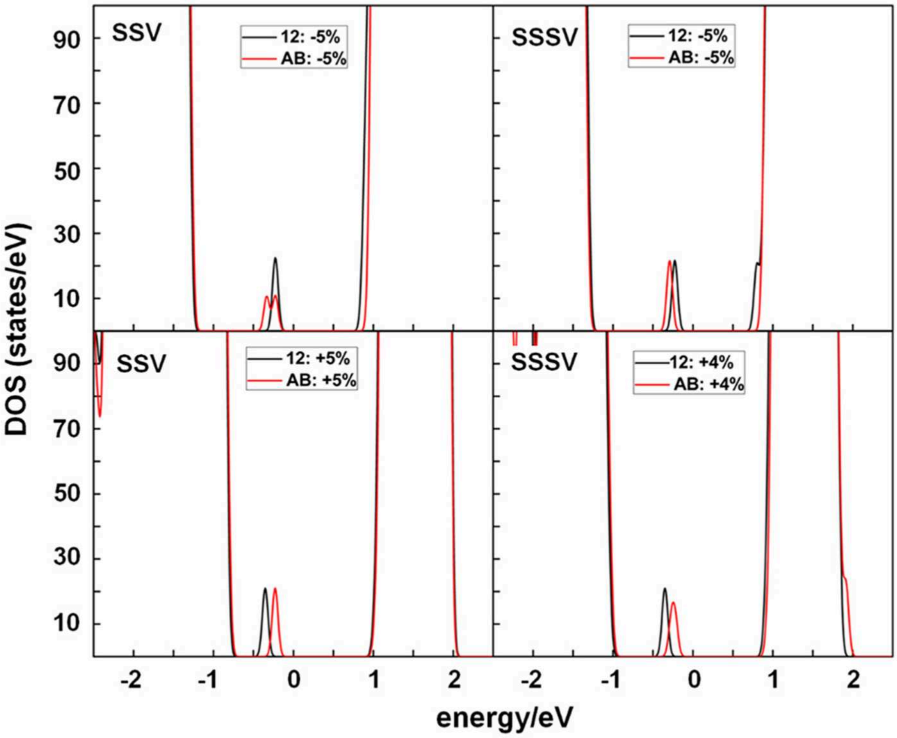

FIGURE 8 | Densities of states (DOS) summed over spin projections and all atoms for a SSV and SSSV under −5%, and +5%, or +4% strain with AB and 12 Ce^{3+} configurations and 5 × 5 periodicity. The Fermi level is set as the zero energy value, below which the states are occupied.

vacant site. **Figure 8** compares the total DOS of the strained SSV and SSSV with the AB and 12 configurations and shows that under surface compression, the characteristic polaron peaks of the AB configuration lie lower in energy than those of the 12 one, whereas under surface expansion, the situation is reversed. This is in line with the above observed changes in the relative stability of the NN-NN (AB) and NNN-NNN (12) Ce^{3+} configurations for both SSV and SSSV vacancy types (cf. **Figures 3**, **4**) under varying strain, i.e., AB configurations are stable under large compressive strain whereas 12 ones are stable otherwise.

High Vacancy Concentration

In this section we analyze the results for a SSV and a SSSV in the near-surface of CeO_2 (111) under strain with 2 × 2 periodicity (**Figure 9**; **Table S8**), and compare them to those obtained with the 5 × 5 unit cell. In the 2 × 2 unit cell under zero applied stress, the most stable SSV and SSSV configurations have both Ce^{3+} ions in NNN sites, one in the outermost cationic layer, and the other in the layer beneath, i.e., both configurations are labeled as 14 (cf. **Figure 2**), in line with previous calculations (Murgida and Ganduglia-Pirovano, 2013). These SSV (14) and the SSSV (14) configurations are by 0.22 and 0.54 eV more stable, respectively, than the corresponding ones with the Ce^{3+} ions in NN sites (AB). We note that at the lower vacancy concentration (5 × 5 unit cell) and zero applied stress, the SSV and the SSSV configurations with both Ce^{3+} ions in the second coordination shell (12) are by 0.23 and 0.32 eV more stable, respectively, than the corresponding ones with Ce^{3+} ions in the first coordination shell (AB). For the SSV and SSSV oxygen vacancies with 2 × 2 periodicity under 0% strain, the 14 >1B >AB and 14 > 1A ≈ 1D > AD ≈ AB stability trends, respectively, are obtained (**Table S8**) (Ganduglia-Pirovano et al., 2009; Murgida and Ganduglia-Pirovano, 2013). As the tensile strain is increased from 0 to +5%, the SSV- and SSSV-14 configurations remain more stable with respect to the corresponding AB ones. For example, for the +5% stretched surface, the SSV- and SSSV-14 configurations are by 0.23 and 0.53 eV more stable, respectively, than the corresponding SSV- and SSSV-AB ones (**Figure 9**; **Table S8**). However, in line with the results for the lower vacancy concentration (5 × 5 unit cell), for both vacancy types under compressive strain, an increasing preference for configurations with both Ce^{3+} ions in the first coordination shell (AB) is observed. For example, for −5% strain, the SSV-AB configuration is by 0.16 eV more stable than the SSV-14 (**Figure 9**; **Table S8**); for the SSSV, an even larger compressive strain would be needed to observe the crossing between the AB and 14 configurations (cf. **Figure 9**), but the tendency is clear. In summary, for both vacancy concentrations, the ground-state configuration of both vacancy types varies whether tensile or compressive stress is applied, namely, under tensile strain, both Ce^{3+} ions do *not* prefer the first coordination sphere of the vacancy, but under large compressive strain they do.

With respect to the relative stability between the SSV and SSSV when stress is applied and the concentration of vacancies is larger (**Figure 9**), a behavior very similar to that already discussed for the case of low concentration is observed (cf. **Figure S3**, **Figure 5**). In agreement with the literature (Ganduglia-Pirovano

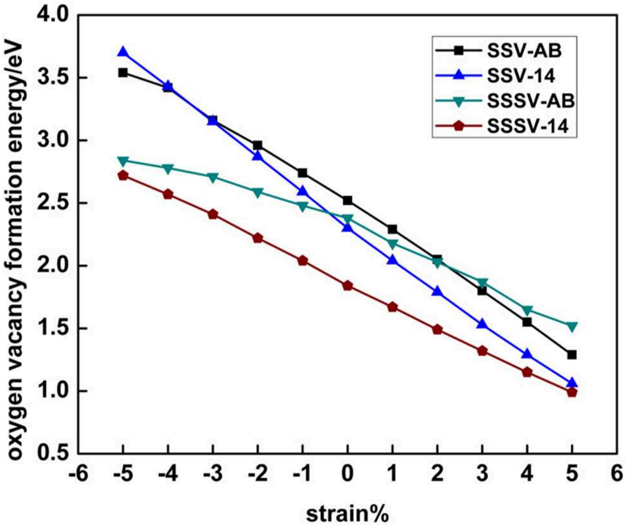

FIGURE 9 | Oxygen vacancy formation energy for single surface (SSV) and subsurface (SSSV) vacancies at the 2 × 2 CeO$_2$ (111) surface as a function of strain and for distinct polaronic structures, which are labeled according to the location of the two Ce^{3+} as shown in **Figure 2**.

et al., 2009; Murgida and Ganduglia-Pirovano, 2013), we find that under 0% tension, the subsurface vacancy position is by 0.46 eV more stable than the surface one; at the lower vacancy concentration the difference is by a factor of two smaller. Under compressive strain, from 0 to −5%, the SSSV remains more stable than the SSV, but the difference becomes larger as the compression increases, for example, under −5% compression, the SSSV is by 0.82 eV more stable than the SSV. However, under tensile strain, the larger relative stability of the SSSV as compared to the SSV becomes smaller and smaller as the strain increases from 0 to +5%, but an even larger tensile strain would be needed to observe the crossing between the corresponding E_f vs. strain curves; at the lower vacancy concentration the crossover occurs at about +3% strain (cf. **Figure 6**). For the higher vacancy concentration, we have also evaluated the bond breaking, E_b, and the relaxation energy, E_r, contributions to the vacancies formation energies as a function of surface strain (**Figure S3**; **Table S11**), which behave similarly to the case of the lower vacancy concentration discussed above. Both contributions resemble straight lines with a different slope for the SSV and SSSV, and the correlation between E_b and strain is negative, whereas that between $-E_r$ and strain is positive. For the −5% compressed surface, both E_b and E_r favor the SSSV by 0.11 and 0.71 eV, respectively, and thus, the SSSV is by 0.82 eV more stable than the SSV. However, for the +5% strained surface, E_b favors the SSV by 0.14 eV and E_r the SSSV by 0.21 eV, and, as a result, the SSSV is only by 0.07 eV more stable than the SSV.

Vacancy Clustering

As mentioned above (section Introduction), under zero applied stress, isolated subsurface vacancies are more stable than surface ones, and the interaction between nearest neighbor vacancies at the surface or in the subsurface is repulsive. We here consider strained reduced surfaces with either first-neighbor vacancy dimers at the surface (SurDimer), or in the subsurface (SubDimer), or pairs with a vacancy separation corresponding to that of third-nearest neighbors in the surface oxygen plane (SurDimer-d), or in the subsurface one (SubDimer-d), cf. **Figure 1**. Due to the large number of possible different configurations of the four Ce^{3+} created upon formation of a vacancy dimer, we have selected a set that mostly involve combinations of nearest-neighbor (A, B, C, D....) or next-nearest-neighbor (1, 2, 3, 4....) sites to the vacancies (**Tables S3–S6**). **Figure 5** shows the averaged vacancy formation energy of the most stable structures as a function of strain (**Table S7**). As expected (Murgida and Ganduglia-Pirovano, 2013; Han et al., 2018), under zero applied stress, the interaction between first-neighbor surface and subsurface vacancies is repulsive; creating two well-separated surface and subsurface vacancies is energetically more favorable by about 0.1 [$\Delta E_f = 2\,E_f$ (Surdimer)− 2 E_f (SSV), cf. Equation 1] and 0.2 eV [$\Delta E_f = 2\,E_f$ (Subdimer)− 2 E_f (SSSV)], respectively, than the corresponding pair formation. Tensile strain not only does not help neither the formation of surface nor subsurface vacancy pairs, but makes the preference for having corresponding isolated species even more pronounced, for example, for +5% tensile strain, by about 0.6 and 0.4 eV, respectively. However, upon lattice compression, the SurDimer and the SubDimer become more stable than the corresponding isolated species, for example, for −5% compressive strain, by about 0.4 and 0.2 eV, respectively, with the SubDimer being by about 0.9 eV more stable than the SurDimer.

In order to understand why compression favors vacancy clustering, for the example of the SurDimer, we have analyzed the two contributions to the vacancy dimer formation energy, namely, the bond breaking energy, E_b, and the energy gained from the structural relaxation in the presence of the vacancies, E_r, and compared them to those of the SSV (**Figure 6**; **Table S9**). **Figure 6** shows that within the −5 to +5% strain interval, creating an unrelaxed SurDimer is always energetically preferred over having two isolated SSV species, for example by 0.7 [$\Delta E_b = 2\ E_b$ (Surdimer)− 2 E_b(SSV)] and 0.6 eV under 0 and −5% strain, respectively (**Table S9**). The reason for this is likely due to the way the four excess electrons are "delocalized" among the nearest-neighbor cations in the unrelaxed structures, i.e., for the SurDimer, the shared cation (B, **Figure 1**) is fully reduced to Ce^{3+}, and the other four (A, C, E, and D), are partially reduced to Ce$^{0.75+}$, whereas in the case of two isolated SSV, the three nearest-neighbor cations of each vacancy would share two excess electrons $(3\times Ce^{0.\hat{6}+})$.

With respect to the energy gained from lattice relaxations, it is always smaller for the SurDimer as compared to two isolated SSV, expectedly, but the difference becomes smaller and smaller as the strain decreases from +5 to −5% (**Table S9**). For instance, under 0% (−5%) strain, the gain amounts to 1.46 (0.96) and 1.86 (1.04) eV/vacancy for the SurDimer and a SSV, respectively. Consequently, under 0% (−5%) strain, $\Delta E_f = \Delta E_b + \Delta E_r = -0.7 + 0.8\ (-0.6 + 0.16) = +0.1\ (-0.44)$, i.e., it is only when the energy gained from lattice relaxations is considered that the preference for dimer formation under compressive strain ($>-2\%$) can be explained.

We finally note that as for the case of the isolated species discussed above, for which compressive (tensile) strain favors NN (NNN) Ce^{3+} configurations, for the dimeric species, a similar tendency is observed, for example, the stable SurDimer and SubDimer configurations under −5% compressive strain have all four Ce^{3+} ions in the first cationic coordination shell of the vacancies (**Tables S3**, **S4**).

CONCLUSION

This work shows the important effect of lattice strain on the relative stability of different types of near-surface oxygen vacancies at the CeO_2 (111) surface, and on their ground-state energy configurations with respect to the localization of the excess charge. We have found three situations of energy crossover: (*i*) isolated surface vs. sub-surface oxygen vacancy species; (*ii*) Ce^{3+} within the first vs. second coordination shell of the vacancies; (*iii*) isolated species vs. first-neighbor vacancy dimers. Under 0% strain, isolated subsurface oxygen vacancies with both Ce^{3+} ions within the second coordination shell of the vacancies are favored, and the interaction between first-neighbor vacancies is repulsive. However, if a large tensile stress is applied, isolated surface vacancies with both Ce^{3+} in the second coordination shell become more stable than the subsurface ones, with both Ce^{3+} in next-nearest neighbor sites too. Moreover, if a large compressive strain is applied, isolated subsurface vacancies are more stable than surface ones, as in the case of 0% strain, but for both vacancy types configurations with both Ce^{3+} in the first coordination shell of the vacancies are favored over those with both Ce^{3+} in the second coordination shell. Finally, under large compressive strain, the formation of first-neighbor vacancy dimers at the surface and in the subsurface, with the four Ce^{3+} in nearest-neighbor sites, is more stable than having the two corresponding isolated species, with the subsurface vacancy dimer being more stable than the surface one.

We have further analyzed the effects of lattice strain on the energy cost to create a single vacancy without allowing for lattice relaxations, as well as on the energy gained due to lattice relaxations, and found that the preference for the surface or subsurface sites is the result of the different dependences of these energies on the applied stress. Regarding the Ce^{3+} switched preference in favor of the first coordination shell of the vacancies under compressive strain, we have inspected the calculated densities of states and found that the Ce^{3+} switched preference is related to the exchange in the relative positions of highest occupied Ce^{3+} f states in the O_{2p}-Ce_{5d} gap region.

Generally speaking, the vacancy structure at ceria surfaces is of importance for technological applications. Clearly, the finding that the relative stabilities of vacancy structures do depend on the applied in-plane strain, particularly in relation to the formation of vacancy aggregates, cannot be ignored when considering that in most applications ceria is employed within a heterostructure or as a supported thin film in which ceria can be strained.

DATA AVAILABILITY

The raw data supporting the conclusions of this manuscript will be made available by the authors, without undue reservation, to any qualified researcher.

AUTHOR CONTRIBUTIONS

MVG-P and YG supervised the whole project. Z-KH and LZ performed the calculations. Z-KH, LZ, MVG-P, and YG wrote the paper. All authors participate in the discussions.

FUNDING

This work has been funded by the National Natural Science Foundation of China (11574340, 21773287) as well as by the US Department of Energy SECA Core Technology Program (DE-NT0006557) and DOE ARPA-E REBELS Program (DE-AR0000502). MVG-P acknowledges support by the MINECO- and MICINN-Spain (CTQ2015-71823-R and RTI2018-101604-B-I00, respectively). The computational resources utilized in this research have been provided by the National Supercomputing Center in Tianjin, the Shanghai Supercomputer Center and the Guangzhou Supercomputer Center, as well as by the National Energy Research Scientific Computing Center, a DOE Office of Science User Facility supported by the Office of Science of the U.S. Department of Energy under Contract No. DE-AC02-05CH11231. This work used the Extreme Science and Engineering Discovery Environment (XSEDE), which is supported by National Science Foundation grant number TG-DMR170045. We thank Gustavo E. Murgida from the CAC-CNEA and CONICET-Argentina for fruitful discussions.

SUPPLEMENTARY MATERIAL

The Supplementary Material for this article can be found online at: https://www.frontiersin.org/articles/10.3389/fchem.2019.00436/full#supplementary-material

REFERENCES

Allen, J. P., and Watson, G. W. (2014). Occupation matrix control of d- and f-electron localisations using DFT+ U. *Phys. Chem. Chem. Phys.* 16, 21016–21031. doi: 10.1039/C4CP01083C

Andersson, D. A., Simak, S. I., Skorodumova, N. V., Abrikosov, I. A., and Johansson, B. (2006). Optimization of ionic conductivity in doped ceria. *Proc. Natl. Acad. Sci. U.S.A.* 103, 3518–3521. doi: 10.1073/pnas.0509537103

Arapan, S., Simak, S. I., and Skorodumova, N. V. (2015). Volume-dependent electron localization in ceria.

Phys. Rev. B 91:125108. doi: 10.1103/PhysRevB.91.125108

Artini, C., Pani, M., Lausi, A., Masini, R., and Costa, G. A. (2014). High temperature structural study of Gd-doped ceria by synchrotron X-ray diffraction (673 K≤ T≤ 1073 K). *Inorg. Chem.* 53, 10140–10149. doi: 10.1021/ic5011242

Castleton, C. W., Kullgren, J., and Hermansson, K. (2007). Tuning LDA+ U for electron localization and structure at oxygen vacancies in ceria. *J. Chem. Phys.* 127, 244704–244704. doi: 10.1063/1.2800015

Conesa, J. C. (2009). Surface anion vacancies on ceria: quantum modelling of mutual interactions and oxygen adsorption. *Catal. Today* 143, 315–325. doi: 10.1016/j.cattod.2008.11.005

Da Silva, J. L. F., Ganduglia-Pirovano, M. V., Sauer, J., Bayer, V., and Kresse, G. (2007). Hybrid functionals applied to rare-earth oxides: the example of ceria. *Phys. Rev. B* 75:045121. doi: 10.1103/PhysRevB.75.045121

De Souza, R. A., Ramadan, A., and Hörner, S. (2012). Modifying the barriers for oxygen-vacancy migration in fluorite-structured CeO_2 electrolytes through strain: a computer simulation study. *Energy Environ. Sci.* 5, 5445–5453. doi: 10.1039/C2EE02508F

Duchon, T. S., Dvorák, F., Aulická, M., Stetsovych, V., Vorokhta, M., Mazurá, I., et al. (2013). Ordered phases of reduced ceria as epitaxial films on Cu(111). *J. Phys. Chem. C* 118, 357–365. doi: 10.1021/jp409220p

Duclos, S. J., Vohra, Y. K., Ruoff, A. L., Jayaraman, A., and Espinosa, G. (1988). High-pressure x-ray diffraction study of CeO_2 to 70 GPa and pressure-induced phase transformation from the fluorite structure. *Phys. Rev. B* 38:7755–7758. doi: 10.1103/PhysRevB.38.7755

Dudarev, S., Botton, G., Savrasov, S., Humphreys, C., and Sutton, A. (1998). Electron-energy-loss spectra and the structural stability of nickel oxide: an LSDA+U study. *Phys. Rev. B* 57:1505. doi: 10.1103/PhysRevB.57.1505

Esch, F., Fabris, S., Zhou, L., Montini, T., Africh, C., Fornasiero, P., et al. (2005). Electron localization determines defect formation on ceria substrates. *Science* 309, 752–755. doi: 10.1126/science.1111568

Fu, Q., Saltsburg, H., and Flytzani-Stephanopoulos, M. (2003). Active nonmetallic Au and Pt species on ceria-based water-gas shift catalysts. *Science* 301, 935–938. doi: 10.1126/science.1085721

Ganduglia-Pirovano, M. V., Da Silva, J. L., and Sauer, J. (2009). Density-functional calculations of the structure of near-surface oxygen vacancies and electron localization on $CeO_2(111)$. *Phys. Rev. Lett.* 102:026101. doi: 10.1103/PhysRevLett.102.026101

Ganduglia-Pirovano, M. V., Hofmann, A., and Sauer, J. (2007). Oxygen vacancies in transition metal and rare earth oxides: current state of understanding and remaining challenges. *Surf. Sci. Rep.* 62, 219–270. doi: 10.1016/j.surfrep.2007.03.002

Grieshammer, S., Nakayama, M., and Martin, M. (2016). Association of defects in doped non-stoichiometric ceria from first principles. *Phys. Chem. Chem. Phys.* 18, 3804–3811. doi: 10.1039/C5CP07537H

Han, X., Amrane, N., Zhang, Z., and Benkraouda, M. (2017). Reply to comment on oxygen vacancy ordering and electron localization in CeO_2: hybrid functional study. *J. Phys. Chem. C* 121, 21084–21086. doi: 10.1021/acs.jpcc.7b02945

Han, Z.-K., Yang, Y.-Z., Zhu, B., Ganduglia-Pirovano, M. V., and Gao, Y. (2018). Unraveling the oxygen vacancy structures at the reduced $CeO_2(111)$ surface. *Phys. Rev. Mater.* 2:035802. doi: 10.1103/PhysRevMaterials.2.035802

Hinterberg, J., Zacherle, T., and De Souza, R. (2013). Activation volume tensor for oxygen-vacancy migration in strained CeO_2 electrolytes. *Phys. Rev. Lett.* 110:205901. doi: 10.1103/PhysRevLett.110.205901

Inaba, H., and Tagawa, H. (1996). Ceria-based solid electrolytes. *Solid State Ionics* 83, 1–16. doi: 10.1016/0167-2738(95)00229-4

Jerratsch, J.-F., Shao, X., Nilius, N., Freund, H.-J., Popa, C., Ganduglia-Pirovano, M. V., et al. (2011). Electron localization in defective ceria films: a study with scanning-tunneling microscopy and density-functional theory. *Phys. Rev. Lett.* 106:246801. doi: 10.1103/PhysRevLett.106.246801

Keating, P., Scanlon, D., and Watson, G. (2009). Intrinsic ferromagnetism in CeO_2: dispelling the myth of vacancy site localization mediated superexchange. *J. Phys. Condens. Matter* 21:405502. doi: 10.1088/0953-8984/21/40/405502

Kresse, G., and Joubert, D. (1999). From ultrasoft pseudopotentials to the projector augmented-wave method. *Phys. Rev. B* 59:1758. doi: 10.1103/PhysRevB.59.1758

Kullgren, J., Hermansson, K., and Castleton, C. (2012). Many competing ceria (110) oxygen vacancy structures: From small to large supercells. *J. Chem. Phys.* 137:044705. doi: 10.1063/1.4723867

Kullgren, J., Wolf, M. J., Castleton, C. W., Mitev, P., Briels, W. J, and Hermansson, K. (2014). Oxygen vacancies versus fluorine at $CeO_2(111)$: a case of mistaken identity? *Phys. Rev. Lett.* 112:156102. doi: 10.1103/PhysRevLett.112.156102

Kullgren, J., Wolf, M. J., Mitev, P. D., Hermansson, K., and Briels, W. J. (2017). DFT-based monte carlo simulations of impurity clustering at $CeO_2(111)$. *J. Phys. Chem. C.* 121:15127 doi: 10.1021/acs.jpcc.7b00299

Li, H.-Y., Wang, H.-F., Gong, X.-Q., Guo, Y.-L., Guo, Y., Lu, G., et al. (2009). Multiple configurations of the two excess 4f electrons on defective $CeO_2(111)$: origin and implications. *Phys. Rev. B* 79:193401. doi: 10.1103/PhysRevB.79.193401

Luches, P., Pagliuca, F., and Valeri, S. (2014). Structural and morphological modifications of thermally reduced cerium oxide ultrathin epitaxial films on Pt (111). *Phys. Chem. Chem. Phys.* 16, 18848–18857. doi: 10.1039/C4CP02723J

Montini, T., Melchionna, M., Monai, M., and Fornasiero, P. (2016). Fundamentals and catalytic applications of CeO_2-based materials. *Chem. Rev.* 116, 5987–6041. doi: 10.1021/acs.chemrev.5b00603

Murgida, G. E., Ferrari, V., Ganduglia-Pirovano, M. V., and Llois, A. M. (2014). Ordering of oxygen vacancies and excess charge localization in bulk ceria: a DFT+ U study. *Phys. Rev. B* 90:115120. doi: 10.1103/PhysRevB.90.115120

Murgida, G. E., and Ganduglia-Pirovano, M. V. (2013). Evidence for subsurface ordering of oxygen vacancies on the reduced $CeO_2(111)$ surface using density-functional and statistical calculations. *Phys. Rev. Lett.* 110:246101. doi: 10.1103/PhysRevLett.110.246101

Namai, Y., Fukui, K. -I., and Iwasawa, Y. (2003). Atom-resolved noncontact atomic force microscopic observations of $CeO_2(111)$ surfaces with different oxidation states: surface structure and behavior of surface oxygen atoms. *J. Phys. Chem. B* 107, 11666–11673. doi: 10.1021/jp030142q

Olbrich, R., Murgida, G. E., Ferrari, V., Barth, C., Llois, A. M., Reichling, M., et al. (2017). Surface stabilizes ceria in unexpected stoichiometry. *J. Phys. Chem. C* 121, 6844–6851. doi: 10.1021/acs.jpcc.7b00956

Paier, J., Penschke, C., and Sauer, J. (2013). Oxygen defects and surface chemistry of ceria: quantum chemical studies compared to experiment. *Chem. Rev.* 113, 3949–3985. doi: 10.1021/cr3004949

Perdew, J. P., Burke, K., and Ernzerhof, M. (1996). Generalized gradient approximation made simple. *Phys. Rev. Lett.* 77:3865. doi: 10.1103/PhysRevLett.77.3865

Pfau, A., and Schierbaum, K. D. (1994). The electronic structure of stoichiometric and reduced CeO_2 surfaces: and XPS, UPS and HREELS study. *Surf. Sci.* 321, 71–80. doi: 10.1016/0039-6028(94)90027-2

Rossignol, S., Gérard, F., Mesnard, D., Kappenstein, C., and Duprez, D. (2003). Structural changes of Ce–Pr–O oxides in hydrogen: a study by in situ X-ray diffraction and Raman spectroscopy. *J. Mater. Chem.* 13, 3017–3020. doi: 10.1039/B306726B

Shoko, E., Smith, M. F., and McKenzie, R. H. (2010). Charge distribution near bulk oxygen vacancies in cerium oxides. *J. Phys. Condens. Matter* 22:223201. doi: 10.1088/0953-8984/22/22/223201

Skorodumova, N., Simak, S., Lundqvist, B. I., Abrikosov, I., and Johansson, B. (2002). Quantum origin of the oxygen storage capability of ceria. *Phys. Rev. Lett.* 89:166601. doi: 10.1103/PhysRevLett.89.166601

Sun, L., Marrocchelli, D., and Yildiz, B. (2015). Edge dislocation slows down oxide ion diffusion in doped CeO_2 by segregation of charged defects. *Nat. Commun.* 6:6294. doi: 10.1038/ncomms7294

Sutton, J. E., Beste, A., and Overbury, S. H. (2015). Origins and implications of the ordering of oxygen vacancies and localized electrons on partially reduced $CeO_2(111)$. *Phys. Rev. B* 92:144105. doi: 10.1103/PhysRevB.92.144105

Torbrügge, S., Reichling, M., Ishiyama, A., Morita, S., and Custance, O. (2007). Evidence of subsurface oxygen vacancy ordering on reduced $CeO_2(111)$. *Phys. Rev. Lett.* 99:056101. doi: 10.1103/PhysRevLett.99.056101

Trovarelli, A. (1996). Catalytic properties of ceria and CeO_2-containing materials. *Catal. Rev.* 38, 439–520. doi: 10.1080/01614949608006464

Vayssilov, G. N., Lykhach, Y., Migani, A., Staudt, T., Petrova, G. P., Tsud, N., et al. (2011). Support nanostructure boosts oxygen transfer to catalytically active platinum nanoparticles. *Nat. Mater.* 10, 310–315. doi: 10.1038/nmat2976

Wang, B., and Cormack, A. N. (2012). Strain modulation of defect structure in gadolinia-doped ceria. *J. Phys. Chem. C* 117, 146–151. doi: 10.1021/jp310518j

Wang, B., Xi, X., and Cormack, A. N. (2014). Chemical strain and point defect configurations in reduced ceria. *Chem. Mater.* 26, 3687–3692. doi: 10.1021/cm500946s

Žguns, P. A., Ruban, A. V., and Skorodumova, N. V. (2019). Influence of composition and oxygen-vacancy ordering on lattice parameter and elastic moduli of $Ce_{1-x}Gd_xO_{2-x/2}$: a theoretical study. *Scr. Mater.* 158, 126–130. doi: 10.1016/j.scriptamat.2018.08.034

Conflict of Interest Statement: The authors declare that the research was conducted in the absence of any commercial or financial relationships that could be construed as a potential conflict of interest.

frontiers in Chemistry

ORIGINAL RESEARCH
published: 06 June 2019
doi: 10.3389/fchem.2019.00212

STM Images of Anionic Defects at CeO_2(111)—A Theoretical Perspective

Matthew J. Wolf [1†], Christopher W. M. Castleton [2,3], Kersti Hermansson [1] and Jolla Kullgren [1]*

[1] Department of Chemistry–Ångström Laboratory, Uppsala University, Uppsala, Sweden, [2] School of Science and Technology, Nottingham Trent University, Nottingham, United Kingdom, [3] Division of Physics and Mathematics/Natural Science Didactics, Mälardalen University, Västerås, Sweden

Edited by:
Maria Veronica Ganduglia-Pirovano,
Institute of Catalysis and Petrochemistry (ICP), Spain

Reviewed by:
Joachim Paier,
Humboldt-Universität zu Berlin, Germany
Niklas Nilius,
University of Oldenburg, Germany

***Correspondence:**
Jolla Kullgren
jolla.kullgren@kemi.uu.se

† Present Address:
Matthew J. Wolf,
Department of Physics, University of Bath, Claverton Down, United Kingdom

Specialty section:
This article was submitted to Physical Chemistry and Chemical Physics,
a section of the journal Frontiers in Chemistry

Received: *07 January 2019*
Accepted: *18 March 2019*
Published: *06 June 2019*

Citation:
Wolf MJ, Castleton CWM, Hermansson K and Kullgren J (2019) STM Images of Anionic Defects at CeO_2(111)—A Theoretical Perspective. Front. Chem. 7:212. doi: 10.3389/fchem.2019.00212

We present a theoretically oriented analysis of the appearance and properties of plausible candidates for the anionic defects observed in scanning tunneling microscopy (STM) experiments on CeO_2(111). The simulations are based on density functional theory (DFT) and cover oxygen vacancies, fluorine impurities and hydroxyl groups in the surface and sub-surface layers. In the surface layer, all three appear as missing spots in the oxygen sublattice in filled state simulated STM images, but they *are* distinguishable in empty state images, where surface oxygen vacancies and hydroxyls appear as, respectively, diffuse and sharp bright features at oxygen sites, while fluorine defects appear as triangles of darkened Ce ions. In the sub-surface layer, all three defects present more complex patterns, with different combinations of brightened oxygen ion triangles and/or darkened Ce ion triangles, so we provide image maps to support experimental identification. We also discuss other properties that could be used to distinguish the defects, namely their diffusion rates and distributions.

Keywords: simulated STM images, cerium dioxide (CeO2), density functional theory, anionic defects, reducible oxide

1. INTRODUCTION

The functional properties of technologically relevant materials can depend critically on the properties of point defects in the lattice structure, which may be present unavoidably as contaminants or introduced deliberately as dopants. For this reason, much research effort goes into identifying and characterizing such defects. In the bulk, typically one must rely on spectroscopic probes, which provide spatially averaged information, but at the surface one can make use of spatially resolving techniques such as scanning tunneling microscopy (STM) and atomic force microscopy (AFM). Of these latter two methods, STM remains more widely used, despite the fact that its applicability is limited to materials with sufficient conductivity, and atomic resolution STM imaging of surfaces is now fairly routine. However, the interpretation of the results of STM experiments is complicated by the fact that the tunneling current depends not only on the topography of the surface, but also on the local electronic structure. Substantial success has been achieved by combining experimental data with the results of electronic structure calculations, most commonly based on density functional theory (DFT) (see e.g., Setvín et al., 2017 for a particularly relevant review of such studies on oxide surfaces).

The focus of the present contribution is the identification of anionic defects at the (111) surface facet of CeO$_2$ (ceria) observed using STM. The earliest such experimental studies were carried out on single crystals obtained commercially, and mainly with negative bias voltages, thereby imaging the filled electronic states (Nörenberg and Briggs, 1997, 1998, 1999; Nörenberg, 2002; Fukui et al., 2003; Namai et al., 2003; Esch et al., 2005). The predominant defects observed were dark "depressions" in this sublattice, which formed triangular and extended linear clusters at higher concentrations, and exhibited sites of enhanced brightness around their edges. However, despite the fact that the samples used in all of these studies were from the same commercial source, the results are not entirely consistent. For instance, apparently similar defects were observed to be mobile at room temperature in one study (Namai et al., 2003), but immobile at temperatures up to 673 K in another (Esch et al., 2005), suggesting that the defects observed in the different experiments might not all be the same species, despite their similar appearances (Campbell and Peden, 2005).

A considerably greater number of studies have been performed on thin ceria(111) films grown on metallic substrates, including Rh(111) (Castellarin-Cudia et al., 2004; Chan and Yuhara, 2015), Ru(0001) (Lu et al., 2006; Zhou et al., 2008; Weststrate et al., 2009; Jerratsch et al., 2011; Hasegawa et al., 2014; Shahed et al., 2014), Cu(111) (Szabova et al., 2012; Hu et al., 2015), Pt(111) (Berner and Schierbaum, 2001; Grinter et al., 2010; Luches et al., 2011) and Au(111) (Zhao et al., 2007; Ma et al., 2008). The coverage, thickness and degree of structural order of the ceria films, as well as the resolution with which they were imaged, vary considerably, making direct comparison between them challenging. Depressions and protrusions, in isolation and in the form of clusters, are commonly observed, both in empty and filled state images.

In **Table 1**, we have attempted to summarize the experimental appearances and assignments of the features observed in filled and empty state STM images of CeO$_2$(111), along with the experimental conditions (temperature and bias voltage), and substrate where applicable. We note that the results of different studies are not entirely consistent, with numerous different features being assigned to oxygen vacancies, with consideration of other possibilities being limited to an assignment of bright protrusions to hydroxyl groups in Shahed et al. (2014).

TABLE 1 | Summary of experimentally observed STM features on ceria (111).

Feature	Assignment	Bias (V)	T (K)	Sample[a]	Reference
Filled states					
Depressions, extended lines	O vacancies	−2.5	773	Single crystal	Nörenberg and Briggs, 1997
Depressions, triangular	Triple O vacancies	−2.5	298	Single crystal	Nörenberg and Briggs, 1997
Protrusions, isolated and clusters	Not assigned	−2.5	298	Single crystal	Nörenberg and Briggs, 1997
Depressions, isolated and clusters	O vacancies	−3	298	Single crystal	Berner and Schierbaum, 2001
Depressions, isolated and clusters	O vacancies	−2	350	Single crystal	Namai et al., 2003
Depressions, isolated, triangular and lines	O vacancies	−3	573	Single crystal	Esch et al., 2005
Triple NNN Protrusions	Sub-surface O vacancies	−3	573	Single crystal	Esch et al., 2005
Depressions, isolated and clusters	O vacancies	−1	298	Au(111)	Zhao et al., 2007
Protrusions, isolated and clusters	Not assigned	−1	298	Au(111)	Zhao et al., 2007
Depressions/Protrusions, isolated and clusters	O vacancies	−1.5	298	Au(111)	Ma et al., 2008
Triple NNN Protrusions	Sub-surface O vacancies	−3	298	Pt(111)	Grinter et al., 2010
Depressions, isolated, triangular and lines	O vacancies	−3	298	Pt(111)	Grinter et al., 2010
Depressions, isolated	Not assigned	−4	573	Single crystal	Shahed et al., 2011
Protrusions, triangular	Hydroxyl groups	−4	150	Ru(0001)	Shahed et al., 2014
Depressions, triangular	O vacancies	−3	150	Ru(0001)	Shahed et al., 2014
Empty states					
Depressions, isolated and clusters	O vacancies	+0.5 to +1	298	Rh(111)	Castellarin-Cudia et al., 2004
Triple NNN Protrusions	Single O vacancy	+3	573	Single crystal	Esch et al., 2005
Large Y shaped clusters	Sub-surface O vacancies	+3	573	Single crystal	Esch et al., 2005
Depressions, triangular	Triple O vacancies	+2.5	298	Ru(0001)	Lu et al., 2006
Depressions, isolated and clusters	Not assigned	+3 to +4	298	Ru(0001)	Zhou et al., 2008
Depressions, extended clusters	Surface roughness	+3 to +4	298	Ru(0001)	Zhou et al., 2008
Depressions/Protrusions, isolated and clusters	O vacancies	+1.5	298	Au(111)	Ma et al., 2008
Depressions, isolated and clusters	Not assigned	+3	298	Ru(0001)	Weststrate et al., 2009
Depressions, clusters	O vacancies	+1 to +3	298	Ru(0001)	Zhou et al., 2010
Protrusions, double and triple	O vacancies	+1	10	Ru(0001)	Jerratsch et al., 2011
Depressions, clusters	O vacancies	+2.5	298	Ru(0001)	Zhou and Zhou, 2012

Bias voltages have been rounded off to the nearest 0.5 V and room temperature is reported as 298 K.

[a] *Ru(0001) means a ceria(111) film on a Ru(0001) substrate, for example.*

With the above discussion in mind, the principal purpose of the present paper is to offer a consistent set of simulated STM images of three particularly plausible candidate defects at anionic sites on $CeO_2(111)$, drawing attention to their similarities and differences, which we believe will aid in the interpretation of STM experiments on this system. We will also discuss other properties which could aid in distinguishing between them, making use of theoretical data available in the literature where available.

The three defects that we consider are oxygen vacancies, fluoride ions, and hydroxyl groups (denoted respectively OV, FI, and OH in the remainder of this paper). Our consideration of the OV defects is natural, given the well known ability and tendency of ceria to release oxygen under oxygen lean conditions, a quality which plays a central role in many of its technological applications (Trovarelli, 2013).

Surface OHs can arise due to the presence of H_2O, which is a ubiquitous molecule even under ultra high vacuum conditions, and there are numerous reports that it reacts with OVs to form hydroxide ions embedded in the surface (Fronzi et al., 2009; Molinari et al., 2012; Mullins et al., 2012).

Finally, our consideration of fluoride ions is primarily due to the observation in Pieper et al. (2012) that fluorine was present in large quantities in single crystalline samples from the same source as those used in Nörenberg and Briggs (1997), Nörenberg and Briggs (1998), Nörenberg and Briggs (1999), Nörenberg (2002), Namai et al. (2003), Fukui et al. (2003), and Esch et al. (2005). Furthermore, it was observed in Zarraga-Colina et al. (2004) and Zarraga-Colina et al. (2005) that if CeO_2 films are grown on CaF, F diffuses into the CeO_2 upon annealing, replacing some of the O ions within the lattice. Taken together, these observations suggest that if CeO_2 is exposed to a source of F, it is likely to become contaminated, and such contamination may be difficult to avoid entirely.

Previously, we concluded that, at least in filled state STM images, fluorine impurities and hydroxyl groups should be difficult to distinguish from oxygen vacancies at $CeO_2(111)$ based on their appearances alone (Kullgren et al., 2014), although OVs and FIs should be distinguishable based on their mobilities, relative concentrations in the surface and sub-surface layers, and tendency to form clusters in the surface layer. In this paper, we expand upon that study, providing a more detailed examination and comparison of the STM appearances of these three oxygen sub-lattice defects (OVs, FIs, and OHs), as well as discussing the results of related studies by other authors. We present both filled and empty state simulated STM images of the three defect species, both when located in the surface layer itself (section 3.2) and when located in the first oxygen sub-surface layer (section 3.3), and relate those images both to the local topography and to the electronic structure. In sections 3.4, 3.5 and 3.6 we discuss other distinguishing characteristics of the three defects, namely the positions of the f electron levels of the associated Ce^{3+} ions, the defects' mobilities and their distributions. We then conclude in section 4.

2. COMPUTATIONAL DETAILS

We carried out Kohn–Sham density functional theory (DFT) calculations using the projector augmented wave (PAW) formalism (Blöchl, 1994), as implemented in the Vienna Ab initio Simulation Package (Kresse and Hafner, 1993; Kresse and Furthmüller, 1996a,b; Kresse and Joubert, 1999) (VASP), version 5.3.5. We used the Perdew–Burke–Ernzerhof (PBE) functional (Perdew et al., 1996, 1997), augmented with a Hubbard-like (effective) U term in the simplified, rotationally invariant form introduced by Dudarev et al. (1998); Himmetoglu et al. (2014). The projectors that were used in the calculations of the occupation matrix were those associated with the PAW potentials, as is done by default in VASP, and we used a value of $U = 5$ eV (Nolan et al., 2005; Andersson et al., 2007; Castleton et al., 2007). The core electrons were described with the "standard" PBE derived PAW potentials distributed with VASP, in which the cores comprise the [Kr]4d electrons of Cerium and the 1s electrons of oxygen and fluorine. Aspherical contributions from the gradient corrections inside the PAW spheres were taken into account. The Kohn–Sham states for the valence electrons were expanded over the set of all plane waves of kinetic energy less than a cut-off value of 400 eV. Energies were converged to 1×10^{-5} eV, and forces to 1×10^{-2} eV/Å. We also used the Occupation Matrix Control (OMC) method in the implementation of B. Dorado and co-workers (Dorado et al., 2009) to avoid the problems associated with the existence of *electronic* self-consistent "local minima," or "meta-stable" states, corresponding to different shapes and/or orientations of the f orbital that is occupied on a given Ce^{3+} ion.

For the structural model of $CeO_2(111)$, we used a periodic slab exposing a $p(5 \times 5)$ supercell of the (111) surface facet on both sides, with a thickness of three O–Ce–O triple layers; this leads to a formula for the stoichiometric slab of $Ce_{75}O_{150}$. A vacuum gap equivalent to the height of 5 bulk triple layers, which is more than 15 Å, was also used. Due to the large supercell used in our calculations, we found that it was sufficient to restrict sampling of the Brillouin zone to the Γ point.

Densities of states were produced by smearing the one-electron spectrum using a normalized Gaussian function with a width of 0.1 eV. Simulated STM images were produced under the Tersoff–Hamann approximation (Tersoff and Hamann, 1983, 1985), that is to say, directly from the local density of states (LDOS) obtained from partial charge densities calculated with VASP. The charge density was smeared with a Gaussian function with a width of 0.1 Å, and then linearly interpolated onto a fine 2D grid parallel to, and at a height 2.8 Å above, the upper surface of the slab; we found that increasing the distance any further introduced considerable numerical noise into the images. The partial charge densities were generated by summing the charge densities of all states within -3.0 eV or $+3.0$ eV of the Fermi level, assumed to be in the middle of the gap, for filled and empty state images, respectively. We note that the simulation protocol used here, which is based on the PBE+U functional, underestimates the band gaps somewhat, yielding O-2p → Ce-4f and O-2p → Ce-5d gaps of 2.25 and 5.20 eV, respectively. However, we find the simulated STM images to be rather insensitive to the precise value of the limit for the summation of states (and therefore the precise positions of the Fermi level and the band edges) with in general, although we present additional images when this is not the case.

3. RESULTS

3.1. Preliminary Considerations

3.1.1. Imaging the Stoichiometric Surface

Simulated filled and empty state images of stoichiometric $CeO_2(111)$ are shown in **Figure 1**.

The (filled) valence band states of ceria derive (primarily) from 2p orbitals of the O^{2-} ions, with a smaller contribution from 4f orbitals of the Ce^{4+} ions in the layer beneath them, so it is natural that the topmost surface O^{2-} ions are what is imaged at negative bias voltages.

Regarding empty state images, some authors have suggested that they are due to electrons tunneling into conduction band states derived (primarily) from Ce 5d orbitals (Esch et al., 2005), rather than states derived (primarily) from Ce 4f orbitals, due to the more compact nature of the latter. However, the available experimental spectral data, summarized in Castleton et al. (2007), place the Ce 5d and 4f band edges at approximately 6 eV and 3 eV, respectively, above the valence band maximum (Wuilloud et al., 1984; Marabelli and Wachter, 1987; Pfau and Schierbaum, 1994; Mullins et al., 1998). It seems reasonable to assume that the Fermi level is below the unoccupied Ce 4f states, as it must be unless the sample is very heavily reduced indeed. We can therefore surmise that tunneling into the Ce 5d states is rather unlikely unless very high positive biases are used.

Given the above discussion, we therefore assume that in empty state imaging, electrons tunnel into states that derive mainly from Ce 4f orbitals. Note that the surface oxygen ions also contribute to the unoccupied states, and since they are in the layer above the Ce ions, they are also partly visible at positive bias voltages.

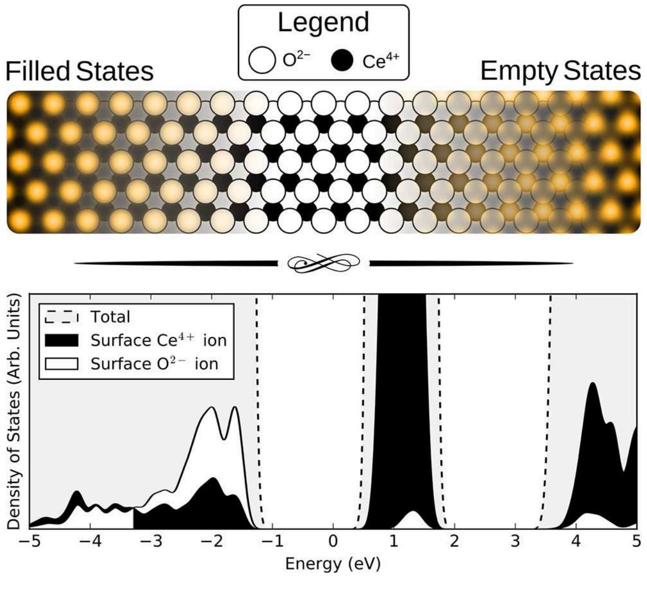

FIGURE 1 | (Upper) Simulated STM images of the stoichiometric $CeO_2(111)$ surface using bias voltages of −3.0 V (filled states) and +3.0 V (empty states). The location of the ions is indicated by superimposing the STM images over a schematic top-view of the surface with white and black circles corresponding to oxygen and cerium ions, respectively. **(Lower)** Density of states (DOS) plots for the stoichiometric slab. Total DOS shown (gray) with dashed lines and projections onto a surface oxygen ion and a surface cerium ion are shown by white and black filled curves, respectively.

3.1.2. Locations of Ce^{3+} Ions

All three defects introduce excess electrons into the lattice; in ceria, these electrons localize on individual Ce sites, reducing their charge states from +4 to +3, forming polarons. In order to maintain charge neutrality, OVs introduce two such Ce^{3+} ions, while FIs and OHs introduce one each.

The energetically preferential location of these Ce^{3+} ions in the vicinity of OVs has been the subject of much debate in the literature. The current consensus, based on theoretical calculations, is that the Ce^{3+} are located preferentially at next-nearest neighbor (NNN) sites to OVs (Murgida and Ganduglia-Pirovano, 2013; Sutton et al., 2015). In contrast, the single Ce^{3+} associated with an FI is preferentially located at a nearest neighbor (NN) site (Kullgren et al., 2014; Wolf et al., 2017), while for a surface OH, the two locations have essentially identical energies (Fernández-Torre et al., 2014; Kullgren et al., 2014; Wolf et al., 2017).

In principle, the Ce^{3+} ions (polarons) which charge compensate the substitional ions should break the threefold rotational symmetry of the lattice around the latter, but at higher temperatures, the electrons can hop between equivalent sites, so that the symmetry is restored (on average) on the time-scale required to obtain an STM image; indeed, this would appear to be the case for most of the experimental images in the literature, in which the rotational symmetry is preserved. For this reason, we present both images with the Ce^{3+} at specific locations, and images that have been rotationally averaged around the substitional ion.

3.2. STM Images of Defects in the Surface Layer

3.2.1. Filled State Images

The simulated filled state STM images of the three surface anionic defects, with the associated Ce^{3+} ions at either nearest neighbor (NN) or next nearest neighbor (NNN) locations, are shown in the bottom row of panels of **Figure 2**.

In the filled state images, the main feature of all three defects is a dark "depression" at the lattice site of the defect center. For the surface OV, this is simply due to the absence of the ion and the associated electron density. The reason for the reduced tunneling current in the case of the fluoride or hydroxide ion in the filled state image can be understood by examining the partial density of states projected onto the defects (see **Figure 3**). Both the OH and the FI make their main contributions to the local density of occupied states at lower energies than the surrounding surface oxygen ions. Hence, despite the fact that both defects protrude from the surface, they are essentially invisible unless the bias voltage is large enough to allow tunneling from these states. At more negative bias voltages, both OH and FI begin to appear, with the OH being more visible than the FI for a given voltage, which in turn would be more visible than an OV. Thus, in principle, very

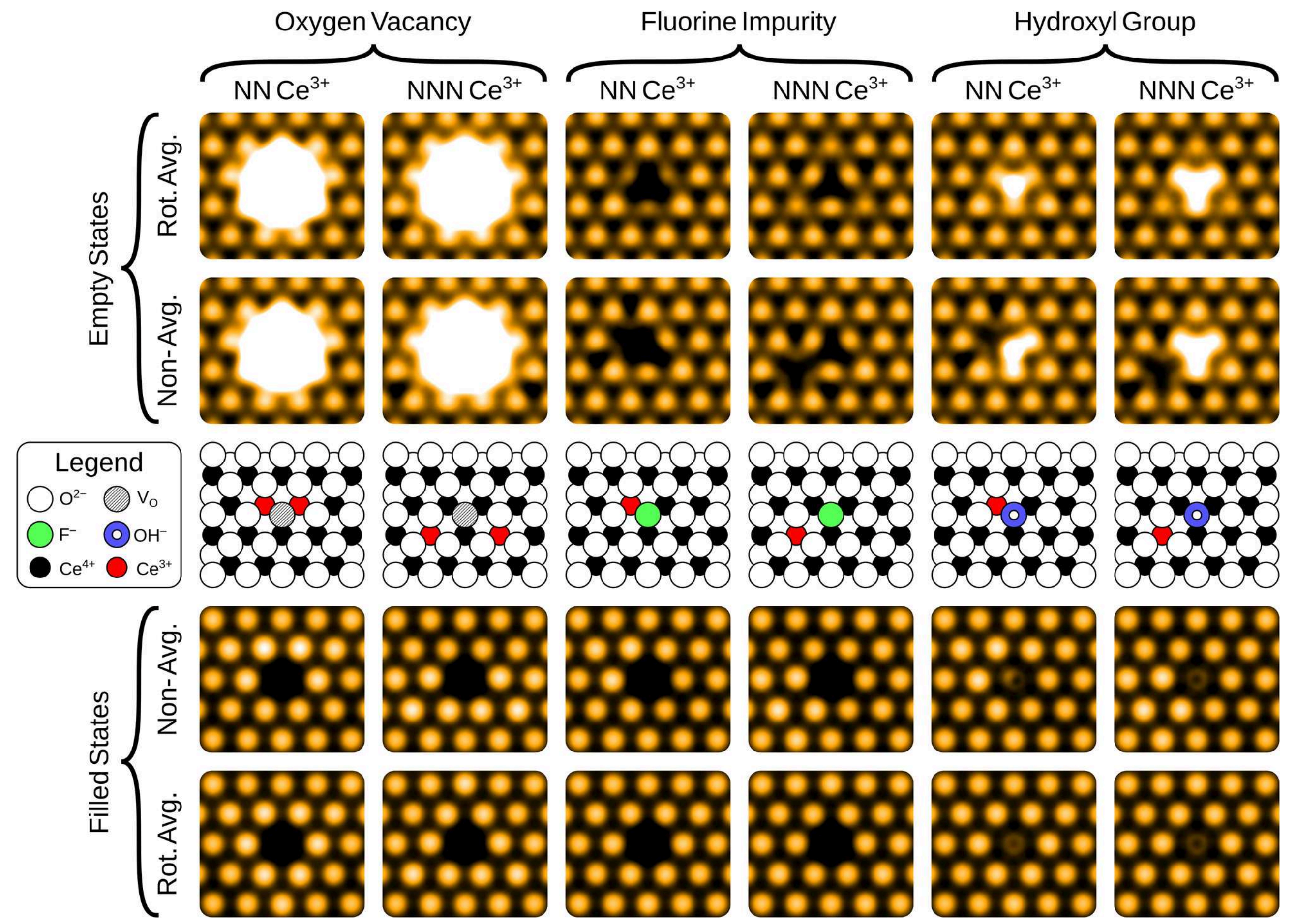

FIGURE 2 | Simulated filled and empty state images of the three surface anionic defects, with the associated Ce^{3+} ions at either nearest neighbor (NN) or next nearest neighbor (NNN) lattice sites. The precise locations of the Ce^{3+} ions are shown in the schematics, for comparison with the non-rotationally averaged images.

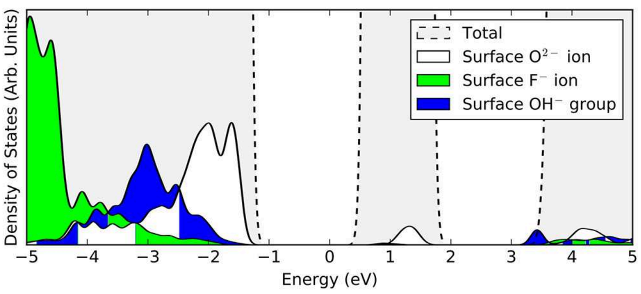

FIGURE 3 | Projected densities of states (PDOS) of a surface oxygen ion (white), surface fluorine ion (green), and a surface hydroxyl group (blue). The total density of states of the stoichiometric slab (gray) is highlighted by the dashed lines.

sensitive STM measurements should be able to distinguish them by their relative apparent depth profile for a *fixed* bias voltage which probes states deep in the valence band.

Moving on to more subtle features of the STM images, we note that some of the oxygen ions in the vicinity of the central depressions are brighter than others. These features are correlated with the positions of the Ce^{3+} ions, and is easy to understand based on the fact that Ce^{3+} ions are larger than Ce^{4+} ions, and they are negatively charged with respect to the lattice. Both of these effects will cause the negatively charged O^{2-} ions to be repelled out of the surface. However, in some publications, an enhanced brightness was reported *between* certain pairs of the surrounding surface O ions (see e.g., Esch et al., 2005; Grinter et al., 2010). Such features have been explained as being due to a relaxation of pairs of surface O ions toward one another Esch et al. (2005). We found that we were only able to reproduce such effects using a $p(2 \times 2)$ surface supercell, as was done in Esch et al. (2005), which corresponds to a much higher defect concentration than that observed in the corresponding experiments. When we use larger $p(4 \times 4)$ or $p(5 \times 5)$ supercells, corresponding more closely to the experimental concentrations, we find a much weaker pairing, and furthermore it is rotated by 120°, i.e., it is between ions which are symmetrically inequivalent to those for which pairing was observed in the experiments in Esch et al. (2005). However, we note that our simulations are performed under the Tersoff–Hamann approximation (as were those in Esch et al., 2005), and thus (a) do not fully treat orbital directionality and (b) do not include the effects of the tip. Given the very low tunneling current of the measurements, it is possible that there are angular effects and/or non-negligible tip–surface interactions, which may be responsible for these features; in any case their origin remains unexplained. Furthermore, the pairing is not observed in all experiments (see Shahed et al., 2011 for example), which could be due to weaker tip–surface interactions.

3.2.2. Empty State Images

The empty state images of the three surface defects are given in the top row of **Figure 2**. At positive bias, the OV appears bright compared to its surroundings, due to a large, diffuse state centered on the vacancy, in agreement with images in Jerratsch et al. (2011). At +3.0 V bias the diffuse state spans the six closest cerium ions at the surface, while at a lower bias of +2.0 V, this diffuse state is transformed into a single or triple protrusion of Ce^{4+} ions neighboring the OV, as shown in **Figure 4**. The simulated empty state image of OH at positive bias voltages is also bright. Here, we find a rather localized feature at the OH, as compared to the more diffuse feature of the OV in the same bias voltage range. In contrast to the OV and OH, the FI is actually somewhat dark in the empty state image, which would make it more readily distinguishable from the other two defects than they would be from each other. In agreement with Jerratsch et al. (2011) we also find that Ce^{3+} ions appear dark due to their empty states being shifted toward higher energies.

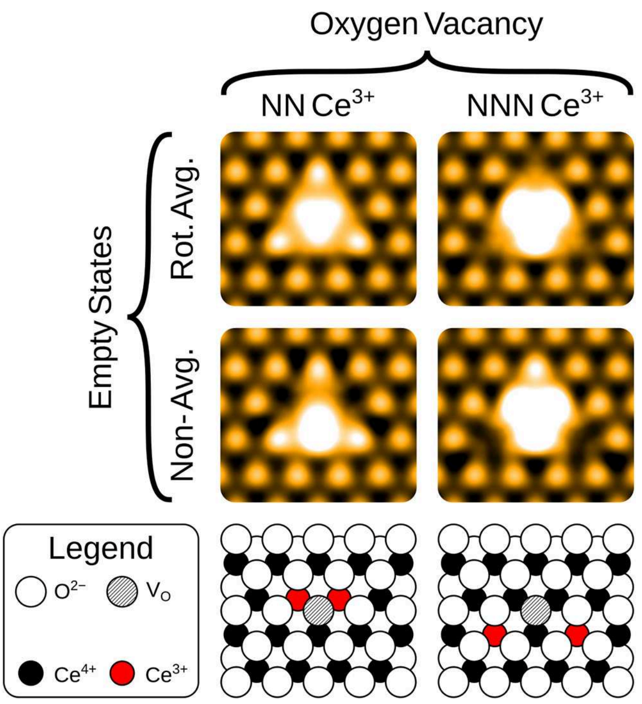

FIGURE 4 | Simulated empty images at a bias voltage of 2.0 eV of a surface OV, with the associated Ce^{3+} ions at either nearest neighbor (NN) or next nearest neighbor (NNN) lattice sites. The precise locations of the Ce^{3+} ions are shown in the schematics, for comparison with the non-rotationally averaged images.

3.3. STM Images of Defects in the Sub-Surface Layer

3.3.1. Filled State Images

The filled state STM appearances of the defects in the first oxygen sub-surface (third atomic) layer are shown in the bottom row of **Figure 5**. In contrast to the surface defects, their appearance is due primarily to the effect the defects have on the surface layer ions above them, rather than imaging the defect site itself. Hence, the apparent topography is a closer reflection of the actual surface topography (i.e., the relative heights of the surface ions).

Triangular protrusions in experimental filled state images have been ascribed to sub-surface oxygen vacancies (Esch et al., 2005; Grinter et al., 2010; Jerratsch et al., 2011). Our simulated images of a sub-surface OV do produce such a protrusion, although we also find that it should be accompanied by a significant depression of the three closest surface oxygen ions, which relax into the surface due to the presence of the vacancy beneath them. The magnitude of this effect depends upon the locations of the Ce^{3+} ions; in the lowest energy NNN configuration, the ions relax downwards by 0.19 Å, while with NN localization, this is reduced to 0.09 Å.

For the sub-surface FI, the main effect for NN localization is the outward relaxation by 0.05 Å. This is also seen if the electrons are at NNN positions, but then it is accompanied by a slight inward relaxation of the three nearest surface O ions, by 0.04 Å. Both of these effects are similar for the OV, but more subtle due to the smaller degree of relaxation.

The sub-surface OH is somewhat different from the other two defects. The triple protrusion is again present, and the associated displacement of the ions is of similar magnitude to the surface FI with NN localization, namely 0.05 Å. However, the more striking feature is the apparent protrusion of the three nearest neighbor oxygen ions, which are pushed out of the surface by the OH by 0.05 Å. This produces a small, bright triangle with the opposite orientation relative to the underlying lattice, as compared to the sub-surface oxygen vacancy. A careful analysis of the partial density of states suggests that the reason why these ions appear brighter, despite being at a similar height, is that the states associated with them are pushed up slightly in energy, likely due to the presence of the proton between them.

3.3.2. Empty State Images

The empty state images, shown in the top row of **Figure 5**, all follow similar patterns. Again, the Ce^{3+} ions appear as dark depressions in all cases, due to the unoccupied states being pushed upwards in energy. For the OV, with NNN localization, we also see a triangular protrusion associated with the Ce^{4+} ions being repelled upward by the defect. We note that this pattern was suggested to be the fingerprint of a surface OV in the combined experimental and theoretical work of Jerratsch et al. (2011). While their observations in empty state images were matched to a single protrusion at negative bias, identification based solely on empty state imaging could lead to mis-interpreting sub-surface OVs as surface OVs, especially at low positive bias where the two appear very much alike (see **Figure 4**). There is a similar, but more subtle protrusion for the FI.

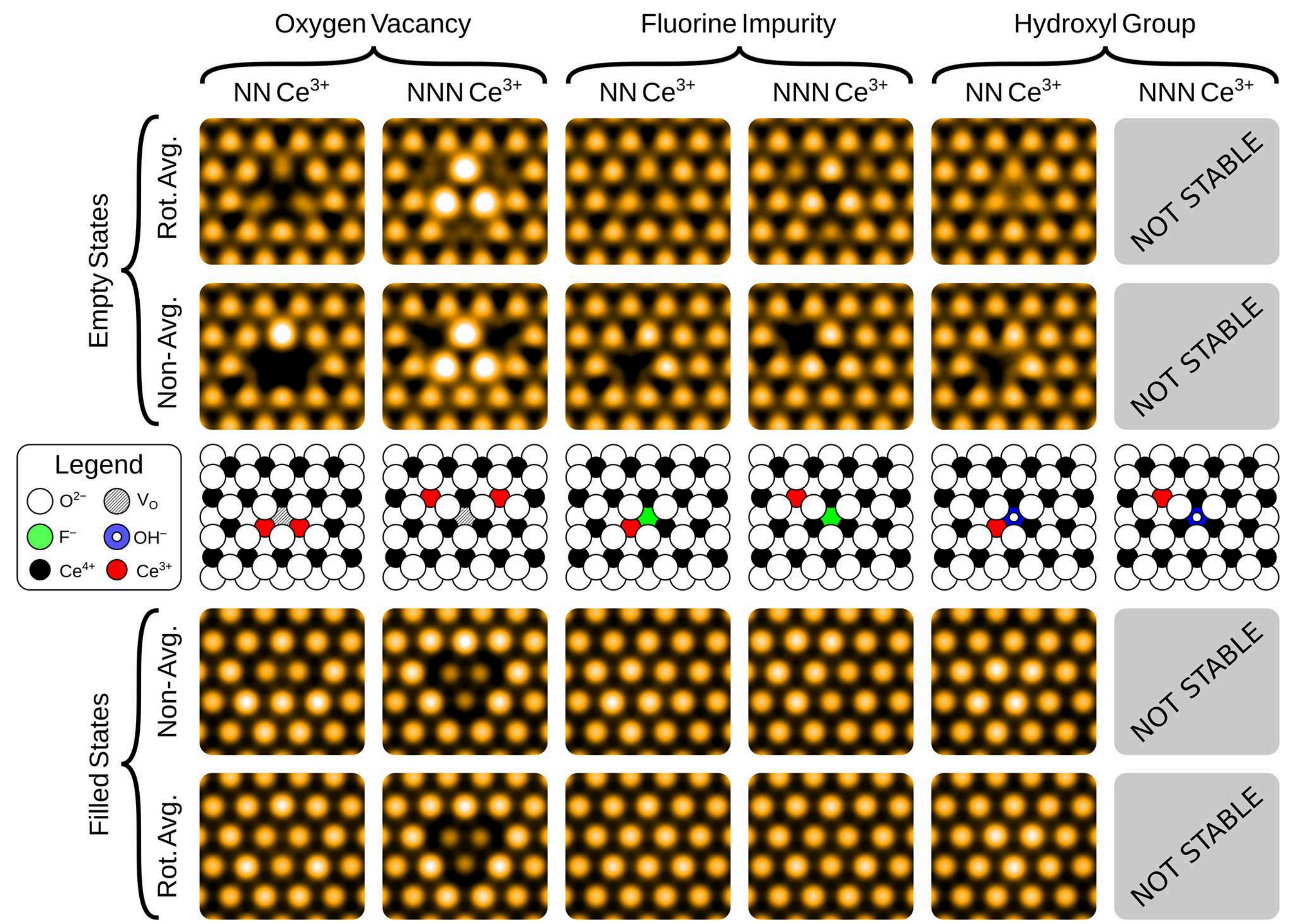

FIGURE 5 | Simulated filled and empty state images of the three sub-surface anionic defects, with the associated Ce^{3+} ions at either nearest neighbor (NN) or next nearest neighbor (NNN) lattice sites. The precise locations of the Ce^{3+} ions are shown in the schematics, for comparison with the non-rotationally averaged images.

3.4. f-Electron Spectral Features

Scanning tunneling spectroscopy (STS) has been performed on $CeO_2(111)$ thin films to determine the energy levels of localized f electrons on Ce^{3+} ions located near defects. This provides another possible way to distinguish between defects that share the same gross appearance. Therefore, we have plotted in **Figure 6** the eigenvalues of the f-electron states associated with all of the defects studied herein. They fall in a range from 0.72 to 0.86 eV with respect to the valence band edge. In the combined experimental and theoretical work by Jerratsch et al. (2011) such spectral features were used to discriminate between defects with different Ce^{3+} localization patterns.

3.5. Diffusion Rates

The diffusion barrier for OVs at $CeO_2(111)$ has been calculated by a number of authors (Plata et al., 2013; Su et al., 2016). The values are generally quite small, i.e., below 0.5 eV, which is consistent with the experimentally observed high ionic conductivity of the material; indeed, this is a property of the material which is exploited in many of its technological applications.

In Kullgren et al. (2014), a diffusion mechanism of the FI was considered which involves it moving out of the lattice position to a site on top of a neighboring Ce^{4+} ion; with the OV thus formed moving simultaneously to a sub-surface position. The barrier height was calculated to be 1.47 eV, which we re-calculate using our current computational set-up to be 1.42 eV.

In Fernández-Torre et al. (2014), a diffusion barrier was presented for surface OH groups. The mechanism involves the transfer of the proton between a surface and sub-surface oxygen site, with a reported activation energy of 1.8 eV. Here, we considered an alternative mechanism similar to that of FI diffusion, in which the entire OH group moves up on to a surface Ce^{4+} ion. We find the barrier height for such a process to be 1.50 eV, i.e., 0.3 eV lower than the barrier reported in Fernández-Torre et al. (2014), and much more similar to the barrier for FI diffusion.

We used these values to calculate diffusion rates from an Arrhenius expression at 77 K, 300 K and 600 K, along with a

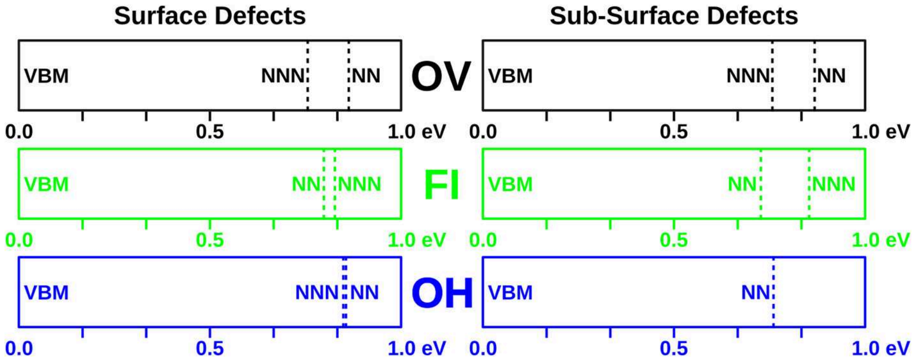

FIGURE 6 | f electron eigenvalues of the defects studied in this work. Positions of f-levels with respect to the valence band for all defects with nearest (NN) and next nearest neighbor (NNN) localization are indicated.

prefactor of $1 \times 10^{13} s^{-1}$. These values, are collected in **Table 2**. Furthermore, given that the diffusion path for the latter two defects considered here requires the concerted motion of both the defects themselves, and a sub-surface oxygen ion, the actual rate is likely to be lower than that calculated here. We therefore conclude that OVs are too mobile to be imaged by STM, for which a single scan takes on the order of minutes, unless experiments are conducted at temperatures significantly lower than room temperature. FIs and OHs on the other hand, should be immobile for sufficiently long for them to be imaged within the full range of temperatures used in experiments reported in the literature.

We note that it has been demonstrated that migration of charged defects on the ceria surface could proceed via a diabatic channel, in which case the activation energy barriers may be drastically increased, by as much as a factor of three (Lustemberg et al., 2016). However, this only applies to migrating species that change their charge state during the transition. For the defects considered here the migrating species remain in the same charge state in the initial, final and transition states.

3.6. Defect Distributions and Interactions

For non-interacting defects of a given species, the proportion of surface to sub-surface defects at thermal equilibrium can be determined by evaluating an appropriate Boltzmann factor. The energy difference between an isolated surface and sub-surface defect of the same type is +0.12 eV for the OV, −0.48 eV for an FI and −1.45 eV for an OH (with a negative value indicating greater stability in the surface layer), according to our calculations. Using these values to calculate the Boltzmann factors at 600 K (within the range of temperatures used in Nörenberg and Briggs, 1999; Nörenberg, 2002; Namai et al., 2003; Esch et al., 2005) suggests that the number of surface OVs for each sub-surface OV is at most 1×10^{-1}, for FIs at least 1×10^{4} and at least 1×10^{12} for OHs. These values, along with analogous ones calculated for $T = 77$ K and $T = 300$ K, are collected in **Table 3**, and can be summarized by saying that under most conditions one would expect to see OVs in the sub-surface layer, but FIs and OHs in the surface layer.

TABLE 2 | Defect diffusion rates of isolated defects (in s^{-1}) from the Arrhenius equation, using a pre-factor of 1×10^{13} s^{-1}.

T (K)	OV	FI	OH
77	1.88×10^{-20}	1.47×10^{-80}	7.60×10^{-86}
300	3.98×10^{4}	1.49×10^{-11}	6.55×10^{-13}
600	6.31×10^{8}	1.22×10^{1}	2.56

TABLE 3 | Relative proportions of isolated surface to sub-surface defects of a given species from Boltzmann factors.

T (K)	OV	FI	OH
77	1.40×10^{-8}	2.61×10^{31}	8.03×10^{94}
300	9.64×10^{-3}	1.16×10^{8}	2.29×10^{24}
600	9.82×10^{-2}	1.08×10^{4}	1.51×10^{12}

However, at higher defect concentrations, interactions between defects will necessarily become important; indeed, one of the enduring points of interest regarding the defects observed in experimental images is their distribution, and in particular, their tendency to form linear and triangular clusters at the surface. DFT simulations have shown that surface OVs do not exhibit any tendency toward NN clustering (Conesa, 2009; Zhang et al., 2009; Sutton et al., 2015), based on comparisons of total energies. On the other hand, both surface FIs (Kullgren et al., 2014) and OHs have been calculated to be stable as constituents of NN dimers (Fernández-Torre et al., 2014) although the binding energies are small (< 0.1 eV/dimer).

Furthermore, combinations of surface OVs, along with sub-surface OVs or sub-surface OHs have also been considered in the DFT study in Wu and Gong (2016), although all of those combinations were shown subsequently to be unstable with respect to decomposition into their isolated constituents (Wolf et al., 2016).

The above conclusions are based solely on differences in total energies, but more recently, the importance of configurational entropy in determining distributions of OVs and FIs has been studied. In Kullgren et al. (2017), DFT-based Monte Carlo simulations showed that OHs have far less tendency to form NN clusters than FIs, and that OHs instead tend to form clusters in which they are located at next-nearest-neighbor sites. For FIs, large and compact clusters are most abundant at 300 K while at 600 K straight and hooked linear clusters are abundant.

DFT based Monte Carlo calculations have also been performed including both surface and sub-surface OVs at a variety of temperatures and levels of reduction (Han et al., 2018). At lower concentrations (10% and 15%) and/or temperature (80 K) the number of NN clusters at the surface was found to be very small, although the numerous sub-surface vacancies do exhibit p(2×2) ordering, consistent with the interpretation of low temperature AFM experiments (Torbrügge et al., 2007). Meanwhile at higher temperatures and levels of reduction, numerous linear NN clusters were observed.

However, standard Monte Carlo simulations such as those described above do not take into account kinetic effects, which must be significant due to the high mobility of OVs. Indeed, the surface OV clusters are reported by Han et al. to be abundant only in simulations performed at temperatures at which OVs are expected to be mobile on the time-scale of STM experiments (see **Table 2**). Although it is conceivable that OVs which comprise parts of clusters could be significantly less mobile than isolated OVs, calculations that address this possibility have not been reported.

4. CONCLUSION

STM images of the ceria (111) surface exhibit a number of point defects in an otherwise regular hexagonal pattern. These features are commonly assigned to surface oxygen vacancies, although alternative interpretations have been proposed. In this contribution, we have used Density Functional Theory (DFT) with the PBE+U functional to examine three likely candidates for anionic defects on $CeO_2(111)$, namely oxygen vacancies (OV), fluorine impurities (FI) and hydroxyl groups (OH), in both the surface and the first sub-surface layers. We have presented and analyzed a consistent set of simulated STM images for them under the Tersoff–Hamann approximation.

Based on our results we suggest that missing spots in the *filled state* images at the surface oxygen lattice could be caused by *any* of the three defects considered here. However, the corresponding empty state images of the three defects are rather different to one another. The clean surface in this case shows spots at Ce sites, and against this background, surface OVs appear as large, bright features centered at oxygen sites, and OHs give smaller but more intense features also at oxygen sites. The FI signature is also centered on an oxygen site, but consists of a triangle of darkened Ce ions surrounding it, relative to the background lattice.

The appearance of the sub-surface defects in filled state images is mainly a reflection of topographical changes at the surface (relaxation of ions) induced by those defects. In filled state images, OVs produce triangular protrusions of next nearest neighbor surface oxygen ions similar to those observed in some experiments (cf. Esch et al., 2005; Grinter et al., 2010), but they also produce a rather striking triangular depression *inside* the protruding triangle, to an extent that may in fact render it difficult to distinguish from a triangular surface defect cluster of either OV, OH or FI. The FI reproduces both of these features, but the contrast variations are more subtle, while the OH produces only protrusions. In the empty state images we note that Ce^{4+} which are nearest neighbors to a sub-surface OV appear bright. A similar but much more subtle effect is also seen for sub-surface FI.

In general, our simulations suggest that missing spots in the *empty state* images, at the cerium lattice, can be caused by Ce^{3+} that are *not* nearest or next nearest neighbor to a surface vacancy, or nearest neighbor to a surface hydroxide.

Regarding their physical properties other than appearances, calculations indicate that OVs are most stable at the sub-surface and that they diffuse rapidly unless the temperature is kept much below room temperature. OVs do not have a strong *energetic* tendency to cluster, although DFT-based Monte Carlo simulations suggest that, given sufficient vacancy concentration and temperature, clusters can emerge. However, their amounts seem to be appreciable only when the temperature is too high for them to be imaged. In contrast, both FI and OH are quite stable at the surface and diffuse slowly. FI's show a tendency for clustering in the surface layer over a wide range of temperatures and concentrations, with OH representing an intermediate case.

AUTHOR CONTRIBUTIONS

MJW and JK performed the calculations and prepared the first version of the manuscript. All authors were involved in the planning of the work, the analysis and interpretation of the results and in the finalization of the text.

ACKNOWLEDGMENTS

This work was supported financially by the Swedish Research Council (VR), the Swedish National Strategic e-Science programme eSSENCE, and Åforsk. Some of the calculations were performed on resources provided by the Swedish National Infrastructure for Computing (SNIC) at UPPMAX and NSC.

REFERENCES

Andersson, D. A., Simak, S. I., Johansson, B., Abrikosov, I. A., and Skorodumova, N. V. (2007). Modeling of CeO_2, Ce_2O_3, and CeO_{2-x} in the LDA+U formalism. *Phys. Rev. B* 75:035109. doi: 10.1103/PhysRevB.75.035109

Berner, U., and Schierbaum, K. (2001). Cerium oxide layers on Pt(111): A scanning tunneling microscopy study. *Thin. Solid Films* 400, 46–49. doi: 10.1016/S0040-6090(01)01446-8

Blöchl, P. E. (1994). Projector augmented-wave method. *Phys. Rev. B* 50:17953. doi: 10.1103/PhysRevB.50.17953

Campbell, C. T., and Peden, C. H. F. (2005). Oxygen vacancies and catalysis on ceria surfaces. *Science* 309, 713–714. doi: 10.1126/science.1113955

Castellarin-Cudia, C., Surnev, S., Schneider, G., Podlucky, R., Ramsey, M. G., and Netzer, F. P. (2004). Strain-induced formation of arrays of catalytically active sites at the metal–oxide interface. *Surf. Sci.* 554, L120–L126. doi: 10.1016/j.susc.2004.01.059

Castleton, C. W. M., Kullgren, J., and Hermansson, K. (2007). Tuning LDA+*U* for electron localization and structure at oxygen vacancies in ceria. *J. Chem. Phys.* 127:244704. doi: 10.1063/1.2800015

Chan, L. H., and Yuhara, J. (2015). Growth and structure of ultrathin cerium oxide films on Rh(111). *J. Chem. Phys.* 143:074708. doi: 10.1063/1.4929349

Conesa, J. C. (2009). Surface anion vacancies on ceria: Quantum modelling of mutual interactions and oxygen adsorption. *Catal. Today* 143, 315–325. doi: 10.1016/j.cattod.2008.11.005

Dorado, B., Amadon, B., Freyss, M., and Bertolus, M. (2009). DFT+*U* calculations of the ground state and metastable states of uranium dioxide. *Phys. Rev. B* 79:235125. doi: 10.1103/PhysRevB.79.235125

Dudarev, S. L., Botton, G. A., Savrasov, S. Y., Humphreys, C. J., and Sutton, A. P. (1998). Electron-energy-loss spectra and the structural stability of nickel oxide: An LSDA+*U* study. *Phys. Rev. B* 57:1505. doi: 10.1103/PhysRevB.57.1505

Esch, F., Fabris, S., Zhou, L., Montini, T., Africh, C., Fornasiero, P., et al. (2005). Electron localization determines defect formation on ceria substrates. *Science* 309, 752–755. doi: 10.1126/science.1111568

Fernández-Torre, D., Carrasco, J., Ganduglia-Pirovano, M. V., and Pérez, R. (2014). Hydrogen activation, diffusion, and clustering on $CeO_2(111)$: A DFT+*U* study. *J. Chem. Phys.* 141:014703. doi: 10.1063/1.4885546

Fronzi, M., Piccinin, S., Delley, B., Traversa, E., and Stampfl, C. (2009). Water adsorption on the stoichiometric and reduced $CeO_2(111)$ surface: A first-principles investigation. *Phys. Chem. Chem. Phys.* 11, 9188–9199. doi: 10.1039/b901831j

Fukui, K.-I., Takakusagi, S., Tero, R., Aizawa, M., Namai, Y., and Iwasawa, Y. (2003). Dynamic aspects and associated structures of $TiO_2(110)$ and $CeO_2(111)$ surfaces relevant to oxide catalyses. *Phys. Chem. Chem. Phys.* 5, 5349–5359. doi: 10.1039/b307879e

Grinter, D. C., Ithnin, R., Pang, C. L., and Thornton, G. (2010). Defect structure of ultrathin ceria films on Pt(111): Atomic views from scanning tunnelling microscopy. *J. Phys. Chem. C* 114, 17036–17041. doi: 10.1021/jp102895k

Han, Z.-K., Yang, Y.-Z., Zhu, B., Ganduglia-Pirovano, M. V., and Gao, Y. (2018). Unraveling the oxygen vacancy structures at the reduced $CeO_2(111)$ surface. *Phys. Rev. Mater.* 2:035802. doi: 10.1103/PhysRevMaterials.2.035802

Hasegawa, T., Shahed, S. M. F., Sainoo, Y., Beniya, A. I. N., Watanabe, Y., and Komeda, T. (2014). Epitaxial growth of $CeO_2(111)$ film on Ru(0001): Scanning tunneling microscopy (STM) and x-ray photoemission spectroscopy (XPS) study. *J. Chem. Phys.* 140:044711. doi: 10.1063/1.4849595

Himmetoglu, B., Floris, A., Gironcoli, S., and Cococcioni, M. (2014). Hubbard-corrected DFT energy functionals: The LDA+*U* description of correlated systems. *Int. J. Quant. Chem.* 114, 14–49. doi: 10.1002/qua.24521

Hu, S., Wang, Y., Wang, W., Han, Y., Fan, Q., Feng, X., Xu, Q., and Zhu, J. (2015). Ag nanoparticles on reducible $CeO_2(111)$ thin films: Effect of thickness and stoichiometry of ceria. *J. Phys. Chem. C* 119, 3579–3588. doi: 10.1021/jp511691p

Jerratsch, J.-F., Shao, X., Nilius, N., Freund, H.-J., Popa, C., Ganduglia-Pirovano, M. V., et al. (2011). Electron localization in defective ceria films: A study with scanning-tunneling microscopy and density-functional theory. *Phys. Rev. Lett.* 106:246801. doi: 10.1103/PhysRevLett.106.246801

Kresse, G., and Furthmüller, J. (1996a). Efficiency of ab-initio total energy calculations for metals and semiconductors using a plane-wave basis set. *Comp. Mater. Sci.* 6, 15–50. doi: 10.1016/0927-0256(96)00008-0

Kresse, G., and Furthmüller, J. (1996b). Efficient iterative schemes for *ab initio* total-energy calculations using a plane-wave basis set. *Phys. Rev. B* 54:11169. doi: 10.1103/PhysRevB.54.11169

Kresse, G., and Hafner, J. (1993). *Ab initio* molecular dynamics for liquid metals. *Phys. Rev. B* 47:558. doi: 10.1103/PhysRevB.47.558

Kresse, G., and Joubert, D. (1999). From ultrasoft pseudopotentials to the projector augmented-wave method. *Phys. Rev. B* 59:1758. doi: 10.1103/PhysRevB.59.1758

Kullgren, J., Wolf, M. J., Castleton, C. W. M., Mitev, P., Briels, W. J., and Hermansson, K. (2014). Oxygen vacancies versus fluorine at $CeO_2(111)$: A case of mistaken identity? *Phys. Rev. Lett.* 112:156102. doi: 10.1103/PhysRevLett.112.156102

Kullgren, J., Wolf, M. J., Mitev, P. D., Hermansson, K., and Briels, W. J. (2017). DFT-based monte carlo simulations of impurity clustering at $CeO_2(111)$. *J. Phys. Chem. C* 121, 15127–15134. doi: 10.1021/acs.jpcc.7b00299

Lu, J.-L., Gao, H.-J., Shaikhutdinov, S., and Freund, H.-J. (2006). Morphology and defect structure of the $CeO_2(111)$ films grown on Ru(0001) as studied by scanning tunneling microscopy. *Surf. Sci.* 600, 5004–5010. doi: 10.1016/j.susc.2006.08.023

Luches, P., Pagliuca, F., and Valeri, S. (2011). Morphology, stoichiometry, and interface structure of CeO_2 ultrathin films on Pt(111). *J. Phys. Chem. C* 115, 10718–10726. doi: 10.1021/jp201139y

Lustemberg, P., Pan, Y., Shaw, B.-J., Grinter, D., Pang, C., Thornton, G., et al. (2016). Diffusion barriers block defect occupation on reduced $CeO_2(111)$. *Phys. Rev. Lett.* 116:236101. doi: 10.1103/PhysRevLett.116.236101

Ma, S., Rodriguez, J., and Hrbek, J. (2008). STM study of the growth of cerium oxide nanoparticles on Au(111). *Surf. Sci.* 602, 3272–3278. doi: 10.1016/j.susc.2008.08.021

Marabelli, F., and Wachter, P. (1987). Covalent insulator $CeO_2(111)$: Optical reflectivity measurements. *Phys. Rev. B* 36, 1238–1243. doi: 10.1103/PhysRevB.36.1238

Molinari, M., Parker, S. C., Sayle, D. C., and Islam, M. S. (2012). Water adsorption and its effect on the stability of low index stoichiometric and reduced surfaces of ceria. *J. Phys. Che. C* 116, 7073–7082. doi: 10.1021/jp300576b

Mullins, D. R., Albrecht, P. M., Chen, T.-L., Calaza, F. C., Biegalski, M. D., Christen, H. M., et al. (2012). Water dissociation on $CeO_2(100)$ and $CeO_2(111)$ thin films. *J. Phys. Chem. C* 116, 19419–19428. doi: 10.1021/jp306444h

Mullins, D. R., Overbury, S. H., and Huntley, D. R. (1998). Electron spectroscopy of single crystal and polycrystalline cerium oxide surfaces. *Surf. Sci.* 409, 307–319. doi: 10.1016/S0039-6028(98)00257-X

Murgida, G. E., and Ganduglia-Pirovano, M. V. (2013). Evidence for subsurface ordering of oxygen vacancies on the reduced $CeO_2(111)$ surface using density-functional and statistical calculations. *Phys. Rev. Lett.* 110:246101. doi: 10.1103/PhysRevLett.110.246101

Namai, Y., Fukui, K.-I., and Iwasawa, Y. (2003). Atom-resolved noncontact atomic force microscopic and scanning tunneling microscopic observations of the structure and dynamic behavior of $CeO_2(111)$ surfaces. *Catal. Today* 85, 79–91. doi: 10.1016/S0920-5861(03)00377-8

Nolan, M., Grigoleit, S., Sayle, D. C., Parker, S. C., and Watson, G. W. (2005). Density functional theory studies of the structure and electronic structure of pure and defective low index surfaces of ceria. *Surf. Sci.* 576, 217–229. doi: 10.1016/j.susc.2004.12.016

Nörenberg, H. (2002). Scanning tunnelling microscopy investigations of nanostructures on single crystalline TiO_2 and CeO_2. *Mater. Sci. Technol.* 18, 755–758. doi: 10.1179/026708302225003875

Nörenberg, H. and Briggs, G. A. D. (1997). Defect structure of nonstoichiometric $CeO_2(111)$ surfaces studied by scanning tunneling microscopy. *Phys. Rev. Lett.* 79:4222. doi: 10.1103/PhysRevLett.79.4222

Nörenberg, H., and Briggs, G. A. D. (1998). Surface structure of $CeO_2(111)$ studied by low current STM and electron diffraction. *Surf. Sci.* 402, 734–737. doi: 10.1016/S0039-6028(97)00999-0

Nörenberg, H., and Briggs, G. A. D. (1999). Defect formation on $CeO_2(111)$ surfaces after annealing studied by STM. *Surf. Sci.* 424, L352–L355. doi: 10.1016/S0039-6028(99)00212-5

Perdew, J. P., Burke, K., and Ernzerhof, M. (1996). Generalized gradient approximation made simple. *Phys. Rev. Lett.* 77:3865. doi: 10.1103/PhysRevLett.77.3865

Perdew, J. P., Burke, K., and Ernzerhof, M. (1997). Erratum: Generalized gradient approximation made simple. *Phys. Rev. Lett.* 78:1396. doi: 10.1103/PhysRevLett.78.1396

Pfau, A., and Schierbaum, K. D. (1994). The electronic structure of stoichiometric and reduced CeO_2 surfaces: An XPS, UPS and HREELS study. *Surf. Sci.* 321, 71–80. doi: 10.1016/0039-6028(94)90027-2

Pieper, H. H., Derks, C., Zoellner, M. H., Olbrich, R., Tröger, L., Schroeder, T., et al. (2012). Morphology and nanostructure of $CeO_2(111)$ surfaces of single crystals and Si(111) supported ceria films. *Phys. Chem. Chem. Phys.* 14, 15361–15368. doi: 10.1039/c2cp42733h

Plata, J. J., Márquez, A. M., and Sanz, J. F. (2013). Transport properties in the $CeO_{2-x}(111)$ surface: From charge distribution to ion-electron collaborative migration. *J. Phys. Chem. C* 117, 25497–25503. doi: 10.1021/jp4066532

Setvín, M., Wagner, M., Schmid, M., Parkinson, G. S., and Diebold, U. (2017). Surface point defects on bulk oxides: Atomically-resolved scanning probe microscopy. *Chem. Soc. Rev.* 46, 1772–1784. doi: 10.1039/C7CS00076F

Shahed, S. M. F., Hasegawa, T., Sainoo, Y., Watanabe, Y., Isomura, N., Beniya, A., et al. (2014). STM and XPS study of $CeO_2(111)$ reduction by atomic hydrogen. *Surf. Sci.* 628, 30–35. doi: 10.1016/j.susc.2014.05.008

Shahed, S. M. F., Sainoo, Y., and Komeda, T. (2011). Scanning tunneling microscope study of surface morphology variation of $CeO_2(111)$ with changing annealing condition. *Japanese J. Appl. Phys.* 50:08LB05. doi: 10.1143/JJAP.50.08LB05

Su, Y.-Q., Filot, I. A. W., Liu, J.-X., Tranca, I., and Hensen, E. J. M. (2016). Charge transport over the defective $CeO_2(111)$ surface. *Chem. Mater.* 28, 5652–5658. doi: 10.1021/acs.chemmater.6b01548

Sutton, J. E., Beste, A., and Overbury, S. H. (2015). Origins and implications of the ordering of oxygen vacancies and localized electrons on partially reduced $CeO_2(111)$. *Phys. Rev. B* 92:144105. doi: 10.1103/PhysRevB.92.144105

Szabová, L., Stetsovych, O., Dvořák, F., Farnesi Camellone, M., Fabris, S., Mysliveček, J., et al. (2012). Distinct physicochemical properties of the first ceria monolayer on Cu(111). *J. Phys. Chem. C* 116, 6677–6684. doi: 10.1021/jp211955v

Tersoff, J., and Hamann, D. R. (1983). Theory and application for the scanning tunneling microscope. *Phys. Rev. Lett.* 50, 1998. doi: 10.1103/PhysRevLett.50.1998

Tersoff, J., and Hamann, D. R. (1985). Theory of the scanning tunneling microscope. *Phys. Rev. B* 31:805. doi: 10.1103/PhysRevB.31.805

Torbrügge, S., Reichling, M., Ishiyama, A., Morita, S., and Custance, O. (2007). Evidence of subsurface oxygen vacancy ordering on reduced $CeO_2(111)$. *Phys. Rev. Lett.* 99:056101. doi: 10.1103/PhysRevLett.99.056101

Trovarelli, A. (2013). *Catalysis by Ceria and Related Materials, 2nd Edn*. London: Imperial College Press.

Weststrate, C. J., Westerström, R., Lundgren, E., Mikkelsen, A., Andersen, J. N., and Resta, A. (2009). Influence of oxygen vacancies on the properties of ceria-supported gold. *J. Phys. Chem. C* 113, 724–728. doi: 10.1021/jp8088116

Wolf, M. J., Kullgren, J., Broqvist, P., and Hermansson, K. (2017). Fluorine impurities at $CeO_2(111)$: Effects on oxygen vacancy formation, molecular adsorption, and surface re-oxidation. *J. Chem. Phys.* 146:044703. doi: 10.1063/1.4973239

Wolf, M. J., Kullgren, J., and Hermansson, K. (2016). Comment on "Clustering of oxygen vacancies at $CeO_2(111)$: Critical role of hydroxyls". *Phys. Rev. Lett.* 117:279601. doi: 10.1103/PhysRevLett.117.279601

Wu, X.-P., and Gong, X.-Q. (2016). Clustering of oxygen vacancies at $CeO_2(111)$: Critical role of hydroxyls. *Phys. Rev. Lett.* 116:086102. doi: 10.1103/PhysRevLett.116.086102

Wuilloud, E., Delley, B., Schneider, W.-D., and Baer, Y. (1984). Spectroscopic evidence for localized and extended f-symmetry states in $CeO_2(111)$. *Phys. Rev. Lett.* 53, 202–205. doi: 10.1103/PhysRevLett.53.202

Zarraga-Colina, J., Nix, R. M., and Weiss, H. (2004). A novel approach to the epitaxial growth of CeO_2 films on Si(111). *Surf. Sci.* 563, L251–L255. doi: 10.1016/j.susc.2004.06.156

Zarraga-Colina, J., Nix, R. M., and Weiss, H. (2005). Growth, structure, and stability of ceria films on Si(111) and the application of CaF_2 buffer layers. *J. Phys. Chem. B* 109, 10978–10985. doi: 10.1021/jp0508296

Zhang, C., Michaelides, A., King, D. A., and Jenkins, S. J. (2009). Oxygen vacancy clusters on ceria: Decisive role of cerium f electrons. *Phys. Rev. B* 79:075433. doi: 10.1103/PhysRevB.79.075433

Zhao, X., Ma, S., Hrbek, J., and Rodriguez, J. A. (2007). Reaction of water with Ce-Au(111) and CeO_x/Au(111) surfaces: Photoemission and STM studies. *Surf. Sci.* 601, 2445–2452. doi: 10.1016/j.susc.2007.04.106

Zhou, J., Baddorf, A. P., Mullins, D. R., and Overbury, S. H. (2008). Growth and characterization of Rh and Pd nanoparticles on oxidized and reduced $CeO_x(111)$ thin films by scanning tunneling microscopy. *J. Phys. Chem. C* 112, 9336–9345. doi: 10.1021/jp711198c

Zhou, Y., Perket, J. M., Crooks, A. B., and Zhou, J. (2010). Effect of ceria support on the structure of Ni nanoparticles. *J. Phys. Chem. Lett.* 1, 1447–1453. doi: 10.1021/jz1003044

Zhou, Y., and Zhou, J. (2012). Ti/$CeO_x(111)$ interfaces studied by XPS and STM. *Surf. Sci.* 606, 749–753. doi: 10.1016/j.susc.2012.01.003

Conflict of Interest Statement: The authors declare that the research was conducted in the absence of any commercial or financial relationships that could be construed as a potential conflict of interest.

frontiers in Chemistry

ORIGINAL RESEARCH
published: 22 May 2019
doi: 10.3389/fchem.2019.00203

Multiscale Modeling of Agglomerated Ceria Nanoparticles: Interface Stability and Oxygen Vacancy Formation

Byung-Hyun Kim [1,2], Jolla Kullgren [1], Matthew J. Wolf [1], Kersti Hermansson [1]* and Peter Broqvist [1]**

[1] Department of Chemistry—Ångström Laboratory, Uppsala University, Uppsala, Sweden, [2] Platform Technology Laboratory, Korea Institute of Energy Research, Daejeon, South Korea

The interface formation and its effect on redox processes in agglomerated ceria nanoparticles (NPs) have been investigated using a multiscale simulation approach with standard density functional theory (DFT), the self-consistent-charge density functional tight binding (SCC-DFTB) method, and a DFT-parameterized reactive force-field (ReaxFF). In particular, we have modeled $Ce_{40}O_{80}$ NP pairs, using SCC-DFTB and DFT, and longer chains and networks formed by $Ce_{40}O_{80}$ or $Ce_{132}O_{264}$ NPs, using ReaxFF molecular dynamics simulations. We find that the most stable {111}/{111} interface structure is coherent whereas the stable {100}/{100} structures can be either coherent or incoherent. The formation of {111}/{111} interfaces is found to have only a very small effect on the oxygen vacancy formation energy, E_{vac}. The opposite holds true for {100}/{100} interfaces, which exhibit significantly lower E_{vac} values than the bare surfaces, despite the fact that the interface formation eliminates reactive {100} facets. Our results pave the way for an increased understanding of ceria NP agglomeration.

Keywords: multiscale modeling, density functional theory, self-consistent charge density functional tight binding, reducible oxides, cerium dioxide, nanoparticles, agglomeration

Edited by:
*Maria Veronica Ganduglia-Pirovano,
Institute of Catalysis and
Petrochemistry (ICP), Spain*

Reviewed by:
*Michael Nolan,
University College Cork, Ireland
Sergey M. Kozlov,
King Abdullah University of Science
and Technology, Saudi Arabia*

***Correspondence:**
*Jolla Kullgren
jolla.kullgren@kemi.uu.se
Kersti Hermansson
kersti@kemi.uu.se
Peter Broqvist
peter.broqvist@kemi.uu.se*

Specialty section:
*This article was submitted to
Physical Chemistry and Chemical
Physics,
a section of the journal
Frontiers in Chemistry*

Received: *09 January 2019*
Accepted: *18 March 2019*
Published: *22 May 2019*

Citation:
*Kim B-H, Kullgren J, Wolf MJ,
Hermansson K and Broqvist P (2019)
Multiscale Modeling of Agglomerated
Ceria Nanoparticles: Interface Stability
and Oxygen Vacancy Formation.
Front. Chem. 7:203.
doi: 10.3389/fchem.2019.00203*

INTRODUCTION

Synthesized ceria samples often appear in the form of agglomerates of nanoparticles (NPs) (Wang and Feng, 2003; Mai et al., 2005; Du et al., 2007; Lin et al., 2012; Liu et al., 2015; Schlick et al., 2016; Lykaki et al., 2017). In most cases, agglomeration degrades the total catalytic performance due to the elimination of reactive surfaces (Li et al., 2003; de Diego et al., 2005). However, in some cases, agglomeration has been found to enhance the catalytic performance due to favorable properties of the interface itself, e.g., by facilitating the formation of critical defects (Maillard et al., 2005). For ceria, only a small fraction of the numerous published studies in recent years have scrutinized the nature of native interfaces. On the experimental side, Wang and Feng (2003) synthesized ceria NPs of truncated octahedral shape and of sizes of 3–10 nm, and noted that the agglomeration of their ceria NPs could be correlated with the disappearance of accessible {100} facets during growth. The resulting agglomerates consisted of NPs in the range of ∼1 μm in diameter and with each consecutive NP pair forming a coherent interface, i.e., perfectly matching their lattices across the interface by sharing a common {111} facet. Reactivity was not discussed in that study, but in a series of papers, Hojo et al. (2010) and Feng et al. (2012, 2016) reported that the atomic structure and local oxygen dynamics are modified by the formation of grain boundaries in thin-films of ceria. They also concluded that grain boundaries can be stabilized by the presence of oxygen vacancies.

On the theoretical side, Sayle and co-workers have used force-field simulations to investigate structure-property relationships for ceria nanostructures and have for example investigated nanocubes, nanorods, nanochains, and mesoporous structures (Sayle et al., 2005, 2011; Jeyaranjan et al., 2018). In one of their studies, ceria nanochains were generated via oriented attachment (OA) and used as model systems to explain the mechanism for ceria nanorod formation (Sayle et al., 2011). Sk et al. (2014) performed density functional theory (DFT) calculations for self-assembled one and two dimensional nanoceria networks. Thus, they studied nanowires and nanogrids built from corner-sharing Ce ions or from sharing of oxygen terminated {100} facets; the latter requiring an energy cost to reduce one side of the {100} facets of the NPs prior to agglomeration. For future reference, we note that the periodic boundary conditions used in Sk et al. (2014) induce constraints on the possible NP interfaces that can be modeled. To the best of our knowledge, detailed theoretical investigations at the atomic scale of *aperiodic* ceria NP interfaces and their redox activity are lacking in the scientific literature. The present study primarily deals with the interface between two ceria NPs and the specific oxygen chemistry that may accompany it.

In this work, we will show that stable ceria-ceria interface structures formed between agglomerated ceria NPs display oxygen redox properties that are quite different from those of either the bare surface or the bulk material, and that this is true both for the "rim" region and the "internal" region of the interface, and both for *coherent* and *incoherent* interfaces. Here the term "rim" refers to interface regions where the constituent atoms are exposed while the term "internal" refers to regions where they are not. Our model systems are ceria NP pairs, with an outlook toward chains at the end of the article.

Our method is a *sequential multiscale simulation approach* linking three levels of theory along the multiscale ladder, namely Hubbard augmented DFT (DFT+U) (Perdew et al., 1996; Dudarev et al., 1998), the self-consistent-charge density functional tight-binding approach (SCC-DFTB+U) (Elstner et al., 1998; Aradi et al., 2007; Kullgren et al., 2017), and finally, for stoichiometric NPs, also the reactive force-field (ReaxFF) method (van Duin et al., 2001; Broqvist et al., 2015). The SCC-DFTB method is an approximate DFT method, which combines an electronic structure description at the minimal basis-set level with a Coulombic expression for long-range interactions. The charges are of Mulliken type and are calculated self-consistently (SCC) in the simulation depending on the elements and the geometric structure. The ReaxFF method, finally, is an advanced bond-order-dependent force-field method, which allows for the description of dissociation and formation of chemical bonds in various kind of compounds.

Moving from DFT to SCC-DFTB to ReaxFF implies a scheme taking us from fine-grained toward more coarse-grained materials models, namely from electrons to atoms in the prevailing MODA language's model entities (Anne de Baas, 2018), as promoted within the European Materials Modeling Council (EMMC, 2019). We use a consistent parameterization of the SCC-DFTB and ReaxFF interaction models which are both trained against DFT+U data. These parameterization efforts were described in detail in previous publications (Broqvist et al., 2015; Kullgren et al., 2017). In the present paper, however, we mostly move in the opposite direction, from SCC-DFTB to DFT, using the former method to screen many NP assembly structures, the most stable of which are subsequently scrutinized using DFT. Finally we make use of the ReaxFF model for ceria to perform long MD simulations during the initial stages of nanoceria agglomeration. In the following, we will often omit the U term in our notation for DFT and SCC-DFTB not to burden the text, but it is in fact present in all our electronic calculations of (partially) reduced ceria systems.

We will present the stable ceria interface structures found and their effects on the oxygen vacancy formation energy, which we will use as a key descriptor of oxygen chemistry. We find that while agglomeration of course lowers the NPs' surface areas, the interface-specific defects might lead to an activation of agglomerated NPs toward redox processes. Finally, we also discuss how to extend our findings into larger interface systems using the ReaxFF method. Here we will briefly address the mechanism of NP agglomeration and relate to the concept of OA which has been amply discussed in the literature (Si et al., 2006; Du et al., 2007; Lin et al., 2012; Raju et al., 2014; Zhang and Banfield, 2014), and where nano-crystallites collide and interact favorably, e.g., by sharing some common crystallographic orientations, resulting in the formation of interfaces between the NPs.

INTERFACE CONSTRUCTION PROTOCOL AND COMPUTATIONAL METHODS

In this work, as mentioned, we use a computational protocol based on a combination of electronic structure methods, namely the SCC-DFTB and DFT methods, to study ceria NP interface structures. SCC-DFTB is roughly 2 orders of magnitude faster than standard (semilocal, i.e., "GGA"-type) DFT calculations. With a proper parameterization, the accuracy with respect to the training set will be close to that of the underlying DFT method. This agreement will be reported in the section Consistency Between the Methods That We Have Used. The considerable speedup compared to DFT makes SCC-DFTB a valuable tool for the investigaton of a large number of interface structures, which is exactly the way we have used it here.

The SCC-DFTB calculations were performed using the DFTB+ code (Elstner et al., 1998; Aradi et al., 2007). The parameters describing the Slater-Koster tables and repulsive potentials for ceria have been generated and thoroughly tested previously (Kullgren et al., 2017). DFT calculations in the implementation with plane waves and pseudopotentials were performed using the Vienna *ab-initio* simulation package (VASP) (Kresse and Hafner, 1993, 1994; Kresse and Furthmüller, 1996a,b). The exchange correlation energy was described within the generalized gradient approximation (GGA) following the work of Perdew-Burke-Ernzerhof (PBE) (Perdew et al., 1996).

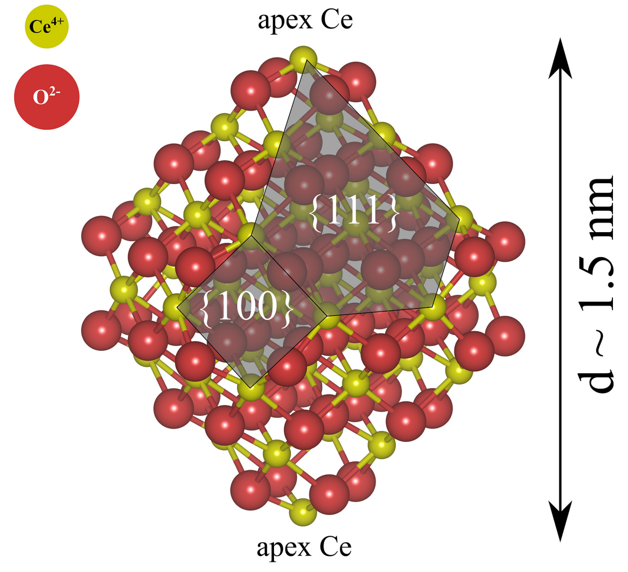

FIGURE 1 | Atomic structure of a stoichiometric truncated octahedral $Ce_{40}O_{80}$ NP optimized at the DFT+U ($U = 5$ eV) level in this work. Red and yellow spheres indicate O^{2-} and Ce^{4+}, respectively.

Pseudopotentials of the Projector Augmented Wave (PAW) type were used to describe the core electrons (Blöchl, 1994; Kresse and Joubert, 1999). The Kohn-Sham single-electron wave functions were expanded by plane waves with a cut-off energy of 408 eV. To accurately treat the strongly correlated Ce *4f* states, the rotationally invariant Hubbard correction scheme from Dudarev et al. (1998) with a U-value of 5 eV on the Ce *4f* states was applied. Previous studies have shown that this U-value gives a good description of the electronic properties of reduced ceria (Castleton et al., 2007; Loschen et al., 2008; Kullgren et al., 2013; Du et al., 2018). In all calculations, the Brillouin zone was sampled at the Γ-point. All structures were pre-optimized using SCC-DFTB. Some were selected and subsequently geometry optimized at the DFT level of theory. Geometry optimizations for all modeled structures were carried out until the maximal force acting on any one atom was <0.02 eV/Å.

We have primarily studied NP pairs, $(NP)_2$, formed by two stoichiometric truncated octahedral ceria NPs with the chemical formula $Ce_{40}O_{80}$. The two NPs were connected via low-index facets, forming {111}/{111} or {100}/{100} interfaces. The *free* solid-vacuum {111} surfaces of stoichiometric ceria are known to be the most stable ones and they make up the largest surface area on the isolated $Ce_{40}O_{80}$ particles (see **Figure 1**). *Free* {100} surfaces are the most reactive low-index surfaces of ceria and have been found to be present on truncated octahedral NPs in UHV (Zhang et al., 2011; Lin et al., 2014).

To generate representative NP interfaces we placed two identical NPs, facet to facet at a distance of 2.7 Å in a periodic cell of the dimensions, 4.5 × 3 × 3 nm^3. Reference calculations were performed for the isolated $Ce_{40}O_{80}$ NP, placed in a 3 × 3 × 3 nm^3 box. One such particle is approximately 15 Å in diameter. We used rather large cell sizes to prevent image-image interactions between particles in neighboring supercells. The same supercell sizes were used in both the DFT and the SCC-DFTB calculations. The final optimized structures were analyzed in terms of stability, structural parameters and electronic properties, as defined in the Results and Discussion section. The calculations for the O_2 molecule in its ground triplet electronic state were also performed, using a large periodic cell, 3 × 3 × 3 nm^3.

In summary, the following stoichiometric systems are examined by electronic structure methods in this study: an isolated truncated $Ce_{40}O_{80}$ labeled NP (**Figure 1**), and a number of $(Ce_{40}O_{80})_2$ systems labeled $(NP)_2$. Reduced systems, where one neutral O atom was removed from (various locations on) the ceria particle to form half an oxygen molecule, were also studied for both the NP and the $(NP)_2$ systems.

RESULTS AND DISCUSSION

Consistency Between the Methods That We Have Used

The DFTB parameters (the entries in the Slater-Koster table and the V_{rep} parameters) used here were trained against DFT calculations (Kullgren et al., 2017). In Kullgren et al. (2017), the DFTB model was subjected to an extended validation process, and passed the test of reproducing the reference DFT results with respect to NP structures as well as oxygen vacancy formation energies in ceria bulk and at the low-index surfaces. In the present paper, the DFTB model was further validated for some of the interface structures, and we find that calculated energies, such as the interface formation energy, $E_{interface}$, and the oxygen vacancy formation energy, E_{vac}, from SCC-DFTB are in reasonably good agreement with those from DFT (see the correlation in **Figure 2** and **Table S-I**). Moreover, the optimized DFT and SCC-DFTB structures are found to differ by <1% in terms of bond lengths. This consistency is a great advantage in our approach to generating interface models, as it reduces the number of computationally expensive DFT energy evaluations. We find that the computational approach used here, i.e., pre-screening using SCC-DFTB followed by full structural optimisations using DFT for selected systems is an efficient and useful protocol.

Identifying Stable Coherent and Incoherent Interfaces

For the single NP, we use a prototypical model structure (**Figure 1**), namely a stoichiometric $Ce_{40}O_{80}$ particle, which is a truncated octahedron exposing eight large {111} facets and six small {100} facets, two of which are decorated with an apex Ce ion. Ceria NPs exhibiting truncated octahedral shapes have been reported in many experiments (Wang and Feng, 2003; Mai et al., 2005; Du et al., 2007; Tan et al., 2011; Wang and Mutinda, 2011; Lin et al., 2012; Cordeiro et al., 2013; Florea et al., 2013; Liu et al., 2015) and previous theoretical studies have shown the truncated octahedral NPs to be stable also under vacuum conditions [see e.g., (Fronzi et al., 2009)].

SCC-DFTB calculations were performed to examine the stabilities of the NP pairs with respect to variation of the angle of rotation of "the second" NP with respect to "the first," where the axis of rotation is the direction joining the two centers-of-mass of the constituent NPs. Shifting one NP with respect to the other was also considered, leading to an interface which is a continuation of the bulk fluorite structure, i.e., a *coherent* interface. In this way, {111}/{111} and {100}/{100} interfaces were formed. After the SCC-DFTB pre-screening, four final structures emerged from our search for stable $(NP)_2$ agglomerates: one with the two NPs joined by {111} faces, and three which were joined by {100} faces; they were subjected to subsequent DFT optimizations. All figures and tables in the following are based on DFT results, except the very last figure which will show results from ReaxFF MD simulations.

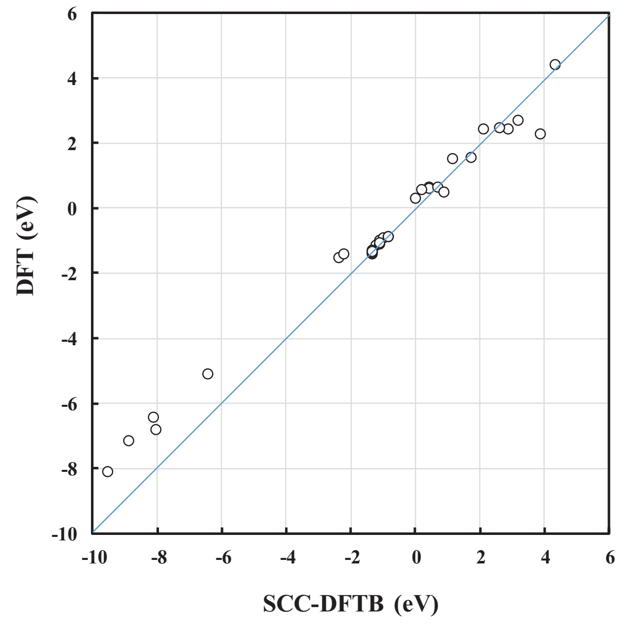

FIGURE 2 | Correlation plot between SCC-DFTB and DFT calculated energies, such as the $E_{\text{interface}}$ and E_{vac} of NP and $(NP)_2$ systems.

The {111}/{111} Interface

Here we note that shifting one NP with respect to the other NP, parallel to the interface, is essential in order to avoid the Coulomb repulsion between ions of the same type; see the cross-sectional view to the right in **Figure 3**. The most stable structure of the {111}/{111} interface is obtained by shifting one NP to match the stacking sequence of the other NP. As can be seen in **Figure 3**, the interface structure formed by attaching {111} to {111} facets is coherent. Hereafter, we use the label "$(NP)_2$-111-shift" to refer to agglomerated NPs with the {111}/{111} interface structures obtained by shifting.

The interface formation energy, $E_{\text{interface}}$, is calculated by the following equation:

$$E_{\text{interface}} = E_{\text{tot}}\,[(NP)_2] - 2 \times E_{\text{tot}}\,[NP] \tag{1}$$

where $E_{\text{tot}}[(NP)_2]$ is the total energy of agglomerated NPs with an interface and $E_{\text{tot}}[NP]$ is that of the isolated NP. To aid in the comparison of interface stabilities, especially for interfaces with oxygen vacancies, we will primarily use $E_{\text{interface}}$ values but also discuss the role of the interface area with normalized interface energies. Our calculated $E_{\text{interface}}$ of the $(NP)_2$-111-shift interface is −8.12 eV, as listed in **Table 1**. Note that a hexagonal close packed type {111}/{111} interface, which can be considered as a stacking fault, was also tested and found to be far less stable (by 2.72 eV) than the $(NP)_2$-111-shift interface.

The {100}/{100} Interface

The protocol for finding stable {100}/{100} interfaces included a scan of the angle of rotation of one NP with respect to the other from 0 to 45° with an increment of 1°. Following this pre-screening, three distinctly different stable structures were found, c.f. **Figure 4** and **Table 1**. They are either rotated by 15 or 45° with respect to each other, or by shifting one NP in a direction perpendicular to the interface normal by half of the lattice parameter so as to match the bulk fluorite structure. We will refer to them as "$(NP)_2$-100-rot15," "$(NP)_2$-100-rot45,"

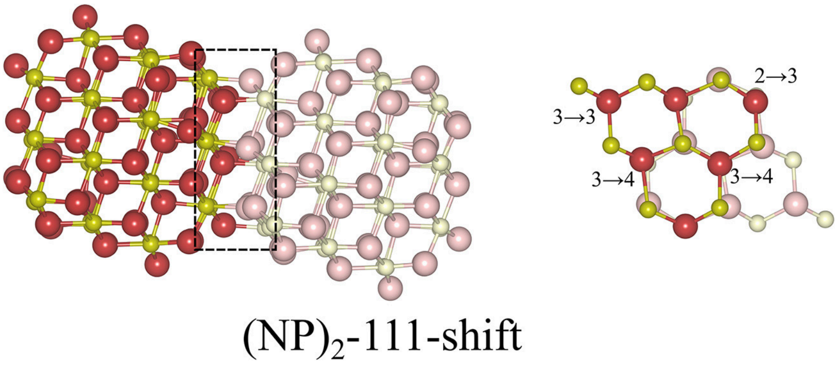

FIGURE 3 | Atomic configuration of the most stable structure that we found for the {111}/{111} interface. It was obtained by shifting one NP with respect to the other. In order to distinguish two NPs clearly, solid and pale colors are used for each NP. The left panel is a side-view, the right panel a cross-sectional view of the interface region, which has been framed in the left figure. The numbers in the right panel indicate the change of coordination number of oxygen ions from the isolated NP to the $(NP)_2$ structure. The oxygen ions which are not marked are symmetry-related to one of the marked ones.

TABLE 1 | Results for the stoichiometric systems, namely for the four stable DFT-optimized NP pairs found in this work, based on the truncated octahedral $Ce_{40}O_{80}$ NP.

Surface/interface label	**Interfaces involved**	**$E_{\text{interface}}$ (eV)**	**Number[a] of**			**Δ(bonds)[b]**	**Figure**
			$O_{CN=2}$	**$O_{CN=3}$**	**$O_{CN=4}$**		
NP(111)	–	–	2	4	0	–	**Figure 1**
NP(100)	–	–	4	0	0	–	**Figure 1**
$(NP)_2$-111-shift	NP(111)/NP(-1-1-1)	−8.12	0	6	6	+10	**Figure 3**
$(NP)_2$-100-rot15	NP(100)/NP(-100)	−7.19	4	4	0	+4	**Figure 4A**
$(NP)_2$-100-shift	NP(100)/NP(-100)	−6.82	2	4	2	+8	**Figure 4B**
$(NP)_2$-100-rot45	NP(100)/NP(-100)	−5.13	0	8	0	+8	**Figure 4C**

Data for the single NP itself is given as references. The table lists the notation, the interfacial energy, $E_{interface}$, calculated according to Equation (1), the number of surface/interface oxygen ions with certain coordination numbers (CNs), the number of new Ce–O bonds created on interface formation, and the figures where the DFT-optimized structures are shown. The interface notation NP(111)/NP(-1-1-1) refers to all symmetry-equivalent combinations, which is of course also true for the (111) surface notation.

[a] *Number of surface or interface O ions with CN=2, CN=3, CN=4 (Thus $O_{CN=2}$, for example, means that all these O atoms in the interface region have exactly two nearest-neighbor Ce ions each).*

[b] *Sum of the coordination numbers of all O ions in the interface region (they are depicted in* ***Figures 3, 4****) minus the sum of the coordination numbers of the same atoms in the isolated NPs. Neighbors within a distance limit of 2.6 Å were counted.*

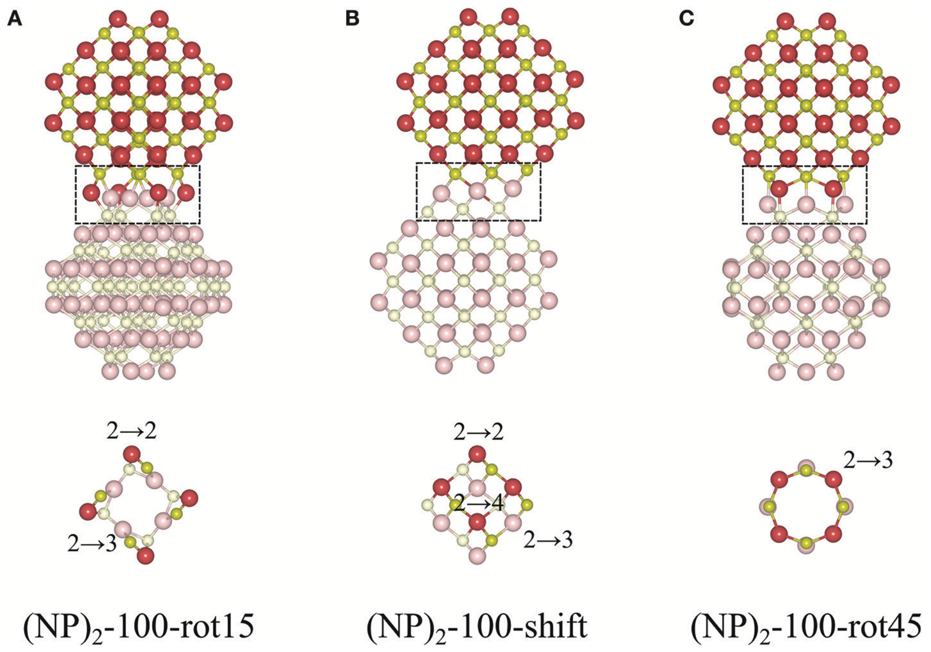

FIGURE 4 | Atomic configurations of the most stable structures of agglomerated $Ce_{40}O_{80}$ NPs with an {100}/{100} interface. **(A)** 15° relative rotation of the NPs, **(B)** a relative shift of the NPs, and **(C)** 45° relative rotation of the NPs. In each case, the upper row shows a side-view of the particle, and the bottom row gives a cross-sectional view through the interface region, which has been marked in the top row. The color scheme and the number scheme in the bottom row are the same as in **Figure 3**.

and "$(NP)_2$-100-shift" in the following. Thus, our results show that the {100}/{100} interface structures can be either coherent or incoherent: the {100}/{100} interface obtained by shifting is coherent while the {100}/{100} interfaces obtained by rotating by 15 or 45° are incoherent. In the literature, it has been suggested (Sk et al., 2014) that the formation of {100}/{100} interfaces requires that one side of a truncated ceria surface be cerium-terminated (having oxygen vacancies at a {100} surface) while the opposite side needs to be oxygen-terminated in order to match the crystal ordering when two particles agglomerate. However, this is a restriction following the use of periodic boundary conditions, where one NP formed an interface between a cerium-terminated surface and an oxygen-terminated surface of the same NP. When we give full freedom to the relaxation and formation of the {100}/{100} interface, such constraints do not exist.

The calculated $E_{\text{interface}}$ values for the agglomerated NPs with the 15 and 45° rotation is −7.19 and −5.13 eV, respectively, and for "$(NP)_2$-100-shift", it is −6.82 eV. Thus, if the NPs are stoichiometric, the {111}/{111} interface (−8.12 eV) is more stable than the {100}/{100} interface structures, likely due to the denser and larger contact areas of the former. It is important to note that for the reported interface energies, the contact areas are very different. The approximate area of the (111) facet on the free $Ce_{40}O_{80}$ NP is 43.8 Å^2 and that of the (100) facet is only 13.3 Å^2. This implies that the normalized interface energy per interface area will be much larger in case of the {100}/{100} interface. For the most stable {111}/{111} and {100}/{100} interfaces on the $(NP)_2$ agglomerate, we get −2.97 J/m^2 (−0.19 eV/Å^2) and −8.66 J/m^2 (−0.54 eV/Å^2), respectively. It is interesting to compare these values with the calculated surface energies of 0.71 J/m^2 and 1.54 J/m^2 for the extended (111) and (100) surfaces, respectively (Kullgren et al., 2017). The calculated surface energy of the (100) surface in Kullgren et al. (2017) was obtained for a reconstructed (100) surface where half of the terminal O ions on the (100) surface were moved to the opposite face to compensate the polarity of the surface. The normalized interface energy in the limit of an infinite interface will be twice the negative surface energy, and thus becomes −1.42 and −3.08 J/m^2, respectively. We note that the calculated normalized nano-interface energies reveal stronger adhesion by at least a factor of 2 compared to the limiting values. This reflects the fact that the surfaces on the small $Ce_{40}O_{80}$ NP mainly consist of rim atoms. Thus, even though the {111}/{111} interface on a total energy scale is more stable than the {100}/{100} interfaces, the latter has a stronger adhesion per unit area, and it may very well form in experiments through an initial first approach via the OA mechanism, and then become kinetically trapped (Si et al., 2006; Tan et al., 2011; Florea et al., 2013).

The interatomic distance within each nearest neighbor (NN) pair, Ce—O, Ce—Ce, and O—O at the rim of the interface of the three {100} systems, $(NP)_2$-100-rot15, -rot45, and -shift, are further analyzed here. First, let us discuss the NN distances of all constituent pairs at the {100} facets that are *not* involved in the interface formation. They are found to be identical with those of the isolated single $Ce_{40}O_{80}$ NP; this indicates that the effect of interface formation on the structural distortion is localized at the interface. Intuitively, one could imagine that the interface stability will correlate with the number of bonds formed upon agglomeration. We have therefore calculated coordination numbers and coordination number differences, Δ(bonds), for the all studied interfaces, c.f. **Table 1**. We note that while this hypothesis can be used to explain why $(NP)_2$-100-rot15 is the most stable interface among the three {100} systems, it fails to discriminate between the different {100}/{100} interfaces. The calculated Δ(bonds) for $(NP)_2$-100-rot15, -rot45, and -shift is +4, +8, and +8, respectively. Here, the NN distances of Ce—Ce and O—O, which will cause repulsive forces and thereby result in a less negative $E_{\text{interface}}$ (less stable interface), give a better correlation, c.f. **Figure 5**, which shows the calculated $E_{\text{interface}}$ vs. average O—O NN distance. The average O—O NN distance at the {100} facet in the isolated $Ce_{40}O_{80}$ NP is 2.56 Å, and at the interfaces the resulting distances are 2.86, 2.54, and 2.74 Å for $(NP)_2$-100-rot15, -rot45, and -shift, respectively. For $(NP)_2$-100-rot45 which is the least stable interface structure among our model interfaces, all the distances of O—O NN pairs at the interface are shorter than 2.56 Å. On the other hand, the interface formation by rotating 15° eliminates these short O—O NN pairs at the interface. We conclude that the larger stability of $(NP)_2$-100-rot15 is attributed to the stretching of the short O—O pairs at the interface, which mitigates repulsion.

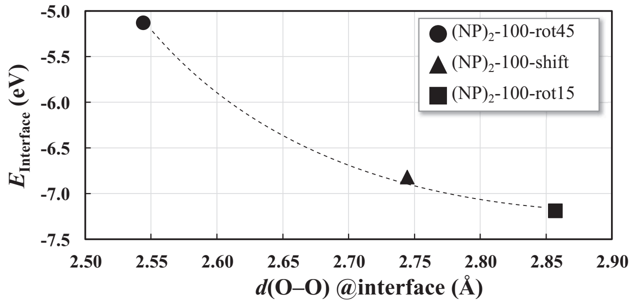

FIGURE 5 | $E_{\text{interface}}$ as a function of the O–O nearest-neighbor distances averaged over the 8 O ions in the interface region of each of the three "100" interfaces displayed in **Figure 4**. The curve is a guide to the reader's eye.

The presence of O—O pairs with short distances affects the electronic properties of agglomerated ceria NPs. This is seen in the electronic projected density of states (PDOS) for the three {100}/{100} interface systems when compared to the isolated NP (see **Figure 6**). Here, most notably, we find a clear peak at the valence band maximum in the PDOS for the isolated NP and $(NP)_2$-100-rot45 interface. Interestingly, the magnitude of the peak is found to be smaller in case of the $(NP)_2$-100-shift and -rot15 interfaces (see the black arrows in **Figure 6**). From the PDOS, it is clearly seen that this peak primarily originates from terminal O ions at the (100) facets (see the dashed red lines in **Figure 6**). We find that they are preserved for $(NP)_2$-100-rot45 whereas in the $(NP)_2$-100-shift and -rot15 interfaces, they are effectively quenched (compare solid green lines in **Figure 6**). Thus, in a sense, the $(NP)_2$-100-rot45 interface structure may be regarded as *electronically* analogous to the free {100} facets of isolated $Ce_{40}O_{80}$ NPs. For $(NP)_2$-100-rot15 and -shift, on the other hand, the surface states are significantly reduced by the interface formation.

Oxygen Chemistry

Oxygen vacancies play a central role in the redox chemistry of ceria and we have investigated whether and how the oxygen vacancy formation energy, E_{vac}, is affected by the creation of an interface between the NPs. E_{vac} is here calculated in the usual way, i.e., as

$$E_{\text{vac}} = E_{\text{tot}}\left[\text{NP} + n\text{V}_{\text{O}}\right] - E_{\text{tot}}\left[\text{NP}\right] + n \times \frac{1}{2} E\left[\text{O}_2(g)\right] \quad (2)$$

where $E_{\text{tot}}[\text{NP} + n\text{V}_{\text{O}}]$ and $E_{\text{tot}}[\text{NP}]$ are the total energies of the system with and without the number of oxygen vacancies, $n\text{V}_{\text{O}}$, respectively. $E[O_2(g)]$ is the energy of an O_2 molecule in its ground triplet electronic state.

First we give a general remark, namely that we find that in all cases, for the interfaces as well as for the single NP, the oxidation states of the apex Ce ions (determined from the 4f-electron occupancy) change from 4+ to 3+ after the oxygen

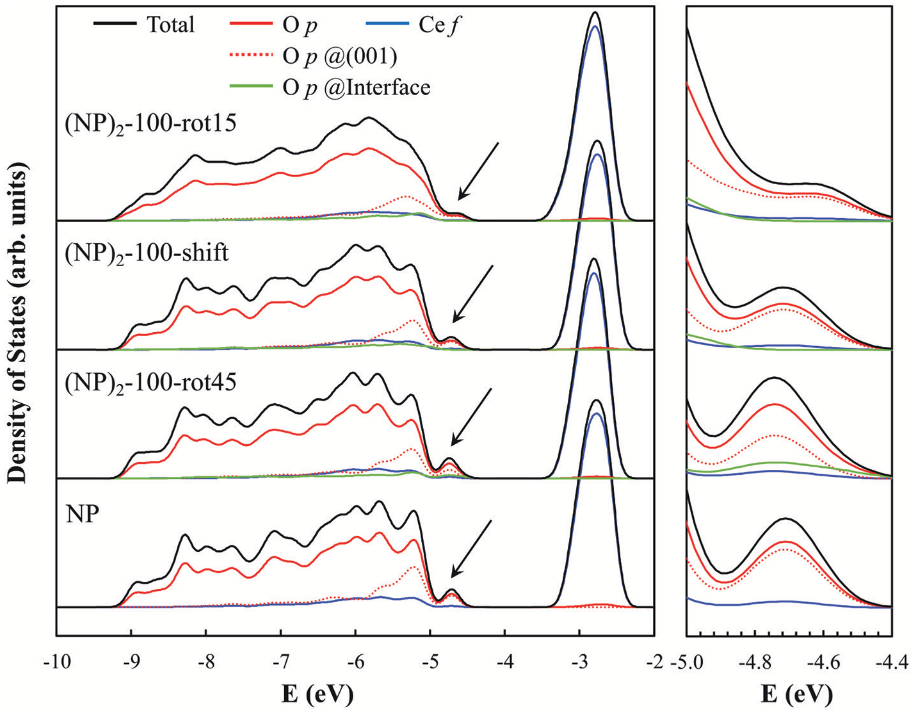

FIGURE 6 | Electronic PDOS for the three "100"-connected $(NP)_2$ systems as well as for the single NP (as a reference). The PDOS diagrams were aligned with respect to the core levels of the O atoms at the center of each NP system. The black arrows in the left panel indicate the surface states induced by the terminal O^{2-} ions at the free {100} facets of the single NP and $(NP)_2$ systems, and especially so at the $(NP)_2$-100-rot45 interface (see text); these states are magnified in the rightmost panel. The computed band gaps [VB(O 2*p*) → CB(Ce 4*f*)] for $(NP)_2$-100-rot15, -shift, -rot45 and the isolated NP are 1.25, 1.49, 1.36, and 1.53 eV, respectively.

vacancy formation. The apex Ce ions are marked in **Figure 1** for the isolated NP and are present in all the $(NP)_2$ systems as well but are not so easy to discern in the figures. The locations of the excess electrons created at the interface is consistent with several previous single-NP studies in the literature, which reported that the two Ce^{3+} ions are preferentially located at the apex sites where the coordination numbers of the Ce ions are the lowest (see Loschen et al., 2007, 2008; Kullgren et al., 2013; Sk et al., 2014).

Let us now consider oxygen vacancy formation at different surfaces and sub-surface positions on an *isolated NP* as shown in **Figure 1**. The vacancy will be labeled according to the facet involved and the label of the surface of sub-surface O removed, as listed in the second column in **Table 2**. The resulting E_{vac} values are also given in the table. The smallest E_{vac} value, i.e., the energetically most stable site for an oxygen vacancy to be formed in an isolated NP is the 2-coordinated O^{2-} site at the {100} facet ("$O_{(100)}$" in **Figure 7A**) with $E_{\mathrm{vac}} = +0.55$ eV, which is in good agreement with the previous DFT work published by the group of Neyman et al., showing that a low-coordinated oxygen vacancy formation costs the least energy (Migani et al., 2010). Oxygen vacancies at the {111} facet (see **Figure 7A**) fall in the range from +1.50 to +1.91 eV depending on their vicinity to the {100} facets; the further from the {100} facet, the higher the E_{vac} value.

We find that the most preferable site for an oxygen vacancy to form at *the {111}/{111} interface* is at a 3-coordinated O^{2-} site (labeled $O^{A}_{\mathrm{interface}}$ in **Figure 7B**) with a formation energy of +0.59 eV which is similar to the corresponding site in the isolated NP. For $O^{B}_{\mathrm{interface}}$, E_{vac} is +1.31 eV. When an oxygen vacancy was formed at $O^{*}_{\mathrm{interface}}$, the vacancy was found to be healed by O′ which was originally located behind the adjacent Ce, which

TABLE 2 | Vacancy formation energies, E_{vac}, for the formation of one and two vacancies at the surface/interface according to Equation (2).

System	Label of 1st removed O	Coordination number	E_{vac}, 1st (eV)	E_{vac}, 2nd (eV)
NP(111)	(111) (A)[a]	3	+1.50	Not done
	(111) (B)[a]	3	+1.75	Not done
	(111) (C)[a]	3	+1.91	Not done
	(100)[a]	2	+0.55	Not done
	Sub-(111)[a]	4	+1.83	Not done
$(NP)_2$-111-shift	Interface (A)[b]	3	+0.59	+0.72
	Interface (B)[b]	4	+1.31	Not done
$(NP)_2$-100-rot15	Interface (A)[c]	2	+0.28	+0.26
	Interface (B)[c]	3	+0.69	Not done
$(NP)_2$-100-shift	Interface (A)[d]	4	+0.24	+0.56
	Interface (B)[d]	2	+0.31	Not done
	Interface (C)[d]	3	+0.37	Not done
$(NP)_2$-100-rot45	Interface[e]	3	−1.53	+0.11

For the $(NP)_2$ systems, a 2nd vacancy was created by removal of each of the remaining interface O ions in turn, but only one of them at a time; the lowest value found is reported as the 2nd E_{vac} in the table. [a]***Figure 7A***. [b]***Figure 7B***. [c]***Figure 8A***. [d]***Figure 8B***. [e]***Figure 8C***.

results in the same structure as when the vacancy was created at $O^A_{interface}$. We conclude that for a pair of truncated octahedral NPs joined by an {111}/{111} interface, which is coherent, the interface formation has none (or a very small) effect on the oxygen vacancy formation capability at the interface.

For *the {100}/{100} interfaces*, the structures and oxygen site labeling schemes are shown in **Figure 8** and their coordination numbers and E_{vac} values are given in **Table 2**. We find that here the oxygen vacancy formation behavior is different from both that of the isolated NP and that of the {111}/{111} interface. For the most stable configuration among the {100}/{100} interface structures, $(NP)_2$-100-rot15, the lowest E_{vac} value (+0.28 eV) is about half of the lowest value for the isolated NP, which was already small (+0.55 eV) (c.f. **Figure 8A**). In fact, all the {100}/{100} interfaces display very small E_{vac} values despite the fact that the interfaces themselves are quite stable. The reason is no doubt connected to the fact that new bonds are formed between the NPs but the NN coordination numbers are modest in these structures: enough to hold the particles strongly together but not enough to hang on to O ions if the opportunity for reduction arises. This is true not only at the rims of these interfaces, but throughout the cross-section, as the coordination number is maintained also in the middle of the cross-section.

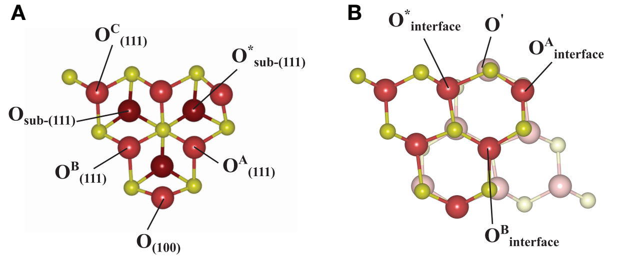

NP(111) facet

$(NP)_2$-111-shift interface

FIGURE 7 | Atom labeling scheme used in the text and in **Table 2** for discussion of oxygen vacancy formation at **(A)** the {111} facet of the isolated $Ce_{40}O_{80}$ NP and at **(B)** the $(NP)_2$-111-shift interface formed from it. The same color scheme as in **Figure 3** has been used, except that the sub-surface oxygens in **(A)** are colored dark red. In both **(A)** and **(B)**, the left-most Ce atom in the upper row and the right-most Ce atom in the bottom row in **(B)** are the "apex Ce" marked in **Figure 1**.

The ultimate oxygen lability is demonstrated by the $(NP)_2$-100-rot45 interface which has a large negative E_{vac}, −1.53 eV, meaning that, thermodynamically speaking, this oxygen vacancy would be formed spontaneously at the interface (and have a stabilizing effect on the interface). A second oxygen can also easily be removed, at hardly any cost (c.f. **Table 2**). The E_{vac} values of the second oxygen vacancy lies in the range from +0.11 to +0.56 eV for all the {100}/{100} interface structures. Under alternating reducing and oxidizing conditions, i.e., when the chemical potential of oxygen changes, E_{vac} will change accordingly. At some point, E_{vac} will turn negative and vacancies will stabilize the interface. Thus, reducing conditions may promote the stability of the interface significantly by oxygen removal from the interface.

The decreased E_{vac} value at {100}/{100} interfaces can be understood by examining the average NN O—O distance at the interface. We find that the occurrence of short O—O pairs at the interface (discussed above) diminishes after the oxygen vacancy formation. For example, the average NN O—O distance of $(NP)_2$-100-rot45 increases significantly, from 2.54 to 2.85 Å, when an oxygen vacancy is formed at the interface. It is then also observed that the two Ce^{3+} ions are generated at the apexes of the agglomerated NPs. We have found (not shown here) that these generated Ce^{3+} ions can be further utilized as adsorption sites for incoming oxygen molecules from the surroundings, similar to the phenomenon of *supercharged oxygen storage capacity* discussed earlier in the literature for ceria NPs (Kullgren et al., 2013; Renuka et al., 2015).

In summary, we find that {100}/{100} interface formation can lower E_{vac} significantly. In other words, the interface formation eliminates the areas of reactive (100) surfaces but promotes a more facile oxygen extraction, which in turn may promote an increased low-temperature oxygen storage capacity of ceria via the so called supercharging mechanism (Kullgren et al., 2013). **Figure 9** summarizes the relative energies of the interface structures considered in this work as a function of increasing number of oxygen vacancies. The reference system is two isolated NPs at infinite distance, and their oxygen vacancies are created by

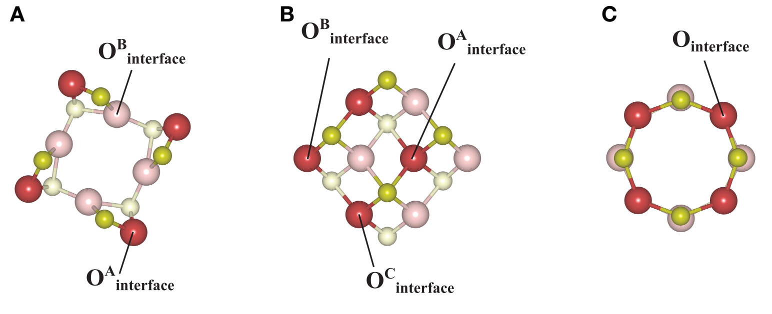

$(NP)_2$-100-rot15

$(NP)_2$-100-shift

$(NP)_2$-100-rot45

FIGURE 8 | Atom labeling scheme used in the text and in **Table 2** for discussion of oxygen vacancy formation at **(A)** the $(NP)_2$-100-rot15, **(B)** the $(NP)_2$-100-shift, and **(C)** the $(NP)_2$-100-rot45 interface structures.

removing neutral O atoms from a {100} facet of each NP. While the {111}/{111} interface is more stable for the stoichiometric cases, we find that the {100}/{100} interface promotes a lower E_{vac} compared to the {111}/{111} interface. Interestingly, in the same comparison, oxygen vacancy formation at the {111}/{111} interface slightly increases E_{vac}. As a result, in the presence of two oxygen vacancies, the stabilities of {100}/{100} interface structures, here $(NP)_2$-100-rot15 and -rot45, become comparable with that of the {111}/{111} interface (see **Figure 9**). This result paves the way not only for understanding the engineering of the interface structure of nanoceria for improved low-temperature redox activity, but also for suggesting experimental guidelines to control a growth direction of ceria nanowires. For example, our results suggest that under oxidizing conditions, a preferential growth direction of agglomerated NPs would be ⟨111⟩ while the {100}/{100} interface can be formed dominantly under reducing conditions.

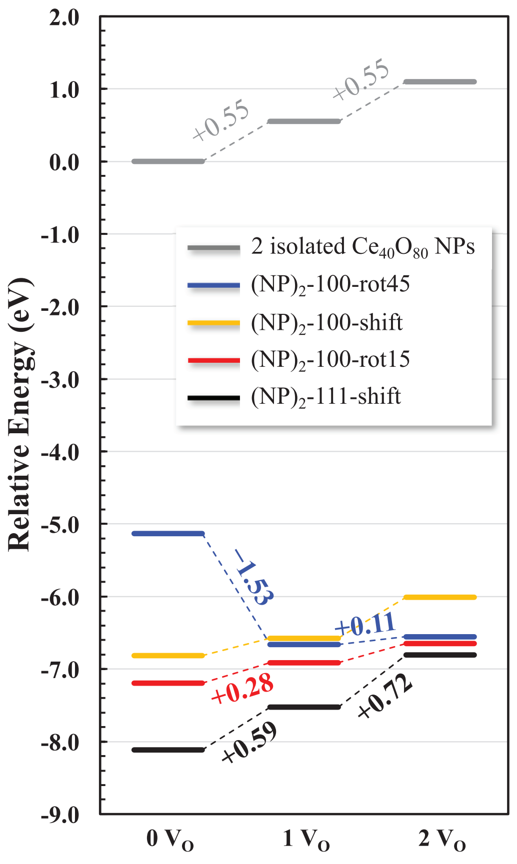

FIGURE 9 | Relative energy diagram for oxygen reduction of agglomerated NPs. Numbers along the pathway denote the corresponding E_{vac}. Two isolated NPs constitute the reference system.

Extrapolation to Larger Systems

One might raise a question whether the interface construction procedure used in this work will also apply to larger systems and what role the interface area plays. To answer these questions, we constructed interfaces between two $Ce_{132}O_{264}$ NPs as shown in **Figure 10**. The {111}/{111} interface can still be formed following a continuation of bulk fluorite (see **Figure 10A**), and one might expect that the interface formation will be similar to that of the smaller system, $Ce_{40}O_{80}$, albeit with a larger area of overlap. However, for {100}/{100} interfaces, the interface construction by rotation does not work since it requires a large rearrangement of constituent ions at the interface which will induce a distortion of the structure. For example, since the interface structure of $(Ce_{132}O_{264})_2$-100-rot15 (**Figure 10B**) contains overlapping Ce and O ions at the center of the interface, it is impossible to avoid the repulsion between these unless the whole interface structure is distorted, which obviously requires a huge amount of energy. "Overlapping ions" here means that if the interface region is seen in a projection perpendicular to the interface, then the Ce ions in the two constituent NPs would (almost) overlap with each other, and similarly for the O ions. Interface construction by shifting also suffers from O ion overlaps as the interface area becomes larger. For a $(Ce_{132}O_{264})_2$-100-shift NP dimer, constructed as shown in **Figure 10C**, there are 36 overlapping O ions at the interface, but only two sites are available for Ce—O bonding (dashed circle in **Figure 10C**). To prevent this overlapping and produce a coherent bulk fluorite structure at the interface as was achieved for $(Ce_{40}O_{80})_2$-100-shift, at

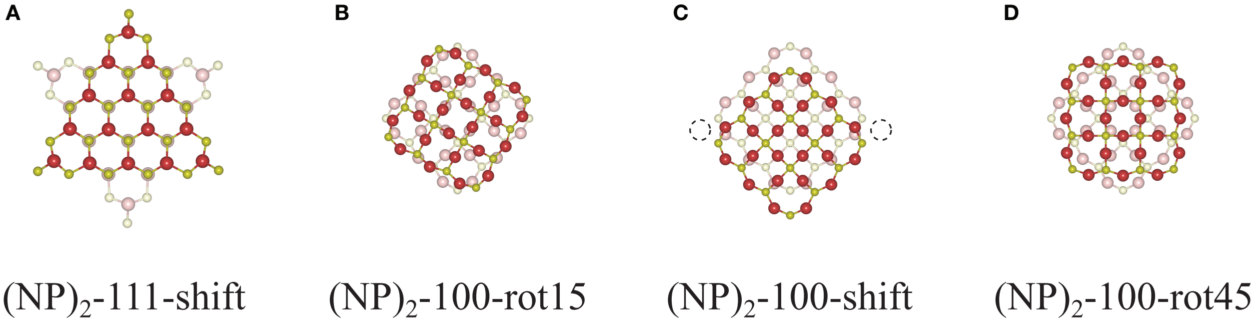

FIGURE 10 | Cross-sectional views of the interface structures of **(A)** $(NP)_2$-111-shift, **(B)** $(NP)_2$-100-rot15, **(C)** -shift, and **(D)** -rot45 of two unrelaxed agglomerated $Ce_{132}O_{264}$ NPs (taken from truncated DFT bulk structures).

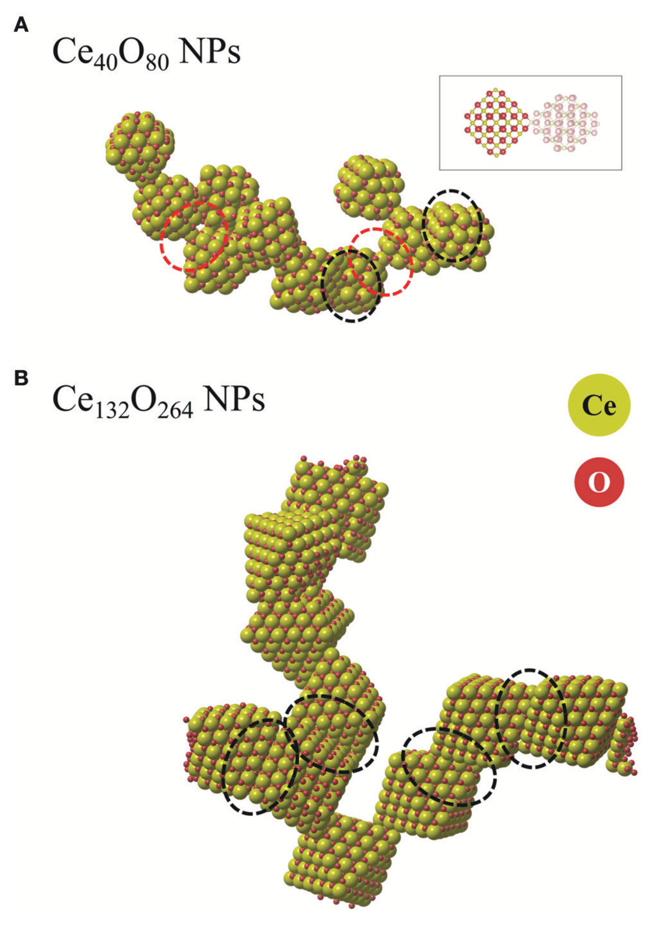

FIGURE 11 | Snapshots from ReaxFF MD simulations of agglomerated NPs of **(A)** $Ce_{40}O_{80}$ and **(B)** $Ce_{132}O_{264}$. The ionic radius of Ce ions was enlarged for the sake of clarity. Red and black dashed ovals indicate apex/{100} interfaces and {111}/{111} interfaces, respectively. The inset indicates the atomic configuration of an apex/{100} interface.

least 16 O ions need to be removed at the interface. Needless to say, the stoichiometric interface structure of $(Ce_{132}O_{264})_2$-100-rot45 as shown in **Figure 10D** would be very unstable due to the overlapped ions at the interface. However, they could be stabilized at reducing conditions by oxygen removal from the interface.

For the large NPs as well as for the smaller ones, we have also performed ReaxFF molecular dynamics (MD) simulations addressing the dynamics of the agglomeration process. The parameter set of ReaxFF used here was derived by us from DFT data (Broqvist et al., 2015). Further technical details about the validation of the parameters of ReaxFF are presented in the **Supplemental Material**. Two simulations extending over 5 ns at 400 K using the NVT ensemble, one with 10 $Ce_{40}O_{80}$ NPs and one with 10 larger $Ce_{132}O_{264}$ NPs, were performed in the current study. The former system consists of particles exposing four small {100} facets each (c.f. **Figure 1**), while the latter represents a system of particles exposing only one, albeit larger, {100} facet per particle. One might say the MD simulations are too short to capture the entire agglomeration process. However, they are long enough to include the coalescence and initial restructuring of the interfaces. In the case of a low particle density (as we have here) we expect that the effective barrier to transform a meta-stable {100}/{100} interface into the energetically more stable {111}/{111} interface must be bound by the interface energy of the former. The magnitude of the interface energy is larger than 5 eV which is large enough to permit long-lived interfaces, even if they happen to be meta-stable ones. The real barrier could obviously be quite different since particles forming the interface may slide or rotate while still maintaining contact. One aim with these MD simulations is therefore to look for indications of dynamical changes in the interface structures formed.

Figures 11A,B compare representative snapshots from the two simulations. We first note that the $Ce_{40}O_{80}$ NPs form an isolated agglomerate while the $Ce_{132}O_{264}$ NPs form an extended two-dimensional web. In both cases, we observe that various kinds of interfaces are formed, not only the energetically stable {111}/{111} interfaces as we described in the earlier section, but also {111}/{100}, apex/{100}, and partially matched {111}/{111} interfaces. This observation is in line with the theoretical findings of Fichthorn and co-workers (Alimohammadi and Fichthorn, 2009; Raju et al., 2014) who showed that titania NPs prefer to aggregate in the direction of approach in vacuum, which suggests that the interface formation may not always follow the thermodynamically most stable pathway. For example, in the system of the smaller particles ($Ce_{40}O_{80}$), we do not observe any formation of the energetically stable {100}/{100} interfaces, but instead find the coherent {111}/{111} interfaces, incoherent {111}/{100} interfaces, and apex/{100}. We attribute this fact to the strong variation in interface energy with respect to particle rotation, which implies that particles have to meet at "just the right" angle to form the {100}/{100} interface. We observe two interfaces where the apex ion of one particle binds to the center of a {100} facet of another particle (apex/{100}). We note the similarity of this structure to the interface presented in the theoretical work by Sk et al. (2014), although, in our case the two particles are rotated with respect to each other. In this structure (**Figure 11A**), a positively charged Ce ion at one apex is bonded to a square of negatively charged O ions on the {100} facet. The interface is seen to readily rotate during the MD simulation. For comparison, we calculated $E_{\text{interface}}$ of the apex/{100} interface energy using Equation (1) at the DFT level to be −1.87 eV. This value is significantly smaller in magnitude than that of the {100}/{100} interfaces which range from −5.1 to −7.2 eV. Nevertheless, the energy is not small enough to rule out that apex/{100} interfaces, once formed, could have a substantial life time, clearly longer than the short simulation time used here. The snapshot from the MD simulation of the $Ce_{132}O_{264}$ system shown in **Figure 11B** dominantly displays the formation of {111}/{111} interfaces. This is in good agreement with an experimental finding (c.f. Figure 7B in Florea et al., 2013). As discussed for overlapping ions of larger NPs above, the fact that {100}/{100} interfaces are not found in our agglomerate of $Ce_{132}O_{264}$ NPs is likely due to the repulsion between overlapping Ce and O ions, respectively. However, under reducing conditions such interfaces might be more likely to form, which is an interesting topic for further study.

CONCLUSIONS

In this work, we addressed the effects that agglomeration may have on the stability and redox activity of ceria NPs. We applied a computational protocol based on a multiscale simulation approach combining three levels of theory, namely DFT, SCC-DFTB and ReaxFF. In particular, we have studied the formation of $Ce_{40}O_{80}$ pairs using DFT and SCC-DFTB, and larger agglomerates of $Ce_{40}O_{80}$ or $Ce_{132}O_{264}$ NPs in MD simulations with ReaxFF.

The most stable {111}/{111} interface structure was found to be coherent, i.e., it exhibits a continuation of the bulk structure, whereas the stable {100}/{100} structures can be either coherent or incoherent. A systematic study of the implications of interface formation on the oxygen chemistry revealed that (i) {111}/{111} interface formation has only a very small effect on the redox activity, and (ii) E_{vac} decreases significantly for oxygen atoms in the vicinity of {100}/{100} interfaces. We conclude that while interface formation eliminates reactive {100} facets, it promotes an enhanced low-temperature redox activity involving the extraction of lattice oxygen; the net result might be an overall increased oxygen storage capacity of ceria.

AUTHOR CONTRIBUTIONS

B-HK has performed the simulations and drafted the first version of the manuscript. All other authors have been equally involved in the planning of the work and in the finalization of the text.

FUNDING

This work was supported by the Swedish Research Council (VR) and the Swedish strategic e-science research programme eSSENCE, and the Sweden-Korea program within The Swedish Foundation for International Cooperation in Research and Higher Education (STINT). B-HK acknowledges support by Nano-Material Technology Development Program through the National Research Foundation of Korea (NRF) funded by the Ministry of Science and ICT (NRF-2016M3A7B4024138). JK acknowledges support from Åforsk. The calculations were performed on resources provided by the Swedish National Infrastructure for Computing (SNIC) at UPPMAX and NSC. This work was also supported by the National Institute of Supercomputing and Network/Korea Institute of Science and Technology Information with supercomputing resources including technical support (KSC-2018-S1-0012).

SUPPLEMENTARY MATERIAL

The Supplementary Material for this article can be found online at: https://www.frontiersin.org/articles/10.3389/fchem.2019.00203/full#supplementary-material

REFERENCES

Alimohammadi, M., and Fichthorn, K. A. (2009). Molecular dynamics simulation of the aggregation of titanium dioxide nanocrystals: preferential alignment. *Nano Lett.* 9, 4198–4203. doi: 10.1021/nl9024215

Anne de Baas (2018). *Review of Materials Modelling VI RoMM; Vocabulary, Classification and Metadata for Materials Modelling*. European Commission (MODA).

Aradi, B., Hourahine, B., and Frauenheim, T. (2007). DFTB+, a sparse matrix-based implementation of the DFTB method. *J. Phys. Chem. A* 111, 5678–5684. doi: 10.1021/jp070186p

Blöchl, P. E. (1994). Projector augmented-wave method. *Phys. Rev. B* 50, 17953–17979. doi: 10.1103/PhysRevB.50.17953

Broqvist, P., Kullgren, J., Wolf, M. J., van Duin, A. C. T., and Hermansson, K. (2015). ReaxFF force-field for ceria bulk, surfaces, and nanoparticles. *J. Phys. Chem. C* 119, 13598–13609. doi: 10.1021/acs.jpcc.5b01597

Castleton, C. W., Kullgren, J., and Hermansson, K. (2007). Tuning LDA + U for electron localization and structure at oxygen vacancies in ceria. *J. Chem. Phys.* 127:244704. doi: 10.1063/1.2800015

Cordeiro, M. A. L., Weng, W., Stroppa, D. G., Kiely, C. J., and Leite, E. R. (2013). High resolution electron microscopy study of nanocubes and polyhedral nanocrystals of cerium(IV) oxide. *Chem. Mater.* 25, 2028–2034. doi: 10.1021/cm304029s

de Diego, L. F., Gayán, P., García-Labiano, F., Celaya, J., Abad, A., and Adánez, J. (2005). Impregnated CuO/Al_2O_3 oxygen carriers for chemical-looping combustion: avoiding fluidized bed agglomeration. *Energy Fuels* 19, 1850–1856. doi: 10.1021/ef050052f

Du, D., Wolf, M. J., Hermansson, K., and Broqvist, P. (2018). Screened hybrid functionals applied to ceria: effect of Fock exchange. *Phys. Rev. B* 97:235203. doi: 10.1103/PhysRevB.97.235203

Du, N., Zhang, H., Chen, B., Ma, X., and Yang, D. (2007). Ligand-free self-assembly of ceria nanocrystals into nanorods by oriented attachment at low temperature. *J. Phys. Chem. C* 111, 12677–12680. doi: 10.1021/jp074011r

Dudarev, S. L., Botton, G. A., Savrasov, S. Y., Humphreys, C. J., and Sutton, A. P. (1998). Electron-energy-loss spectra and the structural stability of nickel oxide: an LSDA+U study. *Phys. Rev. B* 57, 1505–1509. doi: 10.1103/PhysRevB.57.1505

Elstner, M., Porezag, D., Jungnickel, G., Elsner, J., Haugk, M., Frauenheim, T., et al. (1998). Self-consistent-charge density-functional tight-binding method for simulations of complex materials properties. *Phys. Rev. B* 58, 7260–7268. doi: 10.1103/PhysRevB.58.7260

EMMC (2019). *The EMMC-CSA is a Project Under the European Union's Horizon 2020 Research and Innovation Programme Under Grant Agreement No 72386.* The European Materials Modelling Council. Available online at: https://emmc.info/

Feng, B., Hojo, H., Mizoguchi, T., Ohta, H., Findlay, S. D., Sato, Y., et al. (2012). Atomic structure of a $\Sigma 3$ [110]/(111) grain boundary in CeO_2. *Appl. Phys. Lett.* 100:073109. doi: 10.1063/1.3682310

Feng, B., Sugiyama, I., Hojo, H., Ohta, H., Shibata, N., and Ikuhara, Y. (2016). Atomic structures and oxygen dynamics of CeO_2 grain boundaries. *Sci. Rep.* 6:20288. doi: 10.1038/srep20288

Florea, I., Feral-Martin, C., Majimel, J., Ihiawakrim, D., Hirlimann, C., and Ersen, O. (2013). Three-dimensional tomographic analyses of CeO_2 nanoparticles. *Cryst. Growth Des.* 13, 1110–1121. doi: 10.1021/cg301445h

Fronzi, M., Soon, A., Delley, B., Traversa, E., and Stampfl, C. (2009). Stability and morphology of cerium oxide surfaces in an oxidizing environment: a first-principles investigation. *J. Chem. Phys.* 131:104701. doi: 10.1063/1.3191784

Hojo, H., Mizoguchi, T., Ohta, H., Findlay, S. D., Shibata, N., Yamamoto, T., et al. (2010). Atomic structure of a CeO_2 grain boundary: the role of oxygen vacancies. *Nano Lett.* 10, 4668–4672. doi: 10.1021/nl1029336

Jeyaranjan, A., Sakthivel, T. S., Molinari, M., Sayle, D. C., and Seal, S. (2018). Morphology and crystal planes effects on supercapacitance of CeO_2 nanostructures: electrochemical and molecular dynamics studies. *Part. Part. Syst. Charact.* 35:1800176. doi: 10.1002/ppsc.201800176

Kresse, G., and Furthmüller, J. (1996a). Efficient iterative schemes for ab initio total-energy calculations using a plane-wave basis set. *Phys. Rev. B* 54, 11169–11186. doi: 10.1103/PhysRevB.54.11169

Kresse, G., and Furthmüller, J. (1996b). Efficiency of ab-initio total energy calculations for metals and semiconductors using a plane-wave basis set. *Comput. Mat. Sci*. 6, 15–50. doi: 10.1016/0927-0256(96)00008-0

Kresse, G., and Hafner, J. (1993). Ab initio molecular dynamics for liquid metals. *Phys. Rev. B* 47, 558–561. doi: 10.1103/PhysRevB.47.558

Kresse, G., and Hafner, J. (1994). Ab initio molecular-dynamics simulation of the liquid-metal-amorphous-semiconductor transition in germanium. *Phys. Rev. B* 49, 14251–14269. doi: 10.1103/PhysRevB.49.14251

Kresse, G., and Joubert, D. (1999). From ultrasoft pseudopotentials to the projector augmented-wave method. *Phys. Rev. B* 59, 1758–1775. doi: 10.1103/PhysRevB.59.1758

Kullgren, J., Hermansson, K., and Broqvist, P. (2013). Supercharged low-temperature oxygen storage capacity of ceria at the nanoscale. *J. Phys. Chem. Lett.* 4, 604–608. doi: 10.1021/jz3020524

Kullgren, J., Wolf, M. J., Hermansson, K., Köhler, C., Aradi, B., Frauenheim, T., et al. (2017). Self-consistent-charge density-functional tight-binding (SCC-DFTB) parameters for ceria in 0D to 3D. *J. Phys. Chem. C* 121, 4593–4607. doi: 10.1021/acs.jpcc.6b10557

Li, W., Liang, C., Zhou, W., Qiu, J., Sun, G., and Xin, Q. (2003). Preparation and characterization of multiwalled carbon nanotube-supported platinum for cathode catalysts of direct methanol fuel cells. *J. Phys. Chem. B* 107, 6292–6299. doi: 10.1021/jp022505c

Lin, M., Fu, Z. Y., Tan, H. R., Tan, J. P. Y., Ng, S. C., and Teo, E. (2012). Hydrothermal synthesis of ceo$_2$ nanocrystals: ostwald ripening or oriented attachment? *Cryst. Growth Des.* 12, 3296–3303. doi: 10.1021/cg300421x

Lin, Y., Wu, Z., Wen, J., Poeppelmeier, K. R., and Marks, L. D. (2014). Imaging the atomic surface structures of CeO$_2$ nanoparticles. *Nano Lett.* 14, 191–196. doi: 10.1021/nl403713b

Liu, J., Yan, L., Chen, X., Wang, S., Zhang, M., and Tian, C. (2015). Direct synthesis of hollow polyhedral ceria nano powders via a template-free mixed solvothermal route. *J. Rare Earth* 33, 892–897. doi: 10.1016/S1002-0721(14)60501-9

Loschen, C., Carrasco, J., Neyman, K. M., and Illas, F. (2007). First-principles LDA+U and GGA+U study of cerium oxides: dependence on the effective U parameter. *Phys. Rev. B* 75:035115. doi: 10.1103/PhysRevB.75.035115

Loschen, C., Migani, A., Bromley, S. T., Illas, F., and Neyman, K. M. (2008). Density functional studies of model cerium oxide nanoparticles. *Phys. Chem. Chem. Phys.* 10, 5730–5738. doi: 10.1039/b805904g

Lykaki, M., Pachatouridou, E., Iliopoulou, E., Carabineiro, S. A. C., and Konsolakis, M. (2017). Impact of the synthesis parameters on the solid state properties and the CO oxidation performance of ceria nanoparticles. *RSC Adv.* 7, 6160–6169. doi: 10.1039/C6RA26712B

Mai, H. X., Sun, L. D., Zhang, Y. W., Si, R., Feng, W., Zhang, H. P., et al. (2005). Shape-selective synthesis and oxygen storage behavior of ceria nanopolyhedra, nanorods, and nanocubes. *J. Phys. Chem. B* 109, 24380–24385. doi: 10.1021/jp055584b

Maillard, F., Schreier, S., Hanzlik, M., Savinova, E. R., Weinkauf, S., and Stimming, U. (2005). Influence of particle agglomeration on the catalytic activity of carbon-supported Pt nanoparticles in CO monolayer oxidation. *Phys. Chem. Chem. Phys.* 7, 385–393. doi: 10.1039/B411377B

Migani, A., Vayssilov, G. N., Bromley, S. T., Illas, F., and Neyman, K. M. (2010). Dramatic reduction of the oxygen vacancy formation energy in ceria particles: a possible key to their remarkable reactivity at the nanoscale. *J. Mater. Chem.* 20, 10535–10546. doi: 10.1039/c0jm01908a

Perdew, J. P., Burke, K., and Ernzerhof, M. (1996). Generalized gradient approximation made simple. *Phys. Rev. Lett.* 77, 3865–3868. doi: 10.1103/PhysRevLett.77.3865

Raju, M., van Duin, A. C., and Fichthorn, K. A. (2014). Mechanisms of oriented attachment of TiO$_2$ nanocrystals in vacuum and humid environments: reactive molecular dynamics. *Nano Lett.* 14, 1836–1842. doi: 10.1021/nl404533k

Renuka, N. K., Harsha, N., and Divya, T. (2015). Supercharged ceria quantum dots with exceptionally high oxygen buffer action. *RSC Adv.* 5, 38837–38841. doi: 10.1039/C5RA01161B

Sayle, T., X., Parker, S. C., and Sayle, D. C. (2005). Oxidising CO to CO$_2$ using ceria nanoparticles. *Phys. Chem. Chem. Phys.* 7, 2936–2941. doi: 10.1039/b506359k

Sayle, T. X., Inkson, B. J., Karakoti, A., Kumar, A., Molinari, M., Möbus, G., et al. (2011). Mechanical properties of ceria nanorods and nanochains; the effect of dislocations, grain-boundaries and oriented attachment. *Nanoscale* 3, 1823–1837. doi: 10.1039/c0nr00980f

Schlick, S., Danilczuk, M., Drews, A. R., and Kukreja, R. S. (2016). Scavenging of hydroxyl radicals by ceria nanoparticles: effect of particle size and concentration. *J. Phys. Chem. C* 120, 6885–6890. doi: 10.1021/acs.jpcc.6b00404

Si, R., Zhang, Y.-W., You, L.-P., and Yan, C.-H. (2006). Self-organized monolayer of nanosized ceria colloids stabilized by poly(vinylpyrrolidone). *J. Phys. Chem. B* 110, 5994–6000. doi: 10.1021/jp057501x

Sk, M. A., Kozlov, S. M., Lim, K. H., Migani, A., and Neyman, K. M. (2014). Oxygen vacancies in self-assemblies of ceria nanoparticles. *J. Mater. Chem. A* 2, 18329–18338. doi: 10.1039/C4TA02200A

Tan, J. P. Y., Tan, H. R., Boothroyd, C., Foo, Y. L., He, C. B., and Lin, M. (2011). Three-dimensional structure of CeO$_2$ nanocrystals. *J. Phys. Chem. C* 115, 3544–3551. doi: 10.1021/jp1122097

van Duin, A. C. T., Dasgupta, S., Lorant, F., and Goddard, W. A. I. I. I. (2001). ReaxFF: a reactive force field for hydrocarbons. *J. Phys. Chem. A* 105, 9396–9409. doi: 10.1021/jp004368u

Wang, R., and Mutinda, S. I. (2011). The dynamic shape of ceria nanoparticles. *Chem. Phys. Lett.* 517, 186–189. doi: 10.1016/j.cplett.2011.10.024

Wang, Z. L., and Feng, X. (2003). Polyhedral shapes of CeO$_2$ nanoparticles. *J. Phys. Chem. B* 107, 13563–13566. doi: 10.1021/jp036815m

Zhang, H., and Banfield, J. F. (2014). Interatomic Coulombic interactions as the driving force for oriented attachment. *CrystEngComm* 16, 1568–1578. doi: 10.1039/C3CE41929K

Zhang, J., Kumagai, H., Yamamura, K., Ohara, S., Takami, S., Morikawa, A., et al. (2011). Extra-low-temperature oxygen storage capacity of CeO$_2$ nanocrystals with cubic facets. *Nano Lett.* 11, 361–364. doi: 10.1021/nl102738n

Conflict of Interest Statement: The authors declare that the research was conducted in the absence of any commercial or financial relationships that could be construed as a potential conflict of interest.

frontiers in Chemistry

ORIGINAL RESEARCH
published: 16 April 2019
doi: 10.3389/fchem.2019.00220

First Principles Calculations on the Stoichiometric and Defective (101) Anatase Surface and Upon Hydrogen and H_2Pc Adsorption: The Influence of Electronic Exchange and Correlation and of Basis Set Approximations

Ruth Martínez-Casado [1,2]*, ***Milica Todorović*** [3], ***Giuseppe Mallia*** [4], ***Nicholas M. Harrison*** [4] ***and Rubén Pérez*** [2,5]*

[1] Departamento de Física de Materiales, Universidad Complutense de Madrid, Madrid, Spain, [2] Departamento de Física Teórica de la Materia Condensada, Universidad Autónoma de Madrid, Madrid, Spain, [3] Department of Applied Physics, Aalto University, Espoo, Finland, [4] Department of Chemistry, Imperial College London, White City, London, United Kingdom, [5] Condensed Matter Physics Center (IFIMAC), Universidad Autónoma de Madrid, Madrid, Spain

Edited by:
Javier Carrasco,
CIC Energigune, Spain

Reviewed by:
Annabella Selloni,
Princeton University, United States
Jose Julio Gutierrez Moreno,
Shenzhen University, China

****Correspondence:***
Ruth Martínez-Casado
mariarum@ucm.es
Rubén Pérez
ruben.perez@uam.es

Specialty section:
This article was submitted to Physical Chemistry and Chemical Physics,
a section of the journal Frontiers in Chemistry

Received: *30 November 2018*
Accepted: *20 March 2019*
Published: *16 April 2019*

Citation:
Martínez-Casado R, Todorović M, Mallia G, Harrison NM and Pérez R (2019) First Principles Calculations on the Stoichiometric and Defective (101) Anatase Surface and Upon Hydrogen and H_2Pc Adsorption: The Influence of Electronic Exchange and Correlation and of Basis Set Approximations. Front. Chem. 7:220. doi: 10.3389/fchem.2019.00220

Anatase TiO_2 provides photoactivity with high chemical stability at a reasonable cost. Different methods have been used to enhance its photocatalytic activity by creating band gap states through the introduction of oxygen vacancies, hydrogen impurities, or the adorption of phthalocyanines, which are usually employed as organic dyes in dye-sensitized solar cells. Predicting how these interactions affect the electronic structure of anatase requires an efficient and robust theory. In order to document the efficiency and accuracy of commonly used approaches we have considered two widely used implementations of density functional theory (DFT), namely the all-electron linear combination of atomic orbitals (AE–LCAO) and the pseudo-potential plane waves (PP–PW) approaches, to calculate the properties of the stoichiometric and defective anatase TiO_2 (101) surface. Hybrid functionals, and in particular HSE, lead to a computed band gap in agreement with that measured by using UV adsorption spectroscopy. When using PBE+U, the gap is underestimated by 20 % but the computed position of defect induced gap states relative to the conduction band minimum (CBM) are found to be in good agreement with those calculated using hybrid functionals. These results allow us to conclude that hybrid functionals based on the use of AE–LCAO provide an efficient and robust approach for predicting trends in the band gap and the position of gap states in large model systems. We extend this analysis to surface adsorption and use the AE–LCAO approach with the hybrid functional HSED3 to study the adsorption of the phthalocyanine H_2Pc on anatase (101). Our results suggest that H_2Pc prefers to be adsorbed on the surface Ti_{5c} rows of anatase (101), in agreement with that seen in recent STM experiments on rutile (110).

Keywords: density functional theory, oxides, anatase, hybrid functionals, defects, phthalocyanine

1. INTRODUCTION

TiO_2 is an important technological material with widespread applications in solar cells and photocatalysis (Fujishima and Honda, 1972; Fujishima et al., 2008; Schneider et al., 2014; Stetsovych et al., 2015). Although rutile is the stable bulk phase, anatase nanoparticles are often found to be the most active components in these applications.

Among the possible terminations, the (101) facet is found to be the most stable anatase surface (Labat et al., 2008) and represents a significant portion of the exposed surface area in the equilibrium crystallites that are characteristic of polycrystalline surfaces (Lazzeri et al., 2001; Barnard and Curtiss, 2005). The large anatase band gap (3.2 eV) limits its photocatalytic activity to the small ultraviolet portion of the solar spectrum (Hagfeldt and Grätzel, 1995). This has led to the use of a wide variety of approaches to engineer the band gap in order to enhance the activity. These include the incorporation of metallic and non-metallic ion impurities (Hoffmann et al., 1995). Hydrogen impurities are also usually introduced during processing and have significant influence on material properties, and therefore on the device performance. It is well established that hydrogen defects affect the ionic conductivity, electronic, and optical properties of both the bulk crystal and its surfaces (Amano et al., 2016). Hydrogen binds to lattice O^{2-} ions to form OH^- and this n-dopes the crystal modifying its electronic structure and, at elevated temperatures, proton transport makes a significant contribution to the ionic conductivity (Amano et al., 2016). Oxygen vacancies also play an important role in determining the surface chemistry and electronic properties of TiO_2 (Morgan and Watson, 2010; Pan et al., 2013; Hongfei et al., 2015). Under typical processing conditions the dominant intrinsic defect is the oxygen vacancy, which also n-dopes the crystal and significantly affects photocatalytic properties (Liborio and Harrison, 2008). Previous DFT calculations have shown that TiO_2 typically accommodates n-doping in localized states within the band gaps approximately 1eV below the CBM. These states could extend optical absorption to the visible region (Justicia et al., 2002; Liborio and Harrison, 2008). An alternative, and potentially complementary, approach is to enhance light absorption through surface species as happens in dye-sensitized solar cells (Graetzel, 2001). The details of the binding of the dye molecules to the surface are crucial for the improvement of device performance, with phthalocyanines being the most widely studied sysetm (Godlewski and Szymonski, 2013).

The quantitative analysis, and correct interpretation, of these processes has been assisted by the use of *ab initio* calculations of the surface structure and electronic properties. Anatase, as other reducible oxides, represents a challenge for standard implementations of DFT. Generalized gradient approximations (GGA) functionals often underestimate the band gap (Reshak et al., 2010) and provide a poor description of the localized gap states which are essentially lattice $Ti^{4+}(3d^0)$ ions reduced to $Ti^{3+}(3d^1)$ ions (Wang and Doren, 2005). It has been previously shown that the use of hybrid exchange functionals (where a proportion of Fock exchange is included in the exchange functional) provides a qualitatively correct description of the structure, energetics and electronic properties for many different materials, and in particular, for transition metal oxides (Patel et al., 2012, 2014; Sanches et al., 2014). However, in plane-wave codes, the use of hybrid exchange functionals increases dramatically the computational cost to an extent that prevents studies of complex geometries. For this reason, it is common to use the so-called DFT+U (Anisimov et al., 1993; Stetsovych et al., 2015) approximation, where LDA or GGA functionals are supplemented by an on-site local repulsion term U, representing the Coulombic self-interaction of the Ti 3*d* orbitals. This term partially corrects for the electronic self-interaction error inherent in local approximations to DFT and thus provides a more reliable, if somewhat *ad hoc*, description of the electron localization around Ti^{3+} ions.

In this work, firstly we document the performance of two widely employed DFT implementations (AE–LCAO and PP–PW) for computing the electronic structure of the defective (101) anatase surface using different exchange-correlation functionals. The defects considered are the dominant intrinsic ones for this system: single-atom oxygen sub-surface vacancies and hydrogen adsorbates (Setvin et al., 2013). The implementation of hybrid-exchange functionals using local atomic basis sets, in the CRYSTAL code (Dovesi et al., 2014), is very efficient, even when a high quality all-electron basis sets are used. CRYSTAL has therefore been used to investigate the stoichiometric and defective (101) anatase surface and upon hydrogen and H2Pc adsorption using the Perdew-Burke-Ernzerhof (PBE Perdew et al., 1996a) functional and the hybrid [PBE0 (Perdew et al., 1996b), B3LYP (Becke, 1988), and HSE (Heyd et al., 2003)] functionals. For the PP–PW calculations, only the PBE and PBE+U levels have been considered, rather than hybrid exchange functionals, due to the high computational cost of using hybrid functionals for systematic studies (Wu et al., 2009). In our experience, for PW calculations of the anatase bulk crystal, the computational time increases by three orders of magnitude when using hybrid exchange functionals compared to the AE–LCAO approximation. The comparison of the two approaches allows us to document the effects of the choice of basis set, the pseudopotential and the validity of the empirical PBE+U approach in this system. The PBE+U formalism has been shown to describe qualitatively correctly the defective rutile phase of TiO_2, both in the bulk and on the surface, but the results for anatase surface remain ambiguous (Haa and Alexandrova, 2016). A similar analysis to the one presented here have been reported for bulk anatase (Finazzi et al., 2008; Valentin et al., 2009), but the complexity of the surface chemistry makes clear the value of the present study.

A judicious combination of the PP–PW and AE–LCAO approaches can provide an accurate description of complex defective and hybrid organic/oxide structures needed to understand and to improve the chemical reactivity and the photocatalytic properties. Once we have shown that the AE–LCAO approach with the HSE functional is able to accurately describe this surface, we go one step further by studying the adsorption of the phthalocyanine H_2Pc on anatase (101). In the molecule-surface interaction, the effect of the Van der Waals forces is more important and has been taken into account by adding the D3 dispersion correction (HSED3) (Grimme and Krieg, 2010). We will show an analysis of the optimized structure and stability of this interaction, which will be a valuable tool in order to improve the efficiency of dye-sensitized solar cells. The article is structured as follows. In section 2 details are presented. In sections 3.1 and 3.2 the results for the bulk and stoichiometric anatase (101) surface are shown as a reference. The main features of the oxygen defective anatase (101) surface, together with the adsorption of both hydrogen and phthalocyanine on it are presented in sections 3.3, 3.4, and 3.5, respectively.

2. COMPUTATIONAL DETAILS

The calculations carried out with all-electron linear combination of atomic orbitals (AE–LCAO) have been performed using the CRYSTAL software (Dovesi et al., 2014). In the AE–LCAO formalism implemented in CRYSTAL (Dovesi et al., 2014), the crystalline orbitals are expanded as a linear combination of atom centered Gaussian orbitals with *s*, *p*, or *d* symmetry (the basis set). AE calculations were performed in which there is no shape approximation to the potential or density.

DFT has been applied with the PBE (Perdew et al., 1996a), PBE0 (Perdew et al., 1996b), B3LYP (Becke, 1988), and HSE (Heyd et al., 2003) functionals. The main numerical approximation in these calculations is the choice of the basis set (BS). In order to systematically approach the BS limit, a hierarchy of all-electron basis sets, labeled as BS1, BS2, and BS3 (see **Table 1**), has been selected for O, Ti. The most complete basis set (BS3), which includes extended polarization *d* orbitals for both the Ti and O atoms, has been used for the calculations reported below if not indicated. Apart from the obvious consequences on the structural and electronic properties, the subtle effect of the basis set on the description of the gap states will be discussed at the end of section 3.3. For the H_2Pc molecule, we used BS4 in order to reduce the BS superposition error. In the H_2Pc-anatase analysis we perform only AE–LCAO calculations with the HSE functional by adding the D3 dispersion correction (Grimme and Krieg, 2010), which is crucial for this kind of interactions.

In the CRYSTAL (Dovesi et al., 2014) calculations, integration over the reciprocal space was carried out using Monkhorst-Pack (MP) meshes of 8 × 8 × 8 for the anatase bulk and 4 × 4 × 1 for the periodic slab representing the surface. The Coulomb and exchange series are summed directly in direct space and truncated using overlap criteria with thresholds of [7,7,7,7,14] (Pisani et al., 1988). The self-consistent field (SCF) algorithm was set to converge at the point at which the change in energy was $< 10^{-7}$ Hartree per unit cell. Structural optimisation of both the bulk cell parameters and internal coordinates was performed using the Broyden-Fletcher-Goldfarb-Shanno scheme. Convergence was determined from the root-mean-square (rms) and the absolute value of the largest component of the forces. The thresholds for the maximum and the rms forces (the maximum and the rms atomic displacements) have been set to 0.00045 and 0.00030 (0.00180 and 0.0012) in atomic units. Geometry optimisation was terminated when all four conditions were satisfied simultaneously.

TABLE 1 | All-electron basis set hierarchy for Ti, O, H, N, and C.

	Ti	O	H	N	C
BS1	8-6411d(1)	8-611	3-1p(1)	—	—
BS2	8-6411d(11)	8-611	3-1p(1)	—	—
BS3	8-6411d(11)	8-611d(1)	3-1p(1)	—	—
BS4	8-6411d(311)	8-411d(11)	3-11p(1)	6-311d(1)	6-311d(1)

Calculations performed using the VASP code (Kresse and Furthmueller, 1996) include projected augmented wave (PAW) pseudopotentials (Bloechl, 1994; Kresse and Joubert, 1999) and a plane wave basis set with a cutoff of 500 eV. The SCF cycle stopping criterion was 10^{-6} eV. The PBE exchange-correlation functional was supplemented with an onsite $U = 4$eV terms on the Ti 3*d* orbitals to describe better the electronic structure of the (101) anatase surface and the electron localization on Ti^{4+} sites associated with the creation of its most common point defects. Ti PP is described by 4 valence electrons and O by 6 valence electrons. Previous studies on the anatase surface showed this U value provides the best description for the position of the defect-induced Ti gap states with respect to the conduction band minimum of TiO_2 (Cheng and Selloni, 2009; Aschauer et al., 2010; Stetsovych et al., 2015). We included 15 Å of vacuum in order to isolate the two sides of the slab. Defect geometries were accessed using the robust Conjugate Gradient algorithm. Structural optimisation was halted when the value of the largest component of the forces reached a threshold value of 0.01 eV/Å. The Brillouin zone was sampled by a 6 × 6 × 2 MP mesh in bulk anatase calculations, and at Γ point in surface calculations in order to reduce the computational cost. Surface electronic properties were extracted from static calculations featuring a 4 × 4 × 1 MP mesh.

3. RESULTS AND DISCUSSION

3.1. Bulk

The anatase structure belongs to the $I4_1/amd$ tetragonal space group and the unit cell is defined by the lengths of lattice vectors a and c and the oxygen internal coordinate u. The primitive cell contains two atoms in the asymmetric unit: a Ti ion at (0,0,0) and an O ion at (0,0,u), in fractional coordinates. Anatase is an indirect band-gap semiconductor with an optical band gap of approximately 3.2 eV (measured by using UV adsorption spectroscopy) (Reddy et al., 2003). Anatase bulk lattice parameters have been relaxed with AE–LCAO and the DFT functionals: PBE, PBE0, B3LYP, HSE and HSED3. The computed structures and eigenvalue gaps (here, referred to as band gaps for convenience) are presented in **Table 2**, and compared to the structure deduced from X-ray diffraction and the optical band gap measured using UV adsorption spectroscopy (Reddy et al., 2003). It is clear from **Table 2** that the best agreement, for both lattice parameters and band gap, is obtained with the HSE functional. The results obtained within the HSED3 approach are also reported in **Table 2**, showing no significant changes with respect to pure HSE. The B3LYP lattice parameters and band gap are very similar to the ones previously

TABLE 2 | AE–LCAO and PP–PW relaxed lattice parameters and band gap for bulk anatase with respect to the experimental value measured by using X-ray diffraction and the adsorption spectrum (Reddy et al., 2003), respectively.

	a(Å)	c(Å)	Indirect band gap (bulk) (eV)
AE–LCAO PBE	3.803 (0.3 %)	9.770 (1.5 %)	2.12 (-33.7%)
PP–PW PBE	3.809 (0.5%)	9.724 (1.0%)	2.09 (-34.7%)
AE–LCAO PBE0	3.766 (-0.6 %)	9.655 (0.3 %)	4.26 (33.1%)
AE–LCAO B3LYP	3.790 (0.03 %)	9.776 (1.6 %)	3.77 (17.8%)
AE–LCAO HSE	3.766 (-0.6 %)	9.661 (0.4%)	3.63 (13.4%)
AE–LCAO HSED3	3.756 (-0.9 %)	9.522 (1.0%)	3.61 (12.8%)
PP–PW PBE+U	3.855 (1.7%)	9.842 (1.5%)	2.57 (-19.7%)
Observed (Reddy et al., 2003)	3.790	9.625	3.20

The percentage error with respect to the experiment is reported in parenthesis.

obtained in the literature (Labat et al., 2008; Sanches et al., 2014). The eigenvalue gap is an estimate of the fundamental band gap. When using HSE and HSED3, the 13% overestimation of the optical band gap is not unreasonable as the optical gap is expected to be less than the fundamental gap due to the exciton binding energy. A comparison of the DOS calculated with PP–PW (PBE and PBE+U) and AE–LCAO (PBE, B3LYP and HSE) is presented in **Figure 1**. All DOS reported are plotted relative to the CBM to aid comparison. It is important to highlight the good agreement between AE–LCAO and PP–PW approaches with the same functional (PBE). Both methods provide a very similar band gap and lattice parameters suggesting that the PP–PW and local basis set approaches provide a very similar description of the electronic structure in both the valence and conduction bands. The projected density of states (DOS) for bulk anatase performed with AE–LCAO (HSE) shows that the conduction band is largely made up of Ti 3d orbitals and the upper valence band of O 2p orbitals, as one expects from a simple ionic model of the bonding.

3.2. Stoichiometric (101) Surface

The (101) surface has two possible terminations, both resulting in stoichiometric, nonpolar surfaces. In this study we consider the low-energy termination (Sanches et al., 2014), where, as shown in **Figure 2A**, one of each of the following atoms are exposed per periodic cell: O_{2c},O_{3c},Ti_{5c} and Ti_{6c} producing the characteristic saw-tooth (101) surface structure. The 2c, 3c, 5c, and 6c indexes represent the two, three, 5 and 6 fold–coordinated atoms, respectively. The surface was modeled with a 2D periodic slab that includes four TiO_2 trilayers with the in–plane periodicity given by a 1×3 supercell of the conventional surface cell.

The fact that both the AE–LCAO and PP–PW approaches provide a very similar description at the PBE level suggests that the plane-wave and local Gaussian orbital basis sets used are both well converged and that the pseudopotentials are describing the valence-core interactions adequately. This also facilitates the comparison of the results of PP–PW-PBE+U calculations with AE–LCAO-HSE and -B3LYP calculations, as we can be confident that the numerical approximations used are equivalent. This allows us to assess the accuracy of the widely used DFT+U approach.

An analysis of the DOS for the stoichiometric anatase (101) calculated with AE–LCAO and HSE (**Figure 3**) exhibits a similar structure to that seen in the bulk crystal. The conduction band is mainly composed of Ti 3d orbitals and the upper valence band of O 2p orbitals. In order to separate the surface contribution from that of the bulk, the DOS have been plotted in four different ways: projected (PDOS) on the most important atoms of the top layer (O_{2c}, O_{3c}, Ti_{5c}, and Ti_{6c}) (**Figure 3A**), PDOS on the two top trilayers (**Figure 3B**), total DOS (**Figure 3C**), and PDOS on the two bottom trilayers (**Figure 3D**).

The computed DOS of the stoichiometric surface using the PP–PW (PBE+U) and AE–LCAO (HSE and B3LYP) approximations are compared in **Figure 3**. It can be seen that the global hybrid (B3LYP) and screened exchange (HSE) approaches produce very similar band width, shape and band gap. The empirical PBE+U method yields similar band widths but a significantly smaller band gap.

In **Table 3** the bond distances and atom height (with respect to the position of the first oxygen atom of the second trilayer) using PP–PW (PBE+U) and AE–LCAO (HSE and B3LYP) are reported for the selected atoms of the surface layer. The surface structure is found to be relatively insensitive to both the numerical approximation and to the exchange correlation functional used.

3.3. Oxygen Vacancy on (101) Anatase

A simple model of the reduced anatase surface can be generated by oxygen desorption induced by heating. Although, as the least coordinated, the outermost O_{2c} oxygen atoms might be expected to be the first to leave the surface, previous work (Setvin et al., 2013) has shown that these surface vacancies are unstable and quickly evolve to form subsurface vacancies. We therefore consider a subsurface oxygen vacancy model where an oxygen atom is removed from the second trilayer of the surface (see **Figure 2C**).

The extra two electrons left after the vacancy formation could form an F-center at the vacant lattice site or enter the Ti 3*d* band and, potentially, localize to form Ti^{3+} species. A number of previous theoretical studies have described the formation of these localized states (Lindan et al., 1997; Muscat et al., 1999; Chen et al., 2001; Deak et al., 2015). The ground state considered here corresponds to the occupation of a localized 3*d* orbital on each of two next-nearest neighbors, a Ti_{5c} atom in the first trilayer and a Ti_{6c} in the third trilayer (cyan atoms in **Figure 2C**). A previous PP–PW (PBE+U) study also suggested that this configuration for the reduced titanium ions is the most stable (Stetsovych et al., 2015). This is also the case in calculations based on hybrid functionals. For example, the configuration where two nearest neighbor Ti ions are reduced (magenta atoms in **Figure 2C**) is a local energy minimum but has an energy 0.82 eV higher than the one described above. The reduction of two Ti^{4+} ions is confirmed by the spin–polarized DOS presented in **Figure 4**. The two Ti^{3+} ions have a magnetic moment of 0.90 and 0.91 μ_B for AE–LCAO (3LYP), 0.92 and 0.91 μ_B for AE–LCAO (HSE) and 0.91 and 0.89 μ_B for PP–PW (PBE+U). The new localized states, mainly formed by Ti

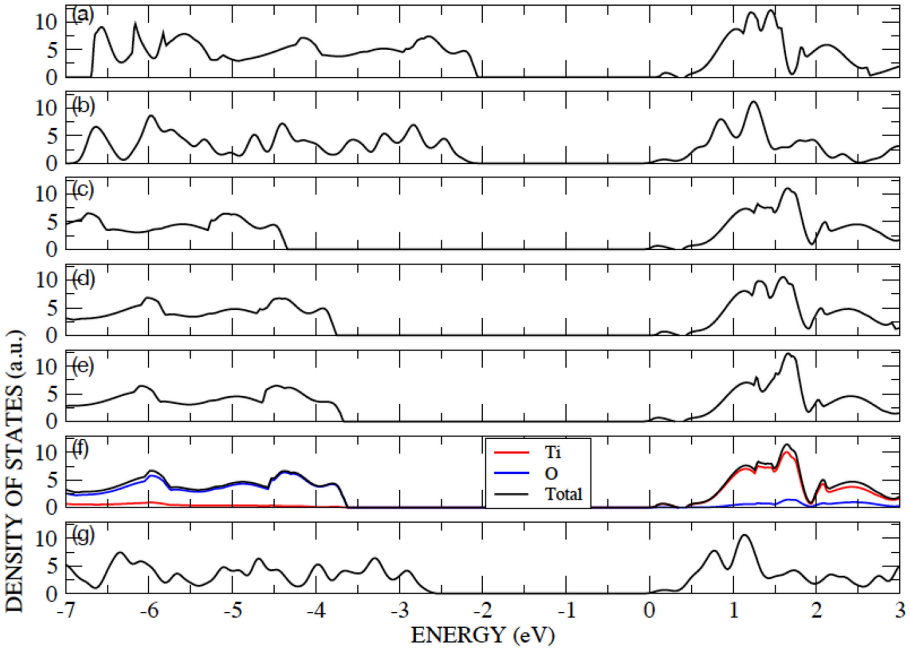

FIGURE 1 | Color online) Density of states for bulk anatase performed with: **(a)** AE–LCAO (PBE), **(b)** PP–PW (PBE), **(c)** AE–LCAO (PBE0), **(d)** AE–LCAO (B3LYP), **(e)** AE–LCAO (HSED3) **(f)** AE–LCAO(HSE) and **(g)** PP–PW (PBE+U). Projected DOS is also shown for AE–LCAO (HSE).

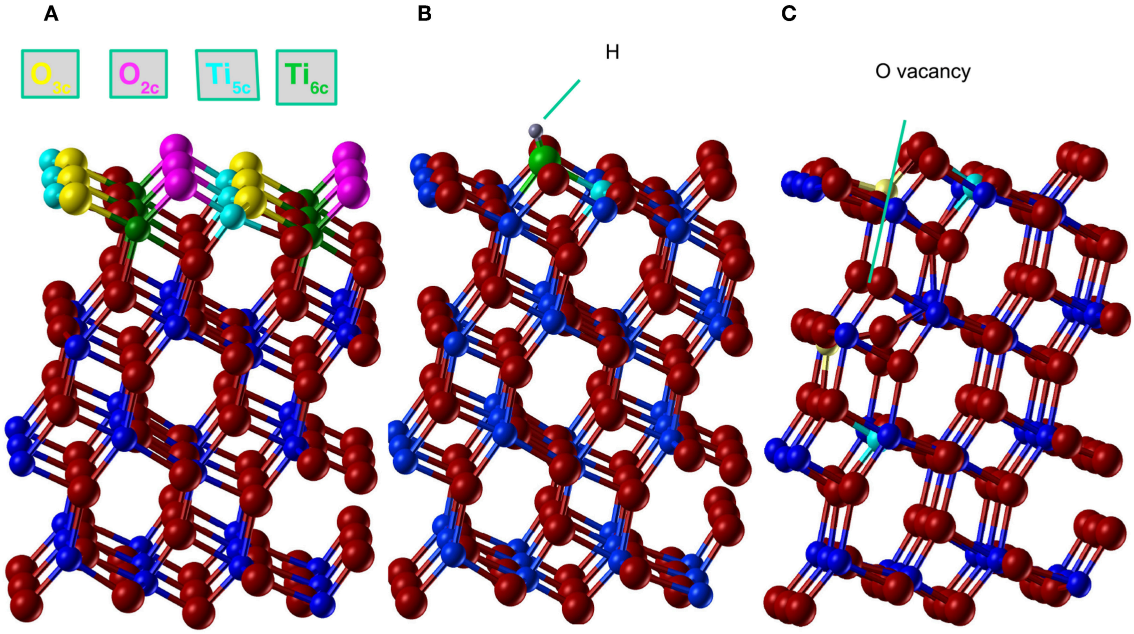

FIGURE 2 | (Color online) Anatase (101) structure relaxed with AE–LCAO (HSE). **(A)** Stoichiometric surface, oxygen and titanium atoms are plotted in red and blue, respectively. The coordination of atoms in the top layer is represented in cyan (Ti_{5c}), green (Ti_{6c}), magenta (O_{2c}), and yellow (O_{3c}). **(B)** H adsorption, where H atom is represented in gray, the O_{2c} bonded to H in green and the spin polarized Ti_{5c} in cyan, **(C)** O monovacancy, where the spin polarized Ti_{5c} atoms are represented in cyan (minimum energy configuration) and yellow (alternative configuration of the spin).

3*d* orbitals from the Ti_{6c} in the third trilayer and the Ti_{5c} in the first trilayer, appear at 1.0 and 1.3 eV below the conduction band for AE–LCAO (HSE). PP–PW (PBE+U) gives a very similar result (1.1, 1.3 eV), while AE–LCAO–B3LYP predicts those states to be deeper in the band gap (1.2, 1.5 eV). The AE–LCAO (HSE) calculation is in good agreement with photoemission

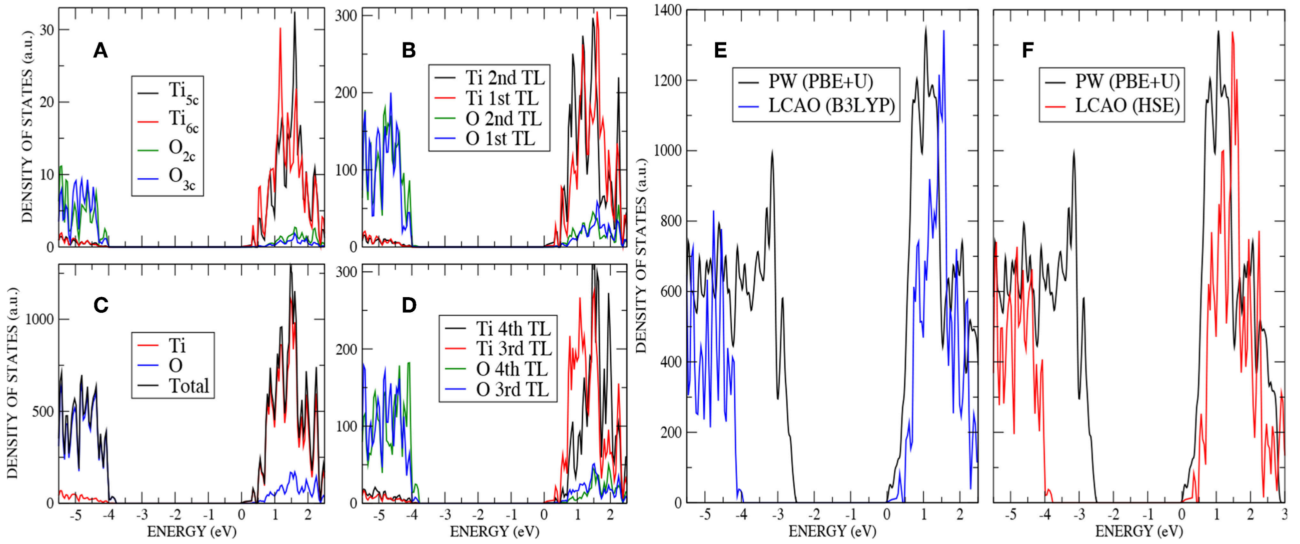

FIGURE 3 | (Color online) Stoichiometric anatase (101) : **(A)** PDOS on the most important atoms (O_{2c},O_{3c},Ti_{5c} and Ti_{6c}) of the top layer by using AE–LCAO (HSE), **(B)** PDOS on the two top trilayers by using AE–LCAO (HSE), **(C)** DOS by using AE–LCAO (HSE), **(D)** PDOS on the two bottom trilayers by using AE–LCAO (HSE) (bulk-like region), **(E)** DOS comparison of AE–LCAO (B3LYP) and PP–PW (PBE+U), and **(F)** DOS comparison of AE–LCAO (HSE) and PP–PW (PBE+U).

TABLE 3 | Bond distance and height of relevant atoms in the top layer (Å) for AE–LCAO and PP–PW in the anatase (101) stoichiometric surface, hydrogen adsorption and oxygen monovacancy.

	Ti_{5c}-O_{2c}	Ti_{6c}-O_{2c}	H-O_{2c}	Ti_{5c} height	Ti_{6c} height	O_{2c} height	H height
PP–PW(PBE+U)							
stoichiometric	1.86	1.90	—	2.64	2.01	3.48	—
Hads	2.07	2.05	0.97	2.72	1.87	3.55	4.46
Ovac	2.04	1.76	—	2.71	2.5	3.81	—
AE–LCAO(B3LYP)							
stoichiometric	1.83	1.84	—	2.67	2.13	3.54	—
Hads	2.02	2.05	0.96	2.66	1.91	3.57	4.26
Ovac	2.02	1.72	—	2.75	2.54	3.83	—
AE–LCAO(HSE)							
stoichiometric	1.83	1.82	—	2.64	2.1	3.50	—
Hads	2.0	2.03	0.96	2.64	1.91	3.54	4.33
Ovac	2.01	1.71	—	2.73	2.53	3.81	—

The height of the atoms is defined with respect to the position of the first oxygen atom of the second trilayer in order to allow a direct comparison.

experiments, which identify a state at around 1 eV bellow the CBM (Thomas et al., 2007).

The relaxed structure for the subsurface vacancy can be seen in **Figure 2C**, where the Ti^{3+} ions depicted in cyan. The charge localization has a profound influence on the structure, as shown by the bond distances and relative height of the key atoms in the top layer in **Table 3**. A significant decrease of the Ti_{6c}-O_{2c} bond is seen. The Ti_{6c}^{3+}-O_{2c} bond is reduced by 0.1 Å, with respect to the Ti_{6c}^{4+}-O_{2c} bond. There are also significant relaxations in the reduced top Ti_{6c}, that changes its coordination from 6 to 5 and moves up by 0.5 Å. In the presence of two polarons and a vacancy, the polaronic distortions might interact and therefore affect the total energy, geometry and position of the gap state. This structural feature appears consistently in all of the calculations presented here and can thus be considered to be insensitive to the approximation of the electronic exchange and correlation.

Previous combined STM/AFM experiments show a strong distortion of the O_{2c} site above the vacancy which is lifted up by 0.3 Å (Stetsovych et al., 2015). PP–PW (PBE+U) and AE–LCAO (B3LYP) support this result with the O_{2c} moving up by 0.28 and 0.31 Å, respectively. AE–LCAO (HSE) reproduces this trend with a normal displacement of 0.38 Å, identical to the PP–PW–PBE+U result.

The four–layer slab used so far is clearly suitable to describe the relaxations in the top layers associated with the creation of the surface and the H–defect. In the case of the subsurface vacancy, where one of the reduced Ti^{3+} ions is located in the third trilayer, one may wonder if an additional trilayer is needed

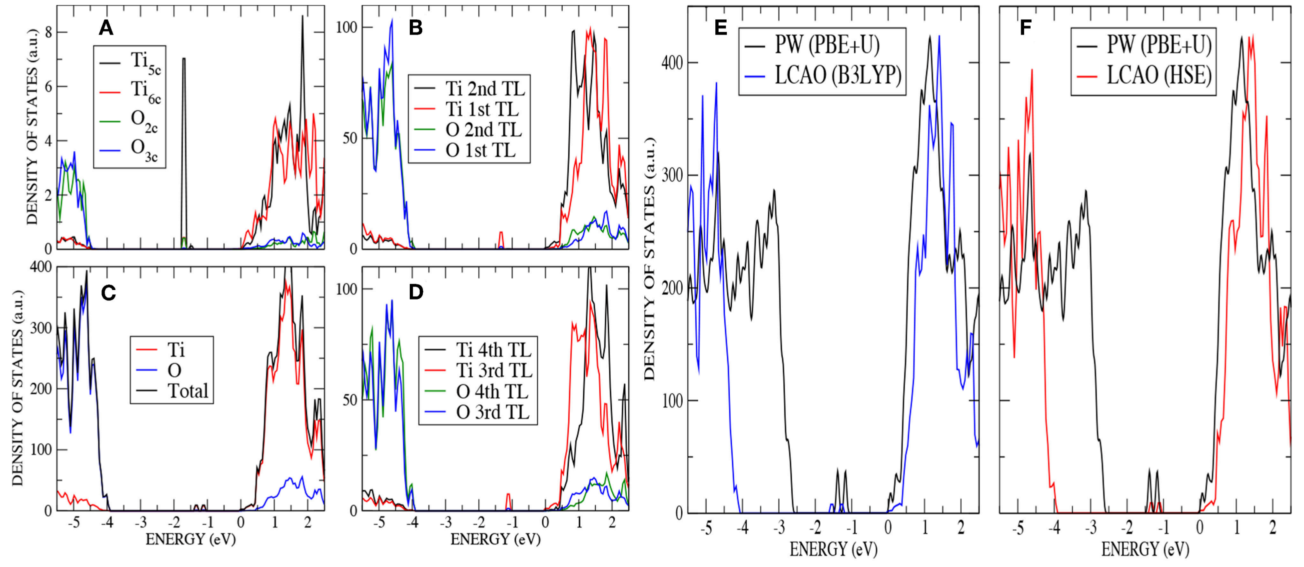

FIGURE 4 | (Color online) O monovacancy on anatase (101) : **(A)** PDOS on the most important atoms (O_{2C},O_{3C},Ti_{5C}, and Ti_{6C}) of the outermost layer by using AE–LCAO (HSE), **(B)** PDOS on the two top trilayers by using AE–LCAO (HSE), **(C)** DOS by using AE–LCAO (HSE), **(D)** PDOS on the two bottom trilayers by using AE–LCAO (HSE) (bulk-like region), **(E)** DOS comparison of AE–LCAO (B3LYP) and PP–PW (PBE+U), and **(F)** DOS comparison of AE–LCAO (HSE) and PW (PBE+U).

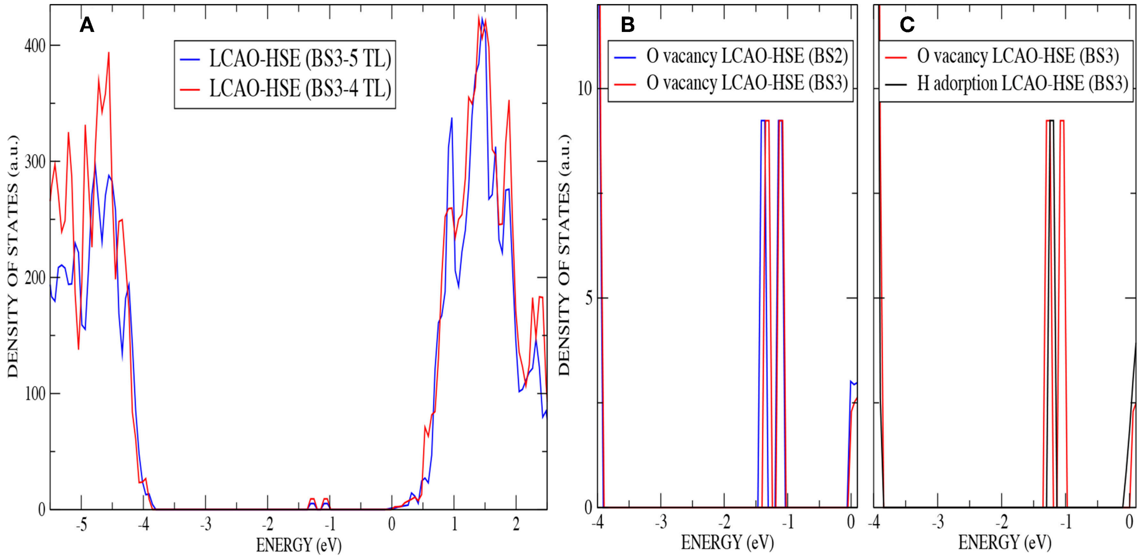

FIGURE 5 | (Color online) **(A)** DOS comparison for the oxygen monovacancy on anatase (101) by using AE–LCAO (HSE) with four and five trilayers **(B)** Band gap for the oxygen monovacancy on anatase (101) by using AE–LCAO (HSE) with BS2 and BS3. **(C)** Band gap for an hydrogen adsorption and oxygen monovacancy on anatase (101) by using AE–LCAO (HSE) with BS3.

in order to relax the local strain induced by the larger ion, as the fourth trilayer has been kept fixed. This strain can be more easily accommodated by atomic relaxations when the reduced ion is located in the first trilayer. This is consistent with the fact that the gap states associated with the two Ti^{3+} ions have different energy, the one associated with the Ti^{3+} in the top trilayer being lowered in energy. Thus, we have optimized the structure of a five–trilayer slab using AE–LCAO–HSE and keeping fixed the fifth (bottom most) trilayer. The structural analysis shows no significant differences, with very similar bond distances among the key atoms and the same surface relaxation pattern, where the O_{2c} above the vacancy moves up again by 0.4 Å. Regarding the electronic properties, a comparison of the DOS calculated with four and five trilayers (see **Figure 5A**) shows that they are nearly identical. The position of the new localized states and local spin magnetic moment (0.94 and 0.93 μ_B) are also very similar to the ones calculated with four trilayers. These results confirm that when the donated electrons are accommodated in the described positions, a four–trilayer slab provides an adequate description.

The localized states associated with the Ti^{3+} ions provide a rigorous test of the flexibility of the local Gaussian basis sets used. The nature of the localized d-state is very different to that of the delocalized d-band of the undoped system. We therefore expect some sensitivity to the flexibility of the basis set used to describe the Ti-d derived orbitals. In **Figure 5B** the DOS in the band gap is displayed for both the oxygen subsurface vacancy with the two basis sets, BS2 and BS3. Although the calculations using BS2 reproduce the surface structure very accurately, the computed position of the defects state relative to the CBM differs by 6% to that predicted by the more flexible BS3. The computational time increases by 33% by using BS3 instead of BS2.

In **Table 4**, AE–LCAO (B3LYP and HSE) calculations show an increase of the surface band gap of around 2% when an oxygen monovacancy is present. This result can be due again to the approximation of considering few layers to simulate the real surface or to the interaction of polaronic distortions as explained above. AE–LCAO (HSE) also describes very similar peaks for the gap state corresponding to the Ti^{3+} ion on the outermost layer in both defects, as it can be seen in **Figure 5C**.

TABLE 4 | Band gap for the stoichiometric anatase (101) and the defective surface by using AE–LCAO and PP–PW.

	Stoichiometric (eV)	H adsorption (eV)	O vacancy (eV)
AE–LCAO B3LYP	3.93	3.86	4.0
AE–LCAO HSE	3.77	3.70	3.83
PP–PW PBE+U	2.41	2.41	2.41

The heterogeneous photocatalysis is based on the ability of photocatalysts to absorb the light energy required to generate electron–hole pairs for a surface reaction. TiO_2 can only absorb ultraviolet (UV) light, but its optical properties can be enhanced by defect engineering. Both oxygen vacancies and hydrogen adsorption give rise to local states below the CB edge, which can extend the light absorption of TiO_2 from the UV to the visible ranges. The formation energy is calculated by using the formula:

$$E_f = E_{def} + 1/2E_{O2} - E_{nodef}, \tag{1}$$

where E_{def} and E_{nodef} are the energies of the defective and non defective anatase(101), respectively, and E_{O2} is the energy of the oxygen molecule. The calculated formation energy with AE–LCAO (HSE) is 2.6 eV, in good agreement with the value 2.9 eV, given in the literature (Haa and Alexandrova, 2016).

3.4. H Adsorption on (101) Anatase

The adsorption mechanism for H investigated here corresponds to the R arrangement in the DFT study by Leconte et al. (2002), since this was found to be the most favorable adsorption mode. A hydrogen atom is adsorbed onto a surface oxygen atom, upon which a reduction of a nearby titanium atom takes place. In our calculation, a neutral H atom is adsorbed to O^{2-} resulting in the formation of OH^- and the donation of an electron to the surface CB.

This electron is transferred to the oxide lattice, and occupies one of the localized 3*d* orbitals of the nearest neighbor Ti_{5c} ions. As a result, this Ti^{4+} ion is reduced and converted to a Ti^{3+} ion. The analysis of the spin (unpaired electrons) population confirms the transfer of an electron onto the Ti ion. The magnetic moment is 0.920 μ_B for PP–PW

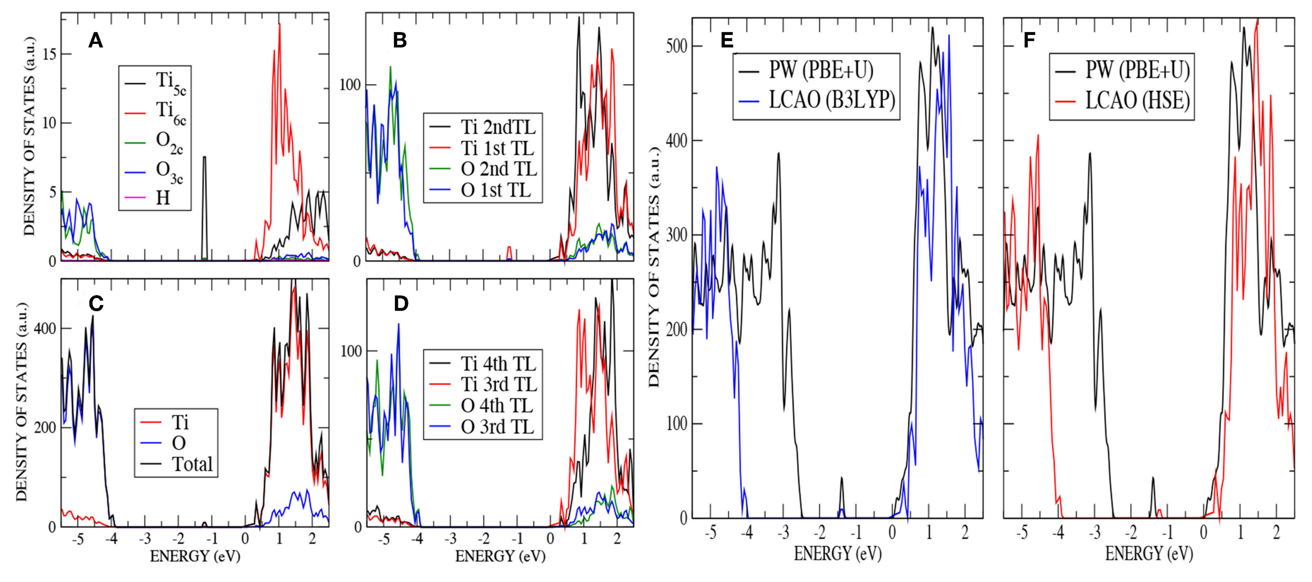

FIGURE 6 | (Color online) H adsorption on anatase (101) : **(A)** PDOS on the most important atoms (O_{2c},O_{3c},Ti_{5c}, and Ti_{6c}) of the top layer by using AE–LCAO (HSE), **(B)** PDOS on the two top trilayers by using AE–LCAO (HSE), **(C)** DOS by using AE–LCAO (HSE), **(D)** PDOS on the two bottom trilayers by using AE–LCAO (HSE) (bulk-like region), **(E)** DOS comparison of AE–LCAO (B3LYP) and PP–PW (PBE+U), and **(F)** DOS comparison of AE–LCAO (HSE) and PP–PW (PBE+U).

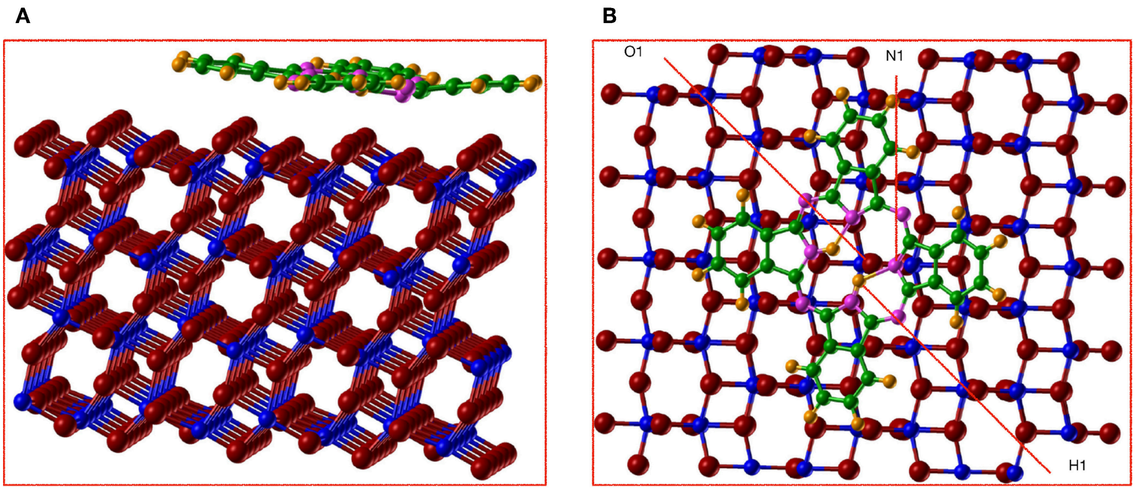

FIGURE 7 | (Color online) **(A)** side view and **(B)** top view of the optimized structure for the adsorption of H_2Pc on anatase (101) by using AE–LCAO (HSE) and centering the molecule on the O_{2c} row. We represent Ti in blue, O in red, N in magenta, C in green, and H in orange.

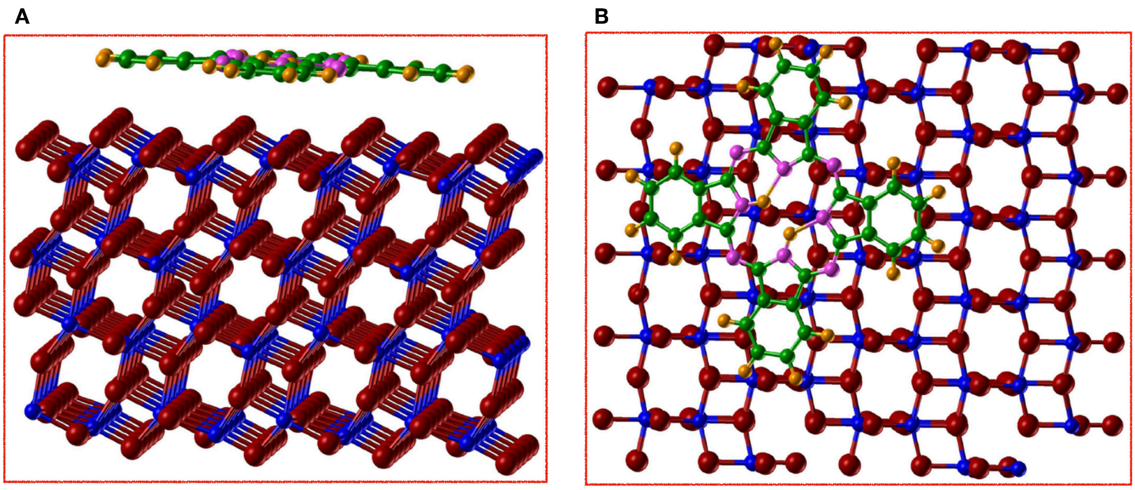

FIGURE 8 | (Color online) **(A)** side view and **(B)** top view of the optimized structure for the adsorption of H_2Pc on anatase (101) by using AE–LCAO (HSE) and centering the molecule on the Ti_{5c} row. We represent Ti in blue, O in red, N in magenta, C in green, and H in orange.

(PBE+U), 0.957 μ_B for AE–LCAO (HSE) and 0.944 μ_B for AE–LCAO (B3LYP). This localization of the electron is due to on–site electronic correlation and therefore one could expect it to be much less when compared to the LDA or GGA approximations.

In **Figure 2B**, the final relaxed structure using the AE–LCAO method and the HSE functional is displayed. The bond distances and atom heights for the key atoms in the top layer calculated with different exchange-correlation functionals are compared in **Table 3**. All the functionals consistently predict the O_{2c} atom bonded to H that moves outwards by 0.13 Å. The height of the H atom above the O_{2c} plane is directly observable in non–contact atomic force microscopy (NCAFM) images (Stetsovych et al., 2015) resulting in a value of 0.11 Å, which is in good agreement with the one predicted here.

The calculated DOS displayed in **Figure 6** –analogous to **Figure 3** for the stoichiometric surface– shows the presence of a localized state 1.2 eV below the conduction band minimum (CBM) for AE–LCAO with HSE (and 1.4 eV for AE–LCAO with B3LYP and PP–PW with PBE+U). This new peak in the band gap, mainly formed by Ti 3*d* states coming from the CBM, is the signature of the reduction of one Ti^{4+} ion of the surface layer to Ti^{3+}. This behavior has been observed in UV absorption spectra and documented in previous calculations of the K atom adsorbed on TiO_2 surface, where the donation of the electron to TiO_2 was localized in a similar state (Muscat et al., 1999). It is remarkable that, in spite of the different position of the valence band maximum, PBE+U predicts a position of that peak with respect to the CBM in agreement with hybrid functionals. In previous infrared spectroscopy experiments and theoretical calculation based on GGA+U on rutile reduced by hydrogen, these gap states have been reported to be in the range 0.75-1.18 eV below the CBM (Cronemeyer, 1959; Finazzi et al., 2008; Islam et al., 2011; Antila et al., 2015), which is consistent with the data presented here. Therefore, both the AE–LCAO and PP–PW implementations predict a similar position of the band gap state due to the localization of the extra electron on the 3d orbital of a Ti_{5c} of the top layer.

It has been stated before that the introduction of defects on TiO_2 can lead to a modification of the band gap value (Naldoni et al., 2012; Mehta et al., 2016). In **Table 4**, a comparison of the computed electronic structure of the stoichiometric and defective surface is presented and the band gap is indicated. The adsorption of hydrogen on anatase (101) leads to a small reduction of the band gap of around 2 % in both the HSE and B3LYP approximations (this result agrees with the value of 1.8% found by diffusion reflectance spectroscopy Mehta et al., 2016). In calculations based on PBE+U the inclusion of defects produces no change in the band gap.

The formation energy is calculated by using the formula:

$$E_f = E_{slab} + E_{H2}/2 - E_{H/slab}, \tag{2}$$

where E_{slab} and $E_{H/slab}$ are the energies of the slabs without and with hydrogen adsorbed on the surface, respectively, and E_H is the energy of atomic hydrogen. The calculated formation energy with AE–LCAO (HSE) is 2.26 eV, in good agreement with the value 2.31 eV, given in the literature (Islam et al., 2011).

3.5. Adsorption of Unsubstituted Phthalocyanine on Anatase(101)

The data presented above suggested that the AE–LCAO-HSE approach is generally the most satisfactory for describing the electronic structure of the stoichiometric and reduced anatase surface. We therefore use this approach to consider the adsorption of H_2Pc on anatase (101). In this calculation we also include the effects of London dispersion interactions through the empirical Grimme D3 correction, as these are likely to play a role in the molecule-surface binding. Initial geometries with the molecule placed centered on O_{2c} or Ti_{5c} rows of the anatase surface have been used in order to explore alternative binding sites on the anatase surface. The optimized structures for both adsorption sites are shown in **Figures 7**, **8**. Local minima are found at both sites. It is perhaps surprising to observe the significant changes in the molecular structure of H_2Pc induced when it is centered on O_{2c}. The molecule becomes non–co–planar and the C-H rings move away from the surface by 0.3–0.4 Å with respect to the central atoms of the molecule, which makes clear the strong repulsion between these rings and the O_{2c}. The reason for this behavior can be the strength of the C-H bond which makes it relatively unreactive. However, the N atoms from the molecule interact strongly with the surface Ti atom, resulting in the N atom placed just on top of the Ti_{5c} (N1 in **Figure 7B**) moving closer to the surface by 0.3 Å, with respect to the rest of the N in the molecule.

The central hydrogens of the molecule form a hydrogen bond of 1.8 Å with the neighboring nitrogens, while one of them (H1) tries to attach to the O_{2c} of the surface. These effects make the O_{2c} (O1) to move up by 0.1 Å. On the contrary when the molecule is centered on Ti_{5c} (**Figure 8**), its remains relatively flat with just variations of 0.1 Å in height between the different atoms. For both sites, H_2Pc is adsorbed with a board altitude that reaches approximately 2.7 Å, in agreement with the result obtained by using STM on rutile (Godlewski and Szymonski, 2013). The calculated adsorption energy is of –3.18 eV with the molecule centered on the oxygen row and of −3.54 eV with the molecule centered on the titanium row. Therefore, the adsorption of H_2Pc is more favorable if the molecule is centered on Ti_{5c} by 0.36 eV. It is clear that when the molecule is adsorbed centered in the O_{2c} the repulsion between the surface and the C-H rings is stronger than the bonds formed.

4. CONCLUSIONS

The AE–LCAO approach is a robust and efficient ab initio method to correctly describe the defects and adsorption of molecules on oxide surfaces. In this work, we have documented the performance of two widely used methods based on Density Functional Theory: linear combination of atomic orbitals (AE–LCAO) and plane waves (PP–PW) to describe the properties of the stoichiometric and defective $TiO_2(110)$ anatase surface. Full relaxation of stoichiometric and defective anatase (101) surfaces has been carried out using the PBE functional and the hybrid PBE0, B3LYP and HSE functionals. For the PP–PW calculations, only the PBE and PBE+U levels of theory have been considered due to the high computational cost of using hybrid functionals for systematic studies. Hybrid functionals, and, in particular, HSE, lead to a computed band gap in excellent agreement with the experimental data. PBE+U underestimates the gap by 20 % but the predicted gap states induced by the defect with respect to the bottom of the conducting band are in good agreement with the hybrid functionals. An understanding of the defective anatase surface is very important for many technological applications. It has been argued that vacancies are very important in the photocatalytic property of surfaces. The formation of mid-gap states, as the ones described here, could improve the photoactivity of the system in the visible light region. Once we have proved that the AE–LCAO approach with the HSE functional is able to accurately describe this surface, we went one step further by studying the adsorption of the phthalocyanine H_2Pc on anatase (101). H_2Pc was placed both on top of the oxygen and titanium rows of anatase (101), with the latter lower in energy by 0.36 eV. This work presents an ab initio study of the adsorption of H_2Pc on anatase (101), and makes clear the influence of the adsorption site in the phthalocyanine-anatase interaction. The AE–LCAO method presented here opens a way to correctly describe the defects and adsorption of molecules on oxide surfaces by using hybrid exchange functionals at a reasonable computational cost, which will be a valuable tool in order to improve the efficiency of dye-sensitized solar cells.

AUTHOR CONTRIBUTIONS

All authors listed have made a substantial, direct and intellectual contribution to the work, and approved it for publication.

FUNDING

We acknowledge financial support from the Spanish MINECO through projects MDM-2014-0377, MAT2014-54484-P, and MAT2017-83273-R and a Juan de la Cierva contract (RM-C). Computer time was provided by the Spanish Supercomputing Network (RES, Spain) at the Magerit Supercomputer (Madrid, Spain) and via the membership of the UK's HEC Materials Chemistry Consortium (GM and NH), which is funded by EPSRC (EP/L000202). This work used the ARCHER UK National Supercomputing Service (http://www.archer.ac.uk).

REFERENCES

Amano, F., Nakata, M., Yamamoto, A., and Tanaka, T. (2016). Effect of ti^{3+} ions and conduction band electrons on photocatalytic and photoelectrochemical activity of rutile titania for water oxidation. *J. Phys. Chem. C* 120:6467. doi: 10.1021/acs.jpcc.6b01481

Anisimov, V. I., Zaanen, J., and Andersen, O. (1993). Density-functional theory and nio photoemission spectra. *Phys. Rev. B* 48:16929. doi: 10.1103/PhysRevB.48.16929

Antila, L. J., Santomauro, F. G., Hammarstroem, L., Fernandes, D. L., and Sa, J. (2015). Hunting for the elusive shallow traps in tio$_2$ anatase. *Chem. Comm.* 51:10914. doi: 10.1039/C5CC02876K

Aschauer, U., Chen, J., and Selloni, A. (2010). Peroxide and superoxide states of adsorbed O_2 on anatase TiO_2 (101) with subsurface defects. *Phys. Chem. Chem. Phys.* 12:12956. doi: 10.1039/c0cp00116c

Barnard, A., and Curtiss, L. (2005). Prediction of tio$_2$ nanoparticle phase and shape transitions controlled by surface chemistry. *Nano Lett.* 5:1261. doi: 10.1021/nl050355m

Becke, A. D. (1988). Density-functional exchange-energy approximation with correct asymptotic behavior. *Phys. Rev. A* 38:3098. doi: 10.1103/PhysRevA.38.3098

Blöchl, P. (1994). Projector augmented-wave method. *Phys. Rev. B* 50:17953. doi: 10.1103/PhysRevB.50.17953

Chen, J., Lin, L.-B., and Jing, F.-Q. (2001). Theoretical study of f-type color center in rutile tio$_2$. *J. Phys. Chem. Solids* 62:1257. doi: 10.1016/S0022-3697(01)00018-X

Cheng, H., and Selloni, A. (2009). Energetics and diffusion of intrinsic surface and subsurface defects on anatase TiO_2(101). *J. Chem. Phys.* 131:054703. doi: 10.1063/1.3194301

Cronemeyer, D. (1959). Infrared absorption of reduced rutile tio$_2$ single crystals. *Phys. Rev.* 113:1222. doi: 10.1103/PhysRev.113.1222

Deak, P., Aradi, B., and Frauenheim, T. (2015). Oxygen deficiency in tio$_2$: Similarities and differences between the ti self-interstitial and the o vacancy in bulk rutile and anatase. *Phys. Rev. B* 92:045204. doi: 10.1103/PhysRevB.92.045204

Dovesi, R., Orlando, R., Erba, A., Zicovich-Wilson, C. M., Civalleri, B., Casassa, S., et al. (2014). Crystal14: a program for the ab initio investigation of crystalline solids. *Int. J. Quantum Chem.* 114:1287. doi: 10.1002/qua.24658

Finazzi, E., Valentin, C. D., Pacchioni, G., and Selloni, A. (2008). Excess electron states in reduced bulk anatase tio$_2$: comparison of standard gga, gga+ u, and hybrid dft calculations. *J. Chem. Phys.* 129:154113. doi: 10.1063/1.2996362

Fujishima, A., and Honda, K. (1972). Electrochemical photolysis of water at a semiconductor electrode. *Nature* 238:37. doi: 10.1038/238037a0

Fujishima, A., Zhang, X., and Tryk, D. A. (2008). Tio$_2$ photocatalysis and related surface phenomena. *Surf. Sci. Rep.* 63:515. doi: 10.1016/j.surfrep.2008.10.001

Godlewski, S., and Szymonski, M. (2013). Adsorption and self-assembly of large polycyclic molecules on the surfaces of tio2 single crystals. *Int. J. Mol. Sci.* 14:2946. doi: 10.3390/ijms14022946

Graetzel, M. (2001). *Nature* 414:338. doi: 10.1038/35104607

Grimme, S., Antony, J., Ehrlich, S., and Krieg, H. (2010). *J. Chem. Phys.* 132:154101. doi: 10.1063/1.3382344

Haa, M.-A., and Alexandrova, A. N. (2016). Oxygen vacancies of anatase(101): extreme sensitivity to the density functional theory method. *J. Chem. Theory Comput.* 12, 2889–2895. doi: 10.1021/acs.jctc.6b00095

Hagfeldt, A., and Grätzel, M. (1995). Light-induced redox reactions in nanocrystalline systems. *Chem. Rev.* 95:49. doi: 10.1021/cr00033a003

Heyd, J., Scuseria, G. E., and Ernzerhof, M. (2003). Hybrid functionals based on a screened coulomb potential. *J.Chem. Phys.* 118:8207. doi: 10.1063/1.1564060

Hoffmann, M. R., Martin, S. T., Choi, W., and Bahnemann, D. W. (1995). Environmental applications of semiconductor photocatalysis. *Chem. Rev.* 95:69. doi: 10.1021/cr00033a004

Hongfei, L., Yuzheng, G., and Robertson, J. (2015). Calculation of tio$_2$ surface and subsurface oxygen vacancy by the screened exchange functional. *J. Phys. Chem. C* 119:18160. doi: 10.1021/acs.jpcc.5b02430

Islam, M. M., Calatayud, M., and Pacchioni, G. (2011). Hydrogen adsorption and diffusion on the anatase tio$_2$(101) surface: a first-principles investigation. *J. Phys. Chem. C* 115:6809. doi: 10.1021/jp200408v

Justicia, I., Ordejon, P., Canto, G., Mozos, J., Fraxedas, J., Battiston, G., et al. (2002). Designed self-doped titanium oxide thin films for efficient visible-light photocatalysis. *Adv. Mater.* 14:1399. doi: 10.1002/1521-4095(20021002)14:19<1399::AID-ADMA1399>3.0.CO;2-C

Kresse, G., and Furthmueller, J. (1996). Efficient iterative schemes for ab initio total-energy calculations using a plane-wave basis set. *Phys. Rev. B* 54:11169. doi: 10.1103/PhysRevB.54.11169

Kresse, G., and Joubert, D. (1999). From ultrasoft pseudopotentials to the projector augmented-wave method. *Phys. Rev. B* 59:1758. doi: 10.1103/PhysRevB.59.1758

Labat, F., Baranek, P., and Adamo, C. (2008). Structural and electronic properties of selected rutile and anatase tio2 surfaces: an ab initio investigation. *J. Chem. Theory Comput.* 4:341. doi: 10.1021/ct700221w

Lazzeri, M., Vittadini, A., and Selloni, A. (2001). Structure and energetics of stoichiometric tio$_2$ anatase surfaces. *Phys. Rev. B* 63:155409. doi: 10.1103/PhysRevB.63.155409

Leconte, J., Markovits, A., Skalli, M. K., Minot, C., and Belmajdoub, A. (2002). Periodic ab initio study of the hydrogenated rutile tio$_2$(1 1 0) surface. *Surf. Sci.* 497:194. doi: 10.1016/S0039-6028(01)01477-7

Liborio, L., and Harrison, N. (2008). Thermodynamics of oxygen defective magneli phases in rutile: a first-principles study. *Phys. Rev. B* 77:104104. doi: 10.1103/PhysRevB.77.104104

Lindan, P., Harrison, N., Gillan, M., and White, J. (1997). First-principles spin-polarized calculations on the reduced and reconstructed tio$_2$(110) surface. *Phys. Rev. B* 55:15919. doi: 10.1103/PhysRevB.55.15919

Mehta, M., Kodan, N., Kumar, S., Kaushal, A., Mayrhofera, L., Walter, M., et al. (2016). Hydrogen treated anatase tio$_2$: a new experimental approach and further insights from theory. *J. Mat. Chem. A* 4:2670. doi: 10.1039/C5TA07133J

Morgan, B., and Watson, G. W. (2010). Intrinsic n-type defect formation in tio$_2$: a comparison of rutile and anatase from gga+u calculations. *J. Phys. Chem. C* 114:2321. doi: 10.1021/jp9088047

Muscat, J., Harrison, N., and Thornton, G. (1999). First-principles study of potassium adsorption on tio$_2$ surfaces. *Phys. Rev. B* 59:15457. doi: 10.1103/PhysRevB.59.15457

Naldoni, A., Allieta, M., Santangelo, S., Marelli, M., Fabbri, F., Cappell, S., et al. (2012). Effect of nature and location of defects on bandgap narrowing in black tio$_2$ nanoparticles. *J. Am. Chem. Soc.* 134:7600. doi: 10.1021/ja3012676

Pan, X., Yang, M.-Q., Fu, X., Zhang, N., and Xu, Y.-J. (2013). Defective tio$_2$ with oxygen vacancies: synthesis, properties and photocatalytic applications. *Nanoscale* 5:3601. doi: 10.1039/c3nr00476g

Patel, M., Mallia, G., Liborio, L., and Harrison, N. (2012). Water adsorption on rutile tio$_2$(110) for applications in solar hydrogen production: a systematic hybrid-exchange density functional study. *Phys. Rev. B* 86:045302. doi: 10.1103/PhysRevB.86.045302

Patel, M., Sanches, F., Mallia, G., and Harrison, N. (2014). A quantum mechanical study of water adsorption on the (110) surfaces of rutile sno$_2$ and tio$_2$: investigating the effects of intermolecular interactions using hybrid-exchange density functional theory. *Phys. Chem. Chem. Phys.* 16:21002. doi: 10.1039/C4CP01824A

Perdew, J. P., Burke, K., and Ernzerhof, M. (1996a). Generalized gradient approximation made simple. *Phys. Rev. Lett.* 77:3865. doi: 10.1103/PhysRevLett.77.3865

Perdew, J. P., Ernzerhof, M., and Burke, K. (1996b). Rationale for mixing exact exchange with density functional approximations. *J.Chem. Phys.* 105:9982. doi: 10.1063/1.472933

Pisani, C., Dovesi, R., and Roetti, C. (1988). *Hartree-Fock ab Initio Treatment of Crystalline Systems*. Berlin: Springer.

Reddy, K. M., Manorama, S. V., and Reddy, A. R. (2003). Bandgap studies on anatase titanium dioxide nanoparticles. *Mater. Chem. and Phys.* 78:239. doi: 10.1016/S0254-0584(02)00343-7

Reshak, A., Stys, D., Auluck, S., and Kityk, I. (2010). Density functional calculations of the electronic structure of 3-phenylamino-4-phenyl-1,2,4-triazole-5-thione. *Phys. Chem. Chem. Phys.* 12:2975. doi: 10.1039/b920743k

Sanches, F. F., Mallia, G., Liborio, L., Diebold, U., and Harrison, N. M. (2014). Hybrid exchange density functional study of vicinal anatase tio$_2$ surfaces. *Phys. Rev. B* 89:1098. doi: 10.1103/PhysRevB.89.245309

Schneider, J., Matsuoka, M., Takeuchi, M., Zhang, J., Horiuchi, Y., Anpo, M., et al. (2014). Understanding tio$_2$ photocatalysis: Mechanisms and materials. *Chem. Rev.* 114:9919. doi: 10.1021/cr5001892

Setvin, M., Aschauer, U., Scheiber, P., Li, Y.-F., Hou, W., Schmid, M., et al. (2013). Reaction of o$_2$ with subsurface oxygen vacancies on tio$_2$ anatase (101). *Science* 341:988. doi: 10.1126/science.1239879

Stetsovych, O., Todorović, M., Shimizu, T. K., Moreno, C., Ryan, J. W., León, C. P., et al. (2015). Atomic species identification at the (101) anatase surface by simultaneous scanning tunnelling and atomic force microscopy. *Nat. Comm.* 6:7265. doi: 10.1038/ncomms8265

Thomas, A. G., Mallick, W. R. F., Kumarasinghe, A. K., Tsoutsou, A. R., Khan, D., Chatwin, N., C., et al. (2007). Comparison of the electronic structure of anatase and rutile tio$_2$ single-crystal surfaces using resonant photoemission and x-ray absorption spectroscopy. *Phys. Rev. B* 75:035105. doi: 10.1103/PhysRevB.75.035105

Valentin, C. D., Pacchioni, G., and Selloni, A. (2009). Reduced and n-type doped tio$_2$: nature of ti^{3+} species. *J. Phys. Chem. C* 113:20543. doi: 10.1021/jp9061797

Wang, Y., and Doren, D. (2005). Electronic structures of v-doped anatase tio$_2$. *Solid State Commun.*136:142. doi: 10.1016/j.ssc.2005.07.014

Wu, X., Selloni, A., and Car, R. (2009). Order-n implementation of exact exchange in extended insulating systems. *Phys. Rev. B* 79:085102. doi: 10.1103/PhysRevB.79.085102

Conflict of Interest Statement: The authors declare that the research was conducted in the absence of any commercial or financial relationships that could be construed as a potential conflict of interest.

frontiers in Chemistry

ORIGINAL RESEARCH
published: 10 April 2019
doi: 10.3389/fchem.2019.00210

The Role of Cation-Vacancies for the Electronic and Optical Properties of Aluminosilicate Imogolite Nanotubes: A Non-local, Linear-Response TDDFT Study

Emiliano Poli[1]*, Joshua D. Elliott[2,3,4], Sergey K. Chulkov[5], Matthew B. Watkins[5]* and Gilberto Teobaldi[6,7,8]*

[1] The Abdus Salam Center for Theoretical Physics, Condensed Matter and Statistical Physics Department, Trieste, Italy, [2] Dipartimento di Fisica e Astronomia "Galileo Galilei", Università degli Studi di Padova, Padova, Italy, [3] CNR-IOM DEMOCRITOS, Consiglio Nazionale delle Ricerche-Istituto Officina dei Materiali, Trieste, Italy, [4] School of Chemical Engineering and Analytical Science, The University of Manchester, Manchester, United Kingdom, [5] School of Mathematics and Physics, University of Lincoln, Brayford Pool, Lincoln, United Kingdom, [6] Daresbury Laboratory, Scientific Computing Department, Science and Technology Facilities Council, Warrington, United Kingdom, [7] Beijing Computational Science Research Centre, Beijing, China, [8] Stephenson Institute for Renewable Energy and Department of Chemistry, University of Liverpool, Liverpool, United Kingdom

Edited by:
Javier Carrasco,
CIC energigune, Spain

Reviewed by:
Rosendo Valero,
University of Barcelona, Spain
Hélio Anderson Duarte,
Federal University of Minas Gerais,
Brazil

***Correspondence:**
Emiliano Poli
epoli@ictp.it
Matthew B. Watkins
mwatkins@lincoln.ac.uk
Gilberto Teobaldi
gilberto.teobaldi@stfc.ac.uk

Specialty section:
This article was submitted to
Physical Chemistry and Chemical
Physics,
a section of the journal
Frontiers in Chemistry

Received: 15 November 2018
Accepted: 18 March 2019
Published: 10 April 2019

Citation:
Poli E, Elliott JD, Chulkov SK,
Watkins MB and Teobaldi G (2019)
The Role of Cation-Vacancies for the
Electronic and Optical Properties of
Aluminosilicate Imogolite Nanotubes:
A Non-local, Linear-Response TDDFT
Study. Front. Chem. 7:210.
doi: 10.3389/fchem.2019.00210

We report a combined non-local (PBE-TC-LRC) Density Functional Theory (DFT) and linear-response time-dependent DFT (LR-TDDFT) study of the structural, electronic, and optical properties of the cation-vacancy based defects in aluminosilicate (AlSi) imogolite nanotubes (Imo-NTs) that have been recently proposed on the basis of Nuclear Magnetic Resonance (NMR) experiments. Following numerical determination of the smallest AlSi Imo-NT model capable of accommodating the defect-induced relaxation with negligible finite-size errors, we analyse the defect-induced structural deformations in the NTs and ensuing changes in the NTs' electronic structure. The NMR-derived defects are found to introduce both shallow and deep occupied states in the pristine NTs' band gap (BG). These BG states are found to be highly localized at the defect site. No empty defect-state is modeled for any of the considered systems. LR-TDDFT simulation of the defects reveal increased low-energy optical absorbance for all but one defects, with the appearance of optically active excitations at energies lower than for the defect-free NT. These results enable interpretation of the low-energy tail in the experimental UV-vis spectra for AlSi NTs as being due to the defects. Finally, the PBE-TC-LRC-approximated exciton binding energy for the defects' optical transitions is found to be substantially lower (up to 0.8 eV) than for the pristine defect-free NT's excitations (1.1 eV).

Keywords: inorganic nanotubes, imogolite nanotubes, defects, DFT, TD-DFT, optical properties, photo-catalysis

INTRODUCTION

By altering the local structure and potential experienced by electrons in insulating or semiconducting materials, point-defects such as atomic-vacancies or interstitial atoms can dramatically affect the physical and chemical properties of the defective host material. Control and tuning of the properties brought about by the presence of defects rest on accurate understanding of their properties at the atomic-scale, which has long motivated strong efforts toward the development and application of accurate, yet computationally viable, approaches for the simulation of defects in solids (Shluger et al., 2003; Ganduglia-Pirovano et al., 2007; Lany and Zunger, 2008; Neugebauer et al., 2014; Walsh and Zunger, 2017; Yin et al., 2018).

The ever-increasing demand for sustainable energy keeps driving research in the development of alternative sustainable technologies for energy production and its efficient use. Photo-catalytic materials (photo-catalysts, PCs) are central to these efforts since they can exploit solar light to access alternative, highly selective, reaction routes for fuels and chemicals production (Kamat, 2007; Sastre et al., 2011, 2012a,b,c; Dietl et al., 2012; de Richter et al., 2013; Maeda, 2013; Baltrusaitis et al., 2014; Fresno et al., 2014; Ismail and Bahnemann, 2014), or environmental remediation (Fujishima et al., 2008; Pelaez et al., 2012; Habisreutinger et al., 2013; Navalón et al., 2013). In this context, the search for affordable high performance, highly selective PCs is an ongoing quest, with growing interest in and appreciation of the potential of aluminosilicate and silicate substrates for selective photo-catalysis (Sastre et al., 2012a,b; Alarcos et al., 2017; Murcia-López et al., 2017). As for any other material, also the ground- and excited-state properties of aluminosilicate and silicate-PCs can be significantly affected by the unavoidable presence of defects (Barrer, 1982; Novatski et al., 2008; Tandia et al., 2011).

The growing research in the photo-catalytic potential of 3D nano- and meso-porous silicates (Sastre et al., 2012a,b; Alarcos et al., 2017; Murcia-López et al., 2017), and parallel substantial progress in the synthesis and characterization of 1D-structured aluminosilicate (AlSi) nanotubes (NTs) based on the imogolite (Imo) structure (Wada et al., 1979; Barron et al., 1982; Theng et al., 1982; Mukherjee et al., 2005, 2007; Levard et al., 2008, 2010; Kang et al., 2010, 2011, 2014; Bottero et al., 2011; Yucelen et al., 2011, 2012b; Zanzottera et al., 2012a,b; Bonelli et al., 2013; Amara et al., 2015; Monet et al., 2018), have prompted recent exploratory computational studies of the potential of Imo-NTs for photo-catalytic applications (Teobaldi et al., 2009; Zhao et al., 2009; Poli et al., 2015, 2016; Elliott et al., 2016).

AlSi Imo-NTs are structurally analogous to the naturally occurring hydrous-aluminosilicate imogolite (Cradwick et al., 1972). Their walls consist of a single layer of octahedrally coordinated aluminum hydroxide with pendant tetrahedral silanol (Si–OH) groups facing the tube cavity (**Figure 1**). The stoichiometric formula of the unit cell is $(Al_2SiO_7H_4)_N$, with N being the number of radially non-equivalent aluminum atoms along the NT circumference (an even number for symmetry reasons). In recent years, control over the structure and functionalization of Imo-NTs has improved greatly. Solution-based synthetic routes to produce single-walled AlSi NTs of controllable radius and length have been defined (Wada et al., 1979; Barron et al., 1982; Theng et al., 1982; Mukherjee et al., 2005, 2007; Levard et al., 2008, 2010; Kang et al., 2010; Yucelen et al., 2011, 2012b) and important post-synthetic, selective functionalization of the outer or inner surface of AlSi NTs (Levard et al., 2010; Bottero et al., 2011; Kang et al., 2011, 2014; Zanzottera et al., 2012a,b; Bonelli et al., 2013; Amara et al., 2015) reported. Further progress has been made in the direct synthesis of methylated (AlSi-Me) (Bottero et al., 2011; Bonelli et al., 2013) or aminated (AlSi-Am) (Kang et al., 2014) AlSi NT derivatives, with methyl ($-CH_3$) or amine ($-NH_2$) moieties in the NT cavity as well as in the creation of hybrid methylated Al(Si/Ge)-Me NTs with tuneable Si/Ge ratio (Amara et al., 2015). Selective amination of the outer surface of AlSi-Me NTs has also been reported (Zanzottera et al., 2012a,b). This synthetic flexibility in turn entails the possibility of widely tuning the NT's properties. Work along this line is ongoing and has led to observation of very encouraging performances of Imo-NTs for chemical separation (Levard et al., 2010; Bottero et al., 2011; Kang et al., 2011, 2014; Zanzottera et al., 2012a,b; Bonelli et al., 2013; Amara et al., 2015), as support for PCs (Katsumata et al., 2013) and as component in hybrid nanocomposites (Marzan and Philipse, 1994). In addition, recent progress in the synthesis of Fe-doped AlSi (and aluminogermanate) NTs (Ma et al., 2012; Arancibia-Miranda et al., 2014; Avellan et al., 2014; Castro et al., 2016; Shafia et al., 2016) has succeeded in introducing absorption of visible (and UV) light, opening new avenues for exploration of the potential of Imo-NTs for both UV and visible light photo-catalytic applications. Recent advances in quantitative structural resolution for (single-walled) Imo-NTs by X-ray scattering (Monet et al., 2018) is expected to further accelerate progress in the development of technological applications based on Imo-NTs. A recent review on Imo-NTs can be found in Paineau (2018).

In spite of the progress in the synthesis and sample-averaged characterization of Imo-NTs (Wada et al., 1979; Barron et al., 1982; Theng et al., 1982; Mukherjee et al., 2005, 2007; Levard et al., 2008, 2010; Kang et al., 2010, 2011, 2014; Bottero et al., 2011; Yucelen et al., 2011, 2012b; Zanzottera et al., 2012a,b; Bonelli et al., 2013; Amara et al., 2015; Monet et al., 2018; Paineau, 2018), the current understanding of point-defects in Imo-NTs is far from complete. To the best of our knowledge, the only experimental investigation of point defects in AlSi Imo-NTs reported to date appears in Yucelen et al. (2012a). By combining different NMR techniques, the authors were able to identify five dominant defect-structures in the AlSi NTs. As explained in Yucelen et al. (2012a), these are based on cation (Al or Si) vacancies, cation (Al→Si) substitution, additional non-stoichiometric Si atoms, and combinations of vacancies with additional atoms (see **Figure 1** for the atomistic models of these defects). Analysis of the experimental results led to the estimation that roughly 16% of the Si atoms in the AlSi NTs are involved in a defect structure. Given the size of Imo-NTs and the challenges in accurate modeling of the proposed defects at the experimental concentrations, to date, these defects have never been studied at Density Functional Theory (DFT) level. Although force-field studies of these defects have appeared in the literature (Liou and Kang, 2016), elucidation of their role for the (defective) AlSi NTs' electronic and optical properties is yet to be accomplished. To this end, and to sustain the growing interest in the optical properties of Imo-NTs and their Fe-doped variants (Arancibia-Miranda et al., 2014; Avellan et al., 2014; Shafia et al., 2015, 2016; Castro et al., 2016), here we present a computational study of

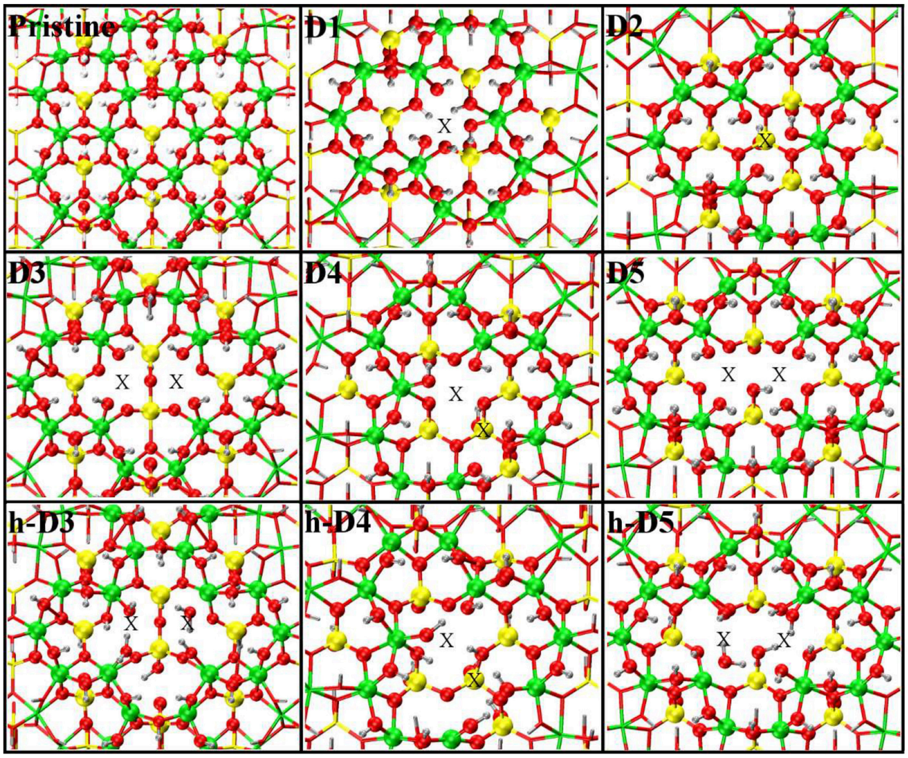

FIGURE 1 | Close up of the atomic structures for the pristine NT, the defects proposed in Yucelen et al. (2012a) (D1–D5), and the protonated defects h-D3, h-D4, and h-D5. Al, green; Si, yellow; O, red; H, silver. An X marker has been used to indicate the position of the missing (Al or Si) atom in the pristine lattice and of the additional Si atoms.

the role of the NMR-inferred defect structures for the optical and electronic properties of AlSi NTs.

Compromising between AlSi NTs' challenging size, the necessity of simulating models sufficiently large to enable full relaxation of the defects and their coexistence with unperturbed lattice regions in the NT-models as well as the far from solved challenges in accurate simulation of excited states properties for solid-state systems (Gonze et al., 1995; Ghosez et al., 1997; Onida et al., 2002; Bernasconi et al., 2011, 2012; Tomic et al., 2014; Ullrich and Yang, 2014; Casida and Huix-Rotllant, 2016; Strand et al., 2019), here we turn to a recent implementation (Strand et al., 2019) of a non-local [PBE0-TC-LRC (Guidon et al., 2009)], linear-response [LR (Casida, 2009)] time-dependent DFT (TDDFT) approach in the Tamn-Dancoff approximation [TDA (Hirata and Head-Gordon, 1999)], that enables computationally viable LR-TDA-TDDFT simulation for model systems of roughly 1,000 atoms. Although of finite accuracy, especially for the optical properties of defect-free NTs (vide infra), the approach provides an arguably reasonable and timely first step in the elucidation of the optical properties of Imo NTs and defects therein, contributing to research in Imo-NTs and, more generally, to the ongoing work on accurate yet viable simulation of excite-state properties in defective solids, NTs included.

The paper is organized as follows: after presentation of the atomic composition and structure for the NMR-inferred defects and computational methods used (section Methods), we present our results in section Results and Discussion. First, we numerically determine the smallest simulation cell capable of accommodating the defect-induced distortions in the presence of effectively unperturbed lattice regions in the NT model (section Determination of the Supercell Size). Structural analysis of the optimized models is presented in section Optimized Defect Structures, followed by characterization of their electronic properties (section Electronic Structure of the Defective NTs). The calculated optical absorption properties are presented in section Optical properties of defects and discussed with respect to available experimental UV-vis spectra for AlSi NTs. We finally present our conclusions in section Conclusions.

METHODS

The Atomic Structure of the NMR-Inferred Defects

For our computational study, we started from the atomic structure of the five main defects inferred from NMR experiments on the AlSi Imo-NTs (Yucelen et al., 2012a). They can be seen in **Figure 1** and are described and labeled as follows:

- **D1** is a single Al-vacancy. By disrupting the gibbsite $Al(OH)_3$ backbone of the NT, D1 introduces additional Al-OH dangling groups in the NTs framework, which would otherwise not be present in the defect-free NTs.

TABLE 1 | Stoichiometric formula and resulting charge for the considered defect models.

#Defect	Model stoichiometry	Net charge
D1	$(Al_2SiO_7H_4)_{71}SiAlO_7H_7$	0
D2	$(Al_2SiO_7H_4)_{71}Si_2AlO_8H_5$	0
D3	$(Al_2SiO_7H_4)_{71}SiO_5H_2$	−4
D4	$(Al_2SiO_7H_4)_{71}Si_2O_7H_4$	−2
D5	$(Al_2SiO_7H_4)_{71}SiO_6H_4$	−4
h-D3	$(Al_2SiO_7H_4)_{71}SiO_5H_6$	0
h-D4	$(Al_2SiO_7H_4)_{71}Si_2O_7H_6$	0
h-D5	$(Al_2SiO_7H_4)_{71}SiO_6H_8$	0

- **D2** presents an additional Si-atom in the inner wall of the NTs, leading to the occurrence of a Si-O-Si bridge in the inner wall of the NTs. It is worth recalling that the pristine NT do not contain Si-O-Si bridges, but only pendant silanol (Si-OH) groups.
- **D3** is a double Al-vacancy in the outer gibbsite layer of the NT. NMR data (Yucelen et al., 2012a) suggests the condensation of two Si-OH groups with formation of an *elongated* Si-O-Si bridge, which we also included in our initial geometry ahead of geometry optimization. In the absence of structural relaxation for the rest of the NT-atoms, the elongated nature of the bridge leads to an unusually large Si-O-Si angle of 169° and partially stretched (1.73 Å) Si-O bond lengths.
- **D4** comprises one Al-vacancy in the outer wall, and one extra Si-atom in the inner wall of the NTs. As for D2 and D3, also D4 contains an additional Si-O-Si bridge not present in the pristine NT structure.
- **D5** consists of two neighboring Al-vacancies. In contrast to D3, no Si-O-Si bridge is present, leaving two Si-OH groups dangling around the double-vacancy site.

Table 1 reports the stoichiometry of the defect models for the adopted x3 periodic repeat of the NT (vide infra, section Determination of the Supercell Size). Given the water-phase synthesis of the AlSi NTs (Mukherjee et al., 2005, 2007; Levard et al., 2008), it is inevitable that counter-cations or protons (in the water solution) will compensate the negative charge of D3, D4, and D5. These considerations prompted us to model three additional structures, one for each negatively charged defect, neutralizing the original negative excess charge by protonation of the defect-site. These structures, labeled **h-D3**, **h-D4** and **h-D5** are also displayed in **Figure 1**. Inclusion in the simulation of larger counter-cations [possibly Keggins ions as experimentally observed during the NT synthesis (Casey, 2006)] was not considered due to the prohibitive computational cost of this approach.

Computational Methods

Geometry Optimization

Given the extended dimension of the systems considered ($\sim$1,000 atoms) all the defect structures were optimized using the Linear Scaling DFT program ONETEP (Skylaris et al., 2005; Haynes et al., 2006; Hine et al., 2009, 2011) with the PBE (Perdew et al., 1996) approximation to the exchange-correlation (XC) functional, and separable (Kleinman-Bylander) norm-conserving pseudopotentials (Gonze et al., 1991) for the atomic core levels. The adopted kinetic energy cutoff was 1,000 eV, and 4 (9) valence Non-Orthogonal Wannier Functions (NGWFs) were used for the O (Al, Si) atoms. 1 NGWF was used for the H atoms. In all cases, no truncation of the density kernel ($K^{\alpha\beta}$) was enforced. The localization radius for the valence NGWFs was 8 Bohr. All simulations were performed with periodic boundary conditions ensuring at least 15 Å vacuum separation between replicated images along the non-periodic directions. Along the periodic direction of the NT, the simulation cell contained three-fold (x3) replicas of the NT along its axis (optimized 8.665 Å period), yielding models of $\sim$1,000 atoms. This choice is extensively discussed and motivated in section Determination of the Supercell Size. Geometry-relaxations were performed via the quasi-Newton optimization scheme based on the Broyden-Fletcher-Goldfarb-Shanno (BFGS) algorithm (Pfrommer et al., 1997). All the atoms of the defective NT-models were left free to relax. The geometry optimization threshold for the atomic forces was 0.05 eV/Å. Consistent with the absence of any dangling bonds (vide infra), singlet spin-states were tested to be energetically favored over alternative spin-polarized solutions.

Hubbard-Corrected, Non-local DFT, and LR-TDDFT Simulations

Following geometry relaxation, the optimized defect models were used for single-point non-local hybrid DFT and LR-TDDFT simulations using the CP2K package (VandeVondele et al., 2005). CP2K uses a mixed Gaussian and plane wave basis set, where atom-centered Gaussian orbitals are used to represent the wavefunction, while the electronic density is represented by an expansion of plane waves.

Through all our calculations, we used Goedecker-Teter-Hutter (GTH) norm-conserving pseudopotentials (Goedecker et al., 1996) to model the electron-ion interactions. We adopted the molecularly optimized (MOLOPT) DZVP-SR basis set (VandeVondele and Hutter, 2007) for all atoms and the auxiliary density matrix method (ADMM) (Guidon et al., 2010) to compute the exchange integrals, using the cpFIT3 basis set for all the elements present in our systems.

Hubbard-corrected (PBE+U) simulations were also performed with the CP2K code applying an isotropic $U = 7$ eV correction on the 2p subspace of the O-atoms. The U-value was taken from earlier benchmarked studies of Al-doped bulk SiO2 (Nolan and Watson, 2006; Mao et al., 2017).

For hybrid DFT and LR-TDDFT simulations, we used the PBE0-TC-LRC XC-functional (Guidon et al., 2009) with 25% Hartree-Fock (HF) exact-exchange mixing and a real-space cut-off of 8 Å, beyond which a long-range correction [based on the spherically averaged PBE exchange hole (Ernzerhof and Perdew, 1998)] is used.

Optical spectra were computed both at the independent-particle level making use of the Fermi Golden Rule (Read and Needs, 1991; Motta et al., 2010) and via the linear-response (LR) time-dependent DFT (TDDFT) formalism (Casida, 2009) recently implemented, in the Tamn-Dancoff approximation

[TDA (Casida, 2009)], in CP2K by two authors of the present paper (Strand et al., 2019). In all cases, the first 60 virtual states were converged for each defect structure using a cutoff of 500 Ry. The absorption spectra were reproduced using a Gaussian broadening of 0.3 eV. Consistent with the closed-shell ground-state for the considered systems, and based on the expected extremely low probability of a singlet to triplet transition due to spectroscopic selection rules, only singlet excitation were considered in the LR-TDA-TDDFT calculations. The real space cutoff of 8 Å was numerically tested to best compromise between (i) convergence in excitation energies (50 meV) and absorption intensities (5%) sufficient to discriminate between the main features in the simulated optical spectra, and (ii) practical viability of the simulations on Tier0 High Performance Computing resources (**Figures S1, S2** in the Supporting Information).

Depending on the choice of the method used to simulate optical absorption, different quantities were calculated and are accordingly displayed. For the FGR approach, we computed the imaginary part of the dielectric function (ε_2). Conversely, for the LR-TDA-TDDFT approach, we computed the absorbance (e, L mol^{-1} cm^{-1}) from the calculated oscillator strengths for each optical excitation following the standard procedure reported in http://gaussian.com/uvvisplot/.

RESULTS AND DISCUSSION

Determination of the Supercell Size

When simulating defects by means of periodic DFT simulation approaches as used here, the size of the periodic cell containing the defect is one of the critical aspects to be numerically checked. To reduce the computational cost without introducing (finite-size) errors in the simulations, the simulation cell should be as small as possible yet capable to preserve bulk-like, unperturbed regions around the defect site following structural relaxation.

For this initial benchmark, we focused on D1. The optimized structure of the AlSi NT in Yucelen et al. (2012a) (24 Al-atoms in the circumference, 336 atoms in total) was modified to recover the same D1 composition and structure derived from the NMR study in Yucelen et al. (2012a). The same procedure was repeated for two larger systems made up by two (672 atoms) and three (1,008 atoms) NT-repeat units, respectively.

The structure of these three differently sized models of D1 was optimized by fully relaxing all the atoms in the simulation cells. We then analyzed the defect-induced atomic-displacements as a function of the distance from the defect site (**Figure 2A**). For a suitably sized model, the regions furthest from the defect site should maintain the same atomic structure as in the perfect, defect-free, system.

To facilitate the analysis, the NT-atoms were divided in different groups based on their distance from the defect-center (**Figure 2**). The atoms directly bonded to a missing atom in the defect structures are referred to as nearest neighbors **(NN)**. The atoms separated by one bond from the NN atoms are marked second nearest neighbors **(SNN)**. The atoms within a 10 Å distance from the defect-sites (but further from the defect center than the SNN atoms) have been inserted in a group called first shell **(FS)**. Accordingly, the FS group does not include NN and SNN atoms. The same approach has been used for atoms within a 15 Å (second shell, **SS**) and 20 Å (third shell, **TS**) distance from the center of the defect-site. The computed displacements from the initial bulk-like positions were then group-averaged, obtaining the ⟨Δ*r*⟩ values shown in **Figure 2**.

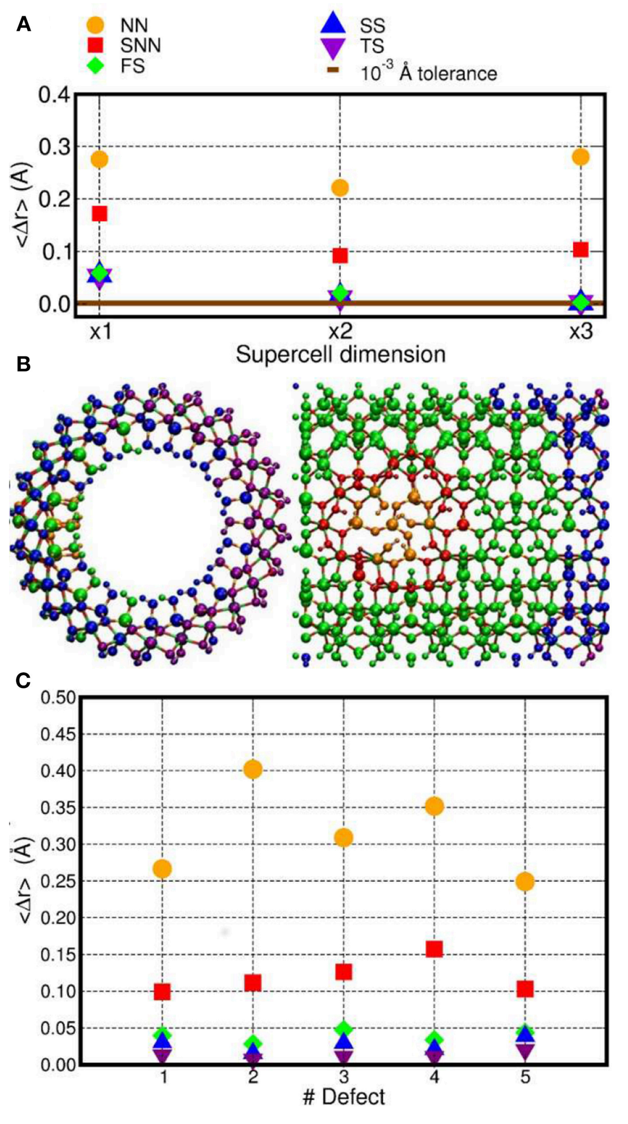

FIGURE 2 | (A) Computed average atomic-displacements from initial bulk-like positions (⟨Δ*r*⟩, Å) for the optimized D1 model as a function of the number of NT-repeat units in the simulation cell (supercell dimension). See text for the definition of the NN, SNN, FS, SS, and TS labeling for the different group of atoms as a function of their distance from the center of the D1 defect. **(B)** Front and side view of the x3 AlSi NT model hosting D1. The atoms have been colored as a function of their ⟨Δ*r*⟩ value. Same color labeling as in **(A)**. **(C)** Computed ⟨Δ*r*⟩ for the D1–D5 models (x3 supercell).

The simulation-cell containing two AlSi NT repeat units shows small but non-negligible displacements for the SS and TS atoms (⟨Δ*r*⟩ ~10^{-2} Å. Conversely, the supercell containing three AlSi NT repeat-units presents negligible ⟨Δ*r*⟩ ≤10^{-3} Å values for all the (FS, SS and TS) atoms further than the SNN group. The extremely small displacements for the TS atoms demonstrates that the simulation cell with three NT repeat units suffer from very limited (i.e., negligible) finite-size effects and enable modeling of regions of the defective NT with a pristine unperturbed structure.

The same analysis was repeated also for all the others defects in **Table 1** using the largest x3 simulation cell. The results are shown in **Figure 2B**. Exception made for D3, the average relaxation-displacements for the atoms further than the SNN (i.e., >15 Å away from the defect site) are in the order of 10^{-2} Å or less for all defects D2 to D5. The larger $\langle \Delta r \rangle$ values for D3 can be ascribed to its more extended structure (**Figure 1**), leading to a longer-range perturbation of the host lattice. The computed $\langle \Delta r \rangle < 10^{-2}$ Å value for the TS atoms (further than 20 Å from the defect center) of D3, nevertheless suggest rather contained finite-size effects also for this defect, when modeled in a x3 supercell of the AlSi NT.

Overall, the results in **Figure 2A** demonstrates that, for atoms belonging to the TS groups (hence furthest from the defect-site within the periodic simulation cell), the defect-induced perturbation are very effectively screened, leading to negligible displacements from bulk-like positions. On the basis of these results, a x3 simulation cell with three NT repeat units was used for the electronic structure characterization. This choice permits to simulate defects concentrations involving $\sim$10% of the Si-atoms in the cells (for D1), which slightly underestimates the experimentally determined value of 16% (Yucelen et al., 2012a). Accordingly, and pending limitations of the adopted PBE XC-functional and neglect of solvent in the simulations, the considered models should provide a reasonable representation of the defects in AlSi NTs.

Optimized Defect Structures

The atomic structure for defects D1 to D5 in Yucelen et al. (2012a) were obtained from a combination of several NMR techniques ("^{1}H–^{29}Si and ^{1}H–^{27}Al FSLG-HETCOR, ^{1}H CRAMPS, and ^{1}H–^{29}Si CP/MAS"), *without* further refinement via energy-based geometry optimization. In the following, we accordingly analyse in detail the role of (DFT) energy-based geometry optimization (in vacuo) for the atomic structure of the defects D1 to D5 both qualitatively and quantitatively.

The optimized structures for the D1-5 and h-D3-5 defects are shown in **Figure 3**. The D1 optimized structure presents a water (H_2O) molecule coordinated to an Al-atom adjacent to the defect site. The formation (*condensation*) of one Al-coordinated H_2O molecule is due to the transfer of one H-atom from a dangling –OH group to an adjacent one. As for D1, also optimization of D5 leads to condensation of one H_2O molecule that remains coordinated to one of the Al-atoms closest to the center of the defect-site.

Optimization of the D2 structure leads to local re-organization of the local hydrogen-bond network both inside and outside the NT-cavity with no H_2O condensation. A qualitatively similar relaxation (rearrangement of inner and outer hydrogen bonding network with no H_2O condensation) is found also for D4.

Also for D3, the optimized geometry presents noticeable differences with respect to the NMR proposed structure in Yucelen et al. (2012a). Upon DFT-relaxation, the stretched Si-O-Si bridge breaks and the O-atom relaxes toward the closest Si-atom leaving a negatively charged deprotonated O-atom. The computed barrier-less breaking of the originally elongated Si-O-Si bridge is accompanied by extensive reorganization of the AlO_6 octahedron closest to the defect site. This relaxation in turn leads to condensation of a H_2O molecule, which remains coordinated to one Al-atom with additional hydrogen bonding coordination (1.53 Å distance) to one deprotonated O-atom from a neighboring Al-octahedron. This geometry was found to be energetically favored by at least 0.4 eV over the alternative geometries studied (**Figure S3** in the Supporting Information).

The final structure for the protonated defects (h-D3, h-D4, h-D5) are relatively similar to their charged correspondent. However, the presence of additional hydrogen-atoms around the defect sites leads to condensation of an additional H_2O molecule. In all cases, the formed H_2O molecules remain coordinated the Al-atoms nearest to the center of the defects.

Given the strong sensitivity to proton environments in the experiments in Yucelen et al. (2012a), it is possible the deviation between the NMR proposed structure (**Figure 1**) and DFT-optimized one for D1 and D3 (**Figure 3**) may be due to the lack of solvent (H_2O) and/or counterions in the simulations. The prohibitive computational (memory) cost of simulating the present models in the presence of explicit solvation, and the unavailability of DFT-benchmarked force-fields for defects in AlSi NTs, prevent us from further investigating this aspect, that is however worth of specialist method development work.

To provide a more quantitative analysis of the optimized defect structure, we next consider their effects on the three types (Si-O, Al-O, O-H) of bonds in AlSi NTs. Given the computed small average-displacement ($\langle \Delta r \rangle$) for atoms further than the FS group (**Figure 2**), we limit the present analysis to the atoms belonging to the NN and SNN groups. **Figure 4** reports the computed average change in Al-O, Si-O, and O-H bond-lengths ($\left\langle \Delta d \right\rangle$) for the atoms in the NN and SNN groups i.e., those closest to the defect-center. The raw data for this analysis can be found in the Supporting Information (**Table S1**).

In general, the presence of cation vacancies in the AlSi NTs framework causes larger changes in the external Al-O octahedral layer than in the inner Si tetrahedrons. The change in length of the Al-O bonds for the NN, SNN atoms varies from case to case. Whereas, the computed deviations for the Al-O bond-lengths in the NN and SNN groups lie in the 3–10% range ($\sim \; 0.02 - 0.15$ Å), those calculated for the stronger Si-O bonds are consistently smaller than 0.01 Å.

Owing to the creation of alternative local hydrogen-bonding patterns and/or condensation of H_2O (D2, D4, h-D4. h-D5 in **Figure 3**) the occurrence of these defects in the NTs induces substantially larger relaxations (up to $\left\langle \Delta d \right\rangle$ >0.25 Å values in **Figure 4**).

It is useful to note that the modeled barrier-less H_2O condensation is found to take place only in defect structures for which the O-O distance between adjacent Al-OH dangling group or between an Al-OH dangling group and a pristine Al-O(H)-Al bridge is <2.5 Å. In D2, D4, and h-D4 the presence of an extra Si atom increases the distances between the closest dangling

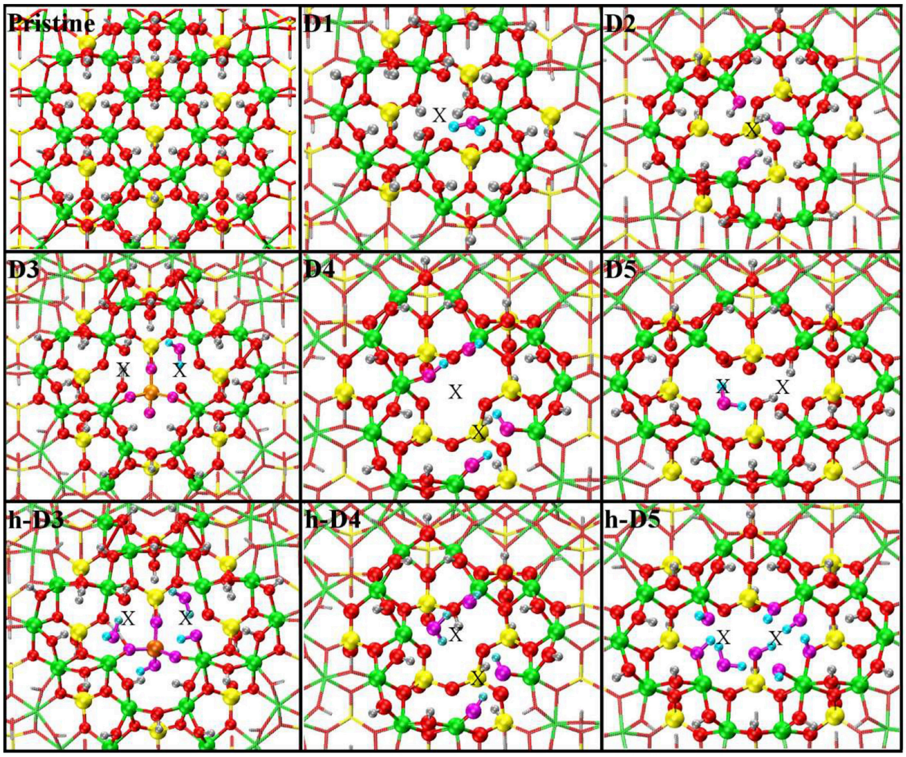

FIGURE 3 | Close up of the optimized atomic structures for the pristine NT, the defects proposed in Yucelen et al. (2012a) (D1–D5), and the protonated defects h-D3, h-D4, and h-D5. Al, green; Si, yellow; O, red; H, silver. To highlight changes from the initial structures in **Figure 1**, an alternative atom-coloring has been used for the dangling -OH groups closest to the defect sites, condensed H_2O molecules, perturbed hydrogen-bonding patterns, and the Si-O-Si bridge in D3 (O, magenta; H, cyan; Si, tangerine). An X marker has been used to indicate the position of the missing (Al or Si) atom in the pristine lattice and of the additional Si atoms.

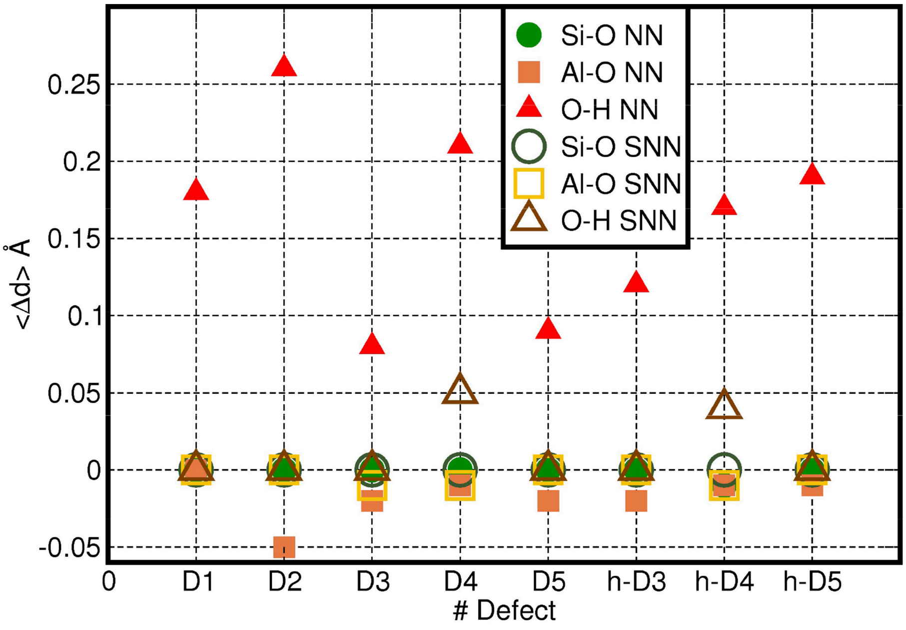

FIGURE 4 | Computed average change in Al-O, Si-O, and O-H bond-lengths ($\langle \Delta d \rangle$, Å) for the NN (filled symbols) and SNN (empty symbols) atoms as a function of the defect-model studied. The adopted reference for each bond type is reported in **Table S1** in the Supporting Information.

Al-OH groups. Provided this condition is not fulfilled, no barrier-less H_2O condensation takes places during the geometry optimization. However, and interestingly, the absence of H_2O condensation during the relaxation of D2, D4, and h-D4 is shown in **Figure 4** to lead to an overall larger structural relaxation around the defect. Altogether, these results suggest that H_2O condensation in non-stoichiometric defective AlSi NTs is an effective mechanism to reduce the spatial-extent of perturbation to the NT-lattice, thence strain.

Electronic Structure of the Defective NTs

As noted above, to the best of our knowledge, the electronic properties of the NMR-inferred defects in Yucelen et al. (2012a) have not been previously considered in the available literature on imogolite, which motivates our interests in the subject and this section. Based on (i) the negligible defect-induced structural distortion computed for the NT-regions farthest from the defect-sites (**Figure 2**), suggesting coexistence of both defect-sites and nearly unperturbed NT-regions in our models, and (ii) the encouraging accuracy of PBE0-related XC-functionals in calculating Kohn-Sham BGs (Guidon et al., 2009, 2010), we expect our results to provide a reasonable approximation of the real NTs (in vacuo).

Figure 5 reports the computed total Density of States (DOS) and defect-site resolved local DOS (LDOS) at both PBE and PBE0-TC-LRC levels. Depending on the defect and its protonation, shallow (h-D5) or deep (D1, D2, D3, D4, D5,h-D3, h-D4) occupied states are introduced in the NT's BG. The ensuing reduction of the energy gap between the highest-energy occupied state and lowest-energy empty state is found to be highly sensitive to the defect composition and structure, with values ranging from 0.25 eV (h-D5) to up to 4.12 eV (D3).

Comparison between the results for the D3-5 defects and their hydrogenated counterparts (h-D3-5) indicates that protonation is effective in turning the deep defect-states of (D3-5) into shallower ones (h-D3-5), with changes as large as 1.5 eV going from D5 to h-D5. For D4, protonation of the defect site leads to shift of the defect states closer to the Valence Band edge and on the SNN atoms. These results hint at the possibility of controlling the energy of the defect states, thence the NT's electronic properties, by altering the pH of the solution the NTs are dissolved in. Although, the absence of implicit or explicit solvent (and control of pH conditions) in our simulations prevents us from drawing firm conclusions on this subject, this result may motivate further experimental research in the pH-dependence of Imo-NTs' optical spectra [not considered in Shafia et al. (2016) and Shafia et al. (2015)].

In all cases, the computed LDOS traces indicate dominant contributions to the occupied defect-states from the NN and SNN atoms closest to the center of the defects. Thus, as shown in **Figure 6**, the occupied defect-states turn out to be highly localized at (or around) the defect site. Conversely, the computed (L)DOS indicate that, for all cases, the CB-edge remains delocalized on the unperturbed NT, being dominated by contributions from the atoms furthest from the defect-sites.

In spite of quantitatively different BG values (**Figure 7**), comparison between the PBE, PBE0-TC-LRC (25 and 12.5% HF exact-exchange mixing) and PBE+U calculated LDOS (**Figure 5** and **Figures S4–S7** in the Supporting Information) reiterates a rather weak dependence of the contributions to the VB-edge and defect-states on the given approximation to the XC-functional. A partial exception to this trend is represented by application of 7 eV Hubbard corrections on the O-atoms (2p subspace) of D2 and h-D5, which results in a slightly enhanced localization of the defect-states. In spite of these small differences, all the computational approaches used agree in predicting the defect states localized at the defect-site.

To further support this statement, we re-optimized the structure for two selected systems, namely the single Al-vacancy (D1) and the mixed Al-vacancy/additional Si system (D4) at both PBE0-TC-LRC and PBE+U=7 eV level. New **Figure S8** in the Supporting information provides a visual comparison between the PBE, PBE+U and PBE0-TC-LRC optimized geometries for D1 and D4. **Figure S9** in the Supporting Information provides a quantification of the deviations of the PBE+U and PBE0-TC-LRC optimized geometries from the PBE-optimized one.

With average deviations smaller than 0.15 Å even for the Nearest Neighbors (NN) atoms (that are directly bonded to a missing/additional atom), the PBE0-TC-LRC geometries are found to be in good agreement with PBE results. As shown in **Figure S8** the deviations are mostly due to small changes in bond-orientations as well as hydrogen bonding patterns. Conversely, use of a rather aggressive U=7 eV correction for the 2p subspace of the O-atoms is found to induce somewhat larger differences between PBE and PBE+U optimized geometries for D1 and D4 (up to ∼0.25 Å average displacement for the NN atoms of D4). The substantially larger (∼0.35 Å) average displacement for the NN atoms of D1 at PBE+U level is due to the absence of water condensation for the PBE+U optimized geometry, in contrast with PBE and PBE0-TC-LRC results.

As the U= 7 eV O(2p) correction was parameterized on experimental data for hole band-gap states in Al-doped SiO_2 (Nolan and Watson, 2006; Mao et al., 2017), a system not containing Al-OH or Al-OH_2 fragments, we are inclined to consider the agreement between PBE and PBE0-TC-LRC results (leading to water condensation) as a robust benchmark of the initially proposed PBE results. Regardless of these specialist and perhaps secondary differences, the good agreement between the differently calculated (L)DOS (**Figure 5** and **Figures S4, S5, S10**) and real-space localization plots (**Figure 6** and **Figures S6, S7, S11**) for D1 and D4 reiterates the conclusion that, pending minor quantitative difference, the physical picture provided by PBE0-TC-LRC refinement of PBE-optimized geometry offer a good compromise between absence of major artifacts and computational costs, at least for the systems considered here.

Altogether, the marked localization of the occupied defect-states, and the computed delocalization of the CB-edge (**Figures 5**, **6**) hint to the possibility of defect-mediated separation of photo-generated e-h pairs via energetically advantageous relaxation of holes to different defect-sites in the NTs. Thus, and pending the actual electron (hole) transfer kinetics which may hinder such separation process, the present

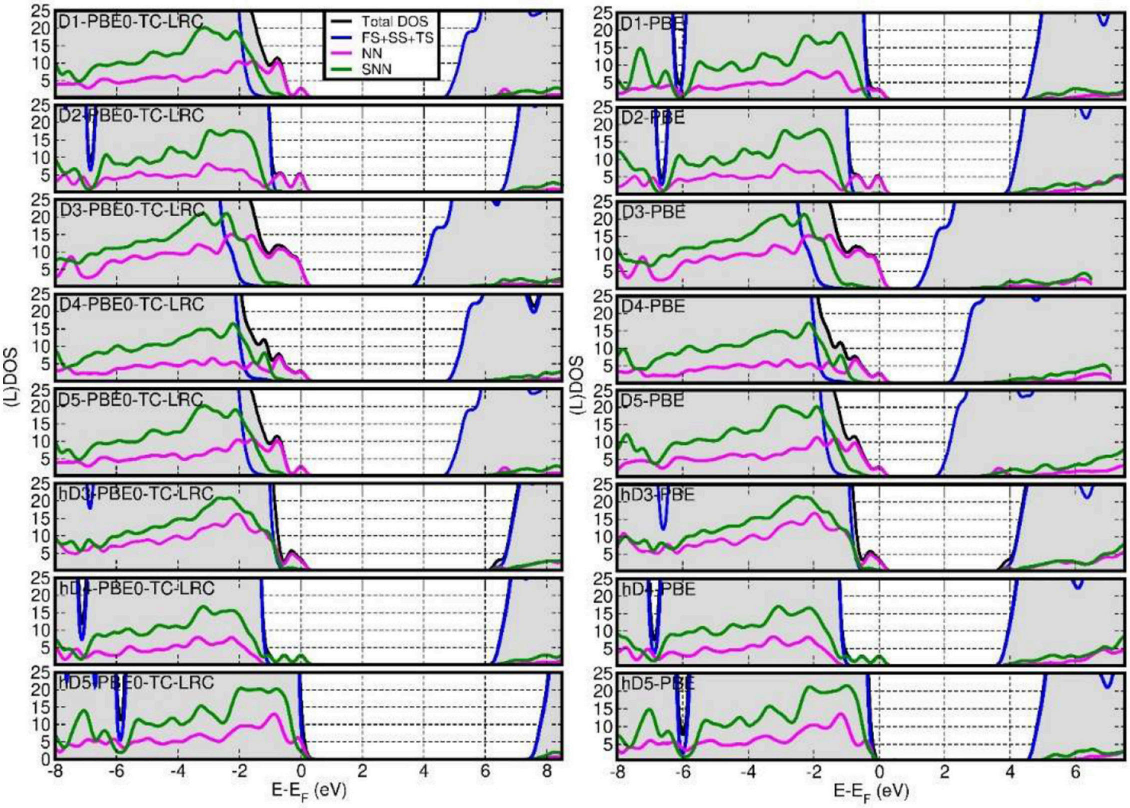

FIGURE 5 | Fermi-energy (E_F) aligned PBE0-TC-LRC **(left)** and PBE **(right)** DOS for all the defects simulated. NN-, SNN- and (FS+SS+TS) resolved local-DOS (LDOS) are also displayed. The energies have been referenced to the highest occupied Kohn-Sham states and the (L)DOS have broadened via 0.1 eV Gaussian smearing. All the computed systems are insulating with no fractional occupancy: occurrence of LDOS traces beyond E_F is due to the applied smearing.

results suggest that cation-vacancies in Imo-NTs could be highly reactive photo-oxidation centers. In addition, the presence of occupied defects states in the BG for defective NTs strengthens earlier suggestions (Levard et al., 2010; Yucelen et al., 2012b) regarding the potential of Imo-NTs as hole-scavengers for molecular photo-catalysts grafted on the NT's wall.

Finally, for the specialist reader we quantify the deviations between PBE and PB0-TC-LRC results for the BGs of the considered systems. As shown in **Figure 7**, not unexpectedly, the PBE-calculated BGs are substantially smaller than the PB0-TC-LRC ones with deviations in the 2.43-2.73 eV range depending on the defect. However, and in spite of the expected underestimation of BGs, the calculated relative energies and amplitudes of the PBE LDOS traces, especially for the occupied states, are in very good agreement with the PB0-TC-LRC ones (**Figure 5**). This result points to a reasonable performance of the PBE functional for the simulation of the relative energy- and real-space localization of occupied cation-vacancy states in Imo-NTs. Not unexpectedly, the results for 12.5% HF mixing are found to lie in between the PBE and PBE0-TH-LRC (25% HF mixing) values. Interestingly, BG values for 12.5% HF mixing appear to be very similar to the PBE+U=7 eV results with relatively limited (300 meV) system-dependent deviations between the two datasets.

As shown in **Figure 7**, for the pristine NTs, the calculated BG is 5.3 eV and 8.0 eV at PBE and PB0-TC-LRC level, respectively. The calculated PBE value of 5.3 eV is in quantitative agreement with earlier results at a similar level of theory (Zhao et al., 2009), and underestimated with respect to the expectedly more accurate PB0-TC-LRC value. Experimentally, aluminosilicate NTs [with 16% of Si atoms involved in defects (Yucelen et al., 2012a)] are observed to start to absorb light at roughly 4.1 eV (300 nm) with a low-energy absorbance shoulder at roughly 5 eV (250 nm) preceding a marked increase in the absorbance at 5.5–6.2 eV (225–200 nm) (Shafia et al., 2015). Tauc-plot processing of the experimental spectra leads to suggestion of an "optical gap" of 4.9 eV for the pristine (direct gap Zhao et al., 2009, Elliott et al., 2016) NTs (Shafia et al., 2015). The marked overestimation (3.1 eV) of the PB0-TC-LRC BG with respect to the low-energy features in the experimental absorption spectra point to possibly crucial roles of both existing defects (Yucelen et al., 2012a) and excitonic relaxations (Ullrich and Yang, 2014) for the optical properties of aluminosilicate NTs. In the following Section we investigate both these points.

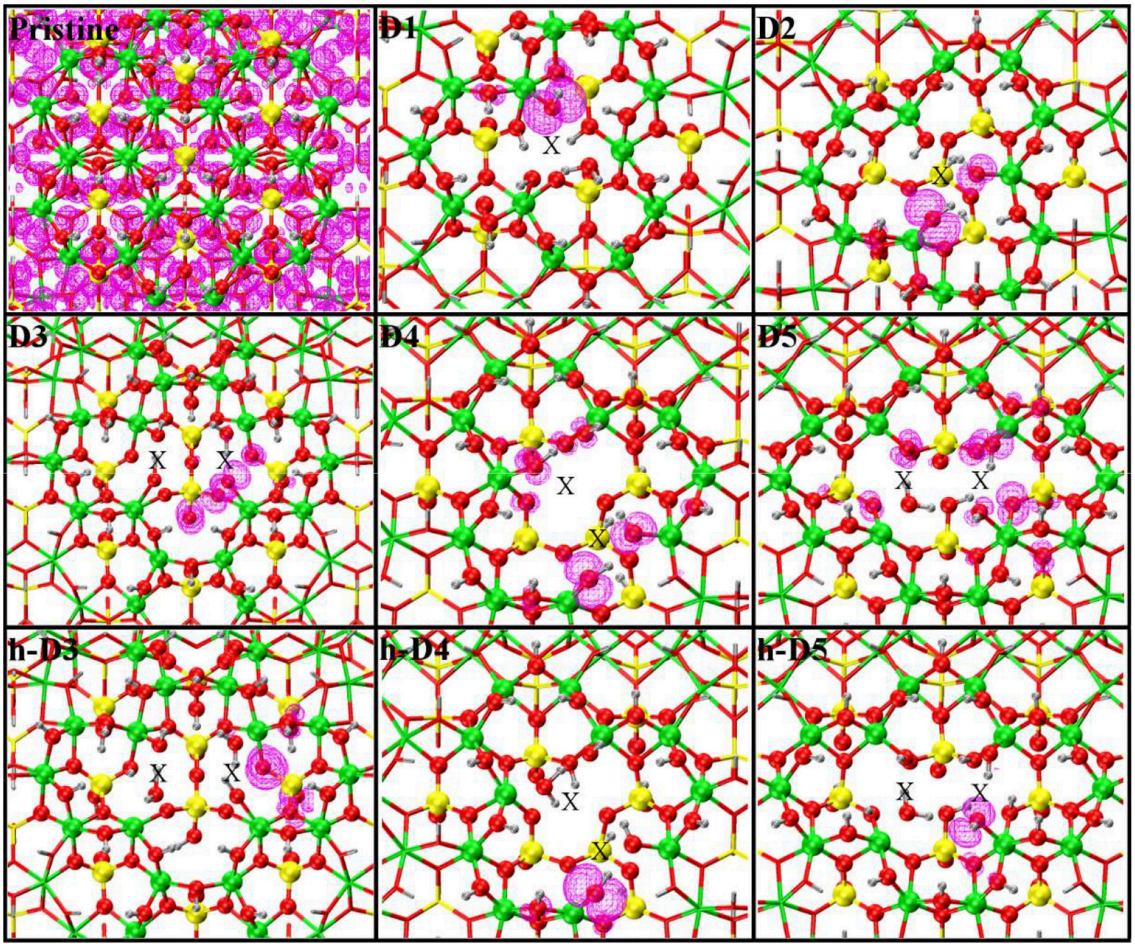

FIGURE 6 | Close up of the optimized defect geometries together with the density-plot of their highest-energy occupied Kohn-Sham states (magenta). Same atomic color labeling as in **Figure 1**. An X marker has been used to indicate the position of the missing (Al or Si) atom in the pristine lattice and of the additional Si atoms.

Optical Properties of Defects

In spite of the growing interest in imogolite NTs, characterization of their optical properties has not been as systematic as the study of their synthesis and potential for chemical separation. To the best of our knowledge, the only UV-vis optical characterization of purified (pristine and Fe-doped) imogolite NTs' samples to date have been published in Shafia et al. (2015) and Shafia et al. (2016). Also to the best of our knowledge, simulation of the optical properties of imogolite nanotubes beyond the independent-particle Fermi Golden Rule (FGR) approximation [with the PBE functional (Elliott et al., 2016; Poli et al., 2016)] is yet to be explored in the literature. To contribute to this knowledge gap, we next investigate the optical properties of the defective NTs-models at different level of theories, analyzing in detail the role of the XC-functional (PBE vs. PBE0-TC-LRC) and optical excitation approach (FGR vs. LR-TDA-TDDFT) for the simulated results.

Figure 8 reports a comparison between the LR-TDA-TDDFT and FGR spectra computed at both PBE0-TC-LRC and PBE level for all the considered defects. We start our analysis from the LR-TDA-TDDFT spectra at PBE0-TC-LRC level that have been computed with that the least aggressive approximations among all the different combinations presented. All the neutral system (pristine NT, D1, D2, h-D3, h-D4, and h-D5) are computed to present a main absorption peak between 6.5 and 7.5 eV. Conversely, for the negatively charged defects (D3, D4, D5), we compute absorbance peaks at lower energy, with D5 presenting a ∼4.5 eV absorption peak. Interestingly, depending on the chemical composition (and charge) of the defect, the computed absorbance peak can be both red-shifted (D1, D2, D3, D4, D5) and blue-shifted (h-D3, h-D4, h-D5) with respect to the defect-free NT's absorbance.

Comparison between the calculated spectra suggests a larger low-energy optical absorbance with respect to the pristine NTs for all the defective structures but D3, whose low-energy absorbance is computed to be strongly suppressed with respect to the defect-free NT (**Tables S5, S11** in the Supporting Information). Thus, the simulations suggest defective NTs sections to absorb more light than defect-free sections. As shown in **Figure 8A**, the calculated absorbance for D1, h-D3, h-D4, h-D5 is 10–20 times

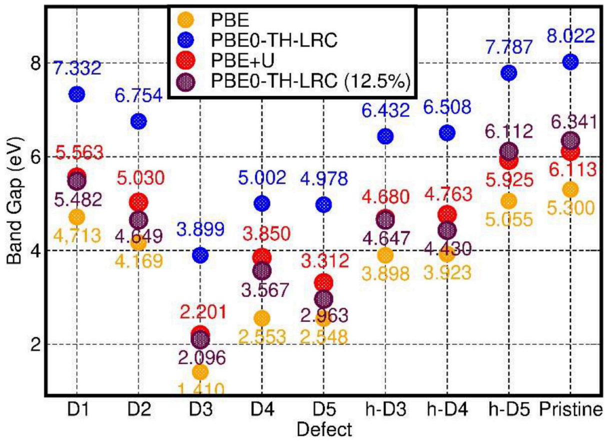

FIGURE 7 | Comparison between the calculated BGs for the considered systems at PBE, PBE0-TH-LRC, PBE+U, and PBE0-TH-LRC (12.5% HF mixing) level.

larger than for the defect-free NTs. Instead, for D2, D5, and D4 the absorbance is twice or comparable to the defect-free NT. Although an immediate connection between the local chemical bonding in the defects and the value of the absorbance cannot be easily drawn, it is interesting to note that protonation of D3, D4, and D5 defects (likely for the defective NTs in water solution at slightly acidic pH as the defect is negatively charged) results in increased optical absorbance. We believe these results motivate further experimental research in the pH-dependence of Imo-NTs's optical properties, an aspect not considered in Shafia et al. (2016) and Shafia et al. (2015).

Before discussing the results of the simulations against published experiments, we recall that as per the NMR study of Yucelen et al. (2012a), up to 16% of Si atoms are involved in a cation vacancy defect and that defects D1 to D5 should be simultaneously present in the NTs. That is, defect-free NTs are not expected to exist, at least for the currently available synthetic routes. We also recall that, experimentally, AlSi NTs start to absorb light at roughly 4.1 eV (300 nm) with a low-energy absorbance shoulder at roughly 5 eV (250 nm) preceding a marked increase in the absorbance for energies larger than 5.5–6.2 eV (225–200 nm) (Shafia et al., 2015).

Based on the computed PBE0-TC-LRC, LR-TDA-TDDFT spectra in **Figure 8A**, it is tempting to tentatively interpret the shape of the experimental spectra in the 300–200 nm (4.1–6.2 eV) region as being due to convolution of the progressively larger absorbance peaks of D5, D4, D2, and D1, with the defect-free NTs contributing -but not dominating- the absorbance around 7 eV. As a direct consequence of the present results, the Tauc-plot derived value of 4.9 eV should likely be re-assigned to a strong defect absorbance (D5), rather than the intrinsic optical-gap of pristine nanotubes (calculated to be a ∼7.0 eV with an approximated –likely underestimated– exciton binding energy of ∼1.1 eV, see below). Given the computed sensitivity to protonation for the absorbance of defects D3 to D5, further experimental research in the dependence of the NTs' UV-vis spectra on the pH conditions would be highly desirable to validate (or confute) the PBE0-TC-LRC, LR-TDA-TDDFT predictions. Recording of spectra below 200 nm would be also highly desirable and strongly contribute to the ongoing work for development of TDDFT strategies to excitons in solids (Gonze et al., 1995; Ghosez et al., 1997; Bernasconi et al., 2011; Tomic et al., 2014; Ullrich and Yang, 2014).

We have also quantified the role of HF mixing (25% as per original PBE0-TC-LRC and 12.5%) for the calculated LR-TD-TDDFT optical properties. To this end, **Figure 9** reports a comparison between the PBE, PBE0-TC-LRC (12.5% HF mixing), and PBE0-TC-LRC (25% HF mixing). In general, reduction of the HF mixing from the original 25–12.5% leads to a decrease of both the energy and intensity of the optical absorption peaks. The relative energy and intensity ranking for the defect considered remains qualitatively unaltered by reduction of the HF mixing. The only exceptions to this trend are the h-D3 and h-D4 systems that, for 12.5% mixing, are not computed to have the 2nd and 3rd largest absorption peak (as for 25% HF mixing). Decrease of HF mixing from 25 to 12.5% is found also to lead to disappearance of a well-defined low-energy shoulder for D1 and D2, indicative of a different energy distribution for the optically active electronic excitations in the system. In spite of the quantitative dependence of the calculated spectra on the HF mixing in the hybrid-DFT approach, the results of this benchmark strengthen our earlier assignment of the experimental low-energy absorption onset [4.1-6.2 eV, (Shafia et al., 2015)] being due to the NMR-inferred defects in the NTs.

We next consider the difference between the calculated PBE0-TC-LRC Kohn-Sham BGs and the lowest energy LR-TDA-TDDFT excitation as a first approximation to the exciton binding energy in the defective NTs. As explained in Ullrich and Yang (2014) (**Figure 2** and related discussion), the approximation stems from (i) the PBE0-TC-LRC BG being used instead of the true *quasi-particle gap*, and (ii) the approximated PBE0-TC-LRC description of the many-body e-h interactions leading to stabilization of the exciton (as measured by the exciton binding energy). Therefore, although encouraged by previous successful applications of unscreened non-local XC-functionals (e.g., B3LYP) with non-local long-range terms in the xc-kernel (f_{xc}) (Bernasconi et al., 2011, 2012; Tomic et al., 2014; Ullrich and Yang, 2014), a note of caution is in place, especially in the absence of many-body benchmark results on defective Imo-NTs' true quasi-particle gap, a quantity not available in the literature and well beyond our computational resources. Moreover, due to the use of real-space cut-off for the exchange integrals in our simulations at PBE0-TC-LRC (Guidon et al., 2009; Strand et al., 2019), the use of a long-range (semi-local) correction may prevent quantitative description of diffuse excitations leading to highly delocalized electron-hole pairs (Gonze et al., 1995; Ghosez et al., 1997; Ullrich and Yang, 2014). In spite of this limitation, the localized nature of the defect occupied states (dominating the low energy optical excitations, vide infra) and the inclusion of exact-exchange to within a 8 Å, should jointly contribute to contain the deficiencies intrinsic to the adopted approach. As noted in the methods section (see also **Figures S1, S2**), the adopted 8 Å cutoff was numerically checked to yield excitation

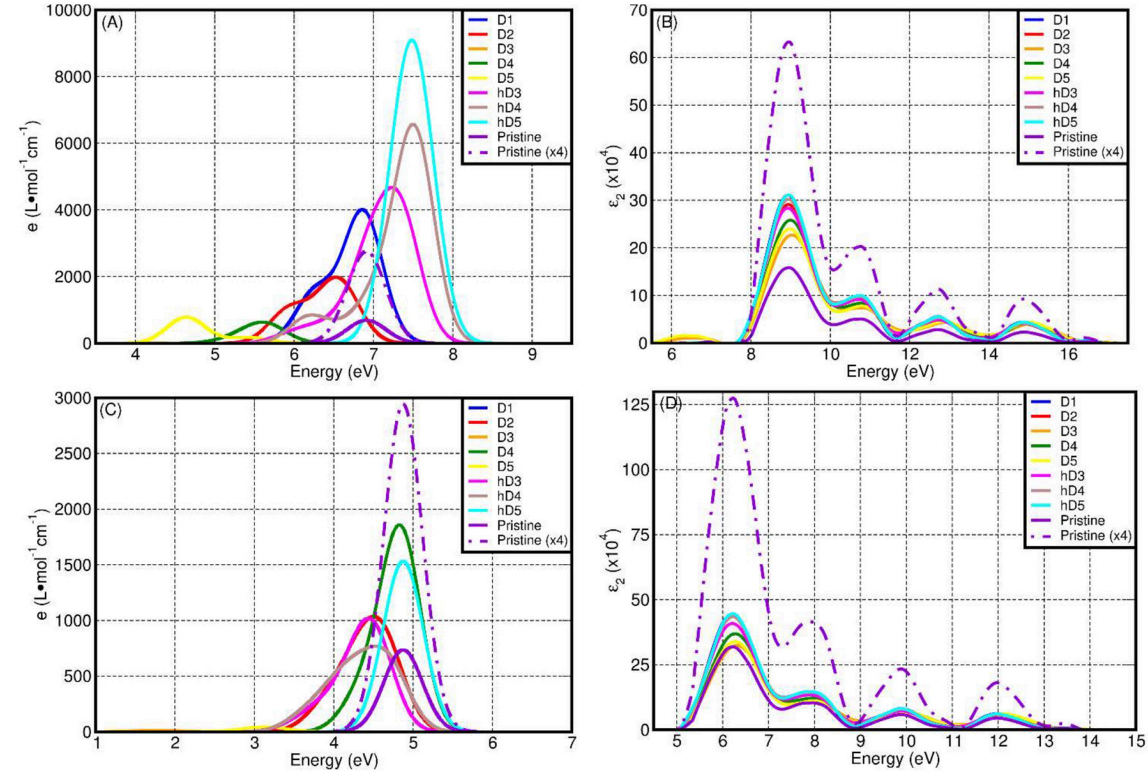

FIGURE 8 | Computed LR-TDA-TDDFT optical spectra at PBE0-TC-LRC **(A)** and PBE **(C)** level of theory for all the systems considered, together with the corresponding FGR spectra, also at PBE0-TH-LRC **(B)** and PBE **(D)** level. Owing to the substantially lower computed absorbance, the D3 traces in **(A,C)** cannot be resolved for the adopted scale of the y-axis.

energies (∼7 eV defect-free NT absorbance-peak included) converged to within 0.05 eV for D1, which, at least to our minds, vouches for a favorable compromise between accuracy and computational viability of the present approach for the system studied.

As shown in **Figure 10**, the computed energies differences (approximated exciton binding energies) are consistently larger than 0.3 eV and can be as large as ∼1.1 eV for the pristine NT and D1. By comparing the results in **Figure 10** with the computed measures of defect-induced structural relaxation (**Figure 2**), it transpires that, at least for the system studied, the exciton binding energy decreases as a function of the defect-induced structural reorganization (D1: ∼1.1 eV, D2: ∼0.9 eV, D3-5, and h-D3-5: < 0.6 eV). Thus, disruption of the cylindrical symmetry for the NT, appears to reduce the excitonic binding energy, at least for the modeled systems in vacuo.

Reduction of the HF mixing from 25 (standard PBE0-TH-LRC) to 12.5% leads to a parallel substantial (up to nearly 400 meV for the pristine NT) decrease in the approximated exciton binding energy for all the cases apart from the negatively charged defects (D3, D4, and D5). For the latter cases, the computed differences in approximated exciton binding energies are smaller than 20 meV. This result in turn suggests a reduced role for non-local interactions (as captured by the HF contribution to the XC-functional) for the low-energy excitations of these systems. As also evident from **Figure 10**, in spite of quantitative differences, use of both 25 and 12.5 % HF mixings consistently leads to smaller (approximated) exciton binding energy for the systems characterized by larger structural relaxation, strengthening the earlier conclusions based on original PBE0-TH-LRC (25% HF mixing) results.

In an attempt to further investigate the nature of the absorbance peaks and low-energy shoulders in **Figure 8**, we next analyse, for each considered case, the five excitations with the largest oscillator strength. **Tables S3–S11** and **Figures S12–S20** in the Supporting Information reveal the presence of at least one secondary excitation with non-negligible oscillator strength for D1, D2, and h-D4. These secondary excitations are, respectively 0.62 eV (D1), 0.87 eV (D2), and 1.34 eV (h-D4) lower in energy with respect to the main peak. In spite of the complex composition of calculated absorbance spectrum, the largest oscillator strength excitations in **Tables S3–S10** and **Figures S12–S19** consistently involve transitions from defect-localized orbitals to delocalized CB orbitals (in general far from the defective part of the NTs). Combined with the substantial reduction (>0.5 eV) in the approximated exciton binding energy for all the NMR-inferred defects but D1 and D2 (**Figure 9**), it is unavoidable to note that altogether these results point to the possibility of defect-mediated exciton-separation in AlSi NTs, with creation of highly-localized oxidative states

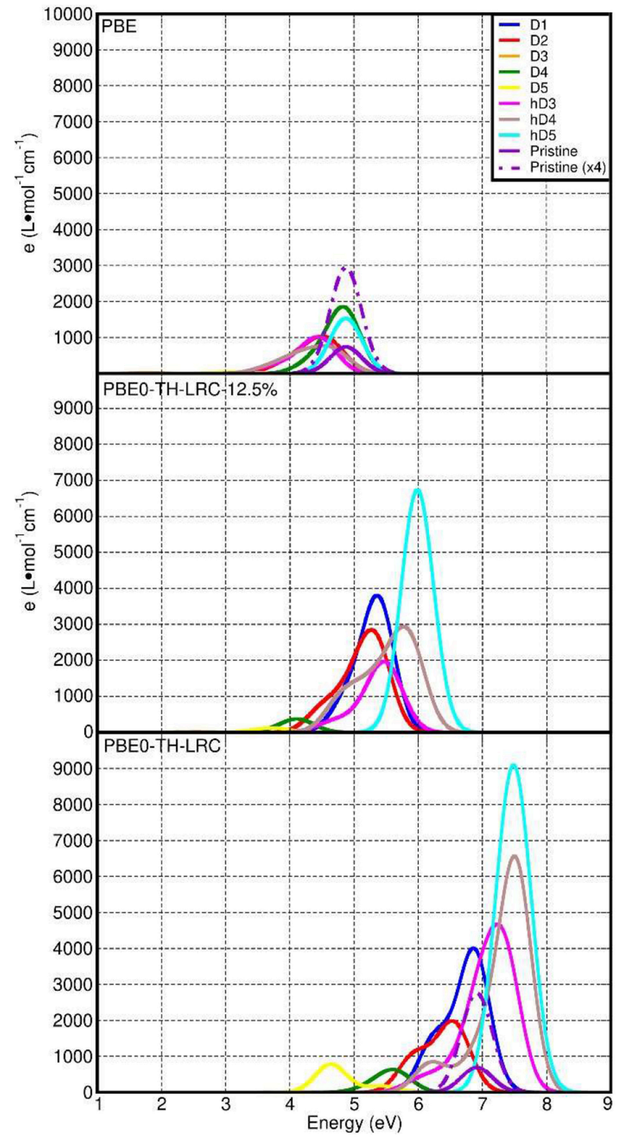

FIGURE 9 | Comparison between the computed LR-TDA-TDDFT optical spectra at PBE **(top)**, PBE0-TH-LRC (12.5% HF mixing, **middle**) and PBE0-TH-LRC (25% HF mixing, **bottom**) level of theory for all the systems considered. The use of the same scale for the x- and y-axis to favor comparison leads to some PBE and PBE0-TH-LRC (12.5% HF mixing) traces being not visible in the plots.

at the defect-sites. Given the ongoing experimental work in development of (UV-light) sustainable photo-catalytic strategies for selective production (oxidation) of high-value chemicals (Sastre et al., 2012a,b; Alarcos et al., 2017; Murcia-López et al., 2017), and the absence of experimental results on the excitonic binding energies in Imo-NTs, these results prompt for interest, further research (and validation opportunities) by the experimental community. The current unavailability of excited state gradients in the used implementation of LR-TDA-TDDFT (Strand et al., 2019), prevents us from further exploring this point by simulation.

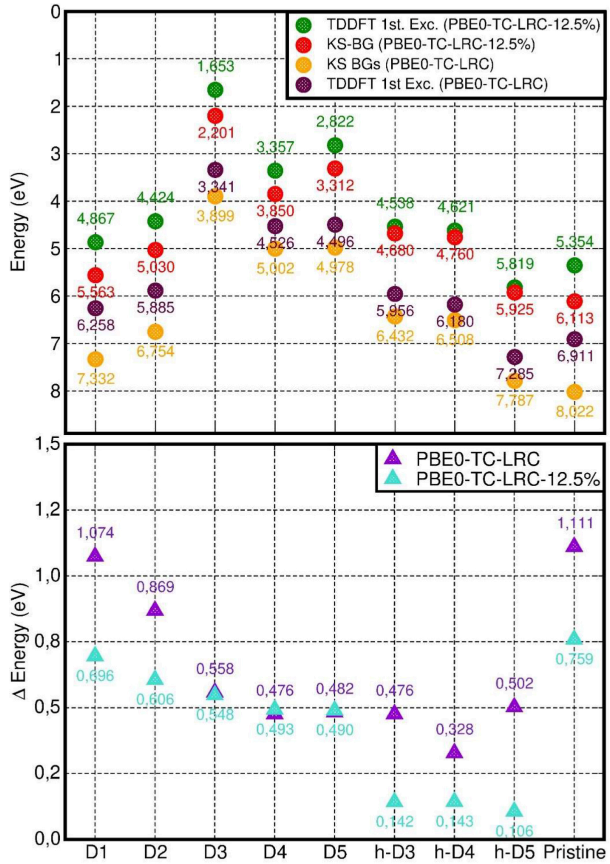

FIGURE 10 | Top: computed PBE0-TC-LRC Kohn-Sham BG and LR-TDA-TDDFT lowest energy excitation energy ("1st Exc"). **Bottom:** difference between the calculated Kohn-Sham BG and LR-TDA-TDDFT 1st excitation energy.

Finally, for the specialist reader we briefly discuss the dependence of the computed spectra on the simulation protocol. We start by considering the role of the xc-functional for the computed LR-TDA-TDDFT spectra. Due to both the BG underestimation (**Figure 7**) and the lack of non-local terms in the xc-kernel (f_{xc}) (Gonze et al., 1995; Ghosez et al., 1997; Bernasconi et al., 2011, 2012; Tomic et al., 2014; Ullrich and Yang, 2014), the PBE LR-TDA-TDDFT spectra (**Figure 8C**) deviates from the PBE0-TC-LRC ones both in terms of computed absorbance values (reduced for PBE) and relative energy of the absorbance peaks. Apart from D5, the absorption peak for all the defects and the pristine NT is now computed between 4.2 and 5 eV. The largest (smallest) absorbance is computed for the D1 and D4 (D3 and D5). That is, at odds with the PBE0-TC-LRC results, protonation is not modeled to increase optical absorbance at PBE-level, in contrast with PBE0-TC-LRC results. **Table S2** in the Supporting Information reports a comparison between the approximated (LR-TDA-TDDFT) exciton binding energies at PBE0-TC-LRC (see also **Figure 10**) and PBE level. Apart from the pristine nanotubes, D1 and D2 the approximated (LR-TDA-TDDFT) exciton binding energies are found not to majorly change depending on the use of the semi-local PBE or non-local PBE0-TC-LRC (the computed changes are smaller than ∼0.1 eV). This results suggest that depending on the structural reorganization of the defects (smaller for D1 and D2, larger for the other defects in **Figure 2**), long-range effects become progressively more screened and less important for the electronic and optical properties of Imo-NTs. The agreement between 25 and 12.5% HF mixing results for D3-D5 in **Figure 10** strengthens this conclusion.

Regardless of the use of PBE0-TC-LRC or PBE, simulation of the spectra at the independent-particle level via the FGR consistently lead to an absorbance maximum at ∼9 (PBE0-TC-LRC) and 6.2 eV (PBE) with qualitatively similar computed spectra. It thus emerges that, regardless of the XC-functional used, application of the FGR prevents the eventual use of the computed absorbance spectra to distinguish between defects and pristine NTs. Accordingly, and not unexpectedly, it transpires that use of the LR-TDA-TDDFT approximation at PBE0-TC-LRC level appears to offer the most favorable accuracy-viability compromise for the study of the optical properties of point-defects in Imo-NTs, at least out of the simulation protocols explored. Given the availability of experimental spectra for Fe-doped aluminosilicate NTs (Shafia et al., 2015, 2016) future work will investigate the performance of the present PBE0-TC-LRC, LR-TDA-TDDFT approach on these systems to sustain research both in the Imo-NTs area and simulation of optical properties in (1D) solids.

CONCLUSIONS

Simulation of the five NMR-inferred defect structures (D1 to D5) for AlSi NTs (Yucelen et al., 2012a) and their protonated counterparts (h-D3 to h-D5) indicates that:

i) The presence of defects induces local deformations in the NT structure that can be suitably simulated in models based on a x3 repeat unit of the NTs. The defect-induced deformations affect primarily the outer Al-O(H) octahedrons and the external O-H hydrogen-bonding network.
ii) All the considered defects leads to the appearance of occupied shallow or deep defect-states highly-localized at the defect-site. The energy-position of these states is computed to be strongly sensitive to protonation of the defect site.
iii) Owing to the absence of dangling bonds in the considered systems, the occurrence of defect-induced shallow or deep sates is found to be rather insensitive to the use of the PBE, PBE+U = 7 eV, PBE-TC-LRC (25% HF mixing) or BE-TC-LRC (12.5 HF mixing).
iv) With the exception of D3, the low-energy optical absorbance of the defects is generally substantially (x2-x20) larger than for defect-free NTs. Protonation of the defect sites leads to increase of the optical absorbance.
v) Based on the calculated PBE0-TC-LRC, LR-TDA-TDDFT spectra, the experimental low energy (4.1–6.2 eV) absorbance tail for AlSi NTs can be interpreted as due to the convolution of the optical absorbance of the NMR-inferred defects.
vi) The differences between the calculated PBE0-TC-LRC Kohn-Sham BGs and the lowest energy LR-TDA-TDDFT excitation, a first approximate measure of the exciton binding energies, are found to be systematically reduced from 1.1 (defect-free NT) to <0.5 eV at the defect sites.

Based on the current lack of experimental results on the electronic and optical properties of defects in imogolite NTs, we believe the present results will be a positive complement to research in the field.

AUTHOR CONTRIBUTIONS

EP executed the simulations and analyzed the results in collaboration with JE, MW, and GT. SC and MW implemented and tested the used TDDFT formalism in CP2K. EP and GT wrote the initial draft of the manuscript. All the authors contributed to the final version of the manuscript.

ACKNOWLEDGMENTS

EP, JE, and GT acknowledge support from EPSRC UK (EP/I004483/1, EP/K013610/1, EP/P022189/1, and EP/P020194/1). EP acknowledges support from CINECA (ICT-CMSP-2018). Via membership of the UK's HEC Materials Chemistry Consortium (EP/L000202) and UKCP Consortium (EP/K013610/1 and EP/P022189/1), this work made use also of the ARCHER UK and UK Materials and Molecular Modeling Hub (EP/P020194/1) High-Performance Computing facilities. MW and SC acknowledge support from EPSRC UK (EP/P022235/1) and an ARCHER eCSE (eCSE03-11).

SUPPLEMENTARY MATERIAL

The Supplementary Material for this article can be found online at: https://www.frontiersin.org/articles/10.3389/fchem.2019.00210/full#supplementary-material

REFERENCES

Alarcos, N., Cohen, B., Ziółek, M., and Douhal, A. (2017). Photochemistry and photophysics in silica-based materials: ultrafast and single molecule spectroscopy observation. *Chem. Rev.* 117, 13639–13720. doi: 10.1021/acs.chemrev.7b00422

Amara, M. S., Paineau, E., Rouzière, S., Guiose, B., Krapf, M. E. M., Tache, O., et al. (2015). Hybrid, tunable-diameter, metal oxide nanotubes for trapping of organic molecules. *Chem. Mater*. 27, 1488–1494. doi: 10.1021/cm503428q

Arancibia-Miranda, N., Escudey, M., Pizarro, C., Denardin, J. C., García-González, M. T., Fabris, J. D., et al. (2014). Preparation and characterization of a single-walled aluminosilicate nanotube-iron oxide composite: its applications to removal of aqueous arsenate. *Mater. Res. Bull.* 51, 145–152. doi: 10.1016/j.materresbull.2013.12.014

Avellan, A., Levard, C., Kumar, N., Rose, J., Olivi, L., Masion, A., et al. (2014). Structural incorporation of iron into Ge–imogolite nanotubes: a promising step for innovative nanomaterials. *RSC Adv.* 4, 49827–49830. doi: 10.1039/C4RA08840A

Baltrusaitis, J., Jansen, I., and Schuttlefield Christus, J. D. (2014). Renewable energy based catalytic CH4 conversion to fuels. *Catal. Sci. Technol.* 4:2397. doi: 10.1039/c4cy00294f

Barrer, R. M. (1982). *Hydrothermal Chemistry of Zeolites*. New York, NY: Academic Press.

Barron, P. F., Wilson, M. A., Campbell, A. S., and Frost, R. L. (1982). Detection of imogolite in soils using solid-state ^{29} Si NMR. *Nature* 299, 616–618. doi: 10.1038/299616a0

Bernasconi, L., Tomic, S., Ferrero, M., Rérat, M., Orlando, R., Dovesi, R., et al. (2011). First-principles optical response of semiconductors and oxide materials. *Phys. Rev. B* 83:195325. doi: 10.1103/PhysRevB.83.195325

Bernasconi, L., Webster, R., Tomic, S., and Harrison, N. M. (2012). Optical response of extended systems from time-dependent Hartree-Fock and time-dependent density-functional theory. *J. Phys.* 367:012001. doi: 10.1088/1742-6596/367/1/012001

Bonelli, B., Armandi, M., and Garrone, E. (2013). Surface properties of alumino-silicate single-walled nanotubes of the imogolite type. *Phys. Chem. Chem. Phys.* 15:13381. doi: 10.1039/c3cp51508g

Bottero, I., Bonelli, B., Ashbrook, S. E., Wright, P. A., Zhou, W., Tagliabue, M., et al. (2011). Synthesis and characterization of hybrid organic/inorganic nanotubes of the imogolite type and their behaviour towards methane adsorption. *Phys. Chem. Chem. Phys.* 13, 744–750. doi: 10.1039/C0CP00438C

Casey, W. H. (2006). Large aqueous aluminum hydroxide molecules. *Chem. Rev.* 106, 1–16. doi: 10.1021/cr040095d

Casida, M. E. (2009). Time-dependent density-functional theory for molecules and molecular solids. *J. Mol. Struct.* 914, 3–18. doi: 10.1016/j.theochem.2009.08.018

Casida, M. E., and Huix-Rotllant, M. (2016). Progress in Time-dependent density-functional theory. *Ann. Rev. Phys. Chem.* 63, 287–323. doi: 10.1146/annurev-physchem-032511-143803

Castro, C., Arancibia-Miranda, N.,Acuña-Rougier, C., Escudey, M., and Tasca, F. (2016). Spectroscopic and electrochemical studies of imogolite and fe-modified imogolite nanotubes. *Nanomaterials* 6:E28. doi: 10.3390/nano6020028

Cradwick, P. D., Wada, K., Russell, J. D., Yoshinaga, N., Masson, C. R., and Farmer, V. C. (1972). Imogolite, a hydrated aluminium silicate of tubular structure. *Nat. Phys. Sci.* 240, 187–189. doi: 10.1038/physci240187a0

de Richter, R. K., Ming, S., and Caillol, S. (2013). Fighting global warming by photocatalytic reduction of CO2 using giant photocatalytic reactors. *Renew. Sust. Energy Rev.* 19, 82–106. doi: 10.1016/j.rser.2012.10.026

Dietl, N., Schlangen, M., and Schwarz, H. (2012). Thermal hydrogen-atom transfer from methane: the role of radicals and spin states in oxo-cluster chemistry. *Angew. Chem. Int. Ed.* 51, 5544–5555. doi: 10.1002/anie.201108363

Elliott, J. D., Poli, E., Scivetti, I., Ratcliff, L. E., Andrinopoulos, L., Dziedzic, J., et al. (2016). Chemically selective alternatives to photoferroelectrics for polarization-enhanced photocatalysis: the untapped potential of hybrid inorganic nanotubes. *Adv. Sci.* 4:1600153. doi: 10.1002/advs.201600153

Ernzerhof, M., and Perdew, J. P. (1998). Generalized gradient approximation to the angle- and system-averaged exchange hole. *J. Chem. Phys.* 109:3313. doi: 10.1063/1.476928

Fresno, F., Portela, R., Suárez, S., and Coronado, J. M. (2014). Photocatalytic materials: recent achievements and near future trends. *J. Mater. Chem. A* 2:2863. doi: 10.1039/c3ta13793g

Fujishima, A., Zhang, X., and Tryk, D. A. (2008). TiO_2 photocatalysis and related surface phenomena. *Surf. Sci. Rep.* 63, 515–582. doi: 10.1016/j.surfrep.2008.10.001

Ganduglia-Pirovano, M. V., Hofmann, A., and Sauer, J. (2007). Oxygen vacancies in transition metal and rare earth oxides: Current state of understanding and remaining challenges. *Surface Science Reports.* 62, 219–270. doi: 10.1016/j.surfrep.2007.03.002

Ghosez, P., Gonze, X., and Godby, R. W. (1997). Long-wavelength behavior of the exchange-correlation kernel in the Kohn-Sham theory of periodic systems. *Phys. Rev. B* 56:1281. doi: 10.1103/PhysRevB.56.12811

Goedecker, S., Teter, M., and Hutter, J. (1996). Separable dual-space Gaussian pseudopotentials. *Phys. Rev. B* 54, 1703–1710. doi: 10.1103/PhysRevB.54.1703

Gonze, X., Ghosez, P., Godby, R. W. (1995). Density-polarization functional theory of the response of a periodic insulating solid to an electric field. *Phys. Rev. Lett.* 74, 4035–4038. doi: 10.1103/PhysRevLett.74.4035

Gonze, X., Stumpf, R., and Scheffler, M. (1991). Analysis of separable potentials. *Phys. Rev. B* 44, 8503–8513. doi: 10.1103/PhysRevB.44.8503

Guidon, M., Hutter, J., and VandeVondele, J. (2009). Robust periodic hartree–fock exchange for large-scale simulations using gaussian basis sets. *J. Chem. Theory Comput.* 5, 3010–3021. doi: 10.1021/ct900494g

Guidon, M., Hutter, J., and VandeVondele, J. (2010). Auxiliary density matrix methods for Hartree–Fock exchange calculations. *J. Chem. Theory Comput.* 6, 2348–2364. doi: 10.1021/ct1002225

Habisreutinger, S. N., Schmidt-Mende, L., and Stolarczyk, J. K. (2013). Photocatalytic reduction of CO2 on TiO2 and other semiconductors. *Angew. Chem. Int. Ed.* 52, 7372–7408. doi: 10.1002/anie.201207199

Haynes, P. D., Skylaris, C. K., Mostofi, A. A., and Payne, M. C. (2006). ONETEP: linear-scaling density-functional theory with local orbitals and plane waves. *Phys. Status Solidi B* 243, 2489–2499. doi: 10.1002/pssb.200541457

Hine, N. D. M., Haynes, P. D., Mostofi, A. A., Skylaris, C. K., and Payne, M. C. (2009). Linear-scaling density-functional theory with tens of thousands of atoms: expanding the scope and scale of calculations with ONETEP. *Comput. Phys.* Commun. 180, 1041–1053. doi: 10.1016/j.cpc.2008.12.023

Hine, N. D. M., Robinson, M., Haynes, P. D., Skylaris, C. K., Payne, M. C., and Mostofi, A. A. (2011). Accurate ionic forces and geometry optimization in linear-scaling density-functional theory with local orbitals. *Phys. Rev. B* 83:195102. doi: 10.1103/PhysRevB.83.195102

Hirata, S., and Head-Gordon, M. (1999). Time-dependent density functional theory within the Tamm–Dancoff approximation. *Chem. Phys. Lett.* 314, 291–299. doi: 10.1016/S0009-2614(99)01149-5

Ismail, A. A., and Bahnemann, W. (2014). Photochemical splitting of water for hydrogen production by photocatalysis: a review. *Sol. Energy Mater. Sol. C* 128, 85–101. doi: 10.1016/j.solmat.2014.04.037

Kamat, P. V. (2007). Meeting the clean energy demand: nanostructure architectures for solar energy conversion. *J. Phys. Chem. C* 111, 2834–2860. doi: 10.1021/jp066952u

Kang, D. Y., Brunelli, N. A., Yucelen, G. I., Venkatasubramanian, A., Zang, J., Leisen, J., et al. (2014). Direct synthesis of single-walled aminoaluminosilicate nanotubes with enhanced molecular adsorption selectivity. *Nat. Commun.* 5:3342. doi: 10.1038/ncomms4342

Kang, D. Y., Zang, J., Jones, C. W., and Nair, S. (2011). Single-walled aluminosilicate nanotubes with organic-modified interiors. *J. Phys. Chem. C* 115, 7676–7685. doi: 10.1021/jp2010919

Kang, D. Y., Zang, J., Wright, E. R., McCanna, A. L., Jones, C. W., and Nair, S. (2010). Dehydration, dehydroxylation, and rehydroxylation of single-walled aluminosilicate nanotubes. *ACS Nano* 4, 4897–4907. doi: 10.1021/nn101211y

Katsumata, K., Hou, X., Sakai, M., Nakajima, A., Fujishima, A., Okada, K., et al. (2013). Visible-light-driven photodegradation of acetaldehyde gas catalyzed by aluminosilicate nanotubes and Cu(II)-grafted TiO2 composites. *Appl. Catal. B* 138, 243–252. doi: 10.1016/j.apcatb.2013.03.004

Lany, S., and Zunger, A. (2008). Assessment of correction methods for the band-gap problem and for finite-size effects in supercell defect calculations: case studies for ZnO and GaAs. *Phys. Rev. B.* 78:235104. doi: 10.1103/PhysRevB.78.235104

Levard, C., Rose, J., Masion, A., Doelsch, E., Borschneck, D., and Olivi, L. (2008). Synthesis of large quantities of single-walled aluminogermanate nanotube. *J. Am. Chem. Soc.* 130, 5862–5863. doi: 10.1021/ja801045a

Levard, C., Rose, J., Thill, A., Masion, A., Doelsch, E., Bottero, J. Y., et al. (2010). Formation and growth mechanisms of imogolite-like aluminogermanate nanotubes. *Chem. Mater.* 22, 2466–2473. doi: 10.1021/cm902883p

Liou, K. H., and Kang, D. Y. (2016). Defective single-walled aluminosilicate nanotubes: structural stability and mechanical properties. *ChemNanoMat* 2, 189–195. doi: 10.1002/cnma.201500185

Ma, W., Yah, W. O., Otsuka, H., and Takahara, A. (2012). Application of imogolite clay nanotubes in organic–inorganic nanohybrid materials. *J. Mater. Chem.* 22, 11887–11892. doi: 10.1039/c2jm31570j

Maeda, K. (2013). Z-scheme water splitting using two different semiconductor photo-catalysts. *ACS Catal.* 3, 1486–1503. doi: 10.1021/cs4002089

Mao, F., Gao, C. Z., Wang, F., Zhang, C., and Zhang, F. S. (2017). Ab initio study of ferromagnetism induced by electronic hole localization in Al-doped -SiO2. *J. Phys. Chem. C* 121:23055. doi: 10.1021/acs.jpcc.7b06680

Marzan, L. L., and Philipse, A. P. (1994). Synthesis of platinum nanoparticles in aqueous host dispersions of inorganic (imogolite) rods. *Colloid Surf. A* 90, 95–109. doi: 10.1016/0927-7757(94)02888-5

Monet, G., Amara, M. S., Rouzière, S., Paineau, E., Chai, Z., Elliott, J. D., et al. (2018). Structural resolution of inorganic nanotubes with complex stoichiometry. *Nat. Commun.* 9:2033. doi: 10.1038/s41467-018-04360-z

Motta, C., Giantomassi, M., Cazzaniga, M., Gal-Nagy, K., and Gonze, X. (2010). Implementation of techniques for computing optical properties in 0–3 dimensions, including a real-space cutoff, in ABINIT. *Comput. Mater. Sci.* 50, 698–703. doi: 10.1016/j.commatsci.2010.09.036

Mukherjee, S., Bartlow, V. M., and Nair, S. (2005). Phenomenology of the growth of single-walled aluminosilicate and aluminogermanate nanotubes of precise dimensions. *Chem. Mater*. 17, 4900–4909. doi: 10.1021/cm0505852

Mukherjee, S., Kim, K., and Nair, S. (2007). Short, highly ordered, single-walled mixed-oxide nanotubes assemble from amorphous nanoparticles. *J. Am. Chem. Soc*. 129, 6820–6826. doi: 10.1021/ja070124c

Murcia-López, S., Bacariza, M. C., Villa, K., Lopes, J. M., Henriques, C., Morante, J. R., et al. (2017). Controlled photocatalytic oxidation of methane to methanol through surface modification of beta zeolites. *ACS Catal.* 7:2878. doi: 10.1021/acscatal.6b03535

Navalón, S., Dhakshinamoorthy, A., Alvaro, M., and Garcia, H. (2013). Photocatalytic CO(2) reduction using non-titanium metal oxides and sulfides. *ChemSusChem* 6, 562–577. doi: 10.1002/cssc.201200670

Neugebauer, J., Kresse, G., Janotti, A., and Van de Walle, C. G. (2014). First-principles calculations for point defects in solids. *Rev. Mod. Phys.* 86:253. doi: 10.1103/RevModPhys.86.253

Nolan, M., and Watson, G. W. (2006). Hole localization in Al doped silica: A DFT+U description. *J. Chem. Phys.* 125:144701. doi: 10.1063/1.2354468

Novatski, A., Steimacher, A., Medina, A. N., Bento, A. C., and Baesso, M. L., Boulon, G. et al. (2008). Relations among non-bridging oxygen, optical properties, optical basicity, and colour centre formation in CaO–MgO aluminosilicate glasses. *J. Appl. Phys.* 104:094910. doi: 10.1063/1.3010306

Onida, G., Reining, L., and Rubio, A. (2002). Electronic excitations: density-functional versus many-body Green's-function approaches. *Rev. Mod. Phys*. 74, 601–659. doi: 10.1103/RevModPhys.74.601

Paineau, E. (2018). Imogolite nanotubes: a flexible nanoplatform with multipurpose applications. *Appl. Sci*. 8:1921. doi: 10.3390/app8101921

Pelaez, M., Nolan, N. T., and Pillai, S. C. (2012). A review on the visible light active titanium dioxide photocatalysts for environmental applications. *Appl. Catal. B* 125, 331–349. doi: 10.1016/j.apcatb.2012.05.036

Perdew, J. P., Burke, K., and Ernzerhof, M. (1996). Generalized gradient approximation made simple. *Phys. Rev. Lett*. 77, 3865–3868. doi: 10.1103/PhysRevLett.77.3865

Pfrommer, B. G., Côté, M., Louie, S. G., and Cohen, M. L. (1997). Relaxation of crystals with the Quasi-Newton method. *J. Comput. Phys*. 131, 233–240. doi: 10.1006/jcph.1996.5612

Poli, E., Elliott, J., Hine, N. D. M., Mostofi, A., Teobaldi, G. (2015). Large-scale density functional theory simulation of inorganic nanotubes: a case study on Imogolite nanotubes. *Mater. Res. Innov*. 19:S272–S282. doi: 10.1179/1432891715Z.0000000001560

Poli, E., Elliott, J. D., Ratcliff, L. E., Andrinopoulos, L., Dziedzic, J., Hine, N. D., et al. (2016). The potential of imogolite nanotubes as (co-)photocatalysts: a linear-scaling density functional theory study. *J. Phys. Condens. Matter* 28:074003. doi: 10.1088/0953-8984/28/7/074003

Read, A. J., and Needs, R. J. (1991). Calculation of optical matrix elements with nonlocal pseudopotentials. *Phys. Rev. B* 44, 13071–13073. doi: 10.1103/PhysRevB.44.13071

Sastre, F., Corma, A., and García, H. (2012a). 185 nm photoreduction of CO2 to methane by water. Influence of the presence of a basic catalyst. *J. Am. Chem. Soc*. 134, 14137–14141. doi: 10.1021/ja304930t

Sastre, F., Corma, A., and García, H. (2012b). Deep UV photocatalytic activation of ethane on silica surfaces. *Appl. Catal. B* 128, 84–90. doi: 10.1016/j.apcatb.2012.09.046

Sastre, F., Fornés, V., Corma, A., and García, H. (2011). Selective, room-temperature transformation of methane to C1 oxygenates by deep UV photolysis over zeolites. *J. Am. Chem. Soc*. 133, 17257–17261. doi: 10.1021/ja204559z

Sastre, F., Fornés, V., Corma, A., and García, H. (2012c). Conversion of methane into C1 oxygenates by deep-UV photolysis on solid surfaces: influence of the nature of the solid and optimization of photolysis conditions. *Chem. Eur. J*. 18, 1820–1825. doi: 10.1002/chem.201102273

Shafia, E., Esposito, S., Armandi, M., Manzoli, M., Garrone, E., and Bonelli, B. (2016). Isomorphic substitution of aluminium by iron into single-walled alumino-silicate nanotubes: a physico-chemical insight into the structural and adsorption properties of Fe-doped imogolite, microporous and mesoporous. *Materials* 224, 229–238. doi: 10.1016/j.micromeso.2015.11.044

Shafia, E., Esposito, S., Manzoli, M., Chiesa, M., Tiberto, P., Bonelli, B., et al. (2015). Al/Fe isomorphic substitution versus Fe_2O_3 clusters formation in Fe-doped aluminosilicate nanotubes (imogolite). *J. Nanopart. Res*. 17:336. doi: 10.1007/s11051-015-3130-2

Shluger, A. L., Foster, A. S., Gavartin, J. L., and Sushko, P. V. (2003). "Models of defects in wide-gap oxides: Perspective and challenges". In *Nano and Giga Challenges in Microelectronics*, eds J. Greer, Korkin, and J. Labanowski (Amsterdam: Elsevier), 151–222. doi: 10.1016/B978-044451494-3/50005-6

Skylaris, C. K., Haynes, P. D., Mostofi, A. A., and Payne, M. C. (2005). Introducing ONETEP: linear-scaling density functional simulations on parallel computers. *J. Chem. Phys*. 122:84119. doi: 10.1063/1.1839852

Strand, J., Chulkov, S. K., Watkins, M. B., and Shluger, A. L. (2019). First principles calculations of optical properties for oxygen vacancies in binary metal oxides. *J. Chem. Phys*. 150:044702. doi: 10.1063/1.5078682

Tandia, A., Timofeev, N. T., Mauro, J. C., and Vargheese, K. D. (2011). Defect-mediated self-diffusion in calcium aluminosilicate glasses: a molecular modeling study. *J. Non-Crystalline Solids*. 357, 1780–1786. doi: 10.1016/j.jnoncrysol.2010.12.078

Teobaldi, G., Beglitis, N. S., Fisher, A. J., Zerbetto, F.,Hofer, W. A. (2009). Hydroxyl vacancies in single-walled aluminosilicate and aluminogermanate nanotubes. *J. Phys. Condens. Matter* 21:195301. doi: 10.1088/0953-8984/21/19/195301

Theng, B. K. G., Russell, M., Churchman, G. J. , and Parfitt, R. L. (1982). Surface properties of allophane, halloysite, and imogolite. *Clays Clay Miner*. 30, 143–149. doi: 10.1346/CCMN.1982.0300209

Tomic, S., Bernasconi, L., Searle, B. G., and Harrison, N. M. (2014). Electronic and optical structure of wurtzite CuInS2. *J. Phys. Chem. C* 118, 14478–14484. doi: 10.1021/jp411213d

Ullrich, C. A., and Yang, Z. (2014). "Excitons in time-dependent density-functional theory," in *Density-Functional Methods for Excited States. Topics in Current Chemistry*, Vol 368, eds N. Ferré, M. Filatov, M. Huix-Rotllant (Cham: Springer), 185–217.

VandeVondele, J., and Hutter, J. (2007). Gaussian basis sets for accurate calculations on molecular systems in gas and condensed phases. *J. Chem. Phys*. 127:114105. doi: 10.1063/1.2770708

VandeVondele, J., Krack, M., Mohamed, F., Parrinello, M., Chassaing, T., and Hutter, J. (2005). Quickstep: Fast and accurate density functional calculations using a mixed Gaussian and plane waves approach. *Comput. Phys. Commun.* 167, 103–128. doi: 10.1016/j.cpc.2004.12.014

Wada, S.-I., Eto, A., and Wada, K. (1979). Synthetic allophane and imogolite. *J. Soil Sci.* 30, 347–355. doi: 10.1111/j.1365-2389.1979.tb00991.x

Walsh, A., Zunger, A. (2017). Instilling defect tolerance in new compounds. *Nature Mat.*16, 964–967. doi: 10.1038/nmat4973

Yin, W. J., Wen, B., Zhou, C., Selloni, A., and Liu, L. M. (2018). Excess electrons in reduced rutile and anatase TiO2. *Surf. Sci. Rep*. 73, 58–82. doi: 10.1016/j.surfrep.2018.02.003

Yucelen, G. I., Choudhury, R. P., Leisen, J., Nair, S., and Beckham, H. W. (2012a). Defect structures in aluminosilicate single-walled nanotubes: a solid-state nuclear magnetic resonance investigation. *J. Phys. Chem. C*. 116, 17149–17157. doi: 10.1021/jp3059728

Yucelen, G. I., Choudhury, R. P., Vyalikh, A., Scheler, U., Beckham, H. W., and Nair, S. (2011). Formation of single-walled aluminosilicate nanotubes from molecular precursors and curved nanoscale intermediates. *J. Am. Chem. Soc.* 133, 5397–5412. doi: 10.1021/ja111055q

Yucelen, G. I., Kang, D. Y., Guerrero-Ferreira, R. C., Wright, E. R., Beckham, H. W., and Nair, S. (2012b). Shaping single-walled metal oxide nanotubes from precursors of controlled curvature. *Nano. Lett.* 12, 827–832. doi: 10.1021/nl203880z

Zanzottera, C., Armandi, M., Esposito, S., Gorrone, E., and Bonelli, B. (2012a). Physico-chemical properties of imogolite nanotubes functionalized on both external and internal surfaces. *J. Phys. Chem. C* 116:20417. doi: 10.1021/jp3061637

Zanzottera, C., Vicente, A., Celasco, E., Fernandez, C., Garrone, E., and Bonelli, B. (2012b). Physico-chemical properties of imogolite nanotubes functionalized on both external and internal surfaces. *J. Phys. Chem. C* 116, 7499–7506. doi: 10.1021/jp301177q

Zhao, M., Xia, Y., and Mei, L. (2009). Energetic minimum structures of imogolite nanotubes: a first-principles prediction. *Phys. Chem. C* 113, 14834–14837. doi: 10.1021/jp9056169

Conflict of Interest Statement: The authors declare that the research was conducted in the absence of any commercial or financial relationships that could be construed as a potential conflict of interest.

frontiers in Physics

ORIGINAL RESEARCH
published: 29 March 2019
doi: 10.3389/fphy.2019.00043

Mechanisms of Oxygen Vacancy Aggregation in SiO_2 and HfO_2

David Z. Gao [1,2,3], Jack Strand [1]*, Manveer S. Munde [1,4] and Alexander L. Shluger [1]

[1] Department of Physics and Astronomy, University College London, London, United Kingdom, [2] Nanolayers Research Computing LTD., London, United Kingdom, [3] Department of Physics, Norwegian University of Science and Technology, Trondheim, Norway, [4] Materials Science Center, Faculty of Physics, Philipps University Marburg, Marburg, Germany

Dielectric oxide films in electronic devices undergo significant structural changes during device operation under bias. These changes are usually attributed to aggregation of oxygen vacancies resulting in formation of oxygen depleted regions and conductive filaments. However, neutral oxygen vacancies have high diffusion barriers in ionic oxides and their interaction and propensity for aggregation are still poorly understood. In this paper we briefly review the existing data on static configurations of neutral dimers and trimers of oxygen vacancies in technologically relevant SiO_2 and HfO_2 and then provide new results on the structure and properties of these defects in amorphous SiO_2 and HfO_2. These results demonstrate weak interaction between neutral O vacancies, which does not explain their quick aggregation. We propose that trapping of electrons, injected from an electrode, by the vacancies may result in creation of new neutral vacancies in the vicinity of pre-existing vacancies. We describe this mechanism in a-SiO_2 and demonstrate that this process becomes more efficient as the vacancy clusters grow larger.

Keywords: dielectric oxides, oxygen vacancies, Density Functional Theory, SiO_2, HfO_2

Edited by:
Maria Veronica Ganduglia-Pirovano, Instituto de Catálisis y Petroleoqumica (ICP), Spain

Reviewed by:
Cesare Franchini, University of Vienna, Austria
Alejandro Strachan, Purdue University, United States

***Correspondence:**
Jack Strand
jack.strand.14@ucl.ac.uk

Specialty section:
This article was submitted to Physical Chemistry and Chemical Physics, a section of the journal Frontiers in Physics

Received: *16 November 2018*
Accepted: *07 March 2019*
Published: *29 March 2019*

Citation:
Gao DZ, Strand J, Munde MS and Shluger AL (2019) Mechanisms of Oxygen Vacancy Aggregation in SiO_2 and HfO_2. Front. Phys. 7:43. doi: 10.3389/fphy.2019.00043

1. INTRODUCTION

Crystalline and amorphous SiO_2 and HfO_2 are important materials for microelectronics as dielectric layers in transistors and memory cells, fiber optics, mirror coatings, resistive random access memory (ReRAM), and neuromorphic cells (see [1–3]). Under an applied stress bias, field-effect transistors (FETs) experience a gradual increase in gate leakage, noise signal, threshold voltage shift, decrease of trans-conductance, and other degradation effects, which are accelerated by strong bias and may lead to dielectric breakdown [1, 4]. These effects have generally been attributed to defect generation and aggregation in oxide layers [1, 4, 5]. The creation of new defects is associated with structural changes in the oxide and requires significant energy [1, 6, 7]. In particular, the aggregation of oxygen vacancies as a result of electrically stressing sub-stoichiometric amorphous SiO_x ($x = 1.32$) films is thought to facilitate the dielectric breakdown of complementary metal-oxide-semiconductor (CMOS) devices [8–10] and electroforming in resistive random access memory cells [3, 11, 12]. However, the fundamental atomistic mechanisms behind these processes are still poorly understood. Both the creation of additional oxygen vacancies and the interaction of diffusing vacancies have been proposed as mechanisms for vacancy aggregation.

Clustering of O vacancies is known to occur in the bulk and at surfaces of *reducible* oxides, such as e.g., TiO_2 [13, 14], CeO_2 [15, 16], and $SrTiO_3$ [17]. It is much less understood in *nonreducible* wide band gap oxides, such as MgO, SiO_2, and HfO_2. The formation of pairs of O vacancies has been suggested in heavily thermochemically reduced MgO [18]. Recent simulations [19, 20] have shed some light on the formation of O-vacancy clusters in SiO_2 and HfO_2. Computational modeling was used to investigate the structures and binding energies of vacancy dimers and trimers in amorphous (a)-SiO_2, the energy barriers for the diffusion of individual vacancies, and whether this diffusion can be stimulated by trapping of injected electrons at vacancies [19]. The calculations of di- and tri-vacancy clusters demonstrate that there are favorable sites for vacancy aggregation in a-SiO_2 with maximum binding energies of approximately 0.13 and 0.18 eV, respectively. However, an average neutral vacancy diffusion barrier was calculated to be 4.6 eV [19], rendering the clustering of randomly distributed neutral vacancies via diffusion unfeasible.

The calculations performed in Bradley et al. [20] demonstrate that the formation of neutral oxygen vacancy dimers, trimers and tetramers in monoclinic HfO_2 is accompanied by an energy gain with respect to the separated vacancies, which depends on the size and shape of the aggregate. In the most strongly bound configurations, vacancies are unscreened by Hf cations and form voids within the crystal, with the larger aggregates having larger energy gain per vacancy (0.11–0.18 eV). The negatively charged di-vacancy was found to have similar binding energies to the neutral one, while the positively charged di-vacancy was found to be unstable. Thus, the aggregation process of either neutral or negatively charged oxygen vacancies in m-HfO_2 is energetically feasible. However, the energy barrier for the diffusion of neutral O vacancies is about 2.4 eV [21], again suggesting that aggregation of vacancies via diffusion processes is too slow to explain e.g., electroforming in HfO_2 films.

The realization that the formation of oxygen vacancy clusters in a-SiO_2 and m-HfO_2 via thermally activated diffusion is inefficient implies that an alternative mechanism should be responsible for the aggregation of oxygen vacancies under electrical stress. In particular, O-vacancy aggregation could result from *creation* of new vacancies near the pre-existing vacancies. To achieve that, an O atom should be displaced from its lattice position to an interstitial site, creating an O-vacancy at the original site and an interstitial O ion, i.e., a Frenkel defect pair.

To put this mechanism in the context of previous studies, we briefly review the structure and characteristics of vacancy dimers and trimers in a-SiO_2 and crystalline and a-HfO_2. We then discuss the mechanisms of Frenkel defect creation in SiO_2 and HfO_2 facilitated by electron injection and show how similar mechanisms can produce new O-vacancies in the vicinity of pre-existing O-vacancies on the example of a-SiO_2. We demonstrate that two electrons trapped at a pre-existing O-vacancy facilitate the formation of a new O-vacancy and an interstitial O^{2-} ion and that this process becomes more probable as the vacancy clusters grow larger.

2. METHODS OF CALCULATIONS

The initial non-defective amorphous structures of SiO_2 and HfO_2 were obtained using classical molecular dynamics and a melt and quench procedure, which is described in detail in prior publications [22, 23]. DFT was then used to optimize starting amorphous geometries, calculate their electronic structures, and study the properties of neutral and charged O defects in the material. Ten periodic models of a-SiO_2 containing a total of 216 atoms each were produced using the ReaxFF force-field [24, 25] implemented in the LAMMPS code [26] and an NPT ensemble. ReaxFF was selected because it was originally parameterized to reproduce the properties of small clusters and silica polymorphs [24, 25] and reproduces the structural characteristics of silica glass well [27]. The initial models of a-HfO_2 structures were created using the pair potentials [28] and the LAMMPS package [26]. Nine periodic models of a-HfO_2, each containing 324 atoms, have been generated using classical molecular dynamics and a melt and quench procedure in an NPT ensemble. The Berendsen thermostat and barostat were used to control the simulations. The melt cooling rates were 8 and 0.75 K/ps for SiO_2 and HfO_2, respectively. We note that using an NPT ensemble creates distribution of densities of amorphous samples. In this work we used densities corresponding to experimental samples, as discussed in El-Sayed et al. [22] and Kaviani et al. [23].

Most DFT calculations were performed using the Gaussians and Plane Waves [29] method as implemented in the CP2K code [30]. The PBE0-TC-LRC [31] nonlocal functional was selected to accurately reproduce the band gap of a-SiO_2 and used in conjunction with the auxiliary density matrix method (ADMM) [32] to mitigate the computational expense. Finally, we used the MOLOPT basis set [33] along with the corresponding pseudopotentials (GTH) [34] and a 400 Ry plane wave cutoff. This method predicts an average band gap of 8.1 eV for amorphous SiO_2. The densities, radial distribution functions, distributions of Si-O bonds and Si-O-Si angles, as well as neutron structure factors of a-SiO_2 models used in this work have been evaluated in El-Sayed et al. [22] and showed good agreement with prior theoretical [27, 35] and experimental [36] studies. This analysis demonstrated that these amorphous models are able to produce disordered continuous random networks that accurately represent the structure of a-SiO_2.

The densities of the DFT optimized a-HfO_2 structures used in this work are in the experimentally determined range of $9.6 - 9.7\ \mathrm{g\ cm^3}$ [23]. Contrary to a-SiO_2, a-HfO_2 samples are characterized by distributions of coordinations of Hf and O ions and bond lengths. In particular, around 56% of the Hf atoms are bonded to 6 oxygen atoms, 38% are bonded to 7, and 6% to 5 oxygen atoms. On the other hand, 83% of the oxygen atoms are 3 coordinated, and there are about 6% of 2 coordinated oxygen atoms. These are in good agreement with previous studies, as discussed in detail in Kaviani et al. [23]. The one-electron band gap of initial structures does not contain localized states due to under-coordinated atoms and the band gap determined as a difference between the energies of HOMO and LUMO Kohn-Sham (K-S) energies is equal to 6.0 eV on average (ranging from 5.8 to 6.2 eV in different structures).

The formation energy of a vacancy was calculated using the standard formula

$$E_F = E_{Vac} - E_{Bulk} + \mu_O + q(E_{Fermi} + E_{VBM}), \qquad (1)$$

where E_{Vac} and E_{Bulk} are the total energies of the vacancy and pure cell, respectively. μ_{O} is the chemical potential of oxygen, q is the charge state of the vacancy, and E_{Fermi} is the Fermi level referenced to the energy eigenvalue of the valence band maximum, E_{VBM}. When modeling charged vacancies, charge corrections due to the interaction of periodic images were evaluated using the Lany and Zunger method [37, 38], with a dielectric constant of 3.9 for a-SiO_2 and 20 for a-HfO_2, and a Madelung constant of 2.8373 for the cubic cells. The population analysis of electronic states was carried out using the Bader method [39]. For the sake of convenience, all charges will be given in units of electron charge.

3. NEUTRAL DI- AND TRI-VACANCIES IN A-SIO$_2$ AND A-HFO$_2$

3.1. Vacancy Clusters in a-SiO$_2$

As observed consistently in previous work, the removal of an oxygen atom results in the formation of a Si-Si bond at the vacancy site ranging from 2.20 to 2.80 Å in length [19, 40–43]. This creates a doubly occupied defect state within the band gap between 0.39 and 1.34 eV above the valence band maximum (VBM), with the LUMO also positioned within the band gap between 7.04 and 8.20 eV above the VBM [40, 42]. However, such data with regards to di- and tri-vacancy clusters has not been previously published.

In the current study, we have analyzed a total of 25 di-vacancy structures and 12 tri-vacancy clusters using the sampling method described in detail in Munde et al. [19]. Typical configurations of di- and tri-vacancies in a-SiO_2 are shown in **Figure 1**. As illustrated, an oxygen tri-vacancy can exhibit three possible configurations: (i) the three vacancies are situated within a 3-member ring; (ii) the three vacancies diverge from a central Si atom to give a "Y" configuration; and (iii) the three vacancies form a chain. Our previous results have suggested that the 3-member ring and Y-geometry are energetically favorable when compared to the vacancy chain [19]. In all cases, the removal of additional oxygen atoms results in further network distortion. Si-Si bond lengths range from 2.20 to 3.00 Å and 2.40 to 3.00 Å in di- and tri-vacancy clusters, respectively. One can attribute the increase in the lower limit to bond length to a decrease in atomic density around the vacancy cluster site.

In all cases considered, occupied states are observed within the band gap. For the di-vacancy case, a single state is observed between 1.27 and 1.97 eV above the VBM with a mean of 1.52 eV. For the tri-vacancy case, two states are observed at 0.35 to 2.04 eV and 1.40 to 2.47 eV above the VBM, with mean values of 1.23 and 1.97 eV, respectively. These states result from the pairing up of electrons from the remaining Si atoms when an oxygen atom is removed. The LUMO is positioned 5.64 to 7.68 eV and 6.10 to 6.92 eV above the VBM for di- and tri-vacancies, with mean values of 6.86 and 6.54 eV, respectively. **Figure 2** illustrates how the LUMO state consists of an electron localized around a cluster site, with the shape of the orbital being dependent on the cluster geometry. In the di-vacancy and 3-member ring tri-vacancy cases (**Figures 2A,B**), the orbital lobes are situated above and below the plane of three Si atoms. This is different for the "Y" geometry and vacancy chain cases (**Figures 2C,D**), where orbital lobes are shared between the four Si atoms making up the vacancy. Typical density of states plots are shown in **Figure 3** for a monovacancy and its corresponding di-vacancy and tri-vacancy. The formation of these states on average ever deeper in the band gap suggests that larger clusters may facilitate conduction processes such as trap-assisted tunneling.

3.2. Vacancy Clusters in a-HfO$_2$

To study the interaction between vacancies in a-HfO_2 we performed calculations for 15 different vacancy configurations. To produce di-vacancy models we take a subset of 9 single

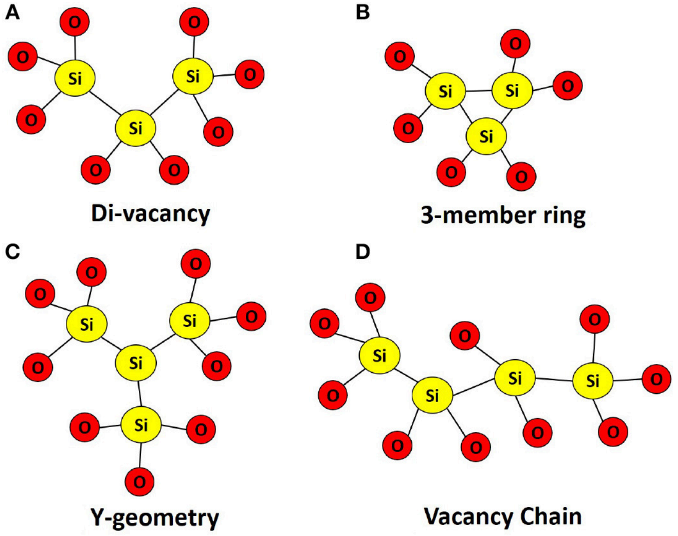

FIGURE 1 | Typical geometries of **(A)** Oxygen di-vacancy in a-SiO_2, **(B–D)** Oxygen tri-vacancies in a-SiO_2. Oxygen tri-vacancies can occur in one of three configurations: a 3-member Ring; a "Y-geometry"; and as a vacancy chain.

vacancies, and for each vacancy in this subset produce 3 di-vacancies by removing adjacent oxygen atoms. This produces 27 di-vacancy models in total. The choice of the original set of parent vacancies reflected the distribution of coordination numbers of oxygen atoms in our a-HfO_2 models. In this approach, the second vacancy probes the local environment around the preexisting vacancy. Vacancy dimers can form as a result of vacancy diffusion, which is inefficient for neutral vacancies, or as a result of formation of new vacancies as a result of electron trapping by pre-existing vacancies discussed below. Efficiency of these processes is governed by energy barriers.

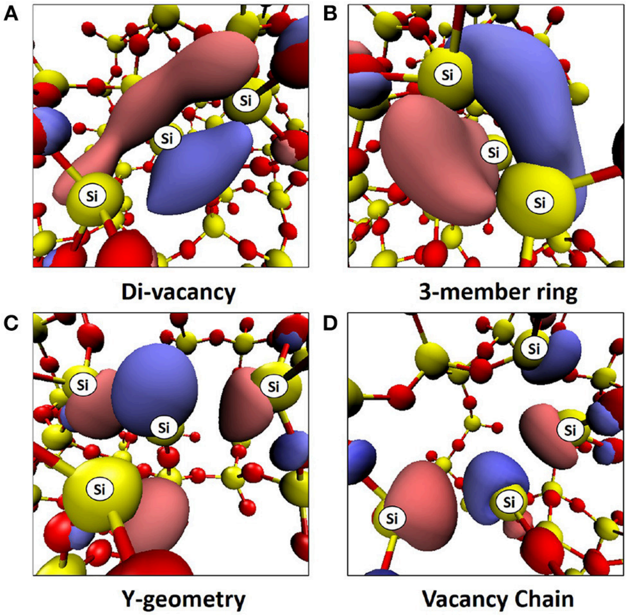

FIGURE 2 | Typical LUMOs from **(A)** Oxygen di-vacancy in a-SiO_2, **(B)** 3-member ring type tri-vacancy in a-SiO_2, **(C)** Y-geometry type tri-vacancy in a-SiO_2, **(D)** Vacancy chain type tri-vacancy in a-SiO_2. Positive and negative iso-surfaces are shown in blue and red with iso values of ±0.05, respectively. The Si atoms belonging to each vacancy cluster are labeled.

The interaction between neutral vacancies in a di-vacancy can be quantified by comparing the energy required to produce the first vacancy and then the second vacancy nearby. The first formation energy is calculated using Eq. 1. The second formation energy, $E_{\mathrm{F}}^{\mathrm{2nd}}$, is calculated using E_{Vac} in place of E_{Bulk}, that is $E_{\mathrm{F}}^{\mathrm{2nd}} = E_{\mathrm{Divac}} - E_{\mathrm{Vac}} + \mu_{\mathrm{O}}$. If $E_{\mathrm{F}}^{\mathrm{2nd}}$ is lower than E_{F}, the vacancies are said to be "attractive," If $E_{\mathrm{F}}^{\mathrm{2nd}} > E_{\mathrm{F}}$, the vacancies are said to be "repulsive." We note that the notion of "attractive," and "repulsive" is blurred in amorphous structures as defect formation energy strongly depends on the local environment. We have checked that all geometric configurations of vacancy dimers are fully converged and hence variations in second vacancy formation energy are caused by the difference in the local environment of each site as well as by the overlap of the vacancy wavefunctions forming bonding states (see **Figure 4**). We have also carried out "reversibility" tests where the O atom is placed back into the vacancy and the geometry is optimized again. In all cases the system returns to the original geometry and total energy, indicating that the formation of the second vacancy does not cause topological changes of the local environment.

The standard deviation of vacancy formation energies for our set of vacancies is 0.2 eV. Therefore we investigate the shift of the formation energy distribution by comparing average formation energies. On average, the second vacancy formation energy is 0.1 eV lower than that of the first. The standard deviation, however, is 0.4 eV. This means that some di-vacancy configurations will be of the "repulsive" type, even though the

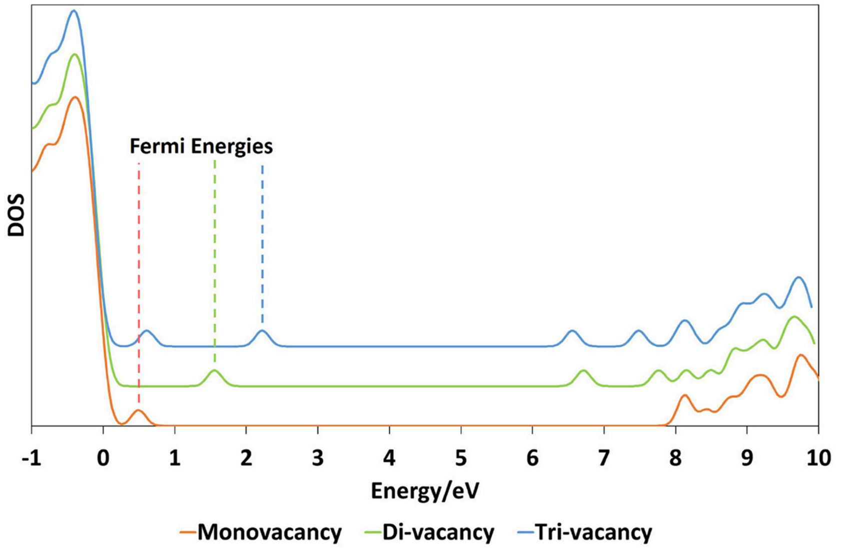

FIGURE 3 | Example density of states plots for a monovacancy together with its corresponding di-vacancy and tri-vacancy. For clarity, the energy levels on the plot have been broadened using Gaussians with a FWHM of 0.1 eV. The dotted lines indicate the position of the Fermi energy for each configuration.

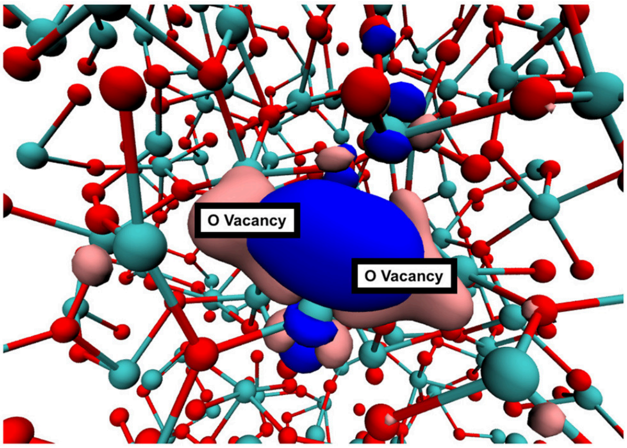

FIGURE 4 | A typical oxygen di-vacancy in a-HfO_2. The pink and blue surfaces show the $|\psi|^2$ of the defects states. In this configuration, the vacancy states combine and look similar to bonding and antibonding orbitals.

average case is "attractive." A typical di-vacancy configuration in a-HfO_2 is shown in **Figure 4**. Interaction between the vacancies is visualized by the plot of the di-vacancy doubly occupied electron states. Instead of two localized states adjacent to one another, the plot shows two states which are extended across the vacancies in a bond-like fashion. This type of molecular bonding type configuration corresponds to the majority of cases (approximately 80 %).

Further stabilization is possible for tri-vacancy clusters. The interaction in tri-vacancies can be quantified in a similar manner to di-vacancies by comparing the third vacancy formation energy with that of the second. It is found that the third vacancy formation energy is, on average, 0.2 eV lower than the second. Oxygen tri-vacancies have two general configurations, they can be organized in a linear or triangular fashion (see **Figure 5**). Similar to a-SiO_2, the interaction between vacancies in a more compact triangular configurations is stronger-the formation energy of triangular clusters is, on average, 0.2 eV lower than that of linear clusters. The standard deviation of the tri-vacancy formation energy distribution is 0.5 eV. This means that, similar to the di-vacancy case, there exists tri-vacancy aggregates that are of the repulsive type, despite the fact that, on average, tri-vacancies are attractive.

Therefore, the vacancy aggregation mechanism is the one in which the presence of a vacancy (or vacancies) lowers the formation energy required to produce an adjacent vacancy. This increases the rate of multi-vacancy generation relative to isolated vacancy generation.

4. ROLE OF ELECTRON INJECTION IN O-VACANCY CREATION

In many applications, amorphous SiO_2 and HfO_2 films are sandwiched between electrodes with often strong (of the order of 1V/nm) electric field applied across them. Under such conditions, extra electrons can tunnel into the oxide conduction band or into defect states inside the oxide by TAT. These effects are known to cause degradation of performance of oxide layers as dielectric in devices [1, 4]. In particular, it has recently been suggested that electrons injected into a-SiO_2 can be trapped in the amorphous matrix at structural precursor sites and form deep electron states in the band gap [44]. These intrinsic trapping sites have been identified as wide O–Si–O angles ($> 132°$) in the continuous random network structure and can accommodate up to two electrons (see **Figure 6**). The formation of these bi-electron states lowers the energy barrier to create a neutral O-vacancy in a-SiO_2 from about 8 eV to an average of 0.7 eV [45]. As a result of this process, an interstitial O^{2-} ion is created in the amorphous network, as shown in **Figures 6A–C**. The concentration of precursor sites for intrinsic electron traps in a-SiO_2 has been estimated at 4×10^{19} [44]. More information on the structure of electron traps, their optical absorption, EPR signatures, and a detailed description of electron injection facilitated Frenkel defect creation in a-SiO_2 can be found in prior publications [44, 45].

We note that neutral O-vacancies and negatively charged O^{2-} interstitial ions created by this mechanism have an average recombination barrier of 0.8 eV [45]. The formation energy diagram for O vacancies in a-SiO_2 is shown in **Figure 7**. The structural disorder of the amorphous material results in a wide range of local structures and hence a wide range of formation energy values. The charge transition levels of these vacancies exhibit a similar spread with an average 0/–1 charge transition level of 6.9 eV and an average –1/–2 charge transition level of 7.0 eV. Our results indicate that the charge transition levels which correspond to negatively charged vacancies are well positioned in relation to the conduction band of Si [46] and Fermi level position of some metal electrodes [47]. Thus, the newly created O vacancies can support trap assisted electron tunneling through a-SiO_2 in Si/SiO_2/metal stacks. The O^{2-} ions can diffuse away through the oxide via a previously studied pivot mechanism [45] which is characterized by a low 0.3 eV energy barrier. Under some conditions, oxygen has been observed to release into the gas phase [11].

A qualitatively similar mechanism for the formation of pairs of neutral O-vacancies and interstitial O^{2-} ions in monoclinic and amorphous HfO_2 has been proposed in Bradley et al. [48] and Kaviani et al. [49]. Extra electrons injected into monoclinic (m)-HfO_2 can form relatively shallow polaron and bi-polarons with trapping energies of about 0.3 eV [50]. Simulations [48] demonstrate that the formation of stable pairs of neutral oxygen vacancies and interstitial oxygen ions assisted by extra electrons is thermodynamically feasible and requires overcoming activation barriers of about 2.0 eV. This barrier is reduced to <1.3 eV if two extra electrons are initially trapped at a pre-existing O-vacancy. This results in the formation of another O-vacancy nearby and a mobile interstitial O^{2-} ion. The created O di-vacancy is stabilized by weak attraction between neutral vacancies, as described above. This leads to further lowering of the formation energy of the defect pair. The binding energy per vacancy in larger oxygen-vacancy aggregates increases as the aggregate grows, facilitating the formation of defect pairs next to larger vacancy aggregates.

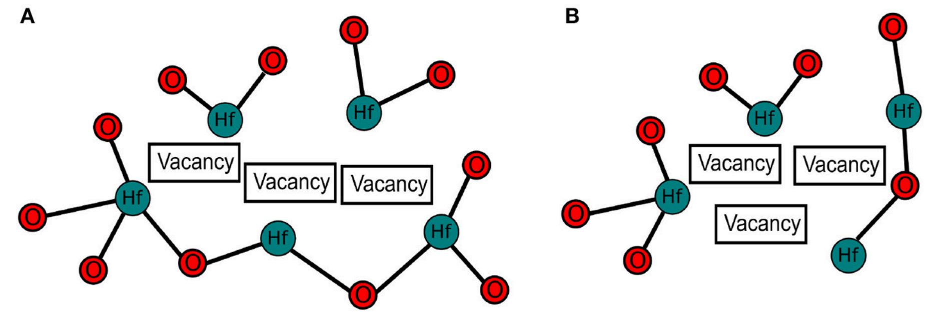

FIGURE 5 | Schematic of the two types of oxygen tri-vacancy in a-HfO_2. **(A)** shows the the linear type of configuration. **(B)** shows the triangular type of configuration. On average, triangular type tri-vacancies are lower in energy.

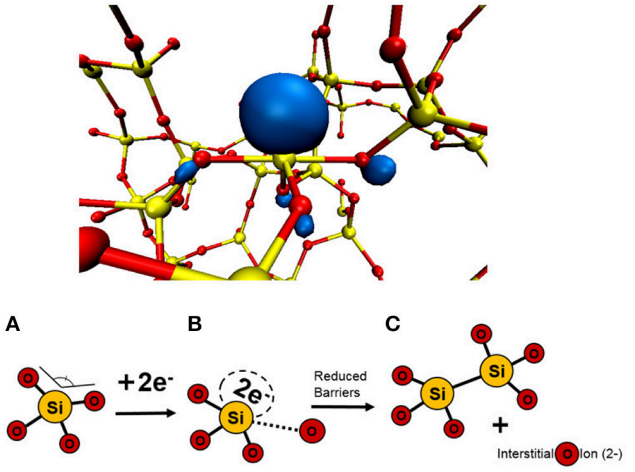

FIGURE 6 | Schematic illustrating how trapping of two electrons at a precursor site facilitates creation of neutral O vacancy and interstitial O^{2-} ion [45]. **(A)** Wide angle intrinsic traps in the amorphous network can trap two electrons. **(B)** Trapped electrons on the precursor reduce the barrier for O interstitial to be displaced. **(C)** O^{2-} ion is displaced to create a vacancy-ion pair.

In amorphous HfO_2, extra electrons injected from an electrode form deep polaron and bi-polaron states [23]. Extra electrons localize in energetically deep states at intrinsic structural traps in a-HfO_2 such as under-coordinated Hf ions or Hf ions with elongated Hf-O bonds, both of which are associated with a lowering of the electrostatic potential for an electron. The estimated density of such sites [23] in a-HfO_2 is about 2×10^{21} cm^{-3}. The structure and spectroscopic properties of these electron traps are described in detail in Kaviani et al. [23] and Strand et al. [51]. The bi-polaron formation causes strong Hf-O bond weakening manifested in significant (about 0.8 Å) ionic displacements. Similar to a-SiO_2, thermal activation of these bi-polarons may cause the formation of Frenkel defects in a-HfO_2 [49].

How electron trapping at pre-existing O-vacancies could facilitate the formation of new O-vacancies in a-SiO_2 is discussed below.

5. CREATION OF VACANCIES NEAR EXISTING VACANCIES

As discussed above, O-vacancies in amorphous SiO_2 and HfO_2 create deep states in the band gap where electrons can tunnel from Si and other electrodes. One of the possible mechanisms of O-vacancy aggregation is via creation of new vacancies near the pre-existing ones. Below we consider whether this process can be facilitated by electron trapping by O-vacancies in a-SiO_2. The cost of creating an oxygen vacancy depends greatly on the local environment. Not only is there a spread of formation energies owing to the disorder, but pre-existing vacancies can affect both the position and the barrier for forming a new vacancy. The presence of an existing vacancy close to the bi-polaron may either facilitate or hinder the next vacancy-creation process.

This can be manifested in several ways: (i) Electron trapping in a vacancy can facilitate the formation of a new vacancy nearby. (ii) Distortion of the surrounding network caused by electron trapping in a vacancy can create another precursor site for electron trapping nearby. Further electron trapping at these precursor sites can facilitate the creation of new vacancies. (iii) Aggregation of several vacancies can distort the surrounding network and enhance local electric field under electrical stress, facilitating creation of new vacancies. Below we consider mechanisms of some of these processes on the example of a-SiO_2.

5.1. Correlated Vacancy Creation in SiO_2

In a-SiO_2, an O-vacancy can trap up to two electrons [52]. When two electrons localize onto an O-vacancy, the defect distorts as the two 3-coordinated Si atoms displace to point away from each other, as shown in **Figure 8**. As a result of this distortion, there is a small chance that one of the lobes of the HOMO localized on Si atoms of the vacancy will point directly at a neighboring 4-coordinated Si atom, facilitating the Si-Si bond formation by expelling an O atom. The HOMO of a negatively charged O vacancy is shown in **Figure 8**.

To determine the likelihood of creating another O vacancy near an existing one, 144 possible vacancy geometries were investigated. In 97% of these geometries, the vacancy simply trapped two electrons by distorting, as shown in **Figures 8**, **9B**.

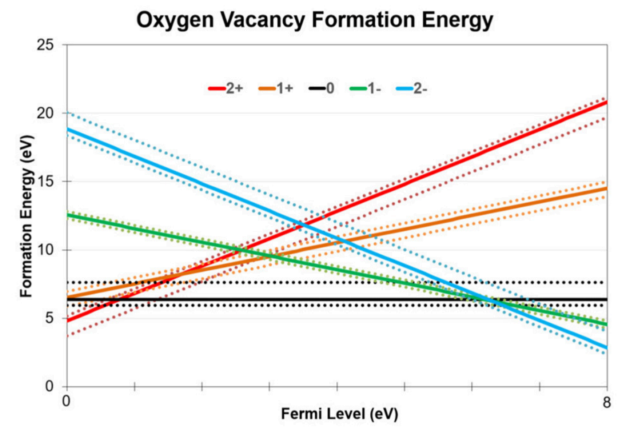

FIGURE 7 | O vacancy formation energies in a-SiO_2 at various charge states as a function of Fermi level. 144 vacancy geometries were calculated for each charge state due to the amorphous nature of our material. The average formation energy of each charge state is plotted using solid lines, while the minimum and maximum values for each charge state is plotted using dotted lines. The crossing point between positive and neutral vacancies is shown to be between 0.5 and 1.0 eV while the crossing point between neutral and negatively charged vacancies is between to be 6.2–7.5 eV.

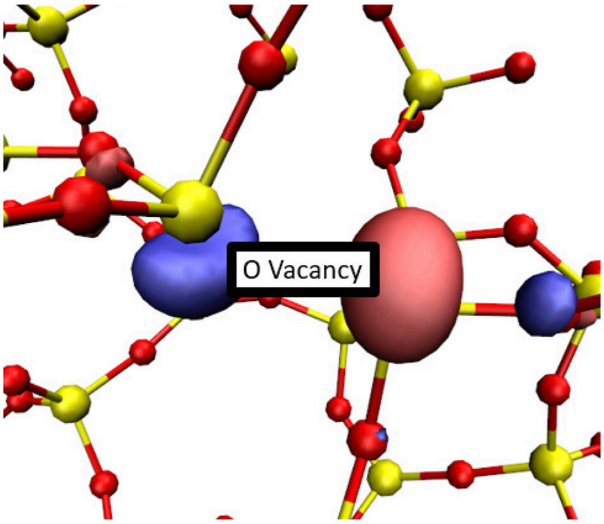

FIGURE 8 | A typical configuration of a doubly-charged O-vacancy in a-SiO_2. Two electrons have been trapped at this vacancy and the Si atoms within the vacancy pivot to point away from each other. Si atoms are shown in yellow while O atoms are shown in red. An iso-surface of the HOMO is shown in blue and pink.

In 2 cases the HOMO happened to point at a neighboring 4-coordinated Si atom, as shown schematically in **Figure 9C**. This configuration facilitates the creation of another O vacancy and O interstitial ion through a process with an average barrier of 1.1 eV. A schematic of formation of another vacancy correlated with the pre-existing vacancy is shown in **Figures 9A–D**. However, it is important to note that this process is relatively rare and was only observed in 2 out of 144 cases considered here.

Another possibility is that new wide O–Si–O angle precursor sites for electron trapping are created when O vacancies are occupied by electrons. Trapping two electrons at these new precursors can lead to creation of O vacancies by the mechanism illustrated in **Figures 6A–C**. The creation of these traps is directly related to the amount of local strain present in the system. Both the creation of new vacancies and the localization of electrons at existing vacancies result in an increase of local network distortion. After the geometry of each doubly negatively charged O vacancy was relaxed, another electron was added into the system to probe whether precursor sites for electron trapping were created. Out of a total of 142 geometries (excluding the two examples of correlated defect creation) a new wide O–Si–O angle intrinsic trapping site was found 38 times. In these cases new wide O–Si–O bond angle sites, which did not exist before, were created by the network distortion induced by the charged vacancy relaxation, as shown in **Figure 10**. Due to flexibility of a-SiO_2 network, wide angle precursors created in this way are not necessarily at neighboring sites to the vacancy responsible for distorting the local geometry. The probability of creating these new precursor sites is about 25%. Trapping two electrons at these new precursor sites generates new O vacancies and interstitial O^{2-} ions, as described above.

Since creation of additional wide O–Si–O angle intrinsic electron traps is associated with the local strain due to the presence of defects, one can expect that increasing the concentration of such defects should increase the probability of generating new precursor sites for electron trapping. As additional vacancies are created near pre-existing ones, the amount of local strain produced increases as well. To investigate this effect, we examined 40 di-vacancy geometries using 214 atom periodic cells. As electrons were added into these simulations, they can either localize in one vacancy, creating an equivalent of one negatively charged vacancy and one neutral vacancy or, if the di-vacancy exhibits a high degree of symmetry, they can be shared between the two, as shown in **Figure 2**. When up to 2 electrons are localized into the di-vacancy, creation of new precursor sites was observed 10 times, the same as for single vacancies. However, when the defect states are fully occupied by 4 electrons, it was observed that in 20 cases out of 40 wide O–Si–O bond angle sites were created due the network distortion caused by electron trapping at existing vacancies. This demonstrates that indeed clustering of O vacancies and electron trapping in them increase the probabilities of creating new vacancies nearby and these of growing new vacancy clusters.

We further investigated this trend by examining whether O tri-vacancies will also induce wide O–Si–O angle precursor sites. To accommodate such large vacancy clusters, we created a library of 648-atom a-SiO_2 cells using the melt and quench procedure described above. These larger amorphous structures were then screened for existing defects or wide O–Si–O angle intrinsic traps and 5 defect-free geometries were selected. Using these large cells, three libraries of tri-vacancy geometries were created to account for the more variable structure of these larger clusters. The first set of tri-vacancy geometries consisted of examples where the three defects were tightly clustered. The second set was composed of examples where the three defects were arranged in a linear array. Finally, in the third set of geometries each contained three loosely associated vacancies within two nearest neighbor sites of each other. Ten geometries from each set were selected for analysis at random and each of them was simulated with 1–6 extra electrons in the system.

In 23 out of 30 geometries, strain-induced wide O–Si–O angle electron traps were observed after all the pre-existing vacancies were charged. These newly created intrinsic traps were evenly distributed between the three types of tri-vacancy geometries, indicating that their exact configuration does not have a large effect on the correlated creation of new defects. When the tri-vacancy structures were charged with up to 2 electrons a new intrinsic trap was observed in 8 cases and when they were charged with up to 4 electrons a new intrinsic trap was observed in 14 geometries.

These results suggest that, as the size of O vacancy clusters increases, the likelihood of creating another vacancy nearby increases as well. Single vacancies have a 25% chance of inducing a wide O-Si-O angle intrinsic electron trap when charged, di-vacancies have a 50% chance, and tri-vacancies are the most likely to create a nearby intrinsic trap with a 77% chance. It also indicates that a significant portion of the network distortion that is responsible for the newly formed traps can be attributed to the localization of injected electrons rather than the presence of the vacancy cluster itself.

The mechanism of creation of a second O-vacancy facilitated by an electron trapping at a pre-existing vacancy in m-HfO_2 has been described in Bradley et al. [48]. The qualitative similarities in vacancy formation and aggregation processes in a-SiO_2 and a-HfO_2 suggest that such mechanisms can be operational also in a-HfO_2. They will be discussed in a separate publication.

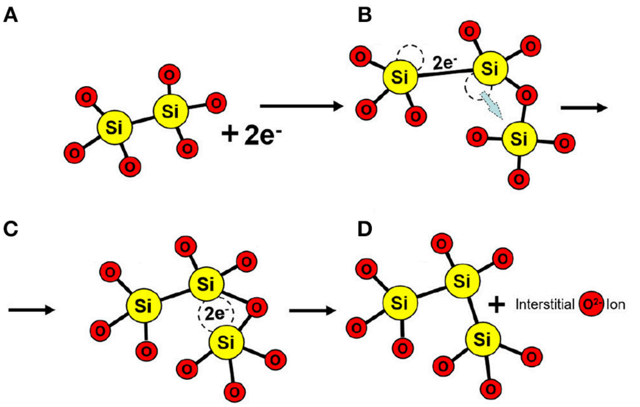

FIGURE 9 | Schematic illustrating the correlated defect creation mechanism. **(A)** O Vacancies can trap up to two electrons; and **(B)** distort the amorphous structure. **(C)** In rare cases, the HOMO of the charged vacancy points toward a neighboring Si atom and forms a bond to **(D)** create a new vacancy and interstitial O.

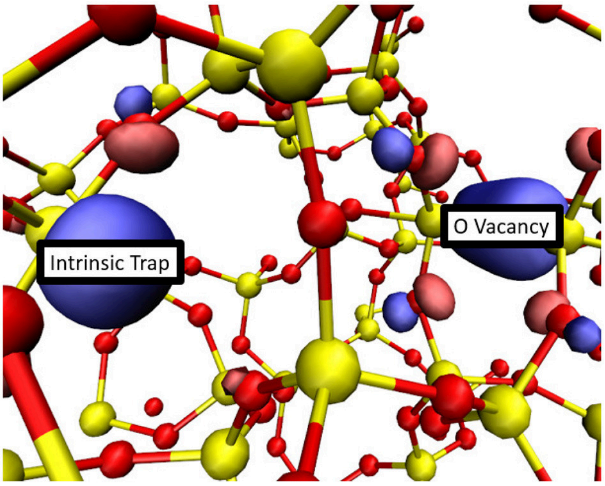

FIGURE 10 | The HOMO of a doubly negative O vacancy and a strain-induced wide O-Si-O angle intrinsic electron trap. In about 25% of geometries the third electron injected into a system which already contains a doubly negatively charged O vacancy localized onto a newly created intrinsic trap. Si atoms are shown in yellow while O atoms are shown in red. An iso-surface of the HOMO is shown in blue and pink.

6. CONCLUSIONS

Understanding the mechanisms of aggregation of oxygen vacancies in dielectric oxides is important for improving their performance in electronics, sensors, catalysis and other applications under electrical stress and different types of irradiation. We reviewed the initial stages of O-vacancy clustering in two prototype wide bandgap oxides, SiO_2 and HfO_2, and demonstrated that this is energetically favorable in some vacancy configurations. However, barriers for neutral O-vacancy diffusion in both materials are high and their aggregation via thermally activated diffusion is unfeasible at room temperature. As an alternative mechanism of vacancy aggregation, we considered how new O-vacancies can be created as a result of electron trapping by pre-existing ones on the example of a-SiO_2. These electrons can be injected via tunneling from an electrode in a device or produced under irradiation process. The results demonstrate that trapping two electrons at O vacancy sites in a-SiO_2 induces local distortion in the amorphous network such that new O–Si–O precursor sites for electron trapping are created with a probability of about 25%. These sites can trap two extra electrons, producing a new vacancy nearby. As the size of the O vacancy clusters increases, the likelihood of creating another vacancy nearby increases as well. Di-vacancies have a 50% chance, and tri-vacancies are the most likely to create a nearby intrinsic trap with a 77% chance.

These results suggest that electron trapping at oxygen vacancies in amorphous and crystalline oxides may facilitate the creation of new vacancies and this process becomes more efficient as vacancy clusters grow larger because this requires less activation. Previous results suggest that a similar mechanism can be also operational in m-HfO_2. We hope that these results will stimulate further studies of oxygen vacancy aggregation in other functional oxides, such as Al_2O_3 and Ga_2O_3 as well as in nitrides.

DATA AVAILABILITY

The datasets generated for this study are available on request to the corresponding author.

AUTHOR CONTRIBUTIONS

DG and MM have performed and analyzed calculations for oxygen vacancy aggregation in a-SiO_2 and wrote the corresponding parts of the paper. JS has performed and analyzed calculations for oxygen vacancy aggregation in a-HfO_2 and wrote the corresponding parts of the paper. AS coordinated the research, participated in analyzing the results and wrote and edited the paper.

FUNDING

We acknowledge funding provided by the UK Engineering and Physical Sciences Research Council (EPSRC) under grants No. EP/K01739X/1 and EP/P013503/1 and by the Leverhulme Trust RPG-2016-135. JS is funded by EPSRC grant no. EP/G036675/1 to the Center for Doctoral Training. Computer facilities on Archer service have been provided via the UKs HPC Materials Chemistry Consortium (EPSRC Grant No. EP/L000202).

ACKNOWLEDGMENTS

The authors are grateful to L. Larcher, A. Padovani, and G. Bersuker for valuable and stimulating discussions. Part of the results presented in this paper were previously published in The 2018 IEEE Reliability Physics Symposium [53].

REFERENCES

1. Fleetwood DM. *Defects in Microelectronic Materials and Devices*. Fleetwood DM, Pantelides ST, Schrimph RD, editors. Boca Raton, FL: CRC Press (2009).
2. Kuzum D, Yu S, Wong HSP. Synaptic electronics: materials, devices and applications. *Nanotechnology*. (2013) **24**:382001. doi: 10.1088/0957-4484/24/38/382001
3. Mehonic A, Shluger AL, Gao D, Valov I, Miranda E, Ielmini D, et al. Silicon oxide (SiO_x): a promising material for resistance switching? *Adv Mater*. (2018) **30**:1801187. doi: 10.1002/adma.201801187
4. Grasser T. *Bias Temperature Instability for Devices and Circuits*. Grasser T editor. New York, NY: Springer Science & Business Media (2013).
5. McPherson J. Time dependent dielectric breakdown physics-Models revisited. *Microelectron Reliab*. (2012) **52**:1753–60. doi: 10.1016/j.microrel.2012.06.007
6. Foster AS, Gejo FL, Shluger AL, Nieminen RM. Vacancy and interstitial defects in hafnia. *Phys Rev B*. (2002) **65**:174117. doi: 10.1103/physrevb.65.174117
7. Gao DZ, Strand J, El-Sayed AM, Shluger AL. Role of electron and hole trapping in the degradation and breakdown of SiO_2 and HfO_2 films. In: *2018 IEEE International Reliability Physics Symposium (IRPS)*. (2018). p. 5A.2–1–5A.2–7.
8. Degreave R, Kaczer B, Groeseneken G. Degradation and breakdown in thin oxide layers: mechanisms, models and reliability prediction. *Microelectron. Reliab*. (1999) **39**:1445–60.
9. Green ML, Gusev EP, Degraeve R, Garfunkel EL. Ultrathin (<4 nm) SiO_2 and Si–O–N gate dielectric layers for silicon microelectronics: understanding the processing, structure, and physical and electrical limits. *J Appl Phys*. (2001) **90**:2057–121. doi: 10.1063/1.1385803
10. Padovani A, Gao DZ, Shluger AL, Larcher L. A microscopic mechanism of dielectric breakdown in SiO_2 films: An insight from multi-scale modeling. *J Appl Phys*. (2017) **121**:155101. doi: 10.1063/1.4979915
11. Mehonic A, Buckwell M, Montesi L, Munde MS, Gao DZ, Hudziak S, et al. Nanoscale transformations in metastable, amorphous, silicon Rich silica. *Adv Mater*. (2016) **28**:7486–93. doi: 10.1002/adma.201601208
12. Ambrogio S, Magyari-Kope B, Onofrio N, Islam MM, Duncan D, Nishi Y, et al. Modeling resistive switching materials and devices across scales. *J Electroceram*. (2017) **39**:39–60. doi: 10.1007/s10832-017-0093-y
13. Setvin M, Schmid M, Diebold U. Aggregation and electronically induced migration of oxygen vacancies in TiO_2 anatase. *Phys Rev B*. (2015) **91**:195403. doi: 10.1103/PhysRevB.91.195403
14. Magyari-Kope B, Tendulkar M, Park SG, Lee HD, Nishi Y. Resistive switching mechanisms in random access memory devices incorporating transition metal oxides: TiO_2, NiO and $Pr_{0.7}Ca_{0.3}MnO_3$. *Nanotechnology*. (2011) **22**:254029. doi: 10.1088/0957-4484/22/25/254029
15. Esch F, Fabris S, Zhou L, Montini T, Africh C, Fornasiero P, et al. Electron Localization Determines Defect Formation on Ceria Substrates. *Science*. (2005) **309**:752–5. doi: 10.1126/science.1111568
16. Wang L, Yu Y, He H, Zhang Y, Qin X, Wang B. Oxygen vacancy clusters essential for the catalytic activity of CeO_2 nanocubes for o-xylene oxidation. *Sci Rep*. (2017) **7**:12845. doi: 10.1038/s41598-017-13178-6
17. Eom K, Choi E, Choi M, Han S, Zhou H, Lee J. Oxygen vacancy linear clustering in a perovskite oxide. *J Phys Chem Lett*. (2017) **8**:3500–5. doi: 10.1021/acs.jpclett.7b01348
18. Henderson B, Wertz JE. Defects in the alkaline earth oxides. Defects in the alkaline earth oxides. *Adv Phys*. (1968) **17**:749–855. doi: 10.1080/00018736800101386
19. Munde MS, Gao DZ, Shluger AL. Diffusion and aggregation of oxygen vacancies in amorphous silica. *J Phys*. (2017) **29**:245701. doi: 10.1088/1361-648X/aa6f9a
20. Bradley S, Bersuker G, Shluger A. Modelling of oxygen vacancy aggregates in monoclinic HfO_2: can they contribute to conductive filament formation? *J Phys*. (2015) **27**:415401. doi: 10.1088/0953-8984/27/41/415401
21. Capron N, Broqvist P, Pasquarello A. Migration of oxygen vacancy in HfO_2 and across the HfO_2/SiO_2 interface: a first principles investigation. *Appl Phys Lett*. (2007) **91**:192905. doi: 10.1063/1.2807282
22. El-Sayed AM, Watkins MB, Afanas'ev VV, Shluger AL. Nature of intrinsic and extrinsic electron trapping in SiO_2. *Phys Rev B*. (2014) **89**:125201. doi: 10.1103/PhysRevB.89.125201
23. Kaviani M, Strand J, Afanas'ev VV, Shluger AL. Deep electron and hole polarons and bipolarons in amorphous oxide. *Phys Rev B*. (2016) **94**:020103. doi: 10.1103/PhysRevB.94.020103
24. van Duin ACT, Strachan A, Stewman S, Zhang Q, Xu X, Goddard W. ReaxFF$_{SiO}$ reactive force field for silicon and silicon oxide systems. *J Phys Chem A*. (2003) **107**:3803. doi: 10.1021/jp0276303
25. Fogarty JC, Aktulga HM, Grama AY, van Duin ACT, Pandit SA. *J Chem Phys*. (2010) **132**:174704. doi: 10.1063/1.3407433
26. Plimpton S. Fast parallel algorithms for short-range molecular dynamics. *J Comp Phys*. (1995) **117**:1. doi: 10.1006/jcph.1995.1039
27. Yu Y, Wang B, Wang M, Sant G, Bauchy M. Revisiting silica with ReaxFF: towards improved predictions of glass structure and properties via reactive molecular dynamics. *J Non-Cryst Solids*. (2016) **443**:148–54. doi: 10.1016/j.jnoncrysol.2016.03.026
28. Broglia G, Ori G, Larcher L, Montorsi M. Molecular dynamics simulation of amorphous HfO_2 for resistive RAM applications. *Model Simul Mater Sci Eng*. (2014) **22**:065006. doi: 10.1088/0965-0393/22/6/065006
29. Lippert G, Hutter J, Parrinello M. A hybrid Gaussian and plane wave density functional scheme. *Mol Phys*. (1997) **92**:477–87. doi: 10.1080/002689797170220

30. VandeVondele J, Krack M, Mohamed F, Parrinelo M, Chassaing T, Hutter J. Quickstep: fast and accurate density functional calculations using a mixed Gaussian and plane waves approach. *Comput Phys Commun*. (2005) **167**:103. doi: 10.1016/j.cpc.2004.12.014
31. Guidon M, Hutter J, VandeVondele J. Robust periodic Hartree-Fock exchange for large-scale simulations using Gaussian basis sets. *J Chem Theory Comput*. (2009) **5**:3013. doi: 10.1021/ct900494g
32. Guidon M, Hutter J, VandeVondele J. Auxiliary density matrix methods for hartreefock exchange calculations. *J Chem Theory Comput*. (2010) **8**:2348. doi: 10.1021/ct1002225
33. VandeVondele J, Hutter J. Gaussian basis sets for accurate calculations on molecular systems in gas and condensed phases. *J Chem Phys*. (2007) **127**:114105. doi: 10.1063/1.2770708
34. Goedecker S, Teter M, Hutter J. Separable dual-space Gaussian pseudopotentials. *Phys Rev B*. (1996) **54**:1703. doi: 10.1103/PhysRevB.54.1703
35. Vollmayr K, Kob W, Binder K. Cooling-rate effects in amorphous silica: a computer-simulation study. *Phys Rev B*. (1996) **54**:15808. doi: 10.1103/PhysRevB.54.15808
36. Susman S, Volin KJ, Price DL, Grimsditch M, Ringo JP, Kalia RK, et al. Intermediate-range order in permanently densified vitreous SiO_2: a neutron-diffraction and molecular-dynamics study. *Phys Rev B*. (1991) **43**:1194. doi: 10.1103/PhysRevB.43.1194
37. Lany S, Zunger A. Accurate prediction of defect properties in density functional supercell calculations. *Model Simul Mater Sci Eng*. (2009) **17**:084002. doi: 10.1088/0965-0393/17/8/084002
38. Murphy ST, Hine NDM. Anisotropic charge screening and supercell size convergence of defect formation energies. *Phys Rev B*. (2013) **87**:094111. doi: 10.1103/PhysRevB.87.094111
39. Bader RFW. *Atoms in Molecules: A Quantum Theory*. Oxford: Oxford University Press (1990).
40. El-Sayed AM. *Atomistic Modelling of Charge Trapping Defects in Silicon Dioxide*. London: University College London (2015).
41. Martin-Samos L, Limoge Y, Richards N, Crocombette JP, Roma G, Anglada E, et al. Oxygen neutral defects in silica: Origin of the distribution of the formation energies. *Europhys Lett*. (2004) 66:680. doi: 10.1209/epl/i2003-10247-3
42. Mukhopadhyay S, Sushko P, Stoneham AM, Shluger AL. Modeling of the structure and properties of oxygen vacancies in amorphous silica. *Phys Rev B*. (2004) **19**:195203. doi: 10.1103/PhysRevB.70.195203
43. Sushko P, Mukhopadhyay S, Stoneham AM, Shluger AL. Oxygen vacancies in amorphous silica: structure and distribution of properties. *Microelectron Eng*. (2005) **80**:292–5. doi: 10.1016/j.mee.2005.04.083
44. El-Sayed AM, Watkins MB, Shluger AL, Afanas'ev VV. Identification of intrinsic electron trapping sites in bulk amorphous silica from *ab initio* calculations. *Microelectron Eng*. (2013) **109**:68–71. doi: 10.1016/j.mee.2013.03.027
45. Gao DZ, El-Sayed AM, Shluger AL. A mechanism for Frenkel defect creation in amorphous SiO_2 facilitated by electron injection. *Nanotechnology*. (2016) **27**:505207. doi: 10.1088/0957-4484/27/50/505207
46. Afanas'ev V, Kolomiiets N, Houssa M, Stesmans A. Internal photoemission metrology of inhomogeneous interface barriers. *Phys Stat Solidi A*. (2017) **215**:1700865. doi: 10.1002/pssa.201700865
47. Yeo YC, King TJ, Hu C. Metal-dielectric band alignment and its implications for metal gate complementary metal-oxide-semiconductor technology. *J Appl Phys*. (2002) **92**:7266–71. doi: 10.1063/1.1521517
48. Bradley SR, Shluger AL, Bersuker G. Electron-injection-assisted generation of oxygen vacancies in monoclinic HfO_2. *Phys Rev Appl*. (2015) **4**:064008. doi: 10.1103/PhysRevApplied.4.064008
49. Strand J, Kaviani M, Shluger AL. Defect creation in amorphous HfO_2 facilitated by hole and electron injection. *Microel Eng*. (2017) **178**:279–83. doi: 10.1016/j.mee.2017.05.005
50. Ramo DM, Shluger A, Gavartin J, Bersuker G. Theoretical prediction of intrinsic self-trapping of electrons and holes in monoclinic HfO_2. *Phys Rev Lett*. (2007) **99**:155504. doi: 10.1103/PhysRevLett.99.155504
51. Strand J, Kaviani M, Afanas'ev VV, Lisoni JG, Shluger AL. Intrinsic Electron Trapping in Amorphous Oxides. *Nanotech*. (2018) **29**:125703. doi: 10.1088/1361-6528/aaa77a
52. Kimmel AV, Sushko PV, Shluger AL, Bersuker G. A microscopic mechanism of dielectric breakdown in SiO_2 films: An insight from multiscale modelling. *Electrochem Soc Trans*. (2009) **19**:3–17. doi: 10.1063/1.4979915
53. Gao D, Strand J, El-Sayed AM, Shluger A, Padovani A, Larcher L. Role of electron and hole trapping in the degradation and breakdown of SiO_2 and HfO_2 films. In: *Reliability Physics Symposium (IRPS), 2018 IEEE International*. IEEE (2018). p. 5A–2.

Conflict of Interest Statement: The authors declare that the research was conducted in the absence of any commercial or financial relationships that could be construed as a potential conflict of interest.

ORIGINAL RESEARCH
published: 13 March 2019
doi: 10.3389/fchem.2019.00104

Partial Oxidation of Methane to Syngas Over Nickel-Based Catalysts: Influence of Support Type, Addition of Rhodium, and Preparation Method

Consuelo Alvarez-Galvan [1]*, Mayra Melian [1], Laura Ruiz-Matas [1], Jose Luis Eslava [1], Rufino M. Navarro [1], Mahdi Ahmadi [2†], Beatriz Roldan Cuenya [2,3] and Jose Luis G. Fierro [1]

[1] Structure and Reactivity Department, Instituto de Catálisis y Petroleoquímica, CSIC, Madrid, Spain, [2] Department of Physics, University of Central Florida, Orlando, FL, United States, [3] Department of Interface Science, Fritz Haber Institute of the Max Planck Society, Berlin, Germany

OPEN ACCESS

Edited by:
Claudio Cazorla,
University of New South Wales,
Australia

Reviewed by:
Benjaram M. Reddy,
Indian Institute of Chemical
Technology (CSIR), India
Tim Schäfer,
University of Göttingen, Germany

***Correspondence:**
Consuelo Alvarez-Galvan
c.alvarez@icp.csic.es

†Present Address:
Mahdi Ahmadi,
Cornell University, Ithaca, NY,
United States

Specialty section:
This article was submitted to
Physical Chemistry and Chemical
Physics,
a section of the journal
Frontiers in Chemistry

Received: 16 November 2018
Accepted: 11 February 2019
Published: 13 March 2019

Citation:
Alvarez-Galvan C, Melian M,
Ruiz-Matas L, Eslava JL, Navarro RM,
Ahmadi M, Roldan Cuenya B and
Fierro JLG (2019) Partial Oxidation of
Methane to Syngas Over
Nickel-Based Catalysts: Influence of
Support Type, Addition of Rhodium,
and Preparation Method.
Front. Chem. 7:104.
doi: 10.3389/fchem.2019.00104

There is great economic incentive in developing efficient catalysts to produce hydrogen or syngas by catalytic partial oxidation of methane (CPOM) since this is a much less energy-intensive reaction than the highly endothermic methane steam reforming reaction, which is the prominent reaction in industry. Herein, we report the catalytic behavior of nickel-based catalysts supported on different oxide substrates (Al_2O_3, CeO_2, La_2O_3, MgO, and ZrO_2) synthesized via wet impregnation and solid-state reaction. Furthermore, the impact of Rh doping was investigated. The catalysts have been characterized by X-ray diffraction, N_2 adsorptiondesorption at −196°C, temperature-programmed reduction, X-ray photoelectron spectroscopy, O_2-pulse chemisorption, transmission electron microscopy, and Raman spectroscopy. Supported Ni catalysts were found to be active for CPOM but can suffer from fast deactivation caused by the formation of carbon deposits as well as via the sintering of Ni nanoparticles (NPs). It has been found that the presence of Rh favors nickel reduction, which leads to an increase in the methane conversion and yield. For both synthesis methods, the catalysts supported on alumina and ceria show the best performance. This could be explained by the higher surface area of the Ni NPs on the alumina surface and presence of oxygen vacancies in the CeO_2 lattice, which favor the proportion of oxygen adsorbed on defect sites. The catalysts supported on MgO suffer quick deactivation due to formation of a NiO/MgO solid solution, which is not reducible under the reaction conditions. The low level of carbon formation over the catalysts supported on La_2O_3 is ascribed to the very high dispersion of the nickel NPs and to the formation of lanthanum oxycarbonate, through which carbon deposits are gasified. The catalytic behavior for catalysts with ZrO_2 as support depends on the synthesis method; however, in both cases, the catalysts undergo deactivation by carbon deposits.

Keywords: syngas, methane, partial oxidation, nickel, rhodium, catalyst

INTRODUCTION

The production of synthesis gas from methane is an important process for converting natural gas, one of the most abundant and cleanest-burning fossil fuels, into value-added high-quality liquid products (Gas-to-liquid technology, GTL). Steam reforming (SRM) has been the preferred technology for the industrial production of synthesis gas from methane to produce ammonia or methanol (Rostrup-Nielsen et al., 2002; Navarro et al., 2007a,b). Nevertheless, SRM is a highly energy-intensive process [Equation 1], and more energy-efficient alternatives to produce synthesis gas are sought.

$$CH_4 + H_2O \leftrightarrows CO + 3H_2 \quad \Delta H^0_{298K} = +206\ \mathrm{kJ/mol} \tag{1}$$

Among the alternatives, the catalytic partial oxidation for the production of synthesis gas from methane (CPOM) is more energy efficient since it has fast kinetics and is exothermic, thus avoiding the need of large reactors and large amounts of superheated steam (Bharadwaj and Schmidt, 1995). In addition, the stoichiometry of the CPO [Equation 2] produces a synthesis gas with an H_2/CO ratio of 2:1, which enables its direct utilization for methanol or Fischer-Tropsch synthesis without additional adjustment.

$$CH_4 + ½O_2 \leftrightarrows CO + 2H_2 \tag{2}$$

The catalytic partial oxidation of methane to syngas is challenging due to the difficulty in controlling the reaction selectivity toward total combustion. Several studies have been performed in the literature to describe the reaction mechanism involved in the CPOM and two reaction mechanisms have been proposed (Dissanayake et al., 1991; Hickman and Schmidt, 1992): the "direct mechanism," in which CH_4 and O_2 react on the catalyst surface to yield CO and H_2, and the "combustion-reforming mechanism," in which CH_4 and O_2 react first to form H_2O and CO_2 and then, with the excess methane, the dry reforming of CO_2 [Equation 3] and steam reforming [Eq.4] produce the final CO and H_2.

$$CH_4 + CO_2 \leftrightarrows 2CO + 2H_2 \tag{3}$$
$$CH_4 + H_2O \leftrightarrows CO + 3H_2 \tag{4}$$

Due to the excessive temperature gradients at high conversion rate, the exothermic nature of the reaction and fast deactivation due to carbon deposition on the catalyst's surface, the development of efficient catalysts for the CPOM has been challenging. NPs of noble metals [Pt (Ji et al., 2001), Rh (Ruckenstein and Wang, 1999; Puolakka and Krause, 2007), Ru (Ashcroft et al., 1990), Pd (Vernon et al., 1990)] and non-noble metals [mainly Ni and Co (Wang and Ruckenstein, 2001)] supported on various oxide substrates have been studied in the CPOM reaction. Nickel is one of the most widely used active phases for CPOM (Miao et al., 1997; Ostrowski et al., 1998; Takehira et al., 2004; Wang et al., 2004). As compared to noble metals, nickel is inexpensive but suffers from deactivation on-stream as a consequence of several processes such as sintering, carbon deposition (Claridge et al., 1993) or solid-state reactions of nickel with the substrate. From the large body of work developed on the CPOM reaction, it is clear that the activity and stability of nickel catalysts depend on both the active phase and the support. Metal particle size was proven to be an important factor for the initial intrinsic activity and for the rate of deactivation, with both decreasing with increasing active metal particle sizes (Barbier and Marecot, 1986; Barbier, 1987). The influence of the support on the performance of Ni-based catalysts has been widely studied in the literature (Tsipouriari et al., 1998). Non-reducible Al_2O_3 is one of the most studied oxides as support for Ni catalysts because of its thermal stability and high ability to disperse Ni nanoparticles (NPs) (Hu and Ruckenstein, 1998; Ostrowski et al., 1998; Zhang et al., 2000); however, its application for CPOM reaction is limited because of the relatively high deactivation of Ni NPs by sintering and the formation of coke deposits (Lu et al., 1998). Magnesium oxide is another non-reducible support widely studied to disperse stable Ni particles (Choudhary et al., 1998a; Ruckenstein and Hu, 1999; Nishimoto et al., 2004). In this case the formation of a solid solution between nickel and magnesia ($Mg_{1-x}Ni_xO$) only allows for the reduction of a small fraction of the nickel that remains in close interaction with the basic MgO substrate, favoring this structure for the production of syngas by CPOM with high activity (Requies et al., 2005). Lanthanum oxide has also been used as a support for Ni catalysts (Tsipouriari et al., 1998; Nishimoto et al., 2004). For the Ni/La_2O_3 catalysts, good stability was reported and attributed to the increased metal-support interface because the nickel NPs are decorated by $La_2O_2CO_3$ species that promote the gasification of coke. Reducible supports (CeO_2, ZrO_2) have been also studied as systems to disperse active and stable nickel particles for CPOM. CeO_2 is known for its ability to improve the dispersion and stabilization of small nickel metal NPs and for its high oxygen storage/transport capacity, which allows for continuous removal of carbonaceous deposits from active sites (Choudhary et al., 1993; Diskin et al., 1998). In addition, under reducing conditions, the SMSI (*Strong Metal-Support Interaction*) effect could be observed on ceria, which in turn affects the stability and activity of the dispersed nickel particles (Trovarelli, 1996). Zirconia is another support that shows interesting properties for the dispersion of active and stable Ni NPs. However, the application of ZrO_2 for CPOM reaction is debatable, since this support decreases the availability of the oxygen that participates in the direct CPOM to synthesis gas, resulting in a decrease in activity (Pompeo et al., 2005).

The incorporation of a second metal to the Ni-based catalysts is a common practice designed to improve catalyst stability. The beneficial effect of adding small amounts of precious metals such as Ru, Pt, Pd, Ir, and Rh to a Ni catalyst was previously demonstrated (Tomishige et al., 2002). Rh is one of the most promising metals (Tanaka et al., 2010a). The improvement was explained in terms of the H-spillover from the noble metal towards the non-noble metal, helping the non-noble metal surface to stay metallic (Chen et al., 1997).

As stated above, efficient Ni catalysts for the CPOM reaction require control over the electronic and structural properties of the nickel NPs, which could be achieved by the careful selection of the support and synthesis procedure. In this context, the main objective of this work is to study the influence of different supports (Al_2O_3, CeO_2, La_2O_3, MgO, ZrO_2) with different textural and surface (basicity, reducibility) properties on the activity, selectivity and stability of Ni-based catalysts for the CPOM reaction at atmospheric pressure. Two different synthesis methods have been used: (I) impregnation over different commercial supports and (II) solid state reaction. The influence of a small amount of Rh over the reducibility and reactivity of the catalysts has been tackled. Using various characterization techniques, we will establish structure-activity relationships that indicate which catalyst properties determine its reactivity and thus give us a way to improve the catalytic performance of the systems.

The Ni catalysts have been characterized by X-ray diffraction, nitrogen adsorption-desorption, temperature programmed reduction, X-ray photoelectron spectroscopy, oxygen-pulse chemisorption, transmission electron microscopy, and Raman spectroscopy. The evolution of the structure and morphology of the catalysts is reported and correlated to its catalytic performance.

MATERIALS AND METHODS

Preparation of Catalysts

Catalysts Prepared by Impregnation of Commercial Supports

Ni (5% weight) catalysts supported on commercial Al_2O_3 (Johnson Matthey, 99.97%), CeO_2 (Johnson Matthey, 96%), La_2O_3 (Fluka Chemika, 99.98%), MgO (Fluka Chemika, >98%) and ZrO_2 (Johnson Matthey, 99.5%) were prepared by wet impregnation. First, the supports were thermally stabilized by calcination at 850°C over 3 h. Then, they were sieved between 212 and 425 μm. The corresponding amount of $Ni(NO_3)_2 \cdot 6\ H_2O$ (Aldrich Chemie) was dissolved in distilled water. Each support was impregnated with this solution by rotary evaporation (70°C, 1 h). Then, the obtained solid was dried at 110°C for 2 h and calcined at 500°C for 3 h.

Catalysts Prepared by Solid State Reaction

The RhNi (0.1% Rh, 10% Ni, weight) catalysts, supported on Al_2O_3, CeO_2, La_2O_3, MgO, and ZrO_2, were prepared by mixing and grounding in an agate mortar the corresponding amounts of $Ni(NO_3)_2{\cdot}6H_2O$ (assay > 98.5%, Aldrich) and the nitrates of the support cations ($Mg(NO_3)_2{\cdot}6H_2O$ (Scharlau, 98%), $La(NO_3)_2{\cdot}6H_2O$ (Johnson Matthey, 99.9%), $Al(NO_3)_3{\cdot}9H_2O$ (99.997% Sigma Aldrich), $Ce(NO_3)_3{\cdot}6H_2O$ (Johnson Matthey, 99.5%), and $ZrO(NO_3)_2{\cdot}xH_2O$, 99.9%), respectively. Since the Rh amount is very small, the method to incorporate this element was based on dissolving the corresponding amount of dicarbonyl(acetylacetonate) Rh(I) ($Rh(CO)_2acac$) (Sigma Aldrich, purum) in acetone and adding this solution dropwise to the powder mixture of nickel nitrate and the corresponding support cation nitrate, thoroughly removing it with a spatula. Then, each mixture was dried at 110°C for 2 h and calcined at 500°C for 3 h. Finally, the samples were ground and sieved between 212 and 425 μm.

Characterization Techniques

X-Ray Diffraction

XRD patterns were recorded on a Seifert 3000 powder diffractometer using Cu Kα radiation ($\lambda = 0.15418$ nm) generated at 40 kV and 40 mA. Scans were recorded at a rate of 0.02°/s for 2θ diffraction angles between 10 and 90°.

N_2 Adsorption-Desorption Isotherms

Textural properties were evaluated by N_2 adsorption-desorption isotherms of the samples recorded at liquid nitrogen temperature with a Micromeritics ASAP2000 apparatus. Samples were degassed at 150°C under vacuum overnight. Specific areas were calculated by applying the BET method.

Temperature Programmed Reduction

Temperature-programmed reduction (TPR) experiments were carried out using a semiautomatic Micromeritics TPD/TPR 2900 apparatus equipped with a TC detector. Prior to the reduction experiments, the samples (ca. 30 mg) were thermally treated under air stream at 300°C to remove moisture. TPR profiles were obtained by heating the samples under a 10% H_2/Ar flow (50 mL/min) from 25 to 800°C with a linear rate of 10°C/min.

Oxygen Chemisorption Capacity

Oxygen chemisorption capacity was determined by O_2-pulse chemisorption. First, the catalyst sample (60–70 mg) was inserted in a U-quartz reactor and heated to 500°C in argon, maintaining this temperature for 15 minutes. Then, the temperature was decreased to room temperature and the sample was reduced under a H_2/Ar flow (10% H_2) up to 750°C over 60 minutes. Finally, the carrier gas was changed to helium, and once the baseline was stabilized, O_2 pulses were injected until the O_2 detected peaks showed the same area.

X-Ray Photoelectron Spectroscopy

To extract information about the chemical state and composition of the Ni-supported samples, XPS measurements were acquired using a monochromatic X-ray source (Al Kα, 1486.6 eV) operating at 200 W and a hemispherical electron analyzer (Phoibos 100, SPECS GmbH). The high-resolution data were acquired with a pass energy of 18 eV. CasaXPS software was used to analyze the data.

X-ray photoelectron spectra of the RhNi supported samples were recorded on a VG Escalab 200R spectrometer equipped with a hemispherical electron analyzer and Mg Kα ($h{\cdot}\nu = 1253.6$ eV) X-ray source (12 kV and 10 mA). The powder samples were degassed at 150°C for 1 h before being transferred into the analysis chamber. Charge effects on the samples were corrected by fixing the binding energies of the C1s peak at 284.9 eV due to adventitious carbon. This reference gave binding energy values with an accuracy of ±0.1 eV. The data were treated with the "XPS peak" software. The spectra were decomposed with the least squares fitting routine using Gaussian/Lorentzian functions after subtracting the Shirley background.

Raman Spectroscopy

Raman spectra of the samples were recorded in air, under ambient conditions (being the samples hydrated by air humidity), using a single monochromator Renishaw inVia 1000 system equipped with a thermoelectrically cooled CCD detector and holographic super-Notch filter. The samples were excited with 535 nm (1800 lines/mm).

Catalytic Activity Tests

The catalytic behavior of the different catalyst precursors for the partial oxidation of methane to syngas was studied under atmospheric pressure at 750°C using a stainless-steel fixed bed reactor (length = 150 mm, internal diameter = 9 mm) placed inside a hinged oven. The catalysts (100 mg) were subjected to pretreatment under 50 mL_N/min of H_2/N_2 (10% H_2, molar) for the Ni-supported samples or under N_2 flow at 750°C for 1 h for the RhNi-supported samples, prior to the reaction. Then, the reactants were fed to the reactor (22.6 mL_N/min N_2, 6 mL_N/min O_2, and 12 mL_N/min CH_4). The reaction stream was analyzed on-line by gas chromatography (Varian 45-GC) with a thermal conductivity detector, equipped with a 5A molecular sieve (CP7538) to separate H_2, N_2, CH_4 y CO and a PoraBOND Q (CP7354) column to separate CO_2 and H_2O with a thermal conductivity detector. Argon was used as a carrier gas in order to increase the sensitivity for H_2 detection.

Methane conversion, CO selectivity, H_2 yield and H_2/CO ratio were defined as follows:

$$CH_4 conversion\ (\%) = \frac{CH_4\ molar\ flow\ (inlet) - CH_4\ molar\ flow\ (outlet)}{CH_4\ molar\ flow\ (inlet)} \cdot 100$$

$$H_2\ yield\ (\%) = \frac{H_2\ molar\ flow\ (oulet)}{2 \cdot CH_4\ molar\ flow\ (inlet)} \cdot 100$$

$$CO\ selectivity\ (\%) = \frac{CO\ molar\ flow\ (oulet)}{CH_4\ molar\ flow\ (inlet) - CH_4\ molar\ flow\ (outlet)} \cdot 100$$

$$\frac{H_2}{CO}(molar\ ratio) = \frac{H_2 molar\ flow\ (oulet)}{CO\ molar\ flow\ (outlet)}$$

RESULTS AND DISCUSSION

The catalysts have been analyzed before reaction (section Physicochemical Characterization of Calcined and Reduced Samples) by XRD, adsorption-desorption of N_2 at −196°C, TPR, and XPS and after reaction (section Physicochemical Characterization of Used Catalysts) by XRD, Raman spectroscopy and XPS. Finally, the results from the activity tests are presented and discussed (section Activity Tests).

Physicochemical Characterization of Calcined and Reduced Samples

Structural Properties

X-ray diffraction patterns of nickel-supported catalysts prepared by the wetness impregnation method and acquired after calcination (before reduction) are depicted in the first line of **Figure 1**. These diagrams show the diffraction lines corresponding to each support (Al_2O_3: 00-048-0367; CeO_2, cubic phase: 01-075-0076; La_2O_3, hexagonal: 01-074-2430; MgO, cubic phase: 01-075-0447 and monoclinic ZrO_2: 01-078-1807). The crystallinity of the supports is very different, being higher for the MgO-supported catalyst. Only for the ceria- and zirconia-supported catalysts is it possible to distinguish the main diffraction line related to NiO crystallites (cubic phase (01-073-1519), corresponding to the (200) diffraction plane. By applying the Scherrer equation, an average domain of NiO crystallites was measured (**Table 1**). On the other hand, the crystalline domains differ among the different supports, although being smaller and quite similar for the alumina and lanthana-supported catalysts.

For the Ni/MgO and Ni/Al_2O_3 catalysts, the peaks corresponding to nickel oxide overlap with those corresponding to the respective supports. SimilarQ16ly, in the Ni/La_2O_3 catalyst, the incorporated NiO reacts on the La_2O_3 surface to form a $LaNiO_3$ phase (00-012-0751), whose peaks overlap with those corresponding to La_2O_3. On the other hand, for the Ni-MgO sample, the formation of a NiO-MgO solid solution cannot be discarded since their diffraction lines coincide with those of MgO.

The Rh-Ni/Al_2O_3 catalyst prepared by impregnation shows a diffractogram similar to that of the Ni/Al_2O_3 catalyst (not displayed). In order to determine the particle size of nickel and rhodium particles, the Rh-Ni/Al_2O_3 catalyst was reduced according to the same activation procedure used for the activity tests and studied by STEM, **Figure 2**. Rh NPs appear as finely dispersed particles with an average size less than 1 nm. Ni NPs are also observed and present larger size (average around 8 nm).

In addition, the XRD patterns of Rh-promoted Ni-supported catalysts, prepared by solid state reaction, were recorded. The XRD patterns of the calcined ones (before reduction) are shown in **Figure 1** (line 2). As for the catalysts prepared by impregnation, the diffraction lines are mainly ascribed to the corresponding supports. In the case of the lanthana-supported catalyst, the formation of the $LaNiO_3$ phase cannot be discarded. For the catalyst supported on magnesia, the diffraction lines corresponding to MgO and a Ni-Mg-O solid solution cannot be distinguished because of their strong overlap (Arena et al., 1996). The formation of the Ni-Mg-O solid solution is due to the relatively high calcination temperature used in the catalyst preparation. Concerning the zirconia-supported catalyst, for this preparation method, zirconia crystallizes in the tetragonal phase.

Rh reflections were not observed, as expected from the very small crystallite size. Concerning the presence of crystalline nickel species, only in the case of the catalyst supported on CeO_2 was it possible to observe a small diffraction line of the (2 0 0) plane of NiO. The crystallinity of the catalysts considerably changed; being higher for the MgO-supported catalyst and lower for the Al_2O_3-supported one. The XRD diagram of this last catalyst indicates its amorphous nature, since the calcination temperature was not high enough to get a crystalline structure of alumina. The temperature range needed to form the gamma phase of alumina is 600–875°C (Sathyaseelan et al., 2013).

The Scherrer equation was applied to these X-ray diffraction diagrams, and the average domain sizes of the different crystalline phases are shown in **Table 2**. For these calcined samples, prepared by solid-state reaction, the average domain size among the

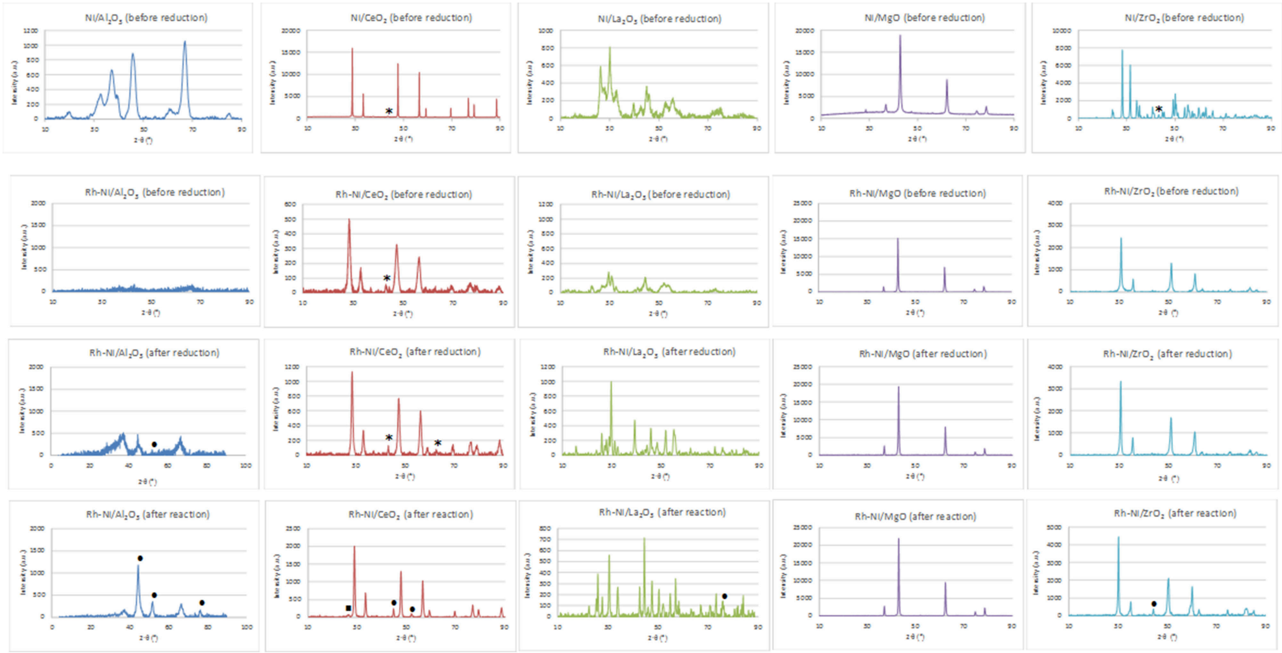

FIGURE 1 | XRD of Ni (prepared by impregnation) and RhNi samples (prepared by solid state reaction) (NiO (01-073-1519): ∗; Ni^0 (00-001-1258): ● ; CeO$_{2-x}$ (00-049-1415): □).

TABLE 1 | Average domain sizes for calcined samples (before reduction) prepared by impregnation (determined by the Scherrer equation).

Sample	Phase	hkl	2·θ (°)	*t* (nm)	Phase	hkl	2·θ (°)	*t* (nm)
Ni/Al$_2$O$_3$	Al$_2$O$_3$	4-4-2	66.867	5.0				
Ni/CeO$_2$	CeO$_2$	1-1-1	28.743	58.3	NiO	2-0-0	43.466	19.6
Ni/La$_2$O$_3$	La$_2$O$_3$	1-0-0	26.366	5.5				
Ni/MgO	MgO	2-0-0	42.782	15.1				
Ni/ZrO$_2$	ZrO$_2$	1-1-1	28.115	29.2	NiO	2-0-0	43.218	18.9

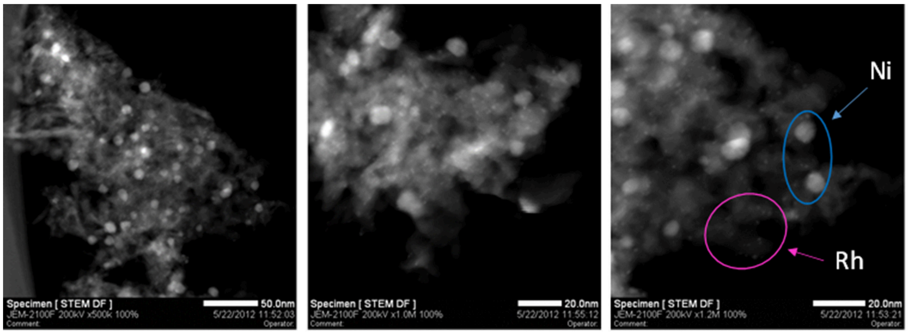

FIGURE 2 | STEM micrographs of sample Rh-Ni/Al$_2$O$_3$ prepared by impregnation.

different supports did not change as much as that which occurred for the calcined samples prepared by impregnation of commercial supports. Moreover, it is noteworthy that the crystalline domains of NiO, if they could be observed, were smaller than those obtained for the samples prepared by impregnation of the commercial supports (**Table 1**).

This figure also shows the XRD patterns of the reduced catalysts (**Figure 1**, line 3). The diffraction lines correspond

TABLE 2 | Average domain sizes for calcined samples (before reduction), fresh reduced catalysts and catalysts after reaction prepared by solid state reaction.

Sample	Phase	hkl	2·θ (°)	*t* (nm)	Phase	hkl	2·θ (°)	*t* (nm)
CALCINED SAMPLES (BEFORE REDUCTION)								
Rh-Ni/CeO_2	CeO_2	1-1-1	28.592	8.2	NiO	2-0-0	43.242	12.5
Rh-Ni/La_2O_3	La_2O_3 cubic	4-0-0	30.733	6.4	La_2O_3 hexag.	0-1-1	29.381	8.6
Rh-Ni/MgO	MgO	2-0-0	42.878	29.6				
Rh-Ni/ZrO_2	ZrO_2	1-1-1	30.575	17.4				
FRESH REDUCED CATALYSTS								
Rh-Ni/Al_2O_3					Ni^0	2-0-0	52.041	13.5
Rh-Ni/CeO_2	CeO_2	1-1-1	28.548	11.3	NiO	0-1-2	43.261	19.4
Rh-Ni/La_2O_3	La_2O_3 hexag.	0-1-1	29.8968	20.5	Ni^0	1-1-1	44.440	21.0
Rh-Ni/MgO	MgO	2-0-0	42.8532	22.0				
Rh-Ni/ZrO_2	ZrO_2	1-1-1	30.4207	15.8				
CATALYSTS AFTER REACTION								
Rh-Ni/Al_2O_3					Ni^0	2-0-0	51.764	7.4
Rh-Ni/CeO_2	CeO_2	1-1-1	28.804	17.2	Ni^0	1-1-1	44.7199	21.3
Rh-Ni/La_2O_3	$La_2O_2CO_3$	1-0-3	30.614	21.4	Ni^0	2-2-0	75.8017	12.8
Rh-Ni/MgO	MgO	2-0-0	42.889	26.4				
Rh-Ni/ZrO_2	ZrO_2	1-0-1	30.218	20.7	Ni^0	1-1-1	44.3868	19.2

basically to that of the supports. In the case of the lanthana-supported catalyst, the XRD profile consists of overlapping lines of La_2O_3, La_2NiO_4 (tetragonal, 01-079-0953) and $La(OH)_3$ (hexagonal, 01-083-2034) as a result of the strong interaction between nickel and lanthana (Pantaleo et al., 2015). Only for the catalyst supported on alumina and lanthana, low intensity peaks assigned to Ni metal [at 51.8°, plane (200)] can be distinguished. On the other hand, diffraction lines assigned to NiO are observed in the ceria-supported samples, indicating that at least part of the nickel phase cannot be reduced.

Textural Properties

Nitrogen adsorption-desorption isotherms of Ni- and Rh-Ni-supported catalysts are displayed in **Figure 3** and the surface areas are summarized in **Table 3**. These isotherms, which are of type IV, are assigned to mesoporous materials. All isotherms display a type H3 hysteresis loop, indicating that the catalysts contain a mesoporous network consisting of slit-type pores. In the relative pressure range of 0.7–1, the loop originates from larger and usually disordered interparticle pores (Sing et al., 1985).

For the Ni catalysts prepared by impregnation, it can be seen that the adsorbed amount of N_2 is higher for the catalysts supported on alumina and magnesia and smaller for the ceria- and zirconia-supported ones. This is in accordance with the large crystallite size of these commercial supports and their low surface area (see **Table 3**), which in turn decreases the dispersion of the nickel phase, as can be derived from the X-ray diffraction diagrams (**Figure 1**) and the average crystalline domains determined for supported NiO NPs (**Table 1**).

For the catalysts supported on alumina and magnesia, a decrease in surface area is observed, which is explained by the blockage of part of the porous lattice by nickel oxide NPs. On the contrary, for the samples supported on ceria, lanthana, and zirconia, an increase in surface area is observed, which might be attributed to the contribution of these NiO surface NPs. The catalyst with the largest surface area is, by far, the one supported on alumina, followed by that supported on magnesia. The other catalysts show BET surface area values one order of magnitude lower, being the lowest that supported on ceria.

On the contrary, the Rh-Ni calcined catalyst, prepared by solid state reaction and supported on ceria, presents larger porosity as derived from the higher extent of nitrogen adsorption and the larger hystheresis loop shifted to high relative P/P_0 pressure, indicating the formation of larger pores.

The alumina-supported Rh-Ni calcined catalyst prepared by solid state reaction, presents a H_2 hysteresis loop in the range of small mesopores at relative pressures of 0.4–0.6, indicating that the catalysts contain complex mesoporous networks consisting of pores with ill-defined shapes. From the nitrogen adsorption values, it can be seen that this preparation method gives catalysts with more uniform textural properties than those prepared by impregnation of commercial supports. This is reflected in the surface areas that are between 6 and 39 m^2/g for the samples used in the reaction, the trend being as follows: Rh-Ni/Al_2O_3 > Rh-Ni/CeO_2 > Rh-Ni/ZrO_2 > Rh-Ni/MgO ∼ Rh-Ni/La_2O_3. The highest surface area was obtained for the ceria-supported catalyst as a consequence of the formation of small nanocrystals (Kundakovic and Flytzani-Stephanopoulos, 1998).

The reduction of these Rh-Ni catalysts produced a change in surface area with respect to the corresponding calcined counterparts, increasing for lanthana and magnesia-supported catalysts and decreasing for the other ones. The used catalysts showed a decrease in surface area due to sintering, with the exception of those supported on alumina and zirconia, for which the surface area slightly increased.

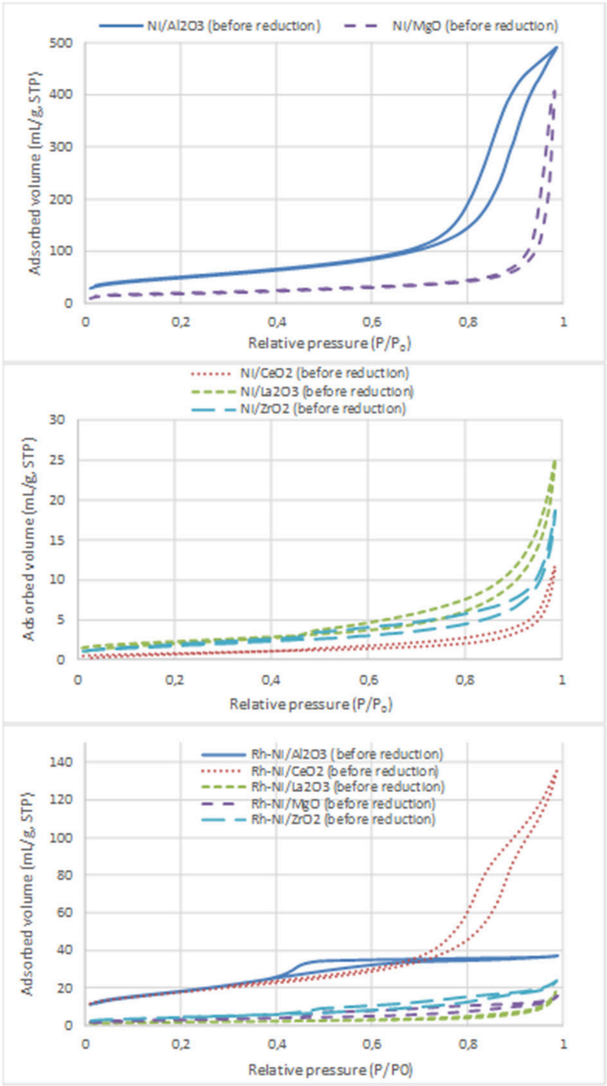

FIGURE 3 | N_2 adsorption-desorption isotherms of the calcined samples (Ni catalysts, prepared by impregnation and Rh-Ni catalysts prepared by solid-state reaction).

TABLE 3 | BET surface areas of commercial supports, of calcined Ni samples prepared by impregnation, and Rh-Ni samples prepared by solid state reaction (calcined, reduced and after reaction).

BET surface areas of supports and catalysts (m^2/g)				
COMMERCIAL SUPPORTS				
Al_2O_3	CeO_2	La_2O_3	MgO	ZrO_2
182.5	1.2	1.7	164.6	5.4
CATALYSTS PREPARED BY IMPREGNATION OF COMMERCIAL SUPPORTS				
Ni/Al_2O_3	Ni/CeO_2	Ni/La_2O_3	Ni/MgO	Ni/ZrO_2
(Calcined samples)				
176.9	3.1	8.2	60.5	6.5
CATALYSTS PREPARED BY SOLID STATE REACTION				
$Rh\text{-}Ni/Al_2O_3$	$Rh\text{-}Ni/CeO_2$	$Rh\text{-}Ni/La_2O_3$	Rh-Ni/MgO	$Rh\text{-}Ni/ZrO_2$
(Calcined samples)				
66.6	63.8	6.1	10.9	16.0
(Fresh reduced catalysts)				
37.9	43.0	12.5	15.4	8.4
(Catalysts after reaction)				
38.5	23.6	5.5	5.7	9.6

Redox Properties

The reduction profiles of the different catalysts prepared by impregnation and by solid state reaction are shown in **Figure 4**. The reduction profiles of Ni catalysts prepared by impregnation are depicted in **Figure 4A**. The H_2 consumption profile corresponding to the alumina-supported sample shows a very small contribution around 300°C due to the reduction of free NiO particles and wide consumption between 400 and 850°C, which indicates the formation of nickel oxide particles with different interactions with the support. The consumption at temperatures higher than 700°C is related to the reduction of nickel aluminate (Poncelet et al., 2005).

For the calcined Ni/CeO_2 sample, two peaks are observed: the first one is centered around 320°C and is ascribed to the reduction of free NiO NPs, while the second and wider one, centered around 780°C, is associated with the reduction of surface ceria and NiO NPs strongly interacting with the support. The consumption at the highest recorded temperature is explained by the reduction of some bulk ceria (Zhang et al., 2008).

The reduction profile of $Ni\text{-}La_2O_3$ calcined sample is characterized by two consumption peaks, the first one centered around 330°C and the second one around 580°C, both due to the 2-step reduction of the perovskite $LaNiO_3$ (see Equations 5, 6), formed during the calcination step (Barbero et al., 2003) .

$$LaNiO_3 + 1/2H_2 \rightarrow \; LaNiO_{2.5} + 1/2H_2O \tag{5}$$

$$LaNiO_{2.5} + H_2 \rightarrow \; 1/2La_2O_3 + Ni + H_2O \tag{6}$$

In the first step at lower temperature, Ni^{3+} species stabilized in the perovskite structure are reduced to Ni^{2+}, and the resulting compound, $LaNiO_{2.5}$, is an oxygen-deficient structure. In the second reduction step, a complete reduction of nickel to metallic nickel is achieved, and a system based on finely dispersed Ni^0 particles supported on a La_2O_3 matrix is obtained.

The reduction profile of the Ni/MgO calcined sample is characterized by very low H_2 consumption, indicative of an extensive formation of a Ni-Mg-O solid solution (Kirillov et al., 2011), which is difficult to reduce under the conditions used in TPR (Temperature Programmed Reduction) analysis. The peak around 330○C is related to the reduction of free NiO particles. The consumption between 400 and 800○C is assigned to the reduction of Ni^{2+} species in the outer or subsurface layers of the MgO lattice. For higher temperatures, H_2 consumption might be due to the reduction of Ni^{2+} taking place in the Ni-Mg-O solid solution (Wang et al., 2009a). For Ni/ZrO_2, a main reduction peak centered at 320°C, with a shoulder around 350°C can be

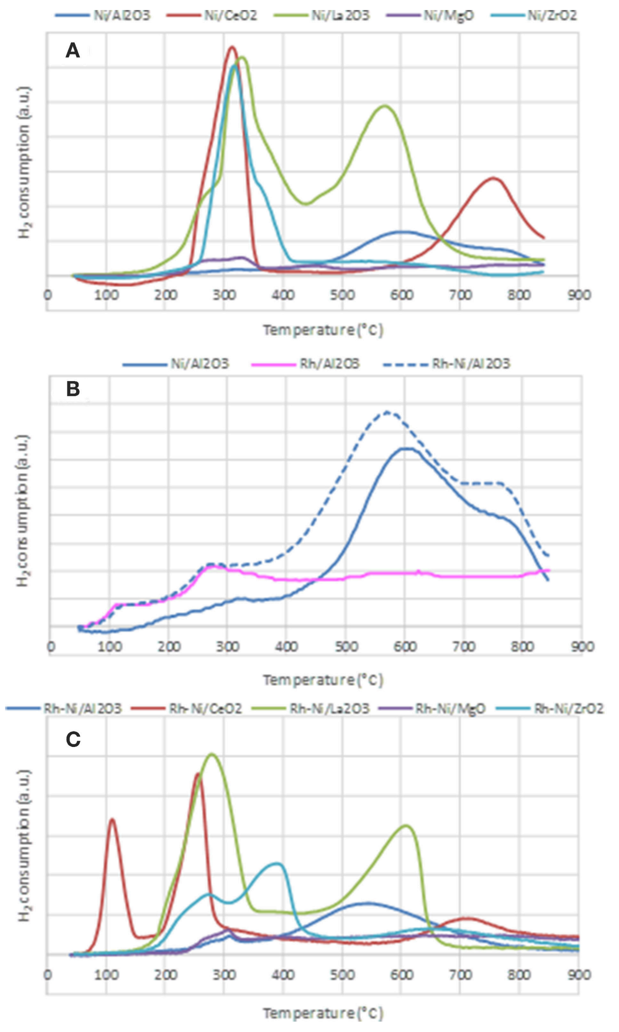

FIGURE 4 | Temperature Programmed Reduction profiles of the calcined samples, prepared by impregnation **(A,B)** and prepared by solid state reaction **(C)**.

found. The main H_2 consumption is due to the reduction of free NiO NPs and the minor one, at some higher temperature, to the reduction of NiO strongly interacting with the support (Wang et al., 2009b).

Figure 4B depicts the reduction profiles of the calcined samples Ni/Al_2O_3, Rh/Al_2O_3, and $Rh\text{-}Ni/Al_2O_3$, prepared by impregnation of commercial alumina. The reduction profile of Ni/Al_2O_3 has already been described above. The reduction profile of the Rh/Al_2O_3 sample shows two small contributions ascribed to the reduction of Rh_2O_3 to Rh^0. As reported in the literature, it is expected that calcination at 500○C causes a fraction of the Rh phase to interact strongly with alumina, with Rh becoming incorporated into the surface layer of this support and, thus, being difficult to reduce. Therefore, the peak around 125○C is attributed to the reduction of rhodium oxide particles containing low interaction with the support, and the second one, around 280○C, is due to the reduction of rhodium oxide species with strong interaction with alumina (Burch et al., 1996). The profile of the Rh-Ni/sample reflects the reduction of both Rh oxide and Ni oxide species. However, a shift to lower temperatures as compared to that of Ni/Al_2O_3 can clearly be observed. This is because the presence of noble metals facilitates the reduction of nickel oxide via a hydrogen-spillover mechanism (Tanaka et al., 2010b; Berger-Karin et al., 2011).

Figure 4C displays the TPR profiles of the Rh-Ni calcined samples prepared by solid-state reaction. The profile of the sample supported on alumina shows two contributions, a minor one around 310°C, attributed to the reduction of free NiO particles, and a second one, very wide and centered around 550°C, assigned to the reduction of Ni species strongly interacting with the support. As commented above, the reduction of nickel aluminate occurred at temperatures greater than 800°C. For the $Rh\text{-}Ni/CeO_2$ sample, the profile shows three different peaks: the lowest temperature peak, around 125°C, is assigned to the reduction of free Rh_2O_3 NPs. As the area of this peak is much higher than that corresponding to the total reduction of Rh in the sample, the consumption of hydrogen by ceria must be considered (Li et al., 2016).

The second one would be an overlapping peak comprising the reduction of Rh species strongly interacting with the support and the reduction of free NiO particles, while the third one, in the range of 650–800 °C, would be due to the reduction of complex NiOx species strongly interacting with the support, as well as surface ceria reduction. Finally, at temperatures higher than 800°C, the TCD signal is attributed to the reduction of bulk CeO_2 species. Comparison of the reduction profiles of $Rh\text{-}Ni/CeO_2$ and Ni/CeO_2 indicates that the presence of Rh promotes CeO_2 reduction, since the reduction profile of the Rh-Ni sample is shifted to lower temperatures, which can be attributed to hydrogen spillover during RhO_x reduction (Ocsachoque et al., 2016).

The reduction profile of the lanthana-supported Rh-Ni also showed two components—similar to what occurred in the Rh-free counterpart—due to the reduction of $LaNiO_3$ which is known to occur in two stages. As commented above, the first was due to the reduction of Ni^{3+} to Ni^{2+}, which is shifted to lower temperatures in comparison to Ni/La_2O_3, and the second saw $LaNiO_{2.5}$ be reduced to finely dispersed metallic nickel NPs supported on La_2O_3.

The TPR profile of Rh-Ni/MgO is characterized by very low H_2 consumption, as was the case for the Ni/MgO, which is due to the formation of Ni-Mg spinel in a larger extent during the calcination step. The small contribution found that around 300°C is attributed to the reduction of free NiO species. A small and wide peak was observed in the range of 400–750°C, which is associated to the reduction of Ni^{2+} interacting with the MgO lattice in external and subsurface layers. H_2 consumption at temperatures higher than 750–800°C is likely associated to the reduction of Ni^{2+} in NiO-MgO solid-solution (Wang et al., 2009a). The reduction profile of $Rh\text{-}Ni/ZrO_2$ shows three contributions: the first one, centered around 275°C, is assigned to the reduction of Rh oxide interacting with the support and also to free NiO particles; the second one, around 400°C, is due to surface nickel species interacting with the support, whereas the high temperature and wide reduction peak is due to the reduction of Ni^{2+} species inserted into the bulk zirconia lattice (Singha et al., 2016).

The interaction of nickel species with the support is one of the factors that influence the reactivity of the catalysts. In principle, a strong interaction among both phases is beneficial to stabilize the supported metal NPs, decreasing the deactivation by sintering (Ruckenstein and Wang, 1999).

Surface Composition

The binding energies of the Ni 2p, Al 2p, Ce $3d_{5/2}$, La $3d_{5/2}$, Mg 2p, and Zr $3d_{5/2}$ core levels, surface atomic ratios of Ni/(support cation) and metallic Ni and nickel oxide proportions have been determined by XPS. For the samples supported on ceria and lanthana, the analysis of the Ni $2p_{3/2}$ level is difficult since this level overlaps with the La $3d_{3/2}$ and Ce $3d_{5/2}$ levels and the quantification was done after careful deconvolution of both spectra.

The Ni 2p XPS core level region was fitted with three doublets assigned to metallic Ni (2p3/2, 852.5 eV), Ni^{2+} (2p3/2,855–856.2 eV), and satellite features (861, 878.2 eV). An example of a fitted spectrum for the Ni/MgO sample is shown in **Figure 5A**. The percentage of phase content for each metallic and metal oxide species was calculated by integrating the fitted XPS data of each sample before and after the reaction. The evolution of the Ni oxidation state is shown in **Figure 5B**. Thus, for the calcined Ni samples, the concentration of surface metallic nickel shows the following trend: $La_2O_3 > CeO_2 > MgO > Al_2O_3 > ZrO_2$. The highest metallic nickel exposure was extracted for the sample supported on lanthana, related to the formation of $LaNiO_3$, in which nickel is atomically distributed in the perovskite lattice. In the other extreme is the sample supported on zirconia, with the lowest metallic nickel proportion. For this series, the trend found for the surface Ni/substrate ratio is the following: $La_2O_3 > MgO > ZrO_2 > CeO_2 > Al_2O_3$. The highest value found for the catalyst supported on lanthana is explained by the atomic nickel dispersion achieved in $LaNiO_3$ perovskite. The others follow the same trend of the surface areas of the substrates, with lower dispersion being found with a smaller surface area of the support, with the exception of the Ni/Al_2O_3 sample, for which the formation of some proportion of nickel aluminate is not discarded.

For the calcined Rh-Ni samples, the binding energy found for the Ni $2p_{3/2}$ level, around 856 eV and accompanied by a satellite peak around 6 eV higher, is characteristic of Ni^{2+} species. Rh was not analyzed since its low amount makes it difficult to be detected. The binding energies found for the support cation indicate that the surface support phases are as follows: Al_2O_3, CeO_2, La_2O_3, MgO, and ZrO_2. The C 1s spectra show a peak around 290 eV, corresponding to surface carbonates for the lanthana and magnesia-supported catalyst precursor, being much intense for the lanthana-supported one. The Ni/M (M: Al, Ce, La, Mg, Zr) surface ratios are compiled in **Table 4**. These ratios change considerably depending on the support type. The trend found is $CeO_2 > La_2O_3 > ZrO_2 > Al_2O_3 > MgO$. The higher ratios obtained for ceria and lanthana-supported catalyst precursors are characteristic of a highly dispersed nickel phase. The low Ni/Mg ratio is due to the formation of a Ni-Mg-O solid solution (Arena et al., 1996; Barbero et al., 2003). The C 1s core-level spectrum of the lanthana-supported catalyst precursor shows a component around 289–290 eV due to the presence of carbonates, which is in accordance with the strong basic character of this oxide.

Physicochemical Characterization of Used Catalysts

Structural Properties

Rh-Ni catalysts after reaction have been structurally characterized by X-ray diffraction. X-ray diffraction patterns, depicted in **Figure 1**, showed that the reaction lead to structural changes in all the catalysts, as observed by comparing with the XRD patterns of fresh reduced samples. An increase in crystalline domain size of the support can be observed for the catalysts Rh-Ni/CeO_2, Rh-Ni-MgO, and Rh-Ni/ZrO_2 (**Table 2**). For the catalyst supported on lanthana, the support is based on lanthanum oxycarbonate (Requies et al., 2005; Navarro et al., 2007a), being formed by a reaction between La_2O_3 and CO_2. Except for the RhNi/MgO catalyst, the other diffractograms show lines corresponding to metallic nickel, with its crystalline domain size being higher for the catalyst supported on ceria and smaller for the one supported on alumina. On the other hand, for the catalyst supported on ceria, diffraction lines corresponding to the formation of oxygen defective ceria (CeO_{2-x}) can be observed (peak around 26.2°, ascribed to the diffraction plane (2 2 2), PDF card 00-049-1415).

Carbon Formation

For CPOM, carbon deposition can take place by the Boudouard reaction ($2\ CO\ \Delta\ C + CO_2$) and by the direct decomposition of methane ($CH_4\ \Delta\ C + 2\ H_2$), (Pena et al., 1996). The characterization of carbon deposits on the spent catalysts was carried out by Raman spectroscopy (spectra are shown in **Figure 6**). For each sample, at least three Raman spectra were recorded in different areas to assure the homogeneity of the composition.

Raman spectra of carbon exhibited two quite sharp modes, the G (graphitic) peak around 1590 cm^{-1} and the D (disordered) peak around 1350 cm^{-1}, which is related to the formation of carbon nanoparticles, amorphous carbon, or defective carbon filaments (Ozdemir et al., 2010; Lopez-Fonseca et al., 2012). The ceria-supported catalysts showed low intense peaks of carbon deposits. This is due to the widely reported oxygen mobility of the ceria surface (Dong et al., 2002). The low carbon formation in lanthana-supported catalysts is ascribed to the surface $La_2O_2CO_3$ species, well known as gasifier agents of C precursors.

As observed in **Figure 6**, in the samples in which peaks corresponding to carbon deposits are found, with the exception of Ni/ZrO_2, the graphitic band is higher than that of the disorder carbon one, particularly in the catalyst Rh-Ni/ZrO_2 (Song et al., 2008). This spent catalyst presents an additional band around 1570 cm^{-1} as a consequence of the splitting of the G band, which is characteristic of carbon nanotubes (Kogler et al., 2014). The formation of different types of carbon seems to be related to the crystal phase of zirconia. As reported in the literature, a

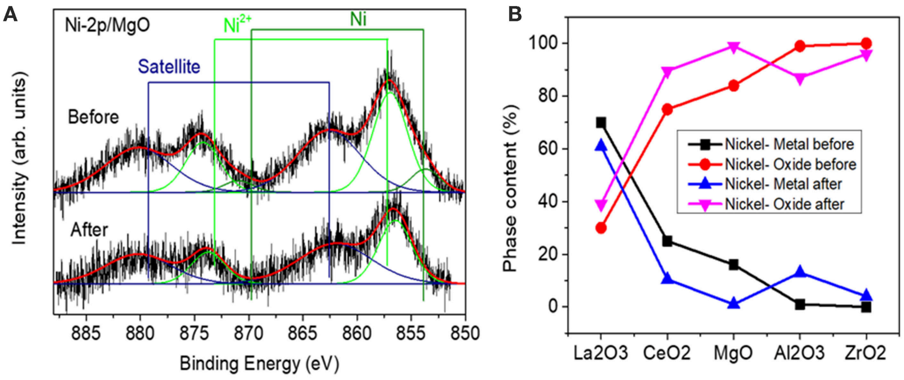

FIGURE 5 | (A) Example of a fitted spectrum for the Ni/MgO sample **(B)** Relative content of metallic nickel and nickel oxide species extracted from the analysis of Ni-2p XPS data measured before and after reaction.

TABLE 4 | Binding energies (eV) and atomic surface ratios of calcined RhNi samples (M: Al, Ce, La, Mg, Zr) prepared by solid state reaction.

Sample	Ni2p$_{3/2}$	M2p(3d)	Ni/M at	CO$_3^{2-}$/M at
RhNi/Al$_2$O$_3$	856.0	74.5	0.044	–
RhNi/CeO$_2$	856.2	883.1	0.497	–
RhNi/La$_2$O$_3$	855.6	834.7	0.389	1.303
RhNi/MgO	855.8	50.2	0.013	0.191
RhNi/ZrO$_2$	855.5	182.2	0.263	–

monoclinic phase favors the formation of encapsulating carbon and, for the tetragonal phase, the formation of carbon nanotubes is more likely (Zhang et al., 2015).

Surface Composition

Ni-supported catalysts were analyzed after reaction by XPS. **Figure 5** shows the content of metallic Ni (%) and the nickel oxide (%) for each one. If these values are compared to those obtained for the catalysts before reaction (fresh calcined), a change of the surface metallic nickel exposure concentration can be observed depending on the catalyst type. Thus, for the samples supported on alumina and zirconia, an increase in the surface metallic nickel % is obtained, contrary to our observation for the other samples. On the other hand, in order to compare the evolution of the surface composition during reaction, another parameter has been compared for all the catalysts, which is depicted in **Figure 7** and represents the ratio between the total Ni 2p area in the catalyst after and before reaction. These results point out that the total surface Ni area of the Ni catalyst supported on lanthana does not evolve significantly during reaction; on the contrary, the catalyst supported on alumina undergoes the greatest decrease in total surface nickel concentration.

Activity Tests

Ni-based catalysts prepared by impregnation were tested for the partial oxidation of methane to syngas and/or hydrogen. CH_4 conversion, H_2 yield, CO selectivity and H_2/CO molar ratio versus reaction time are depicted in **Figure 8**. The catalytic behavior highly depends on the type of support. The most active, selective and stable catalyst is the one on alumina. The counterpart supported on magnesia, which suffers a drastic deactivation, shows the worst catalytic behavior. The beginning of the reaction depends on the catalyst support.

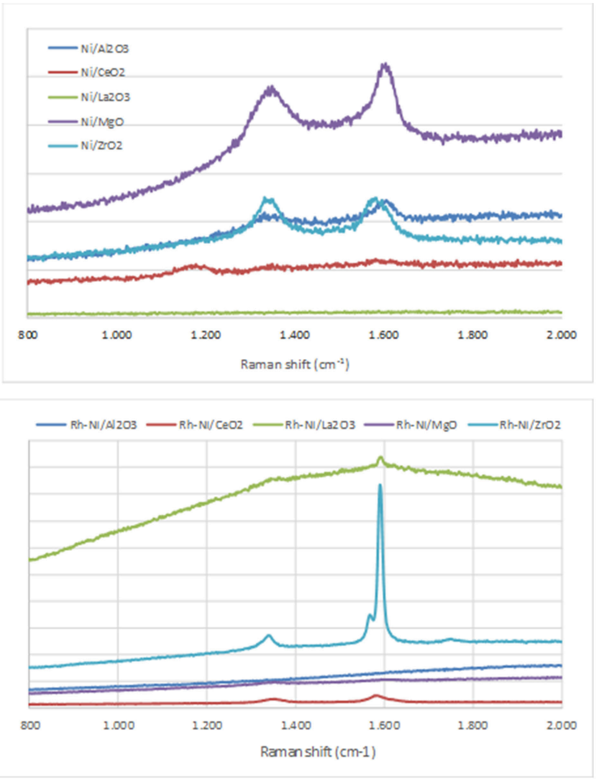

FIGURE 6 | Raman spectra of the catalysts after reaction (Ni catalysts, prepared by impregnation and Rh-Ni catalysts prepared by solid-state reaction).

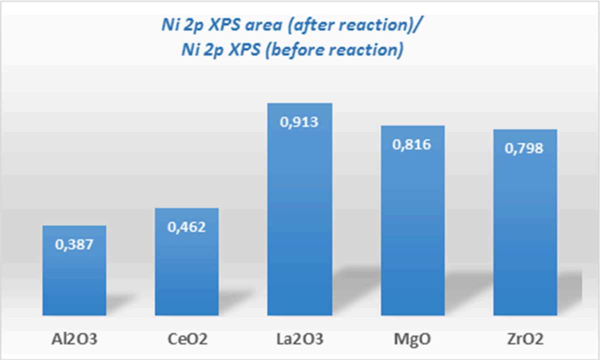

FIGURE 7 | Ratio of Ni to substrate before and after the reaction of Ni catalysts supported on different substrates (prepared by impregnation) extracted from the analysis of XPS data.

The reactivity trends observed with the other catalysts are as follows: Ni/CeO_2 > Ni/ZrO_2 > Ni/La_2O_3. However, these catalysts suffer a different deactivation rate, but similar values for methane conversion, H_2 yield and CO selectivity were found after 6 h of reaction. The better performance showed by the Ni/Al_2O_3 catalyst is mainly attributed to a relatively high level of nickel dispersion, favored by the higher surface area of the alumina support.

Although the metal-to-oxide ratio for Ni/La_2O_3 (before and after reaction) (**Figure 5**) is much higher than the analogous ratios of the other catalysts, and the Ni 2p area barely decreases during reaction (**Figure 7**), in agreement with earlier findings (Requies et al., 2005), this catalyst does not appear to be very active for CPOM. Since the analysis of the Raman spectra rules out the carbon formation and therefore carbon deposition on nickel species, the observed deactivation should be due to sintering and/or the coverage of nickel species by lanthana carbonates, which are produced by the adsorption of CO_2 formed during the reaction (Requies et al., 2005). The deactivation of this catalyst is explained by its metal/support ratio (**Figure 5**), far from the optimum to favor the selectivity to methane partial oxidation, for this type of support. Furthermore, the oxidation of nickel particles at the beginning of the reaction would lead to lower selectivity toward syngas or hydrogen formation, increasing the selectivity toward total oxidation and, consequently, catalyst deactivation.

As reported in the literature, the catalytic performance of a catalyst based on Ni/MgO depends on its composition, preparation conditions, and even the properties of the MgO support (Hu and Ruckenstein, 2004; Nguyen et al., 2016). The fast deactivation observed for the Ni/MgO catalyst is due to the low fraction of metallic Ni on the catalyst surface (∼7%). Indeed, this Ni-loading is far below the optimal range (10-35%). As a consequence, this catalyst shows very low activity for CPOM (Ruckenstein and Hu, 1999), with only CO_2 and carbon as products after 4 h on-stream. Moreover, the nickel fouling leads to a substantial decrease in the Ni-support ratio (**Figure 5**). The deactivation of the Ni/ZrO_2 catalyst is mainly related to the formation of carbon deposits (**Figure 6**), which agrees with the results reported in the literature (Pengpanich et al., 2004; Larimi and Alavi, 2012).

The H_2/CO ratios are higher than 2 and lower than 2.7, except for the catalyst supported on magnesia, because this catalyst behaves as a combustion catalyst. For the other catalysts, the trend found for the H_2/CO ratio mainly depends on the extent of the Boudouard reaction ($2\ CO\ \Delta\ CO_2 + C$) and reverse water gas shift reaction, rWGS ($CO_2 + H_2\ \Delta\ CO + H_2O$), with this ratio being higher when the Boudouard reaction occurs at a large extent and the rWGS reaction at a low extent (Albarazi et al., 2013). Thus, it appears that a direct correlation between the Raman peaks related to carbon formation (**Figure 6**) and the H_2/CO ratio can be observed.

Figure 9 shows activity tests with monometallic Ni and Rh catalysts supported on alumina and with the bimetallic counterpart. Methane conversions and H_2 yields clearly show that adding a small amount of Rh to the nickel catalyst results in an improvement in the catalytic performance of the Ni-based catalyst. This is reasonably explained by the higher reduction degree of surface nickel particles by the H_2 spillover originating on Rh NPs (see **Figure 4**). The Rh monometallic catalyst suffers from fast deactivation produced as a consequence of the low amount of active phase (Hohn and Schmidt, 2001; Berger-Karin et al., 2011).

For the catalyst series prepared by the solid-state reaction based on Rh and Ni as active phases (**Figure 10**), the best performance is also obtained with the catalyst supported on alumina. The ceria-supported catalyst showed also good performance with a H_2 yield similar after 6 h on stream, even having a lower surface area (**Table 3**). The low deactivation of the RhNi/CeO_2 catalyst by carbon formation is a consequence of the oxygen mobility and storage of the ceria support promoted by the redox pair Ce(IV)/Ce(III) (Pantaleo et al., 2016), which is known to play a key role in this reaction (Ding et al., 2015). The results obtained by O_2 pulses at reaction temperature point out that the extent of O_2 chemisorbed in this catalyst is 1.344 mmol/g, a much higher amount than on the other catalysts (RhNi/Al_2O_3: 0.127; RhNi/La_2O_3: 0.144; RhNi/MgO: 0.299; RhNi/ZrO_2: 0.546 mmol/g).

The other catalysts undergo fast deactivation with time on-stream. The deactivation of the catalyst supported on zirconia is explained by the fouling of active phases, since they underwent extensive carbon formation. The deactivation rate of the zirconia-supported bimetallic catalysts is higher than that observed for the monometallic counterpart. The different crystalline phases of zirconia (monoclinic for the monometallic catalyst, prepared by impregnation, and tetragonal, for the bimetallic one, prepared by solid state reaction), may have an influence on carbon formation. As reported in the literature, the ability of CO_2 activation, which is essential to remove the surface carbon species, is related to the crystal phase of ZrO_2 since different active sites are expected to be present on the different surfaces (Zhang et al., 2015). Thus, it has been reported that CO_2 reacts by the reverse Boudouard reaction, with carbon species resulting from methane dissociation to CO (Baerns et al., 1997). The higher CO_2 adsorption capacity of m-ZrO_2 is attributed to the

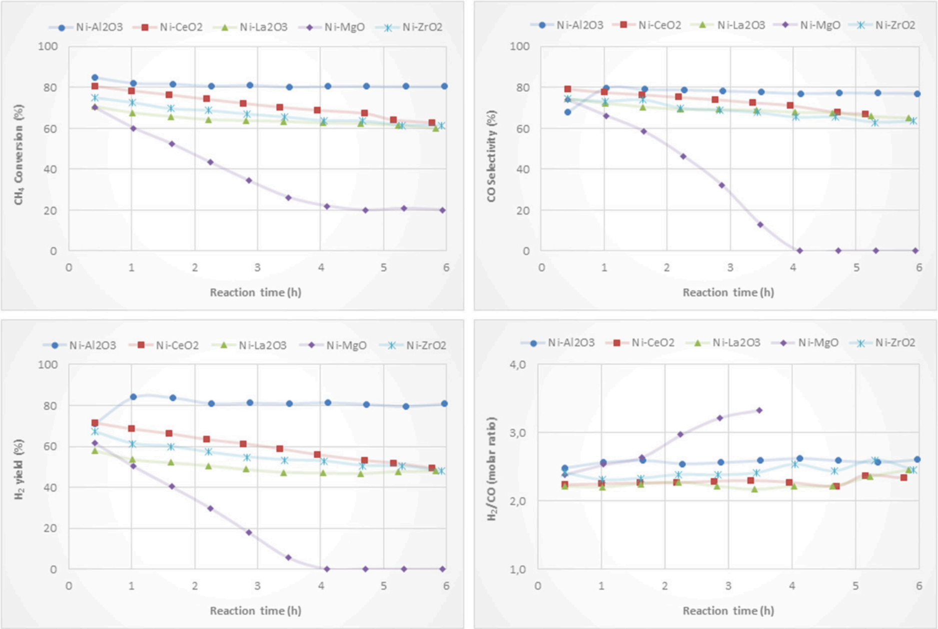

FIGURE 8 | Catalytic performance of Ni catalysts (prepared by impregnation) for CPOM: CH_4 conversion, H_2 yield, CO selectivity and H_2/CO molar ratio.

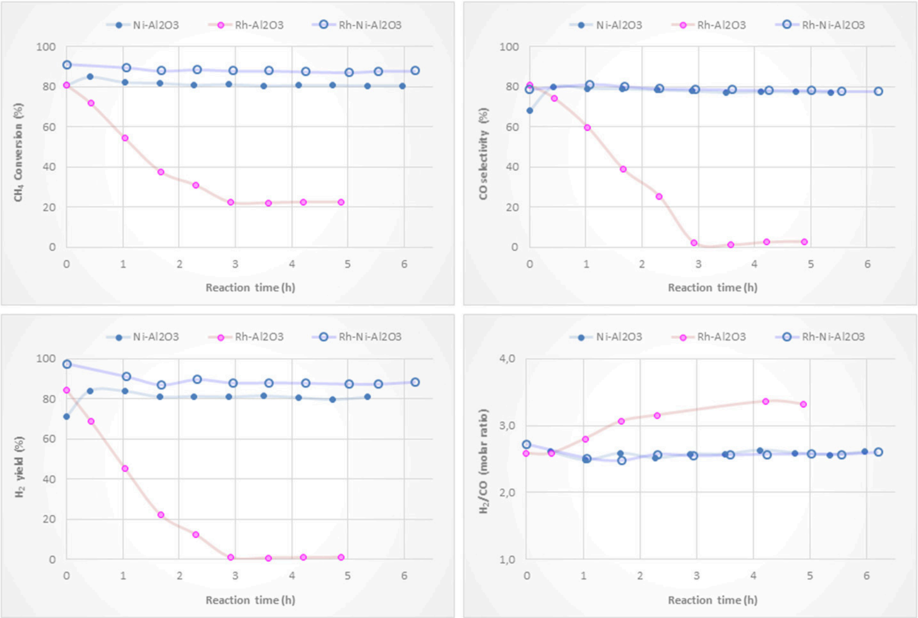

FIGURE 9 | Catalytic performance of Ni/Al_2O_3, Rh/Al_2O_3 and RhNi/Al_2O_3 catalysts (prepared by impregnation) for CPOM: CH_4 conversion, H_2 yield, CO selectivity and H_2/CO molar ratio.

higher concentration and basicity of the hydroxyl groups on this polymorph, as well as to the stronger Lewis basicity of O_2-anions (Pokrovski et al., 2001). This fast deactivation during CPOM has also been reported in a study using a monoclinic zirconia-supported Ni catalyst, also prepared by solid state reaction (Choudhary et al., 1998b).

Another factor influencing the reactivity of this catalyst is the sintering of nickel produced by hot spot formation in the catalyst bed, because the space velocity may not be high enough (Tang et al., 1998; Hohn and Schmidt, 2001). Since the interaction of metallic nickel particles on ZrO_2 is relatively weak, the catalysts are prone to deactivate by sintering of nickel particles (Barbero

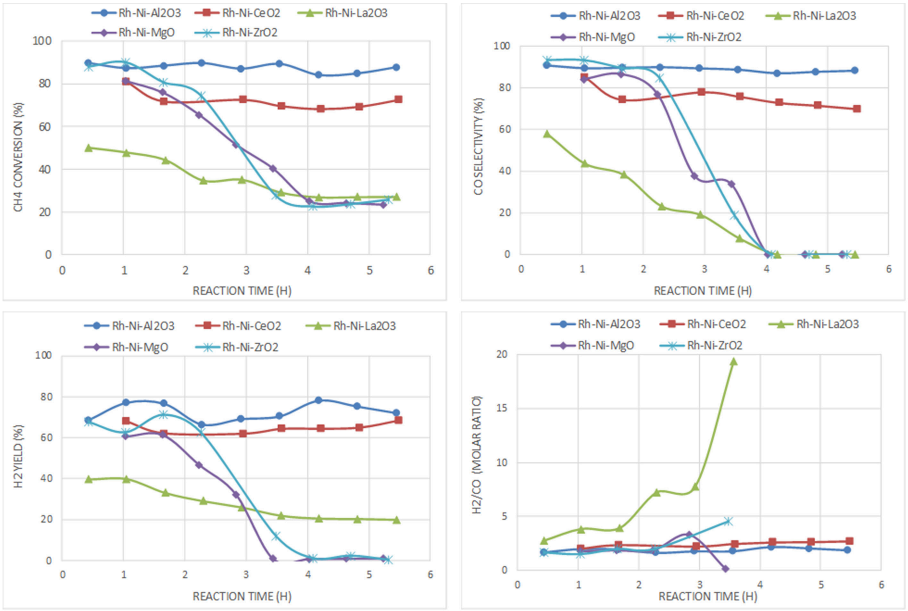

FIGURE 10 | Catalytic performance of Rh-Ni catalysts (prepared by solid state reaction) for CPOM: CH_4 conversion, H_2 yield, CO selectivity and H_2/CO molar ratio.

et al., 2003). Such species can be observed in the XRD diffraction lines of the spent catalyst (**Table 2**).

For the catalyst supported on magnesia, in which mainly an unreduced Ni-Mg-O solid solution was found that was inactive for the CPOM reaction, the decrease in selectivity toward syngas or H_2 was influenced by the low surface proportion of metallic nickel (Requies et al., 2005). Therefore, this catalyst deactivated gradually due to its oxidation (Nurunnabi et al., 2006). Although this mixed oxide phase inhibits carbon deposition, especially from CO disproportionation (Tang et al., 1998), the surface content of nickel produced from Ni-Mg-O reduction is too low (or the MgO surface proportion too large). The analysis by Raman spectroscopy of this catalyst after reaction revealed the near absence of carbon, which runs contrary to the result obtained for the monometallic catalyst (Ni/MgO). This is explained by the role of Rh, which enhances the resistance to carbon deposition (Nurunnabi et al., 2006).

In the case of the catalyst supported on lanthana, it displays the worst catalytic performance, with an initial methane conversion of 50%, which is almost half the conversion achieved by the other catalysts. Its deactivation is not due to an extensive carbon formation, since only a small peak around 1,600 cm^{-1}, attributed to graphitic carbon, is observed (**Figure 6**). In this catalyst, carbon is gasified by lanthanum oxycarbonate species (**Figure 1**) that limits deactivation to some extent.

In summary, the most active and selective catalysts are those supported on alumina and ceria. The comparison between Ni/Al_2O_3 and $RhNi/Al_2O_3$, as well as between Ni/CeO_2 and $RhNi/CeO_2$, points out that the bimetallic ones are more active, selective and stable. This is influenced by the greater metal-support interface achieved in these catalysts, prepared by solid state reaction, by the higher intrinsic activity of Rh and its role favoring the reduction of Ni.

The catalysts that have showed better activity per surface area for CPOM under the reaction conditions used in this research are those supported on ceria (Ni/CeO_2 and $RhNi/CeO_2$). In these catalysts, methane is dissociated on nickel particles, and C species migrate to the interface with the support to form CO (Dong et al., 2002). The bimetallic catalyst showed higher methane conversion, higher selectivity to H_2 and syngas and higher stability as a consequence of the larger metal-support interface. One of the properties that improved the catalytic behavior of this system is the non-stoichiometry of ceria, in which there is more oxygen mobility as compared to the other supports, which plays a key role in oxygen adsorption and carbon gasification (Pengpanich et al., 2004).

CONCLUSIONS

Catalysts based on Ni, Rh, and Rh-Ni supported on Al_2O_3, CeO_2, La_2O_3, MgO, and ZrO_2 have been prepared by wet impregnation of commercial supports and by solid state reaction. The catalysts have been tested for CPOM and it was found that their performance depends on the support type and on the preparation method. It can also be observed that a small amount of Rh promotes the reduction of Ni species, improving the catalytic performance. Regardless of the preparation method, the most active, selective and stable catalysts are those supported on alumina, which is mainly due to the higher dispersion of the nickel particles. The Ni/CeO_2 catalyst shows the best behavior per surface area, in which the lack of stoichiometry of the CeO_2 is a key property influencing the reactivity and stability. The catalyst composition of $RhNi-CeO_2$ prepared by solid state reaction yields higher activity and stability than that of Ni-CeO_2, prepared by impregnation. The fast deactivation of the catalysts supported on magnesia is explained by the low amount of active Ni sites, which leads to the combustion of methane, rather than to its selective oxidation. For the catalysts supported on lanthana, the deactivation is ascribed to the nickel content being lower than the optimum required amount on this type of support, resulting in the oxidation of nickel. The deactivation of the zirconia-supported catalysts is ascribed to the extensive formation of carbon, being less pronounced in the Ni/ZrO_2 catalyst due to the higher basicity of monoclinic zirconia in comparison to the tetragonal phase of RhNi/ZrO_2.

DATA AVAILABILITY

All datasets generated for this study are included in the manuscript and/or the supplementary files.

AUTHOR CONTRIBUTIONS

CA-G, MM, LR-M, and JE contributed to the preparation, characterization of catalysts and catalytic activity tests. RN contributed to tune up the reaction system and GC. MA, BR, and JF discussed the XPS results. CA-G discussed the results obtained by the other characterization techniques and the catalytic activity tests data.

FUNDING

CA-G gratefully acknowledges financial support from CSIC (Consejo Superior de Investigaciones Científicas) by a grant (PA1003284) through the Program Programa de Ayudas a Investigadores del CSIC para la realización de estancias en centros de investigación extranjeros.

ACKNOWLEDGMENTS

CA-G would like to thank all the members of Roldan Group for their hospitality during her stay at University of Central Florida (Orlando, USA). We acknowledge support toward the publication fee by the CSIC Open Access Publication Support Initiative through its Unit of Information Resources for Research (URICI).

REFERENCES

Albarazi, A., Beaunier, P., and Da Costa, P. (2013). Hydrogen and syngas production by methane dry reforming on SBA-15 supported nickel catalysts: on the effect of promotion by $Ce_{0.75}Zr_{0.25}O_2$ mixed oxide. *Int. J. Hydrogen Energy* 38, 127–139. doi: 10.1016/j.ijhydene.2012.10.063

Arena, F., Frusteri, F., Parmaliana, A., Plyasova, L., and Shmakov, A. N. (1996). Effect of calcination on the structure of Ni/MgO catalyst: An x-ray diffraction study. *J. Chem. Soc. Farad. Transact.* 92, 469–471. doi: 10.1039/ft9969200469

Ashcroft, A. T., Cheetham, A. K., Foord, J. S., Green, M. L. H., Grey, C. P., Murrell, A. J., et al. (1990). Selective oxidation of methane to synthesis gas-using transition-metal catalysts. *Nature* 344, 319–321. doi: 10.1038/344319a0

Baerns, M., Buyevskaya, O. V., Mleczko, L., and Wolf, D. (1997). "Catalytic partial oxidation of methane to synthesis gas - Catalysis and reaction engineering," in *Natural Gas Conversion Iv,* eds M. dePontes, R. L. Espinoza, C. P. Nicolaides, J. H. Scholtz, and M. S. Scurrell. (Amsterdam: Elsevier Science Bv), 421–428

Barbero, J., Pena, M. A., Campos-Martin, J. M., Fierro, J. L. G., and Arias, P. L. (2003). Support effect in supported Ni catalysts on their performance for methane partial oxidation. *Catal. Lett.* 87, 211–218. doi: 10.1023/a:1023407609626

Barbier, J. (1987). *Catalyst Deactivation,* eds B. Delmon and G. F. Froment. Amsterdam: Elsevier.

Barbier, J., and Marecot, P. (1986). Effect of presulfurization on the formation of coke on supported metal-catalysts. *J. Catal.* 102, 21–28. doi: 10.1016/0021-9517(86)90136-3

Berger-Karin, C., Radnik, J., and Kondratenko, E. V. (2011). Mechanistic origins of the promoting effect of tiny amounts of Rh on the performance of NiOx/Al_2O_3 in partial oxidation of methane. *J. Catal.* 280, 116–124. doi: 10.1016/j.jcat.2011.03.010

Bharadwaj, S. S., and Schmidt, L. D. (1995). Catalytic partial oxidation of natural-gas to syngas. *Fuel Process. Technol.* 42, 109–127. doi: 10.1016/0378-3820(94)00098-e

Burch, R., Loader, P. K., and Cruise, N. A. (1996). An investigation of the deactivation of Rh/alumina catalysts under strong oxidising conditions. *Appl. Catal. A Gen.*147, 375–394. doi: 10.1016/s0926-860x(96)00212-8

Chen, Y. G., Tomishige, K., Yokoyama, K., and Fujimoto, K. (1997). Promoting effect of Pt, Pd and Rh noble metals to the Ni0.03Mg0.97O solid solution catalysts for the reforming of CH_4 with CO_2. *Appl. Catal. A Gen.*165, 335–347. doi: 10.1016/s0926-860x(97)00216-0

Choudhary, V. R., Rajput, A. M., and Mamman, A. S. (1998a). NiO alkaline earth oxide catalysts for oxidative methane-to-syngas conversion: Influence of alkaline earth oxide on the surface properties and temperature-programmed reduction/reaction by H_2 and methane. *J. Catal.* 178, 576–585. doi: 10.1006/jcat.1998.2197

Choudhary, V. R., Rajput, A. M., Prabhakar, B., and Mamman, A. S. (1998b). Partial oxidation of methane to CO and H_2 over nickel and/or cobalt containing ZrO_2, ThO_2, UO_2, TiO_2, and SiO_2 catalysts. *Fuel* 77, 1803–1807. doi: 10.1016/s0016-2361(98)00072-6

Choudhary, V. R., Rane, V. H., and Rajput, A. M. (1993). Selective oxidation of methane to Co and H2 over unreduced Nio-rare earth oxide catalysts. *Catal. Lett.* 22, 289–297. doi: 10.1007/bf00807236

Claridge, J. B., Green, M. L. H., Tsang, S. C., York, A. P. E., Ashcroft, A. T., and Battle, P. D. (1993). A study of carbon deposition on catalysts during the partial oxidation of methane to synthesis gas. *Catal. Lett.* 22, 299–305. doi: 10.1007/bf00807237

Ding, C. M., Ai, G. G., Zhang, K., Yuan, Q. B., Han, Y. L., Ma, X. S., et al. (2015). Coking resistant Ni/ZrO_2@SiO_2 catalyst for the partial oxidation of methane to synthesis gas. *Int. J. Hydrogen Energy* 40, 6835–6843. doi: 10.1016/j.ijhydene.2015.03.094

Diskin, A. M., Cunningham, R. H., and Ormerod, R. M. Z. (1998). The oxidative chemistry of methane over supported nickel catalysts. *Catal. Today* 46, 147–154. doi: 10.1016/s0920-5861(98)00336-8

Dissanayake, D., Rosynek, M. P., Kharas, K. C. C., and Lunsford, J. H. (1991). Partial oxidation of methane to carbon-monoxide and hydrogen over a Ni/Al_2O_3 catalyst. *J. Catal.* 132, 117–127. doi: 10.1016/0021-9517(91)90252-y

Dong, W. S., Jun, K. W., Roh, H. S., Liu, Z. W., and Park, S. E. (2002). Comparative study on partial oxidation of methane over Ni/ZrO_2, Ni/CeO_2 and Ni/Ce-ZrO_2 catalysts. *Catal. Lett.* 78, 215–222. doi: 10.1023/a:1014905318290

Hickman, D. A., and Schmidt, L. D. (1992). The role of boundary-layer mass-transfer in partial oxidation selectivity. *J. Catal.* 136, 300–308. doi: 10.1016/0021-9517(92)90063-n

Hohn, K. L., and Schmidt, L. D. (2001). Partial oxidation of methane to syngas at high space velocities over Rh-coated spheres. *Appl. Catal. A Gen.* 211, 53–68. doi: 10.1016/s0926-860x(00)00835-8

Hu, Y. H., and Ruckenstein, E. (1998). Catalyst temperature oscillations during partial oxidation of methane. *Ind. Eng. Chem. Res.* 37, 2333–2335. doi: 10.1021/ie980027f

Hu, Y. H., and Ruckenstein, E. (2004). "Catalytic conversion of methane to synthesis gas by partial oxidation and CO_2 reforming," in *Advances in Catalysis*, Vol 48, eds B. C. Gates and H. Knozinger. (San Diego, CA: Elsevier Academic Press Inc), 297–345.

Ji, Y. Y., Li, W. Z., Xu, H. Y., and Chen, Y. X. (2001). A study of carbon deposition on catalysts during the catalytic partial oxidation of methane to syngas in a fluidized bed. *React. Kinet. Catal. Lett.* 73, 27–32. doi: 10.1023/a:1013952216199

Kirillov, V. A., Fedorova, Z. A., Danilova, M. M., Zaikovskii, V. I., Kuzin, N. A., Kuzmin, V. A., et al. (2011). Porous nickel based catalysts for partial oxidation of methane to synthesis gas. *Appl. Catal. A Gen.* 401, 170–175. doi: 10.1016/j.apcata.2011.05.018

Kogler, M., Kock, E. M., Perfler, L., Bielz, T., Stoger-Pollach, M., Hetaba, W., et al. (2014). methane decomposition and carbon growth on Y_2O_3, yttria-stabilized zirconia, and ZrO_2. *Chem. Mater.* 26, 1690–1701. doi: 10.1021/cm404062r

Kundakovic, L., and Flytzani-Stephanopoulos, M. (1998). Cu- and Ag-modified cerium oxide catalysts for methane oxidation. *J. Catal.* 179, 203–221. doi: 10.1006/jcat.1998.2213

Larimi, A. S., and Alavi, S. M. (2012). Ceria-Zirconia supported Ni catalysts for partial oxidation of methane to synthesis gas. *Fuel* 102, 366–371. doi: 10.1016/j.fuel.2012.06.050

Li, Y., Wang, X. X., and Song, C. S. (2016). Spectroscopic characterization and catalytic activity of Rh supported on CeO_2-modified Al_2O_3 for low-temperature steam reforming of propane. *Catal. Today* 263, 22–34. doi: 10.1016/j.cattod.2015.08.063

Lopez-Fonseca, R., Jimenez-Gonzalez, C., de Rivas, B., and Gutierrez-Ortiz, J. I. (2012). Partial oxidation of methane to syngas on bulk $NiAl_2O_4$ catalyst. Comparison with alumina supported nickel, platinum and rhodium catalysts. *Appl. Catal. A Gen.* 437, 53–62. doi: 10.1016/j.apcata.2012.06.014

Lu, Y., Xue, J. Z., Yu, C. C., Liu, Y., and Shen, S. K. (1998). Mechanistic investigations on the partial oxidation of methane to synthesis gas over a nickel-on-alumina catalyst. *Appl. Catal. A Gen.* 174, 121–128. doi: 10.1016/s0926-860x(98)00163-x

Miao, Q., Xiong, G. X., Sheng, S. S., Cui, W., Xu, L., and Guo, X. X. (1997). Partial oxidation of methane to syngas over nickel-based catalysts modified by alkali metal oxide and rare earth metal oxide. *Appl. Catal. A Gen.* 154, 17–27. doi: 10.1016/s0926-860x(96)00377-8

Navarro, R. M., Alvarez-Galvan, M. C., Villoria, J. A., Gonzalez-Jimenez, I. D., Rosa, F., and Fierro, J. L. G. (2007a). Effect of Ru on $LaCoO_3$ perovskite-derived catalyst properties tested in oxidative reforming of diesel. *Appl. Catal. B Environ.* 73, 247–258. doi: 10.1016/j.apcatb.2006.12.013

Navarro, R. M., Pena, M. A., and Fierro, J. L. G. (2007b). Hydrogen production reactions from carbon feedstocks: fossils fuels and biomass. *Chem. Rev.* 107, 3952–3991. doi: 10.1021/cr0501994

Nguyen, T. H., Lamacz, A., Krzton, A., Liszka, B., and Djega-Mariadassou, G. (2016). Partial oxidation of methane over Ni-0/La_2O_3 bifunctional catalyst III. Steady state activity of methane total oxidation, dry reforming, steam reforming and partial oxidation. sequences of elementary steps. *Appl. Catal. B Environ.* 182, 385–391. doi: 10.1016/j.apcatb.2015.09.016

Nishimoto, H., Nakagawa, K., Ikenaga, N., Nishitani-Gamo, M., Ando, T., and Suzuki, T. (2004). Partial oxidation of methane to synthesis gas over oxidized diamond catalysts. *Appl. Catal. A Gen.* 264, 65–72. doi: 10.1016/j.apcata.2003.12.029

Nurunnabi, M., Fujimoto, K., Suzuki, K., Li, B. T., Kado, S., Kunimori, K., et al. (2006). Promoting effect of noble metals addition on activity and resistance to carbon deposition in oxidative steam reforming of methane over NiO-MgO solid solution. *Catal. Commun.* 7, 73–78. doi: 10.1016/j.catcom.2005.09.002

Ocsachoque, M. A., Russman, J. I. E., Irigoyen, B., Gazzoli, D., and Gonzalez, M. G. (2016). Experimental and theoretical study about sulfur deactivation of Ni/CeO_2 and Rh/CeO_2 catalysts. *Mater. Chem. Phys.* 172, 69–76. doi: 10.1016/j.matchemphys.2015.12.062

Ostrowski, T., Giroir-Fendler, A., Mirodatos, C., and Mleczko, L. (1998). Comparative study of the catalytic partial oxidation of methane to synthesis gas in fixed-bed and fluidized-bed membrane reactors - part I: a modeling approach. *Catal. Today* 40, 181–190. doi: 10.1016/s0920-5861(98)00006-6

Ozdemir, H., Oksuzomer, M. A. F., and Gurkaynak, M. A. (2010). Preparation and characterization of Ni based catalysts for the catalytic partial oxidation of methane: effect of support basicity on H_2/CO ratio and carbon deposition. *Int. J. Hydrogen Energy* 35, 12147–12160. doi: 10.1016/j.ijhydene.2010.08.091

Pantaleo, G., La Parola, V., Deganello, F., Calatozzo, P., Bal, R., and Venezia, A. M. (2015). Synthesis and support composition effects on CH_4 partial oxidation over Ni-CeLa oxides. *Appl. Catal. B Environ.* 164, 135–143. doi: 10.1016/j.apcatb.2014.09.011

Pantaleo, G., La Parola, V., Deganello, F., Singha, R. K., Bal, R., and Venezia, A. M. (2016). Ni/CeO_2 catalysts for methane partial oxidation: Synthesis driven structural and catalytic effects. *Appl. Catal. B Environ.* 189, 233–241. doi: 10.1016/j.apcatb.2016.02.064

Pena, M. A., Gomez, J. P., and Fierro, J. L. G. (1996). New catalytic routes for syngas and hydrogen production. *Appl. Catal. A Gen.* 144, 7–57. doi: 10.1016/0926-860x(96)00108-1

Pengpanich, S., Meeyoo, V., and Rirksomboon, T. (2004). Methane partial oxidation over Ni/CeO_2-ZrO_2 mixed oxide solid solution catalysts. *Catal. Today* 93–5, 95–105. doi: 10.1016/j.cattod.2004.06.079

Pokrovski, K., Jung, K. T., and Bell, A. T. (2001). Investigation of CO and CO_2 adsorption on tetragonal and monoclinic zirconia. *Langmuir* 17, 4297–4303. doi: 10.1021/la001723z

Pompeo, F., Nichio, N. N., Ferretti, O. A., and Resasco, D. (2005). Study of Ni catalysts on different supports to obtain synthesis gas. *Int. J. Hydrog. Energy* 30, 1399–1405. doi: 10.1016/j.ijhydene.2004.10.004

Poncelet, G., Centeno, M. A., and Molina, R. (2005). Characterization of reduced alpha-alumina-supported nickel catalysts by spectroscopic and chemisorption measurements. *Appl. Catal. A Gen.* 288, 232–242. doi: 10.1016/j.apcata.2005.04.052

Puolakka, K. J., and Krause, A. O. I. (2007). Combined CO_2 reforming and partial oxidation of fuel compounds. *Catal. Lett.* 116, 87–93. doi: 10.1007/s10562-007-9112-y

Requies, J., Cabrero, M. A., Barrio, V. L., Guemez, M. B., Cambra, J. F., Arias, P. L., et al. (2005). Partial oxidation of methane to syngas over Ni/MgO and Ni/La_2O_3 catalysts. *Appl. Catal. A Gen.* 289, 214–223. doi: 10.1016/j.apcata.2005.05.002

Rostrup-Nielsen, J. R., Sehested, J., and Norskov, J. K. (2002). "Hydrogen and synthesis gas by steam- and CO_2 reforming," in *Advances in Catalysis,* Vol 47, eds B. C. Gates and H. Knozinger (San Diego, CA: Elsevier Academic Press Inc), 65–139.

Ruckenstein, E., and Hu, Y. H. (1999). Methane partial oxidation over NiO MgO solid solution catalysts. *Appl. Catal. A Gen.* 183, 85–92. doi: 10.1016/s0926-860x(99)00047-2

Ruckenstein, E., and Wang, H. Y. (1999). Effect of support on partial oxidation of methane to synthesis gas over supported rhodium catalysts. *J. Catal.* 187, 151–159. doi: 10.1006/jcat.1999.2593

Sathyaseelan, B., Baskaran, I., and Sivakumar, K. (2013). Phase transition behavior of nanocrystalline Al_2O_3 Powders. *Soft Nanosci. Lett.* 69–74.

Sing, K. S. W., Everett, D. H., Haul, R. A. W., Moscou, L., Pierotti, R. A., Rouquerol, J., et al. (1985). Reporting physisorption data for gas solid systems with special reference to the determination of surface-area and porosity (recommendations 1984). *Pure Appl. Chem.* 57, 603–619. doi: 10.1351/pac198557040603

Singha, R. K., Shukla, A., Yadav, A., Adak, S., Iqbal, Z., Siddiqui, N., et al. (2016). Energy efficient methane tri-reforming for synthesis gas production over highly coke resistant nanocrystalline Ni-ZrO_2 catalyst. *Appl. Energy* 178, 110–125. doi: 10.1016/j.apenergy.2016.06.043

Song, Y. Q., He, D. H., and Xu, B. Q. (2008). Effects of preparation methods of ZrO_2 support on catalytic performances of Ni/ZrO_2 catalysts in methane partial oxidation to syngas. *Appl. Catal. A Gen.* 337, 19–28. doi: 10.1016/j.apcata.2007.11.032

Takehira, K., Shishido, T., Wang, P., Kosaka, T., and Takaki, K. (2004). Autothermal reforming of CH_4 over supported Ni catalysts prepared from Mg-Al hydrotalcite-like anionic clay. *J. Catal.* 221, 43–54. doi: 10.1016/j.jcat.2003.07.001

Tanaka, H., Kaino, R., Nakagawa, Y., and Tomishige, K. (2010a). Comparative study of Rh/MgO modified with Fe, Co or Ni for the catalytic partial oxidation of methane at short contact time. Part II: catalytic performance and bed temperature profile. *Appl. Catal. A Gen.* 378, 187–194. doi: 10.1016/j.apcata.2010.02.018

Tanaka, H., Kaino, R., Okumura, K., Kizuka, T., Nakagawa, Y., and Tomishige, K. (2010b). Comparative study of Rh/MgO modified with Fe, Co or Ni for the catalytic partial oxidation of methane at short contact time. Part I: characterization of catalysts. *Appl. Catal. A Gen.* 378, 175–186. doi: 10.1016/j.apcata.2010.02.017

Tang, S., Lin, J., and Tan, K. L. (1998). Partial oxidation of methane to syngas over Ni/MgO, Ni/CaO and Ni/CeO_2. *Catal. Lett.* 51, 169–175. doi: 10.1023/a:1019034412036

Tomishige, K., Kanazawa, S., Sato, M., Ikushima, K., and Kunimori, K. (2002). Catalyst design of pt-modified Ni/Al_2O_3 catalyst with flat temperature profile in methane reforming with CO_2 and O_{-2}. *Catal. Lett.* 84, 69–74. doi: 10.1023/a:1021076601653

Trovarelli, A. (1996). Catalytic properties of ceria and CeO_2-containing materials. *Catal. Rev. Sci. Eng.* 38, 439–520. doi: 10.1080/01614949608006464

Tsipouriari, V. A., Zhang, Z., and Verykios, X. E. (1998). Catalytic partial oxidation of methane to synthesis gas over Ni-based catalysts - I. Catalyst performance characteristics. *J. Catal.* 179, 283–291. doi: 10.1006/jcat.1998.2182

Vernon, P. D. F., Green, M. L. H., Cheetham, A. K., and Ashcroft, A. T. (1990). Partial oxidation of methane to synthesis gas. *Catal. Lett.* 6, 181–186. doi: 10.1007/bf00774718

Wang, H. T., Li, Z. H., and Tian, S. X. (2004). Effect of promoters on the catalytic performance of Ni/$A_{l2}O_3$ catalyst for partial oxidation of methane to syngas. *React. Kinet. Catal. Lett.* 83, 245–252. doi: 10.1023/B:REAC.0000046083.76225.a0

Wang, H. Y., and Ruckenstein, E. (2001). Conversions of methane to synthesis gas over Co/gamma-Al_2O_3 by CO_2 and/or O_2. *Catal. Lett.* 75, 13–18. doi: 10.1023/a:1016719703118

Wang, Y. H., Liu, H. M., and Xu, B. Q. (2009a). Durable Ni/MgO catalysts for CO_2 reforming of methane: activity and metal-support interaction. *J. Mol. Catal. A Chem.* 299, 44–52. doi: 10.1016/j.molcata.2008.09.025

Wang, Y. Q., Wang, W. J., Hong, X. B., and Li, B. B. (2009b). Zirconia promoted metallic nickel catalysts for the partial oxidation of methane to synthesis gas. *Catal. Commun.* 10, 940–944. doi: 10.1016/j.catcom.2008.12.034

Zhang, X. P., Zhang, Q. D., Tsubaki, N., Tan, Y. S., and Han, Y. Z. (2015). "Influence of zirconia phase on the performance of Ni/ZrO_2 for carbon dioxide reforming of methane," in *Advances in Co_2 Capture, Sequestration, and Conversion,* eds F. Jin, L. N. He, and Y. H. Hu (Washington, DC: Amer Chemical Soc), 135–153.

Zhang, Y. H., Xiong, G. X., Sheng, S. S., and Yang, W. S. (2000). Deactivation studies over NiO/gamma-Al_2O_3 catalysts for partial oxidation of methane to syngas. *Catal. Today* 63, 517–522. doi: 10.1016/s0920-5861(00)00498-3

Zhang, Y. W., Zhou, J. H., Chen, Y., Wang, Z. H., Liu, J. Z., and Cen, K. F. (2008). Hydrogen iodide decomposition over nickel-ceria catalysts for hydrogen production in the sulfur-iodine cycle. *Int. J. Hydrogen Energy* 33, 5477–5483. doi: 10.1016/j.ijhydene.2008.07.007

Conflict of Interest Statement: The authors declare that the research was conducted in the absence of any commercial or financial relationships that could be construed as a potential conflict of interest.

frontiers in Chemistry

ORIGINAL RESEARCH
published: 12 March 2019
doi: 10.3389/fchem.2019.00114

Pt/CeO$_2$ and Pt/CeSnO$_x$ Catalysts for Low-Temperature CO Oxidation Prepared by Plasma-Arc Technique

Tatyana Y. Kardash[1,2]*, Elizaveta A. Derevyannikova[1], Elena M. Slavinskaya[1,2], Andrey I. Stadnichenko[1,2], Vasiliy A. Maltsev[3], Alexey V. Zaikovskii[3], Sergey A. Novopashin[3], Andrei I. Boronin[1,2]* and Konstantin M. Neyman[4,5,6]*

[1] Boreskov Institute of Catalysis, Siberian Branch of the Russian Academy of Sciences, Novosibirsk, Russia, [2] Novosibirsk State University, Novosibirsk, Russia, [3] Kutateladze Institute of Thermophysics, Siberian Branch of the Russian Academy of Sciences, Novosibirsk, Russia, [4] Departament de Ciència dels Materials i Química Física, Universitat de Barcelona, Barcelona, Spain, [5] Institut de Química Teòrica i Computacional, Universitat de Barcelona, Barcelona, Spain, [6] ICREA (Institució Catalana de Recerca i Estudis Avançats), Barcelona, Spain

OPEN ACCESS

Edited by:
Javier Carrasco,
CIC energigune, Spain

Reviewed by:
Arturo Martinez-Arias,
Instituto de Catálisis y Petroleoquímica (ICP), Spain
Jose A. Rodriguez,
Brookhaven National Laboratory (DOE), United States

***Correspondence:**
Tatyana Yu. Kardash
kardash@catalysis.ru
Andrei I. Boronin
boronin@catalysis.ru
Konstantin M. Neyman
konstantin.neyman@icrea.cat

Specialty section:
This article was submitted to Physical Chemistry and Chemical Physics,
a section of the journal Frontiers in Chemistry

Received: 26 November 2018
Accepted: 13 February 2019
Published: 12 March 2019

Citation:
Kardash TY, Derevyannikova EA, Slavinskaya EM, Stadnichenko AI, Maltsev VA, Zaikovskii AV, Novopashin SA, Boronin AI and Neyman KM (2019) Pt/CeO$_2$ and Pt/CeSnO$_X$ Catalysts for Low-Temperature CO Oxidation Prepared by Plasma-Arc Technique. Front. Chem. 7:114.
doi: 10.3389/fchem.2019.00114

We applied a method of plasma arc synthesis to study effects of modification of the fluorite phase of ceria by tin ions. By sputtering active components (Pt, Ce, Sn) together with carbon from a graphite electrode in a helium ambient we prepared samples of complex highly defective composite PtCeC and PtCeSnC oxide particles stabilized in a matrix of carbon. Subsequent high-temperature annealing of the samples in oxygen removes the carbon matrix and causes the formation of active catalysts Pt/CeO$_x$ and Pt/CeSnO$_x$ for CO oxidation. In the presence of Sn, X-Ray Diffraction (XRD) and High-Resolution Transmission Electron Microscopy (HRTEM) show formation of a mixed phase CeSnO$_x$ and stabilization of more dispersed species with a fluorite-type structure. These factors are essential for the observed high activity and thermic stability of the catalyst modified by Sn. X-Ray Photoelectron Spectroscopy (XPS) reveals the presence of both Pt^{2+} and Pt^{4+} ions in the catalyst Pt/CeO$_x$, whereas only the state Pt^{2+} of platinum could be detected in the Sn-modified catalyst Pt/CeSnO$_x$. Insertion of Sn ions into the Pt/CeO$_x$ lattice destabilizes/reduces Pt^{4+} cations in the Pt/CeSnO$_x$ catalyst and induces formation of strikingly high concentration (up to 50% at.) of lattice Ce^{3+} ions. Our DFT calculations corroborate destabilization of Pt^{4+} ions by incorporation of cationic Sn in Pt/CeO$_x$. The presented results show that modification of the fluorite lattice of ceria by tin induces substantial amount of mobile reactive oxygen partly due to affecting geometric parameters of ceria by tin ions.

Keywords: platinum, ceria, tin, CO oxidation, plasma arc synthesis, DFT calculations, Pt/CeO$_2$ catalyst

INTRODUCTION

Pollution of biosphere with toxic emissions is becoming increasingly urgent due to the rapid increase in electric and thermal power production, the production growth in metallurgical and chemical industries as well as growing number of vehicles. Among the most effective methods of solving this problem is efficient catalytic oxidation of CO and hydrocarbons (Farrauto and Bartholomew, 1997; Muraki and Zhang, 2000). The increasing restrictions of the standards for the automotive emissions require either improvement of existing catalysts or creation of fundamentally new ones (Trovarelli, 1996; Montini et al., 2016; Trovarelli and Llorca, 2017).

Broadening temperature ranges of catalysts action and maintaining their activity are important challenges therefore. In this regard, the use of conventional three-component formulations based on PGM-CeO_2-MO_x (where PGM are platinum group metals and MO_x are modifying metal oxides) is still promising for catalytic oxidation of CO and hydrocarbons. Palladium is the most commonly used PGM. It is characterized as a PGM very strongly interacting with CeO_2. According to Fornasiero et al. (Cargnello et al., 2012; Monai et al., 2015), PdO nanoparticles decorated with cerium oxide (core-shell structures Pd@CeO_2) are promising materials for the efficient oxidation of methane and other hydrocarbons. Such Pd@CeO_2 structures are capable of oxidizing methane at 200–250°C. However, Farrauto (Farrauto, 2012) pointed out that due to the phase transition PdO-Pd at ∼800°C the creation of thermally stable ($T > 800°C$) catalysts on the basis of this Pd form is difficult. Such a conclusion emphasizes the importance of the strong metal-support interaction (SMSI) effect for palladium, platinum and other PGMs for creation of thermally stable catalysts (Figueroba et al., 2016, 2017; Lykhach et al., 2017a).

The realization of the SMSI effect in PGM-CeO_2 systems depends crucially on the synthesis procedure. Different synthetic approaches are used to obtain PGM-CeO_2 catalysts with desired improved characteristics (Boronin et al., 2009; Gulyaev et al., 2012, 2014b; Slavinskaya et al., 2015, 2016, 2018; Vasilchenko et al., 2016; Derevyannikova et al., 2017; Kardash et al., 2017; Kibis et al., 2017). Novel physical preparation methods that utilize the action of thermal and electrical fields, such as laser ablation, magnetron sputtering, "solution-combustion" and plasma methods attracted attention of many research groups (Bera et al., 2003; Baidya et al., 2009; Hegde et al., 2009; Gupta and Hegde, 2010; Hinokuma et al., 2014; Slavinskaya et al., 2016, 2018; Vasilchenko et al., 2016; Stadnichenko et al., 2018, 2019). These methods allow obtaining of highly dispersed PGM forms (ions and clusters) on the surface and inside ceria, which ensures the maximal SMSI effect and appearance of new highly active surface species.

Recently we have developed and applied a plasma-arc method (PAS) for synthesis of Pd/CeO_2 catalysts (Gulyaev et al., 2014b; Kardash et al., 2017). The PAS method is based on the sputtering of a specific anode material in a vacuum chamber filled with an inert gas under action of a plasma arc discharge. The anode material consists of a graphite rod, in the center of which a mixture of dispersed carbon and PGM metal powders, cerium and/or other components is placed. Sputtering of the anode leads to the appearance of atomic components of carbon and atomically dispersed metals in the arc. Diffusion and convection of the components in a buffer gas leads to their heterogeneous condensation. The condensation products are deposited on the cooled screen. The synthesized material consists of nanoparticles embedded in a carbon matrix. Subsequent high-temperature annealing in oxygen converts the synthesized carbon-based composite into an active oxide catalyst for low-temperature CO oxidation (LTO CO).

The aim of this work was to establish, weather the PAS method also allows obtaining joint phase of Pt and CeO_2, where Pt is in a highly dispersed ionic state similar to that of Pd in the Pd-doped CeO_2 joint phase $Pd_xCe_{1-x}O_{2-\delta}$ (Primavera et al., 1998; Priolkar et al., 2002; Scanlon et al., 2011; Gulyaev et al., 2014a; Neitzel et al., 2016). Assuming that stable Pt^{2+} and Pt^{4+} (Bruix et al., 2014) species are formed in the PAS synthesis, it was important to determine concentration of these in the prepared samples and their influence on the catalytic activity

In order to increase the thermal stability and redox ability of the catalysts, Sn was used as a modifying element of the catalysts. Sn^{4+} is assumed to substitute Pt^{4+} and Ce^{4+} in the fluorite structure (Matolín et al., 2008; Zeng et al., 2012; Ayastuy et al., 2014). The formation of the joint $Ce_{1-x}Sn_xO_y$ phase was expected to promote the generation of defects and oxygen vacancies in the prepared samples of catalysts, thus increasing their oxygen storage capacity (OSC) and the catalytic activity in LTO CO (Tolla et al., 1999; Nguyen et al., 2003; Gupta et al., 2010). Our previous studied of the Pd/CeO_2-SnO_{2-x} catalysts showed that introduction of Sn into PdCeC formulations during the PAS synthesis formed nano-heterogeneous composites after calcination of the PdCeSnC composite. The obtained catalysts were stable against sintering and crystallization to large particles (Kardash et al., 2017). As a result, LTO CO activity was preserved even after calcination at 1,000°C. One of the objectives of this study was to determine the thermal stability of composite Pt/CeO_2-SnO_2 catalysts and to compare their catalytic properties with those of the unmodified by Sn Pt/CeO_2 catalysts prepared under the same PAS conditions.

Also in this paper we present density functional (DFT) calculations of platinum species stabilized either by pure ceria nanoparticles or ceria nanoparticles modified by tin ions. The calculations of these models allowed establishing the most stable structures and the effect of tin substitution on the properties of Pt/CeO_2 nanoparticles. Our DFT calculations corroborate the effect of embedded tin on the state of platinum ions in the CeO_2 lattice.

Obtained experimental and theoretical data showed that the PAS method allows obtaining highly defective ceria particles and ionic platinum species. Modification with tin leads to increased thermal stability of platinum catalysts, higher amount of reactive oxygen in the catalysts and enhanced catalytic activity of the latter in the low-temperature regime of CO oxidation.

EXPERIMENTAL

Catalysts Synthesis

PAS method was applied to obtain PtCeC and PtCeSnC composite materials. We refer to the detailed description of the procedure in our previous work (Kardash et al., 2017). To obtain oxide catalysts, the synthesized PtCe(Sn)C composites were calcined in air at 600, 800, and 900°C. **Table 1** presents the chemical composition and characteristics of the obtained Pt/Ce and Pt/CeSn catalysts.

Methods

The Specific Surface

The specific surface (SBET) of the samples was determined by BET method (Lowell et al., 2006), using argon thermal desorption with a Sorbtometr-M adsorption analyzer.

TABLE 1 | Chemical compositions and BET specific surface area of the prepared samples.

Sample	Chemical composition, % wt*			S_{BET}, m^2/g			
	Pt	CeO_2	SnO_2	600°C	700°C	800°C	900°C
Pt/Ce	4.6	88	–	110	71	48	10
Pt/CeSn	2.4	12	79	60	39	27	16

**The rest is carbon and water.*

Analysis of the Chemical Composition

Analysis of the chemical composition was performed by X-ray fluorescence (XRF) method on an ARL PERFORM analyzer with a Rh anode of an X-ray tube. Chemical compositions of tin and cerium oxides were determined using calibrations; the determination of Pt was carried out using the external standard method.

X-Ray Diffraction (XRD)

X-ray diffraction (XRD) patterns were recorded on a Bruker D8 Advance instrument using CuKα radiation and the Bragg-Brentano focusing geometry. The aperture of the Soller slits on the primary and reflected beams was 2.5°. LynxEye (Bruker) multi strip detector was employed for intensity measurements. Data acquisition was performed in the 2θ range of 15–100°, at a 0.05° step and counting time of 2 s. Phase analysis was carried out using the ICDD PDF 2 database (Powder Diffraction File PDF-2. International Center for Diffraction Data. USA. 2009). Structural data were taken from the structural database ICSD (Hellenbrandt, 2004). Rietveld refinement for quantitative analysis was carried out with the help of the software package Topas V.4.3 (Coelho, 2005). The instrumental broadening was described with metallic silicon as a reference material. The diffraction line profiles were analyzed using the fundamental parameter approach. The lengths of coherent scattering domain were calculated from LVol-IB values (i.e., volume weighted mean column lengths based on integral breadth).

Electron Microscopy

Electron microscopy investigation was performed using JEM-2010 (JEOL Ltd., Japan) and JEM-2200FS (JEOL Ltd., Japan) electron microscopes operated at 200 kV for obtaining High Resolution Transmission Electron Microscopy (HRTEM) images. High-Angle Annular Dark-Field mode in a Scanning Transmission Electron Microscope (STEM HAADF) was employed together with Energy Dispersive X-ray (EDX) spectroscopy. Samples for the TEM study were prepared on the perforated carbon film mounted on a copper grid.

Temperature Programmed Reaction With CO (TPR-CO)

The reaction mixture containing 1.0 vol.% CO, 0.5 vol.% Ne in flowing He was fed at a rate of 100 cm^3/min to the catalyst sample (0.2 g) preliminary cooled in the reactor to −10°C. As the steady-state concentrations of CO and CO_2 were established, the sample was heated from −10 to 450°C at 10°C/min heating rate. The concentrations of CO, CO_2, O_2, H_2, and H_2O were measured during the reaction. Before each TPR-CO experiment the catalysts were pretreated by 20%O_2/He gas mixture at 450°C during 2 h with subsequent cooling in this gas mixture. After the cooling the catalysts were purged in helium.

Investigation of Catalytic Properties

Investigation of catalytic properties of the synthesized samples was performed in an automated setup with a flow reactor and mass-spectrometric analysis of the gas mixture using the temperature-programmed reaction (TPR-CO-O_2). A sample with the particle sizes of 0.25–0.5 mm was mounted in a stainless steel reactor. The reaction mixture containing 0.2 vol.% CO, 1.0 vol.% O_2, 0.5 vol.% Ne in flowing He was fed at a rate of 1,000 cm^3/min to the initial catalyst cooled to −10°C. For the Pt/Ce catalysts calcined at 600, 700, 800, and 900°C weight of samples employed for catalytic testing was 0.3, 0.36, 0.4, and 0.62 g, respectively; for the Pt/CeSn catalysts calcined at 600, 700, 800, and 900°C −0.3, 0.34, 0.35, and 0.34 g. The catalyst was heated in the reaction mixture from −10 to 450°C at a rate of 10°C/min with subsequent cooling and repeated heating in the reaction mixture. The concentrations of CO, O_2, and CO_2 were monitored in the course of reaction at a frequency of 0.34 Hz.

X-Ray Photoelectron Spectroscopy (XPS)

X-ray photoelectron spectroscopy (XPS) measurements used an ES-300 (KRATOS Analytical) photoelectron spectrometer equipped with a MgKα ($h\nu = 1253.6$ eV) radiation source. The spectrometer was calibrated using the Au4$f_{7/2}$ (84.0 eV) and Cu2$p_{3/2}$ (932.7 eV) lines of pure metallic surfaces of Au and Cu, respectively. The U''' component of the Ce3d spectral line (E_b = 916.7 eV) served as a standard for calibration of XPS spectra. The program of processing spectral data created by us, XPS-Calc, was used for the mathematical treatment of the XPS spectra. This software has previously been applied for different systems, including Pt/CeO_2 and Pt/Al_2O_3 catalysts (Ivanova et al., 2010; Svintsitskiy et al., 2015; Stadnichenko et al., 2017, 2019). The Shirley model and the Gauss–Lorentz functions were used for background subtraction and curve fitting, respectively.

DFT Calculations

DFT calculations were carried out employing PW91 exchange-correlation functional (Perdew et al., 1992) in the plane-wave VASP code (Kresse and Hafner, 1993) for periodic boundary conditions. Plane-wave basis sets with a cut-off energy of 415 eV were used. Core-valence electron interactions were described by projector-augmented wave method (Kresse and Joubert, 1999). In order to properly localize Ce4f electrons in partially reduced Ce^{3+} ions, an on-site Coulombic correction (U_{eff} = 4.0 eV) (Anisimov et al., 1997; Dudarev et al., 1998; Loschen et al., 2007) was applied to 4f electrons in all Ce atoms. Our Pt- and Sn-containing models (see **Supplementary Material**) were based on a model stoichiometric ceria nanoparticle $Ce_{40}O_{80}$ ca. 1.5 nm large (Migani et al., 2010). Our previous calculations of this type of models resulted in several predictions subsequently confirmed experimentally (Bruix and Neyman, 2016, 2019). Each model nanoparticle was positioned in a rectangular periodically repeated cell of 2.2 × 1.9 × 1.9 nm. Spin-polarized Γ-point calculations of all model nanoparticles under scrutiny were performed with the single-point total energy convergence tolerance of 2×10^{-5} eV. Optimization of positions of all atoms constituting a given model was continued until the maximum forces acting on each atom were <0.02 eV/Å.

RESULTS

TEM Study of the As-Prepared by Plasma-Arc Synthesis PtCeC and PtCeSnC Composites

The composite material PtCeC obtained by PAS consists of highly dispersed nanoparticles embedded within a matrix of amorphous carbon. **Figure 1** shows typical TEM images of this material with 1 to 10 nm large nanoparticles. The analysis of interatomic distances features that nanoparticle structure corresponds to Ce_2O_3 (ICDD PDF-2 #00-023-1048). The reflections on the Fourier image displayed in **Figure 1B** reveal the interplanar distances of 0.32 and 0.3316 nm corresponding to the (002) and (100) reflections of a Ce_2O_3 trigonal structure. We detected a similar microstructure for a PdCeC composite prepared by PAS (Gulyaev et al., 2014b).

Morphology of the as-prepared PtCeSnC composite is characterized by the presence of two types of nanoparticles: a highly dispersed fraction with sizes 1–10 nm and a fraction of larger particles with sizes from 10 to 40 nm. **Figure 2A** shows typical images of the PtCeSnC composite.

Larger particles (see **Figure 2B**) exhibit a core-shell-shell structure. The outer shell has lower density than the core and is built of amorphous carbon. The core of the particles contains tin. The analysis of the crystalline structure of the inner particle core shows the distance 0.3 nm, which could be assigned to different phases: SnO_2 (Pbcn) [0.30 nm (113)], SnO (P4/nmm) [0.299 nm (101)], Sn ($I4_1$/amd) [0.29 nm (200)], see **Figure 2C**. The next crystalline shell of the particles shows the distances of 0.31 and 0.33 nm, which are unambiguously related to the (113) and (112) reflections of SnO_2 (Pbcn). The observation of higher density of the particle core suggests that the core structure is related to Sn. Hence, a large fraction of the core-shell-shell particles appears to feature a composition Sn-SnO_2-C, where C is amorphous carbon.

Structural analysis of the dispersed particles of the as-prepared PtCeSnC composite showed the distances of 0.3 nm and 0.29 nm, which could be related to (002) and (101) reflections of the Ce_2O_3 correspondently, see **Figure 2D**.

Characterization of the Calcined Pt/Ce and Pt/CeSn Samples

Our earlier studies of catalysts prepared by PAS (Kardash et al., 2017) showed that calcination at temperatures above 600°C causes burning of carbon in PtCeC and PtCeSnC composites and transforms them into oxide materials. The chemical composition analysis was performed for the calcined samples (see **Table 1**). One can see that after calcination at 600–800°C the Pt/Ce sample exhibits a higher specific surface area than the Pt/CeSn sample. However, after calcination at 900°C the specific surface area of the Pt/CeSn sample becomes higher than that of the Pt/Ce sample, which indicates a stabilizing effect of Sn preventing particle sintering.

Figure 3 presents XRD patterns of the calcined Pt/Ce and Pt/CeSn samples. **Table 2** shows the results of a quantitative phase analysis obtained by the Rietveld refinement of the XRD data.

CeO_2 phase with a fluorite-type structure is a major component in the Pt/Ce sample. The lattice parameter of the fluorite phase and mean particle size estimated from the XRD data are shown in **Table 2**. For the Pt/CeSn sample, the oxides SnO_2 (cassiterite, ICDD PDF-2 #00-034-0394) and CeO_2 (ICDD PDF #00-029-1484) are the major phases. Note, that the CeO_2 fluorite phase exhibits smaller particles in the Pt/CeSn sample compared to the Pt/Ce sample for all calcination temperatures. This observation implies that addition of SnO_2 to the composite allows stabilizing the CeO_2 particle size against sintering.

Additional peaks were detected in the Pt/CeSn sample, corresponding to the unstable orthorhombic SnO_2 phase (ICDD PDF-2 #04-015-3275). According to the literature data, this form of SnO_2 can be built at high pressures and temperatures (Gracia et al., 2007). The fraction of the orthorhombic SnO_2 phase is decreased upon sample calcination. We assume that this unstable phase can result from a rapid oxidation of the PtSnCeC composites, when they are exposed to the atmosphere upon taking out of the synthesis chamber. This phase could be stabilized by the carbon matrix within core-shell-shell nanoparticles. However, the subsequent calcination of the composite transforms it into a stable cassiterite phase.

Metallic Pt phase was not detected in the samples calcined at 600°C. Peaks corresponding to metallic Pt appear on the XRD patterns only after calcination of the Pt/CeSn sample at 700°C and of the Pt/Ce sample at 900°C. However, the Rietveld refinement shows that the content of metallic Pt is lower than the analytical amount of Pt in the sample. This indicates the presence of Pt in highly dispersed states in the samples calcined at 600°C and even higher temperatures.

Total amount of SnO_2 in the Pt/CeSn sample is less than detected by the XRF analysis. It implies that a part of Sn is embedded in the CeO_2 lattice. This assumption is supported by decreasing of the fluorite lattice parameter from 5.411 Å for CeO_2 in the Pt/Ce sample to 5.401 Å in the Pt/CeSn sample. Relying on the difference in the radii of the Ce^{4+}/Ce^{3+} cations and Sn^{4+} cations, it is possible to estimate the composition of the $Ce_{1-x}Sn_xO_y$ joint fluorite phase. For the Pt/CeSn-600 sample, the estimated composition of the fluorite phase is

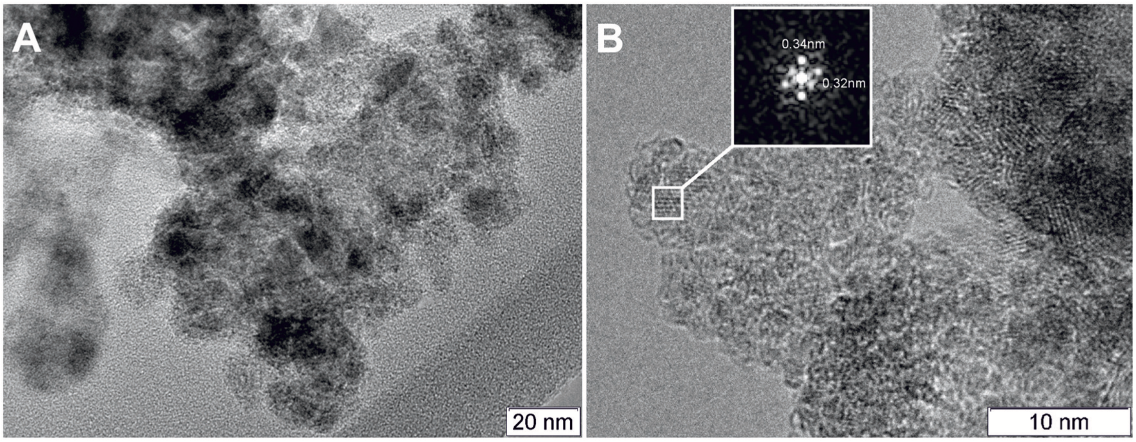

FIGURE 1 | TEM image of the PtCeC composite **(A)** and Fourier image of the crystal lattice of a nanoparticle **(B)**.

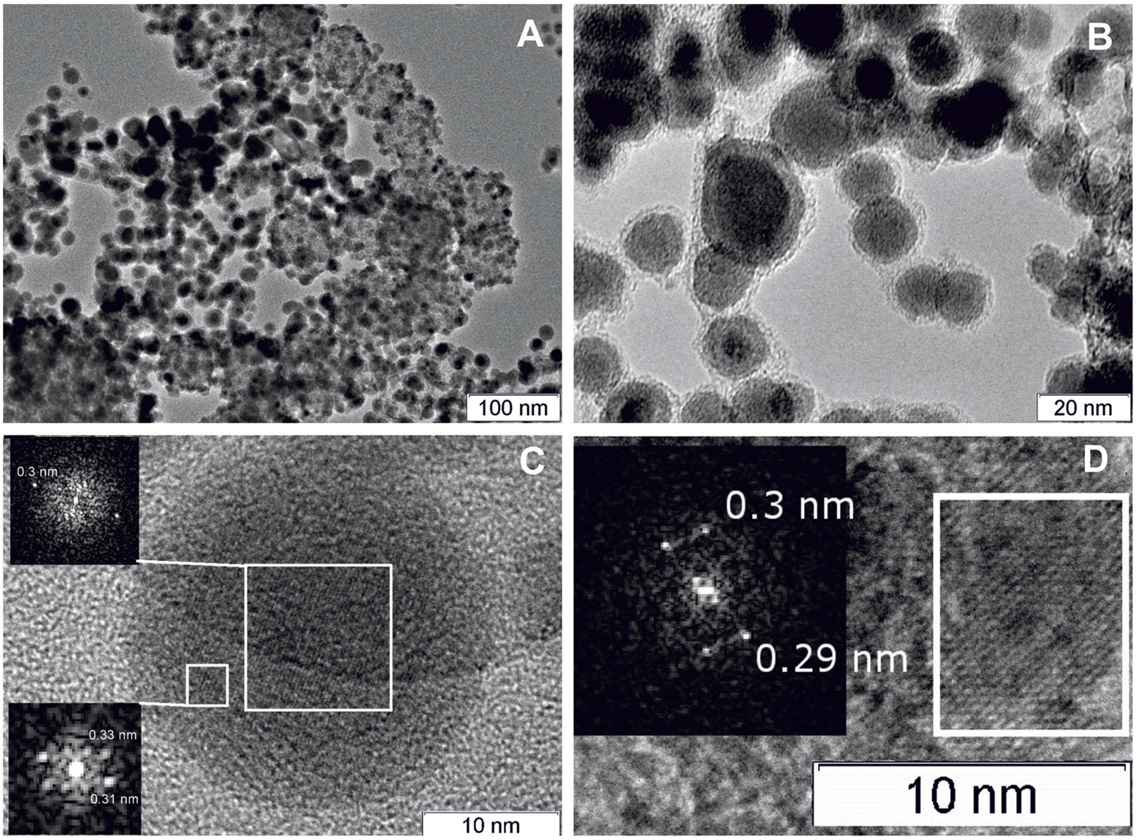

FIGURE 2 | TEM image of the PtCeSnC composite **(A)**, TEM image of large core-shell-shell particles **(B)**. HRTEM image and Fourier image of the lattice of core-shell-shell particles Sn@SnO$_2$@C **(C)**. HRTEM image and Fourier image of the crystal lattice of small Ce$_2$O$_3$ particles within amorphous carbon matrix **(D)**.

$Ce_{0.93}Sn_{0.07}O_{2-\delta}$. However, the so determined tin content in the fluorite structure is underestimated, since the calculation did not take into account that the fluorite lattice parameter can increase with decreasing particle size to 1–3 nm (Tsunekawa et al., 2004; Baranchikov et al., 2010).

In line with these considerations, the nearest 8 Sn-O and 8 Sn-Ce distances calculated by DFT for the model tin-doped nanoparticles $SnCe_{39}O_{80}$ and Pt/$SnCe_{39}O_{80}$ with Sn^{4+} dopant located in an inner Ce^{4+} position are shorter than the corresponding Ce-O and Ce-Ce distances in the pristine

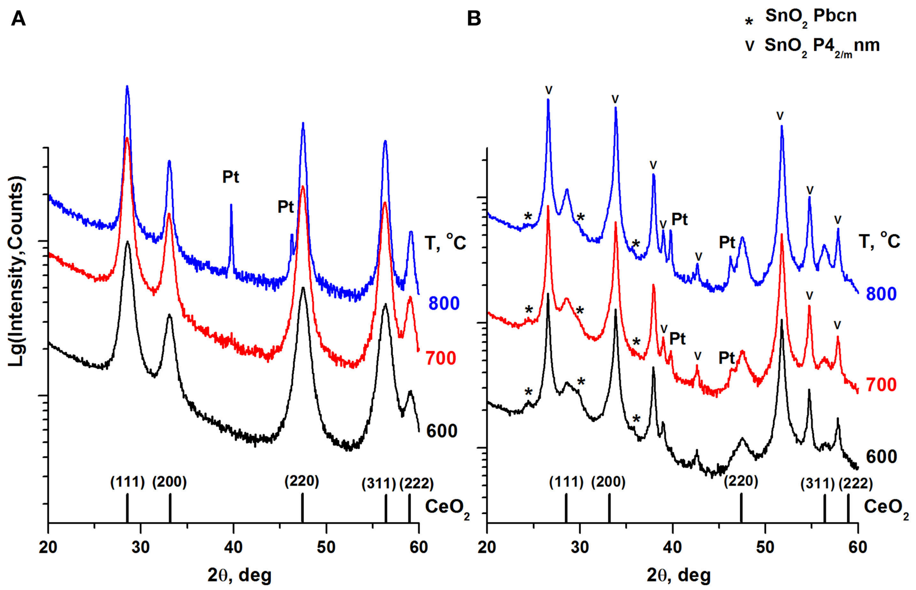

FIGURE 3 | XRD patterns of the Pt/Ce **(A)** and Pt/CeSn **(B)** samples calcined at different temperatures. The graph at the bottom shows the positions of CeO$_2$ fluorite phase reflections and corresponding Miller indexes. Symbol (*) indicates an unstable orthorhombic form of SnO$_2$, the symbol (v) indicates reflections of a cassiterite SnO$_2$ phase.

TABLE 2 | Phase composition of the Pt/Ce and Pt/CeSn samples calcined at different temperatures T$_{calc}$, lattice parameter (a) and particle mean size (D) of the fluorite phase.

Sample	T$_{calc}$, °C	Phase composition, % wt				Parameters of the fluorite phase	
		CeO$_2$ Fm3m	SnO$_2$ P4$_{2/}$mnm	SnO$_2$ Pbcn	Pt	a, Å	D, nm
Pt/Ce	600					5.415 (1)	6.6 (1)
	700	100	–	–	–	5.415 (4)	8.6 (1)
	800	98 (1)	–	–	2 (1)	5.413 (3)	12.7 (1)
Pt/CeSn	600	24 (7)	64 (6)	12 (3)	-	5.404 (1)	3.5 (5)
	700	20 (5)	70 (5)	9 (3)	0.4 (1)	5.401 (2)	3.0 (1)
	800	21 (4)	79 (4)	-	0.7 (1)	5.406 (2)	4.2 (1)

The standard deviations of the calculated values are given in parentheses.

$Ce_{40}O_{80}$ particle (see **Figure 4** and **Supplementary Material**). Namely, the average distances Ce-O and Ce-Ce in $Ce_{40}O_{80}$ are 2.326 Å and 3.741 Å, respectively, whereas the corresponding average distances Sn-O and Sn-Ce are 2.229 Å and 3.707 Å in the $SnCe_{39}O_{80}$ particle and 2.222 Å and 3.706 Å in the $Pt/SnCe_{39}O_{80}$ particle. Our calculations of the latter with the doping Sn occupying various cationic positions of the CeO$_2$ lattice showed (see **Supplementary Figure 1**) that the location of the Sn^{4+} dopant inside the nanoparticle is moderately stabilized, by 14–36 kJ/mol, compared to its surface location on the (111) terrace of the nanoparticle. Interestingly, a notably more stable location was calculated for a surface corner position of the dopant, where it substitutes a partially reduced Ce^{3+} cation and acquires a quite unusual Sn^{3+} state. We note in passing that such special corner sites O$_4$ exposed by nanostructured ceria are able to bind very strongly atoms of various metals in the form of cations (Figueroba et al., 2016, 2017; Neitzel et al., 2016).

Figures 5, **6** show TEM images of the Pt/CeSn and Pt/Ce samples calcined at 600°C. The TEM data corroborate that calcination of the composites causes removal of the amorphous carbon matrix and crystallization of the formed oxide structures. Two particle types are observed in the Pt/CeSn-600 sample: larger ones with the sizes of 20–50 nm and smaller ones with the sizes of 5–15 nm (**Figure 5A**). A detailed analysis of the structure of the material showed that the larger particles belong to SnO$_2$ (P4$_2$/mnm) (**Figure 5B**). The crystal structure analysis of the smaller particles revealed that they correspond to a cubic fluorite-type structure (**Figure 5C**). These findings agree with the XRD analysis data showing that fluorite-type particles are smaller than those of tin oxides type.

The cerium and tin distribution in the Pt/CeSn-600 sample was investigated by means of EDX. **Figure 6** displays HAADF-STEM images and the corresponding EDX maps for cerium and tin. As can be seen from the TEM images, cerium and tin are distributed over the entire volume of the sample, and no

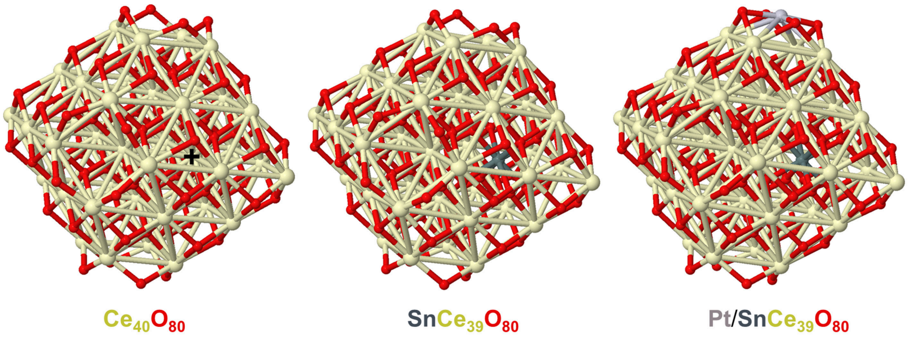

FIGURE 4 | Geometric structures of CeO_2-based nanoparticles calculated to analyze effects of doping Sn ions on the nearest distances from the latter to O and Ce ions. Color coding for atoms: Ce—beige, O—red, Sn—dark gray, Pt—light gray. The nearest distances to the Ce^{4+} ion marked by + in the $Ce_{40}O_{80}$ model: Ce-O-2.292, 2.292, 2.293, 2.295, 2.358, 2.358, 2.361, 2.361 (average 2.326); Ce-Ce-3.732, 3.734, 3.737, 3.738, 3.744, 3.746, 3.747, 3.752 (average 3.741). The nearest distances to the Sn^{4+} ion in the $SnCe_{39}O_{80}$ model: Sn-O-2.181, 2.184, 2.187, 2.189, 2.264, 2.269, 2.276, 2.280 (average 2.229); Sn-Ce-3.687, 3.687, 3.688, 3.693, 3.717, 3.724, 3.726, 3.730 (average 3.707). The nearest distances to the Sn^{4+} ion in the Pt/$SnCe_{39}O_{80}$ model: Sn-O-2.175, 2.176, 2.205, 2.210, 2.238, 2.246, 2.260, 2.266 (average 2.222); Sn-Ce-3.682, 3.691, 3.691, 3.700, 3.714, 3.717, 3.725, 3.726 (average 3.706). All the distances are in Å. Atomic coordinates and total energies of the displayed structures are given in the **Supplementary Material**.

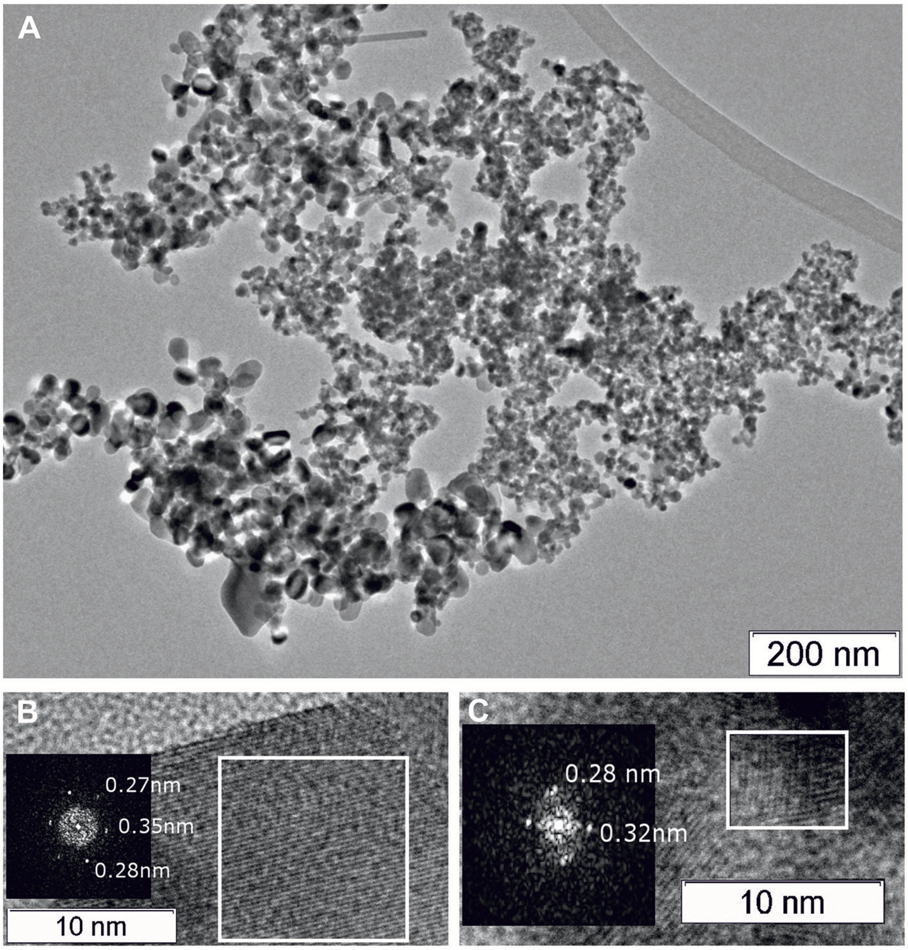

FIGURE 5 | TEM images of the Pt/CeSn-600 sample **(A)**. A HRTEM and Fourier image of the crystal lattice of the SnO_2 cassiterite phase **(B)**, HRTEM and Fourier image of the CeO_2 fluorite phase **(C)**.

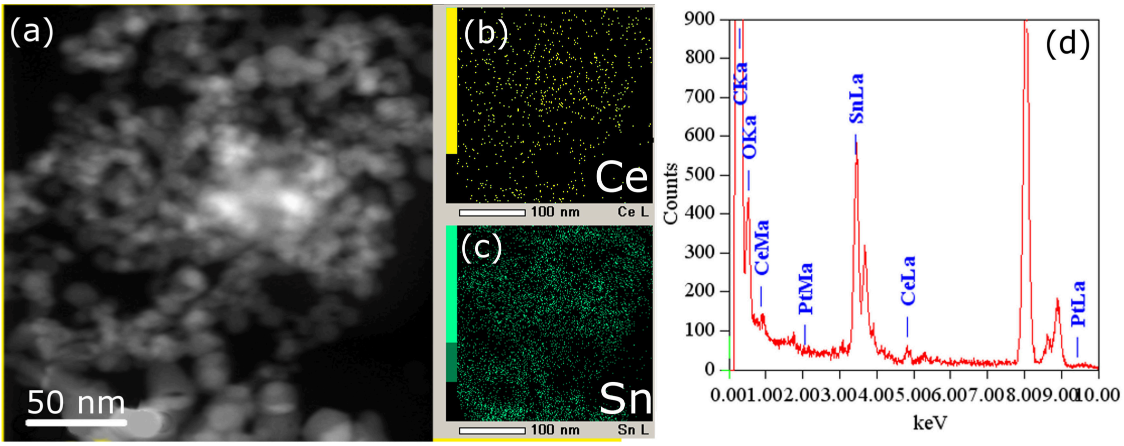

FIGURE 6 | HAADF-STEM image **(a)** and corresponding EDX-mapping **(b,c)** patterns (CeL signal is shown in yellow, SnL signal is shown in green) of the Pt/CeSn-600 sample, **(d)** EDX analysis of the sample composition.

individual CeO$_2$ particles were detected there. This is consistent with the XRD data for the Pt/CeSn-600 sample showing the formation of composites built from SnO$_2$ and Ce$_{1-x}$Sn$_x$O$_2$ nanoparticles. The EDX data on the sample composition agree with the chemical analysis data.

Figure 7 displays TEM images for the Pt/Ce-600 sample. Nanocrystalline blocks with sizes 5–10 nm are observed. The detected distances correspond to the cubic fluorite-type ceria.

XPS spectra of the Pt/Ce and Pt/CeSn samples calcined at 600 and 900°C are shown in **Figures 8**, **9**. The quantitative analysis data and the Pt4f binding energy values determined from the XPS spectra for the Pt/Ce-600 and Pt/CeSn-600 samples are presented in **Table 3**. According to these spectroscopic data all samples contain significant amounts of carbon, concentration of which varies from 27 to 35 at. %. From the analysis of the C1s spectra (not shown) it follows that the detected carbon is represented mainly by amorphous carbon or hydrocarbon groups. The share of oxygen-containing carbon groups, including carbonates, is at most 5–10% (**Table 3**). Such notable content of carbon in the samples obtained by sputtering in an electric arc discharge is not surprising, since the sputtering of atomically dispersed metals and species from graphite carbon rod occurs simultaneously.

Analysis of the charge states of platinum in a series of samples was carried out using the spectra curves fitting. Fitted Pt4f spectra are presented in **Figure 8**. Upon decomposition into individual components, metallic platinum ($E_b = 71.1$ eV) could not be detected in samples calcined at 600°C. In the Pt/Ce-600 sample platinum is present in two states characterized by $E_b(\mathrm{Pt4f}_{7/2}) =$ 72.7 and 74.5 eV. Formally, these states can be referred to as Pt^{2+} and Pt^{4+}. In the remaining samples in the presence of tin, only the state Pt^{2+} with $E_b(\mathrm{Pt4f}_{7/2}) = 72.8$ eV was detected, but not the state Pt^{4+}.

After calcination at 900°C, the Pt^{2+} species are preserved. However, a new state with $E_b(\mathrm{Pt4f}_{7/2}) = 70.9$ eV appears. This state is referred to as Pt^0, and its appearance is in a good agreement with XRD data. After calcination at 900°C, the surface Pt concentration decreases, which could be attributed to sintering of Pt particles.

Figure 9 shows Ce3d spectra for the Pt/Ce-600 and Pt/CeSn-600 samples, and Sn3d for the Pt/CeSn-600 sample. The Sn3d spectra show only one main doublet with $E_b(\mathrm{Sn3d}_{5/2}) = 486.9$ eV attributable to Sn^{4+} (Moulder et al., 1992). Ce3d spectra were decomposed into individual components of Ce^{4+} species (V, V$''$, V$'''$ and U, U$''$, U$'''$) and Ce^{3+} species (V^0, V$'$ and U^0, U$'$) in accordance with literature data (Anandan and Bera, 2013; Zhu et al., 2014). The analysis shows that the quantity of Ce^{3+} species is increased significantly in the Pt/CeSn-600 sample. In the Pt/Ce-600 sample, only 6 at.% of Ce^{3+} is detected, whereas 49% of cerium is in the Ce^{3+} state in the Pt/CeSn-600 sample.

Such a high amount of Ce^{3+} species in the Pt/CeSn-600 sample could be explained by the XRD and TEM data, which show the formation of the Sn-doped fluorite phase Ce$_{1-x}$Sn$_x$O$_{2-\delta}$. When Sn^{4+} substitutes cerium in the fluorite phase, the Ce^{3+} in the position of Ce^{4+} could be generated together with an oxygen vacancy according the electroneutrality requirement: $\mathrm{CeO_2} \rightarrow \mathrm{Sn_{Ce}} + V_{\mathrm{O}}^{\bullet\bullet} + 2\mathrm{Ce'_{Ce}}$, where $V^{\bullet\bullet}$ – is an oxygen vacancy with −2 charge, $\mathrm{Ce'_{Ce}}$–is a Ce^{3+} in the Ce^{4+} position.

Sn atoms were shown in a combined experimental and DFT study to easily reduce ceria nanoparticles, both bare and doped by Pt atoms acquiring the oxidation state +2 (Lykhach et al., 2017b). First, only Ce^{4+} cations were partially reduced upon interactions of atomic Sn with Pt/ceria nanoparticles, but already a moderate increase of Sn content resulted in the reduction of cationic Pt^{2+} species to essentially neutral atomic ones prone to form Pt clusters. Using the same computational approach and similar model Pt/ceria nanoparticles we computationally investigated in the present work stability of Pt dopants in a much more labile +4 state in ceria nanostructures in the presence of minimal amounts of Sn. **Figure 10** shows that the interaction

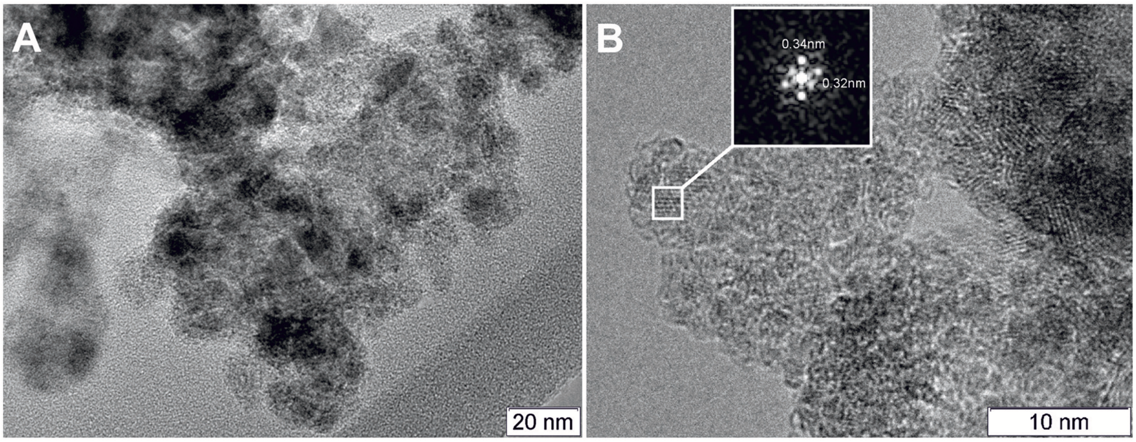

FIGURE 7 | **(A)** TEM image of the Pt/Ce-600 sample, and **(B)** HRTEM and Fourier image of the CeO$_2$ crystal lattice.

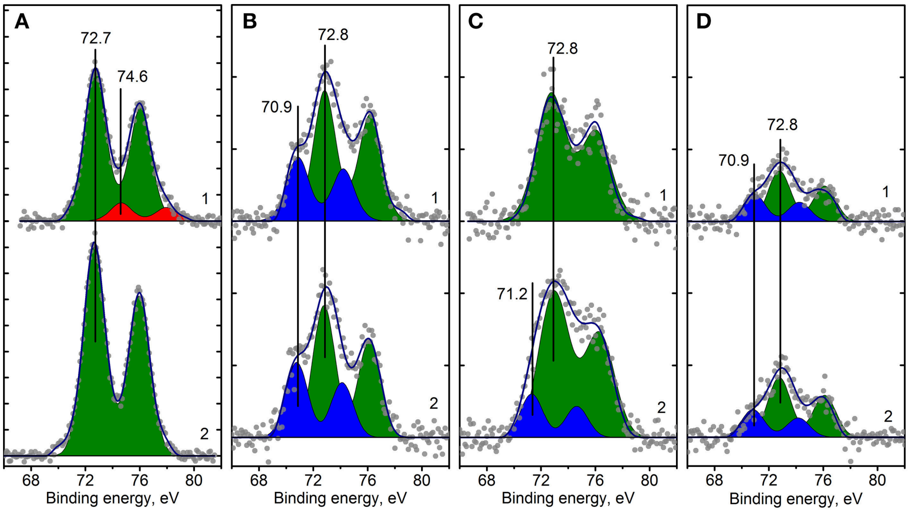

FIGURE 8 | Curve fitted Pt4f XPS spectra for Pt/Ce-600 **(A)**, Pt/Ce-900 **(B)**, Pt/CeSn-600 **(C)** and Pt/CeSn-900 **(D)** samples, before (curves 1) and after CO+O$_2$ reaction (curves 2). Ticks range on the Y-axis is 50 counts.

with a model particle Pt^{2+}/Pt^{4+}Ce$_{39}$O$_{80}$ of just one Sn atom can already slightly favor partial reduction of Pt^{4+} remote from Sn by 8 Å. In the presence of two doping Sn atoms (see **Figure 10**, bottom panels) we also succeed to optimize a local-minimum structure Sn$_2$Pt^{2+}/Pt^{4+}Ce$_{39}$O$_{80}$ with the inner Pt atom in the highest oxidation state +4. This structure is over 40 kJ/mol less stable than the corresponding structure Sn$_2$Pt^{2+}/Pt^{2+}Ce$_{39}$O$_{80}$, where Pt^{4+} is reduced to Pt^{2+}. These calculated data substantiate and explain our experimental observations on the absence of the Pt^{4+} XPS signals, when Sn component is added to the Pt-ceria samples.

Catalytic Properties and TPR-CO Data

Figure 11 presents temperature dependencies of the CO conversion over the prepared Pt/Ce and Pt/CeSn catalysts and **Table 4** shows temperatures for the 10% (T$_{10}$) and 50% (T$_{50}$) CO conversion.

The Pt/Ce and Pt/CeSn catalysts, calcined at 600°C (**Figure 11A**), are characterized by unusual behavior of CO conversion at varying temperature. Up to 100 °C the observed CO conversion either quite weakly depends on temperature (Pt/CeSn) or even decreases with temperature increase (Pt/Ce). The conversion of CO at −10°C is 63 and 26% for Pt/Ce and Pt/CeSn, respectively. The temperature of the 10% CO conversion is significantly below room temperature (**Table 4**).

The presence of several regions in the CO conversion curve with different temperature dependencies, i.e., with different observed activation energies, indicates the presence of active centers of different nature triggering different CO oxidation mechanisms.

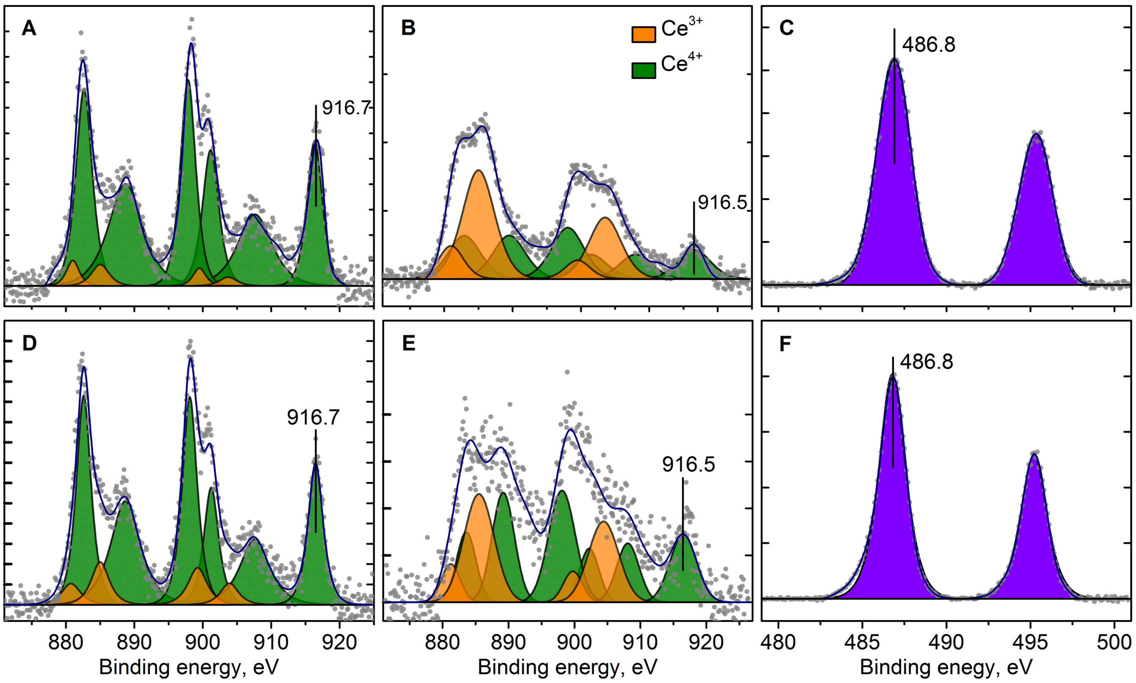

FIGURE 9 | Curve fitted Ce3d **(A,B,D,E)** and Sn3d **(C,F)** XPS spectra for Pt/Ce-600 **(A,D)**, Pt/CeSn-600 **(B,C,E,F)** before **(A,B,C)** and after CO+O$_2$ reaction **(D,E,F)** respectively. Ticks range on the Y-axis is 500 counts.

TABLE 3 | Quantitative composition of the catalyst surface and the XPS binding energy values E$_b$ of individual states of the elements in the Pt/Ce-600 and Pt/CeSn-600 catalysts.

Sample	Pt/Ce		Pt/CeSn	
	E_b (eV)	Concentration, % at.	E_b (eV)	Concentration, % at.
Pt4f		0.65		0.26
Pt^{2+}	72.7	0.58	72.7	0.26
Pt^{4+}	74.6	0.07	–	–
C1s		34.83		27.56
C$_1$	284.8	30.42	285.5	25.88
C$_2$	288.6	4.41	289.0	1.68
Sn3d	–	0	486.9	18.62
Ce3d	916.7	24.85	916.5	7.30
O1s	529.4	39.67	530.9	46.25
Ce/Sn		100:0		28:72
Ce^{3+}/Ce (%)		6		49

The calcination of catalysts at temperatures above 700°C leads to the disappearance of the low-temperature activity. The T$_{10}$ values increase by more than 150°C. The 50% conversion of CO (T$_{50}$) increases by 215 and 110°C for Pt/Ce and Pt/CeSn, respectively after calcination of the catalysts at 800°C. Catalysts calcination at 900°C results in the increase of T$_{50}$ by 10°C for Pt/Ce and by 20°C for Pt/CeSn catalysts.

The TOF values at 150°C are 0.005 and 0.020 for the Pt/Ce-700 and Pt/CeSn-700 samples, respectively (see **Table 5**). Furthermore, after calcination at 800 and 900°C the Pt/CeSn samples show higher TOF values than the Pt/Ce samples. These results indicate that the promotion by tin leads to an increase in both thermal stability and catalyst activity in the medium temperature range.

Table 5 also provides activation energy values calculated for CO oxidation reactions on Pt/Ce and Pt/CeSn catalysts calcined at 700, 800, and 900°C. The finding that the activation energy values are quite close to each other indicates that the limiting stages of the CO oxidation catalytic process on different samples under scrutiny are the same and, therefore, the oxidation process is carried out at essentially the same active centers. The data given in **Table 5** was obtained at the temperature range of 100–200°C. It was not possible to get such quantitative data for the low-temperature range of 0–100°C. Nevertheless, it can be assumed that the reaction mechanism is similar in the low-temperature range and is triggered by active centers of the fluorite phase.

The catalysts after CO+O$_2$ reaction were analyzed by XPS. **Figure 8** (curves 2) shows Pt4f lines for the Pt/Ce-600, Pt/Ce-900, Pt/CeSn-600, and Pt/CeSn-900 catalysts after reaction. For the most active catalysts, calcined at 600°C, XPS shows that the fraction of Pt^{2+} ionic species in both Pt/Ce-600 and Pt/CeSn-600 catalysts does not decrease significantly during the catalytic tests. However, we observe some reduction of Pt after the tests: Pt^{4+} species are reduced to Pt^{2+} in the Pt/Ce-600 catalysts; a small fraction of Pt metal is observed in the Pt/CeSn-600 catalysts. This is an indication that some Pt cations are reduced in CO+O$_2$ mixture. Yet, most of Pt^{2+} is preserved after the catalytic tests.

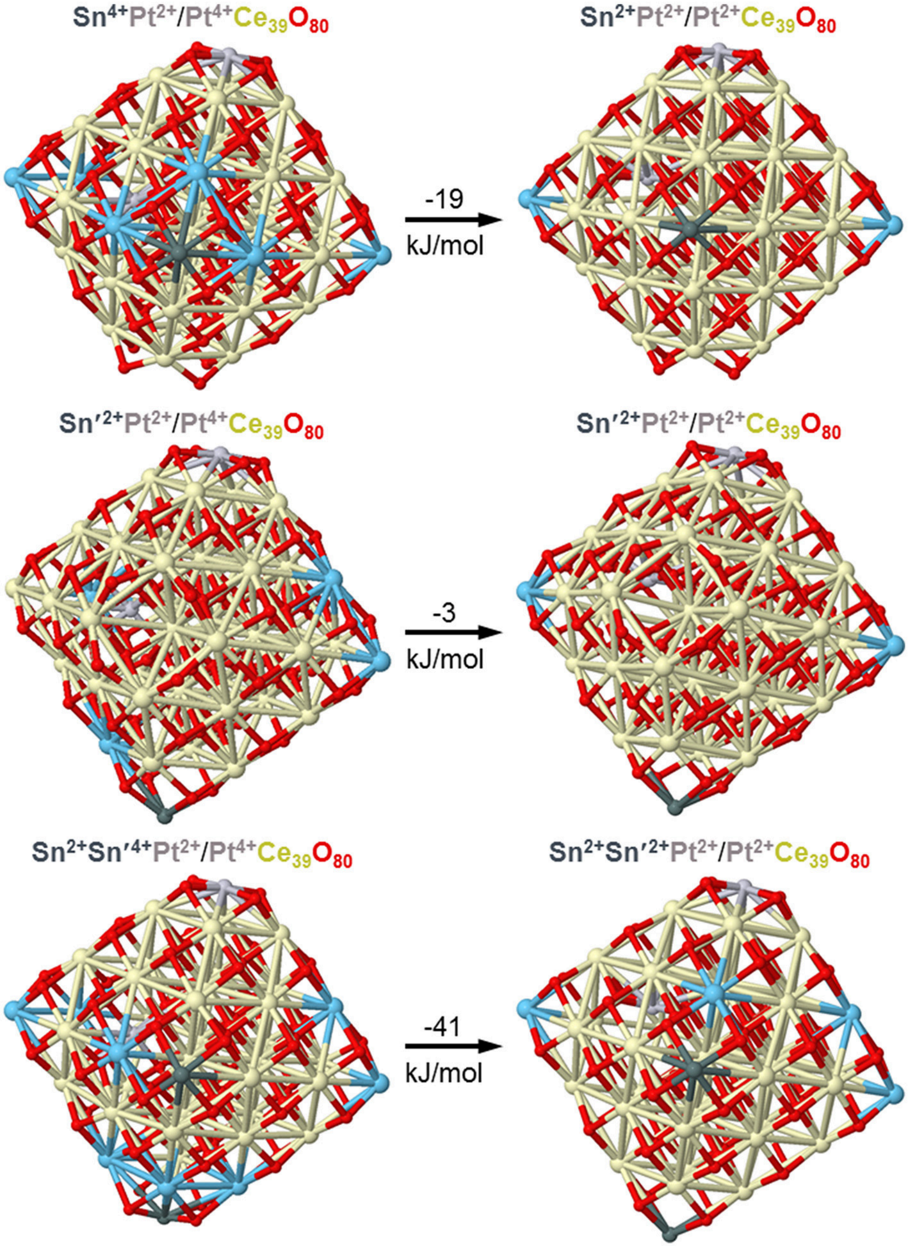

FIGURE 10 | DFT optimized structures and relative energies of model Pt/PtCe$_{39}$O$_{80}$ nanoparticles interacting with one and two Sn atoms illustrating interplay of Pt^{4+} and Pt^{2+} oxidation states. Color coding for atoms: Ce^{4+}-beige, Ce^{3+}–light blue, O—red, Sn—dark gray, Pt—light gray. Atomic coordinates and total energies of the structures are given in the **Supplementary Material**.

Furthermore, no changes in the Pt states were detected in the samples calcined at 800 and 900°C. **Figures 9D–F** shows that Ce and Sn oxidation states of the catalysts are not changed too. This observation was expected, since the catalytic reaction CO+O$_2$ is carried out not in a stoichiometric mixture, but in an excess of oxygen (O$_2$: CO ratio = 5: 1).

Figure 12 presents results for the catalysts obtained by the method of temperature-programmed reaction with CO (TPR-CO). The study of our catalysts by the TPR-CO method in the absence of the gas-phase oxygen allowed us to characterize the reactivity of oxygen present in the catalysts to carbon monoxide. Spectra of both CO absorption and CO$_2$ emission during TPR-CO are presented for the Pt/Ce, Pt/CeSn and pristine CeO$_2$ samples calcined at 600°C.

For the pristine CeO$_2$, CO consumption and CO$_2$ release begin above 200°C. Addition of Pt leads to a strong activation of oxygen present in ceria revealed by lowering initial temperatures of the CO consumption and the CO$_2$ release to just 20 and 45°C, respectively. The promotion by tin causes a further decrease of the reactions begin temperature by 20°C, i.e.,

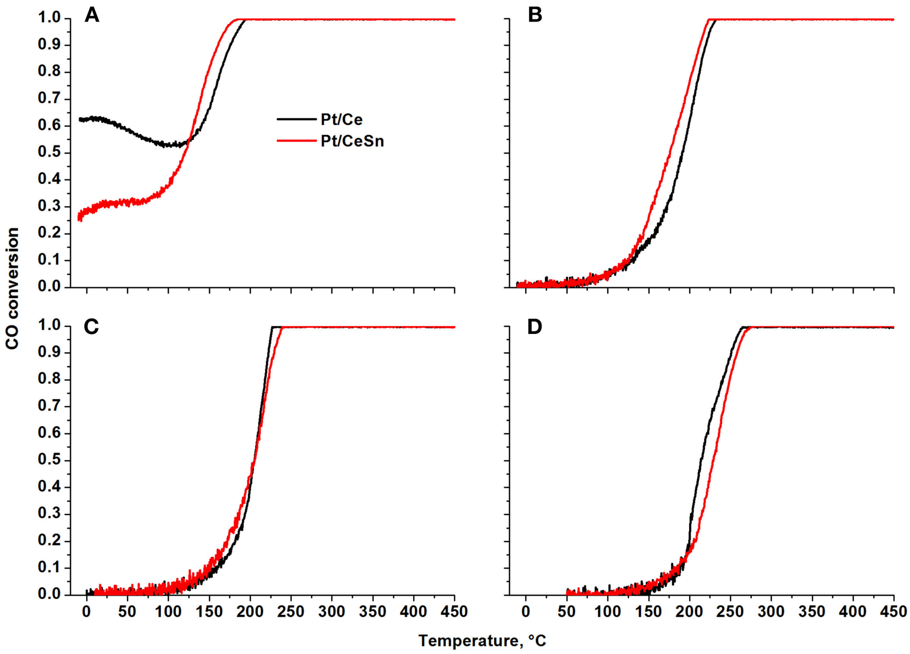

FIGURE 11 | Temperature dependencies of CO conversion (TPR-CO+O$_2$) for the Pt/Ce and Pt/CeSn catalysts calcined at different temperatures: **(A)** 600°C, **(B)** 700°C, **(C)** 800°C, and **(D)** 900°C.

TABLE 4 | Catalytic characteristics in CO oxidation of the samples calcined at different temperatures T_{calc}.

T_{10}, T_{50}, °C	T_{calc}, °C	Pt/Ce	Pt/CeSn
T_{10}, °C	600	<-20	<-20
	700	126	122
	800	159	146
	900	182	182
T_{50}, °C	600	<-10	118
	700	191	175
	800	204	205
	900	215	228

TABLE 5 | TOF and activation energy E_a values for CO oxidation over the Pt/Ce and Pt/CeSn samples calcined at 700, 800, and 900°C and featuring specific surface area S_{BET}.

Sample	Pt,%	S_{BET}, m^2/g	E_a, kcal/mol	*TOF × 10^3, s^{-1}
Pt/Ce-700	4.58	71	8.3	5.4
Pt/CeSn-700	2.37	39	9.2	19.8
Pt/Ce-800	4.58	48	10.8	1.5
Pt/CeSn-800	2.37	27	11.3	12.8
Pt/Ce-900	4.58	10	17	0.7
Pt/CeSn-900	2.37	16	12.7	7.5

**TOF(s^{-1}) = W/C_{Pt}, where W—reaction rate (molecules/cm^2 s), C_{Pt}–Pt concentration calculated from Pt content in the catalyst (XPS).*

to 0 and 25°C, respectively. These data suggest that the addition of tin to the catalysts leads to weaker binding of the lattice oxygen in them. TPR-CO spectra of the catalysts under study reveal three peaks at the temperatures of 20–200°C (peak 1), 200–350°C (peak 2) and above 350°C (peak 3). The first two peaks appear to result from CO interactions with reactive oxygen activated during formation of the Pt—Ce catalyst due to appearance of ionic platinum in the (PtCe)O$_2$ mixed phase.

At temperature above 350°C the profiles of CO consumption and CO$_2$ release match. According to Giordano et al. (2000), diffusion of oxygen from the support volume to the surface and interaction with gas-phase CO begins at these temperatures. H$_2$ release is observed in our experiments during such a process. It was suggested (Zhu et al., 2004) that H$_2$ and CO$_2$ release could be observed during the TPR-CO experiments due to a reaction of CO with surface hydroxo-groups of the catalyst: $CO(ads) + 2OH^-(support) \rightarrow CO_2(gas) + H_2(gas) + O^{2-}(support)$.

Addition of Sn to the catalysts leads to a decrease in the area of the peak 1 due to a decrease in the CeO$_2$ content. The areas of the peaks 2 and 3 are increased due to increased amount of reactive oxygen species. **Table 6** shows that the amount of consumed CO and released CO$_2$ for the Pt/CeSn-600 catalyst is almost 3 times higher than that for the Pt/Ce-600 catalyst. This corroborates that the modification of our Pt/Ce catalyst by tin noticeably increases the amount of oxygen reactive at low temperatures in the Pt/CeSn catalyst. Notably, the catalysts calcined at temperatures above 600°C lose their high low-temperature oxidative activity. However, the observation of higher TOF values for Pt/CeSn catalysts compared to the corresponding Pt/Ce catalysts prepared by calcination at the

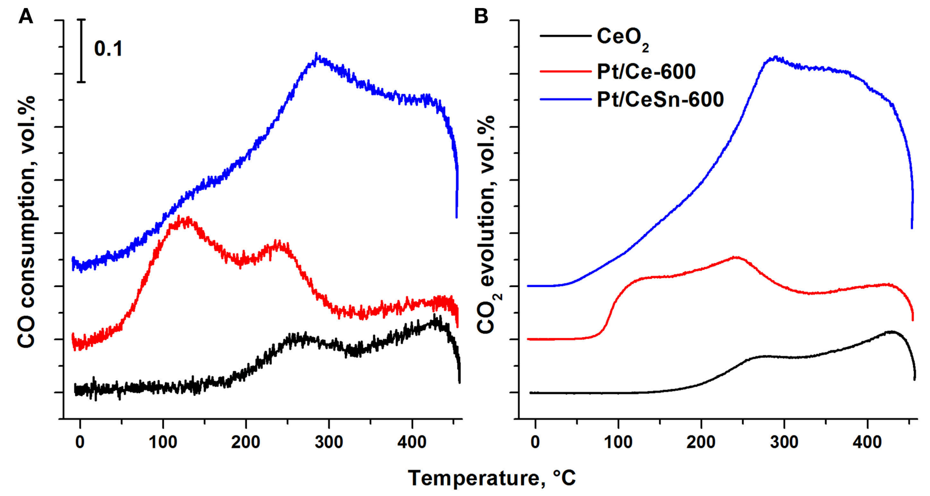

FIGURE 12 | Temperature dependence of the CO consumption **(A)** and CO_2 evolution **(B)** during the TPR-CO for the catalysts Pt/Ce-600, Pt/CeSn-600 and pristine CeO_2-600.

TABLE 6 | CO consumption and CO_2 evolution during the TPR-CO.

Sample	CO, μmol/g	CO_2, μmol/g	*CO/Pt	*CO_2/Pt
Pt/Ce-600	1,121	975	4.8	4.2
Pt/CeSn-600	2,753	3,093	23.8	26.7

**CO/Pt and *CO_2/Pt are molar ratios of the CO consumed and CO_2 evolved during the TPR-CO to the Pt content in the catalyst, respectively.*

same temperatures indicates increased thermal stability of the Sn-containing catalysts.

DISCUSSION

To achieve effective low-temperature oxidation of CO over ceria-based catalysts particle size in them should not exceed 10 nm (Boronin et al., 2009; Kurnatowska et al., 2012). In such cases a SMSI effect between dispersed ceria and ionic forms of the active component is possible, which can result in the formation of a large number of oxygen vacancies and mobile oxygen species with increased diffusion and reactivity.

In this work we used plasma arc synthesis to obtain highly dispersed ceria particles and mixed phases with tin dioxide. TEM data show that the as-prepared condense PtCeC and PtCeSnC substances are nanocomposites, in which the Ce and Sn components are in the form of semi-oxidized particles with Ce_2O_3, SnO, and SnO_2 crystalline structures coated with amorphous carbon. However, according to the reducing conditions of the synthesis, the initial particles should be in metallic state. We assume that the semi-oxidized nanoparticles Ce_2O_3 and SnO are formed, when samples are exposed to the atmosphere after opening the chamber, in which plasma arc synthesis was performed. Considering high reactivity of cerium and tin metal particles their partial surface oxidation occurs even despite the diffusion difficulties of oxygen molecules into the carbon matrix. As a result, formation of core-shell structures Ce_2O_3@C in the PtCeC composite and of core-shell-shell structures Sn@SnO@C in the PtCeSnC composite takes place.

Subsequent calcination of the nanocomposites in an oxygen atmosphere at $T > 600$ °C results in burning out of the amorphous carbon matrix and conversion of the components into oxidized forms. Our TEM and XRD data show that phases with a fluorite structure (CeO_2 and Sn-doped CeO_2) and cassiterite (SnO_2) are formed, with fluorite particles being much smaller (3–4 nm) than SnO_2 particles (9–12 nm). We note that so small CeO_2 particles were not obtained in our previous studies of samples prepared by co-precipitation and solution-combustion methods (Slavinskaya et al., 2015; Vasilchenko et al., 2016). Our XRD data reveal formation of a mixed $Ce_{1-x}Sn_xO_{2-\delta}$ phase. Furthermore, XPS data show that the state of Pt in the Pt/CeSn-600 catalysts is characterized only by Pt^{2+} ions, which significantly differs from the state of platinum in the Pt/Ce-600 catalyst (Pt^{2+}/Pt^{4+}) and also indicates the influence of tin ions on the surface state of the fluorite phase in Sn-modified catalysts. Our DFT calculations showed that the presence of Sn^{4+} ions in ceria nanoparticles facilitates Pt^{4+} reduction to Pt^{2+}. In addition, very stable square planar structures PtO_4 were formed (Bruix et al., 2014; Figueroba et al., 2017) when platinum interacted with nanostructured CeO_2 surface. It can be speculated that the presence of embedded tin ions boosts formation of such stable structures. Along with the effect of tin on the state of platinum, the Ce3d spectra show a significant increase in the concentration of Ce^{3+} ions. Namely, the concentration of Ce^{3+} ions in the Pt/CeSn catalysts reaches 50 % at., while in the Pt/Ce catalysts the Ce^{3+} concentration is 15–20% at. These data indicate that the number of oxygen vacancies in the Sn-modified catalysts is significantly higher.

Key factor for the implementation of efficient CO oxidation in PGM-ceria systems is the formation of mobile highly reactive oxygen species. TPR-CO experiments allowed us to establish the effect of mobile oxygen formation in the catalysts synthesized by PAS. For these catalysts, the starting temperature of the interaction with CO is 20–50°C. At temperatures up to 200°C a significant amount of oxygen is released due to interaction with CO. This low-temperature mobile oxygen is generated in both Pt/Ce and Pt/CeSn catalysts, but there is a difference. In fact, a significant part of mobile oxygen is released from the Pt/Ce-600 catalyst with a peak with $T_{max} = 100°C$, while from the Pt/CeSn-600 catalysts mobile oxygen is released in the whole temperature range from 20 to 450°C, and its amount is more than 2.5 times higher than in the case of Pt/Ce-600 catalyst. Obviously, this effect is directly related to the modification of the CeO$_2$ fluorite phase by Sn^{4+} ions.

Our DFT modeling allows estimating effects of Sn^{4+} doping ions in near-surface Ce^{4+} positions of ceria nanoparticles on the reducibility of the latter (see **Figure 13**). In line with experimental observations (*vide supra*), the substitution of a Ce^{4+} cation in the lattice of ceria by Sn^{4+} greatly facilitates formation of oxygen vacancies O$_v$ in the immediate vicinity of the dopant. Indeed, the lowest vacancy formation energy E_{Ov} (calculated with respect to ½ O$_2$) for removal of the first O atom located near Sn^{4+} is almost 80 kJ/mol smaller than when the vacancy

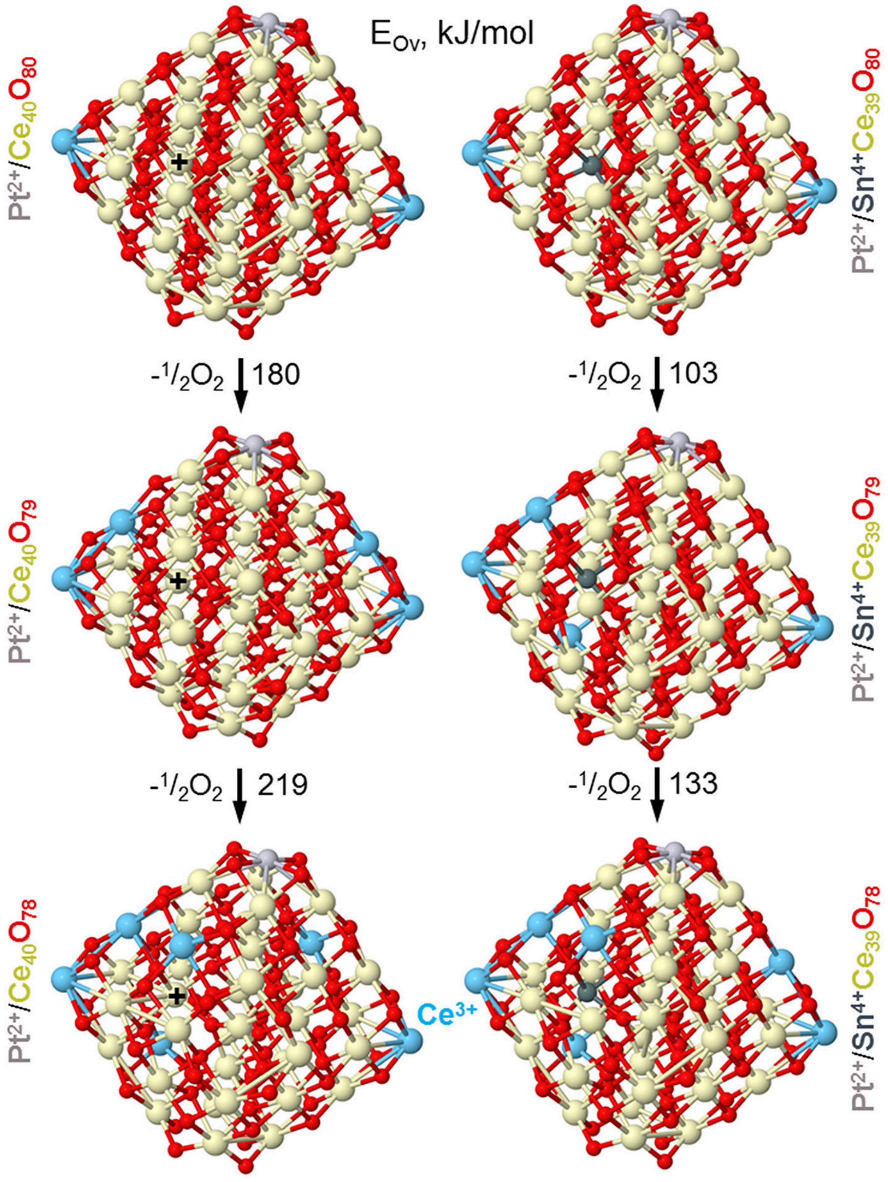

FIGURE 13 | Optimized structures of nanoparticles Pt/Ce$_{40}$O$_{80-n}$ and Pt/SnCe$_{39}$O$_{80-n}$ corresponding to formation of the first and second oxygen vacancies (Ov) with the lowest energy E_{Ov} in the vicinity of Sn^{4+} and Ce^{4+} ions located in the same near-surface cationic position labeled by +. Color coding for atoms: Ce^{4+}–beige, Ce^{3+}–light blue, O—red, Sn—dark gray, Pt—light gray. Atomic coordinates and total energies of the structures are given in the **Supplementary Material**.

is created near Ce^{4+} cation occupying the same site. Calculated E_{Ov} value for creating the second O_v around the Sn^{4+} cation decreases even somewhat more with respect to the Ce^{4+} site. Notably, both the first and the second E_{Ov} values for the Sn^{4+} dopant case are very low, 103 and 133 kJ/mol, respectively. These E_{Ov} values are close to those calculated using the same DFT scheme for Pt-ceria nanocomposites, where predicted high oxygen mobility was confirmed experimentally (Vayssilov et al., 2011). Thus, the present low E_{Ov} values corroborate very high oxygen mobility in nanostructured ceria induced by doping with Sn. Our calculations indicate that at least two mobile reactive O atoms can be easily generated by the presence of one Sn^{4+} cation in ceria lattice, with concomitant creation of four reduced Ce^{3+} ions, in full agreement with our experimental observations. The enhanced mobility of oxygen is related to strongly distorted oxygen coordination of Sn^{4+} compared to Ce^{4+} most favorably surrounded by cubes of eight O^{2-} anions. The calculated eight nearest Ce-O and Sn-O distances (in Å) are: for Ce^{4+} in $Pt^{2+}/Ce_{40}O_{80}$—2.28×2, 2.31×2, 2.33, 2.34, 2.35, 2.36 and for Sn^{4+} in $Pt^{2+}/SnCe_{39}O_{80}$—2.11, 2.12, 2.14, 2.15, 2.22, 2.27, 2.35, 2.54 (see sketches of these models in the upper panels of **Figure 13** and atomic coordinates in the **Supplementary Material**).

Although the amount of mobile oxygen is generally higher for the Pt/CeSn-600 catalyst, this is probably not the only important factor for low-temperature oxidation reactivity. Our CO conversion data show that the catalytic activity in the range of 0–100°C is slightly lower for the Pt/CeSn-600 catalysts than for the Pt/Ce-600 ones. Most likely, the amount of mobile oxygen affects the catalytic activity above 100°C, when the TOF values are higher for the Pt/CeSn-800 and Pt/CeSn-900 catalysts. The six-fold difference in TOF values for the Pt/Ce and Pt/CeSn catalysts calcined at 900°C reinforces notably higher activity of the latter at temperatures above 100°C. According to the experimental data, Pt^{2+} and Pt^{4+} ions are present in catalytically active centers of the Pt/Ce-600 samples. In the Pt/CeSn-600 samples, doping Sn species can replace Pt^{4+} ions and also induce additional reduction of Ce^{4+} ions.

Application of plasma arc synthesis makes it possible to mix catalysts components at the cluster and nanoscale level. Due to the mixing of components takes place in the carbon matrix, which suppresses sintering at the sputtering stage, formation of highly dispersed oxide structures during annealing in oxygen atmosphere is possible. In the processes of annealing and burning of carbon, nanoparticles of CeO_2 and SnO_2 interact in the contact area.

CONCLUSIONS

We prepared complex PtCeC and PtCeSnC composites in the form of highly defective oxide particles stabilized in carbon matrices using a plasma arc synthesis method. High-temperature annealing of the prepared samples in oxygen removes the carbon matrix and results in the formation of Pt/CeO_x and $Pt/CeSnO_x$ samples that actively catalyze CO oxidation. In the presence of Sn XRD analysis shows formation of a mixed phase CeSnOx and stabilization of more dispersed species with a fluorite-type structure, the factors significantly contributing to the high activity and thermal stability of the catalyst modified by Sn.

XPS analysis indicates the presence of both Pt^{2+} and Pt^{4+} cationic states in the catalyst Pt/CeO_x, whereas only the state Pt^{2+} could be detected in the catalyst $Pt/CeSnO_x$. Insertion of Sn ions in the fluorite lattice of Pt/CeO_x does not stabilize Pt^{4+} state in the $Pt/CeSnO_x$ catalyst, but induces formation of remarkably high concentration (50%) of lattice Ce^{3+} ions. Results of our DFT calculations corroborate destabilization of Pt^{4+} ions by incorporation of Sn cations into the fluorite structures of Pt/CeO_x nanoparticles.

Our TPR-CO experiments show the presence of loosely bound active oxygen in the Pt/CeO_x and $Pt/CeSnO_x$ catalysts in contrast with the similarly prepared pristine CeO_x catalyst. CO_2 evolution in the gas phase upon interaction of the Pt/CeO_x and $Pt/CeSnO_x$ catalysts with CO takes place in the temperature range 0–200°C, while no reaction of the CeO_x catalyst with CO could be detected at these temperatures. The TPR-CO results that the ignition temperature of CO oxidation over the $Pt/CeSnO_x$ catalyst is lower than that over the Sn-free Pt/CeO_x catalyst strongly suggest the presence of more reactive oxygen species in the Sn-modified catalyst. Moreover, incorporation of Sn causes increased amounts of the loosely bound highly reactive oxygen (enhanced oxygen storage capacity). According to our DFT calculations, doping Sn cations are somewhat more energetically stable inside ceria nanoparticles than on their surface. The calculations also provide an atomic-level explanation for the observed low-temperature generation of surprisingly abundant reactive oxygen and reduced Ce^{3+} species in the presence of Sn in ceria, which is related to strongly distorted Sn-O coordination sphere compared to that of Ce-O.

Along with the effect of Sn incorporation in the fluorite lattice of CeO_2 we also document interactions of tin and cerium oxides at the nanoscale, which stabilize highly dispersed cerium oxide species crucial for the observed enhanced stability of the modified by tin $Pt/CeSnO_x$ catalysts.

DATA AVAILABILITY

The data that support the findings of this study are included in this published article and the **Supplementary Material.** Extra data are available from the corresponding authors upon reasonable request.

AUTHOR CONTRIBUTIONS

TK, ED, ES, AS, VM, AZ, and SN performed experiments. KN performed DFT modeling, analyzed the calculated data, and was involved in the preparation of the manuscript. TK, ED, ES, and AS were involved in the analysis of the experimental data and the preparation of the manuscript. AB supervised the experimental work and was involved in the analysis of the experimental data and the preparation of the manuscript.

FUNDING

This work was conducted within the framework of the budget project #AAAA-A17-117041710084-2 for Boreskov Institute of Catalysis. This work was also supported by the Russian Foundation for Basic Research (grants no. 17-03-00754 and 17-43-540738). KN gratefully acknowledges a support by the Spanish grants PRX17/00348, CTQ2015-64618-R, and MDM-2017-0767 as well as by the 2017SGR13 grant of the Generalitat de Catalunya.

ACKNOWLEDGMENTS

Computer resources and technical support for the DFT modeling have been partly provided by the Red Española de Supercomputación (Barcelona, Spain).

SUPPLEMENTARY MATERIAL

The Supplementary Material for this article can be found online at: https://www.frontiersin.org/articles/10.3389/fchem.2019.00114/full#supplementary-material

REFERENCES

Anandan, C., and Bera, P. (2013). XPS studies on the interaction of CeO_2 with silicon in magnetron sputtered CeO_2 thin films on Si and Si_3N_4 substrates. *Appl. Surf. Sci.* 283, 297–303. doi: 10.1016/j.apsusc.2013.06.104

Anisimov, V. I., Aryasetiawan, F., and Lichtenstein, A. I. (1997). First-principles calculations of the electronic structure and spectra of strongly correlated systems: the LDA + U method. *J. Phys.* 9:767. doi: 10.1088/0953-8984/9/4/002

Ayastuy, J. L., Iglesias-González, A., and Gutiérrez-Ortiz, M. A. (2014). Synthesis and characterization of low amount tin-doped ceria ($Ce_XSn_{1-X}O_{2-\delta}$) for catalytic CO oxidation. *Chem. Eng. J.* 244, 372–381. doi: 10.1016/j.cej.2014.01.077

Baidya, T., Gupta, A., Deshpandey, P. A., Madras, G., and Hegde, M. S. (2009). High oxygen storage capacity and high rates of CO oxidation and NO reduction catalytic properties of $Ce_{1-x}Sn_xO_2$ and $Ce_{0.78}Sn_{0.2}Pd_{0.02}O_{2-\delta}$. *J. Phys. Chem. C.* 113, 4059–4068. doi: 10.1021/jp8060569

Baranchikov, A. E., Polezhaeva, O. S., Ivanov, V. K., and Tretyakov, Y. D. (2010). Lattice expansion and oxygen non-stoichiometry of nanocrystalline ceria. *CrystEngComm* 12, 3531–3533. doi: 10.1039/c0ce00245c

Bera, P., Gayen, A., Hegde, M. S., Lalla, N. P., Spadaro, L., Frusteri, F., et al. (2003). Promoting effect of CeO_2 in combustion synthesized Pt/CeO_2 catalyst for CO oxidation. *J. Phys. Chem. B.* 107, 6122–6130. doi: 10.1021/jp022132f

Boronin, A. I., Slavinskaya, E. M., Danilova, I. G., Gulyaev, R. V., Amosov, Y. I., Kuznetsov, P. A., et al. (2009). Investigation of palladium interaction with cerium oxide and its state in catalysts for low-temperature CO oxidation. *Catal. Today* 144, 201–211. doi: 10.1016/j.cattod.2009.01.035

Bruix, A., Lykhach, Y., Matolínov,á, I., Neitzel, A., Skála, T., Tsud, N., et al. (2014). Maximum noble-metal efficiency in catalytic materials: atomically dispersed surface platinum. *Angewan. Chem. Int. Ed.* 53, 10525–10530. doi: 10.1002/anie.201402342

Bruix, A., and Neyman, K. M. (2016). Modeling ceria-based nanomaterials for catalysis and related applications. *Catal. Lett.* 146, 2053–2080. doi: 10.1007/s10562-016-1799-1

Bruix, A., and Neyman, K. M. (2019). "How to design models for ceria nanoparticles: Challenges and strategies for describing nanostructured reducible oxides," in *Frontiers of Nanoscience,* Vol. 12, eds Bromley, S. T. and Woodley, S. M (Oxford: Elsevier), 55–99.

Cargnello, M., Delgado, Jaén, J. J., Hernández garrido, J. C., Bakhmutsky, K., Montini, T., et al. (2012). Exceptional activity for methane combustion over modular Pd@CeO_2 subunits on functionalized Al_2O_3. *Science* 337, 713–717. doi: 10.1126/science.1222887

Coelho, A. A. (2005). *TOPAS.Graphics Based Profile and Structureanalysis Software, Version 3.0*, Madison, WI: Bruker AXS, Inc.

Derevyannikova, E. A., Kardash, T. Y., Kibis, L. S., Slavinskaya, E. M., Svetlichnyi, V. A., Stonkus, O. A., et al. (2017). The structure and catalytic properties of Rh-doped CeO_2 catalysts. *Phys. Chem. Chem. Phys.* 19, 31883–31897. doi: 10.1039/C7CP06573F

Dudarev, S. L., Botton, G. A., Savrasov, S. Y., Humphreys, C. J., and Sutton, A. P. (1998). Electron-energy-loss spectra and the structural stability of nickel oxide: an LSDA+U study. *Phys. Rev. B* 57:1505. doi: 10.1103/PhysRevB.57.1505

Farrauto, R. J. (2012). Low-temperature oxidation of methane. *Science* 337, 659–660. doi: 10.1126/science.1226310

Farrauto, R. J., and Bartholomew, C. H. (1997). *Fundamentals of Industrial Catalytic Processes*. London: Blackie Academic and Professional.

Figueroba, A., Bruix, A., Kovács, G., and Neyman, K. M. (2017). Metal-doped ceria nanoparticles: stability and redox processes. *Phys. Chem. Chem. Phys.* 19, 21729–21738. doi: 10.1039/C7CP02820B

Figueroba, A., Kovacs, G., Bruix, A., and Neyman, K. M. (2016). Towards stable single-atom catalysts: strong binding of atomically dispersed transition metals on the surface of nanostructured ceria. *Catal. Sci. Technol.* 6, 6806–6813. doi: 10.1039/C6CY00294C

Giordano, F., Trovarelli, A., De Leitenburg, C., and Giona, M. (2000). A model for the temperature-programmed reduction of low and high surface area ceria. *J. Catal.* 193, 273–282. doi: 10.1006/jcat.2000.2900

Gracia, L., Beltrán, A., and Andrés, J. (2007). Characterization of the High-pressure structures and phase transformations in SnO_2. a density functional theory study. *J. Phys. Chem. B* 111, 6479–6485. doi: 10.1021/jp067443v

Gulyaev, R. V., Kardash, T. Y., Malykhin, S. E., Stonkus, O. A., Ivanova, A. S., and Boronin, A. I. (2014a). The local structure of $Pd_xCe_{1-x}O_{2-x-\delta}$ solid solutions. *Phys. Chem. Chem. Phys.* 16, 13523–13539. doi: 10.1039/C4CP01033G

Gulyaev, R. V., Slavinskaya, E. M., Novopashin, S. A., Smovzh, D. V., Zaikovskii, A. V., Osadchii, D. Y., et al. (2014b). Highly active $PdCeO_x$ composite catalysts for low-temperature CO oxidation, prepared by plasma-arc synthesis. *Appl. Catal. B* 147, 132–143. doi: 10.1016/j.apcatb.2013.08.043

Gulyaev, R. V., Stadnichenko, A. I., Slavinskaya, E. M., Ivanova, A. S., Koscheev, S. V., and Boronin, A. I. (2012). *In situ* preparation and investigation of Pd/CeO_2 catalysts for the low-temperature oxidation of CO. *Appl. Catal. A* 439–440, 41-50. doi: 10.1016/j.apcata.2012.06.045

Gupta, A., and Hegde, M. S. (2010). $Ce_{0.78}Sn_{0.2}Pt_{0.02}O_{2-\delta}$: A new non-deactivating catalyst for hydrogen production via water-gas shift reaction. *Appl. Catal. B* 99, 279–288. doi: 10.1016/j.apcatb.2010.06.034

Gupta, A., Kumar, A., Hegde, M. S., and Waghmare, U. V. (2010). Structure of $Ce_{1-x}Sn_xO_2$ and its relation to oxygen storage property from first-principles analysis. *J. Chem. Phys.* 132, 194702. doi: 10.1063/1.3425662

Hegde, M. S., Madras, G., and Patil, K. C. (2009). Noble metal ionic catalysts. *Accounts Chem. Res.* 42, 704–712. doi: 10.1021/ar800209s

Hellenbrandt, M. (2004). The inorganic crystal structure database (ICSD)—present and future. *Crystallography Rev.* 10, 17–22. doi: 10.1080/08893110410001664882

Hinokuma, S., Fujii, H., Katsuhara, Y., Ikeue, K., and Machida, M. (2014). Effect of thermal ageing on the structure and catalytic activity of Pd/CeO_2 prepared using arc-plasma process. *Catal. Sci. Technol.* 4, 2990–2996. doi: 10.1039/C4CY00291A

Ivanova, A. S., Slavinskaya, E. M., Gulyaev, R. V., Zaikovskii, V. I., Stonkus, O. A., Danilova, I. G., et al. (2010). Metal-support interactions in Pt/Al_2O_3 and Pd/Al_2O_3 catalysts for CO oxidation. *Appl. Catal. B* 97, 57–71. doi: 10.1016/j.apcatb.2010.03.024

Kardash, T. Y., Slavinskaya, E. M., Gulyaev, R. V., Zaikovskii, A. V., Novopashin, S. A., and Boronin, A. I. (2017). Enhanced thermal stability of Pd/Ce–Sn–O catalysts for CO oxidation prepared by plasma-Arc synthesis. *Topics Catal.* 60, 898–913. doi: 10.1007/s11244-017-0755-7

Kibis, L. S., Kardash, T. Y., Derevyannikova, E. A., Stonkus, O. A., Slavinskaya, E. M., Svetlichnyi, V. A., et al. (2017). Redox and catalytic properties of $Rh_xCe_{1-x}O_{2-\delta}$ solid solution. *J. Phys. Chem. C* 121, 26925–26938. doi: 10.1021/acs.jpcc.7b09983

Kresse, G., and Hafner, J. (1993). Ab initio molecular dynamics for liquid metals. *Phys. Rev. B* 47, 558–561. doi: 10.1103/PhysRevB.47.558

Kresse, G., and Joubert, D. (1999). From ultrasoft pseudopotentials to the projector augmented-wave method, *Phys. Rev. B* 59:1758. doi: 10.1103/PhysRevB.59.1758

Kurnatowska, M., Kepinski, L., and Mista, W. (2012). Structure evolution of nanocrystalline $Ce_{1-x}Pd_xO_{2-y}$ mixed oxide in oxidizing and reducing atmosphere: Reduction-induced activity in low-temperature CO oxidation. *Appl. Catal. B* 117–118, 135–147. doi: 10.1016/j.apcatb.2011.12.034

Loschen, C., Carrasco, J., Neyman, K. M., and Illas F. (2007). First principles LDA+U and GGA+U study of cerium oxides: dependence on the effective U-parameter. *Phys. Rev. B* 75:035115. doi: 10.1103/PhysRevB.75.035115

Lowell, S., Shields, J. E., Thomas, M. A., and Thommes, M. (2006). *Characterization of Porous Solids and Powders: Surface Area, Pore Size and Density.* Amsterdam: Springer.

Lykhach, Y., Bruix, A., Fabris, S., Potin, V., Matolinova, I., Matolín, V., et al. (2017a). Oxide-based nanomaterials for fuel cell catalysis: the interplay between supported single Pt atoms and particles. *Catal. Sci. Technol.* 7, 4315–4345. doi: 10.1039/C7CY00710H

Lykhach, Y., Figueroba, A., Skála, T., Duchon, T., Tsud, N., Aulická, M., et al. (2017b). Redox-mediated conversion of atomically dispersed platinum to sub-nanometer particles. *J. Mater. Chem. A,* 5, 9250–9261. doi: 10.1039/C7TA02204B

Matolín, V., Cabala, M., Cháb, V., Matolínov,á, I., Prince, K. C., Skoda, M., et al. (2008). A resonant photoelectron spectroscopy study of $Sn(O_x)$ doped CeO_2 catalysts. *Surface Interface Analy.* 40, 225–230. doi: 10.1002/sia.2625

Migani, A., Vayssilov, G. N., Bromley, S. T., Illas, F., and Neyman, K. M. (2010). Dramatic reduction of the oxygen vacancy formation energy in ceria particles: a possible key to their remarkable reactivity at the nanoscale. *J. Mater. Chem.* 20, 10535–10546. doi: 10.1039/c0jm01908a

Monai, M., Montini, T., Chen, C., Fonda, E., Gorte, R. J., and Fornasiero, P., et al. (2015). Methane catalytic combustion over hierarchical Pd@CeO_2/Si-Al_2O_3: effect of the presence of water. *ChemCatChem* 7, 2038–2046. doi: 10.1002/cctc.201402717

Montini, T., Melchionna, M., Monai, M., and Fornasiero, P. (2016). Fundamentals and catalytic applications of CeO_2-based materials. *Chem. Rev.* 116, 5987–6041. doi: 10.1021/acs.chemrev.5b00603

Moulder, J. F., Stickle, W. F., Sobol, P. E., and Bomben, K. D. (1992). *Handbook of X-ray Photoelectron Spectroscopy*. Minnesota: Perkin-Elmer Corp, Eden Prairie.

Muraki, H., and Zhang, G. (2000). Design of advanced automotive exhaust catalysts. *Catal. Today* 63, 337–345. doi: 10.1016/S0920-5861(00)00477-6

Neitzel, A., Figueroba, A., Lykhach, Y., Skála, T., Vorokhta, M., Tsud, N., et al. (2016). Atomically dispersed Pd, Ni, and Pt species in ceria-based catalysts: principal differences in stability and reactivity. *J. Phys. Chem. C* 120, 9852–9862. doi: 10.1021/acs.jpcc.6b02264

Nguyen, T. B., Deloume, J. P., and Perrichon, V. (2003). Study of the redox behaviour of high surface area CeO_2-SnO_2 solid solutions. *Appl. Catal. A* 249, 273–284. doi: 10.1016/S0926-860X(03)00223-0

Perdew, J. P., Chevary, J. A., Vosko, S. H., Jackson, K. A., Pederson, M. R., Singh, D. J., et al. (1992). Atoms, molecules, solids, and surfaces: applications of the generalized gradient approximation for exchange and correlation. *Phys. Rev. B* 46, 6671–6687. doi: 10.1103/PhysRevB.46.6671

Primavera, A., Trovarelli, A., De Leitenburg, C., Dolcetti, G., and Llorca, J. (1998). "Reactivity and characterization of Pd-containing ceria-zirconia catalysts for methane Combustion," in *Studies in Surface Science and Catalysis*, Vol. 119, eds A. Parmaliana, D. Sanfilippo, F. Frusteri, A. Vaccari, and F. Arena (Amsterdam: Elsevier).

Priolkar, K. R., Bera, P., Sarode, P. R., Hegde, M. S., Emura, S., Kumashiro, R., et al. (2002). Formation of $Ce_{1-x}Pd_xO_{2-\delta}$ Solid Solution in Combustion-Synthesized Pd/CeO_2 Catalyst: XRD, XPS, and EXAFS Investigation. *Chem. Mater.* 14, 2120–2128. doi: 10.1021/cm0103895

Scanlon, D. O., Morgan, B. J., and watson, G. W. (2011). The origin of the enhanced oxygen storage capacity of $Ce_{1-x}(Pd/Pt)_xO_2$. *Phys. Chem. Chem. Phys.* 13, 4279–4284. doi: 10.1039/c0cp01635g

Slavinskaya, E. M., Gulyaev, R. V., Zadesenets, A. V., Stonkus, O. A., Zaikovskii, V. I., Shubin, Y. V., et al. (2015). Low-temperature CO oxidation by Pd/CeO_2 catalysts synthesized using the coprecipitation method. *Appl. Catal. B* 166–167, 91–103. doi: 10.1016/j.apcatb.2014.11.015

Slavinskaya, E. M., Kardash, T. Y., Stonkus, O. A., Gulyaev, R. V., Lapin, I. N., Svetlichnyi, V. A., et al. (2016). Metal-support interaction in Pd/CeO_2 model catalysts for CO oxidation: from pulsed laser-ablated nanoparticles to highly active state of the catalyst. *Catal. Sci. Technol.* 6, 6650–6666. doi: 10.1039/C6CY00319B

Slavinskaya, E. M., Stadnichenko, A. I., Muravyov, V. V., Kardash, T. Y., Derevyannikova, E. A., Zaikovskii, V. I., et al. (2018). Transformation of a Pt–CeO_2 mechanical mixture of pulsed-laser-ablated nanoparticles to a highly active catalyst for carbon monoxide oxidation. *ChemCatChem* 10, 2232–2247. doi: 10.1002/cctc.201702050

Stadnichenko, A. I., Kibis, L. S., Svintsitskiy, D. A., Koshcheev, S. V., and Boronin, A. I. (2018). Application of RF discharge in oxygen to create highly oxidized metal layers. *Surface Eng.* 34, 1–5. doi: 10.1179/1743294415Y.0000000010

Stadnichenko, A. I., Muravev, V. V., Koscheev, S. V., Zaikovskii, V. I., Aleksandrov, H. A., Neyman, K. M., et al. (2019). Study of active surface centers of Pt/CeO_2 catalysts prepared using radio-frequency plasma sputtering technique. *Surface Sci.* 679, 273–283. doi: 10.1016/j.susc.2018.10.002

Stadnichenko, A. I., Muravev, V. V., Svetlichnyi, V. A., and Boronin, A. I. (2017). Platinum state in highly active Pt/CeO_2 catalysts from the X-ray photoelectron spectroscopy data. *J. Struct. Chem.* 58, 1152–1159. doi: 10.1134/S0022476617060129

Svintsitskiy, D. A., Kibis, L. S., Stadnichenko, A. I., Koscheev, S. V., Zaikovskii, V. I., and Boronin, A. I. (2015). Highly oxidized platinum nanoparticles prepared through radio-frequency sputtering: thermal stability and reaction probability towards CO. *ChemPhysChem* 16, 3318–3324. doi: 10.1002/cphc.2015 00546

Tolla, B., Demourgues, A., Isnard, O., Menetrier, M., Pouchard, M., Rabardel, L., et al. (1999). Structural investigation of oxygen insertion within the $Ce_2Sn_2O_7$-$Ce_2Sn_2O_8$ pyrochlore solid solution by means of *in situ* neutron diffraction experiments. *J. Mater. Chem.* 9, 3131–3136. doi: 10.1039/a905914h

Trovarelli, A. (1996). Catalytic properties of ceria and CeO_2-Containing materials. *Catal. Rev. Sci. Eng.* 38, 439–520. doi: 10.1080/01614949608006464

Trovarelli, A., and Llorca, J. (2017). Ceria catalysts at nanoscale: how do crystal shapes shape catalysis? *ACS Catal.* 7, 4716–4735. doi: 10.1021/acscatal.7b01246

Tsunekawa, S., Ito, S., and Kawazoe, Y. (2004). Surface structures of cerium oxide nanocrystalline particles from the size dependence of the lattice parameters. *Appl. Phys. Lett.* 85, 3845–3847. doi: 10.1063/1.1811771

Vasilchenko, D. B., Gulyaev, R. V., Slavinskaya, E. M., Stonkus, O. A., Shubin, Y. V., Korenev, S. V., et al. (2016). Effect of Pd deposition procedure on activity of Pd/$Ce_{0.5}Sn_{0.5}O_2$ catalysts for low-temperature CO oxidation. *Catal. Commun.* 73, 34–38. doi: 10.1016/j.catcom.2015.10.012

Vayssilov, G. N., Lykhach, Y., Migani, A., Staudt, T., Petrova, G. P., Tsud, N., et al. (2011). Support nanostructure boosts oxygen transfer to catalytically active platinum nanoparticles. *Nat. Mater.* 10, 310–315. doi: 10.1038/nmat2976

Zeng, X., Zhang, R., Xu, X., and Wang, X. (2012). Study on ceria-modified SnO_2 for CO and CH_4 oxidation. *J. Rare Earths* 30, 1013–1019. doi: 10.1016/S1002-0721(12)60171-9

Zhu, H., Qin, Z., Shan, W., Shen, W., and Wang, J. (2004). Pd/CeO_2-TiO_2 catalyst for CO oxidation at low temperature: a TPR study with H_2 and CO as reducing agents. *J. Catal.* 225, 267–277. doi: 10.1016/j.jcat.2004.04.006

Zhu, Y., Jain, N., Hudait, M. K., Maurya, D., Varghese, R., and Priya, S. (2014). X-Ray Photoelectron spectroscopy analysis and band offset determination of CeO2 deposited on epitaxial (100), (110), and (111)Ge. *J. Vac. Sci. Technol. B Microelectron. Nanom. Struct.* 32:011217. doi: 10.1116/1.4862160

Conflict of Interest Statement: The authors declare that the research was conducted in the absence of any commercial or financial relationships that could be construed as a potential conflict of interest.

frontiers in Chemistry

ORIGINAL RESEARCH
published: 12 February 2019
doi: 10.3389/fchem.2019.00067

Activation of Water on MnO_X-Nanocluster-Modified Rutile (110) and Anatase (101) TiO_2 and the Role of Cation Reduction

*Stephen Rhatigan and Michael Nolan**

Tyndall National Institute, University College Cork, Cork, Ireland

Surface modification of titania surfaces with dispersed metal oxide nanoclusters has the potential to enhance photocatalytic activity. These modifications can induce visible light absorption and suppress charge carrier recombination which are vital in improving the efficiency. We have studied heterostructures of Mn_4O_6 nanoclusters modifying the TiO_2 rutile (110) and anatase (101) surfaces using density functional theory (DFT) corrected for on-site Coulomb interactions (DFT + U). Such studies typically focus on the pristine surface, free of the point defects and surface hydroxyls present in real surfaces. In our study we have considered partial hydroxylation of the rutile and anatase surfaces and the role of cation reduction, via oxygen vacancy formation, and how this impacts on a variety of properties governing the photocatalytic performance such as nanocluster adsorption, light absorption, charge separation, and reducibility. Our results indicate that the modifiers adsorb strongly at the surface and that modification extends light absorption into the visible range. MnO_X-modified titania can show an off-stoichiometric ground state, through oxygen vacancy formation and cation reduction spontaneously, and both modified rutile and anatase are highly reducible with moderate energy costs. Manganese ions are therefore present in a mixture of oxidation states. Photoexcited electrons and holes localize at cluster metal and oxygen sites, respectively. The interaction of water at the modified surfaces depends on the stoichiometry and spontaneous dissociation to surface bound hydroxyls is favored in the presence of oxygen vacancies and reduced metal cations. Comparisons with bare TiO_2 and other TiO_2-based photocatalyst materials are presented throughout.

Keywords: TiO2, water activation, reduction, oxygen vacancies, photocatalysis

Edited by:
Javier Carrasco,
CIC energigune, Spain

Reviewed by:
Jose J. Plata,
Universidad de Sevilla, Spain
Li-Min Liu,
Beihang University, China

****Correspondence:***
Michael Nolan
michael.nolan@tyndall.ie

Specialty section:
This article was submitted to
Physical Chemistry and Chemical
Physics,
a section of the journal
Frontiers in Chemistry

Received: *12 October 2018*
Accepted: *24 January 2019*
Published: *12 February 2019*

Citation:
Rhatigan S and Nolan M (2019)
Activation of Water on
MnO_X-Nanocluster-Modified Rutile
(110) and Anatase (101) TiO_2 and the
Role of Cation Reduction.
Front. Chem. 7:67.
doi: 10.3389/fchem.2019.00067

INTRODUCTION

Photocatalysts are semiconductor materials which absorb photons of energies in excess of the bandgap to produce electron-hole pairs. These charge carriers separate and migrate to the surface of the catalyst where they drive chemical reactions *via* reduction and oxidation of adsorbed species. Photocatalysis has a variety of applications, including, but not limited to, the solar production of hydrogen from water splitting (Ni et al., 2007; Fujishima et al., 2008; Maeda and Domen, 2010; Jiang et al., 2017).

A practical photocatalyst must meet a number of criteria, such as visible light absorption, efficient charge carrier separation, stability, and active surface sites for the adsorption of feedstock species. Reducible metal cations in the catalyst can be important for enhancing the activity of the catalyst toward the difficult step of water dissociation. The development of metal oxide photocatalysts is of interest as these materials are cheap, earth abundant and, in many instances, non-toxic. Indeed, the most widely studied photocatalyst is titanium dioxide (TiO_2) (Ni et al., 2007; Fujishima et al., 2008; Dimitrijevic et al., 2011; Pelaez et al., 2012; Habisreutinger et al., 2013; Tada et al., 2014; Etacheri et al., 2015) which was first demonstrated as a photoanode for water splitting by Fujishima and Honda (1972). The large bandgap (>3 eV) means that photoactivity is restricted to the UV and has limited the real-world application of TiO_2-based photocatalyst technologies. As a result, significant scientific effort has focused on extending the light absorption edge of TiO_2 to longer wavelengths.

Substitutional doping of TiO_2 with cations and/or anions is a widely studied approach to inducing visible light absorption through the emergence of impurity-derived energy levels in the TiO_2 bandgap (Di Valentin et al., 2007; Czoska et al., 2008; Haowei et al., 2008; Ikeda et al., 2008; Gai et al., 2009; Nie et al., 2009; Valentin et al., 2009; Xu et al., 2009; Yang et al., 2009; Yu et al., 2009; Zhu et al., 2009; Long and English, 2010a,b; Zhang et al., 2010; Zheng et al., 2010; Herrmann, 2012; Etacheri et al., 2015; Li, 2015; Na Phattalung et al., 2017). First principles studies of such doped systems typically focus on bandgap reduction (Cui et al., 2008; Yang et al., 2009; Zhu et al., 2009; Long and English, 2010a,b; Zhang et al., 2010, 2014; Chand et al., 2011; Guo and Du, 2012; Na Phattalung et al., 2017) and questions of charge localization and surface reactivity are often overlooked. These are important considerations as dopant-derived defect states have been shown to act as recombination centers (Herrmann, 2012; Etacheri et al., 2015; Li, 2015) and photocatalysis is generally a surface mediated phenomenon.

Studies of the chemistry and electronic properties of surfaces and interfaces are key to understanding and screening materials for photocatalysis. The enhanced performance of the benchmark material, P25, which consists of chemically interfaced rutile and anatase phases, has been attributed to the favorable alignment of the conduction and valence bands at the interface which facilitates charge transfer between phases and the suppression of charge carrier recombination (Scanlon et al., 2013). In addition, the interface can promote the formation of active catalytic sites. This effect can be tuned by considering heterostructures with metal oxides of different compositions. Such heterostructures have been realized experimentally and shown to exhibit enhanced photocatalytic activity (Boppana and Lobo, 2011; Boppana et al., 2013; Chae et al., 2017; Sotelo-Vazquez et al., 2017; Wang et al., 2017). Nanostructuring of metal oxides has been investigated as an approach to enhancing charge transfer kinetics and increasing surface area while providing low-coordinated metal and oxygen sites for the adsorption of feedstock species (Gordon et al., 2012; Bhatia and Verma, 2017; Zhang et al., 2017a; Ong et al., 2018). Further, nanostructuring can also facilitate the reduction of metal cations.

Surface modification of metal oxide surfaces with dispersed metal oxide nanoclusters combines the properties of hetero- and nano-structuring. Sub-nm nanoclusters of iron oxide were deposited on TiO_2 surfaces *via* chemisorption-calcination cycle (CCC) (Jin et al., 2011; Tada et al., 2014) and atomic layer deposition (ALD) (Libera et al., 2010). FeO_x-modified TiO_2 exhibited bandgap reduction and enhanced visible light photocatalytic activity. The modification was shown to suppress carrier recombination as indicated by photoluminescence spectroscopy (Jin et al., 2011). The red-shift in light absorption was attributed to cluster-derived states above the valence band maximum (VBM) which were identified by X-ray photoelectron spectroscopy (XPS) and density functional theory (DFT) simulations (Jin et al., 2011; Nolan, 2011a; Tada et al., 2014).

These studies, and the subsequent development of similar systems, (Jin et al., 2012; Boppana et al., 2013; Iwaszuk et al., 2013; Bhachu et al., 2014; Fronzi et al., 2016a) mean that a multitude of nanocluster-surface composites can be investigated. Considerations for tuning these systems for optimal performance include composition, surface termination, nanocluster size, and stoichiometry; all of which contribute to the light absorption properties, charge carrier mobility and surface reactivity. DFT simulations can be used to illuminate the properties underpinning experimental observations (Nolan, 2011a; Jin et al., 2012; Nolan et al., 2012; Iwaszuk et al., 2013) and to screen candidate materials worthy of further investigation (Park et al., 2009; Graciani et al., 2010; Nolan, 2011b, 2012, 2018; Iwaszuk and Nolan, 2013; Lucid et al., 2014; Nolan et al., 2014; Fronzi et al., 2016b; Rhatigan and Nolan, 2018a,b).

In the present study we use first principles DFT calculations to examine the photocatalytic properties of manganese oxide modified TiO_2, using model systems of Mn_4O_6-nanoclusters modifying the rutile (110) and anatase (101) surfaces and consider the role of partial surface hydroxylation in the interfacial chemistry. Our analysis includes an assessment of the stability of the composite surfaces, their ground state stoichiometry and reducibility *via* oxygen vacancy formation. Point defects, such as oxygen vacancies, are active sites at metal oxide surfaces and can be produced thermally. A more reducible surface will lose oxygen more readily and be more active in solar thermal (Muhich et al., 2016) or Mars and van Krevelen processes 1954, (Ganduglia-Pirovano et al., 2007). Computed density of states plots elucidate the impact of modification on the light absorption properties and a model for the photoexcited state (Di Valentin and Selloni, 2011) is used to examine charge separation and localization. Finally, we study the interaction of water with the modified surfaces and focus particularly on the role of oxygen vacancies and reduced cations on water adsorption. We identify the characteristics of activation, such as dissociation, geometry distortions and charge transfer to the adsorbed species. The importance of oxygen vacancies as active sites for water dissociation at the rutile (110) surface (Schaub et al., 2001; Henderson et al., 2003) and ceria surfaces (Mullins et al., 2012) has been widely discussed and reduced Ti^{3+} ions have been shown to be active in the chemistry at titania surfaces

(Lira et al., 2011; Xiong et al., 2012). For anatase TiO_2, oxygen vacancies have been shown to be more stable at subsurface and bulk sites than on the surface (He et al., 2009; Scheiber et al., 2012). However the surface can be reduced by electron bombardment (Scheiber et al., 2012; Setvin et al., 2016) and the reaction of these vacancy sites with water and O_2 results in water dissociation. These studies highlight the necessity of engineering photocatalytic surfaces for which vacancies can be produced with moderate energy costs.

MnO_x is an interesting modifier as manganese is a multi-valent, reducible element which crystallizes in oxides with a variety of oxidation states; (Franchini et al., 2007) this will have implications for the light absorption properties and reducibility of sub-nm nanoclusters of MnO_x dispersed at the titania surfaces. We have previously studied similar systems of MnO_x-modified TiO_2, in collaboration with experiment, to interrogate their activity for CO_2 capture and reduction (Schwartzenberg et al., 2017). In the present study, we focus on the potential for these catalysts to be active toward water activation. Furthermore, we investigate the impact of surface hydroxylation on the reduction of the heterostructures *via* oxygen vacancy formation and apply a model for photoexcitation to examine the associated energetics and charge localization. In reference Schwartzenberg et al. (2017), the Mn_4O_6-TiO_2 composites were found to be stoichiometric in the ground state for both modified rutile and anatase, albeit with moderate costs to produce reducing oxygen vacancies (+0.59 eV for rutile and +1.1 eV for anatase). However, the impact of surface hydroxyls on the formation of oxygen vacancies was not investigated; in this paper we show that vacancy formation is in fact promoted with hydroxyls already present at the TiO_2 surfaces. The photoexcited state model, which examines localization of electrons and holes at nanocluster metal and oxygen sites, sheds light on experimental observations which suggest that the MnO_x-modifiers may facilitate recombination (Schwartzenberg et al., 2017). In addition, active oxygen vacancy sites play a crucial role in the subsequent interaction of water molecules and their adsorption modes. In particular, dissociation is favored for the reduced systems; this is an important step in the water oxidation reaction.

METHODOLOGY

Periodic plane wave DFT calculations are performed using the VASP5.4 code (Kresse and Hafner, 1994; Furthmüller et al., 1996) with an energy cut-off of 400 eV. The core-valence interaction is described with projector augmented wave (PAW) potentials, (Blöchl, 1994; Kresse and Joubert, 1999) with 4 valence electrons for Ti, 6 for O, 13 for Mn and 1 for H species. The Perdew-Wang (PW91) approximation to the exchange-correlation functional is used (Perdew et al., 1996).

The TiO_2 rutile (110) and anatase (101) substrates are modeled as 18 and 12 atomic layer slabs, respectively. The bulk lattice parameters for rutile were computed as a = 4.639 Å and c = 2.974 Å, and the rutile (110) surface was modeled with a (2 × 4) surface expansion. For anatase the bulk lattice parameters are a = 3.814 Å and c = 9.581 Å and a (1 × 4) expansion was used for the anatase (101) surface. These parameters correspond to surface areas per supercell of 13.120 × 11.896 Å and 10.312 × 15.255 Å for rutile (110) and anatase (101), respectively. The surfaces are separated from their periodic images by vacuum gaps of 20 Å, as used in our previous studies (Fronzi and Nolan, 2017; Schwartzenberg et al., 2017; Nolan, 2018; Rhatigan and Nolan, 2018a,b). Γ-point sampling is used and the convergence criteria for the energy and forces are 10^{-4} eV and 0.02 $eVÅ^{-2}$, respectively. All calculations are spin polarized.

A Hubbard U correction is implemented to consistently describe the partially filled Mn 3d states and reduced Ti^{3+} states (Anisimov et al., 1991; Dudarev et al., 1998). The values of U used are U(Ti) = 4.5 eV and U(Mn) = 4 eV and these have been chosen based on previous work on TiO_2 (Morgan and Watson, 2007; Nolan et al., 2008; Iwaszuk and Nolan, 2011; Nolan, 2011a; Fronzi et al., 2016a; Fronzi and Nolan, 2017; Rhatigan and Nolan, 2018a) and manganese oxides (Franchini et al., 2007; Kitchaev et al., 2016).

To model surface hydroxylation (before the nanoclusters are adsorbed) and the impact on the heterostructure chemistry, four water molecules are dissociatively adsorbed at the clean rutile (110) and anatase (101) surfaces which gives a partial coverage of 50%. The computed energy gain when the TiO_2 surfaces are hydroxylated at half coverage is −1.03 eV per water molecule for rutile (110) and −0.8 eV for anatase (101), referenced to the total energy of four gas phase water molecules. These indicate favorable water adsorption and surface hydroxylation and these models have been used in our previous studies (Fronzi et al., 2016a; Fronzi and Nolan, 2017; Schwartzenberg et al., 2017; Rhatigan and Nolan, 2018a). The nature of water molecules adsorbed at metal oxide surfaces, and in particular TiO_2 surfaces, is widely investigated both experimentally and computationally (Valdés et al., 2008; Fronzi and Nolan, 2017; Rhatigan and Nolan, 2018a) and readers are referred to reference (Mu et al., 2017) for a review of the state of the art. These models are representative of hydroxylated rutile and anatase surfaces, while we are not attempting to describe the most stable solutions for water or dissociative water adsorption at these titania surfaces (Fronzi et al., 2016a; Fronzi and Nolan, 2017; Rhatigan and Nolan, 2018a). The hydroxylated surfaces are denoted by OH-r110 and OH-a101. For the O^{2-} ions of the pristine titania surfaces, computed Bader charges are in the range of 7.3–7.4 electrons and this is our reference. After hydroxylation, Bader charges for those oxygen atoms of the surface to which H atoms are adsorbed increase to values in the range 7.6–7.7 electrons, with similar values for oxygen ions of the water-derived hydroxyls.

The Mn_4O_6 nanocluster (see **Supporting Information**) was adsorbed in different configurations at the hydroxylated rutile (110) and anatase (101) surfaces and the adsorption energies are computed using:

$$E_{ads} = E_{surf+A} - E_{surf} - E_A \qquad (1)$$

where E_{surf+A}, E_{surf} and E_A are the energies of the adsorbate-surface composite system, the hydroxylated titania surface and the gas phase nanocluster, respectively.

For the reduction of the composite surface, each of the six O sites of the supported nanocluster is considered for the formation of an oxygen vacancy, O_V. One oxygen ion is removed from the Mn_4O_x cluster and the vacancy formation energy is calculated as:

$$E_{vac} = E\,(Mn_4O_{x-1}) + 1/2E(O_2) - E\,(Mn_4O_x) \quad (2)$$

where the first and third terms on the right hand side are the total energy of the cluster-surface composite with and without an oxygen vacancy and the energy is referenced to half the total energy for molecular O_2. Having identified the most stable structure with a single O_V, the calculation is repeated for each of the five remaining O sites to determine the most stable structure with two O_V. Oxidation states are investigated with Bader charge analysis and computed spin magnetizations.

We apply a model for photoexcitation to the ground state configuration of each modified surface and to the unmodified OH-r110 and OH-a101 surfaces for comparison. This model involves imposing a triplet electronic state on the system (Di Valentin and Selloni, 2011) to promote an electron to the conduction band, with a corresponding hole in the valence band. The analysis of the energies and charge localization is discussed in more detail in the **Supporting Information**.

For the interaction of water with the modified surfaces, H_2O molecules are adsorbed in various configurations at the oxygen deficient systems and the adsorption energies are calculated as:

$$E_{ads} = E_{surf+H_2O} - E_{surf} - E_{H_2O} \quad (3)$$

where E_{surf+H_2O}, E_{surf} and E_{H_2O} refer to the energies of the H_2O molecule and modified surface in interaction, the modified surface, and the gas phase H_2O, respectively.

Oxygen atoms of the surface, cluster and surface-bound hydroxyls are denoted O_S, O_C and O_{OH}, respectively, and similar notation is adopted for OH groups. For the interaction of water with the modified surfaces, water-derived oxygen and hydroxyls are denoted O_W and OH_W.

RESULTS

Stoichiometric Mn_4O_6-Modified TiO_2 OH-Rutile (110) and OH-Anatase (101)

Figures 1A,B show the adsorption energies and relaxed atomic structures of the stoichiometric Mn_4O_6-nanocluster modifying the OH-r110 and OH-a101 surfaces. The large, negative adsorption energies indicate that the nanocluster-surface interaction is favorable and that the nanoclusters will be stable against desorption and aggregation (Fronzi et al., 2016b; Nolan et al., 2016; Fronzi and Nolan, 2017; Nolan, 2018; Rhatigan and Nolan, 2018a,b). For Mn_4O_6-OH-r110 (**Figure 1A**), three Mn ions are 4-fold coordinated and to each of these is bound a terminal OH. Of these OH groups, one has migrated from a Ti site in the rutile surface to an Mn ion of the cluster (OH_{OH}) and two OH groups result from the migration of hydrogen from surface hydroxyls to O_C atoms (OH_C). The fourth Mn ion is 5-fold coordinated and is bound to three O_C and two O_S ions (one bridging O_S and one in-plane O_S). Five O ions of the OH-r110 surface bind with Mn of the nanocluster (three O_S and two O_{OH}) and two O_C ions bind to Ti of the surface. Mn-O distances are in the range 1.8–2.1 Å; the shorter distances involve 2-fold coordinated O ions and for Mn bound to the in-plane O_S ion the Mn-O distance is 2.2 Å. Ti ions which bind to the nanocluster migrate out from the surface by 0.1 Å, however, distortions to the geometry of the rutile (110) surface are minimal.

For Mn_4O_6-OH-a101 (**Figure 1B**), three Mn ions are 4-fold coordinated and one Mn is 5-fold coordinated. Five O_C sites are 2-fold coordinated with one O_C ion binding to three Mn ions and a H atom which has migrated from a bridging O_S site. Of the six interfacial bonds between the Mn_4O_6 nanocluster and OH-a101, three involve Mn and OH_{OH} groups; two involve Mn and bridging O_S sites and the sixth is a Ti-O_C bond. Mn-O distances are in the range 1.7–2.1 Å.

For Mn_4O_6 adsorbed at OH-r110 and OH-a101, the computed Bader charge for each of the Mn ions is 11.3 electrons, which are typical of Mn^{3+} ions (see **Table 1**).(Schwartzenberg et al., 2017) The spin magnetizations for these sites are each 3.9 μ_B, which reflects the $3d^4$ configuration of the Mn^{3+} ion.

For the Mn_4O_6 nanocluster adsorbed at OH-a101, there is an accumulation of positive charge at those O_C sites which are doubly-coordinated to Mn ions of the nanocluster. Computed Bader charges of 7.0 electrons for these O_C sites compare with 7.3–7.7 electrons computed for O^{2-} anions of the OH-a101 surface. The nanocluster-surface interaction is not as strong at the OH-a101 surface as indicated by the smaller adsorption energy. The consequence of this is that the supported nanocluster retains characteristics of the gas phase, for which the O_C ions have computed Bader charges in the range 7.0–7.1 electrons.

Reduction of Mn_4O_6-Modified TiO_2 OH-Rutile (110) and OH-Anatase (101) Via Oxygen Vacancy Formation

The most stable modified surfaces with a single O_V are shown in **Figure 1C** for Mn_4O_5-OH-r110 and **Figure 1D** for Mn_4O_5-OH-a101. For the modified OH-r110 surface the formation energy of a single O_V is −0.26 eV and this formation energy indicates that O_V will form spontaneously. The next three most stable vacancy sites have formation energies in the range 0.60–0.82 eV. After formation of the most stable vacancy, two Mn ions are 3-fold coordinated and the third and fourth Mn cations are 4- and 5-fold coordinated. Two bridging and one in-plane surface oxygen are bound to Mn ions of the nanocluster. Two O_C ions bind to surface Ti sites while three O_C ions are bound only to Mn and H ions.

The formation of the neutral oxygen vacancy releases two electrons. Bader charge analysis reveals that the electrons localize at the 3-fold coordinated Mn sites of the nanocluster. The computed Bader charges on these sites increase from 11.3 to 11.5 electrons; see (**Table 1**) for computed Bader charges of reduced Ti and all Mn sites. The computed spin magnetizations are 4.6 μ_B for these Mn sites; this is typical of the formation of reduced Mn^{2+} ions which has an electronic configuration of $3d^5$.

The most favorable structure with one O_V is more stable than the second most favorable by 0.9 eV. However, the relaxed atomic structures of these configurations are very similar (compare

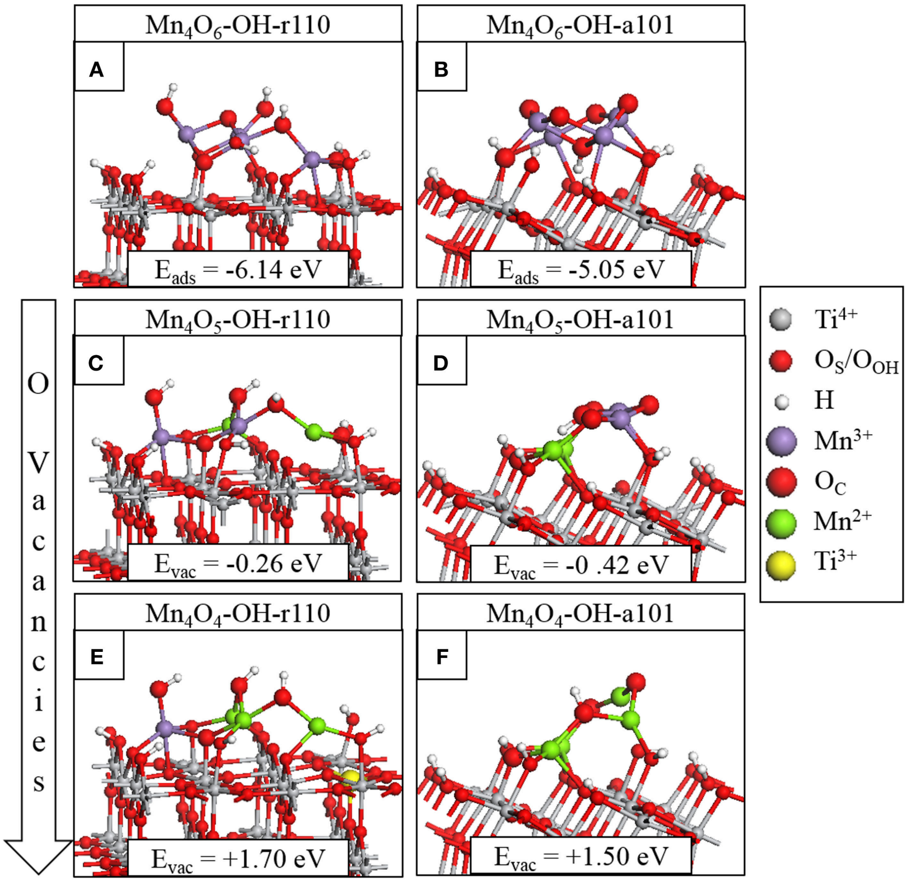

FIGURE 1 | Relaxed atomic structures of Mn_4O_x modifying the hydroxylated titania surfaces. The stoichiometric composites are shown in **(A)** for Mn_4O_6-OH-r110 and **(B)** for Mn_4O_6-OH-a101; the nanocluster adsorption energies are included in the inset. The atomic structures after formation of the most stable single O_V are shown in panels **(C)** for Mn_4O_5-OH-r110 and **(D)** for Mn_4O_5-OH-a101. The atomic structures of the most stable composites with two O_V are shown in panels **(E)** for Mn_4O_4-OH-r110 and **(F)** for Mn_4O_4-OH-a101. The energy costs to produce O_V are included and computed relative to the structure with one less O_V. Atomic species and oxidation states are indicated by the colors in the legend on the right hand side.

TABLE 1 | Computed Bader charges for the manganese ions in the supported nanoclusters before and after formation of one or more O_V.

Surface	**OH-r110**				**OH-a101**		
Modifier	**Mn_4O_6**	**Mn_4O_5**	**Mn_4O_4**		**Mn_4O_6**	**Mn_4O_5**	**Mn_4O_4**
Mn_I	11.3	**11.5**	**11.5**	Mn_I	11.3	**11.5**	**11.5**
Mn_{II}	11.3	11.2	11.2	Mn_{II}	11.3	11.3	**11.6**
Mn_{III}	11.3	11.2	**11.5**	Mn_{III}	11.3	11.3	**11.6**
Mn_{IV}	11.3	**11.5**	**11.5**	Mn_{IV}	11.3	**11.5**	**11.5**
Ti_I	1.3	1.3	**1.7**				

Also included are Bader charges for titanium ions of the support which are reduced after vacancy formation. Reduced Mn^{2+} and Ti^{3+} are highlighted in bold.

Figure 1C with **Figure S3A**). The difference in energy arises from the distibution of excess charge. For the O_V structure shown in **Figure S3A**, one excess charge localizes at a 5-fold coordinated surface Ti site for which the Bader charge increases from 1.3 to 1.7 electrons. A computed spin magnetization of 1.0 μ_B reflects the $3d^1$ configuration of reduced Ti^{3+}.

For the modified OH-a101 surface, the most stable O_V has a formation energy of −0.42 eV which indicates that it will spontaneously form, so that the ground state is off-stoichiometric (vacancy formation energies for other sites of the nanocluster were in the range 0.5–1.3 eV). This compares with Mn_4O_6 modifying bare anatase (101) which was found to be stoichiometric in the ground state (Schwartzenberg et al., 2017). After the formation of this O_V, two Mn ions relax toward the titania surface and bind with bridging O_S sites so that, in this configuration, each Mn ion is 4-fold coordinated. Bader charge analysis and computed spin densities indicate that two Mn ions are reduced to Mn^{2+}, having computed Bader charges of 11.5 electrons and computed spin magnetisations of 4.6 μ_B. The next most stable structure with one O_V is shown in **Figure S3B**; in this configuration three Mn ions are reduced to Mn^{2+} and this is accompanied by an accumulation of postive charge on 2-fold coordinated O_C ions for which the Bader charges were computed as 7.0 electrons.

The formation of the second O_V has a moderate energy cost for both MnO_x-modified TiO_2 surfaces, however the modified anatase surface is reducible at a lower energy cost. Given that the anatase surface is more easily hydroxylated, (Mu et al., 2017) which these results indicate promotes vacancy formation, one would expect more O_V present on modified anatase. That O_V formation is more facile for modified anatase corroborates previous experimental work on MnO_x-TiO_2 (Schwartzenberg et al., 2017). The most stable configurations of the heterostructures with two O_V are shown in **Figure 1E** for Mn_4O_4-OH-r110 and **Figure 1F** for Mn_4O_4-OH-a101. For the Mn_4O_4-OH-r110 surface, the two most stable O_C sites for formation of a second O_V had similar formation energies. One such configuration is described here and the other is included in the **Supporting Information**. For the structure shown in **Figure 1E**, the removed O_C ion was 2-fold coordinated to a cluster Mn and surface Ti ion. After vacancy formation the Mn ion binds to a bridging O_S ion and remains 3-fold coordinated. In this configuration three Mn ions are reduced; the Bader charges and spin magnetizations for these sites are 11.5 electrons and 4.6 μ_B, respectively. Similarly, for the Ti site to which the removed O_C was bound, the Bader charge and spin magnetization are 1.7 electrons and 1.0 μ_B. Hence, the Mn_4O_4-OH-r110 heterostructure with two oxygen vacancies has one Ti^{3+} and three Mn^{2+} ions.

For the modified OH-a101 surface, a 3-fold coordinated O_C site, which forms a hydroxyl group bridging two Mn ions, has the lowest cost to produce a second O_V. One Mn ion that was bound to the removed O_C atom is 2-fold coordinated, having been originally coordinated to three O_C ions and one O_{OH} ion. The second Mn ion is 3-fold coordinated, having been 4-fold coordinated prior to vacancy formation. The H ion which was bound to the removed O_C migrates to another O_C ion. In this Mn_4O_4-OH-a101 configuration, there are four Mn^{2+} ions, with computed Bader charges of 11.5–11.6 electrons and spin magnetizations of 4.6 μ_B.

Additional structures with two O_V are presented in **Figure S3C** for Mn_4O_4-OH-r110 and **Figure S3D** for Mn_4O_4-OH-a101; these are close in energy to the configurations described above, and differ in the distribution of excess charge over Mn and Ti sites. Hence, Mn and Ti sites should be present at the surface in a variety of oxidation states.

The localization of electrons at Ti and Mn sites is also accompanied by localized geometry distortions. The cation-O distances increase by ∼0.1 Å after reduction, reflecting the larger ionic radii of Mn^{2+} and Ti^{3+} compared to $Mn^{3+}$and Ti^{4+} (Shannon and Prewitt, 1969).

Electronic Properties of Mn_4O_x-Modified TiO_2 OH-Rutile (110) and OH-Anatase (101)

The projected electronic density of states (PEDOS) for the heterostructures are presented in **Figure 2**. Since the heterostructures are off-stoichiometric in the ground state, the PEDOS plot for Mn_4O_6-OH-r110 and Mn_4O_6-OH-a101 have been omitted from this figure and are included in the **Supporting Information** for completeness. The top panels of **Figure 2** show the PEDOS of modified OH-r110 for (A) the ground state with one O_V and (B) the reduced state with two O_V. The PEDOS plots show that occupied nanocluster-derived states (Mn 3d and O_C 2p) extend to 0.3 and 0.8 eV above the VBM of the rutile support for Mn_4O_5- and Mn_4O_4-OH-r110, respectively. Unoccupied Mn 3d-derived states also emerge in the titania band gap at 0.1 and 0.3 eV below the conduction band minimum (CBM) for the ground state with one O_V and the reduced state with two O_V. Additional states emerge in the band gap due to occupied Ti^{3+} states (see inset of **Figure 2B**), for the heterostructure with two O_V.

The bottom panels of **Figure 2** display the PEDOS of the modified OH-a101 surface for (C) the ground state, with one O_V, and (D) reduced state with two O_V. The PEDOS plot for the ground state, with one O_V, shows that occupied Mn 3d- and O_C 2p-derived states extend to 1.3 eV above the titania derived VBM, while unoccupied Mn 3d states emerge at 1 eV below the CBM, leading to a significant reduction in the computed energy gap relative to TiO_2. For the reduced structure, with two O_V, each of the Mn ions is reduced to Mn^{2+}, and the highest occupied of these states is 1 eV above the VBM. The lowest energy, unoccupied state is Mn-derived and is 1 eV below the CBM. For Mn_4O_4-OH-a101 the energy gap is 0.6 eV, with our DFT+U set-up showing a reduction over unmodified anatase.

These features of the PEDOS for Mn_4O_x-TiO_2 can be attributed to formation of interfacial bonds, the presence of low-coordinated Mn and O_C sites and the facile formation of O_V in the supported metal oxide nanocluster. Modification pushes the VBM to higher energy and results in the emergence of empty states below the CBM; these effects, and the consequent red shift, are greater for modified anatase, consistent with previous reports (Schwartzenberg et al., 2017). These metal oxide nanocluster-modified surfaces are of interest for the oxygen evolution half reaction (OER) of the water splitting process and in this context raising the VBM from that of TiO_2 and toward the water oxidation potential is a desirable effect. Lowering of the titania CBM from its favorable position straddling the water reduction potential is detrimental to the hydrogen evolution reaction (HER) activity. However, as H adsorbs too strongly at metal oxide surfaces, such heterostructures will in any case not be suitable photocathodes for water splitting.

Photoexcitation Model

We apply the model for the photoexcited state to the ground state systems, Mn_4O_5-OH-r110 and Mn_4O_5-OH-a101. **Table 2** presents the computed vertical, singlet-triplet and electron-hole trapping energies, as discussed in the **Supporting Information**. As can be seen from the values listed in **Table 2**, the underestimation of the bandgap inherent in approximate DFT is present in our DFT+U computational set-up. Our goal in choosing +U corrections is to consistently describe the localization of electrons and holes rather than reproduce the bandgap of bulk TiO_2, which is not advised. Comparison of these computed energies across different structures nonetheless yields useful qualitative information about the effect of surface modification and results for the unmodified OH-r110 and OH-a101 surfaces are included for reference. In particular, $E^{vertical}$ is analogous to the optical band gap, and a reduction in this value

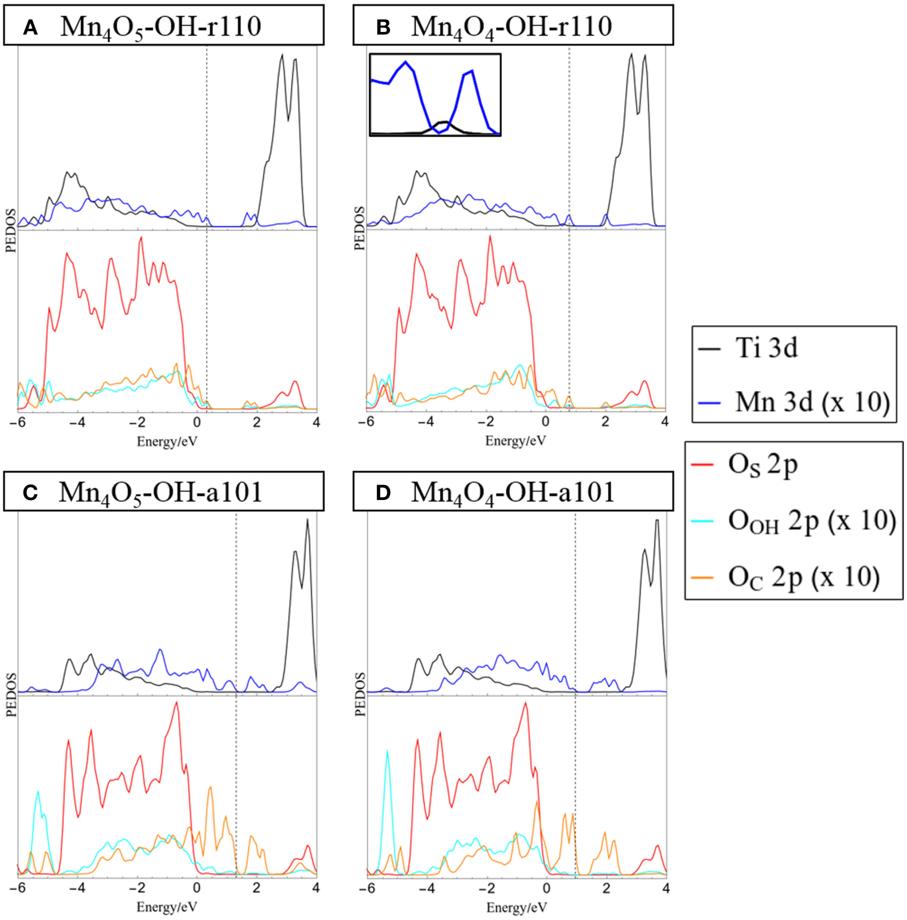

FIGURE 2 | Projected electronic density of states (PEDOS) plots for **(A)** Mn_4O_5-, and **(B)** Mn_4O_4-OH-r110 and **(C)** Mn_4O_5-, and **(D)** Mn_4O_4-OH-a101. The computed valence band max is set to 0 eV and the Fermi energy is indicated with a dashed line. The top half of each panel displays Ti and Mn 3d derived states. The bottom halves of the panels show contributions to the DOS from oxygen 2p states of the surface (O_C), surface bound hydroxyls (O_{OH}) and nanocluster (O_C). Inset in panel **(B)** shows the mid-gap occupied Ti 3d states in the range [0 eV, 1 eV].

TABLE 2 | Vertical singlet-triplet energy difference ($E^{vertical}$), the relaxed singlet-triplet energy difference (E^{excite}) and the relaxation energy (E^{relax}) for Mn_4O_5-OH-r110 and Mn_4O_5-OH-a101.

Composite structure	$E^{vertical}$ (eV)	E^{excite} (eV)	E^{relax} (eV)
OH-rutile (110)	2.08	1.61	0.46
Mn_4O_5-OH-rutile (110)	2.00	0.68	1.31
OH-anatase (101)	2.71	1.52	1.19
Mn_4O-$_5$-OH-anatase (101)	2.37	0.95	1.43

Values for hydroxylated rutile (110) and anatase (101) surfaces have been included for reference.

for a heterostructure relative to unmodified titania implies that modification leads to a red shift in light absorption.

When comparing Mn_4O_5-OH-r110 with unmodified OH-r110 we can see that the values for $E^{vertical}$ are similar, however E^{excite} is reduced by 0.93 eV for the modified surface. Comparing Mn_4O_5-OH-a101 with unmodified OH-a101, decreases in $E^{vertical}$ and E^{excite} by 0.34 and 0.57 eV, respectively, indicate that modification leads to a significant red shift in light absorption. These results corroborate the analysis of the PEDOS. E^{relax} is the energy gained by the system after structural relaxation in response to the triplet electronic state and is related to the stability of the trapped electron and hole. The relaxation energy is larger for Mn_4O_5-OH-r110 than that computed for unmodified OH-r110 (1.31 vs. 0.46 eV) and reflects the greater flexibility of the modified system in accommodating the triplet electronic state. The relaxation energies for Mn_4O_5-OH-a101 and unmodified OH-a101 are comparable. The mixture of Mn oxidation states and the proximity of the Mn ions to each other at the anatase surface (neighboring Mn-Mn distances are in the range 2.9–3.2 Å for Mn_4O_5-OH-a101 and 3.0–3.9 Å for Mn_4O_5-OH-r110) restricts the degree to which the nanocluster can respond structurally to the localization of photoexcited charges.

Through analysis of Bader charges and spin magnetizations we can determine the electron and hole localization sites and the results of this analysis are represented graphically in **Figure 3**. For Mn_4O_5-OH-r110, in **Figures 3A,B**, the electron localizes at an Mn site; the Bader charge and spin magnetization for this site are 11.5 electrons and 4.6 μ_B after electron localization, which are typical of Mn^{2+} formation. The hole localizes at an O_C site which is 2-fold coordinated to the Mn^{2+} ion and a surface Ti. In this instance the Bader charge is 6.8 electrons and the spin magnetization is 0.8 μ_B, which are consistent with formation of O^-. The Mn^{2+}-O^- distance increases by 0.2 Å, relative to the ground state. The Ti-O^- distance decreases by 0.1 Å.

For Mn_4O_5-OH-a101 (**Figures 3C,D**), the photoexcited electron localizes at an Mn site of the nanocluster, as confirmed by a computed Bader charge of 11.5 electrons and spin magnetization of 4.5 μ_B. The hole state localizes predominantly at an O_C site which bridges Mn^{2+} and Mn^{3+} ions. After hole localization the Bader charge for the O^- ion is 6.7 electrons and the spin magnetization is 0.8 μ_B. The Mn^{2+}-O distances increase by 0.2–0.3 Å.

These results show that the electron localizes at an Mn site of the supported nanocluster and the hole state localizes at a neighboring O_C site. Based on this model for the photoexcited state, we can conclude that modification does not necessarily promote the spatial separation of photoexcited charges. However, both electrons and holes will be available at the modified surface for transfer to adsorbed species.

H_2O Adsorption at Mn_4O_x-Modified OH-Rutile (110) and OH-Anatase (101)

For the interaction of water at the modified surfaces, only those composites with O_V present were considered, as such vacancies are known to be active sites at metal oxide surfaces (Schaub et al., 2001; Wang et al., 2016; Ruiz Puigdollers et al., 2017; Zhang et al., 2017b). Water adsorption is favorable at multiple sites of both modified surfaces and the geometries of the most stable adsorption configurations are displayed in **Figure 4**, while the **Supporting Information** shows other, less stable, water adsorption structures.

We adsorb water in molecular form at the heterostructures and relax the geometry. For Mn_4O_5-OH-r110, shown in **Figure 4A**, water is adsorbed exothermically in molecular form with a computed adsorption energy of −0.75 eV. In this instance, the water molecule binds to a 3-fold coordinated Mn^{2+} site with a Mn-O_W distance of 2.3 Å. **Figure S5A** shows dissociative water adsorption at the Mn_4O_5-OH-r110 surface, which has an adsorption energy of −0.31 eV. Upon dissociation, an H atom migrates to a bridging O_S site and the water-derived hydroxyl (OH_W) is singly coordinated to an Mn site with an Mn-O_W distance of 1.9 Å. The dissociation is accompanied by a transfer of charge from O_W to the nanocluster modifier, indicated by a decrease of 0.4 electrons in the computed Bader charge for the O_W ion. The Bader charges and spin magnetizations of cation sites are unchanged by the adsorption and dissociation.

Water adsorbs molecularly at Mn_4O_5-OH-a101, as shown in **Figure 4B**, with an adsorption energy of −0.74 eV. The H_2O binds to a 4-fold coordinated Mn^{3+} ion with a Mn-O_W distance of 2.2 Å. Since Mn_4O_5-OH-r110 and Mn_4O_5-OH-a101 are the ground states of the systems, the single O_V having formed spontaneously, these composites favor non-stoichiometry so that the strength of interaction with the water molecule is not sufficient to promote spontaneous dissociation and adsorption in molecular form is favored.

The surfaces with two O_V show higher reactivity to water, as indicated by the larger adsorption energies in **Figures 4C,D**. Water adsorbs and spontaneously dissociates at both Mn_4O_4-OH-r110 (**Figure 4C**) and Mn_4O_4-OH-a101 (**Figure 4D**). For Mn_4O_4-OH-r110, the water molecule adsorbs at an O_V site. An H atoms migrates to a bridging O_S site and the OH_W group is doubly coordinated to an Mn and a surface Ti site. The Mn-O_W and Ti-O_W distances are 2.2 Å. Bader charge analysis reveals that 0.3 electrons are transferred from the O_W to the surface. Despite this charge transfer, the Ti ion which binds to OH_W and which was reduced to Ti^{3+} due to O_V formation prior to water adsorption, remains in the Ti^{3+} state. This agrees with work by Henderson et al. in which no charge transfer was observed between Ti^{3+} and bridging hydroxyls bound at oxygen vacancy sites at the TiO_2 rutile (110) surface (Henderson et al., 2003). The reduced Ti site was only oxidized after interaction of O_2 with the Ti^{3+}-OH group. After water adsorption and dissociation the distribution of cation oxidation states is unchanged so that there are three Mn^{2+} ions and one Ti^{3+}. The Bader charge for the bridging O_S site to which the H ion binds increases from 7.3 to 7.7 electrons which, as discussed in the methodology, is typical of hydroxyl formation.

For Mn_4O_4-OH-a101, the water molecule adsorbs at an O_V site and after dissociation an H atom migrates to an O_C ion which shows an increase in Bader charge, from 7.1 to 7.6 electrons. The OH_W group binds to three Mn^{2+} ions; the Bader charges and spin magnetizations for cation sites are unchanged so that these ions are not involved in the charge transfer. However, for the water adsorption configuration shown in **Figure S5D**, an Mn^{2+} ion is re-oxidized to Mn^{3+} after dissociation of the water molecule. In this instance the adsorption energy is −1.89 eV and the OH_W group is singly-coordinated to the re-oxidized Mn ion.

CONCLUSIONS

The properties of Mn_4O_x-modified hydroxylated titania surfaces and their reduction and interaction with water depend on the phase of the TiO_2 substrate. For Mn_4O_6 adsorbed at the hydroxylated anatase (101) surface, one interfacial bond is established between a cluster oxygen ion and the surface and Mn ions bind mostly to oxygen ions of the surface bound hydroxyls. Conversely, for Mn_4O_6 at hydroxylated rutile (110), the nanocluster-surface interaction is more intimate, with Mn ions binding to bridging and in-plane oxygen ions of the rutile surface.

Our results indicate that both Mn_4O_x-OH-r110 and Mn_4O_x-OH-a101 favor non-stoichiometry, in contrast to unhydroxylated modified TiO_2 surfaces, as oxygen vacancies form spontaneously and both composites can be considered highly reducible with moderate energy costs for subsequent oxygen vacancy formation. Bader charge analysis shows that Mn ions are present in a mixture of oxidation states of at the hydroxylated surfaces. Both Mn and Ti ions are reduced in response to vacancy formation.

Modification with Mn_4O_x has a significant impact on the light absorption properties. Occupied Mn 3d states extend the

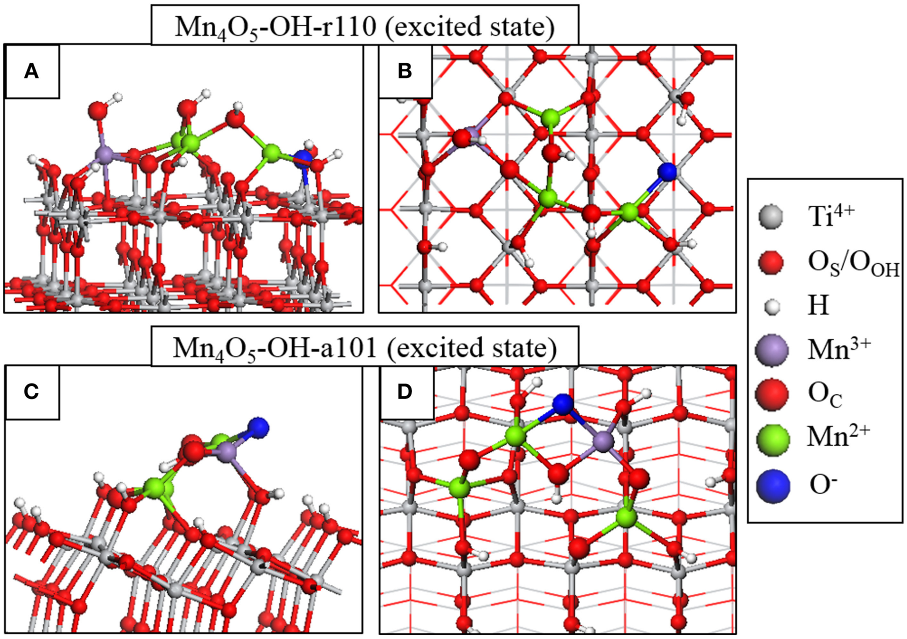

FIGURE 3 | Atomic structure of the fully relaxed triplet electronic state imposed on Mn_4O_6-OH-r110 for **(A)** side and **(B)** top view and Mn_4O_5-OH-a101 for **(C)** side and **(D)** top view. Charge localization and changes in oxidation state are distinguished by color according to the legend on the right hand side.

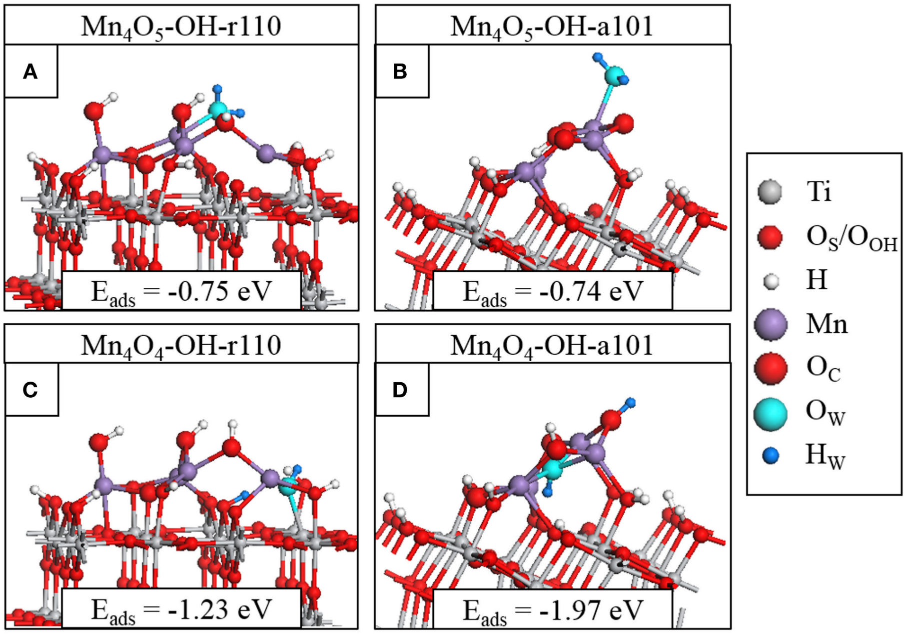

FIGURE 4 | Relaxed atomic structures of the most stable configurations of H_2O adsorbed at **(A)** Mn_4O_5-OH-r110, **(B)** Mn_4O_5-OH-a101, **(C)** Mn_4O_4-OH-r110, and **(D)** Mn_4O_4-OH-a101. Atomic species are distinguished by color according to the legend on the right hand side.

VBM of the composites to higher energies relative to that of the titania support and empty states emerge below the CBM. The consequent red shift in the light absorption edge is confirmed by our model for the photoexcited state. In particular, the vertical energy, analogous to the optical energy gap, decreases significantly for Mn_4O_5-OH-a101 relative to that computed for the unmodified, hydroxylated anatase (101) surface. Analysis of this model shows that electrons and holes localize at Mn and neighboring O_C sites, respectively, so that modification may not promote separation of photoexcited charges, but the trapping energies of the electron and hole are quite high, suggesting high stability.

With regard to water adsorption and activation, the formation of oxygen vacancies has an impact on the strength of interaction and the most favorable adsorption mode of H_2O at the modified surfaces. For Mn_4O_5-OH-a101, with a spontaneously formed O_V, water adsorbs only in molecular form. With formation of reducing oxygen vacancies, water adsorption becomes more exothermic and leads to spontaneous dissociation to surface bound hydroxyls, similar to observations made for water interacting at reduced TiO_2 (Schaub et al., 2001; Henderson et al., 2003) and CeO_2 (Mullins et al., 2012) surfaces.

AUTHOR CONTRIBUTIONS

MN devised the research. SR performed the DFT modeling. Both authors analyzed the results and prepared, reviewed and approved the text of the paper.

ACKNOWLEDGMENTS

We acknowledge support from Science Foundation Ireland through the US-Ireland R and D Parntershop program, Grant number SFI/US/14/E2915 and the ERA.Net for Materials Research and Innovation (M-ERA.Net 2), Horizon 2020 grant agreement number 685451, SFI Grant Number SFI/16/M-ERA/3418 (RATOCAT). We acknowledge access to SFI funded computing resources at Tyndall Institute and the SFI/HEA funded Irish Centre for High End Computing. We are grateful for support from the COST Action CM1104 Reducible Metal Oxides, Structure and Function.

SUPPLEMENTARY MATERIAL

The Supplementary Material for this article can be found online at: https://www.frontiersin.org/articles/10.3389/fchem.2019.00067/full#supplementary-material

REFERENCES

Anisimov, V. I., Zaanen, J., and Andersen, O. K. (1991). Band theory and mott insulators: hubbard U instead of stoner I. *Phys. Rev. B.* 44, 943–954.

Bhachu, D. S., Sathasivam, S., Carmalt, C. J., and Parkin, I. P. (2014). PbO-modified TiO_2 thin films: a route to visible light photocatalysts. *Langmuir* 30, 624–630. doi: 10.1021/la4038777

Bhatia, S., and Verma, N. (2017). Photocatalytic activity of ZnO nanoparticles with optimization of defects. *Mater. Res. Bull.* 95, 468–476. doi: 10.1016/j.materresbull.2017.08.019

Blöchl, P. E. (1994). Projector augmented-wave method. *Phys. Rev. B.* 50, 17953–17979.

Boppana, V., Jiao, B. R., Newby, F., Laverock, D., Smith, J., Lobo, K. E., et al. (2013). Analysis of visible-light-active Sn(ii)–TiO_2 photocatalysts. *Phys. Chem. Chem. Phys.* 15, 6185–6189. doi: 10.1039/c3cp44635b

Boppana, V., Lobo, B. R. (2011). SnOx–ZnGa2O4 photocatalysts with enhanced visible light activity. *ACS Catal.* 1, 923–928. doi: 10.1021/cs200137h

Chae, S. Y., Lee, C. S., Jung, H., Joo, O. S., Min, B. K., et al. (2017). Insight into charge separation in WO_3/$BiVO_4$ heterojunction for solar water splitting. *ACS Appl. Mater. Interfaces*. 9, 19780–19790. doi: 10.1021/acsami.7b02486

Chand, R., Obuchi, E., Katoh, K., Luitel, H. N., and Nakano, K. (2011). Enhanced photocatalytic activity of TiO_2/SiO_2 by the influence of Cu-doping under reducing calcination atmosphere. *Catal. Commun.* 13, 49–53. doi: 10.1016/j.catcom.2011.04.024

Cui, Y., Du, H., and Wen, L. (2008). Doped-TiO2 photocatalysts and synthesis methods to prepare TiO_2 films. *J. Mater. Sci. Technol.* 24, 675–689.

Czoska, A. M., Livraghi, S., Chiesa, M., Giamello, E., Agnoli, S., Granozzi, G., et al. (2008). The nature of defects in fluorine-doped TiO_2. *J. Phys. Chem. C.* 112, 8951–8956. doi: 10.1021/jp8004184

Di Valentin, C., Finazzi, E., Pacchioni, G., Selloni, A., Livraghi, S., and Paganini, M. C. (2007). N-doped TiO_2: theory and experiment. *Chem. Phys.* 339, 44–56. doi: 10.1016/j.chemphys.2007.07.020

Di Valentin, C., and Selloni, A. (2011). Bulk and surface polarons in photoexcited anatase TiO_2. *J. Phys. Chem. Lett.* 2, 2223–2228. doi: 10.1021/jz2009874

Dimitrijevic, N. M., Vijayan, B. K., Poluektov, O. G., Rajh, T., Gray, K. A., and He, H. (2011). Role of water and carbonates in photocatalytic transformation of CO_2 to CH_4 on Titania. *J. Am. Chem. Soc.* 133, 3964–3971. doi: 10.1021/ja108791u

Dudarev, S. L., Botton, G. A., Savrasov, S. Y., Humphreys, C. J., and Sutton, A. P. (1998). Electron-energy-loss spectra and the structural stability of nickel oxide: an LSDA+U study. *Phys. Rev. B.* 57, 1505–1509. doi: 10.1103/PhysRevB.57.1505

Etacheri, V., Di Valentin, C., Schneider, J., Bahnemann, D., and Pillai, S. C. (2015). Visible-light activation of TiO_2 photocatalysts: advances in theory and experiments. *J. Photochem. Photobiol. C: Photochem. Rev*. 25, 1–29. doi: 10.1016/j.jphotochemrev.2015.08.003

Franchini, C., Podloucky, R., Paier, J., Marsman, M., and Kresse, G. (2007). Ground-state properties of multivalent manganese oxides: density functional and hybrid density functional calculations. *Phys. Rev. B*. 75:195128. doi: 10.1103/PhysRevB.75.195128

Fronzi, M., Daly, W., and Nolan, M. (2016b). Reactivity of metal oxide nanocluster modified rutile and anatase TiO_2: oxygen vacancy formation and CO_2 interaction. *App. Catal. A*. 521, 240–249. doi: 10.1016/j.apcata.2015.11.038

Fronzi, M., Iwaszuk, A., Lucid, A., and Nolan, M. (2016a). Metal oxide nanocluster-modified TiO_2 as solar activated photocatalyst materials. *J. Phys.: Condens. Matter*. 28, 074006. doi: 10.1088/0953-8984/28/7/074006

Fronzi, M., and Nolan, M. (2017). Surface modification of perfect and hydroxylated TiO_2 rutile (110) and anatase (101) with chromium oxide nanoclusters. *ACS Omega* 2, 6795–6808. doi: 10.1021/acsomega.7b01118

Fujishima, A., and Honda, K. (1972). Electrochemical photolysis of water at a semiconductor electrode. *Nature* 238, 37–38. doi: 10.1038/238037a0

Fujishima, A., Zhang, X., and Tryk, D., A (2008). TiO2 photocatalysis and related surface phenomena. *Surf. Sci. Rep*. 63, 515–582. doi: 10.1016/j.surfrep.2008.10.001

Furthmüller, J., Hafner, J., and Kresse, G. (1996). Dimer reconstruction and electronic surface states on clean and hydrogenated diamond (100) surfaces. *Phys. Rev. B.* 53, 7334–7351.

Gai, Y., Li, J., Li, S. S., Xia, J. B., and Wei, S. H. (2009). Design of narrow-gap TiO_2: a passivated codoping approach for enhanced photoelectrochemical activity. *Phys. Rev. Lett.* 102:036402. doi: 10.1103/PhysRevLett.102.036402

Ganduglia-Pirovano, M. V., Hofmann, A., and Sauer, J. (2007). Oxygen vacancies in transition metal and rare earth oxides: current state of understanding and remaining challenges. *Surf. Sci. Rep*. 62, 219–270. doi: 10.1016/j.surfrep.2007.03.002

Gordon, T. R., Cargnello, M., Paik, T., Mangolini, F., Weber, R. T., Fornasiero, P., et al. B (2012). Nonaqueous synthesis of TiO2 nanocrystals using TiF_4 to engineer morphology, oxygen vacancy concentration, and photocatalytic activity. *J. Am. Chem. Soc.* 134, 6751–6761. doi: 10.1021/ja300823a

Graciani, J., Plata, J. J., Sanz, J. F., Liu, P., and Rodriguez, J. A. (2010). A theoretical insight into the catalytic effect of a mixed-metal oxide at the nanometer level: the case of the highly active metal/CeO_x/TiO_2(110) catalysts. *J. Chem. Phys.* 132:104703. doi: 10.1063/1.3337918

Guo, M., and Du, J. (2012). First-principles study of electronic structures and optical properties of Cu, Ag, and Au-doped anatase TiO_2. *Physica B* 407, 1003–1007. doi: 10.1016/j.physb.2011.12.128

Habisreutinger, S. N., Schmidt-Mende, L., and Stolarczyk, J. K. (2013). Photocatalytic reduction of CO_2 on TiO_2 and other semiconductors. *Angew. Chem. Int. Ed*. 52, 7372–7408. doi: 10.1002/anie.201207199

Haowei, P., Jingbo, L., Shu-Shen, L., and Jian-Bai, X. (2008). First-principles study of the electronic structures and magnetic properties of 3d transition metal-doped anatase TiO_2. *J. Phys.* 20:125207. doi: 10.1088/0953-8984/20/12/125207

He, Y., Dulub, O., Cheng, H., Selloni, A., and Diebold, U. (2009). Evidence for the predominance of subsurface defects on reduced anatase TiO_2(101). *Phys. Rev. Lett.* 102:106105. doi: 10.1103/PhysRevLett.102.106105

Henderson, M. A., Epling, W. S., Peden, C. H. F., and Perkins, C., L. (2003). Insights into photoexcited electron scavenging processes on TiO_2 obtained from studies of the reaction of O_2 with OH groups adsorbed at electronic defects on TiO_2(110). *J. Phys. Chem. B.* 107, 534–545. doi: 10.1021/jp0262113

Herrmann, J. M. (2012). Detrimental cationic doping of titania in photocatalysis: why chromium Cr^{3+}-doping is a catastrophe for photocatalysis, both under UV- and visible irradiations. *New J. Chem.*. 36, 883–890. doi: 10.1039/c2nj20914d

Ikeda, T., Nomoto, T., Eda, K., Mizutani, Y., Kato, H., Kudo, A., et al. (2008). Photoinduced dynamics of TiO_2 doped with Cr and Sb. *J. Phys. Chem. C.* 112, 1167–1173. doi: 10.1021/jp0752264

Iwaszuk, A., and Nolan, M. (2011). Reactivity of sub 1 nm supported clusters: $(TiO_2)_n$ clusters supported on rutile TiO2 (110). *Phys. Chem. Chem. Phys.* 13, 4963-4973. doi: 10.1039/C0CP02030C

Iwaszuk, A., and Nolan, M. (2013). Lead oxide-modified TiO_2 photocatalyst: tuning light absorption and charge carrier separation by lead oxidation state. *Catal. Sci. Technol.* 3, 2000–2008. doi: 10.1039/c3cy00194f

Iwaszuk, A., Nolan, M., Jin, Q., Fujishima, M., and Tada, H. (2013). Origin of the visible-light response of nickel(ii) oxide cluster surface modified titanium(iv) dioxide. *J. Phys. Chem. C.* 117, 2709–2718. doi: 10.1021/jp306793r

Jiang, C., Moniz, S. J. A., Wang, A., Zhang, T., and Tang, J. (2017). Photoelectrochemical devices for solar water splitting - materials and challenges. *Chem. Soc. Rev.* 46, 4645–4660. doi: 10.1039/C6CS00306K

Jin, Q., Fujishima, M., Nolan, M., Iwaszuk, A., and Tada, H. (2012). Photocatalytic activities of tin(iv) oxide surface-modified titanium(iv) dioxide show a strong sensitivity to the TiO_2 crystal form. *J. Phys. Chem. C.* 116, 12621–12626. doi: 10.1021/jp302493f

Jin, Q., Fujishima, M., and Tada, H. (2011). Visible-light-active iron oxide-modified anatase titanium(iv) dioxide. *J. Phys. Chem. C.* 115, 6478–6483. doi: 10.1021/jp201131t

Kitchaev, D. A., Peng, H., Liu, Y., Sun, J., Perdew, J. P., and Ceder, G. (2016). Energetics of MnO_2 polymorphs in density functional theory. *Phys. Rev. B.* 93:045132. doi: 10.1103/PhysRevB.93.045132

Kresse, G., and Hafner, J. (1994). *Ab initio* molecular-dynamics simulation of the liquid-metal-amorphous-semiconductor transition in germanium. *Phys. Rev. B.* 49, 14251–14269.

Kresse, G., and Joubert, D. (1999). From ultrasoft pseudopotentials to the projector augmented-wave method. *Phys. Rev. B.* 59, 1758–1775.

Li, W. (2015). Influence of electronic structures of doped TiO_2 on their photocatalysis. *Phys. Status Solidi (RRL) – Rapid Res. Lett.* 9, 10–27. doi: 10.1002/pssr.201409365

Libera, J. A., Elam, J. W., Sather, N. F., Rajh, T., and Dimitrijevic, N. M. (2010). Iron(iii)-oxo centers on TiO_2 for visible-light photocatalysis. *Chem. Mater.* 22, 409–413. doi: 10.1021/cm902825c

Lira, E., Wendt, S., Huo, P., Hansen, J. Ø., Streber, R., Porsgaard, S., et al. (2011). The importance of Bulk Ti^{3+} defects in the oxygen chemistry on titania surfaces. *J. Am. Chem. Soc.* 133, 6529–6532. doi: 10.1021/ja200884w

Long, R., and English, N. J. (2010a). First-principles calculation of synergistic (N, P)-codoping effects on the visible-light photocatalytic activity of anatase TiO_2. *J. Phys. Chem. C.* 114, 11984–11990. doi: 10.1021/jp100802r

Long, R., and English, N. J. (2010b). Synergistic effects on band gap-narrowing in titania by codoping from first-principles calculations. *Chem. Mater.* 22, 1616–1623. doi: 10.1021/cm903688z

Lucid, A., Iwaszuk, A., and Nolan, M. (2014). A first principles investigation of Bi_2O_3-modified TiO_2 for visible light activated photocatalysis: the role of TiO_2 crystal form and the Bi^{3+} stereochemical lone pair. *Mater. Sci. Semicond. Process.* 25, 59–67. doi: 10.1016/j.mssp.2014.01.005

Maeda, K., and Domen, K. (2010). Photocatalytic water splitting: recent progress and future challenges. *J. Phys. Chem. Lett.* 1, 2655–2661. doi: 10.1021/jz1007966

Mars, P., and van Krevelen, D. W. (1954). Oxidation carried out by means of vandium oxide catalysts. *Chem. Eng. Sci.* 3, 41–59.

Morgan, B. J., and Watson, G. W. (2007). A DFT + U description of oxygen vacancies at the TiO_2 rutile (1 1 0) surface. *Surf. Sci.* 601, 5034–5041.

Mu, R.,. Zhao, Z.-J., Dohnálek, Z., and Gong, J. (2017). Structural motifs of water on metal oxide surfaces. *Chem. Soc. Rev.* 46, 1785–1806. doi: 10.1039/C6CS00864J

Muhich, C. L., Ehrhart, B. D., Al-Shankiti, I., Ward, B. J., Musgrave, C. B., and Weimer, A. W. (2016). A review and perspective of efficient hydrogen generation via solar thermal water splitting. *Wiley Interdis. Rev.* 5, 261–287. doi: 10.1002/wene.174

Mullins, D. R., Albrecht, P. M., Chen, L., Calaza, F. C., Biegalski, M. D., Overbury, S. H., et al. (2012). Water dissociation on CeO_2(100) and CeO_2(111) thin films. *J. Phys. Chem. C.* 116, 19419–19428. doi: 10.1021/jp306444h

Na Phattalung, S., Limpijumnong, S., and Yu, J. (2017). Passivated co-doping approach to bandgap narrowing of titanium dioxide with enhanced photocatalytic activity. *Appl. Catal. B.* 200, 1–9. doi: 10.1016/j.apcatb.2016.06.054

Ni, M., Leung, M., Leung, K. H., and Sumathy, K. (2007). A review and recent developments in photocatalytic water-splitting using TiO2 for hydrogen production. *Renew. Sustain. Energy Rev.* 11, 401–425. doi: 10.1016/j.rser.2005.01.009

Nie, X., Zhuo, S., Maeng, G., and Sohlberg, K. (2009). Doping of polymorphs for altered optical and photocatalytic properties. *Int. J. Photoenergy*. 2009:294042. doi: 10.1155/2009/294042

Nolan, M. (2011a). Electronic coupling in iron oxide-modified TiO2 leads to a reduced band gap and charge separation for visible light active photocatalysis. *Phys. Chem. Chem. Phys.* 13, 18194–18199. doi: 10.1039/c1cp21418g

Nolan, M. (2011b). Surface modification of TiO_2 with metal oxide nanoclusters: a route to composite photocatalytic materials. *Chem. Commun.* 47, 8617–8619. doi: 10.1039/c1cc13243a

Nolan, M. (2012). First-principles prediction of new photocatalyst materials with visible-light absorption and improved charge separation: surface modification of rutile TiO_2 with nanoclusters of MgO and Ga_2O_3. *ACS Appl. Mater. Interfaces*. 4, 5863–5871. doi: 10.1021/am301516c

Nolan, M. (2018). Alkaline earth metal oxide nanocluster modification of rutile TiO_2 (110) promotes water activation and CO_2 chemisorption. *J. Mater. Chem. A.* 6, 9451–9466. doi: 10.1039/C8TA01789A

Nolan, M., Elliott, S. D., Mulley, J. S., Bennett, R. A., Basham, M., and Mulheran, P. (2008). Electronic structure of point defects in controlled self-doping of the TiO_2 (110) surface: combined photoemission spectroscopy and density functional theory study. *Phys. Rev. B.* 77:235424. doi: 10.1103/PhysRevB.77.235424

Nolan, M., Iwaszuk, A., and Gray, K., A (2014). Localization of photoexcited electrons and holes on low coordinated Ti and O sites in free and supported TiO_2 nanoclusters. *J. Phys. Chem. C.* 118, 27890–27900. doi: 10.1021/jp508822v

Nolan, M., Iwaszuk, A., Lucid, A. K., Carey, J. J., and Fronzi, M. (2016). Design of novel visible light active photocatalyst materials: surface modified TiO_2. *Adv. Mater.* 28, 5425–5446. doi: 10.1002/adma.201504894

Nolan, M., Iwaszuk, A., and Tada, H. (2012). Molecular metal oxide cluster-surface modified titanium dioxide photocatalysts. *Aust. J. Chem.* 65, 624–632. doi: 10.1071/CH11451

Ong, C. B., Ng, L. Y., and Mohammad, A., W (2018). A review of ZnO nanoparticles as solar photocatalysts: synthesis, mechanisms and applications. *Renew. Sustain. Energy Rev.* 81, 536–551. doi: 10.1016/j.rser.2017.08.020

Park, J. B., Graciani, J., Evans, J., Stacchiola, D., Ma, S., Liu, P., et al. (2009). High catalytic activity of Au/CeO_x/TiO_2(110) controlled by the nature of the mixed-metal oxide at the nanometer level. *Proc. Natl. Acad. Sci. U. S. A.* 106, 4975–4980. doi: 10.1073/pnas.0812604106

Pelaez, M., Nolan, N. T., Pillai, S. C., Seery, M. K., Falaras, P., Kontos, A. G., et al. (2012). A review on the visible light active titanium dioxide photocatalysts for environmental applications. *Appl. Catal. B.* 125, 331–349. doi: 10.1016/j.apcatb.2012.05.036

Perdew, J. P., Burke, K., and Ernzerhof, M. (1996). Generalized gradient approximation made simple. *Phys. Rev. Lett.* 77, 3865–3868.

Rhatigan, S., and Nolan, M. (2018a). Impact of surface hydroxylation in MgO-/SnO-nanocluster modified TiO_2 anatase (101) composites on visible light absorption, charge separation and reducibility. *Chin. Chem. Lett.* 29, 757–764. doi: 10.1016/j.cclet.2017.11.036

Rhatigan, S., and Nolan, M. (2018b). CO_2 and water activation on ceria nanocluster modified TiO_2 rutile (110). *J. Mater. Chem. A*. 6, 9139–9152. doi: 10.1039/C8TA01270A

Ruiz Puigdollers, A., Schlexer, P., Tosoni, S., and Pacchioni, G. (2017). Increasing oxide reducibility: the role of metal/oxide interfaces in the formation of oxygen vacancies. *ACS Catal*. 7, 6493–6513. doi: 10.1021/acscatal.7b01913

Scanlon, D. O., Dunnill, C. W., Buckeridge, J., Shevlin, S. A., Logsdail, A. J., Woodley, S. M., et al. (2013). Band alignment of rutile and anatase TiO_2. *Nat. Mater*. 12, 798–801. doi: 10.1038/nmat3697

Schaub, R., Thostrup, P., Lopez, N., Lægsgaard, E., Stensgaard, I., and Nørskov, J. K. (2001). Oxygen vacancies as active sites for water dissociation on rutile TiO_2(110). *Phys. Rev. Lett*. 87, 266104. doi: 10.1103/PhysRevLett.87.266104

Scheiber, P., Fidler, M., Dulub, O., Schmid, M., Diebold, U., Hou, W., et al. (2012). (Sub)Surface Mobility of Oxygen Vacancies at the TiO_2 Anatase (101) Surface. *Phys. Rev. Lett*. 109:136103. doi: 10.1103/PhysRevLett.109.136103

Schwartzenberg, K. C., Hamilton, J., Lucid, W. J., Weitz, A. K., Notestein, E., Gray, K. A.,et al. (2017). Multifunctional photo/thermal catalysts for the reduction of carbon dioxide. *Catal. Today* 280, 65–73. doi: 10.1016/j.cattod.2016.06.002

Setvin, M., Aschauer, U., Hulva, J., Simschitz, T., Daniel, B., Schmid, M., et al. (2016). Following the reduction of oxygen on TiO_2 anatase (101) step by step. *J. Am. Chem. Soc*. 138, 9565–9571. doi: 10.1021/jacs.6b04004

Shannon, R. D., and Prewitt, C. T. (1969). Effective ionic radii in oxides and fluorides. *Acta Crystallogr. Sec. B*. 25, 925–946. doi: 10.1107/S0567740869003220

Sotelo-Vazquez, C., Quesada-Cabrera, R., Ling, M., Scanlon, D. O., Kafizas, A., Thakur, P. K., et al. (2017). Evidence and effect of photogenerated charge transfer for enhanced photocatalysis in WO_3/TiO_2 heterojunction films: a computational and experimental study. *Adv. Funct. Mater*. 27:1605413. doi: 10.1002/adfm.201605413

Tada, H., Jin, Q., Iwaszuk, A., and Nolan, M. (2014). Molecular-scale transition metal oxide nanocluster surface-modified titanium dioxide as solar-activated environmental catalysts. *J. Phys. Chem. C*. 118, 12077–12086. doi: 10.1021/jp412312m

Valdés, Á., Qu, Z. W., Kroes, G. J., Rossmeisl, J., and Nørskov, J. K. (2008). Oxidation and photo-oxidation of water on TiO_2 surface. *J. Phys. Chem. C*. 112, 9872–9879. doi: 10.1021/jp711929d

Valentin, C. D., Pacchioni, G., Onishi, H., and Kudo, A. (2009). Cr/Sb codoped TiO_2 from first principles calculations. *Chem. Phys. Lett*. 469, 166–171. doi: 10.1016/j.cplett.2008.12.086

Wang, F., Wei, S., Zhang, Z., Patzke, G. R., and Zhou, Y. (2016). Oxygen vacancies as active sites for H_2S dissociation on the rutile TiO_2(110) surface: a first-principles study. *Phys. Chem. Chem. Phys*. 18, 6706–6712. doi: 10.1039/C5CP06835E

Wang, J., Li, H., Meng, S., Zhang, L., Fu, X., and Chen, S. (2017). One-pot hydrothermal synthesis of highly efficient SnO_x/Zn_2SnO_4 composite photocatalyst for the degradation of methyl orange and gaseous benzene. *Appl. Catal. B*. 200, 19–30. doi: 10.1016/j.apcatb.2016.06.070

Xiong, L. B., Li, L., Yang, B., and Yu, Y. (2012). Ti^{3+} in the surface of titanium dioxide: generation, properties and photocatalytic application. *J. Nanomater*. 2013:831524. doi: 10.1155/2012/831524

Xu, J.-, Li, P., Lv, L., Zhang, Y., Chen, S., Du, W, et al. (2009). Structural and magnetic properties of Fe-doped anatase TiO_2 films annealed in vacuum. *Chin. Phys. Lett*. 26:097502. doi: 10.1088/0256-307X/26/9/097502

Yang, K., Dai, Y., Huang, B.,0 andWhangbo, M.- H. (2009). Density functional characterization of the visible-light absorption in substitutional C-anion- and C-cation-doped TiO_2. *J. Phys. Chem. C*. 113, 2624–2629. doi: 10.1021/jp808483a

Yu, J., Xiang, Q., and Zhou, M. (2009). Preparation, characterization and visible-light-driven photocatalytic activity of Fe-doped titania nanorods and first-principles study for electronic structures. *Appl. Catal. B*. 90, 595–602. doi: 10.1016/j.apcatb.2009.04.021

Zhang, H., Yu, X., McLeod, J. A., and Sun, X. (2014). First-principles study of Cu-doping and oxygen vacancy effects on TiO_2 for water splitting. *Chem. Phys. Lett*. 612, 106–110. doi: 10.1016/j.cplett.2014.08.003

Zhang, J., Pan, C., Fang, P., Wei, J., and Xiong, R. (2010). Mo + C codoped TiO_2 using thermal oxidation for enhancing photocatalytic activity. *ACS Appl. Mater. Interf*. 2, 1173–1176. doi: 10.1021/am100011c

Zhang, J., Salles, I., Pering, S., Cameron, P. J., Mattia, D., and Eslava, S. (2017a). Nanostructured WO_3 photoanodes for efficient water splitting via anodisation in citric acid. *RSC Adv*. 7, 35221–35227. doi: 10.1039/C7RA05342H

Zhang, Y., Dai, R., and Hu, S. (2017b). Study of the role of oxygen vacancies as active sites in reduced graphene oxide-modified TiO_2. *Phys. Chem. Chem. Phys*. 19, 7307–7315. doi: 10.1039/C7CP00630F

Zheng, J. W., Bhattcahrayya, A., Wu, P., Chen, Z., Highfield, J., Dong, Z., et al. (2010). The origin of visible light absorption in chalcogen element (S, Se, and Te)-doped anatase TiO_2 photocatalysts. *J. Phys. Chem. C*. 114, 7063–7069. doi: 10.1021/jp9115035

Zhu, W., Qiu, X., Iancu, V., Chen, X. Q., Pan, H., Zhang, Z., et al. (2009). Band gap narrowing of titanium oxide semiconductors by noncompensated anion-cation codoping for enhanced visible-light photoactivity. *Phys. Rev. Lett*. 103:226401. doi: 10.1103/PhysRevLett.103.226401

Conflict of Interest Statement: The authors declare that the research was conducted in the absence of any commercial or financial relationships that could be construed as a potential conflict of interest.

frontiers
in Chemistry

ORIGINAL RESEARCH
published: 08 February 2019
doi: 10.3389/fchem.2019.00057

Dynamics of the Interaction Between Ceria and Platinum During Redox Processes

Paola Luches[1], *Gabriele Gasperi*[1,2], *Marc Sauerbrey*[3,4], *Sergio Valeri*[1,2], *Jens Falta*[3,4] and *Jan Ingo Flege*[3,4,5]*

[1] *Istituto Nanoscienze, Consiglio Nazionale delle Ricerche, Modena, Italy,* [2] *Dipartimento di Scienze Fisiche, Informatiche e Matematiche, Università degli Studi di Modena e Reggio Emilia, Modena, Italy,* [3] *Institute of Solid State Physics, University of Bremen, Bremen, Germany,* [4] *MAPEX Center for Materials and Processes, University of Bremen, Bremen, Germany,* [5] *Applied Physics and Semiconductor Spectroscopy, Brandenburg University of Technology Cottbus-Senftenberg, Cottbus, Germany*

The work is focused on understanding the dynamics of the processes which occur at the interface between ceria and platinum during redox processes, by investigating an inverse catalytic model system made of ceria epitaxial islands and ultrathin films supported on Pt(111). The evolution of the morphology, structure and electronic properties is analyzed in real-time during reduction and oxidation, using low-energy electron microscopy and spatially resolved low-energy electron diffraction. The reduction is induced using different methods, namely thermal treatments in ultra-high vacuum and in H_2 as well as deposition of Ce on the oxide surface, while re-oxidation is obtained by exposure to oxygen at elevated temperature. The use of two different epitaxial systems, continuous films and nanostructures, allows determining the influence of platinum proximity on the stabilization of the specific phases observed. The factors that limit the reversibility of the observed modifications with the different oxidation treatments are also discussed. The obtained results highlight important aspects of the cerium oxide/Pt interaction that are relevant for a complete understanding of the behavior of Pt/CeO_2 catalysts.

Keywords: cerium oxide, platinum, LEEM, LEED, reduction

OPEN ACCESS

Edited by:
Maria Veronica Ganduglia-Pirovano,
Instituto de Catálisis y Petroleoquímica
(ICP), Spain

Reviewed by:
Juan De La Figuera,
Instituto de Química Física
Rocasolano (IQFR), Spain
Vladimir Matolin,
Charles University, Czechia

****Correspondence:***
Jan Ingo Flege
flege@b-tu.de

Specialty section:
This article was submitted to
Physical Chemistry and Chemical
Physics,
a section of the journal
Frontiers in Chemistry

Received: *12 October 2018*
Accepted: *21 January 2019*
Published: *08 February 2019*

Citation:
Luches P, Gasperi G, Sauerbrey M,
Valeri S, Falta J and Flege JI (2019)
Dynamics of the Interaction Between
Ceria and Platinum During Redox
Processes. Front. Chem. 7:57.
doi: 10.3389/fchem.2019.00057

INTRODUCTION

The importance of cerium oxide in catalysis is based on its reducibility, namely on the possibility for cerium ions to reversibly switch between the 4+ and the 3+ oxidation state depending on the external conditions (Trovarelli, 1996). This property is closely linked to the material ability to reversibly store and release oxygen ions in redox reactions. In most catalytic applications cerium oxide is combined with metal nanoparticles, which complete the system functionality (Trovarelli, 1996; Cargnello et al., 2012; Trovarelli and Fornasiero, 2013). In particular, a large number of studies have demonstrated that the combination of platinum and cerium oxide allows exploiting the synergy between the two materials to obtain unprecedented activities with a minimal amount of Pt (Pierre et al., 2007; Bruix et al., 2012; Fiala et al., 2015; Jones et al., 2016). The interaction, which influences the catalytic activity, is rather complex and it involves, for example, the stabilization of ionic Pt species at specific defective ceria surface sites in catalysts with ultra-low Pt loading (Bruix et al., 2014) and a relevant charge transfer between Pt nanoparticles and cerium oxide (Lykhach et al., 2015). To identify the functionality of different atomic sites, to clarify some aspects of the interaction and to optimize the activity and/or the selectivity of catalysts, several studies made use of inverse model systems composed of well-controlled epitaxial oxide nanostructures or ultrathin films supported on metal single crystals (Suchorski et al., 2008; Senanayake et al., 2013; Grinter et al., 2016). Such systems are well-suited in particular to focus on the interplay between cerium oxide and the metal, using surface science techniques with high sensitivity and resolution.

The different properties of cerium oxide epitaxial films and nanostructures have been recently reviewed (Luches and Valeri, 2015). In particular, when Pt(111) is used as a substrate the films grow with a good epitaxial quality (Berner and Schierbaum, 2002; Grinter et al., 2010; Luches et al., 2011, 2013), with surface and subsurface oxygen vacancies (Grinter et al., 2010), step edges and domain boundaries (Grinter et al., 2010; Luches et al., 2011) as the dominant defects. The thermal stability of the oxide films indeed depends on the thickness considered, and different surface reconstructions are stabilized by thermally induced reduction (Berner and Schierbaum, 2002; Luches et al., 2014; Grinter et al., 2016). An interfacial charge transfer has been identified (Luches et al., 2015) and proposed to determine the higher reducibility of films of sub-nanometer thickness as compared to the surface of thicker deposits (Gasperi et al., 2016).

To understand the mechanisms that take place in cerium oxide during redox reactions, several recent studies have specifically focused on understanding the reduced phases stabilized on different cerium oxide surfaces (Wilkens et al., 2013a,b; Duchon et al., 2014a,b; Luches et al., 2014; Höcker et al., 2015, 2017; Grinter et al., 2016; Olbrich et al., 2017; Murgida et al., 2018). A large number of different surface reconstructions have been observed, some of which represent the truncation of a metastable bulk phase, while some others, without a bulk counterpart, are stabilized at the surface or at reduced dimensionality. The reducibility of cerium oxide, at the basis of its catalytic activity, is therefore certainly influenced by a number of factors. For example, Kozlov et al. simulated different reduced ultrathin ceria structures, and they showed that their relative stability depends on the surface lattice parameter (Kozlov et al., 2015). Indeed, epitaxial strain is only one of the parameters which may come into play, and also the electronic interaction with the substrate, the oxide surface morphology, the island size, and the temperature may play an important role (Dvorak et al., 2011; Stetsovych et al., 2013; Wilkens et al., 2013a; Luches and Valeri, 2015; Olbrich et al., 2017).

Low-energy electron microscopy (LEEM) has been shown to be able to provide useful information in this context (Flege and Grinter, 2018), allowing to access the dynamic evolution of the morphology during reduction and oxidation cycles with a lateral resolution below 10 nm and simultaneously providing structural information from electron micro-diffraction with a high spatial resolution (∼250 nm) (Höcker et al., 2015, 2017; Grinter et al., 2016). Moreover, the energy-dependent electron reflectivity can provide important fingerprints of the local surface geometric and electronic properties of the investigated systems and in particular of the surface oxidation state of ceria at about 10 nm spatial resolution (Flege et al., 2013).

We report here a spatially resolved dynamic study of the formation of reduced phases at different sites in ceria/Pt systems. We identify in particular the phases which specifically originate from the direct cerium oxide—platinum interaction and the ones which originate at sites which are further from the interface. The obtained results provide a basis for a better understanding of the mechanisms that can occur in ceria-platinum catalysts, which always comprise a high density of interfacial sites.

MATERIALS AND METHODS

A Pt(111) single crystal was used as a support for the cerium oxide epitaxial nanostructures. The Pt surface was cleaned by multiple cycles of sputtering with Ar^+ ions and annealing at 900 K in an oxygen background pressure of 5×10^{-7} Torr, followed by a final heating step at 1,200 K in ultra-high vacuum (UHV). Cerium was deposited by reactive molecular beam epitaxy in oxygen background pressure of 5×10^{-7} Torr using a home-made electron beam evaporator. The nominal thickness of deposited cerium oxide is estimated by considering the cerium flux from the evaporator and the deposition time and it is expressed in monolayer equivalents (MLE), where 1 MLE corresponds to the thickness of an O-Ce-O trilayer, 3.12 Å, fully covering the Pt surface (Sauerbrey et al., 2017). The flux of the evaporator was calibrated using our results from previous works (Luches et al., 2011), in which the thickness of a closed ceria layer on Pt(111) was estimated using a quartz microbalance coupled with scanning tunneling microscopy results. The reduction was performed using three methods, differing for the reducing agent and for the reduction temperature used: thermal treatments at 1,040 K in UHV, thermal treatments at 680 K in H_2 background pressure of 5×10^{-7} Torr, and deposition of cerium at 680 K in UHV on the surface of the film. The thickness of metallic cerium is also expressed in MLE, where 1 MLE CeO_2 ∼1 MLE Ce since the atomic densities of cerium in its metal structure and in the oxide are almost the same. Reduction by cerium deposition in UHV was applied only to closed cerium oxide films, to avoid direct interactions between Ce and Pt, which are known to give origin to ordered alloyed phases (Baddeley et al., 1997; Berner and Schierbaum, 2002; Kemmer et al., 2014). The re-oxidation is performed by thermal treatments at 1,040 K in O_2 background pressure of 1×10^{-7} Torr. Similar thermal treatments were shown to be effective in reducing and oxidizing cerium oxide low dimensional structures in previous studies (Duchon et al., 2014a,b; Luches et al., 2014; Höcker et al., 2015, 2017).

The morphological and structural evolution was investigated *in-situ* using a commercial Elmitec LEEM III system, equipped with multiple apertures in order to perform micro-illumination low-energy electron diffraction (μLEED) from selected areas down to ∼250 nm in diameter. LEEM images and μLEED patterns were acquired in real-time during reduction and oxidation cycles. I-V LEEM curves were also acquired on selected surface areas. The μLEED and LEEM data were processed with the Gxsm software package (Zahl et al., 2010).

RESULTS

The dynamic modification of the structure and morphology of cerium oxide overlayers with reduction and oxidation cycles was

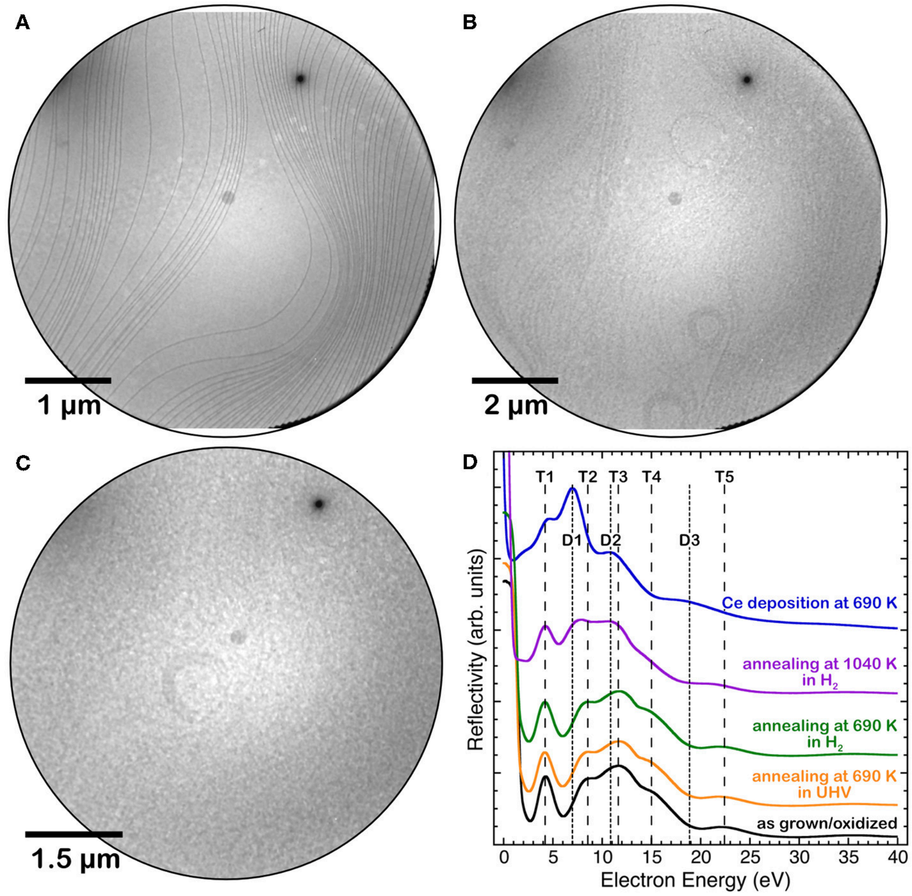

FIGURE 1 | LEEM images of: **(A)** the clean Pt(111) surface, **(B)** a 5 MLE cerium oxide film grown at 720 K, **(C)** the same film after reduction in hydrogen background at 1,040 K. **(D)** I(V)-LEEM spectra of the 5 MLE film after growth at 720 K(black line) and after different reducing treatments: annealing at 690 K in UHV (yellow line), annealing at 690 K in H_2 (green line), annealing at 1,040 K in H_2 (purple line) and Ce deposition in UHV at 680 K on the surface (blue line).

investigated by LEEM and μLEED. I-V curves provide local information on the surface composition. Although the obtained information is only qualitative, the comparison of the curves with the ones obtained on cerium oxide samples with known stoichiometry provides relevant information on the investigated processes (Flege et al., 2013; Höcker et al., 2015). The present study focusses on two different systems: cerium oxide films completely covering the Pt substrate and well-separated cerium oxide islands with part of the substrate surface left uncovered. The continuous cerium oxide films provide essential information to interpret the more complex results obtained on cerium oxide islands. On the other hand, the islands allow for a direct observation of the interactions between the oxide and the metal at the edge sites (see, e.g., Schaefer et al., 2018).

Continuous Cerium Oxide Films

Cerium oxide films fully covering the Pt(111) surface were obtained by depositing nominal amounts of cerium oxide above 5 MLE on the clean substrate kept at 720 K, as in Sauerbrey et al. (2017). **Figure 1** shows the LEEM images of the clean Pt substrate (a) and of the film surface after the growth (b). The film morphology does not show any relevant feature within the resolution of the technique. The I-V curve acquired on the film, shown in **Figure 1D** (black line), has the typical shape observed for stoichiometric cerium oxide films, with a well-resolved feature at 4.5 eV (T1), three partially overlapping features at 9, 12, and 15 eV (T2–T4) and a minor feature at 22.5 eV (T5) (Flege et al., 2013; Höcker et al., 2015). Thermal treatments at 690 K in UHV or in hydrogen background pressure for 50 min did not lead to relevant modifications of the I-V curves (yellow and green lines in **Figure 1D**). On the contrary, a thermal treatment at 1,040 K for 185 min in hydrogen (purple line in **Figure 1D**) leads to significant modifications of the I-V curve, namely to a change in the energy position and relative weight of the features, which are compatible with the formation of a reduced cerium oxide phase (Flege et al., 2013; Höcker et al., 2015). A stronger reducing treatment was performed by depositing approximately 0.5 MLE of Ce in UHV on the surface at 680 K. In this case the I-V curve (blue line in **Figure 1D**) showed a rather marked peak at approximately 8 eV (D1), a contribution at 4.5 eV (T1) and two minor features at 11 and 19 eV (D2, D3), which are well compatible with the formation of a fully reduced Ce_2O_3

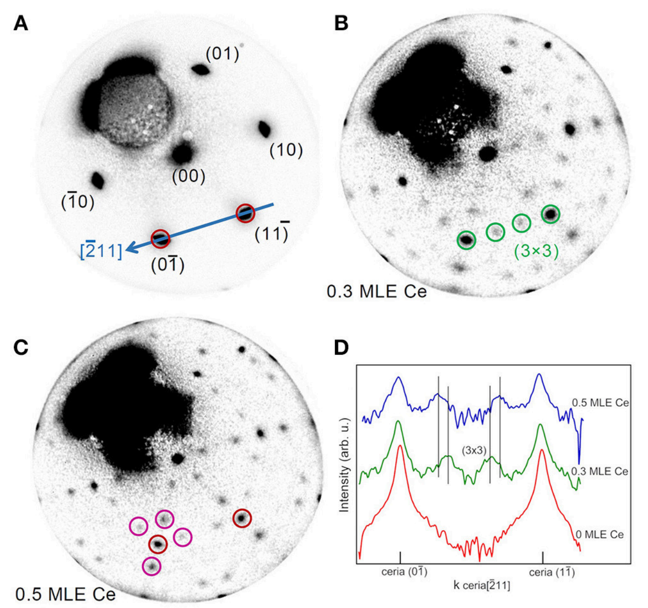

FIGURE 2 | Time-lapse LEED patterns sequence acquired at $E = 40.0$ eV during reduction of a 5 MLE cerium oxide film by Ce deposition at 680 K on the oxide film surface: **(A)** as prepared (0.0 ML Ce); **(B)** after 3,600 s (0.3 ML Ce); **(C)** after 6,000 s of deposition (0.5 ML Ce). **(D)** Profiles of the LEED patterns in **A**, **B**, and **C** along the cerium oxide [101] direction (blue arrow in **A**).

bixbyite phase (Flege et al., 2013; Höcker et al., 2015). The LEEM image acquired after reduction in hydrogen background at 1,040 K (**Figure 1C**) does not show pronounced morphological modifications compared to the image acquired before oxidation (**Figure 1B**).

The evolution of the structure with reducing treatments was followed by LEED. **Figure 2** shows selected patterns acquired during Ce deposition on the film surface, while the full LEED movie is included as **Supplementary Video 1**. Before the treatment the LEED shows only the cerium oxide related spots and no substrate related spot (**Figure 2A**), which indicates that the substrate is fully covered by an epitaxial film with a good crystalline quality. After the deposition of 0.3 MLE of Ce a clear (3 × 3) superstructure appears (**Figure 2B**). This surface periodicity in reduced cerium oxide films was already observed to be formed after Ce deposition on the surface of a 3 nm thick cerium oxide films on Cu(111) followed by annealing at 870 K by Duchon et al. and it was ascribed to the $CeO_{1.67}$ phase with a specific surface structure (Duchon et al., 2014b). Subsequently, the same phase was observed to appear also on ceria films grown on Ru(0001) using thermal reducing treatments (Duchon et al., 2014a; Höcker et al., 2015). By depositing larger amounts of metallic cerium the superstructure-related spots gradually move toward the cerium oxide related spots, reaching a periodicity of approximately (3.5×3.5) after the deposition of 0.5 MLE of Ce. The LEED intensity profiles along the [101] direction, reported in **Figure 2D**, show the shift of the (3×3)-related spots toward the (11) and (10) ceria spots. A previous work by Höcker et al. (2015) demonstrated that if two coexisting phases with slightly different surface periodicities (e.g., 3 × 3 and 4 × 4) gradually transform from one into the other in a non-correlated way, the lattice parameter of the resulting periodicity in LEED patterns progressively changes between the two values determined by the individual phases (Höcker et al., 2015). It seems therefore reasonable to assume that the (3.5 × 3.5) periodicity originates from an incomplete transformation of the (3 × 3) phase into a phase with a (4 × 4) periodicity. The latter corresponds to the bixbyite Ce_2O_3 phase, which was observed to be stabilized by reduction of ceria films on Cu(111) (Duchon et al., 2014b) and on Ru(0001) (Duchon et al., 2014a; Höcker et al., 2015).

In order to investigate the effect of interface proximity on the reduced phases that are stabilized, reduction was induced by cerium deposition on the surface of a much thinner film of 1.5 MLE. **Figure 3** reports a time-lapse LEED pattern sequence during the deposition of selected amounts of cerium, while the full LEED movie is included as **Supplementary Video 2**. Before the treatment (**Figure 3A**) the LEED pattern shows both the spots related to cerium oxide and those related to the Pt(111) surface plus some extra spots (brown circles in **Figure 3A**), probably originating from a non-complete oxidation of the cerium oxide film. After the deposition of ∼0.05 MLE of Ce a well-ordered (3 × 3) phase appears (**Figure 3B**), in analogy with the phase obtained on thicker continuous films after the deposition of 0.3 MLE of Ce (**Figure 2B**). After the deposition of 0.09 MLE of cerium (**Figure 3C**) the (3 × 3) phase disappears and the surface shows a pattern similar to the one observed before reduction (**Figure 3A**), which might be due to random creation of further oxygen vacancies. With further reduction a phase with a (7 × 7) periodicity with respect to the Pt surface becomes clearly visible, which corresponds to an approximate (5 × 5) periodicity with respect to cerium oxide (**Figure 3D**). As the reduction proceeds (**Figures 3E,F**) some of the superstructure spots gradually move toward the main cerium oxide spots finally forming a $5/2(\sqrt{3} \times \sqrt{3})R30°$ reconstruction after the deposition of ∼0.5 MLE of Ce. Also in this case the gradual movement of some of the LEED spots is interpreted as due to two kinds of spatially uncorrelated domains with the (5 × 5) and the $5/2(\sqrt{3} \times \sqrt{3})R30°$ reconstruction which gradually transform one into the other, as in Höcker et al. (2015).

Cerium Oxide Islands

To have more detailed information on the interaction between cerium oxide and Pt, we investigated the processes occurring with thermal reduction on a sample obtained by growing 1.5 MLE cerium oxide on the Pt surface at 1,040 K to allow for the formation of well-separated cerium oxide islands, using the procedures identified in one of our previous studies (Sauerbrey et al., 2017). **Figure 4A** reports a typical LEEM image of the sample surface. The bright features can be ascribed to cerium oxide, which has a higher reflectivity than the bare Pt surface at 12 eV (see **Figure 1D** and Sauerbrey et al., 2017). The lateral size of the ceria features varies between ∼50 and 200 nm and their shape appears mainly irregular, being partially constrained by the substrate step edges. The islands that nucleate on flat areas of the Pt substrate, far from step edges, have a more regular triangular shape as they have grown from a single or only very few nuclei

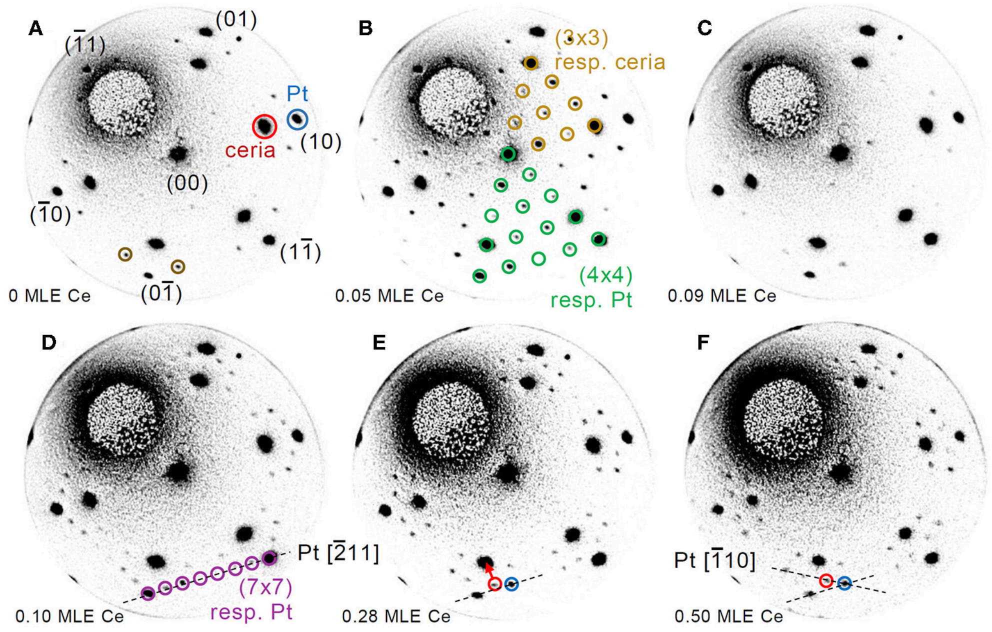

FIGURE 3 | Time-lapse LEED pattern sequence acquired at $E = 40.0$ eV during reduction of a 1.5 MLE cerium oxide film by Ce deposition at 680 K on the oxide film surface: **(A)** as prepared (0.00 ML Ce); **(B)** after 245 s (0.05 ML Ce); **(C)** after 435 s (0.09 ML Ce); **(D)** after 540 s (0.10 ML Ce); **(E)** after 1,425 s (0.28 ML Ce); **(F)** after 2,495 s of deposition (0.50 ML Ce).

(highlighted by white arrows in **Figure 4**). The average height of the islands, estimated using the Pt surface coverage (25 ± 1%) and the cerium oxide equivalent thickness, amounts to approximately 6 ML.

The evolution of the morphology of the sample during thermal treatments at 1,040 K in UHV was followed by LEEM in real-time (see also **Supplementary Video 3**). **Figures 4B–D** represent selected LEEM images during reduction. The image acquired after 440 s (**Figure 4B**) evidences significant morphological modifications of the sample. Most of the islands are surrounded by an area characterized by a very low reflectivity, which appears darker than the substrate. The low-reflectivity phase partially extends also along the step edges, partially decorating them with an almost continuous profile. The extent of the bright part of the islands decreases with reduction, as shown for example by comparing the areas highlighted in green in **Figures 4A,B**. Simultaneously, some of the bright islands increase in size and acquire a more regular triangular shape (blue arrows). With longer times, the low-reflectivity phase surrounding the ceria structures further extends on the substrate surface, while the bright part of the islands decreases in size (areas highlighted in red and yellow in **Figures 4C,D**). The morphology and contrast of the larger triangular islands (white arrows) are almost unchanged, except for a mild decrease in reflectivity. The latter can be rationalized by considering the modifications of the I-V curves induced by the different reduction treatments in **Figure 1D**. The I-V curve T3 peak at 11.6 eV observed in stoichiometric cerium oxide film does not change significantly in intensity after mild reduction treatments, while a pronounced decrease in reflectivity at ∼12 eV is observed after strong reduction. We therefore interpret the mild decrease of reflectivity of the ceria islands as originating from an intermediate reduction, in accordance with previous findings from spatially resolved I(V) analysis for chemical reduction of cerium oxide islands on Ru(0001) (Kozlov et al., 2015). The nature of the phase with a lower reflectivity than Pt at 12 eV is instead less clear, although a similar behavior was observed also on reduced ceria films on a Ru(0001) support (Höcker et al., 2017).

In order to have more information on the nature of the different phases obtained with increasing reduction μLEED images were acquired on selected areas of the fully reduced sample. Regions including mainly the brighter islands (**Figure 4** L1) show dominant spots with hexagonal symmetry ascribed to the Pt(111) surface, together with a pattern of lower intensity and smaller size in reciprocal space, compatible with a reduced cerium oxide phase without specific ordering of oxygen vacancies, considering the decreased reflectivity compared to fully oxidized phases (**Figures 4A,C**). The cerium oxide related spots are 5° rotated with respect to the Pt ones, possibly due to the higher stability of the rotated orientation (Luches et al., 2011; Sauerbrey et al., 2017). On the contrary, on the areas comprising mainly the phase with a reflectivity lower than Pt μLEED shows superstructures with a $5/2(\sqrt{3} \times \sqrt{3})R30^\circ$ periodicity (**Figure 4** L2). In the literature a similar superstructure was observed by LEED at the early stages of Pt-Ce alloy formation and ascribed to a metallic Pt_5Ce alloy (Baddeley et al., 1997; Kemmer et al., 2014). This suggests that there might be a non-negligible tendency for interatomic exchange between cerium oxide and Pt induced by the thermal reduction.

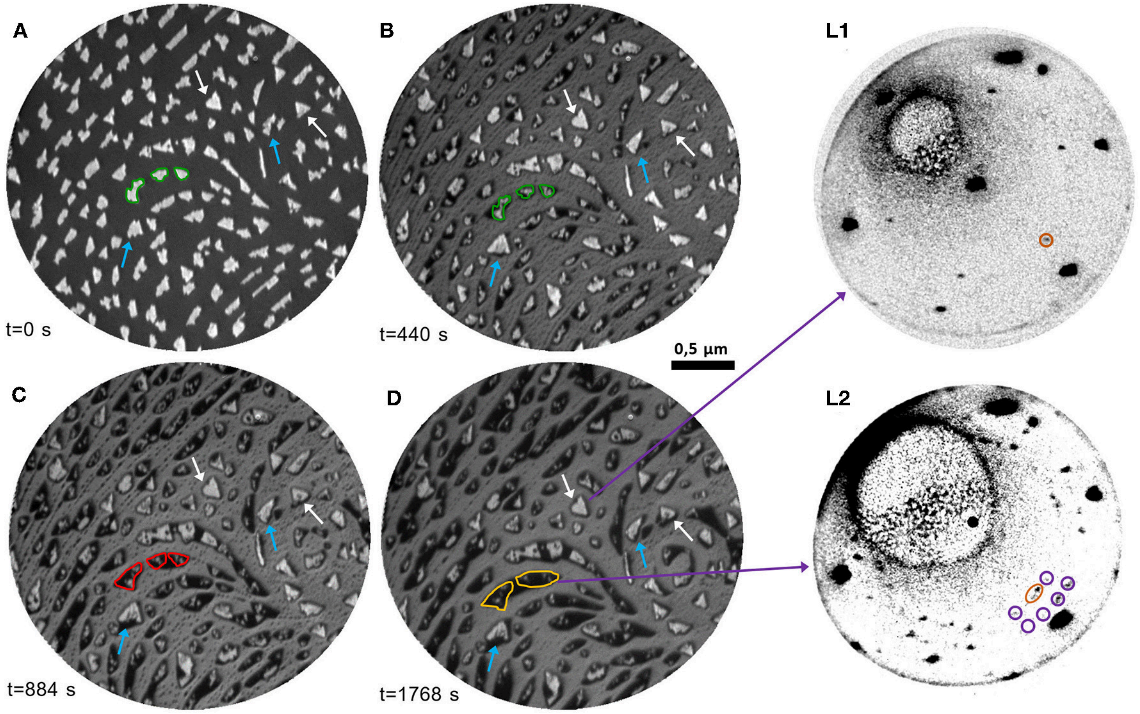

FIGURE 4 | (A–D) Time-lapse LEEM image sequence at $E = 12.0$ eV acquired during thermal reduction in UHV at 1,040 K of cerium oxide islands of nanometric thickness (1.5 MLE): **(A)** before the reduction; **(B)** after 440 s; **(C)** after 884 s; **(D)** after 1,768 s. The edge of selected islands is highlighted in green in **(A)** and reported in **(B)**, to emphasize the decrease of the bright areas and the increase of the dark areas. The expansion of the low-reflectivity phase in the same area with further reduction is highlighted in red in **(C)**, and in yellow in **(D)**. The blue arrows indicate bright islands which become wider and more regular during the first stages of the treatment. The white arrows point at regular triangular islands which undergo only a decrease in reflectivity with the treatment. (L1)-(L2): µLEED patterns ($E = 40.0$ eV) acquired on selected areas of **(D)**: (L1) on a bright triangular island; (L2) on a low-reflectivity area.

Figure 5 reports the I-V curves in selected areas of the 1.5 MLE sample as-prepared, after reduction and after re-oxidation. The spectra obtained on areas between the cerium oxide islands correspond to the one expected for clean platinum, with features at 14 eV (P1) and at 18 eV (P2) (red curve in **Figure 5C**). The as-grown cerium oxide islands exhibit an I-V curve that contains both the cerium oxide related features at 3.5, 8, and 11 eV, T1-T3 in analogy with **Figure 1**, and a weak Pt-related P2 feature at 18 eV (yellow curve in **Figure 5C**). After reduction the I-V curve on the bare substrate areas is not significantly altered (red curve in **Figure 5C**), apart from an overall increase of intensity possibly originating from the desorption of oxygen from the Pt surface. The dark areas have a reflectivity that is lower than that of the Pt at all energies (purple curve in **Figure 5C**). The islands, which still appear bright after reduction, have an I-V curve with a dominant R1 peak at low energies around 4 eV, slightly shifted to higher energies compared to the T1 peak before reduction (yellow curve in **Figure 5C**). A broad feature, R2, appears at 7 eV together with attenuated Pt-related P1 and P2 features at 14 and 18 eV. The regular islands which show a mild reflectivity decrease at ~12 eV with the reducing treatment, like the one highlighted in green in **Figure 4B**, have an I-V curve which appears somewhat intermediate between the ones observed on bright islands and on the low-reflectivity phase (green curve in **Figure 5C**).

A very similar phase with low reflectivity surrounding the brighter islands was also observed after exposure of the ceria islands to hydrogen at a pressure of 1×10^{-7} Torr at 680 K (**Figures 6A,B**). The I-V curves of the different regions, bright islands, dark island areas and substrate (**Figure 6D**), are compatible with the ones observed after the thermal treatment in UHV (**Figure 5**). The LEED pattern acquired on the low reflectivity areas (**Figure 6C**) shows a reconstruction very similar to the one observed after reduction by thermal treatments in UHV (**Figure 4** L2).

The evolution of the morphology of fully reduced cerium oxide islands during oxidation in oxygen background pressure at 1,040 K was also investigated. **Figure 7** reports a time-lapse sequence of LEEM images acquired during the treatment (see also **Supplementary Video 4**). Already after the first few minutes of oxygen exposure the low-reflectivity phase, initially covering a large part of the surface, starts to vanish while the bright areas increase in size and their reflectivity is increased (area highlighted in red in **Figure 7**). New bright islands also appear during the treatment, like for example the one indicated with a yellow arrow in **Figure 7B**. With further oxygen exposure the low-reflectivity phase completely disappears, and it is replaced by bright islands with a non-uniform contrast and an irregular shape. The LEED patterns after re-oxidation are very close

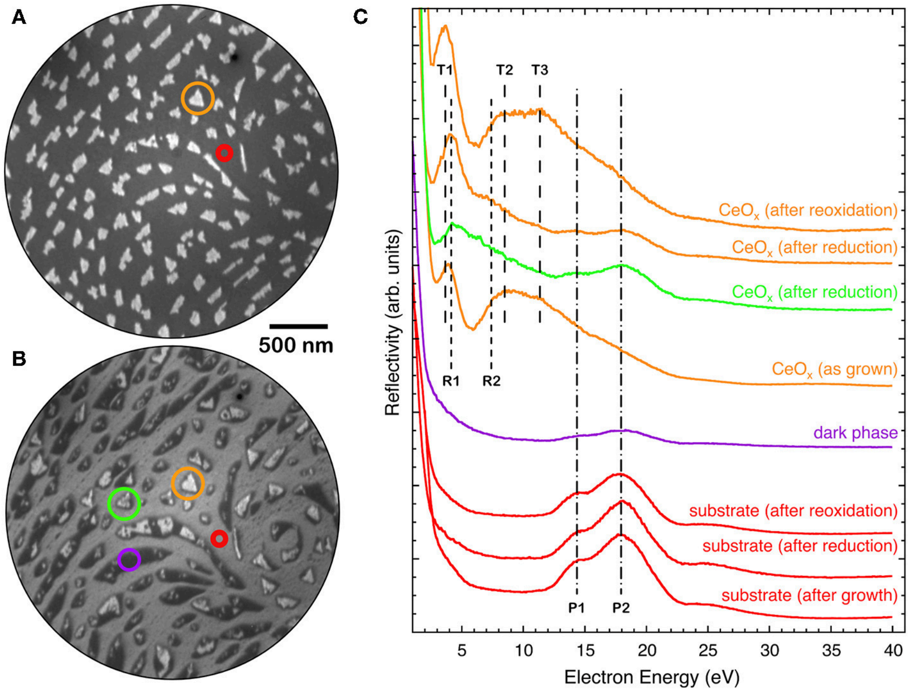

FIGURE 5 | LEEM image ($E = 12.0$ eV) of a 1.5 MLE ceria film **(A)** as prepared and **(B)** after reduction [same as (**Figures 4A,D**)]. **(C)** I-V LEEM curves acquired on selected areas of the as-prepared, reduced and re-oxidized samples: triangular island (orange), substrate (red), low-reflectivity (dark) phase (purple), and island with decreased reflectivity (green).

to the ones acquired before reduction, demonstrating the reversibility of the structure (**Figures 7E,F**). In analogy, also the I-V curves acquired before reduction and after re-oxidation appear very close, demonstrating the reversibility of the surface stoichiometry, while the I-V curves on bare Pt surface areas appear unaltered (**Figure 5C**).

DISCUSSION

The present study points at understanding the dynamics of the processes which occur at the interface between ceria and platinum during redox processes.

The main result of the work is the evidence for a strong interaction between the two materials involving non-negligible mass transport already at the early stages of isothermal reduction starting at the cerium oxide island edge sites (**Figure 3**). At these sites the formation of oxygen vacancies is likely favored by reduced coordination and by the proximity of Pt which possibly induces a decrease in the oxygen vacancy formation energy by charge transfer (Luches et al., 2015). At the earlier reduction stage the stability of cerium oxide islands with irregular shape is significantly lower than the one of islands with regular triangular shape (**Figure 4**), probably because the reduction is more pronounced where the island edges are less regular, which typically implies the presence of kinks and other kinds of defects, and a low structural order in the long range. The thicker and more regular islands are not significantly altered at the investigated temperature at this earlier stage. Some of the thicker islands increase their lateral size at this stage because some of the neighboring islands with smaller lateral size get some mobility and possibly merge with them. At a later stage most of the islands are partially converted into the alloy and their lateral size is decreased. The low-reflectivity phase, which appears and expands with reducing treatments, is ascribed to a surface alloy based on its LEED pattern although it has a reflectivity which is very low at all energies, as expected for a rough surface with a low crystal quality (Sauerbrey et al., 2016). This may indicate that the surface mobility at the used temperature (1,040 K) is not high temperature (1,040 K) is not high enough to reach a good surface ordering, although the long-range ordered Ce-Pt surface alloy. We note that the appearance of a low-reflectivity phase with reduction low-reflectivity phase with reduction was observed also on the Ru(0001) surface, although it did not show any diffraction pattern (Höcker et al., 2017), probably due to the different miscibility of cerium and Ru, given the alloys (Colinet, 1995). A phase with the same surface periodicity (and LEED dynamic) is observed also on a 1.5 MLE cerium oxide films fully covering the Pt surface on which the reduction is induced by cerium deposition at 680 K (**Figure 3F**), and also after reduction of a 1.8 MLE film (grown at 1,040 K) induced by H_2 reduction of a 1.8 MLE film (grown at 1,040 K) induced by H_2 exposure of at 680 K (**Figure 6**). The formation of a surface alloy on thermally reduced ceria films on Pt(111) was also hypothesized based on atomic and Kelvin probe force microscopy experiments (Gasperi et al., 2018). These evidences indicate that surface alloy formation is a process

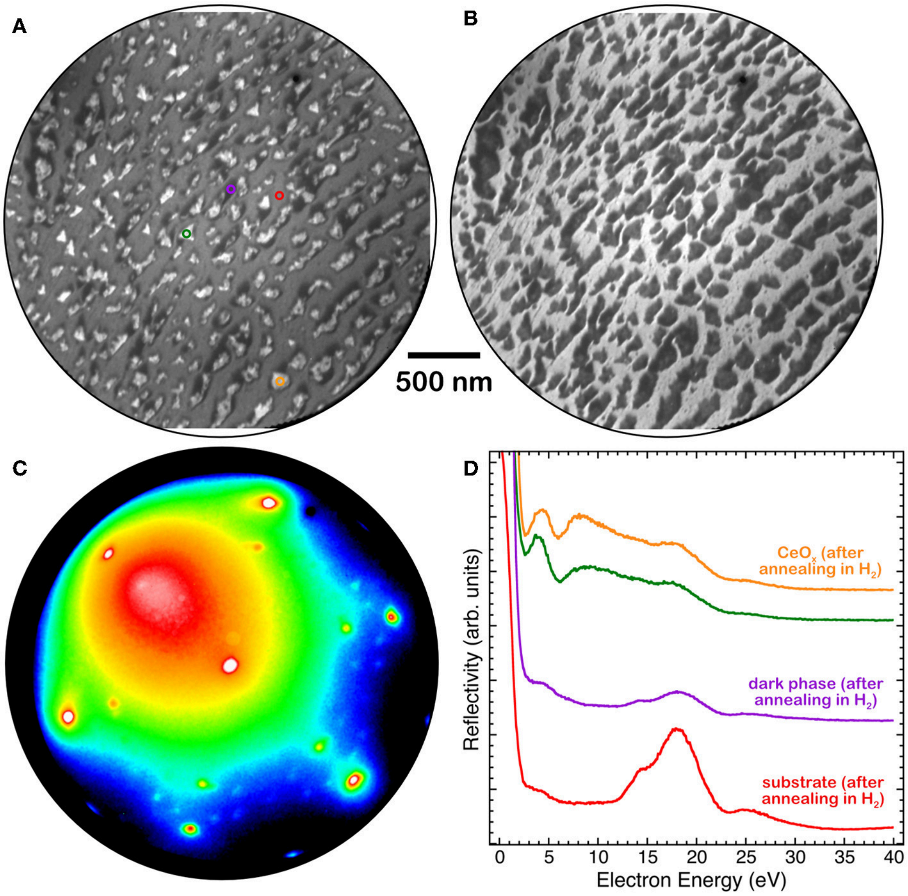

FIGURE 6 | (A) LEEM image at $E = 12$ eV, **(B)** LEEM image at $E = 17$ eV, **(C)** LEED pattern at $E = 40$ eV and **(D)** I-V LEEM curves, acquired on selected areas of a 1.8 MLE cerium oxide film grown at 1,040 K and reduced by H_2 exposure ($P_{H2} = 1 \times 10^{-7}$ Torr) at 680 K: triangular island (orange and green), substrate (red), low-reflectivity (dark) phase (purple).

which also occurs at intermediate temperatures in reducing conditions.

An important aspect is that the extended low reflectivity phase can be transformed back to confined cerium oxide islands by oxidation at elevated temperature (**Figure 7**). The partially reduced bright islands increase in size, suggesting that re-oxidation is more favorable at the step edges between reduced ceria and the Pt-Ce alloy, inducing a preferential oxide formation at the sides of the existing islands accompanied by a progressive shrinking of the low-reflectivity phase. Simultaneously also the reflectivity at 12 eV of partially reduced cerium oxide islands increases, evidencing a change in oxidation state and suggesting a filling of surface oxygen vacancies. Moreover, new bright islands appear in isolated sites of the low reflectivity phase, possibly where some cerium oxide nanostructures below the LEEM resolution were left by the reduction treatment or at some other defect sites created during alloy formation. The resulting different morphology of the ceria islands after re-oxidation is probably due to kinetic barriers which limit the diffusion and originate less regular structures, compared to the ones formed when Ce adatoms are co-deposited with O_2 on the clean, very smooth Pt surface. At the investigated oxygen pressures and temperatures, both the closed films and the ceria islands were fully re-oxidized in relatively short times, of the order of tens of minutes. Indeed, it would be interesting to follow also the dynamics of re-oxidation in different conditions. The efficiency for molecular oxygen dissociation on the Pt surface for example is expected to contribute to the kinetics of re-oxidation at milder oxidizing conditions. We suggest this as a relevant issue to be investigated in future studies, to obtain a complete picture of the redox process. Indeed, a non-negligible and reversible interatomic exchange is likely to occur also in Pt-ceria real catalysts during redox reactions, likely on a shorter length scale determined by the working temperature and by pressure of the reactant. The process needs to be considered in studies devoted to the optimization of cerium oxide/Pt catalysts, for example by minimizing or substituting platinum.

The present work also allows to draw some important considerations on the factors which induce the stabilization of specific reduced phases in cerium oxide. A phase diagram summarizing the phases observed for the different ceria film

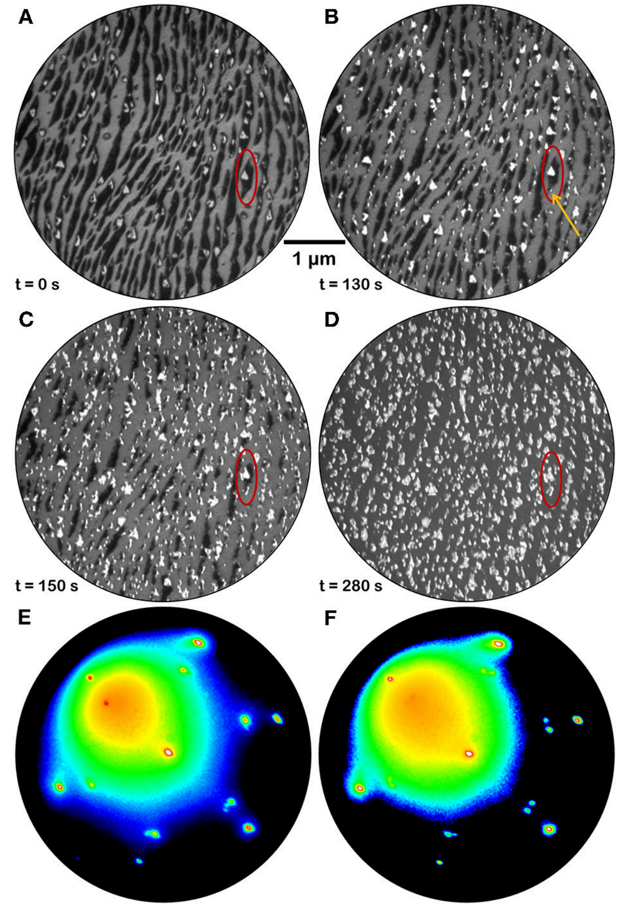

FIGURE 7 | Time-lapse LEEM image sequence at $E = 12.0$ eV acquired during re-oxidation of a fully reduced ceria sample (1.5 MLE) by annealing in O_2 background pressure ($P = 1 \times 10^{-7}$ Torr) at 1,040 K: **(A)** before the re-oxidation; **(B)** after 130 s; **(C)** after 150 s; **(D)** after 280 s. The red ellipse allows to follow the evolution of the morphology in a selected surface region. The orange arrow in **(B)** evidences a bright feature that was absent before the treatment and that is growing with time **(C,D)**. **(E,F)** µLEED patterns ($E = 40$ eV) acquired on two islands of different shape after full reduction and subsequent re-oxidation by exposure to oxygen at $P_{O2} = 1 \times 10^{-7}$ Torr for 5 min at 1,040 K.

thicknesses and at the different reducing conditions is shown in **Figure 8**. The (3 × 3) phase was observed both on 1.5 MLE and on 5 MLE films, although in the first case a much smaller amount of cerium was required for its stabilization. The Pt substrate possibly favors the formation of the (3 × 3) phase which has a surface size compatible with the coincidence cell at the ultrathin limit (Luches et al., 2013). The $CeO_{1.67}$ (3 × 3) phase was already observed in cerium oxide ultrathin films supported on different metal substrates, e.g., Cu(111) (Duchon et al., 2014b; Höcker et al., 2015), while it was not observed on bulk surfaces (Olbrich et al., 2017), although a recent theoretical study showed that it can result from the (111) termination of a metastable bulk Ce_3O_5 phase (Murgida et al., 2018). The reduced dimensionality in the out of plane direction probably plays a role in its stabilization, given the higher structural flexibility of thin films compared to bulk surfaces. The Ce_2O_3 (4 × 4) phase was shown to coexist with the (3 × 3) phase on 5 ML films at the maximum degree of reduction accessed, while on thinner films it was not observed, being probably less stable than other reduced phases. The phase was also observed in previous studies on ultrathin films on different substrates (Duchon et al., 2014a,b; Höcker et al., 2015), as well as on bulk-like surfaces (Olbrich et al., 2017).The reduced (5 × 5) phase, observed in this work on 1.5 MLE films at intermediate reduction (**Figure 3D**), was never observed in previous studies. We speculate that its stabilization may also be ascribed to epitaxy with the Pt substrate, since a 5:7 coincidence between cerium oxide and platinum is possible and it implies a slight surface expansion of the cerium oxide surface lattice (Luches et al., 2013), indeed favored by reduction since Ce^{3+} ions have a larger radius than Ce^{4+} ions. The (5 × 5) phase gradually evolves with further reduction toward the $5/2(\sqrt{3} \times \sqrt{3})R30^\circ$ phase which is related to the initial stages of an alloy formation as discussed above. The alloy was observed at low thickness and moderate degrees of reduction, while for thicker films the onset for alloy formation was found at higher degrees of reduction. The plethora of surface reconstructions, the fast transformation between the different phases and the partially different behavior of cerium oxide layers close to the interface compared to the surface of thin films highlight the complexity of the processes that occur at the interface between these two technologically important materials during redox processes.

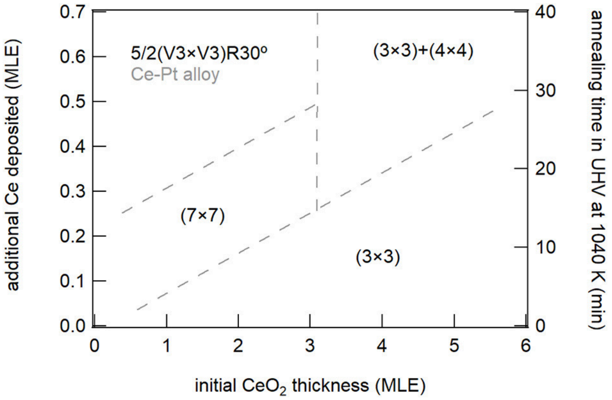

FIGURE 8 | Schematic phase diagram summarizing the different reduced phases observed on the surface of ceria films for the different nominal thicknesses and in the different reducing conditions.

Finally, this work proves that for a thorough understanding of the complex phenomena which occur during reduction and oxidation a real-time investigation not only of the evolution in morphology, but also of the structure and electronic properties is extremely important to fully understand the system behavior.

CONCLUSIONS

We have investigated the dynamic changes in morphology, structure, and electronic properties in cerium oxide films and confined islands with reducing and oxidizing treatments. We relate the observed modifications to the formation of different reduced structural phases, and we discuss the effect of temperature, of dimensionality and of the interaction with platinum for their stabilization. In particular, the $CeO_{1.67}$ (3 × 3) phase gradually transforms into the Ce_2O_3 (4 × 4) bixbyite phase, with increasing reduction in sites which are not in close proximity with the Pt interface. This is in contrast to the very early stage of the reduction process, more prominent where the lateral oxide-metal interface is less smooth and more defective. The resulting (3 × 3) phase is stabilized at milder conditions in ultrathin films due to an important role of the Pt substrate. At higher degrees of reduction the interaction between cerium oxide and Pt induces the formation of more complex phases, and it finally leads to a partial interdiffusion between substrate and overlayer atoms. The structural modifications are reversible with oxidizing treatments, whereas a complete restoration of the original morphology is partially hindered by kinetic barriers.

AUTHOR CONTRIBUTIONS

PL, JIF, JF, and SV conceived and designed the experiment. GG and MS did the sample growth, the measurements and the data analysis. JIF and JF supervised the experiment and the data analysis. PL wrote the manuscript draft. All authors contributed to data interpretation, discussion of results and manuscript critical revisions.

ACKNOWLEDGMENTS

The activity was performed with the support of the COST Action CM1104 Reducible oxide chemistry, structure and functions.

SUPPLEMENTARY MATERIAL

The Supplementary Material for this article can be found online at: https://www.frontiersin.org/articles/10.3389/fchem.2019.00057/full#supplementary-material

Supplementary Video 1 | LEED movie ($E = 40$ eV) during reduction of a 5 ML cerium oxide film by Ce deposition at 680 K on the film surface.

Supplementary Video 2 | LEED movie ($E = 40$ eV) during reduction of a 1.5 ML cerium oxide film by Ce deposition at 680 K on the film surface.

Supplementary Video 3 | LEEM movie ($E = 12$ eV) of cerium oxide islands of nanometric thickness during thermal reduction in UHV at 1,040 K.

Supplementary Video 4 | LEEM movie ($E = 12$ eV) of reduced cerium oxide islands of nanometric thickness during thermal reoxidation at 1,040 K in oxygen background pressure ($P_{O2} = 1 \times 10^{-7}$ Torr).

REFERENCES

Baddeley, C. J., Stephenson, A. W., Hardacre, C., Tikhov, M., and Lambert, R. M. (1997). Structural and electronic properties of Ce overlayers and low-dimensional Pt-Ce alloys on Pt{111}. *Phys. Rev. B* 56, 12589–12598. doi: 10.1103/PhysRevB.56.12589

Berner, U., and Schierbaum, K. D. (2002). Cerium oxides and cerium-platinum surface alloys on Pt(111) single-crystal surfaces studied by scanning tunneling microscopy. *Phys. Rev. B* 65:235404. doi: 10.1103/PhysRevB.65.235404

Bruix, A., Lykhach, Y., Matolínová I., Neitzel, A., Skála, T., Tsud, N., et al. (2014). Maximum noble-metal efficiency in catalytic materials: atomically dispersed surface platinum. *Angew. Chem. Int. Ed.* 53, 10525–10530. doi: 10.1002/anie.201402342

Bruix, A., Rodriguez, J. A., Ramírez, P. J., Senanayake, S. D., Evans, J., Park, J. B., et al. (2012). A new type of strong metal–support interaction and the production of H2 through the transformation of water on Pt/CeO2(111) and Pt/CeOx/TiO2(110) catalysts. *J. Am. Chem. Soc.* 134, 8968–8974. doi: 10.1021/ja302070k

Cargnello, M., Jaén, J. J. D., Garrido, J. C. H., Bakhmutsky, K., Montini, T., Gámez, J. J., et al. (2012). Exceptional activity for methane combustion over modular Pd@CeO2 subunits on functionalized Al2O3. *Science* 337, 713–717. doi: 10.1126/science.1222887

Colinet, C. (1995). The thermodynamic properties of rare earth metallic systems. *J. Alloys Compd.* 225, 409–422. doi: 10.1016/0925-8388(94)07087-3

Duchon, T., Dvorák, F., Aulická, M., Stetsovych, V., Vorokhta, M., Mazur, D., et al. (2014a). Comment on "ordered phases of reduced ceria as epitaxial films on Cu(111)". *J. Phys. Chem. C* 118, 5058–5059. doi: 10.1021/jp412439b

Duchon, T., Dvorak, F., Aulicka, M., Stetsovych, V., Vorokhta, M., Mazur, D., et al. (2014b). Ordered phases of reduced ceria as epitaxial films on Cu(111). *J. Phys. Chem. C* 118, 357–365. doi: 10.1021/jp409220p

Dvorak, F., Stetsovych, O., Steger, M., Cherradi, E., Matolinova, I., Tsud, N., et al. (2011). Adjusting morphology and surface reduction of CeO2(111) thin films on Cu(111). *J. Phys. Chem. C* 115, 7496–7503. doi: 10.1021/jp1121646

Fiala, R., Vaclavu, M., Rednyk, A., Khalakhan, I., Vorokhta, M., Lavkova, J., et al. (2015). Pt–CeOx thin film catalysts for PEMFC. *Catalysis Today* 240 (Pt. B), 236–241. doi: 10.1016/j.cattod.2014.03.069

Flege, J. I., and Grinter, D. C. (2018). *In situ* studies of oxide nucleation, growth, and transformation using slow electrons. *Prog. Surf. Sci.* 93, 21–45. doi: 10.1016/j.progsurf.2018.02.001

Flege, J. I., Kaemena, B., Meyer, A., Falta, J., Senanayake, S. D., Sadowski, J. T., et al. (2013). Origin of chemical contrast in low-energy electron reflectivity of correlated multivalent oxides: the case of ceria. *Phys. Rev. B* 88:235428. doi: 10.1103/PhysRevB.88.235428

Gasperi, G., Amidani, L., Benedetti, F., Boscherini, F., Glatzel, P., Valeri, S., et al. (2016). Electronic properties of epitaxial cerium oxide films during controlled reduction and oxidation studied by resonant inelastic X-ray scattering. *Phys. Chem. Chem. Phys.* 18, 20511–20517. doi: 10.1039/C6CP04407G

Gasperi, G., Luches, P., and Barth, C. (2018). Stability of ultrathin ceria films on Pt(111) exposed to air and treated in redox cycles. *J. Phys. Chem. C* 122, 25954–25963. doi: 10.1021/acs.jpcc.8b07231

Grinter, D. C., Ithnin, R., Pang, C. L., and Thornton, G. (2010). Defect structure of ultrathin ceria films on Pt(111): atomic views from scanning tunnelling microscopy. *J. Phys. Chem. C* 114, 17036–17041. doi: 10.1021/jp102895k

Grinter, D. C., Muryn, C., Sala, A., Yim, C.-M., Pang, C. L., Menteş T. O., et al. (2016). Spillover reoxidation of ceria nanoparticles. *J. Phys. Chem. C* 120, 11037–11044. doi: 10.1021/acs.jpcc.6b03670

Höcker, J., Krisponeit, J. O., Schmidt, T., Falta, J., and Flege, J. I. (2017). The cubic-to-hexagonal phase transition of cerium oxide particles: dynamics and structure. *Nanoscale* 9, 9352–9358. doi: 10.1039/C6NR09760J

Höcker, J., Menteş T. O., Sala, A., Locatelli, A., Schmidt, T., Falta, J., et al. (2015). Unraveling the dynamic nanoscale reducibility (Ce4+ → Ce3+) of CeOx–Ru in hydrogen activation. *Adv. Mater. Interfaces* 2:1500314. doi: 10.1002/admi.201500314

Jones, J., Xiong, H., DeLaRiva, A. T., Peterson, E. J., Pham, H., Challa, S. R., et al. (2016). Thermally stable single-atom platinum-on-ceria catalysts via atom trapping. *Science* 353:150. doi: 10.1126/science.aaf8800

Kemmer, J., Praetorius, C., Krönlein, A., Hsu, P.-J., Fauth, K., and Bode, M. (2014). Structural analysis of the intermetallic surface compound CePt5/Pt(111). *Phys. Rev. B* 90:195401. doi: 10.1103/PhysRevB.90.195401

Kozlov, S. M., Demiroglu, I., Neyman, K. M., and Bromley, S. T. (2015). Reduced ceria nanofilms from structure prediction. *Nanoscale* 7, 4361–4366. doi: 10.1039/C4NR07458K

Luches, P., Giordano, L., Grillo, V., Gazzadi, G. C., Prada, S., Campanini, M., et al. (2015). Atomic scale structure and reduction of cerium oxide at the interface with platinum. *Adv. Mater. Interfaces* 2:1500375. doi: 10.1002/admi.201500375

Luches, P., Pagliuca, F., and Valeri, S. (2011). Morphology, stoichiometry, and interface structure of CeO_2 ultrathin films on Pt(111). *J. Phys. Chem. C* 115, 10718–10726. doi: 10.1021/jp201139y

Luches, P., Pagliuca, F., and Valeri, S. (2014). Structural and morphological modifications of thermally reduced cerium oxide ultrathin epitaxial films on Pt(111). *Phys. Chem. Chem. Phys.* 16, 18848–18857. doi: 10.1039/C4CP02723J

Luches, P., Pagliuca, F., Valeri, S., and Boscherini, F. (2013). Structure of ultrathin CeO_2 films on Pt(111) by polarization-dependent X-ray absorption fine structure. *J. Phys. Chem. C* 117, 1030–1036. doi: 10.1021/jp310375t

Luches, P., and Valeri, S. (2015). Structure, morphology and reducibility of epitaxial cerium oxide ultrathin films and nanostructures. *Materials* 8, 5818–5833. doi: 10.3390/ma8095278

Lykhach, Y., Kozlov, S. M., Skála, T., Tovt, A., Stetsovych, V., Tsud, N., et al. (2015). Counting electrons on supported nanoparticles. *Nat. Mater.* 15:284. doi: 10.1038/nmat4500

Murgida, G. E., Ferrari, V., Llois, A. M., and Ganduglia-Pirovano, M. V. (2018). Reduced CeO2(111) ordered phases as bulk terminations: introducing the structure of Ce3O5. *Phys. Rev. Mater.* 2:083609. doi: 10.1103/PhysRevMaterials.2.083609

Olbrich, R., Murgida, G. E., Ferrari, V., Barth, C., Llois, A. M., Reichling, M., et al. (2017). Surface stabilizes ceria in unexpected stoichiometry. *J. Phys. Chem. C* 121, 6844–6851. doi: 10.1021/acs.jpcc.7b00956

Pierre, D., Deng, W., and Flytzani-Stephanopoulos, M. (2007). The importance of strongly bound Pt–CeO x species for the water-gas shift reaction: catalyst activity and stability evaluation. *Topics Catalysis* 46, 363–373. doi: 10.1007/s11244-007-9013-8

Sauerbrey, M., Gasperi, G., Luches, P., Falta, J., Valeri, S., and Flege, J. I. (2017). Cerium oxide epitaxial nanostructures on Pt(111): growth, morphology and structure. *Topics Catalysis* 60, 513–521. doi: 10.1007/s11244-016-0716-6

Sauerbrey, M., Höcker, J., Wellbrock, M., Schowalter, M., Krisponeit, J.-O., Müller-Caspary, K., et al. (2016). Ultrasmooth Ru(0001) films as templates for ceria nanoarchitectures. *Crystal Growth Design* 16, 4216–4224. doi: 10.1021/acs.cgd.6b00192

Schaefer, A., Hagman, B., Höcker, J., Hejral, U., Flege, J. I., and Gustafson, J. (2018). Thermal reduction of ceria nanostructures on rhodium(111) and re-oxidation by CO2. *Phys. Chem. Chem. Phys.* 20, 19447–19457. doi: 10.1039/C8CP01505H

Senanayake, S. D., Stacchiola, D., and Rodriguez, J. A. (2013). Unique properties of ceria nanoparticles supported on metals: novel inverse ceria/copper catalysts for CO oxidation and the water-gas shift reaction. *Acc. Chem. Res.* 46, 1702–1711. doi: 10.1021/ar300231p

Stetsovych, V., Pagliuca, F., Dvorák, F., Duchon, T., Vorokhta, M., Aulická, M., et al. (2013). Epitaxial cubic Ce2O3 films via Ce-CeO2 interfacial reaction. *J. Phys. Chem. Lett.* 4, 866–871. doi: 10.1021/jz400187j

Suchorski, Y., Wrobel, R., Becker, S., and Weiss, H. (2008). CO Oxidation on a CeOx/Pt(111) inverse model catalyst surface: catalytic promotion and tuning of kinetic phase diagrams. *J. Phys. Chem. C* 112, 20012–20017. doi: 10.1021/jp806033v

Trovarelli, A. (1996). Catalytic properties of ceria and CeO_2-containing materials. *Catalysis Rev.* 38, 439–520. doi: 10.1080/01614949608006464

Trovarelli, A., and Fornasiero, P. (2013). *Catalysis by Ceria and Related Materials.* London: Imperial College Press.

Wilkens, H., Schuckmann, O., Oelke, R., Gevers, S., Reichling, M., Schaefer, A., et al. (2013a). Structural transitions of epitaxial ceria films on Si(111). *Phys. Chem. Chem. Phys.* 15, 18589–18599. doi: 10.1039/c3cp52688g

Wilkens, H., Schuckmann, O., Oelke, R., Gevers, S., Schaefer, A., Bäumer, M., et al. (2013b). Stabilization of the ceria ι-phase (Ce7O12) surface on Si(111). *Appl. Phys. Lett.* 102:111602. doi: 10.1063/1.4795867

Zahl, P., Wagner, T., Möller, R., and Klust, A. (2010). Open source scanning probe microscopy control software package GXSM. *J. Vacuum Sci. Technol. B Nanotechnol. Microelectr. Mater. Proces. Measure. Phenom.* 28, C4E39–C34E47. doi: 10.1116/1.3374719

Conflict of Interest Statement: The authors declare that the research was conducted in the absence of any commercial or financial relationships that could be construed as a potential conflict of interest.

ORIGINAL RESEARCH
published: 07 February 2019
doi: 10.3389/fchem.2019.00037

Oxygen Vacancies in Oxide Nanoclusters: When Silica Is More Reducible Than Titania

Andi Cuko [1,2]***, Stefan T. Bromley*** [1,3] ***and Monica Calatayud*** [2*]

[1] Departament de Ciència de Materials i Química Física, Institut de Química Teòrica i Computacional (IQTCUB), Universitat de Barcelona, Barcelona, Spain, [2] CNRS, Laboratoire de Chimie Théorique, LCT, Sorbonne Université, Paris, France, [3] Institució Catalana de Recerca i Estudis Avançats (ICREA), Barcelona, Spain

Oxygen vacancies are related to specific optical, conductivity and magnetic properties in macroscopic SiO_2 and TiO_2 compounds. As such, the ease with which oxygen vacancies form often determines the application potential of these materials in many technological fields. However, little is known about the role of oxygen vacancies in nanosized materials. In this work we compute the energies to create oxygen vacancies in highly stable nanoclusters of $(TiO_2)_N$, $(SiO_2)_N$, and mixed $(Ti_xSi_{1-x}O_2)_N$ for sizes between $N = 2$ and $N = 24$ units. Contrary to the results for bulk and surfaces, we predict that removing an oxygen atom from global minima silica clusters is energetically more favorable than from the respective titania species. This unexpected chemical behavior is clearly linked to the inherent presence of terminal unsaturated oxygens at these nanoscale systems. In order to fully characterize our findings, we provide an extensive set of descriptors (oxygen vacancy formation energy, electron localization, density of states, relaxation energy, and geometry) that can be used to compare our results with those for other compositions and sizes. Our results will help in the search of novel nanomaterials for technological and scientific applications such as heterogeneous catalysis, electronics, and cluster chemistry.

Keywords: TiO_2, SiO_2, titanosilicates, nanoclusters, oxygen vacancy, reducibility

Edited by:
Javier Carrasco,
CIC Energigune, Spain

Reviewed by:
Gianfranco Pacchioni,
Università degli Studi di Milano Bicocca, Italy
Alexander Shluger,
University College London, United Kingdom

****Correspondence:***
Monica Calatayud
calatayu@lct.jussieu.fr

Specialty section:
This article was submitted to Physical Chemistry and Chemical Physics,
a section of the journal Frontiers in Chemistry

Received: *09 November 2018*
Accepted: *14 January 2019*
Published: *07 February 2019*

Citation:
Cuko A, Bromley ST and Calatayud M (2019) Oxygen Vacancies in Oxide Nanoclusters: When Silica Is More Reducible Than Titania. Front. Chem. 7:37. doi: 10.3389/fchem.2019.00037

INTRODUCTION

Metal oxides are an important class of materials in many scientific and technological fields. Silica and titania are abundant compounds and play crucial roles in geology (Howie, 1964; Lakshtanov et al., 2007; Lyle et al., 2015), astrochemistry (Lambert et al., 2012; Lee et al., 2015; Komatsu et al., 2018), environmental and chemical sciences (Joo et al., 2014; Kapilashrami et al., 2014), biology and medicine (Mal et al., 2003; Nguyen et al., 2005; Das et al., 2009; Bawazer et al., 2012; Lucky et al., 2016; Saroj and Rajput, 2018). Their ability to exchange oxygen drastically determines their properties. In the case of TiO_2, the loss of lattice oxygen results in a change of color from white to blue, the appearance of magnetism, and is connected with photocatalytic properties (Houlihan et al., 1975; Diebold, 2003; Di Valentin et al., 2006; Na-Phattalung et al., 2006; Vásquez et al., 2016; Li et al., 2018). On the other hand, oxygen vacancies present in amorphous silica have been reported to modify its electronic and optical properties (Rudra and Fowler, 1987; Skuja, 1998; Manveer et al., 2017). Oxygen substoichiometry in silica-based materials is linked to dielectric breakdown and electroforming in resistive random access memory devices (McPherson and Mogul, 1998; Yao et al., 2010; Wang et al., 2014; Mehonic et al., 2018). Whereas, the effect of creating an oxygen vacancy in bulk and surfaces of both titania and silica is well-reported, little is known about the role these defects may play in nanosized materials and clusters. By means of density functional theory (DFT) based calculations, we characterise the energetics of creating an oxygen vacancy in silica, titania and titanosilicate clusters recently derived from global optimization studies. Low energy clusters can be generated with cluster beam experiments and stabilized by soft landing techniques. Such studies are increasingly looking into the reactivity of the cluster species formed for technologically important reactions (Yin and Bernstein, 2014; Vajda and White, 2015; Sun et al., 2016). With our work we hope to elucidate the reactivity of such nanoclusters as estimated through their reduction by oxygen removal.

From a computational point of view, the energetic cost of removing a neutral oxygen atom from a stoichiometric metal oxide can be calculated with the following equation:

$$\begin{aligned} \mathrm{M_nO_{2n}} &\rightarrow \mathrm{M_nO_{2n-1}} + 1/2\ \mathrm{O_2} \\ \mathrm{E_{vac}} &= \mathrm{EM_nO_{2n-1}} + 1/2\mathrm{EO_2} - \mathrm{EM_nO_{2n}} \end{aligned} \tag{1}$$

A reducible oxide like titania tends to have small (positive) $\mathrm{E_{vac}}$ values, while the energy to form an oxygen vacancy in an irreducible oxide like silica is relatively higher. $\mathrm{E_{vac}}$ values can thus be used to compare different systems and provide an initial ranking of reducibility (Ganduglia-Pirovano et al., 2007; Deml et al., 2015; Helali et al., 2017). Typical values for bulk and surface E_{vac} values in rutile and anatase $\mathrm{TiO_2}$ are 3.7–4.5 eV whereas for $\mathrm{SiO_2}$ the values are much higher, 5–8 eV (see Sushko et al., 2005). In addition, the localization of the electrons remaining after the removal of the oxygen in the lattice provides crucial information related to the electronic structure of the defective material (Helali et al., 2017):

$$M^{n+} - O^{2-} - M^{n+} \rightarrow M^{n+} - 2e^{-} - M^{n+} + \tfrac{1}{2}O_2 \tag{2}$$

It is commonly accepted that removing an oxygen atom from $\mathrm{TiO_2}$ leads to the formation of paramagnetic $\mathrm{Ti^{3+}}$ sites in both bulk and surfaces (Houlihan et al., 1975; Di Valentin et al., 2006; Li et al., 2018). The electronic state of reduced titania systems is typically open-shell. In amorphous $\mathrm{SiO_2}$ and quartz the removal of a lattice oxygen results in the formation of a Si-Si covalent bond where the electron pair is stabilized by two Si sites (Sushko et al., 2005). In the quartz surface the removal of an oxygen atom leads to an electron pair localized on a surface silicon site (Silvi and D'Arco, 2006; Causà et al., 2015). This typically leads to electronic states that are closed-shell.

We focus on the effects that the system size reduction to the nanoscale has on the type of oxygen defects exhibited and their resultant $\mathrm{E_{vac}}$ values. As has been previously reported for $\mathrm{ZrO_2}$ (Ruiz Puigdollers et al., 2016a,b), $\mathrm{CeO_2}$ (Kozlov et al., 2015), $\mathrm{TiO_2}$ (Morales-García et al., 2018), this may result in a significant change in the materials' properties. Specifically, in this work we investigate the energetic, structural and electronic properties of silica, titania and mixed titanosilicates as regards their tendency to lose neutral oxygen atoms. These properties are then compared between the different oxides and with respect to the system size, including up to the bulk. At the nanoscale level, we consider a set of globally optimized silica and titania clusters with sizes between 2 and 24 $\mathrm{MO_2}$ units. Moreover, we compare our results for these pure oxides with a comparative set of titanosilicate clusters for the size of 10 $\mathrm{MO_2}$ units. At the bulk level, we consider alpha quartz and rutile phases, respectively, for silica and titania, which are the two most stable phases under ambient conditions. Such systems are then reduced by a single and neutral oxygen vacancy and the results are analyzed to elucidate the role of cluster size, structure and oxide type with respect to the formation of oxygen vacancies.

METHODOLOGY

All nanocluster structures selected in this study correspond to the lowest energy global minima candidates currently reported in the literature as derived by us and/or other authors: $\mathrm{SiO_2}$ systems are derived from Flikkema and Bromley (2003, 2004), Lu et al. (2003), Bromley and Flikkema (2005), $\mathrm{TiO_2}$ systems from Hamad et al. (2005), Woodley et al. (2006), Calatayud et al. (2008a), Syzgantseva et al. (2011), Chen and Dixon (2013), Bhattacharya et al. (2015), Aguilera-Granja et al. (2016), Lamiel-Garcia et al. (2017), and finally mixed titanosilicates are taken from Cuko et al. (2018). A two-step procedure is followed to compute $\mathrm{E_{vac}}$ (Equation 1): (i) a selected oxygen atom is removed from a structurally frozen stoichiometric nanocluster and the pre-removal/post-removal energy difference is defined as $\mathrm{E_{unrel}}$, (ii) the post-removal non-stoichiometric nanocluster structure is then fully optimized, with the pre-optimized/post-optimized energy difference defined as $\mathrm{E_{vac}}$. The relaxation energy $\mathrm{E_{rel}}$ is then derived as the difference between $\mathrm{E_{unrel}}$ and $\mathrm{E_{vac}}$. For the smaller sizes, $N = 2$–10, every symmetrically distinct oxygen site was tested and only the most representative ones were reported. For larger sizes, an exhaustive approach was found to be too computationally demanding and a sampling of approximately 10 oxygen sites was performed, always including all symmetrically non-equivalent terminating oxygens. All DFT based calculations involving reduced nanoclusters were carried out using a spin-polarized formalism, employing the PBE0 functional (Adamo and Barone, 1999) and a tier-1/tight numerical basis set as implemented in the FHI-AIMS code (Blum et al., 2009). In most of the calculations, we did not force the spin multiplicity of the system. However, in a few cases, especially for $\mathrm{TiO_2}$ systems, in order to overcome convergence problems, we forced the spin multiplicity to be either an open shell singlet or a triplet. Recently, room temperature ferromagnetism has been reported for zirconia nanoparticles (Rahman et al., 2016; Albanese et al., 2018). This effect might also take place in titania and could be studied by considering multiple vacancies in future works.

RESULTS AND DISCUSSION

Pure $(\mathrm{SiO_2})_N$ Nanoclusters

Figure 1 shows the calculated values of $\mathrm{E_{vac}}$ for the lowest energy $\mathrm{SiO_2}$ nanoclusters together with some selected nanocluster structures. **Figure S1** shows the structures of all stoichiometric silica nanoclusters used in this work and **Table S1** includes the corresponding values of E_{vac}, E_{unrel}, and E_{rel} for the most stable reduced systems. Generally, stoichiometric silica global minimum nanoclusters tend to possess quite open symmetric structures and typically have between 2 and 4 unsaturated (terminal) oxygen sites. The majority of these structures present silanone centers, which are triply-coordinated planar Si centers involving a terminal oxygen atom (i.e., formally >Si=O, but arguably more accurately $>Si^{+}$-O^{-}) (Avakyan et al., 2006; Zwijnenburg et al., 2009). For nearly all the silica nanoclusters considered, the terminal oxygen atoms at these sites are found to cost the least energy to be removed, 2.6–2.8 eV, with E_{vac} increasing slightly and monotonically with the size. The $(SiO_2)_{12}$ nanocluster is the only exception as it only displays non-bridging oxygen (NBO) terminal species (i.e., ≡Si–O species where Si is 4-fold coordinated) rather than silanones. Removing the terminal oxygen atom of an NBO center results in a higher E_{vac} value (3.60 eV) as compared with silanone defects (2.6–2.8 eV). We note that the values of E_{vac} for the removal of oxygen atoms at both silanone and NBO defects are much lower than those for the removal of 2-fold coordinated oxygen atoms in the corresponding bulk systems. From our calculations, for example, we obtained E_{vac} values between 5.06–5.39 eV for a-quartz with a range of vacancy concentrations between 1/24 and 1/3 vacancies per SiO_2 units. These values are also consistent with other work where an E_{vac} value of 5.15 eV was obtained using plane-wave based DFT calculations at the PBE level for the alpha-quartz structure with a vacancy concentration of 1/48 (Helali et al., 2017). We note that, removing a 2-fold oxygen atom in our nanoclusters typically costs between 4.2 and 5.7 eV (see **Figure S2** which shows selected values for $Si_{10}O_{20}$), which is comparable to the E_{vac} values obtained for bulk alpha quartz. This confirms that the terminal silanone oxygens are least energetically costly in silica nanoclusters. From a structural point of view, reducing a silanone defective site in a nanocluster leads to a 2-fold Si site displaying a Si-O distance of 1.71 Å. This is slightly longer than the Si-O bond length of 1.62 Å as calculated by Pacchioni and Ferrario (1998) for a 2-fold coordinated Si defect in alpha quartz using a cluster approach at both wave function theory level employing unrestricted Hartree Fock, and DFT level employing the hybrid B3LYP functional. Further comparing our results with these bulk cluster calculations, in our clusters the O-Si-O angle of a reduced silanone site is found to be between 87 and 111°, depending on whether the defect is part of a two or three membered ring. This compares with a value of 102° found from bulk cluster calculations. Also, the vicinal Si-O-Si^{II} angle (where Si^{II} corresponds to the 2-fold coordinated silicon atom) is found to be between 90 and 133° in our nanoscale clusters against the corresponding values for the same defective site of 141–161° from bulk cluster calculations.

We note that for silica nanoclusters, relaxation is found to have little impact on the energetics of oxygen removal. An analysis of **Figure 1** (see **Table S1** for the values) shows that E_{rel} is generally between 0.06 and 0.12 eV, and is thus <5% of the corresponding E_{vac}. The structures of the relaxed O-deficient nanoclusters are very similar to the original stoichiometric structures. The only exception is the nanocluster structure for $N = 12$ that possesses two NBO sites. Oxygen vacancies originating from 2-fold coordinated oxygen atoms, which at nanoscale are less energetically favored than those generated from mono-coordinated oxygen sites, are also well-studied for bulk silica in the literature (Skuja et al., 1984; Skuja, 1998; Sulimov et al., 2002). Specifically, the ≡Si-Si≡ equilibrium distance is reported to be 2.3–2.5 Å in α-quartz (Skuja et al., 1984; Skuja, 1998; Sulimov et al., 2002). At the nanoscale, after removal of two-coordinated oxygens we find the ≡Si-Si≡ equilibrium distance to be between 2.12–2.37 Å, slightly lower with respect to the range reported for the bulk. Moreover, bulk oxygen removal is known to induce a long range structural distortion and asymmetric relaxation of atoms surrounding the vacancy (Sulimov et al., 2002). Such long-range effects are more difficult to evaluate for clusters for which the sizes range between 5 and 20 Å. However, generally we observe a relatively strong local relaxation for the neighboring atoms, whereas no significant long-range relaxation is observed (usually <0.1 Å of total displacement for distances >3 Å from the vacancy).

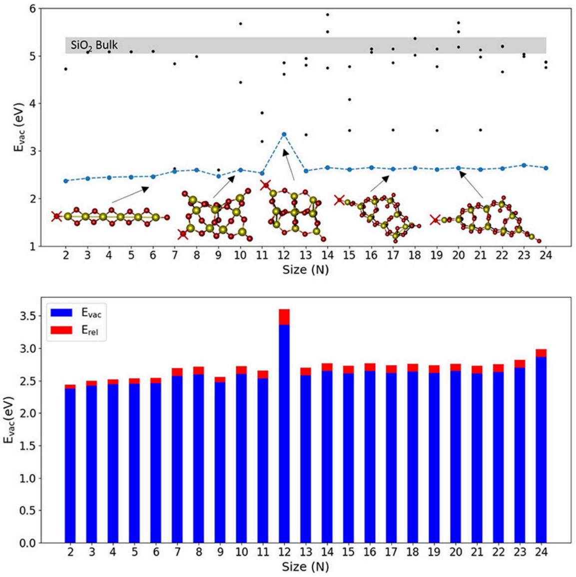

FIGURE 1 | Top: E_{vac} vs. N plot of global minimum isomers for selected $(SiO_2)_N$ nanocluster sizes. Blue line is relative to lowest E_{vac} obtained associated with the removal of O atoms indicated with red crosses. Black points indicate a selection of E_{vac} values obtained from the removal of different sites of O atoms. Light gray region indicates the range of E_{vac} values calculated for α-quartz SiO_2 bulk. Bottom, the corresponding oxygen vacancy formation energy values, E_{vac} (blue), and relaxation energy values, E_{rel} (red), with respect to nanocluster size.

The electronic structure of the oxygen-deficient non-stoichiometric silica clusters is consistently found to be a singlet, as expected. The electron density of the highest occupied state is mainly located on the O-deficient silicon site and has the shape of a *sp* orbital, see **Figure S3**.

Pure $(TiO_2)_N$ Nanoclusters

Figure 2 shows the calculated values of E_{vac} for the lowest energy $(TiO_2)_N$ nanoclusters together with selected nanocluster structures. **Table S1** shows the corresponding values of E_{vac}, E_{unrel}, and E_{rel} obtained and **Figure S4** shows the $(TiO_2)_N$ structures used. It can be observed that the $(TiO_2)_N$ nanocluster structures are more compact and less symmetric than silica clusters for the range selected, with titanium atoms being in 4-, 5-, and 6-fold coordinated environments. Many of these nanocluster structures, especially for sizes smaller than $N = 20$, possess terminal oxygen sites bonded to a Ti atom in a tetrahedral environment (≡Ti–O species). If present, these terminal oxygens are generally the least energetically costly to remove. In some cases (e.g., $N = 4, 9, 11, 12$), although the removal of a terminal oxygen does not have the lowest associated E_{unrel} value, removing a 2-fold oxygen atom nearby can lead to a reduced nanocluster with the same topology as the one that results from removing the terminal oxygen itself. E_{vac} values for $(TiO_2)_N$ nanoclusters are found to oscillate between 2.48 and 5.01 eV and display no clear size-dependent trend, contrary to the case of silica nanoclusters. The energetic cost to remove an oxygen atom seems to depend critically on the structure of each cluster. In very few cases (i.e., $N = 17, 22$), the E_{vac} values for TiO_2 nanoclusters was found to be comparable with that found for SiO_2 nanoclusters. In such cases, after the relaxation, the TiO_2 nanocluster structure was found to have neither terminal oxygen sites (usually the site of the oxygen atom removal) nor 3-fold coordinated Ti defective centers, known to be highly destabilizing when left after the removal of a terminal site. We were not able to obtain a E_{vac} value for bulk systems with the computational setup used for the nanoclusters due to severe convergence problems associated with the presence of Ti^{3+} centers. Other authors have calculated E_{vac} for bulk and surfaces of anatase and rutile using DFT-based calculations employing hybrid functionals incorporating between 20 and 25% Hartree Fock exchange, obtaining values between 4.8 eV (Finazzi et al., 2008; Yamamoto and Ohno, 2012; Deák et al., 2014) and 5.4 eV (Islam et al., 2007; Janotti et al., 2010; Lee et al., 2012). We also note that the E_{vac} value for a terminal oxygen in an anatase bulk cut $(TiO_2)_{35}$ nanoparticle was calculated to be 3.95 eV, using the same methodology as employed herein (Kim et al., 2016). This value is similar to the average value of 3.65 eV, calculated for the lowest E_{vac} values over our set of nanoclusters. Interestingly, for the $(TiO_2)_{35}$ nanoparticle, the removal of an internal bulk-like three-coordinated oxygen resulted in a lower E_{vac} (i.e., 3.65 eV) with respect to that for removing a terminal oxygen atom. This behavior probably derives from the strong geometrical relaxation induced from the vacancy to the already metastable anatase bulk cut structure.

The relaxation of the TiO_2 nanoclusters after oxygen removal is found to involve more energy than in the case of silica nanoclusters. Specifically, the average E_{rel} value for the lowest energy clusters is found to be 1.50 eV, and in some cases it accounts for more than 2.5 eV ($N = 21, 23$). With a few exceptions, such as for $N = 4, 17, 22$, the removal of terminal oxygens induces a moderate degree of local relaxation. However, when 2-fold coordinated oxygen atoms are removed, significant structural rearrangements take place (i.e., $N = 10, 20, 21, 23, 24$). In **Figure S3** we show the O-deficient structure for $N = 11$ where a 2-fold oxygen atom is removed in the presence of a terminal oxygen, which then subsequently moves during the relaxation to fill the vacancy.

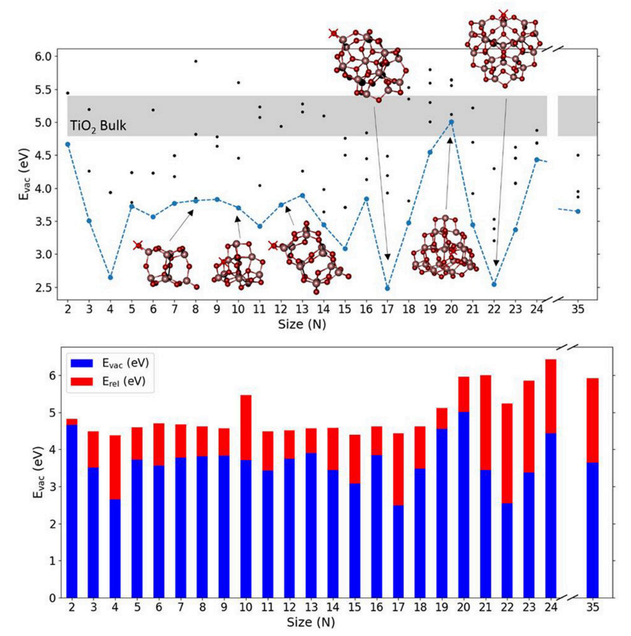

FIGURE 2 | Top: E_{vac} as a function of the system size (N) for the considered $(TiO_2)_N$ nanoclusters. Blue line is relative to lowest E_{vac} obtained associated with the removal of O atoms. Black points indicate a selection of E_{vac} values obtained from the removal of different sites of O atoms. Light gray region indicates the range of calculated TiO_2 bulk E_{vac} values reported in literature (see text). A selection of nanocluster structures is also shown where red crosses indicate the oxygen site that, upon removal, leads to the lowest E_{vac} value. Values of E_{vac} and E_{rel} for the nanoparticle with $N = 35$ are obtained from Kim et al. (2016). Bottom: the corresponding oxygen vacancy formation energies, E_{vac} (blue), and relaxation energies, E_{rel} (red), with respect to nanocluster size.

The electronic structure of the O-deficient clusters is either a triplet with two unpaired electrons occupying two titanium sites or an open shell singlet with unpaired electrons equally delocalized around three Ti centers neighboring the vacancy. **Figure S3** displays the electron density associated with the highest occupied state of the $(TiO_2)_{10}$ and $(TiO_2)_{11}$ nanocluster after the removal of an oxygen atom, which is localized on Ti^{3+} sites that carry the electrons left in the vacancy.

Mixed $(Si_xTi_{1-x}O_2)_N$ Nanoclusters

In order to study the effect of mixing SiO_2 and TiO_2 on E_{vac} values, we have selected $(Ti_xSi_{1-x}O_2)_{10}$ nanoclusters and a Ti content x between 0 and 1. The nanocluster structures used are taken from the global optimized structures reported in Cuko et al. (2018) (see also **Figure S5**). The nanoclusters exhibit different isomers for pure and mixed structures. All the structures possess terminal ≡Ti-O oxygen sites, with the exception of the pure $(TiO_2)_{10}$ nanocluster. The pure silica $(SiO_2)_{10}$ nanocluster displays only silanone terminations, whereas mixed systems display typically two terminal oxygen centers bonded with

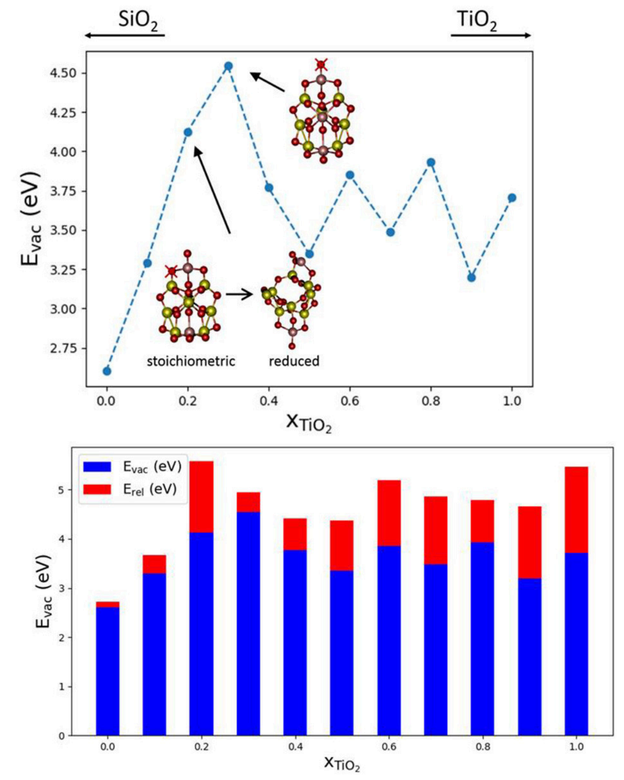

FIGURE 3 | Top: E_{vac} vs. x plot; global minima isomers for $(Ti_xSi_{1-x}O_2)_{10}$ with $0 < x < 1$, the red crosses indicate the O atom that, after removal, leads to the lowest E_{vac}. Bottom, the corresponding oxygen vacancy formation energies, E_{vac} (blue), and relaxation energies, E_{rel} (red), with respect to nanocluster composition.

titanium atoms. The presence of titanium thus seems to allow for relatively more energetically stable terminal oxygen sites than silicon (Cuko et al., 2018). **Figure 3** shows that the E_{vac} values obtained for the mixed nanocluster systems oscillate around 3.7 eV, with the lowest value being found for $x = 0.1$ ($E_{vac} = 3.29$ eV) and the highest value for $x = 0.3$ ($E_{vac} = 4.54$ eV). The mixed nanocluster structure with $x = 0.1$ possesses two terminal oxygen sites bound to a Si and Ti atom. The removal of the terminal oxygen is more energetically facile (i.e., E_{vac} is relatively lower) when it is bound to a silicon atom rather than a titanium atom. As the content of TiO_2 increases, the E_{vac} values are found to initially increase up to $x = 0.30$, and afterwards decrease and oscillate with no obvious trend.

Over the range of $(Ti_xSi_{1-x}O_2)_{10}$ nanoclusters, relaxation effects are relatively less significant for clusters with titania contents of $x = 0.0, 0.1, 0.3$. In the first two cases, indeed, the less energetically costly oxygen to be removed is from a silanone or a Si-NBO site, and therefore, the local structural relaxation effects are similar to those of pure silica systems. The system with $x = 0.2$ is a special case since lowest E_{vac} value we could find is related to the removal of a two coordinated oxygen as shown. The removal of this oxygen atom leads to a significant structural change during the geometry optimization with a consequent relatively large associated E_{rel} value (see **Figure 3**). For higher Ti content, E_{rel} energies are found to be in the range of 0.6–1.5 eV which is typical for pure TiO_2 nanoclusters. Overall, the mixed $(Ti_xSi_{1-x}O_2)_{10}$ nanocluster systems tend to behave more like titania nanoclusters rather than silica nanoclusters in terms of reduction through O-vacancy formation.

DISCUSSION

The results obtained point to a (sub)nanosize dependency of the formation of oxygen vacancies in silica- and titania-based structures. Firstly, the removal of singly-coordinated terminal oxygen atoms is often associated with low E_{vac} values. This is explained by the low energetic cost of breaking an M-O bond compared with the energy required to break two M–O bonds for oxygen atoms in 2-fold coordinated sites. This is observed in the three types of nanoclusters studied in this work and has been reported in the literature for other oxides, especially in systems exhibiting structural stable dangling bonds. For instance, V_2O_5 in bulk, surface and clusters exhibit structurally stable terminal oxygen sites. The coordination of oxygen sites in vanadia is commonly associated with chemical reactivity (Calatayud and Minot, 2006; Ganduglia-Pirovano et al., 2007; Calatayud et al., 2008b). The lower E_{vac} found for nanoclusters compared to bulk values indicates higher reducibility of the nanosized materials as has been reported for other oxide systems like CeO_2 and ZrO_2 (Bruix and Neyman, 2016; Ruiz Puigdollers et al., 2016b).

It is, however, worth noting that the lowest E_{vac} values found for silica clusters, 2.3–3.6 eV, are generally lower than for titania clusters, 2.48–5.01 eV as also shown from **Figures 1**, **2** and **Table S1**. A direct comparison between bulk SiO_2 and bulk TiO_2 was not possible in this study due to the high computational cost and convergence problems with TiO_2 systems. However, there are several studies on O vacancy defects formation in metal oxides (Pacchioni, 2008; Deml et al., 2015; Helali et al., 2017) that agree on associating a higher reducibility to titania (either rutile and anatase phases) with respect to silica bulk (mainly α-quartz). Our results suggest that silica becomes more reducible than titania at the nanoscale, which is contrary to the properties observed for respective bulk materials. The reason for such inverted behavior seems to be connected to the presence of terminal silanone oxygen atoms in low energy silica nanoclusters. The electronic structure (projected density of states) of this site is displayed in **Figure 4**, showing that the energy levels are highly localized in two sharp peaks (one between −9 and −10 eV, and the other between −10.5 and −11.5 eV) associated to higher reactivity. In comparison, the oxygen levels of the 2-fold oxygen in $(TiO_2)_{10}$ are distributed over a 3 eV range of energies (between −9 and −12 eV). In the $(TiO_2)_{11}$ cluster, the electronic energy levels associated with the dangling oxygen lay closer to the Fermi level, between −9 and −11 eV, and those associated with the 2-fold coordinated site levels spread between −9 and −13 eV. The electronic structure of the dangling silanone oxygen in silica is consistent with an enhanced reactivity of this site and with the low E_{vac} values shown. Interestingly, the oxygen vacancy in bulk silica has been reported to exhibit specific electronic transitions associated with the electron pair localized on the

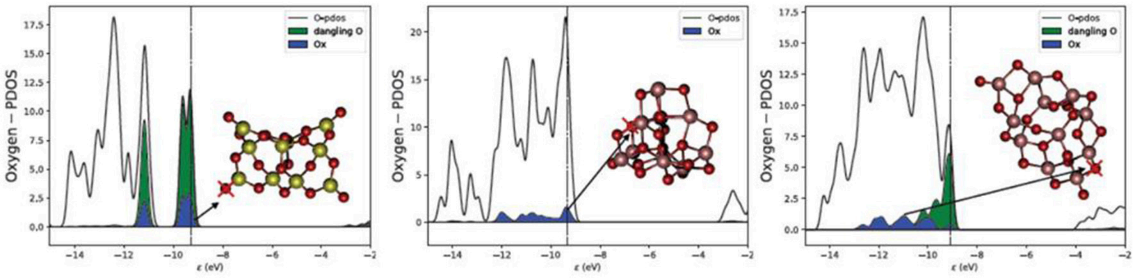

FIGURE 4 | Projected density of states (PDOS) on for oxygen atoms for $(SiO_2)_{10}$ (left), $(TiO_2)_{10}$ (middle), and $(TiO_2)_{11}$ (right). Ox indicates the projection on the oxygen center marked with a cross (blue). Dangling O indicates the projection on all single terminal oxygen sites (green). Vertical lines indicate the position of the Fermi level. The PDOS plot has been smeared for clarity.

silicon atom after reduction (Cannizzo and Leone, 2004; Sushko et al., 2005). We also observe the highest occupied electronic level of O-deficient $(SiO_2)_{10}$ cluster localized on the resulting Si< site (**Figure S3** top right), which is consistent with the presence of an electron pair localized on the silicon site.

A second important point is the structure-dependency of the E_{vac} values. In the case of silica nanoclusters, the E_{vac} value is almost constant and related to the presence of Si sites with dangling silanone oxygen sites. However, titania nanoclusters display a greater range of E_{vac} values, depending on the structure near to the removed oxygen atom. Relaxation effects can also be significantly stronger in titania nanoclusters than in silica nanoclusters, which is consistent with the greater variety of E_{vac} sites and values found. The size dependency of E_{vac} values is also different for each nanomaterial. For the system sizes considered here, the majority of silica nanoclusters exhibit a near constant value of $E_{vac} \sim 2.6$ eV associated with silanone sites, and exceptionally an E_{vac} value of 3.6 eV associated with the NBO in the $(SiO_2)_{12}$ nanocluster. For larger sizes, silica nanoclusters are predicted to become fully-coordinated (Flikkema and Bromley, 2009), which will result in a jump of E_{vac} to near bulk values ~5 eV. As can be seen in **Figure S2**, 2-fold coordinated oxygens cost 4.4–5.5 eV. In the case of pure titania nanoclusters there seems to be no clear trend with size.

Finally, mixing nanosilica and nanotitania results in chemically and structurally rich nanocluster systems displaying a variety of oxygen sites. Interestingly the presence of titanium induces the disappearance of silanone sites in favor of pyramidal ≡Ti–O species. Whereas terminal oxygen sites are relatively unstable when bonded to silicon, they are stabilized when bonded to titanium. As for pure titania nanoclusters, the values of E_{vac} are found to strongly depend on the structure, the coordination of the oxygen removed, and the degree of relaxation after oxygen removal.

In order to further study the role of the chemical nature of Si and Ti in the oxygen vacancy energy, we consider a set of $(Ti_xSi_{1-x}O_2)_{10}$ structural isomers with the same topology (**Figure 5**), with selected compositions between $x = 0$–1. Such isomer structures are global minima for titanosilicates with $x = 0.1$, 0.2, and 0.3, and are slightly less stable than the global minima for pure systems. They have been geometrically optimized in their stoichiometric composition. We then remove each non-equivalent oxygen atom keeping the initial geometry frozen. In **Figure 5** we report the resulting unrelaxed oxygen vacancy formation energies (E_{unrel}).

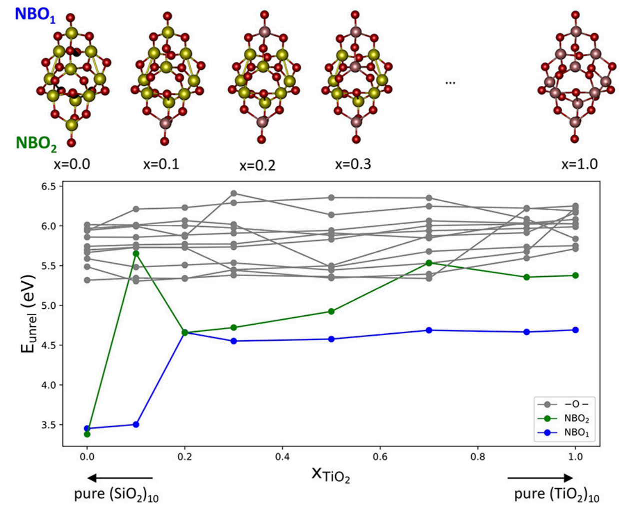

FIGURE 5 | Top: a set of $(Ti_xSi_{1-x}O_2)_{10}$ cluster structures exhibiting the same structural isomer for pure silica ($x = 0$), pure titania ($x = 1$) and all intermediate compositions. Bottom: the corresponding oxygen formation energy without relaxation (E_{unrel}) in eV for all non-equivalent oxygen sites. Vacancies are generated after removing a 2-fold coordinated oxygen (gray), terminal NBO_1 (blue), and terminal NBO_2 (green).

Figure 5 shows E_{unrel} as a function of the mixing composition x_{TiO2} of the cluster. In the plot there are three families of oxygen vacancies according of the type of oxygen removed: the vacancies originating from the removal of two-coordinated oxygen atoms are denoted in gray, whereas those originating from removing the terminal oxygen sites labeled NBO_1 and NBO_2, respectively, are denoted in blue and green. In most of the cases, vacancies at terminal position are found to provide the lowest E_{unrel} value. For the pure silica cluster isomer, the E_{unrel} values for the NBO_1 and NBO_2 are 3.38 and 3.45 eV, respectively, which values are significantly lower than the corresponding values for pure titania systems, 4.69 and 5.38 eV. This result further confirms that the oxygen vacancy formation energy is driven by the presence of unsaturated O centers and, particularly when such centers are bonded to Si atoms, are more easily removed than when they are bonded to Ti atoms. This is clearly seen in the $x = 0.1$ isomer that possesses one terminal oxygen on Si and one on Ti: the E_{unrel} for the Si-bonded oxygen NBO_1 is 3.50 eV whereas for the Ti-bonded oxygen NBO_2 it is 5.65 eV. Although relaxation effects have not been considered, based on the results discussed above, they are not expected to be significant. Therefore, the nature of the cationic site, Si or Ti, seems to critically determine the stabilization of the terminal oxygen deficient systems.

CONCLUSIONS

In this work we use DFT-based calculations employing the PBE0 hydrid functional to explore oxygen vacancy formation in globally optimized TiO_2, SiO_2, and mixed $Ti_xSi_{1-x}O_2$ nanoclusters for sizes between 2 and 24 stoichiometric oxide units. The properties computed (oxygen vacancy formation energies, electronic structure, nanocluster structure, relaxation effects) are found to critically depend on the nature of the oxide. The behavior of silica nanoclusters is found to be rather constant and dominated by the presence of dangling oxygens in silanone $>Si{=}O$ sites. In titania and titanosilicate nanoclusters; however, we find a strong dependence of the properties with respect to the local geometry. When unsaturated oxygen centers are present in the system, removing such centers is energetically less costly than removing two-coordinated oxygen atoms. Since at the nanoscale such unsaturated centers are naturally present in low energy systems, contrary to the bulk and extended surfaces, we can predict that the reduction of nanosized silica clusters is energetically more favorable than in the bulk. Furthermore, we found that the oxygen vacancy formation in silica nanoclusters is also more favorable than from similar-sized low energy titania nanoclusters. This demonstrates the emergence of an unexpected chemical behavior induced by the small size of the systems considered. We hope that our results will help in the search of novel materials for applications in scientific and technological fields such as heterogeneous catalysis, electronics, and cluster chemistry.

AUTHOR CONTRIBUTIONS

AC performed all the calculations, figures, tables, analyzed the data, discussed results, and participated in the elaboration of the manuscript. SB and MC directed the work, discussed the data, and wrote the manuscript.

FUNDING

This research was supported by the H2020 project ITN-EJD-642294 (TCCM: Theoretical Chemistry and Computational Modeling). The Spanish MINECO/AEI-FEDER grant: CTQ2015-64618-R and, in part, Generalitat de Catalunya grants: 2017SGR13 and XRQTC are acknowledged.

ACKNOWLEDGMENTS

We also acknowledge support from the Spanish MCIU Maria de Maeztu award MDM-2017-0767. The GENCI-CINES/IDRIS (Grant 2016-x2016082131, 2017-x2017082131, 2018-x2018082131) and the Red Española de Supercomputación provided valuable computing time.

SUPPLEMENTARY MATERIAL

The Supplementary Material for this article can be found online at: https://www.frontiersin.org/articles/10.3389/fchem.2019.00037/full#supplementary-material

Supplementary Data Sheet 1 | Oxygen vacancy formation energies with and without relaxation (E_{vac}, E_{unrel}, E_{rel}), nanocluster structures employed, E_{vac} values for different O-vacancies, electron density plots of selected O-deficient structures.

REFERENCES

Adamo, C., and Barone, V. (1999). Toward reliable density functional methods without adjustable parameters: the PBE0 model. *J. Chem. Phys.* 110, 6158–6170. doi: 10.1063/1.478522

Aguilera-Granja, F., Vega, A., and Balbás, L. C. (2016). New structural and electronic properties of $(TiO_2)_{10}$. *J. Chem. Phys.* 144, 234312–234312. doi: 10.1063/1.4954060

Albanese, E., Ruiz Puigdollers, A., and Pacchioni, G. (2018). Theory of ferromagnetism in reduced ZrO_{2-x} nanoparticles. *ACS Omega* 3, 5301–5307. doi: 10.1021/acsomega.8b00667

Avakyan, V. G., Sidorkin, V. F., Belogolova, E. F., Guselnikov, S. L., and Gusel'nikov, L. E. (2006). AIM and ELF electronic structure/G2 and G3 π-bond energy relationship for doubly bonded silicon species, H_2Si_X ($X = E^{14}H_2$, $E^{15}H$, E^{16})^1. *Organometallics* 25, 6007–6013. doi: 10.1021/om0605478

Bawazer, L. A., Izumi, M., Kolodin, D., Neilson, J. R., Schwenzer, B., and Morse, D. E. (2012). Evolutionary selection of enzymatically synthesized semiconductors from biomimetic mineralization vesicles. *Proc. Nat. Acad. Sci.* 109, E1705–E1714. doi: 10.1073/pnas.1116958109

Bhattacharya, S., Sonin, B. H., Jumonville, C. J., Ghiringhelli, L. M., and Marom, N. (2015). Computational design of nanoclusters by property-based genetic algorithms: tuning the electronic properties of $(TiO_2)_n$ clusters. *Phys. Rev. B* 91, 241115–241115. doi: 10.1103/PhysRevB.91.241115

Blum, V., Gehrke, R., Hanke, F., Havu, P., Havu, V., Ren, X., et al. (2009). Ab initio molecular simulations with numeric atom-centered orbitals. *Computer Phys. Commun.* 180, 2175–2196. doi: 10.1016/j.cpc.2009.06.022

Bromley, S. T., and Flikkema, E. (2005). Columnar-to-disk structural transition in nanoscale $(SiO_2)_N$ clusters. *Phys. Rev. Lett.* 95:185505. doi: 10.1103/physrevlett.95.185505

Bruix, A., and Neyman, K. M. (2016). Modeling ceria-based nanomaterials for catalysis and related applications. *Catalysis Lett.* 146, 2053–2080. doi: 10.1007/s10562-016-1799-1

Calatayud, M., Maldonado, L., and Minot, C. (2008a). Reactivity of $(TiO_2)_N$ clusters (N = 1-10): probing gas-phase acidity and basicity properties. *J. Phys. Chem. C* 112, 16087–16095. doi: 10.1021/jp802851q

Calatayud, M., and Minot, C. (2006). Reactivity of the V_2O_5-TiO_2-anatase catalyst: role of the oxygen sites. *Top. Catalysis* 41, 17–26. doi: 10.1007/s11244-006-0090-x

Calatayud, M., Tielens, F., and De Proft, F. (2008b). Reactivity of gas-phase, crystal and supported V_2O_5 systems studied using density functional theory based reactivity indices. *Chem. Phys. Lett.* 456, 59–63. doi: 10.1016/j.cplett.2008.03.007

Cannizzo, A., and Leone, M. (2004). Conformational disorder and optical properties of point defects in vitreous silica. *Philos. Mag. A* 84, 1651–1657. doi: 10.1080/14786430310001644440

Causà, M., D'Amore, M., Gentile, F., Menendez, M., and Calatayud, M. (2015). Electron localization function and maximum probability domains analysis of semi-ionic oxides crystals, surfaces and surface defects. *Comput. Theor. Chem.* 1053, 315–321. doi: 10.1016/j.comptc.2014.11.001

Chen, M., and Dixon, D. A. (2013). Tree growth—Hybrid genetic algorithm for predicting the structure of small $(TiO_2)_n$, n = 2–13, nanoclusters. *J. Chem. Theor. Comput.* 9, 3189–3200. doi: 10.1021/ct400105c

Cuko, A., Calatayud, M., and Bromley, S. T. (2018). Stability of mixed-oxide titanosilicates: dependency on size and composition from nanocluster to bulk. *Nanoscale* 10, 832–842. doi: 10.1039/C7NR05758J

Das, K., Bose, S., and Bandyopadhyay, A. (2009). TiO_2 nanotubes on Ti: influence of nanoscale morphology on bone cell–materials interaction. *J. Biomed. Mater. Res. Part A* 90A, 225–237. doi: 10.1002/jbm.a.32088

Deák, P., Kullgren, J., and Frauenheim, T. (2014). Polarons and oxygen vacancies at the surface of anatase TiO_2. *Phys. Status Solidi Rapid Res. Lett.* 8, 583–586. doi: 10.1002/pssr.201409139

Deml, A. M., Holder, A. M., O'Hayre, R. P., Musgrave, C. B., and Stevanovic, V. (2015). Intrinsic material properties dictating oxygen vacancy formation energetics in metal oxides. *J. Phys. Chem. Lett.* 6, 1948–1953. doi: 10.1021/acs.jpclett.5b00710

Di Valentin, C., Pacchioni, G., and Selloni, A. (2006). Electronic structure of defect states in hydroxylated and reduced rutile $TiO_2(110)$ surfaces. *Phys. Rev. Lett.* 97:166803. doi: 10.1103/PhysRevLett.97.166803

Diebold, U. (2003). The surface science of titanium dioxide. *Surf. Sci. Rep.* 48, 53–229. doi: 10.1016/S0167-5729(02)00100-0

Finazzi, E., Valentin, C. D., Pacchioni, G., and Selloni, A. (2008). Excess electron states in reduced bulk anatase TiO_2: comparison of standard GGA, GGA+U, and hybrid DFT calculations. *J. Chem. Phys.* 129:154113. doi: 10.1063/1.2996362

Flikkema, E., and Bromley, S. T. (2003). A new interatomic potential for nanoscale silica. *Chem. Phys. Lett.* 378, 622–629. doi: 10.1016/j.cplett.2003.07.017

Flikkema, E., and Bromley, S. T. (2004). Dedicated global optimization search for ground state silica nanoclusters:$\sim (SiO_2)_N$ (N = 6–12). *J. Phys. Chem. B* 108, 9638–9645. doi: 10.1021/jp049783r

Flikkema, E., and Bromley, S. T. (2009). Defective to fully coordinated crossover in complex directionally bonded nanoclusters. *Phys. Rev. B* 80:035402. doi: 10.1103/PhysRevB.80.035402

Ganduglia-Pirovano, M. V., Hofmann, A., and Sauer, J. (2007). Oxygen vacancies in transition metal and rare earth oxides: current state of understanding and remaining challenges. *Surface Sci. Rep.* 62, 219–270. doi: 10.1016/j.surfrep.2007.03.002

Hamad, S., Catlow, C. R. A., Woodley, S. M., Lago, S., and Mejias, J. A. (2005). Structure and stability of small TiO_2 nanoparticles. *J. Phys. Chem. B* 109, 15741–15748. doi: 10.1021/jp0521914

Helali, Z., Jedidi, A., Syzgantseva, O. A., Calatayud, M., and Minot, C. (2017). Scaling reducibility of metal oxides. *Theor. Chem. Accounts* 136:100. doi: 10.1007/s00214-017-2130-y

Houlihan, J. F., Danley, W. J., and Mulay, L. N. (1975). Magnetic susceptibility and EPR spectra of titanium oxides: correlation of magnetic parameters with transport properties and composition. *J. Solid State Chem.* 12, 265–269. doi: 10.1016/0022-4596(75)90317-5

Howie, R. A. (1964). Pleochroism of orthopyroxenes. *Nature* 204:279. doi: 10.1038/204279a0

Islam, M. M., Bredow, T., and Gerson, A. (2007). Electronic properties of oxygen-deficient and aluminum-doped rutile TiO_2 from first principles. *Phys. Rev. B* 76:045217. doi: 10.1103/PhysRevB.76.045217

Janotti, A., Varley, J. B., Rinke, P., Umezawa, N., Kresse, G., and Van de Walle, C. G. (2010). Hybrid functional studies of the oxygen vacancy in TiO_2. *Phys. Rev. B* 81:085212. doi: 10.1103/PhysRevB.81.085212

Joo, J. B., Dillon, R., Lee, I., Yin, Y., Bardeen, C. J., and Zaera, F. (2014). Promotion of atomic hydrogen recombination as an alternative to electron trapping for the role of metals in the photocatalytic production of H_2. *Proc. Nat. Acad. Sci.* 111, 7942–7947. doi: 10.1073/pnas.1405365111

Kapilashrami, M., Zhang, Y., Liu, Y.-S., Hagfeldt, A., and Guo, J. (2014). Probing the optical property and electronic structure of TiO_2 nanomaterials for renewable energy applications. *Chem. Rev.* 114, 9662–9707. doi: 10.1021/cr5000893

Kim, S., Ko, K. C., Lee, J. Y., and Illas, F. (2016). Single oxygen vacancies of $(TiO_2)_{35}$ as a prototype reduced nanoparticle: implication for photocatalytic activity. *Phys. Chem. Chem. Phys.* 18, 23755–23762. doi: 10.1039/C6CP04515D

Komatsu, M., Fagan, T. J., Krot, A. N., Nagashima, K., Petaev, M. I., Kimura, M., et al. (2018). First evidence for silica condensation within the solar protoplanetary disk. *Proc. Nat. Acad. Sci.* 115, 7497–7502. doi: 10.1073/pnas.1722265115

Kozlov, S. M., Demiroglu, I., Neyman, K. M., and Bromley, S. T. (2015). Reduced ceria nanofilms from structure prediction. *Nanoscale* 7, 4361–4366. doi: 10.1039/C4NR07458K

Lakshtanov, D. L., Sinogeikin, S. V., Litasov, K. D., Prakapenka, V. B., Hellwig, H., Wang, J., et al. (2007). The post-stishovite phase transition in hydrous alumina-bearing SiO_2 in the lower mantle of the earth. *Proc. Nat. Acad. Sci.* 104, 13588–13590. doi: 10.1073/pnas.0706113104

Lambert, J.-F., Sodupe, M., and Ugliengo, P. (2012). Prebiotic chemistry. *Chem. Soc. Rev.* 41, 5373–5374. doi: 10.1039/C2CS90061K

Lamiel-Garcia, O., Cuko, A., Calatayud, M., Illas, F., and Bromley, S. T. (2017). Predicting size-dependent emergence of crystallinity in nanomaterials: titania nanoclusters versus nanocrystals. *Nanoscale* 9, 1049–1058. doi: 10.1039/C6NR05788H

Lee, G., Helling, C., Giles, H., and Bromley, S. T. (2015). Dust in brown dwarfs and extra-solar planets. *A&A* 575:A11. doi: 10.1051/0004-6361/201424621

Lee, H.-Y., Clark, S. J., and Robertson, J. (2012). Calculation of point defects in rutile TiO_2 by the screened-exchange hybrid functional. *Phys. Rev. B* 86:075209. doi: 10.1103/PhysRevB.86.075209

Li, J., Lazzari, R., Chenot, S., and Jupille, J. (2018). Contributions of oxygen vacancies and titanium interstitials to band-gap states of reduced titania. *Phys. Rev. B* 97:041403. doi: 10.1103/PhysRevB.97.041403

Lu, W. C., Wang, C. Z., Nguyen, V., Schmidt, M. W., Gordon, M. S., and Ho, K. M. (2003). Structures and fragmentations of small silicon oxide clusters by ab initio calculations. *J. Phys. Chem. A* 107, 6936–6943. doi: 10.1021/jp027860h

Lucky, S. S., Idris, N. M., Huang, K., Kim, J., Li, Z., Thong, P. S., et al. (2016). *In vivo* biocompatibility, biodistribution and therapeutic efficiency of titania coated upconversion nanoparticles for photodynamic therapy of solid oral cancers. *Theranostics* 6, 1844–1865. doi: 10.7150/thno.15088

Lyle, M. J., Pickard, C. J., and Needs, R. J. (2015). Prediction of 10-fold coordinated TiO_2 and SiO_2 structures at multimegabar pressures. *Proc. Nat. Acad. Sci.* 112, 6898–6901. doi: 10.1073/pnas.1500604112

Mal, N. K., Fujiwara, M., and Tanaka, Y. (2003). Photocontrolled reversible release of guest molecules from coumarin-modified mesoporous silica. *Nature* 421, 350. doi: 10.1038/nature01362

Manveer, S. M., David, Z. G., and Alexander, L. S. (2017). Diffusion and aggregation of oxygen vacancies in amorphous silica. *J. Phys. Condensed Matter* 29:245701. doi: 10.1088/1361-648x/aa6f9a

McPherson, J. W., and Mogul, H. C. (1998). Underlying physics of the thermochemical E model in describing low-field time-dependent dielectric breakdown in SiO_2 thin films. *J. Appl. Phys.* 84, 1513–1523. doi: 10.1063/1.368217

Mehonic, A., Shluger, A. L., Gao, D., Valov, I., Miranda, E., Ielmini, D., et al. (2018). Silicon oxide (SiOx): a promising material for resistance switching? *Adv. Mater.* 30:1801187. doi: 10.1002/adma.201801187

Morales-García, Á., Lamiel-García, O., Valero, R., and Illas, F. (2018). Properties of single oxygen vacancies on a realistic $(TiO_2)_{84}$ nanoparticle: a challenge for density functionals. *J. Phys. Chem. C* 122, 2413–2421. doi: 10.1021/acs.jpcc.7b11269

Na-Phattalung, S., Smith, M. F., Kim, K., Du, M.-H., Wei, S.-H., Zhang, S. B., et al. (2006). First-principles study of native defects in anatase TiO_2. *Phys. Rev. B* 73:125205. doi: 10.1103/PhysRevB.73.125205

Nguyen, T. D., Tseng, H.-R., Celestre, P. C., Flood, A. H., Liu, Y., Stoddart, J. F., et al. (2005). A reversible molecular valve. *Proc. Nat. Acad. Sci. U.S.A.* 102, 10029–10034. doi: 10.1073/pnas.0504109102

Pacchioni, G. (2008). Modeling doped and defective oxides in catalysis with density functional theory methods: room for improvements. *J. Chem. Phys.* 128:182505. doi: 10.1063/1.2819245

Pacchioni, G., and Ferrario, R. (1998). Optical transitions and EPR properties of two-coordinated Si, Ge, Sn and related $H(mathrm{I}),$ $H(mathrm{II}),$

and $H(mathrm{III})$ centers in pure and doped silica from ab initio calculations. *Phys. Rev. B* 58, 6090–6096. doi: 10.1103/PhysRevB.58.6090

Rahman, M. A., Rout, S., Thomas, J. P., McGillivray, D., and Leung, K. T. (2016). Defect-rich dopant-free ZrO_2 nanostructures with superior dilute ferromagnetic semiconductor properties. *J. Am. Chem. Soc.* 138, 11896–11906. doi: 10.1021/jacs.6b06949

Rudra, J. K., and Fowler, W. B. (1987). Oxygen vacancy and the $E_1^{'}$ center in crystalline SiO_2. *Phys. Rev. B* 35, 8223–8230. doi: 10.1103/PhysRevB.35.8223

Ruiz Puigdollers, A., Illas, F., and Pacchioni, G. (2016a). Structure and properties of zirconia nanoparticles from density functional theory calculations. *J. Phys. Chem. C* 120, 4392–4402. doi: 10.1021/acs.jpcc.5b12185

Ruiz Puigdollers, A., Tosoni, S., and Pacchioni, G. (2016b). Turning a nonreducible into a reducible oxide via nanostructuring: opposite behavior of bulk ZrO_2 and ZrO_2 nanoparticles toward H_2 adsorption. *J. Phys. Chem. C* 120, 15329–15337. doi: 10.1021/acs.jpcc.6b05984

Saroj, S., and Rajput, S. J. (2018). Composite smart mesoporous silica nanoparticles as promising therapeutic and diagnostic candidates: recent trends and applications. *J. Drug Deliv. Sci. Technol.* 44, 349–365. doi: 10.1016/j.jddst.2018.01.014

Silvi, B., and D'Arco, P. (Eds.). (2006). *Modelling of Minerals and Silicated Materials*. New York, NY; Boston, MA; Dordrecht; London; Moscow: Kluwer Academic Publishers.

Skuja, L. (1998). Optically active oxygen-deficiency-related centers in amorphous silicon dioxide. *J. Non-Crystalline Solids* 239, 16–48. doi: 10.1016/S0022-3093(98)00720-0

Skuja, L. N., Streletsky, A. N., and Pakovich, A. B. (1984). A new intrinsic defect in amorphous SiO_2: two-fold coordinated silicon. *Solid State Commun.* 50, 1069–1072. doi: 10.1016/0038-1098(84)90290-4

Sulimov, V. B., Sushko, P. V., Edwards, A. H., Shluger, A. L., and Stoneham, A. M. (2002). Asymmetry and long-range character of lattice deformation by neutral oxygen vacancy in ensuremath{alpha}-quartz. *Phys. Rev. B* 66:024108. doi: 10.1103/PhysRevB.66.024108

Sun, X., Zhou, S., Schlangen, M., and Schwarz, H. (2016). Thermal methane activation by $[Si_2O_5].+$ and $[Si_2O_5H_2].+$: reactivity enhancement by hydrogenation. *Angew. Chem. Int. Ed.* 55, 13345–13348. doi: 10.1002/anie.201607864

Sushko, P. V., Mukhopadhyay, S., Stoneham, A. M., and Shluger, A. L. (2005). Oxygen vacancies in amorphous silica: structure and distribution of properties. *Microelectron. Eng.* 80, 292–295. doi: 10.1016/j.mee.2005.04.083

Syzgantseva, O. A., Gonzalez-Navarrete, P., Calatayud, M., Bromley, S., and Minot, C. (2011). Theoretical investigation of the hydrogenation of $(TiO_2)_N$ clusters ($N = 1$–10). *J. Phys. Chem. C* 115, 15890–15899. doi: 10.1021/jp2050349

Vajda, S., and White, M. G. (2015). Catalysis applications of size-selected cluster deposition. *ACS Catalysis* 5, 7152–7176. doi: 10.1021/acscatal.5b01816

Vásquez, G. C., Karazhanov, S. Z., Maestre, D., Cremades, A., Piqueras, J., and Foss, S. E. (2016). Oxygen vacancy related distortions in rutile TiO_2 nanoparticles: a combined experimental and theoretical study. *Phys. Rev. B* 94:235209. doi: 10.1103/PhysRevB.94.235209

Wang, G., Raji, A.-R. O., Lee, J.-H., and Tour, J. M. (2014). Conducting-interlayer SiOx memory devices on rigid and flexible substrates. *ACS Nano* 8, 1410–1418. doi: 10.1021/nn4052327

Woodley, S. M., Hamad, S., Mejías, J. A., and Catlow, C. R. A. (2006). Properties of small TiO_2, ZrO_2 and HfO_2 nanoparticles. *J. Mater. Chem.* 16, 1927–1933. doi: 10.1039/B600662K

Yamamoto, T., and Ohno, T. (2012). A hybrid density functional study on the electron and hole trap states in anatase titanium dioxide. *Phys. Chem. Chem. Phys.* 14, 589–598. doi: 10.1039/C1CP21547G

Yao, J., Sun, Z., Zhong, L., Natelson, D., and Tour, J. M. (2010). Resistive switches and memories from silicon oxide. *Nano Lett.* 10, 4105–4110. doi: 10.1021/nl102255r

Yin, S., and Bernstein, E. R. (2014). Experimental and theoretical studies of H_2O oxidation by neutral $Ti_2O_{4,5}$ clusters under visible light irradiation. *Phys. Chem. Chem. Phys.* 16, 13900–13908. doi: 10.1039/C4CP00097H

Zwijnenburg, M. A., Sokol, A. A., Sousa, C., and Bromley, S. T. (2009). The effect of local environment on photoluminescence: a time-dependent density functional theory study of silanone groups on the surface of silica nanostructures. *J. Chem. Phys.* 131:034705. doi: 10.1063/1.3155083

Conflict of Interest Statement: The authors declare that the research was conducted in the absence of any commercial or financial relationships that could be construed as a potential conflict of interest.

Advantages of publishing in Frontiers

OPEN ACCESS
Articles are free to read
for greatest visibility
and readership

FAST PUBLICATION
Around 90 days
from submission
to decision

HIGH QUALITY PEER-REVIEW
Rigorous, collaborative,
and constructive
peer-review

TRANSPARENT PEER-REVIEW
Editors and reviewers
acknowledged by name
on published articles

Frontiers
Avenue du Tribunal-Fédéral 34
1005 Lausanne | Switzerland

Visit us: www.frontiersin.org
Contact us: info@frontiersin.org | +41 21 510 17 00

REPRODUCIBILITY OF RESEARCH
Support open data
and methods to enhance
research reproducibility

DIGITAL PUBLISHING
Articles designed
for optimal readership
across devices

FOLLOW US
@frontiersin

IMPACT METRICS
Advanced article metrics
track visibility across
digital media

EXTENSIVE PROMOTION
Marketing
and promotion
of impactful research

LOOP RESEARCH NETWORK
Our network
increases your
article's readership